Identifying the metabolic 'Achilles heel' of adult and paediatric glioblastoma multiforme

By

James Ashley Wood MSci

A thesis submitted to the University of Nottingham for the degree of Doctor of Philosophy, July 2018

Supervisors: Prof Richard Grundy

Dr Ruman Rahman

Abstract

Despite substantive efforts to characterise glioblastoma multiforme (GBM) at the molecular level, improvements to the overall survival of patients have yet to be seen within the clinic. Intratumour heterogeneity describes the co-existence of several subpopulations of GBM cells that are genetically distinct. This phenomenon provides one mechanism by which GBM recurs via the presence of resistant subclonal cells. However, questions remain as to whether cancer cell metabolism demonstrates the same level of heterogeneity given the metabolic regulatory role of several oncogenes and tumour suppressors. We applied liquid chromatography-mass spectrometry to profile the metabolome and lipidome of tumour fragments sampled from adult GBM patients. The extent of heterogeneity in metabolomic and lipidomics profiles differed between patients but was predominantly observed between non-invasive and invasive regions. Evidence for normal brain metabolism influencing the metabolomic profile of the invasive region was detected, calling for isolation of the tumour cell component. Despite this caveat, dysregulated proline metabolism was identified for further mechanistic and therapeutic study.

The identification of intratumour metabolic heterogeneity in GBM has therapeutic implications in terms of the utilisation of single-agent therapies targeting metabolism. However, elucidation of a metabolic dependency in GBM cells representing an 'Achilles heel' may circumvent intratumour genetic heterogeneity. Glucose is not the only nutrient utilised by cancer cells. The dependence of GBM cells on external sources of lipid and cholesterol species in the form of lipoproteins was assessed to determine the consequences on cellular viability and metabolism. Growth inhibitory responses were demonstrated under lipoprotein deficient conditions, associated with cell line-specific responses indicative of different metabolic stress responses in adult and paediatric GBM. Consistent observation of reduced cellular cholesterol levels across all cell lines presented a metabolic vulnerability that was pharmacologically replicated using liver X receptor (LXR) agonists. The identification of reduced cellular viability following exposure to LXR agonists and transcriptomic responses associated with a reduced proliferative response provide impetus for further drug development in terms of combination strategies and alleviation of deleterious side-effects.

Acknowledgements

First and foremost, I would like to thank my supervisors Prof Richard Grundy and Dr Ruman Rahman. Their advice and mentorship over the last three years has been priceless, and I hope that they are aware that this PhD opportunity they provided me has equipped me with the necessary skills to succeed in life.

Other members within the Children's Brain Tumour Research Centre (CBTRC) I wish to acknowledge include Mr Stuart Smith for his part in obtaining patient tumour samples and general advice throughout the project, and Dr Anbarasu Lourdusamy for his bioinformatic support. I also wish to thank Dr Jennifer Ward, Dr Rebecca Chapman, Dr Lisa Storer, Dr Maria Estevez Cebrero, Jonathan Rowlinson, Dr Hazel Rogers, and Dr Franziska Linke for demonstrating patience with all my technical enquiries and providing support in any way possible.

This project would not have been possible if it was not for our collaborators. Therefore, much gratitude goes to Prof David Barrett, Dr Dong-Hyun Kim, Dr Catherine Ortori, Dr Salah Abdelrazig, Sergey Evseev, Mohammad Al-natour and other members within the School of Pharmacy for their enthusiasm in the project and willingness to share their analytical expertise using mass spectrometry. I am also grateful to Prof Sean May, Dr Marcos Castellanos-Uribe, Dr Naofel Aljafer and Dr Iqbal Khan for their collaborative support in the transcriptomics aspect of the project.

I also wish to thank past and present members of the CBTRC who have made me most welcome and provided much emotional and professional support. Special mention goes to Jasper Estrañero, who began this journey at same time as me, and Sophie Roper, whose love has helped me reach my highs and pass through my lows. My parents also deserve special mention for their support and desire to see me reach my maximum potential.

Finally and most importantly, I wish to thank the patients who nobly support research, and the funding charities, especially Children's Cancer and Leukaemia Group and Little Princess Trust who contributed to this project, whose passion to see better outcomes for GBM sufferers really is something to be admired.

Contents

List of Figures

List of Tables

List of Common Abbreviations

2HG: D-2-hydroxyglutarate

5-ALA: 5-Aminolevulinic acid

aGBM: Adult glioblastoma multiforme

αKG: α-Ketoglutarate

ANOVA: Analysis of variance

ApoE: Apolipoprotein E

APS: Ammonium persulfate

ATP: Adenosine 5'-triphosphate

BSA: Bovine serum albumin

CIMP: CpG island hypermethylator phenotype

ChIP: Chromatin immunoprecipitation

CNA: Copy number aberration

CNS: Central nervous system

CT: Computerised tomography

DCE: Dynamic contrast-enhanced

ddH_2O: Double distilled water

DEGs: Differentially expressed genes

DMEM: Dulbecco's modified eagle medium

DMSO: Dimethyl sulfoxide

EGFR: Epidermal growth factor receptor

ER: Endoplasmic reticulum

FASN: Fatty acid synthase

FBS: Foetal bovine serum

FDR: False discovery rate

GBM: Glioblastoma multiforme

GO: Gene ontology

GSC: Glioma stem-like cell

Gy: Gray

HCl: Hydrochloric acid

HDL: High-density lipoprotein

HGG: High-grade glioma

HMGCR: 3-hydroxy-3-methylglutaryl-CoA reductase

HMGCS: 3-Hydroxy-3-methylglutaryl-CoA synthase

HPLC: High-performance liquid chromatography

HRP: Horseradish peroxidase

IDH: Isocitrate dehydrogenase

ITH: Intratumour heterogeneity

LA: Linoleic acid

LC: Liquid chromatography

LC-MS: Liquid chromatography-mass spectrometry

LD-BCS: Lipoprotein deficient bovine calf serum

LD-FBS: Lipoprotein deficient serum from foetal calf

LDL: Low-density lipoprotein

LDLR: Low-density lipoprotein receptor

LPDM: Lipoprotein deficient medium

LXR: Liver X receptor

m/*z*: mass-to-charge ratio
MβCD: Methyl-β-cyclodextrin
MeOH: Methanol
MRI: Magnetic resonance imaging
MS: Mass spectrometry
MSEA: Metabolite set enrichment analysis
NAA: N-Acetyl-aspartate
NAAG: N-acetyl-aspartyl-glutamate
NAD(P)+/NAD(P)H: Nicotinamide adenine dinucleotide (phosphate)
NBS: Non-brain stem
NEAAs: Non-essential amino acids
NMR: Nuclear magnetic resonance spectroscopy
OA: Oleic acid
OPLS-DA: Orthogonal partial least squares-discriminant analysis
P/S: Penicillin/streptomycin
P5C: 1-pyrroline-5-carboxylate
PA: Palmitic acid
PAGE: Polyacrylamide gel electrophoresis
PBS: Phosphate buffered saline
PCA: Principle components analysis
PET: Positron emission tomography
PDGFR: Platelet-derived growth factor receptor
PFS: Progression-free survival
pGBM: Paediatric glioblastoma multiforme
pHGG: Paediatric high-grade glioma
PI: Propidium iodide
PTEN: Phosphatase and tensin-homolog
PVDF: Polyvinylidene difluoride
QC: Quality control
ROS: Reactive oxygen species
RIN: RNA integrity number
RIPA: Radioimmunoprecipitation assay
RSD: Relative standard deviation
RTK: Receptor tyrosine kinase
SDS: Sodium dodecyl sulfate
SHMT2: Serine hydroxymethyltransferase 2
SKP2: S-phase kinase-associated protein 2
SNV: Single-nucleotide variant
SOAT1: Sterol O-acyltransferase 1
SREBP1: Sterol regulatory element-binding protein 1
TBST: Tris buffered saline-Tween 20
TCA cycle: Tricarboxylic acid cycle

Chapter 1

Introduction

1. Introduction

Glioblastoma multiforme (GBM) is the third most frequently reported brain tumour (15.1%) and the most common malignant neoplasm of the central nervous system (CNS) to occur in adults (46.1%). GBM is more prevalent in the adult population (15.7%) compared to its prevalence in children and young adults (0-19 years), in which GBM accounts for approximately 3% of all brain and other CNS tumours. Collectively, brain and other CNS tumours are the most common malignancy in the 0-14 years age-group, superseding the incidence rates of leukaemia. Despite advances in cancer therapy and management, brain and CNS tumours still present a substantial clinical challenge with only 73.9% of children and 26.2% of adults surviving 5 years after diagnosis (Ostrom *et al.*, 2017). Indeed, brain and CNS tumours accounts for the highest number of cancer-related death in children.

"Glioma" is an umbrella term for tumours with a glial cell-of-origin including astrocytomas, oligodendrogliomas, ependymomas, and mixed gliomas (Schwartzbaum *et al.*, 2006). The World Health Organisation (WHO) classification system for astrocytic tumours is based on mitotic atypia and microvascular proliferation. Astrocytomas of tumour grade I (pilocytic astrocytoma) and grade II (diffuse astrocytoma) are designated as low-grade gliomas (LGGs), whereas grade III (anaplastic astrocytoma) and grade IV (GBM) tumours are classified as high-grade gliomas (HGGs) (Louis *et al.*, 2016). Paediatric cases of GBM are morphologically indistinguishable from adult cases (Karsy *et al.*, 2012). However, recent studies have revealed genetic and genomic differences that suggest the existence of different biological mechanisms of gliomagenesis in the paediatric and adult setting (Paugh *et al.*, 2010; Schwartzentruber *et al.*, 2012; Sturm *et al.*, 2012).

1.1. Clinical features

1.1.1. Presenting symptoms and diagnostic procedure

Patients with a GBM in the brain present with symptoms that stem from tumour infiltration into brain parenchyma and increased intracranial pressure. Symptoms include persistent headaches, behavioural changes, early morning nausea/emesis, diplopia (double vision), and papilloedema (optic disc swelling). (Fangusaro, 2012). Upon suspicion of a GBM, patients are provisionally assessed for lesions/masses via non-contrast computerised tomography (CT) or magnetic resonance imaging (MRI). Features on CT scans indicative of GBM include thick margins of heterogenous enhancement and hypodense centres indicative of necrosis. Upon MRI, lesions appear as hypo- and hyperintense areas on T1- and T2-weighted scans, respectively (Ahmed *et al.*, 2014). Measurement of relative metabolite concentrations through magnetic resonance spectroscopy can support a diagnosis of GBM following identification of increased choline, lactate, and lipid signals, whereas peak levels of *N*-acetyl acetate and myoinositol are decreased (Bulik *et al.*, 2013). Pathological confirmation of a GBM is conducted through histological analysis of brain tumour biopsies taken at the time of surgery or as a single event if surgery is not safely possible (Fangusaro, 2012).

1.1.2. Incidence and mortality rates

GBM has an annual age-adjusted incidence rate of 3.20 per 100,000 population worldwide. Incidence rates increase with age and are highest within the 75-84 age bracket. The median age at diagnosis is 64 years. Two-year survival rates are 23.5% and 34.3% in the 20+ and 0-19 years age-groups, respectively. These values fall to 6.9% and 17.7% five years after diagnosis and indicate that children and young adults with GBM have a slightly better prognosis compared to older adults, likely reflecting tolerance of adjuvant therapies. In clinical trials examining primary postoperative chemotherapy without radiotherapy, very young children (under 5 years old) with HGGs demonstrated 5-year overall survival ranging between 30.9 to 59% (Dufour *et al.*, 2006; Grundy *et al.*, 2010).

Compared to the respective two- and five-year survival rates of 45.2% and 34.9% for all malignant brain and CNS tumours, this highlights the particularly aggressive nature of GBM (Ostrom *et al.*, 2017). HGGs in adults occur most frequently in supratentorial regions located above the tentorium cerebelli, an extension of the dura matter that separates the cerebellum from the occipital and temporal lobes of the cerebral cortex (Jones and Baker, 2014). In children and young adults, HGGs are reported to occur in several brain regions, most frequently in pontine (43.2%), cerebral hemispheres (25.8%) and thalamus (12.3%), but also in cerebellum (4.5%) and spinal cord (2.6%) (Wolff *et al.*, 2008). Median age at diagnosis varies among the different tumour locations with cerebellar (7.6 y) and pontine (8.0 y) HGGs presenting at a younger age compared to thalamic (11.5 y), supratentorial (11.7 y) and spinal cord (13.0 y) tumours (Kramm *et al.*, 2011; Wolff *et al.*, 2012; Karremann *et al.*, 2013). The 2-year survival rates for paediatric patients with pontine, thalamic or cerebellar HGGs are 13.8%, 20.7%, and 33.0%, respectively (Kramm *et al.*, 2011; Karremann *et al.*, 2013). In supratentorial and spinal cord HGGs, the 2-year survival rates are 52.0% and 55.2%, respectively (Wolff *et al.*, 2012; Karremann *et al.*, 2013). The association of tumour location with age at diagnosis and survival rates in children is summarised in Table 1.1.

Table 1.1. Clinical parameters associated with paediatric HGG tumour location

Tumour location	Pontine	Thalamus	Cerebellum	Supratentorial	Spinal cord
Frequency (%)	43.2	12.3	4.5	25.8	2.6
Median age at diagnosis (years)	8.0	11.5	7.6	11.7	13.0
2-year survival rates (%)	13.8	20.7	33.0	52.0	55.2

Information collated from Karremann et al. (2013), (Kramm et al. (2011), B. Wolff et al. (2012), and J. E. Wolff et al. (2008).

1.1.3. Standard treatment strategies

The standard treatment in adult cases of GBM is maximal resection to remove the bulk of the tumour leaving minimal residual disease. Gross total resection

is difficult to achieve due to tumour cell invasion into the adjacent normal brain parenchyma. This residual disease is responsible for the recurrence of tumours 2-3 cm from the surgical resection margin (Behin *et al.*, 2003). The extent of resection is correlated with progression-free survival (PFS) (Senft *et al.*, 2011) and can be facilitated by administration of 5-aminolevulinic acid (5-ALA) (Stummer *et al.*, 2006). 5-ALA is a precursor of heme and highlights cancerous tissue through accumulation of the fluorescent porphyrin protoporphyrin IX, although the mechanism by which this occurs is contested with evidence in support of decreased ferrochelatase enzyme activity (Kaneko and Kaneko, 2016) and reduced NADPH levels (Kim *et al.*, 2017) as the underlying cause. Fluorescence can be measured from the normal brain in animals albeit at a much lower level (Kaneko and Kaneko, 2016). However, the specific contributions from other cell populations within the tumour, including activated immune cells, to the fluorescent signal has yet to be elucidated. Clinically, 5-ALA fluorescence has been visualised using a modified neurosurgical microscope leading to more complete resection and improved PFS in patients (Della Puppa *et al.*, 2013). Following tumour resection and subject to health, patients are administered radiotherapy with concomitant and adjuvant temozolomide based on statistically significant outcomes in randomised clinical trials (Stupp *et al.*, 2005, 2009).

The initial treatment strategy for a child diagnosed with a HGG is tumour debulking through maximal safe surgical resection, following improved PFS in patients with greater than 90% resection in the Children's Cancer Group (CCG) study-945 (Finlay *et al.*, 1995). Following surgery, combined chemo- and radiotherapy has been adopted as the "standard of care" based on the results of the CCG-943 trial in which patients received weekly vincristine during radiation followed by eight maintenance chemotherapy cycles consisting of prednisone, lomustine, and vincristine (PCV) each administered approximately 6 weeks apart (Sposto *et al.*, 1989). Radiotherapy is given postoperatively in children older than 3 years to prevent tumour progression and recurrence with

50-60 Gray (Gy) delivered in daily fractions of approximately 180-200 cGy over a 6-week period (Fangusaro, 2012). However, younger children (<3 years old) are treated with chemotherapy alone due to treatment-related co-morbidities associated with irradiation, including neurocognitive and endocrinological deficits (Dufour *et al.*, 2006; Grundy *et al.*, 2007, 2010; Sanders *et al.*, 2007).

1.2. Tumour biology

1.2.1. Molecular characteristics of adult GBM

Early assessment of the adult GBM (aGBM) genome using microarray technology highlighted the unique genomic profile of GBM compared to other glial brain tumours (astrocytoma and oligodendroglioma) (Shai *et al.*, 2003). Cohorts containing patients with secondary GBM, which derive from the progression of gliomas initially diagnosed as low-grade, highlighted molecular separation from primary GBM (Godard *et al.*, 2003; Tso *et al.*, 2006) as well as revealing heterogeneity in the molecular pathogenesis of secondary GBM (Maher *et al.*, 2006). Furthermore, several studies showed that a gene-based classification of glioma could be used for diagnostic purposes and delineate prognostic groups with better or worse clinical outcomes (Nutt *et al.*, 2003; Freije *et al.*, 2004; Liang *et al.*, 2005; Shirahata *et al.*, 2007; Gravendeel *et al.*, 2009).

Phillips and colleagues (2006) identified three subtypes of HGG that resembled stages in neurogenesis based on signature genes: Proneural, Mesenchymal, and Proliferative. Prolonged survival in the Proneural subtype was observed along with poor prognostic outcomes associated with the Mesenchymal class in both primary and recurrent tumours (Phillips *et al.*, 2006). An additional molecular subtype, Classical, was delineated in a cohort of 200 GBM samples from The Cancer Genome Atlas (TCGA) network. The Proneural, Classical and Mesenchymal subtypes were each characterised by abnormalities or mutations within platelet-derived growth factor receptor (*PDGFRA*)/isocitrate dehydrogenase (*IDH1*), epidermal growth factor receptor (*EGFR*), and

neurofibromin 1 (*NF1*), respectively (Verhaak *et al.*, 2010). Methylation profiling further subdivided the Proneural subgroup into CpG island methylator phenotype (CIMP)-positive and -negative tumours (Noushmehr *et al.*, 2010; Sturm *et al.*, 2012). Interestingly, plasticity between the Proneural and Mesenchymal subtypes has been shown to occur in an NFκB-dependent manner that may be driven by microglia within the tumour microenvironment (Bhat *et al.*, 2013). A summary of epigenetic and biological features characteristic of each GBM subgroup is presented in Table 1.2.

The therapeutic relevance of the four GBM subtypes is contentious given that IDH mutation status is the only significant molecular indicator of a better prognosis, with Classical, Mesenchymal and IDH-wildtype Proneural subtypes displaying similarly poor survival outcomes (Sturm *et al.*, 2012). Individual tumours can also display multiple gene expression phenotypes (discussed in detail in section 1.4), one of the features of GBM accounting for tumour recurrence in clinical trials of therapies targeting a particular subtype. However, the bulk of the heterogeneity within tumours is removed during surgery, in line with gross total tumour resection as one of the most important prognostic factors (Kreth *et al.*, 2013). Therefore, molecular characterisation of minimal residual disease is most biologically relevant to better inform on prognosis and choice of therapeutic strategy to prevent tumour recurrence.

Table 1.2. Epigenetic and biological subgroups of adult and paediatric GBM

Epigenetic subgroup	IDH	K27	G34	RTK I 'PDGFRA'	MES	RTK II 'Classical'
Characteristic lesions	*IDH*^{mut} *TP53*^{mut}	*H3F3A*^{mut} K27 *TP53*^{mut}	*H3F3A*^{mut} G34 *TP53*^{mut}	*PDGFRA* ampl. *CDKN2A* del.	CNV^{low}	*EGFR* ampl. Chr 7^{+}/Chr 10^{-} *CDKN2A* del.
DNA methylation phenotype	CIMP+	-	CHOP+	-	-	-
Gene expression signature	Proneural	Proneural	Mixed	Proneural	Mesenchymal	Classical
Median age at diagnosis (years)	40	10.5	18	36	47	58
Tumour location	Cerebrum	Midline	Cerebrum	Cerebrum	Cerebrum	Cerebrum

Adapted from Sturm et al. (2012, 2014). Abbreviations: Ampl. – amplification; CHOP – CpG hypomethylator phenotype; CIMP – CpG island hypermethylator phenotype; del. – deletion; IDH – isocitrate dehydrogenase; MES – mesenchymal; Mut – mutated; RTK – receptor tyrosine kinase.

1.2.2. Molecular characteristics of paediatric GBM

Molecular investigations into paediatric GBM (pGBM) initially identified two subsets that were distinct from aGBM and characterised by differential Ras and AKT pathway activation (Faury *et al.*, 2007; Haque *et al.*, 2007). This was partially explained by increased activity of *PDGFRA* through amplification (12% of cases) or somatic-activating mutation (14.4% of non-brainstem (NBS) paediatric HGGs) (Paugh *et al.*, 2010, 2013). Whole-exome sequencing of pGBMs revealed recurrent and hotspot mutations within *H3F3A,* which encodes the replication-independent histone variant H3.3. *H3F3A* mutations were observed in 36% of paediatric cases and 3% of young adults. These mutations caused either a lysine-to-methionine change at position 27 (K27M) or a glycine-to-arginine/valine change at position 34 (G34R/V) and were predominantly observed in younger (median age 11 years) and older patients (median age 20 years), respectively (Schwartzentruber *et al.*, 2012). K27M mutations were almost exclusively found in midline tumours whereas G34R/V mutations were characteristic of supratentorial tumours (Fontebasso *et al.*, 2013), consistent with a better prognosis for the G34R/V subgroup (median of 24 months versus 12 months in K27M mutant tumours) (Schwartzentruber *et al.*, 2012). Figure 1.1 highlights the neuroanatomic locations associated with the two histone H3.3 mutations, as well as genes that are co-mutated at a high frequency.

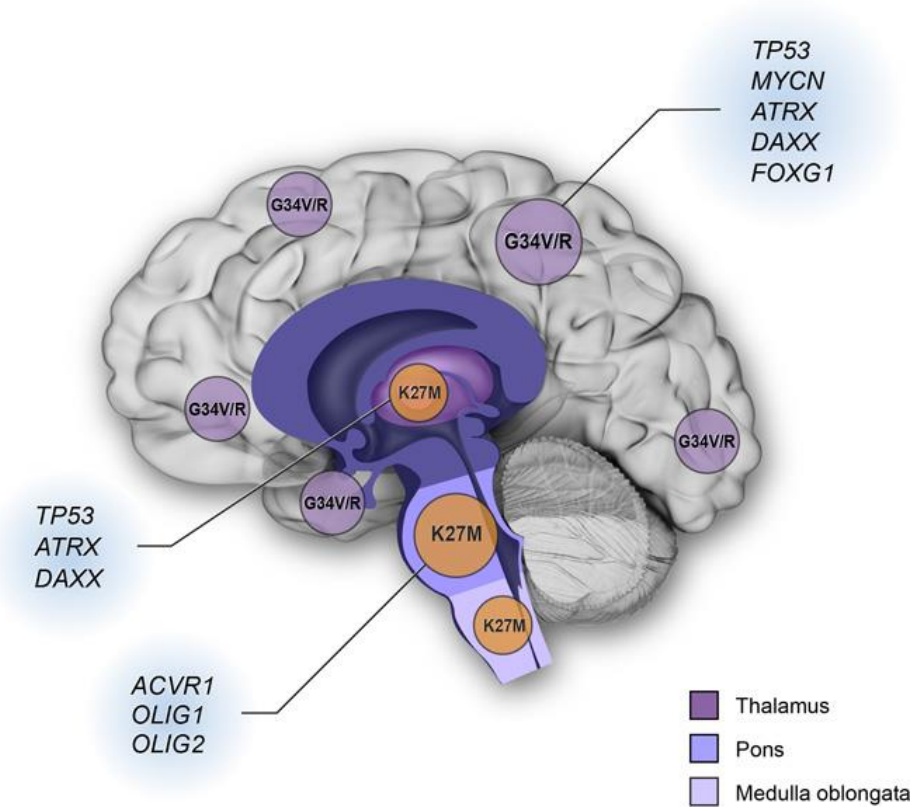

Figure 1.1. Neuroanatomic associations between histone H3.3 mutations and other genetic lesions in paediatric HGGs. K27M and G34V/R are recurrent genetic lesions within *H3F3A*, which encodes the replication-independent histone H3.3. These lesions are characteristic of paediatric HGGs found in midline or cerebral tumours, respectively. ATRX and DAXX encode members of a chromatin remodelling complex which mediates histone H3.3 incorporation at pericentric heterochromatin and telomeres (Schwartzentruber *et al.*, 2012). Activating mutations in *ACVR1* is a frequent observation in histone H3.1 K27M mutant diffuse intrinsic pontine glioma (Taylor *et al.*, 2014). OLIG1/2 and FOXG1 regulate differentiation and self-renewal processes in glial progenitor cells (Meijer *et al.*, 2012; Bulstrode *et al.*, 2017). Figure was taken directly from Lulla, Saratsis, & Hashizume (2016).

Methylation profiling of pGBMs identified 30% to 40% of cases characterised by aberrant DNA methylation patterns as a result of recurrent mutations in either *H3F3A* or *IDH1*, highlighting disrupted epigenetic regulation as a key factor in paediatric gliomagenesis. Integration with the Verhaak expression signatures revealed a Proneural oligodendrocytic expression pattern in tumours within the K27, RTK I (PDGFRA), and IDH clusters, indicating a common cell of origin, whereas G34-mutated tumours displayed mixed results (Sturm *et al.*, 2012). Interestingly, tumours displaying a Mesenchymal gene expression signature contained fewer copy number aberrations (CNAs) and no

characteristic point mutations, consistent with the previous identification of a paediatric HGG (pHGG) subset with stable genomes (Bax *et al.*, 2010). The functional consequence of the K27M mutation has been attributed to global hypomethylation of the repressive H3K27me3 mark leading to aberrant gene activation (Bender *et al.*, 2013). In G34V mutant cells, differential genomic binding of the activating K36 trimethylation mark (H3Kme3) led to a transcriptional program associated with stem-cell maintenance, cell-fate decisions, and self-renewal (Bjerke *et al.*, 2013). Interestingly, *H3F3A* mutations co-occurred with mutations in *ATRX* (α-thalassaemia/mental retardation syndrome X-linked) and *DAXX* (death-domain associated protein) which encode two subunits of a chromatic remodelling complex involved in incorporating H3.3 at pericentric heterochromatin and telomeres. *H3F3A*/*ATRX-DAXX*/*TP53* mutations strongly associated with alternative lengthening of telomeres (Schwartzentruber *et al.*, 2012), a process that lengthens shortened telomeres through homologous recombination, in mechanistic contrast to upregulated telomerase activity, evident in ~90% of all solid cancers (Cesare and Reddel, 2010).

1.2.3. Spectrum of mutations in adult and paediatric GBM

The RB and TP53 pathways are responsible for controlling cell growth and cell death in response to uncontrolled proliferation, respectively. Mutation or homozygous deletion of *TP53* was identified in approximately 55% of pHGGs (Fontebasso *et al.*, 2014; Wu *et al.*, 2014), which is higher than observed in aGBM (35%) (The Cancer Genome Atlas Research Network, 2008). In aGBM, mutations in other members of the *TP53* pathway are frequently observed, including amplification of the p53 negative regulators *MDM2* and *MDM4* in 11% and 4% of tumours, respectively (The Cancer Genome Atlas Research Network, 2008). In paediatric midline HGGs, mutations in other p53 pathway components have only been found in *PPM1D* (Wu *et al.*, 2014), which mediates stress responses downstream of the p38 mitogen-activated protein kinase (p38-MAPK)-p53 signalling axis (Taylor *et al.*, 2014). Mutations within the RB pathway are frequent in aGBM (77%) and most commonly consist of

homozygous deletion of *CDKN2A* and *CDKN2B* in 55% and 53% of patients, respectively (The Cancer Genome Atlas Research Network, 2008). Whole-genome analysis identified loss of *CDKN2A* in approximately 25% of paediatric patients with tumours in NBS locations, indicating that homozygous deletion of RB pathway components is a less frequent event in the childhood setting. pHGGs also display focal amplification of *CDK4* and *CDK6* (Wu *et al.*, 2014), thus presenting an opportunity for the use of small molecule inhibitors such as Palbociclib, Ribociclib, and Abemaciclib for the targeted inhibition of tumourigenic proliferation (Klein *et al.*, 2018).

Activation of the receptor tyrosine kinase (RTK)-RAS-phosphoinositide 3-kinase (PI3K) signalling pathway is a frequent event in paediatric NBS-HGGs (67%) (Wu *et al.*, 2014). The most commonly mutated RTK in pHGGs is *PDGFRA* (30%) (Jones and Baker, 2014). Amplification of *EGFR*, which is observed in 41% of aGBMs (The Cancer Genome Atlas Research Network, 2008), is a relatively rare event in pHGGs (less than 10%) (Qu *et al.*, 2010). Growth factor signalling through RTKs is mediated via the recruitment and activation of PI3K and RAS. PI3K is a heterodimer consisting of a catalytic (p110α) and regulatory subunit (p85), encoded by *PIK3CA* and *PIK3R1*, respectively. Mutations within *PIK3CA* are evident in 5% of pHGGs located in the cerebral cortex, whereas *PIK3R1* mutations are found in 5% to 12% of cases (Fontebasso *et al.*, 2014; Wu *et al.*, 2014). In comparison, mutations affecting PI3K were identified in 15% of aGBMs (The Cancer Genome Atlas Research Network, 2008). Activation of the PI3K pathway is regulated by the phosphatase and tensin homolog (PTEN) tumour suppressor protein. Inactivation of *PTEN* expression through homozygous deletion has been observed in 4% of pHGGs (Fontebasso *et al.*, 2014; Jones and Baker, 2014) but is a more common genetic event in aGBMs (36%) (The Cancer Genome Atlas Research Network, 2008). Alternative activation of the RAS signalling pathway in pHGGs has also been reported in 12% to 25% of cortical HGGs demonstrating mutations in *NF1*, a negative regulator of Ras (Fontebasso *et al.*, 2014; Jones and Baker, 2014).

Of particular relevance to glioma classification are the neomorphic *IDH1* mutations (most commonly R132H). Heterozygous *IDH1* mutations are observed in 12% of GBM cases (Parsons *et al.*, 2008) but are a much more prominent feature of astrocytomas (54%) and oligodendroglial tumours (65%) (Ichimura *et al.*, 2009). Mutant IDH1 is a hallmark feature of secondary GBM, occurring in nearly all cases compared to only 7% of primary GBM patients (Parsons *et al.*, 2008). Neomorphic enzymatic activity of mutant IDH1 leads to the generation of D-2-hydroxyglutarate (2HG) which inhibits α-ketoglutarate (αKG)-dependent dioxygenases, including histone demethylases such as JHDM1A, leading to altered epigenetic regulation (Waitkus, Diplas and Yan, 2016). Interestingly, IDH1 mutant tumours are frequently CIMP-positive (Noushmehr *et al.*, 2010; Sturm *et al.*, 2012). Metabolic changes in response to IDH mutants have been reported and are characterised by decreased glutamate and glutamine levels to sustain tricarboxylic acid (TCA) cycle metabolite pools (Reitman *et al.*, 2011; Ohka *et al.*, 2014). The characteristic molecular profiles of adult and paediatric HGGs are summarised in Table 1.3.

Table 1.3. Pathway mutations characteristic of adult and paediatric GBM.

Category	Adult	Paediatric
Chromatin and transcription regulation	**H3.3 mut. (3%)**	**H3.3 mut. (36%)** - K27M (23%) - G34R/V (12%) H3.1 K27M mut. (5%) ATRX/DAXX mut. (31%) SETD2 mut (15%)
RTK-RAS-PI3K signalling pathway	**RTK-RAS-PI3K pathway (86%)** - *EGFR* ampl. (41%) - *PDGFRA* ampl. (13%) - *ERRB2* ampl. (8%) - *MET* ampl. (4%) - *NF1* mut. (~10%) - *PIK3CA* mut. (~6%) - *PIK3R1* mut. (~6%) - *PTEN* mut./del. (36%)	**RTK-RAS-PI3K pathway (67%)** - *PDGFRA* mut. (30%) - *EGFR* ampl. (10%) - *FGFR1* mut. (4-27% thalamic HGG) - *NF1* mut. (12-25%) - *NTRK* fusion (10%) - *PIK3CA* mut. (5%) - *PIK3R1* mut. (5-12%) - *PTEN* del. (4%)
RB1 and TP53 cell cycle regulation	**RB pathway (77%)** - *CDKN2A* del. (55%) - *CDKN2B* del. (53%) **TP53 pathway** - *TP53* mut. (35%) - *MDM2* ampl. (11%) - *MDM4* ampl. (4%)	**RB pathway (18%)** - *CDKN2A*/*CDKN2B* del. (13%) - *CDKN2B* del. (~25%) ***TP53* pathway (55%)** - *TP53* mut. (19%) - *PPMD1* mut. (2%)
IDH metabolic enzymes	***IDH1* mut. (5-12%)** - Identified in 7% and 83% of primary and secondary cases, respectively	***IDH1* mut. (0-16%)**

Information collated from Fontebasso et al. (2014); Jones & Baker (2014); Parsons et al. (2008); Paugh et al. (2011); Qu et al. (2010); Schwartzentruber et al. (2012); Sturm et al. (2012, 2014); The Cancer Genome Atlas Research Network (2008); Wu et al. (2014). Abbreviations: ampl. – amplification; del. – deletion; mut. – mutation.

1.2.4. Chromosomal aberrations and genomic rearrangements in adult and paediatric GBM

Gain of chromosome 7 and loss of chromosome 10 is the most common gross chromosomal abnormality observed in GBM, accounting for 83-85% of cases (The Cancer Genome Atlas Research Network, 2008; Brennan *et al.*, 2013). The $7^{+}/10^{-}$ genotype is predominantly seen in older (age ≥70 years) rather than younger (age ≤40) patients (Bozdag *et al.*, 2013), consistent with enrichment in the Classical (RTK-II) subtype, minimal presence in the Proneural subtype, and virtual absence in the *H3F3A*- or *IDH*-mutant G-CIMP-positive tumours (Sturm *et al.*, 2012). Other frequent genomic CNAs include gain of chromosome 19 and 20 (35-40%; enriched in the Classical (RTK-II) subtype), and loss of chromosomes 9p (38%), 22q (33%), 13q (33%), 14q (27%) and 6q (22%) (The Cancer Genome Atlas Research Network, 2008; Brennan *et al.*, 2013). In comparison with adult cases, pHGGs are characterised by gain of 1q (19% vs. 9% in aHGG) and loss of 16q (17.5% vs. 7.4% in aHGG). pHGGs also demonstrate a distinct lack of chromosome 7 gain (19% vs 74.1% in aHGG) and 10q loss (15.9% vs 80.4% in aHGG). Association of CNAs with clinico-pathologic parameters revealed a trend towards shorter survival in pHGGs with gain of 1q (Bax *et al.*, 2010).

Chromothripsis (complex chromosomal rearrangements in a single catastrophic event) is a feature of >30% of GBMs (Malhotra *et al.*, 2013). 69% of GBMs demonstrate some form of chromosomal aberration in the form of interchromosomal, intrachromosomal (intergenic), or intragenic rearrangement (Zheng *et al.*, 2013). The most prominent intragenic deletion occurs within regions of the *EGFR* gene encoding either the carboxyl terminus or the extracellular domain, the latter generating the EGFRvIII variant following deletion of exons 2-7 (Cho *et al.*, 2011). pGBMs demonstrate similar chromosomal imbalances (Wong *et al.*, 2006; Qu *et al.*, 2010). A large proportion of pHGGs (34.9%) display large-scale CNAs involving whole chromosomes or chromosomal arms; 17.5% feature numerous intrachromosomal breaks resulting in a highly rearranged genome; and 27.0%

demonstrate single or multiple high-level gene amplifications. In contrast, a number of pHGGs are characterised by stable (balanced) genomes, with either few, low-level focal changes (20.6%) or no detectable copy number changes (12.7%) (Bax *et al.*, 2010). Intragenic deletions within the *PDGFRA* and *EGFR* genes (producing the EGFRvIII variant) have also been identified in pGBMs (Bax *et al.*, 2009; Ozawa *et al.*, 2010). Fusion genes resulting from the structural rearrangement of genomes have been identified in 47% of pHGGs. Recurrent fusion genes involving the three neurotrophin receptor (*NTRK*) genes have been identified in 10% of NBS-HGGs and were particularly prevalent within the infant population (40%). Tumours expressing a *NTRK* fusion gene demonstrate few additional mutations indicating that *NTRK* fusion genes are potent oncogenic drivers in early postnatal brain tumour development (Wu *et al.*, 2014).

1.3. Therapy resistance to conventional and targeted therapies

The identification of recurrent genomic aberrations in GBM has propelled research into genome-directed targeted therapy as a form of personalised medicine. Studies into GBM have revealed an oncogene addiction to EGFR and its constitutively active mutant variant EGFRvIII (Del Vecchio *et al.*, 2012; Fan *et al.*, 2013). Several EGFR inhibitors have been tested as monotherapy in the primary and recurrent GBM setting, including erlotinib, gefitinib, and lapatinib. However, no clinical trial to date has demonstrated therapeutic efficacy in extending overall survival (Bastien, McNeill and Fine, 2015). Inherent mechanisms of EGFR inhibitor resistance have been identified in GBM cell lines and primary tumours, including loss of PTEN tumour suppressor activity (Mellinghoff *et al.*, 2005) and activation of redundant RTKs (Snuderl *et al.*, 2011; Szerlip *et al.*, 2012). Novel adaptive responses to EGFR inhibitor include de-repression of *PDGFRβ* (Akhavan *et al.*, 2013) and downregulation of sensitising EGFRvIII mutants via loss of double minute chromosomes (Nathanson *et al.*, 2014). Resistance to targeted therapy is also an inherent feature of tumour evolution based on a hierarchical model of glioma stem cells or genetically heterogenous clonal subpopulations (Bonavia *et al.*, 2011). Finally, cell-cell

interactions that are either beneficial or detrimental to tumour growth further complicate therapeutic decision-making (Inda *et al.*, 2010; Marusyk *et al.*, 2014).

1.4. Intratumour heterogeneity

Intratumour heterogeneity (ITH) describes the genetic heterogeneity arising from a hierarchy of multiple competing subclones that dynamically changes in response to therapy or pressures within the tumour microenvironment. In 1976, Peter Nowell formulated an evolutionary model of cancer progression based on the sequential stepwise accumulation of advantageous genetic alterations. Nowell proposed that genetic instability in the initial neoplastic clone leads to the establishment of a tumour cell population consisting of variant subclones. Most advanced tumours display genetic instability at either the nucleotide or chromosome level, leading to accelerated evolutionary adaptation and enhanced biological fitness (Swanton, 2012). Current understanding of carcinogenesis stipulates that initial genotoxic disturbances in the tissue microenvironment in the form of inflammation, reactive oxygen species or external carcinogens act upon inherited mutations to instigate hyperplastic growth of the cell of origin. The development of hypoxia within the tissue microenvironment further supports the accumulation of chromosomal abnormalities and mutations following increased reactive oxygen species (ROS) production and acidosis from highly glycolytic cells, ultimately leading to clades of cells displaying diverse genetic and phenotypic traits (Gillies, Verduzco and Gatenby, 2012).

1.4.1. Clinical implications of intratumour heterogeneity

The spatial and temporal aspects of ITH present several issues to clinicians and scientists regarding targeted therapy approaches and biomarker discovery. Historically, biopsy of tumours for diagnostic and therapeutic decision-making purposes, have sampled only a small proportion of the tumour mass (typically central, contrast-enhanced, highly cellular regions), leading to incomplete

characterisation of subclonal dynamics, as seen in renal carcinomas (Gerlinger *et al.*, 2012). In pancreatic cancer, metastatic subclones responsible for seeding secondary metastases have been shown to exist in minor populations in spatially distinct areas of the tumour mass (Yachida *et al.*, 2010). Therefore, implementation of targeted therapies based on the genetic signature of dominant subclones within biopsy samples ultimately fail due to the existence of subdominant populations of therapy-resistant, malignant and infiltrative subclones that escape detection, as is the case in GBM (Johnson *et al.*, 2014). Confounding therapeutic decision making further, interclonal interactions between minor subclones have been identified that drive tumour growth in a non-cell-autonomous manner, leading to new phenotypic traits (Marusyk *et al.*, 2014). Moreover, interactions between cancer cells and the tumour microenvironment, including immune cells and endothelial cells, may help shape the tumour subclone hierarchy by either constraining or promoting tumour growth depending on the context (McGranahan and Swanton, 2017).

The highly dynamic nature of ITH precludes the identification of predictive or prognostic biomarkers, as competition between subclones leads to changes in clonal architecture that evolves over time (Keats *et al.*, 2012). This temporal evolution of ITH has led to tumours being described as “moving targets”, with the complete eradication of the founding clone and all subclones proposed as the only path to achieving a cure (Ding *et al.*, 2012). Exploitation of tumour cell interdependencies to achieve tumour remission has been put forward in an “adaptive therapy” approach. Adaptive therapy departs from the standard Norton-Simon model of treatment, in which patients are given the maximum tolerated dose, to a dynamic metronomic approach that is continuously modulated to enforce a stable tumour burden, allowing fitter chemosensitive subclones to outcompete less-fit therapy-resistant subclones (Gatenby *et al.*, 2009).

1.4.2. Models of intratumour heterogeneity

The parallels between the evolution of tumour cell hierarchies and Darwin's "tree of life" has led to the description of tumour growth as "branching", resulting in a trunk-branch model to conceptualise the development of a single neoplastic founding clone into a heterogeneous subclonal population. Oncogenic drivers present in early clonal progenitors are ubiquitously present within the tumour and represent the "trunk" of the tumour evolutionary tree. Later acquired somatic alterations leading to divergence of tumour subclones represent branch events which are proposed to underlie tumour metastatic progression and therapy resistance (Swanton, 2012). Branched events may be spatially separated within a single biopsy or between regions of the same tumour (Yachida *et al.*, 2010). A 'Big Bang' model of tumour expansion was proposed by Sottoriva and colleagues (2015) following studies in colorectal tumours. In this model, ITH is proposed to occur early after the initial expansion of a neoplastic clone, with most detectable private mutations occurring early after the transition to an advanced tumour. The pervasiveness of genetic alterations within the tumour is dependent on the timing of the event, with early genetic alterations existing throughout the tumour, whereas late events are found as discrete branched populations. Therefore, ITH is proposed to be uniformly high throughout the tumour mass since loss of normal cell adhesion in the early tumour leads to subclone mixing. This early expression of an invasive phenotype implies that some tumours are predisposed to an aggressive phenotype and that malignant potential is determined early (Sottoriva *et al.*, 2015).

1.4.3. Intratumour heterogeneity in adult and paediatric GBM

Adult patients with GBM initially respond to chemoradiation but eventually succumb to recurrent disease (Stupp *et al.*, 2005). The identification of clonal subpopulations that express different RTKs (EGFR, PDGFRA, and MET) in a mutually exclusive manner fuelled interest into characterising intratumour heterogeneity in GBM (Snuderl *et al.*, 2011; Szerlip *et al.*, 2012). Spatiotemporal evaluation of ITH in aGBM was conducted by Sottoriva et al. (2013) in a novel

surgical procedure utilising the fluorescent compound 5-ALA to aid multi-region sampling of the tumour mass in real-time. Analysis of genome-wide CNAs revealed heterogeneity in putative GBM drivers including gain/amplification of *PDGFRA*, *MDM4*, and *AKT3*, and deletion of *PTEN*. Reconstruction of tumour fragment phylogenies to infer GBM evolution based on common, shared and unique genetic events, identified CNAs in *EGFR* and *CDKN2A/B/p14ARF* as early trunk events followed by amplification of *PDGFRA* and deletion of *PTEN* as subsequent branching events (Sottoriva *et al.*, 2013), as summarised in Figure 1.2. A similar sampling strategy coupled with RNA-sequencing of contrast-enhancing (CE) core and non-enhancing (NE) margins of GBM tumours indicated that CE regions were of the Proneural, Classical, or Mesenchymal subtype, whereas the NE regions were predominantly of the neural subtype (Gill *et al.*, 2014). Even more extensive characterisation of ITH in GBM has been conducted at the single-cell level. Single-cell RNA-sequencing revealed a stemness gradient in GBMs that was differentially associated with Verhaak expression signatures, with the more stem-like cells of Proneural and Classical subtype (Patel et al. 2014). Consistent with this, functional profiling of individual clones revealed unique proliferation and differentiation abilities and identified pre-existing treatment-resistant clones within untreated tumours (Meyer *et al.*, 2015). Interestingly, spatiotemporal evolution is evident between primary and recurrent tumours that is related to the distance of recurrence, with greater divergence from the parental genetic landscape in distal compared to local recurrent tumours (J. Kim *et al.*, 2015).

Preliminary evidence of ITH in pHGGs was obtained by Wu et al. (2014) through whole-genome sequencing of samples from 127 patients. Heterogeneity was assessed by calculation of the mutant allele fraction (MAF), a measure of the frequency of single-nucleotide variants (SNVs) in regions with no CNAs or loss-of-heterozygosity. Density plots of MAF values suggested the presence of multiple subclones in pHGGs with multiple distinct peaks observed in 50% of tumours. Read counts of SNVs were used to investigate the clonal architecture

and tumour evolution from diagnosis to relapse or autopsy. In one case, the founder clone harboured a *TP53* truncating mutation and had two descendent subclones in the tumour at diagnosis. Only the founder clone was present in the autopsy along with a descendent subclone with autopsy-specific mutations. A second case had a founder clone with the prototypical pHGG *H3F3A* K27M mutation as well as a *PIK3CA* Q546K mutation. A descendent of the founder subclone harboured additional mutations including a nonsense mutation in *PPM1D*. As in the first case, only the founding clone was present in relapse which gave rise to a dominant subclonal population that acquired additional mutations including *HMGXB3* L611W. This study suggests that ITH is a phenomenon that not only occurs in aGBM but also in pHGG as a driving force of tumour evolution and adaptation (Wu *et al.*, 2014). Although we have generated intra-tumour resected biopsies for paediatric ependymoma (unpublished), multiple region-sampling of pGBM has yet to be conducted to truly characterise ITH. However, evidence from DIPG suggests that ITH may be a feature of HGGs in the childhood as well as the adult setting (Nikbakht *et al.*, 2016). It is important to note that identification of ITH as an inherent feature of both adult and paediatric GBM may not be completely therapeutically relevant since tumour de-bulking surgery removes most of the tumour subclonal hierarchy, leaving few tumour subclones within residual disease. Moreover, disparities between primary and recurrent tumours in terms of the underlying genetic landscape precludes the use of molecular information from the initial occurrence on the informed treatment of secondary tumours. Strategies aimed at isolating invading cells within normal brain tissue will facilitate the development of more clinically relevant therapeutic strategies, as has been shown by Darmanis et al. (2017).

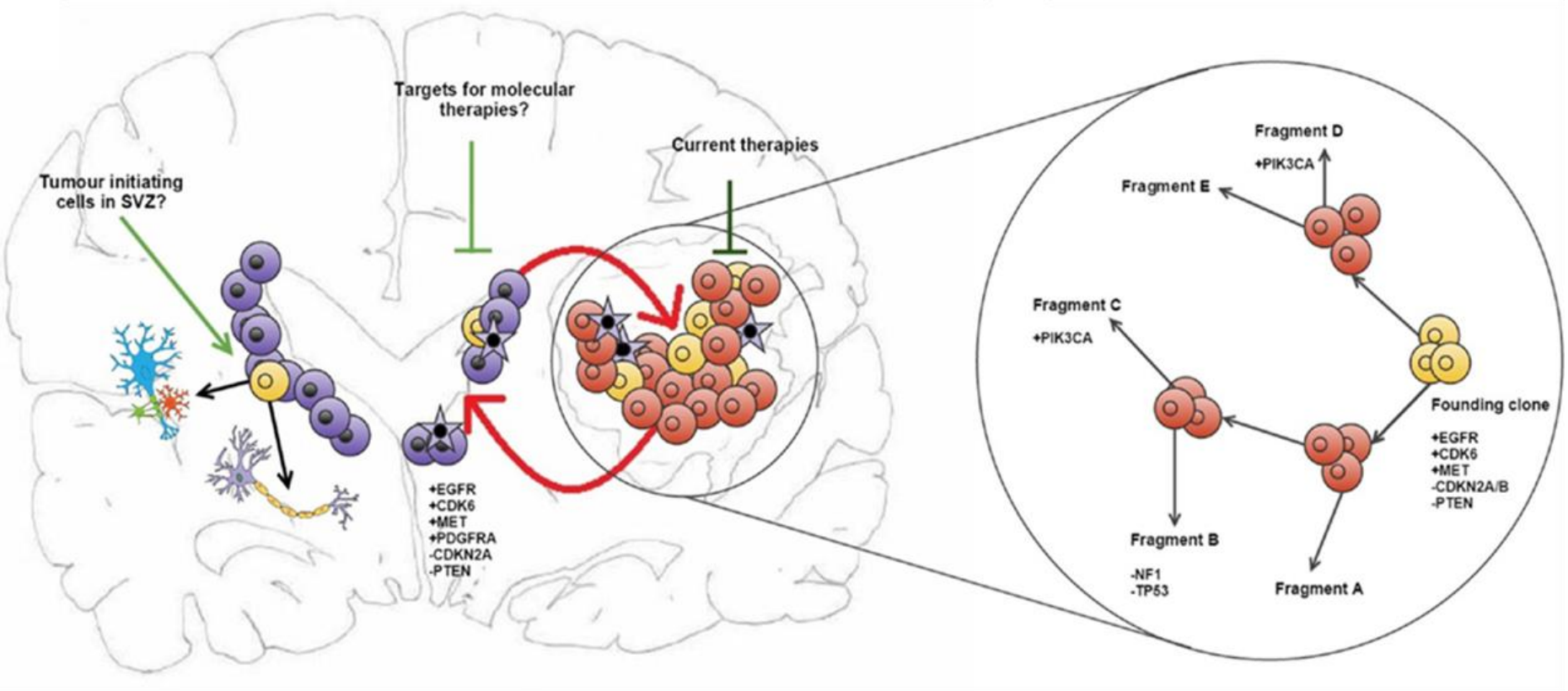

Figure 1.2. Spatiotemporal evolution of aGBM. The diagram represents a summary of the phylogenetic analysis conducted by Sottoriva et al. (2013) of tumour fragments obtained in a multi-region sampling approach. Gain and loss of genetic lesions within tumour subclonal populations (red cells) are displayed reflecting the evolution of the GBM founding clone (yellow cells) over time in response to inherent genetic instability, competition between subclones, and environmental stresses. The founding clone is hypothesised to be derived from tumour initiating cells within in the subventricular zone (SVZ). Figure taken directly from Ellis et al. (2015).

1.5. Tumour metabolism

The genomics era has propelled research into tumour characterisation at the molecular level, leading to increased awareness and understanding of the heterogeneous nature of tumour cell subpopulations. However, much of the heterogeneity observed in tumours comprises passenger mutations with no relevance to driving tumourigenesis. Scientific advancement in cancer research therefore requires functional genomics approaches to determine how the heterogeneous genomic landscape manifests phenotypically in tumour behaviour. Studying tumour metabolism is a means to understanding the functional consequences of the myriad oncogenes and tumour suppressor genes observed. Since several signalling pathways converge on a limited number of metabolic pathways, targeting tumour metabolism may represent a way of circumventing the inherent genetic redundancy evident within cells and between clonal subpopulations that accounts for the failure of targeted therapies over prolonged use. The following sections provide a brief overview of intermediary metabolism and how cancer cells can hijack inherent systems to fuel their bioenergetic and anabolic needs for proliferation.

1.5.1. Aerobic glycolysis and the role of oxidative phosphorylation

The seminal observations made by Otto Warburg in the 1920s regarding aerobic glycolysis fuelled scientific interest into the study of tumour metabolism (Koppenol, Bounds and Dang, 2011). Almost a century on, reprogramming of normal cellular metabolism to meet energetic and biosynthetic needs is now considered a hallmark of cancer (Hanahan and Weinberg, 2011). The Warburg effect describes the phenomenon of cancer cells fermenting glucose into lactate in the presence of oxygen and in preference to complete oxidation of glucose through mitochondrial oxidative phosphorylation (OXPHOS). Partial oxidation of one glucose molecule via glycolysis generates two molecules of adenosine 5'-triphosphate (ATP) compared to ~36 molecules of ATP produced via OXPHOS (Vander Heiden, Cantley and Thompson, 2009). Despite the relative inefficiency of glycolysis compared to OXPHOS in terms of energy generation, cancer cells demonstrate

an increased capacity for glucose uptake and glycolytic flux to account of the energy deficit (Boroughs and DeBerardinis, 2015).

The Warburg effect has been hypothesised to facilitate the generation of intermediates, such as nucleotides, amino acids, and lipids, to build biomass and enable cancer cell proliferation (Figure 1.3) (Vander Heiden, Cantley and Thompson, 2009). Consistent with this, several studies demonstrate the ability of oncogenes to reprogram metabolism directly through regulation of metabolic enzymes or indirectly by activation of signalling pathways that initiate proliferative programs (Figure 1.3) (Boroughs and DeBerardinis, 2015). Oncogenic Ras signalling in pancreatic cancer induces a glycolytic response through the upregulation of glycolysis genes (*GLUT1*, *HK1*, and *LDHA*) with consequent channelling of glucose intermediates into the hexosamine and pentose phosphate pathways (Ying *et al.*, 2012). In glioma, a grade-specific increase in the expression of the pyruvate kinase M2 (PKM2) isoform results in a paradoxical reduction in glycolytic flux, which enables the shuttling of glycolytic intermediates into anabolic pathways (Figure 1.3) (Mukherjee *et al.*, 2013). In direct conflict with Warburg's initial observations, some cancers rely on oxidative phosphorylation to generate energy and metabolic intermediates (Caro *et al.*, 2012). Such behaviour is observed in glioma stem cells which display a preference for oxidative phosphorylation compared to their differentiated progeny, indicating that agents targeting glycolysis may spare this tumour subpopulation (Vlashi *et al.*, 2011).

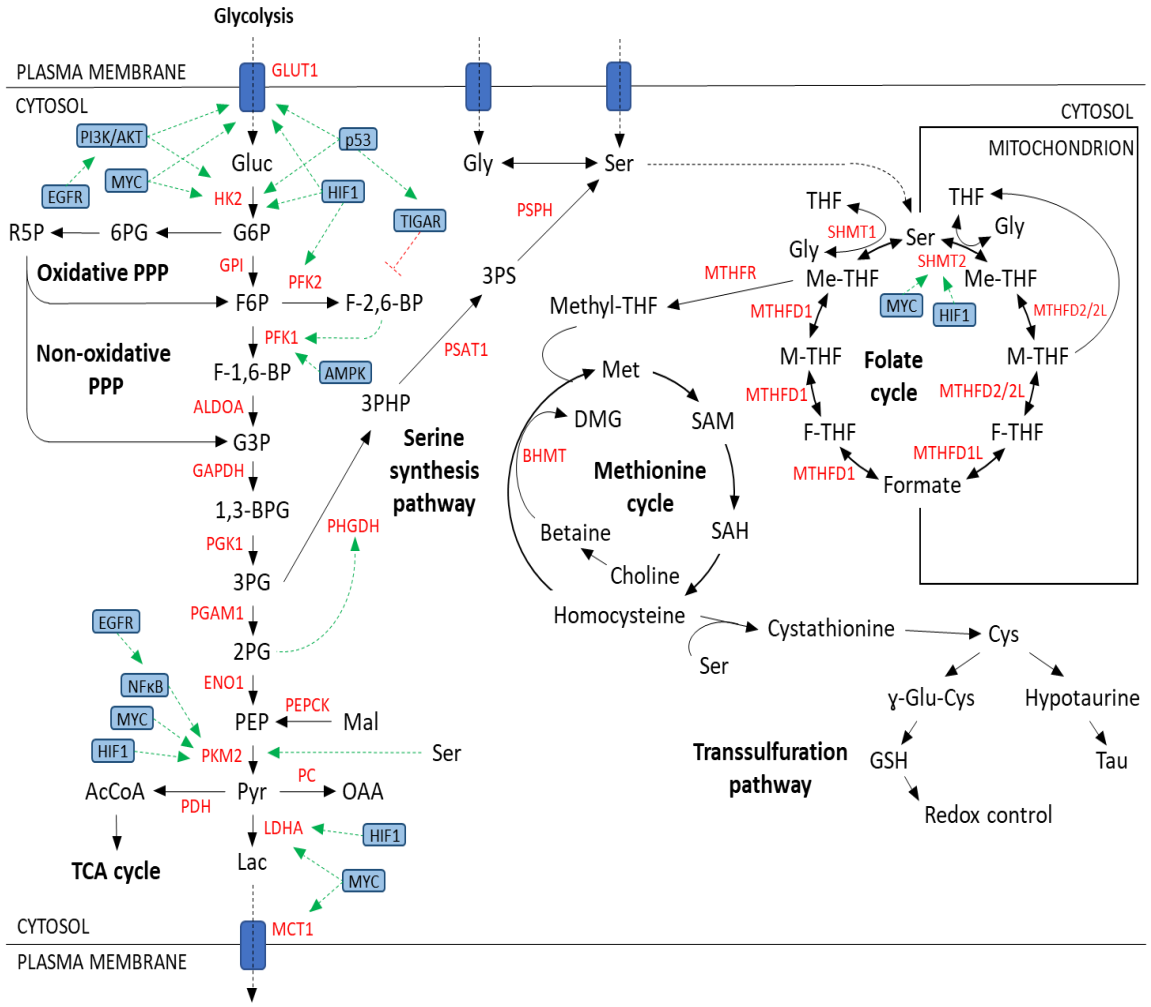

Figure 1.3. Overview of glycolysis, serine synthesis pathway and one-carbon metabolism. Aberrant glycolytic activity manifesting as the "Warburg effect" is a hallmark of cancer. Several oncogenic drivers (blue boxes) regulate glycolysis at early stages by increasing glucose uptake and at the latter stages by shuttling carbon into anabolic pathways rather than the TCA cycle. This is mediated through the increased expression of pyruvate kinase M2 isoform, which has low enzymatic activity in dimeric format. Shuttling of G6P into the oxidative arm of the PPP is an important source of NADPH to be utilised in *de novo* lipid synthesis. Serine derived from *de novo* synthesis or uptake from the extracellular environment is fed into one-carbon metabolism consisting of the folate and methionine cycles. Intermediates generated from the folate cycle are fed into purine synthesis, whereas intermediates from the methionine cycle are used in methyl-transferase reactions and for glutathione (GSH) production within the transsulfuration pathway. Abbreviations: G6P – glucose 6-phospate; F6P – fructose 6-phosphate; F-1,6-BP – fructose- 1,6-bisphosphate; G3P – glyceraldehyde 3-phosphate; 3PG – 3-phosphoglycerate; 2PG – 2-phospho-glycerate; PEP – phosphoenolpyruvate; 6PG – 6-phosphogluconate; R5P – ribose 5-phosphate; 3PHP – 3-phospho-hydroxypyruvate; 3PS – 3-phosphoserine; THF – tetrahydrofolate; Me-THF – 5,10-methylene-THF; M-THF – 5,10-methenyl-THF; F-THF – 10-formyl-THF; DMG – dimethyl-glycine; SAM – S-adenosylmethionine; SAH – S-adenosylhomocysteine. Red – metabolic enzymes; Blue boxes – metabolic regulators; Green pointed arrows – stimulating activity; Red stop arrow – inhibiting activity.

1.5.2. Glutamine and tricarboxylic acid cycle anapleurosis

Other substrates are utilised by cancer cells to complement carbon input from glucose and to maintain survival under low nutrient conditions. Glutamine is a conditional non-essential amino acid that is metabolised by proliferating cells to synthesise hexosamines, nucleotides, and amino acids (Figure 1.4) (DeBerardinis and Cheng, 2010). MYC-overexpressing cancer cells consume glutamine in excess of cellular requirements for protein and nucleotide synthesis in order to sustain metabolite pools within the TCA cycle (Wise *et al.*, 2008), a process referred to as anapleurosis. This occurs through a novel posttranslational mechanism whereby MYC suppresses the expression of MiR-23a and MiR-23b, which target the glutaminase (GLS) mRNA for degradation (Figure 1.4) (Gao *et al.*, 2009). These results indicate that TCA cycle activity is still apparent in cancer cells that have undergone a glycolytic switch, as has been documented in human brain tumours *in situ* through infusion of [U-^{13}C]glucose into patients (Maher *et al.*, 2012). However, the importance of glutamine in TCA cycle anapleurosis is contentious following demonstration of a lack of glutamine oxidation in a nuclear magnetic resonance (NMR) and ^{13}C-labelled isotope infusion study of patient-derived orthotopic models, which instead highlighted glucose and acetate as sustaining metabolite pools (Mashimo *et al.*, 2014). In contrast to the purported role of glutamine in anapleurosis, catapleurosis of glutamine from glutamate and ammonia via glutamine synthetase (GS) has been shown to sustain the proliferation of GBM cells under glutamine-deprived conditions for utilisation in *de novo* purine synthesis (Tardito *et al.*, 2015). In low GS-expressing tumours, glutamine may be obtained by GBM cells from that supplied by normal astrocytes, potentially uncoupling the glutamine-glutamate cycle between astrocytes and neurons and causing epileptic seizures (Rosati *et al.*, 2013).

Anapleurosis is also achieved through conversion of glutamate into aspartate by aspartate transaminase (GOT1), which releases αKG into the TCA cycle (Figure 1.4). Further processing of glutamine-derived aspartate through a series of reactions leads to increased levels of reduced nicotinamide adenine

dinucleotide phosphate (NADPH) via the conversion of malate into pyruvate by malic enzyme (Figure 1.4) (Son *et al.*, 2013). This highlights another important aspect of tumour metabolism – the maintenance of mitochondrial redox balance. Glutamine metabolism in conjunction with the oxidative arm of the pentose phosphate pathway (Figure 1.3) and serine/one-carbon metabolism (Figure 1.4), collectively regulate levels of redox species (Alberghina and Gaglio, 2014). The literature on glutamine metabolism strongly supports a positive impact on tumour growth through the provision of energetic, anabolic, and redox intermediates. Further study into the importance of glutamine in GBM is required, considering the therapeutic effectiveness of glutamine pathway inhibition in other solid cancers (Seltzer *et al.*, 2010).

1.5.3. Conditional non-essential and essential amino acids

Conditional non-essential amino acids are normally not essential except in times of illness and stress. This categorisation includes the following amino acids: arginine, cysteine, glutamine, tyrosine, glycine, ornithine, proline, and serine. Cancer cells are highly dependent on the uptake of exogenous serine for conversion into glycine and intermediates for building nucleotides (Labuschagne *et al.*, 2014). Catabolism of serine by mitochondrial serine hydroxymethyltransferase (SHMT2) feeds carbon into the folate cycle which generates NADPH (Fan *et al.*, 2014). This source of redox potential is particularly important under hypoxic stress, as seen in MYC-amplified neuroblastoma and brain cancer cells within the ischaemic zones of gliomas (Ye *et al.*, 2014; D. Kim *et al.*, 2015). *De novo* synthesis of serine indirectly supports tumour growth via the conversion of 3-phosphohydroxypyruvate (3-PHP) into 3-phosphoserine (3-PS) by phosphoserine aminotransferase 1 (PSAT1) (Figure 1.3), a reaction which fills αKG pools within the TCA cycle (Possemato *et al.*, 2011).

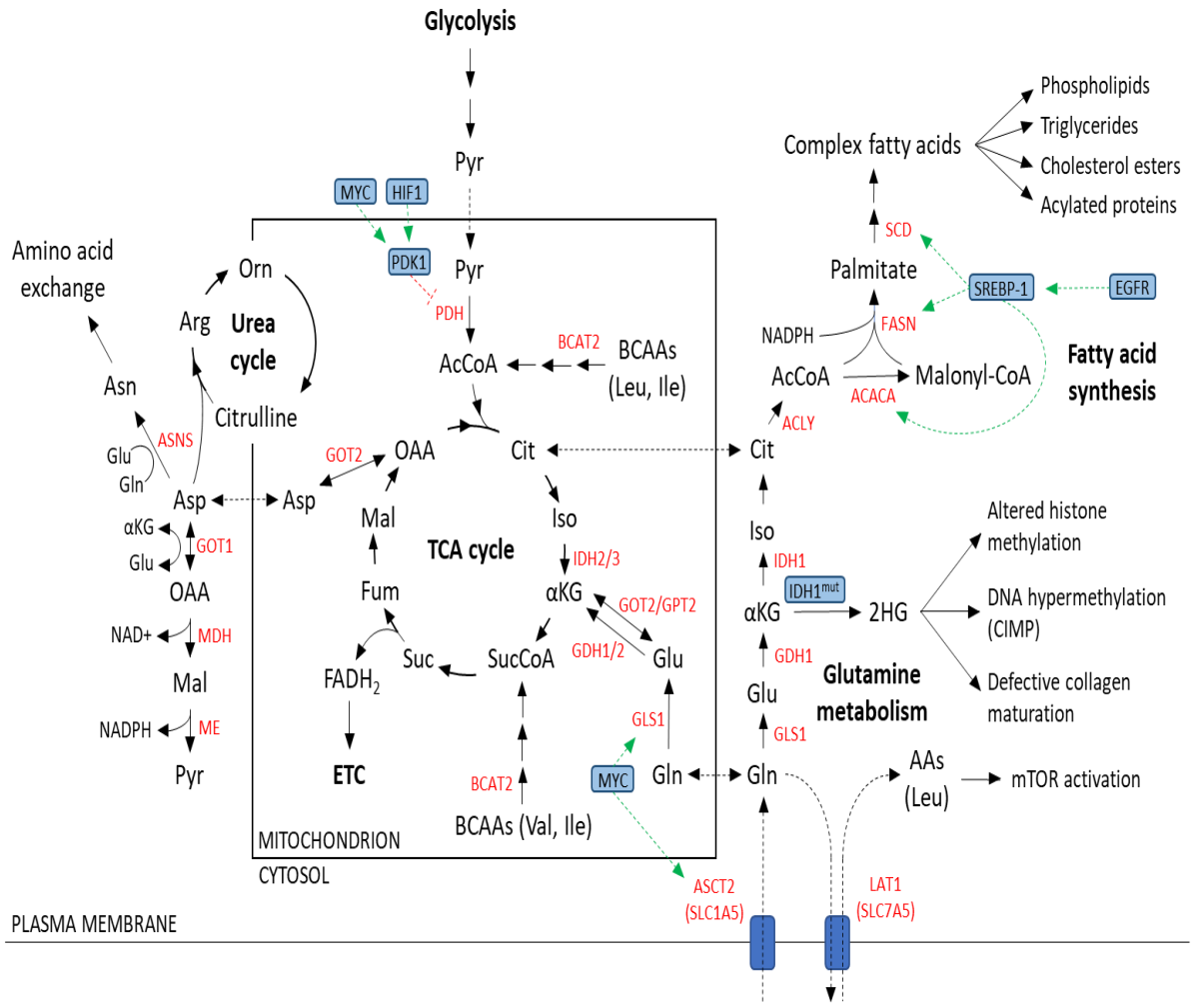

Figure 1.4. Overview of the TCA cycle, glutamine metabolism and fatty acid synthesis. Some cancers are dependent on activity within the TCA cycle to generate ATP from the electron transport chain (ETC). In most cancers, TCA cycle metabolites are utilised in anabolic reactions to generate amino acids and lipids. Oncogenic-regulation of the TCA cycle is primarily conducted by MYC, which activates PDK1 to inhibit PDH activity. Anapleurotic reactions replenishing TCA cycle metabolite pools is largely mediated through the reduction of glutamate into α-KG. Glutaminase 2 (GLS2), which mediates the conversion of glutamine into glutamate, is upregulated following oncogenic MYC activity. Other means of TCA cycle anapleurosis include catabolism of BCAAs by BCAT1, as seen in IDH1-wildtype gliomas only. The most common IDH1 mutation R132H is neomorphic, causing conversion of α-KG into 2HG. 2HG causes alterations to histone methylation, induces CIMP, and interferes with collagen maturation. An unusual effect of 2HG is the greater instability of HIF1 due to stimulation of prolyl hydroxylase activity by 2HG. Latter malignant stages of transformation usually require acquisition of a lipogenic phenotype in which fatty acid synthesis is upregulated to meet cellular demands aberrant proliferation. The master regulator of fatty acid synthesis SREBP-1 is a downstream target of oncogenic EGFR signalling, leading to an increase in *de novo* synthesis as well as uptake of fatty acids. Red – metabolic enzymes; Blue boxes – metabolic regulators; Green pointed arrows – stimulating activity; Red stop arrow – inhibiting activity.

The second product of the SHMT reaction, glycine, is an integral component of the antioxidant molecule, glutathione, and fuels the synthesis of heme contained within cytochromes and oxidative phosphorylation complexes (Amelio *et al.*, 2014). Mass spectrometric analysis of core and release profiles across the NCI-60 cancer cell lines identified a strong correlation between glycine and rates of proliferation (Jain *et al.*, 2012). However, conflicting evidence from Labuschagne and colleagues indicated detrimental effects of high glycine levels due to conversion into serine with consequent depletion of the one-carbon pool (Labuschagne *et al.*, 2014). Another conditional non-essential amino acid with an understudied role in cancer is proline. Oncogenic MYC induces expression of proline biosynthesis enzymes and downregulates the mitochondrial tumour suppressor, proline oxidase/dehydrogenase (POX/PRODH), via MiR-23b*, which is processed from the same GLS-inhibiting MiR-23b transcript (Liu *et al.*, 2012). Interconversion of proline with its catabolic breakdown product 1-pyrroline-5-carboxylate (P5C) contributes to tumour growth by helping recycle NAD(P)H/NAD(P)+ species for use in the glycolysis and oxidative pentose phosphate pathways (Liu *et al.*, 2015).

Essential amino acids cannot be synthesised *de novo* and are obtained solely through nutrition. This categorisation includes the following amino acids: histidine, isoleucine, leucine, methionine, phenylalanine, threonine, tryptophan, valine, and lysine. The branched-chain amino acids (BCAAs: isoleucine, leucine, and valine) are of particular interest in gliomas since tumours carrying wildtype IDH1 display a novel route of TCA cycle anapleurosis through BCAA catabolism. Knockdown of the catabolic BCAA transaminase 1 (BCAT1) enzyme reduced glioma growth, likely due to reduced influx of acetyl-CoA and succinyl-CoA into the TCA cycle. Interestingly, slow-growing IDH mutant gliomas were essentially absent of BCAT1 protein expression as explained by altered epigenetic regulation (Tönjes *et al.*, 2013). An interesting non-energetic, non-anabolic role is shown by tryptophan in cancer immunity. Tryptophan catabolism by indolamine-2,3-dioxygenase (IDO) expressed in tumour cells or antigen-presenting cells generates immunosuppressive

catabolites in the tumour milieu and draining lymph nodes, leading to T-cell anergy and apoptosis (Platten, Wick and Van Den Eynde, 2012).

1.5.4. Lipid metabolism, β-oxidation and lipid droplets

Lipids encompass a vast collection of compounds with glycerol or sphingoid bases connected to highly diverse fatty acid structures. Most normal cells and tissues obtain their lipid requirements through dietary uptake, although systems exist for *de novo* synthesis (Santos and Schulze, 2012). The latter is achieved by the shuttling of carbon into the acetyl-CoA pool through either glycolysis or reductive carboxylation of glutamine (Metallo *et al.*, 2011; Mullen *et al.*, 2011). In cancer, malignant progression is often dependent on the acquisition of a lipogenic phenotype, in which uptake and endogenous synthesis of fatty acids is increased (Menendez and Lupu, 2007). Following covalent modification with coenzyme A (CoA) via fatty acyl-CoA synthetase (ACS), fatty acids enter the bioactive pool and can be esterified with either glycerol or sterol to generate triacylglycerols or sterol esters, respectively (Currie *et al.*, 2013). Further processing of fatty acids provides building blocks to synthesise membrane phospholipids, including phosphatidylcholine, phosphatidylethanolamine, and phosphatidyl-serine, as well as sphingolipids and lysophospholipids (Blom, Somerharju and Ikonen, 2011). Such is the importance of *de novo* fatty acid synthesis that knockdown of ATP citrate lyase (ACLY) subverts the supply of acetyl-CoA units from citrate leading to reduced lipid generation and tumour growth (Bauer *et al.*, 2005; Hatzivassiliou *et al.*, 2005). Fatty acid synthase (FASN), the enzyme complex that mediates *de novo* fatty acid synthesis, is overexpressed in a grade-specific manner in glioma and its inhibition with Orlistat leads to reduced cell growth (Grube *et al.*, 2014). However, cancer cells demonstrate different capacities to induce *de novo* fatty acid synthesis under lipid-poor conditions (Daniëls *et al.*, 2014) and can instead scavenge fatty acids from the extracellular milieu, especially under hypoxic conditions (Young *et al.*, 2013). Oncogenic Ras-driven cells preferably uptake phospholipids with one fatty acid tail (lysophospholipids), rendering these cells resistant to sterol-CoA desaturase (SCD1) inhibition (Kamphorst *et al.*, 2013). A

special case of lipid scavenging is demonstrated by the metabolic cooperation between adipocytes and ovarian cancer cells that have metastasised to the omentum (Nieman *et al.*, 2011).

In addition to their structural and signalling functions, fatty acids are catabolised through mitochondrial β-oxidation. This is the preferred route of energy generation in some cancers (Caro *et al.*, 2012) and can allow cancer cells to survive tumour regression (Viale *et al.*, 2014). Constitutive expression of carnitine palmitoyltransferase 1C (CPT1C), a brain-specific mitochondrial fatty acid transporter, increases fatty acid oxidation, ATP production, and resistance under low nutrient or hypoxic conditions (Zaugg *et al.*, 2011). Blocking CPT1-mediated fatty acid transport into mitochondria using etomoxir inhibited β-oxidation in association with reduced cellular respiratory responses, leading to prolonged survival in models of malignant glioma (Lin *et al.*, 2017).

Excess lipids and cholesterol are stored within lipid droplets (Yue *et al.*, 2014), which are endoplasmic reticulum (ER)-derived cytoplasmic organelles consisting of a neutral lipid core surrounded by a monolayer of phospholipids and associated proteins (Bozza and Viola, 2010). Storage of cholesterol within lipid droplets requires esterification of the hydroxyl group attached to carbon 3 of cholesterol in a reaction catalysed by acyl CoA:cholesterol acyltransferase (ACAT1) (Yue *et al.*, 2014). High lipid droplet content is now considered a hallmark of cancer aggressiveness. In breast cancer, cholesterol ester accumulation and storage within lipid droplets following lipoprotein uptake correlated with tumour aggressiveness and poor clinical outcome (de Gonzalo-Calvo *et al.*, 2015). Lipid storage suppresses cytotoxic ER stress responses under conditions of nutrient and oxygen limitation, and promotes resistance to chemotherapy (Qiu *et al.*, 2015). In GBM, hypoxic induction of fatty acid binding protein 3 (FABP3) and FABP7 led to significant lipid droplet accumulation whilst *de novo* fatty acid synthesis was repressed. These lipid droplets provided a valuable source of ATP through β-oxidation of fatty acids during cycles of hypoxia-reoxygenation and protected against the detrimental effects of

reactive oxygen species (Bensaad *et al.*, 2014). A summary of fatty acid metabolism is presented in Figure 1.5.

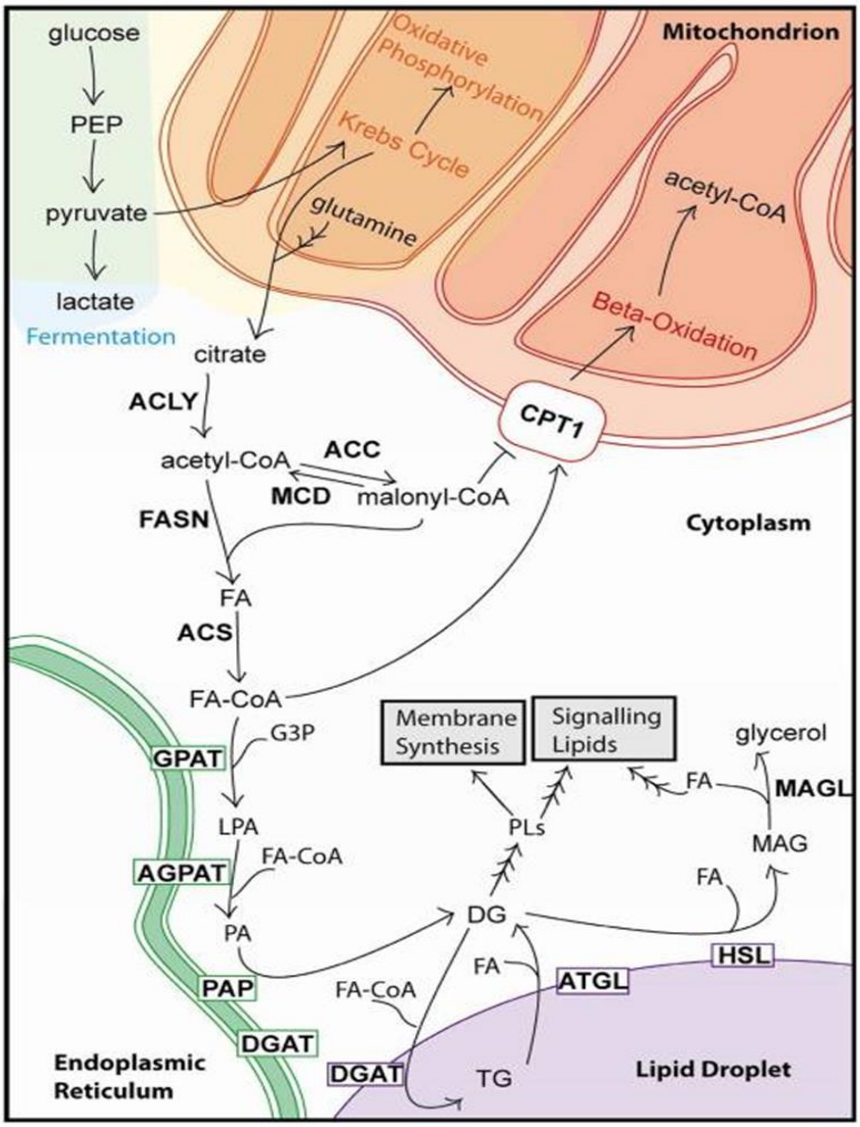

Figure 1.5. Overview of fatty acid synthesis, β-oxidation and lipid droplet metabolism. Cytosolic citrate is converted into acetyl-CoA by ACLY. These units are either converted into malonyl-CoA by acetyl-CoA carboxylases (ACCs) or combined with malonyl-CoA to produce fatty acids (FA) in a reaction catalysed by FASN. Fatty acids are then activated by ACS and channelled into the Kennedy or glycerol-phosphate pathway to form triacylglycerol (TG) for storage within lipid droplets. Diacylglycerols (DG) formed within this pathway can be utilised to make phospholipids (PLs) or converted into monoacylglycerol to recycle into glycerol. Fatty acyl-CoA (FA-CoA) units also provide an energetic substrate through β-oxidation following transport into mitochondria via CPT1. Abbreviations: MCD – malonyl-CoA decarboxylase; GPAT – glycerol-3-phosphate acyltransferase; AGPAT – acylglycerolphosphate acyltransferase; PAP – phosphatidic acid phosphohydrolase; DGAT – diacylglycerol acyltransferase; ATGL – adipose triglyceride lipase; HSL – hormone sensitive lipase; MAGL – monoacylglycerol lipase; LPA – lysophosphatidic acid; PA – phosphatidic acid. Figure taken directly from Currie et al. (2013).

1.5.5. Metabolic plasticity, stress adaptation and intratumour metabolic heterogeneity

The capacity of cancer cells to display metabolic plasticity has confounded efforts to target tumour metabolism and improve survival outcomes. Glucose deprivation in MYC-overexpressing Burkitt lymphoma cells caused glutamine-mediated anapleurosis of TCA cycle metabolites (Le *et al.*, 2012). Similarly, simulation of glucose withdrawal using the glycolysis inhibitor, 2-deoxyglucose, increased the activity of glutamate dehydrogenase (GDH), which catalyses the conversion of glutamine-derived glutamate into αKG (Yang *et al.*, 2009). Deprivation of glutamine itself also elicits several metabolic adaption strategies. Synthesis of the non-essential amino acid, asparagine, prevents glutamine withdrawal-induced apoptosis (Zhang *et al.*, 2014), forming the basis of L-asparaginase treatment seen in paediatric leukaemia and GBM (Panosyan *et al.*, 2014). A novel compensatory response by Ras-transformed cancer cells is the induction of macropinocytosis to obtain glutamine and other amino acids from internalised extracellular proteins (Commisso *et al.*, 2013). Activated Ras also provides nutrients through autophagy leading to replenishment of TCA cycle metabolites, control of lipid pools via fatty acid oxidation, and removal of non-functional mitochondria (J. Y. Guo *et al.*, 2011; Guo *et al.*, 2013). Adaptation to stress imposed by reactive oxygen species under hypoxic conditions is mediated through the AMPK-LKB1 axis in cancer (Shackelford and Shaw, 2009). AMPK negatively regulates the Warburg effect and can inhibit fatty acid synthesis through acetyl-CoA carboxylases, ACC1 and ACC2, to conserve NADPH levels under redox stress (Jeon, Chandel and Hay, 2012; Faubert *et al.*, 2013).

Metabolic pressures within the tumour microenvironment can select for cancer cells with a genotype amenable to survival. Glucose deprivation of colon cancer cells with wild-type *KRAS* alleles led to selection of cells with high levels of GLUT1, with 4% of these survivors acquiring a non-parental *KRAS* mutation (Yun *et al.*, 2009). Whilst the metabolic microenvironment of the tumour can influence the evolution of the genetic landscape, driver mutations and tissue of

origin can dictate whether tumours will be glycolytic or glutaminergic in nature (Yuneva *et al.*, 2007). This was evident in isogenic clonal populations of glioma-initiating cells which showed that early metabolic characteristics persisted into the late stages of tumourigenesis (Saga *et al.*, 2014; Shibao *et al.*, 2017). However, given the intratumour genetic heterogeneity observed broadly across all cancer types, it is not inconceivable that this would manifest phenotypically as spatial metabolic heterogeneity. Strong evidence in support of this has been obtained through mass spectrometric analysis in lung cancer and kidney cancer (Hensley *et al.*, 2016; Okegawa *et al.*, 2017). In glioma, preliminary investigations using concentric regions of tumour tissue identified significantly higher mitochondrial respiratory activity and fewer antioxidant systems in the periphery compared to the tumour centre (Santandreu *et al.*, 2008). The presence of subclones with different metabolic preferences and the ability of cancer cells to alter metabolism following stress insult has precluded successful implementation of single agents targeting one aspect of cancer metabolism, thus requiring the identification of metabolic escape mechanisms and the implementation of combined therapeutic strategies aimed at disrupting multiple metabolic requirements of cancer cell proliferation.

1.6. Cholesterol metabolism in cancer

Cholesterol is a major structural constituent of mammalian cell membranes. By occupying the spaces between sphingolipids (sphingomyelin and glycosphingolipids), cholesterol condenses the packing of membrane molecules to form liquid-ordered domains called lipid rafts (Simons and Ikonen, 2000). A link between cholesterol metabolism and cancer has long been established following the identification of low high-density lipoprotein (HDL) levels in cancer patients (Ho *et al.*, 1978; Vitols *et al.*, 1984, 1990) and high cholesterol content within tumour membranes (Elegbede *et al.*, 1986). The following sections review the mechanisms maintaining cholesterol homeostasis which are often hijacked by cancer cells to fuel tumour growth (Clendening, Pandyra, Boutros, *et al.*, 2010; Llaverias *et al.*, 2011).

1.6.1. *De novo* cholesterol synthesis

Endogenous synthesis of cholesterol occurs via the mevalonate pathway as depicted in Figure 1.6. The initial reaction between acetyl-CoA and acetoacetyl-CoA producing 3-hydroxy-3-methylglutaryl (HMG)-CoA is catalysed by HMG-CoA synthase 1 (HMGCS1). HMG-CoA is then converted into mevalonate by HMG-CoA reductase (HMGCR) in the rate-limiting step of the pathway. Additional enzyme-catalysed reactions generate intermediates used to synthesise fundamental end-products including isoprenoids, dolichol, ubiquinone, and isopentenyl adenine (Goldstein and Brown, 1990). High expression of HMGCR and other mevalonate pathway genes has been associated with a poor prognosis in a meta-analysis of primary breast cancer. Indeed, ectopic expression of HMGCR in mouse embryonic fibroblast cells was shown to cooperate with RAS to promote foci formation in classic transformation experiments. Although this suggests that HMGCR can contribute to transformation, questions remain as to whether dysregulation of HMGCR and the mevalonate pathway is a consequence rather than a cause of aberrant cancer growth (Clendening, Pandyra, Boutros, *et al.*, 2010).

1.6.2. Cholesterol uptake and efflux

Much of the cholesterol needs of peripheral tissues is met by the uptake and distribution of dietary cholesterol via lipoprotein carriers within the bloodstream. This reduces energy expenditure on *de novo* biosynthesis of cholesterol. Circulating low-density lipoproteins (LDLs) are incorporated into cells via receptor-mediated uptake (Figure 1.6) by members of the LDL receptor (LDLR) family (Brown and Goldstein, 1986). Although the blood-brain barrier prevents the transfer of low-density lipoproteins into the CNS, some of the smaller HDL particles traverse into the brain. In addition, astrocytes synthesise apolipoprotein E (ApoE)-containing HDLs to distribute cholesterol within the CNS (Wang and Eckel, 2014). In health, LDL-derived cholesterol initiates feedback mechanisms to maintain cholesterol homeostasis through suppression of HMGCR and LDLR transcription via the sterol regulatory element-binding protein (SREBP) pathway and the activation of ACAT to store

excess free cholesterol in esterified form within lipid droplets (Brown and Goldstein, 1999; Goldstein and Brown, 2009). GBMs display higher LDLR protein levels compared to normal brain concomitant with lower levels of HMGCS1 and HMGCR expression, indicating that lipoprotein uptake is the main mechanism by which this tumour type meets its cholesterol requirements (Villa *et al.*, 2016). Furthermore, interference of GBM lipid storage through inhibition of SOAT1, the key enzyme mediating cholesterol esterification into lipid droplets, suppresses tumour growth and prolongs survival in xenograft models (Geng *et al.*, 2016), highlighting a metabolic vulnerability within GBM.

Cholesterol levels within peripheral tissues are also controlled through efflux in a process called reverse cholesterol transport to prevent the toxic accumulation of free cholesterol. This process is mediated by transporters of the ATP-binding cassette (ABC) superfamily. ABCA1 initiates cholesterol efflux by shuttling cholesterol to lipid-poor ApoA-I leading to discoid HDL formation which is ultimately returned to the liver for excretion as bile (Vedhachalam *et al.*, 2007). ABCG1 cooperates with ABCA1 to facilitate the maturation of nascent HDL particles through the addition of cellular lipids (Kennedy *et al.*, 2005; Phillips, 2014). Control of *de novo* biosynthesis, uptake, and efflux are intricately linked through a series of protein sensors and transcription factors which are discussed next.

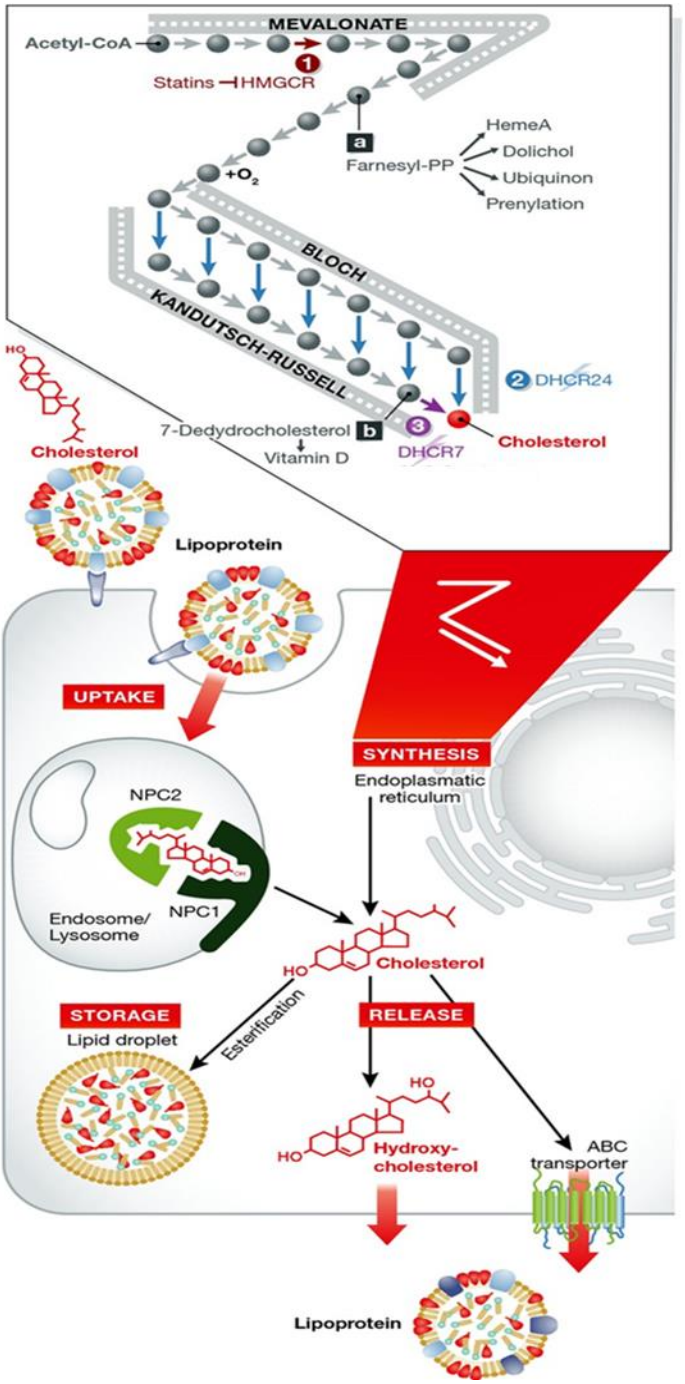

Figure 1.6. Sources of cellular cholesterol. Cells can obtain cholesterol through de novo synthesis. Acetyl-CoA is shuttled into the mevalonate pathway and through a series of enzymatic reactions (including HMGCR) lanosterol is produced. Pathway intermediate farnesyl-pyrophosphate (PP) is a precursor for other biologically active molecules. Lanosterol is then fed into either the Bloch or Kandutsh-Russell pathways, both of which produce cholesterol as the end product but generate C24 double-bond reduced cholesterol at different steps. Cholesterol uptake from the environment is achieved through receptor-mediated endocytosis of lipoproteins to the endosomal/lysosomal compartment, within which Niemann-Pick Type Protein (NPC)1 and 2 mediate the release of cholesterol into the intracellular pool. Cholesterol overload is prevented by storage of excess in lipid droplets, conversion into membrane-permeable oxysterols, or transfer to lipoproteins via ABC transporters. Figure taken directly from Martín, Pfrieger, & Dotti (2014).

1.6.3. Regulation of intracellular cholesterol levels

Cholesterol regulation is mediated at one level by SREBPs bound to the ER membrane (Brown and Goldstein, 1997). Under high sterol conditions, binding of sterols to the sterol-sensing domain of the SREBP-cleavage activating protein (SCAP) leads to retention of SREBPs within the ER via association with insulin-induced gene 1/2 proteins (INSIG1/2) (Goldstein, DeBose-Boyd and Brown, 2006). However, under low sterol conditions or statin-induced inhibition of HMGCR, conformational changes within SCAP cause the translocation of SREBPs to the Golgi where site-1 and -2 proteases cleave SREBPs into their active form (Brown and Goldstein, 1999). Mature SREBP(s) enters the nucleus and induces the transcription of genes containing sterol response elements, including HMGCR and LDLR (Clendening and Penn, 2012). The turnover of HMGCR is also directly regulated by cholesterol as detection of sterols by its sterol-sensing domain leads to binding of INSIG1/2 followed by ubiquitination and degradation (Sever *et al.*, 2004; DeBose-Boyd, 2008).

An additional layer of cholesterol control is mediated through liver X receptors (LXRs), members of the nuclear receptor superfamily of ligand-activated transcription factors (Lin and Gustafsson, 2015). Two LXR isoforms have been identified: LXRβ is ubiquitously expressed whereas LXRα is selectively expressed within metabolically active tissues (Apfel *et al.*, 1994; Willy *et al.*, 1995). LXRs form heterodimers with retinoid X receptors (RXRs) (Repa, Turley, *et al.*, 2000) and are activated by oxysterols, including 24S-hydroxycholesterol (24-OHC), 25-hydroxycholesterol (25-OHC) and 27-hydroxycholesterol (27-OHC) (Janowski *et al.*, 1996; Chen *et al.*, 2007). LXR/RXR heterodimers bind to LXR responsive elements consisting of two 5'-AGGTCA-3' hexameric half-sites separated by a four-nucleotide spacer (DR4 motif) (Apfel *et al.*, 1994; Willy *et al.*, 1995). Upon ligand binding, transcriptional corepressors and coactivators are recruited to facilitate histone modification and chromatin remodelling (Lin and Gustafsson, 2015). Genes targeted for transcription by LXRs include the cholesterol exporters ABCA1 (Venkateswaran *et al.*, 2000), ABCG1 (Kennedy *et al.*, 2005), ABCG5, and ABCG8 (Repa *et al.*, 2002). Complementary to this, LXRs

modulate lipoprotein metabolism by upregulating the inducible degrader of LDLR (IDOL), an E3 ubiquitin ligase that targets LDLR for degradation (Zelcer *et al.*, 2009), as well as lipoprotein lipase (LPL) and phospholipid transfer protein (PLPT) which co-ordinately promote the maturation of HDL particles involved in reverse cholesterol transport (Zhang *et al.*, 2001; Laffitte *et al.*, 2003). Ligand binding to LXRs also shifts the utilisation of acetyl-CoA from *de novo* cholesterol to fatty acid synthesis through transcriptional upregulation of SREBP-1c (Repa, Liang, *et al.*, 2000), FASN (Joseph, Laffitte, *et al.*, 2002), and SCD1 (Chu *et al.*, 2006). Figure 1.7 displays a simplified overview of cholesterol regulation in response to high or low intracellular sterol levels.

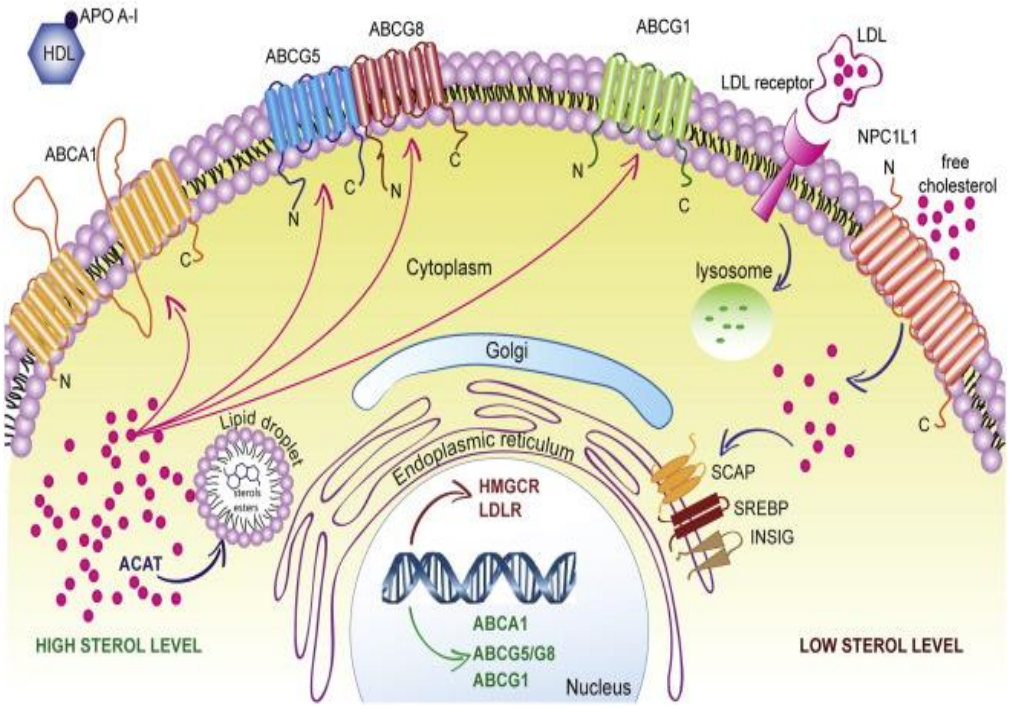

Figure 1.7. Mechanisms of intracellular cholesterol homeostasis. Low intracellular levels of cholesterol cause migration of the SCAP-SREBP complex to the Golgi apparatus where mature SREBP is released upon proteolytic cleavage. SREBP induces *de novo* cholesterol synthesis via HMGCR and Niemann Pick C1-like 1 (NPC1L1)- or LDLR-mediated uptake of cholesterol-containing lipoproteins. NPC1L1 is associated with cholesterol absorption at the brush border membrane of enterocytes. High intracellular levels of cholesterol activate LXR transcriptional activity leading to the upregulation of cholesterol exporters, including ABCA1, ABCG1, and ABCG5/8. Figure taken directly from Bovenga, Sabbà, & Moschetta (2015).

Feedback regulation of cholesterol biosynthesis is mediated by oxysterols rather than cholesterol. Oxysterols increase cholesterol efflux and decrease uptake through the respective transcriptional activity of LXRs and SREBPs, prevent *de novo* cholesterol synthesis through HMGCR, and increase cholesterol esterification and storage (Du, Pham and Brown, 2004; Lin and Gustafsson, 2015). In proliferating cells or under conditions of low sterol availability, oxysterols are inactivated by sulfation via SULT2B1b (Chen *et al.*, 2007), which increases the polarity of oxysterols and facilitates cellular removal via ABCC1 (Bovenga, Sabbà and Moschetta, 2015). In GBM, significantly reduced levels of several oxysterols, including 24-OHC and 27-OHC, were identified in conjunction with low expression of oxysterol-synthesising enzymes. Comparison with normal brain revealed a near 10-fold reduction of CYP46A1, the main enzyme mediating oxysterol synthesis in the brain. Oxysterol catabolism is also deregulated in GBM as shown by higher protein levels of HSD3B7, which breaks down oxysterols, thus providing GBM access to a large supply of cholesterol to maintain tumour growth (Villa *et al.*, 2016).

1.7. Targeting cholesterol metabolism in cancer

1.7.1. Inhibition of *de novo* cholesterol synthesis using statins

Cancer cells can synthesis cholesterol via the shuttling of acetyl-CoA into the mevalonate pathway. The cholesterol–lowering statins were initially identified in a screen for microbial metabolites capable of inhibiting HMGCR, the enzyme responsible for catalysing the rate-limiting step in the mevalonate pathway (Endo, Kuroda and Tanzawa, 1976). Analogs of the original compound, mevastatin, were soon developed and approved for clinical use in the treatment of hypercholesterolemia and chronic heart disease (Endo, 1992). Later studies on cancer cells soon revealed the anti-proliferative effects of statins via cell-cycle arrest or induction of apoptosis. Rao and colleagues (1998) demonstrated cell-cycle arrest in the G1 phase following lovastatin treatment in both normal and tumour breast cell lines resulting from the redistribution of the cyclin-dependent kinase inhibitors (CKIs) p21 and p27 from CDK4 to CDK2

following a decrease in CDK4 protein levels (Rao *et al.*, 1998). The induction of apoptosis by statins appears to be tumour-dependent and influenced by a pre-existing dysregulation of the mevalonate pathway. In multiple myeloma, only tumour cells with deficient upregulation of HMGCR and HMGCS in response to statin exposure demonstrated sensitivity to treatment (Clendening, Pandyra, Li, *et al.*, 2010). The upstream responses leading to apoptosis may include reduced pro-growth and survival signalling from isoprenylated proteins, including RAS and RHO GTPases, due to insufficient levels of the isoprenoids geranylgeranyl pyrophosphate and farnesyl pyrophosphate used for isoprenylation (Wong *et al.*, 2007).

Several large-scale epidemiological studies have supported the cancer-preventative effects of statins (Clendening and Penn, 2012). In glioma, a case-control study conducted in Denmark revealed that long-term (5+ years) use of statins was associated with a reduced glioma risk in men and women compared to non-users, particularly within the ≤60 years age group (Gaist *et al.*, 2013). Contradictory evidence from a UK-based study did not find an inverse association between statin use and glioma risk (Seliger *et al.*, 2016). From an *in vitro* perspective, Yanae and colleagues (2011) demonstrated the cytotoxicity of statins in C6 glioma cells associated with decreased phosphorylation of ERK and AKT following reduced synthesis of geranylgeranyl pyrophosphate (Yanae *et al.*, 2011). Contrary to this, EGFRvIII-expressing GBM cells were shown to be relatively unaffected upon exposure to either lovastatin or atorvastatin compared to normal human astrocytes, a finding supported by lower expression levels of HMGCS1 and HMGCR in GBM compared to normal brain tissue (Villa *et al.*, 2016). In addition, high-dose simvastatin treatment in a GBM mouse model prevented tumour vessel normalisation by reducing the number of pericytic cells along blood vessel walls (Bababeygy *et al.*, 2009). Therefore, several questions remain regarding the use of statins as a preventative or curative treatment approach in glioma.

1.7.2. Regulation of cholesterol influx and efflux using LXR agonists

LXR agonists were initially developed to treat dyslipidaemias related to atherosclerosis and cardiovascular disease (Hong and Tontonoz, 2014). The first synthetic LXR agonist to be developed was T0901317, which predominantly targets the LXRα isoform (Schultz *et al.*, 2000). Application within *in vitro* and *in vivo* models of prostate cancer demonstrated the inhibitory effects of T0901317 on cell proliferation and tumour growth that was dependent upon increased p27 levels at the protein but not mRNA level (Fukuchi *et al.*, 2004). The posttranslational upregulation of p27 by T0901317 is likely mediated through downregulation of the S-phase kinase-associated protein 2 (SKP2), a component of the SCF ubiquitin ligase complex (Hao *et al.*, 2005; Egozi *et al.*, 2007). Indeed, T0901317 reduced SKP2 protein levels in a dose-dependent manner in LNCaP sublines resulting in a reduced percentage of cells in S-phase (Fukuchi *et al.*, 2004). High doses of T0901317 applied to ovarian carcinoma cell lines induced caspase-3/7 activity and increased the percentage of cells in the G_0/G_1-phase, concomitant with higher p21 and p27 protein levels and decreased Rb phosphorylation at $Ser^{807/811}$ (Rough *et al.*, 2010). The anti-proliferative effects of T0901317 have also been shown to be mediated in part through the downstream consequences of cholesterol efflux mediated through upregulation of either ABCA1 or ABCG1 (Fukuchi *et al.*, 2004; Pommier *et al.*, 2010). Through atomic force microscopy, Pommier and colleagues demonstrated a reduction in lipid raft width and height in T0901317-treated LNCaP cells leading to reduced phosphorylation of membrane-localised AKT, an effect rescued by the addition of cholesterol to the growth medium (Pommier *et al.*, 2010). However, the use of T0901317 as an investigative tool in the therapeutic targeting of LXRs has been confounded by the identification of the farnesoid X receptor (FXR; NR1H4) and the pregnane X receptor (PXR; NR1I2) as additional targets for ligand binding and activation (Schultz *et al.*, 2000; Houck *et al.*, 2004; Rough *et al.*, 2010).

The need for more selective LXR agonists led to the development of GW3965, a full agonist of LXRα and LXRβ (Collins *et al.*, 2002). Treatment of the HT29

colon cancer cell line with GW3965 increased the percentage of cells in G1 phase in conjunction with reduced cyclin D1 and Skp2 protein levels and increased p21 and p27 levels at the transcript and protein level, respectively (Lo Sasso *et al.*, 2013). The downregulation of genes associated with cell proliferation in response to LXR agonists may be mediated in part through the E2F family of transcription factors. In cell line models of breast cancer, genes downregulated following GW3965 treatment demonstrated a significant over-representation of promoter regions belonging to the E2F family of transcription factors, consistent with an observed decrease in E2F2 and E2F7 transcript levels. However, no LXRE was located within the regions proximal to the E2F2 gene, indicating that regulation of E2F2 by LXRs may occur via an indirect mechanism (Nguyen-Vu *et al.*, 2013). A novel tumour suppressive mechanism mediated via the tumour stroma was demonstrated in GW3965-treated melanoma. GW3965 inhibited metastatic melanoma invasion and reduced endothelial recruitment in an LXRβ-dependent manner via ligand-induced transcription and secretion of ApoE from tumour as well as stromal cells including macrophages, leukocytes, and endothelial cells (Pencheva *et al.*, 2014). Pencheva and colleagues had previously demonstrated the anti-metastatic properties of secreted ApoE mediated through the LRP1 and LRP8 receptors on melanoma and endothelial cells, respectively (Pencheva *et al.*, 2012).

Besides a cell-cycle regulatory role, LXR agonists can affect tumour cell viability and proliferation through modulation of cholesterol and lipid metabolism (Lin and Gustafsson, 2015). GBM cells expressing a constitutively active EGFR receptor (EGFRvIII) demonstrate increased PI3K pathway activation leading to downstream SREBP-1 cleavage and expression of LDLR, which results in a metabolic dependence on lipoproteins for cell survival and proliferation (Guo *et al.*, 2009). GW3965 induced the expression of the cholesterol exporter ABCA1 and caused IDOL-mediated degradation of LDLR in U87-EGFRvIII xenografts leading to 59% inhibition of tumour growth and a 25-fold increase in apoptosis (D. Guo *et al.*, 2011). Particularly pertinent in the treatment of CNS

tumours is the hurdle of overcoming the blood-brain barrier (Banks, 2016). The partial LXRα/full LXRβ agonist LXR-623 has shown evidence of brain penetrance and demonstrated a therapeutic response against EGFRvIII-expressing GBM cells with little to no effect on the viability of NHAs. LXR-623 increased ABCA1 and IDOL expression and reduced LDLR protein levels in U87EGFRvIII cells leading to reduced LDL uptake and enhanced cholesterol efflux (Villa *et al.*, 2016). The studies above indicate that LXR agonists can target several hallmarks of cancer including cell cycle regulation, cellular metabolism, tumour angiogenesis and the stromal compartment (Figure 1.8), highlighting the need for further drug development and clinical trials of this class of compounds across several cancer types.

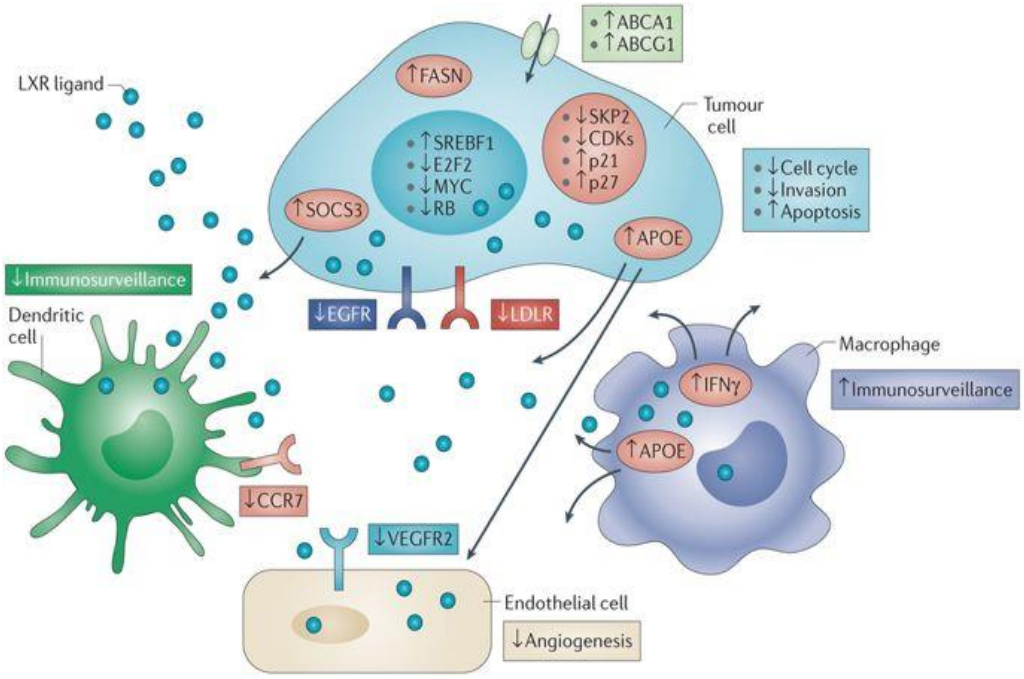

Figure 1.8. Current understanding of the anticancer therapeutic properties of LXR agonists. Activation of LXR transcriptional activity causes cell cycle arrest due to reduced expression of cyclin-dependent kinases (CDKs) and SKP2, which results in higher levels of p21 and p27. In addition to changes to cholesterol-related gene expression, increased expression of SREBF1 leads to higher FASN levels, causing lipotoxicity and the negative side-effect of steatosis. In melanoma, induced expression of APOE decreases invasive potential. Levels of the suppressor of cytokine signalling 3 (SOCS3) involved in the regulation of inflammation are upregulated in prostate cancer following LXR activation. LXR agonists may have both positive and negative consequences on immune surveillance following increased interferon-ɣ (IFNɣ) expression by macrophages and T-cells, and reduced C-C chemokine receptor 7 (CCR7) expression in maturing dendritic cells. Image taken directly from C.-Y. Lin & Gustafsson (2015).

1.8. Analytical profiling of tumour metabolism

The initial investigations into tumour metabolism utilised simple chemical procedures to investigate single metabolites or broad classes of cholesterol and lipids species. The molecular complexity of metabolites and lipids has required the development of instruments capable of delineating species in terms of nuclear magnetic resonance or mass-to-charge ratios, in combination with separation techniques to aid the identification and profiling of the thousands of compounds observed within intermediary metabolism. Progress in "molecular imaging" methods has also enabled the visualisation and measurement of metabolic processes in a spatial context which maintains the structural architecture of tissues, allowing delineation of cancers from normal tissue and compartmentalised read-outs of tumour metabolism within localised microenvironments. This section briefly reviews the technologies available to profile tumour metabolism and outlines the biological information that can be obtained through their use.

1.8.1. Positron emission tomography

Positron emission tomography (PET) images positron-emitting radionuclides that are injected into patients or animals. Spatial aspects of metabolism can be obtained when PET is combined with x-ray CT imaging (Kurhanewicz *et al.*, 2011). [^{18}F]-fluoro-2-deoxyglucose (FDG) is the most commonly used PET tracer since it exploits the high glycolytic rate often displayed by tumours. It is mainly used as a diagnostic tool to stage disease and monitor treatment response but is also used in a laboratory setting to evaluate the efficacy of metabolism-targeting agents (Wei *et al.*, 2008). Other radionuclides tested in brain cancer include tracers for amino acid metabolism (e.g. [^{11}C]methionine, 4-18F-(2S,4R)-fluoroglutamine (Venneti *et al.*, 2015)), DNA synthesis ([^{18}F]fluorothymidine), membrane biosynthesis ([^{18}F]fluorocholine), and hypoxia ([^{18}F]fluoro-misonidazole) (La Fougère *et al.*, 2011).

1.8.2. Nuclear magnetic resonance spectroscopy

Nuclear magnetic resonance spectroscopy uses radiofrequency (RF) waves to probe nuclei that possess magnetic spin, considered to arise from the spinning motion of its electrical charge. 'Spin states' refers to different nuclear energy levels. ^{1}H and ^{13}C nuclei only have two spin states called + ½ ('spin up') and – ½ ('spin down'), whereas 'quadrupolar' nuclei, such as ^{2}H, ^{18}O, and ^{23}Na, have spins > ½. Irradiation of magnetic nuclei with RF waves changes the spin state from the ground state into a higher energy spin state. 'Relaxation' of the magnetic nuclei back to the ground state releases RF waves, which are detected by a radiofrequency coil placed inside the spectrometer. By measuring four parameters of the emitted RF waves – intensity, frequency, relaxation, and phase – NMR can be used to determine chemical and protein structures and its sensitivity enables the detection of molecular interactions, such as occurs between proteins and ligands. Measured resonances are expressed as a chemical shift relative to a standard, such as tetramethylsilane (TMS) in organic solvents and 2,2-dimethyl-2-silapentane-5-sulfonic acid (DSS) in aqueous applications, with units of parts per million (Bothwell and Griffin, 2011).

^{1}H- and ^{13}C-NMR spectroscopy are frequently used in biological investigations of metabolism, particularly in metabolomics studies of altered central carbon metabolism (Markley *et al.*, 2017). ^{31}P-NMR spectroscopy has been utilised to distinguish between phosphocreatine, inorganic phosphate, and ATP. Inorganic phosphate exists either as muscle phosphate ($H_2PO_4^-$) or orthophosphate (HPO_4^{2-}) depending on pH, and therefore equilibrium concentrations can be used to measure pH changes (Bothwell and Griffin, 2011). Phosphate groups have also been investigated within phospholipids by ^{31}P-NMR spectroscopy in order to elucidate total phospholipids (except phosphatidylcholine) and phosphatidylcholine in brain tumours (Srivastava *et al.*, 2010). Other aspects of biology have been examined using alternate magnetic nuclei, including the use of deuterium oxide ($^{2}H_2O$) as a blood flow and tissue perfusion tracer (Ackerman *et al.*, 1987) and ^{15}N-labelled substrates to examine nucleotide and amino acid metabolism (Tardito *et al.*, 2015). Unlike mass spectrometry-based

metabolism studies, NMR has the added benefit of being able to be utilised in real-time to study metabolism *in vivo* (Bastawrous *et al.*, 2018).

1.8.3. Stable-isotope resolved metabolomics

Stable isotope-resolved metabolomics (SIRM) utilises isotopically enriched metabolic substrates to trace their consumption in living systems. Stable isotopes are non-radioactive and include ^{2}H, ^{13}C, or ^{15}N. Crude extracts from living systems containing isotopically labelled metabolites are analysed by either mass spectrometry (MS) or NMR spectroscopy. MS readily determines the number of heavy atoms (isotopologues) incorporated and is often used orthogonally with gas and liquid chromatography methods to resolve large numbers of metabolites. Although ultra-high resolution Fourier-transform MS can resolve non-isomeric metabolites without chromatography, NMR spectroscopy is better suited to determine positional labelling within isotopomers (Bruntz *et al.*, 2017). [$^{13}C_6$]Glucose is a relatively inexpensive tracer used to follow labelling within glycolysis and in other pathways using glycolysis-derived precursors (Sellers *et al.*, 2015). However, glycolytic flux is better resolved using glucose tracers labelled at $^{13}C_1$-2 or $^{13}C_1$-3. [$^{13}C_6$]Glucose also provides maximal labelling of intermediates within the PPP (Bruntz *et al.*, 2017). However, the oxidative and non-oxidative branches of the PPP are better resolved using [$^{13}C_2$-1,2]glucose, which can also be used to estimate PPP activity using the ratio of [$^{13}C_1$-3]lactate to [$^{13}C_2$-2,3]lactate (Ying *et al.*, 2012).

Activity within the TCA cycle can be investigated using ^{13}C-labelled glucose or glutamine (Son *et al.*, 2013; Davidson *et al.*, 2016). [$^{13}C_6$]Glucose enters the TCA cycle as [$^{13}C_2$]acetyl-CoA via pyruvate dehydrogenase and condenses with oxaloacetate to [$^{13}C_2$]citrate in the first round or [$^{13}C_4$]citrate in the second round of the TCA cycle. [$^{13}C_3$]- and [$^{13}C_5$]citrate isotopologues occur following carboxylation of [$^{13}C_3$]pyruvate with unlabelled carbon dioxide and condensation of the resulting [$^{13}C_3$]oxaloacetate with either unlabelled or [$^{13}C_2$]acetyl CoA. The contribution of pyruvate to the TCA cycle via carboxylation alone can be traced using [$^{13}C_2$-3,4]glucose that generates [$^{13}C_1$]pyruvate.

Oxidative and reductive glutamine metabolism can both be monitored using [$^{13}C_5$]glutamine or separately using [$^{13}C_1$]- and [$^{13}C_5$]glutamine, respectively. Oxidation of [$^{13}C_5$]glutamine generates [$^{13}C_4$]succinate, -fumarate, -malate, and -oxaloacetate through the first turn of the TCA cycle, whereas reductive carboxylation of this tracer generates [$^{13}C_5$]citrate that subsequently produces [$^{13}C_3$]oxaloacetate, -malate, and -fumarate (Bruntz *et al.*, 2017). Tracing the ^{15}N isotope also enables measurement of the contribution of glutamine to the synthesis of amino acids and nucleotides (DeBerardinis *et al.*, 2007). Other isotopic tracers used in biological investigations include [^{13}C]serine (Cowin *et al.*, 1996), [^{13}C]glycerol (Qi *et al.*, 2012), and ^{13}C-labelled fatty acids (Kasumov *et al.*, 2005).

1.8.4. Coupled chromatography-mass spectrometry

Mass spectrometry (MS) coupled with chromatographic separation techniques has the capacity to profile thousands of metabolites and lipid species, providing much broader coverage of the metabolome and lipidome compared to ^{1}H-NMR spectroscopy. In this technique, gas or liquid chromatography (LC) is performed initially to separate volatile and non-volatile samples, respectively (Wang *et al.*, 2015). Separated compounds are then ionised and identified based on label-free measurement of mass-to-charge (*m/z)* ratios (Lietz, Gemperline and Li, 2013). Several ionisation techniques have been developed based on the desired application, including electrospray ionisation (ESI), atmospheric chemical ionisation (ACPI), desorption electrospray ionisation (DESI), and matrix-assisted laser desorption/ionisation (MALDI) (Awad, Khamis and El-Aneed, 2015). In ESI, samples in solution are sprayed out into the ionisation source from a spray needle/capillary with a high voltage applied to produce charged droplets, a process called nebulisation. Sheath gas directs the droplets from the capillary tip through a curtain of heated inert gas, such as nitrogen, or a heated capillary to mediate solvent evaporation (Gaskell, 1997). DESI was introduced by Takats and colleagues as an ambient ionisation method that can profile the surface of tissue samples at atmospheric pressure with little to no sample preparation. Ionisation is mediated by charged microdroplets that are carried to the target

surface as part of a fast nebulising gas jet propelled from a high-voltage needle (Takáts *et al.*, 2004). Through an ESI mechanism or heterogeneous charge transfer, molecules from the target surface are ionised and desorbed into a heated capillary leading to a mass spectrometer (Lietz, Gemperline and Li, 2013).

There are different varieties of mass analyser used in metabolomics studies. Quadrupoles are the simplest and consist of four parallel metal rods that filter mass ions in response to a direct current (DC) voltage. By linearly arranging three quadrupole cells, triple quadrupole or QQQ mass analysers were developed which have tandem-MS capabilities, meaning that compound structures can be elucidated through collision-induced decomposition (CID) and detection of the daughter fragments. Time-of-flight (TOF)/MS analysers are based upon the relationship between ion mass and flight velocity along a flight tube leading to different arrival times at the detector (Guilhaus, Mlynski and Selby, 1997). Combining TOF/MS with a quadrupole mass analyser produces the instrument known as quadrupole-time of flight (Q-TOF)/MS with tandem-MS capabilities (Allwood and Goodacre, 2010). To enable detection of low abundance ions, trap-based mass analysers were developed which permit sequential MS (MS^n) by the trapping and re-trapping of mass ions between three electrodes: two hyperbolic metal electrodes with their foci facing each other and a hyperbolic ring electrode positioned half-way between them (Allwood and Goodacre, 2010). In Orbitrap instruments, *m*/*z* ratios are measured as a function of ion frequency during oscillatory motion using a Fourier transformation (Savaryn, Toby and Kelleher, 2016).

1.9. NMR- and MS-based metabolomics analysis of gliomas

Despite only detecting a limited coverage of the metabolome, ^{1}H-NMR spectroscopy can detect distinct metabolic profiles from several CNS tumours, including meningiomas, neuroblastomas, and GBMs (Florian *et al.*, 1995), as well brain metastases (Möller-Hartmann *et al.*, 2002). NMR profiles

characteristic of GBMs include lower myoinositol (MI)/creatine (Cr) and Cr/choline (Cho) ratios in GBMs compared to normal brain (Castillo, Smith and Kwock, 2000; Howe *et al.*, 2003). Interestingly, N-acetyl-aspartate (NAA)/Cr and NAA/Cho levels fall from the tumour periphery to the tumour core and are lower in comparison to normal brain (Goebell *et al.*, 2006). Even further out into contralateral brain, levels of MI and glutamine are increased which is suggestive of mild astrocytosis and early neoplastic infiltration (Kallenberg *et al.*, 2009). Early evidence of intratumour metabolic heterogeneity was provided by Li and colleagues who identified voxels with different values of several metabolic indices based on Cho, Cr, NAA, lactate, and lipid levels (Li *et al.*, 2002).

^{1}H-NMR has also been used to profile lipids and cholesterol species in gliomas. Compared to normal brain, gliomas demonstrated higher total cholesterol content (cholesterol esters and free cholesterol) and triglyceride levels (Srivastava *et al.*, 2010). Tugnoli and colleagues attributed the presence of cholesterol esters and triglycerides within glioma tissue to neovascularisation processes since they positively correlate with lipid extracts taken from human blood. Interestingly, GBMs featured higher quantities of choline-containing phospholipids, including phosphatidylcholine and sphingomyelin, compared to normal brain tissue (Tugnoli *et al.*, 2001), likely reflecting changes to membrane structure due to aberrant biosynthetic and catabolic reactions. These studies demonstrate the versatility of ^{1}H-NMR for classification purposes and as a tool to probe tumour metabolism, particularly when stable isotopic substrates are utilised. However, the drawback to this technique is the poor coverage of the metabolome and lipidome which limits extensive evaluation of tumour metabolism.

An ultrahigh performance liquid chromatography/tandem mass spectrometry (UHPLC/MS-MS)-based metabolomics study of gliomas was performed by Chinnaiyan and colleagues, leading to the identification of three metabolic subgroups: (1) *energetic* – this subgroup displayed a classic glycolytic profile

with accumulation of upstream intermediates of glycolysis; (2) *anabolic* – this subgroup showed elevated levels of metabolites associated with diverted glycolytic intermediates and anabolic metabolism; and (3) *phospholipid catabolism* – this subgroup had an anabolic profile characterised by long-chain fatty acid and lysolipid catabolism. The metabolomics analysis revealed a shift from a classic glycolytic profile in grade III tumours to an anabolic profile in grade IV tumours associated with significantly reduced overall survival. Grade IV gliomas showed a decrease in overall carbohydrate levels, glycolipids, lysolipids, and sterols, in contrast to increased abundances of essential and medium chain fatty acids and metabolites associated with carnitine metabolism. There was also an accumulation of key metabolites within the pentose phosphate pathway and serine metabolism, including 6-phosphoglycerate (6-PG), ribose 5-phosphate (R5P), serine, and glycine. Interestingly, phosphoenolpyruvate (PEP) accumulation in grade IV gliomas strongly correlated with the Mesenchymal subtype, consistent with significantly reduced pyruvate kinase (PK) activity and increased PKM2 expression compared to the Proneural group (Chinnaiyan *et al.*, 2012).

Mass spectrometric analysis of the lipidome in glioma has been conducted through DESI-MS, leading to the elucidation of lipid profiles correlating with glioma subtype, histological grade, and tumour cell concentration. Lipid profiles associated with GBMs feature a high abundance of phosphatidylserine and phosphoinositol species, and can be distinguished from grade II and III astrocytomas by a lack of sulfatides. Delineation of tumour margins was also achieved as the technique was capable of distinguishing a region of GBM with nearly 100% tumour cell concentration from a region of infiltration consisting of mainly grey matter with approximately 30% tumour cell concentration (Eberlin *et al.*, 2012). Stereotactic registration of tumour samples obtained during surgery has been conducted using the neuronavigation pointer (Brainlab) to identify the sampling position on pre-operative 3D MRI. Samples obtained from the same tumour showed heterogeneity in histological grade and tumour cell concentration, with a reduced concentration of tumour cells

observed at the tumour margin. Interestingly, samples from the tumour margin were classified as grade III, whereas samples from the tumour mass were designated as grade II. In one surgical case, samples obtained at the tumour resection margin demonstrated high tumour cell concentration, indicating incomplete surgical removal and the presence of residual tumour. These preliminary studies highlight the potential of DESI-MS as an intraoperative method to characterise brain tumours in near real-time, aiding surgeons to achieve complete surgical resection and better patient outcomes (Eberlin *et al.*, 2013).

1.10. Project rationale and aims

Given the genetic basis underlying certain metabolic phenotypes, we hypothesised that ITH in GBM would manifest at the level of metabolism. Evidence of such a phenomenon has previously been highlighted in lung (Hensley *et al.*, 2016) and kidney (Okegawa *et al.*, 2017) cancers. The identification of intratumour metabolic heterogeneity in GBM would have major implications in the clinic since targeting of metabolism using single agents may have the same drawbacks as previously tested targeted agents, such as RTK inhibitors, in which redundant signalling pathways or subclonal selection allow therapies to be circumvented and resistance to develop. Therefore, there is a strong rationale to elucidate the level of intratumour metabolic heterogeneity observed in GBM. Understanding the genetic basis of such heterogeneity is important to confirm the genetic programming of metabolism, as well as to develop a means to predict metabolic phenotypes based on a genetic signature and enable patient-tailored therapeutic strategies in the clinic. We therefore aimed to characterise the level of intratumour metabolic heterogeneity in GBM using liquid chromatography-mass spectrometry (LC-MS), followed by integration with transcriptomics data to better understand gene-metabolic associations within an *in vivo* context.

Since several proliferative signalling pathways converge on a small number of metabolic pathways, including glycolysis and the TCA cycle, we predicted that

the level of heterogeneity observed at the metabolic level would not equate to the genetic complexity identified in GBM, following the basic metabolic requirements of proliferating cells in terms of anabolic substrates, energy production and balance of redox potential. Therefore, the challenges presented by the identification of intratumour metabolic heterogeneity in GBM may be overcome through the identification of metabolic pathways to which proliferating cancer cells are 'addicted' to in order to maintain survival. Determination of such a metabolic 'Achilles heel' was therefore an aim of this project, which ultimately bears more therapeutic relevance as the identification of a single agent that circumvents intratumour genetic and metabolic heterogeneity as well as displaying efficacy across a broad range of patients is highly desirable.

Chapter 2

Materials and methods

2. Materials and methods

2.1. Patient tissue sample collection for LC-MS-based metabolomic and lipidomic analyses

Patient recruitment was conducted within UK NHS Trust centres at Nottingham Queen's Medical Centre, Leicester Royal Infirmary, and Royal Derby Hospital. Recruitment was extended to international centres including Massachusetts General Hospital, Boston, USA. The study was ethically approved by the National Research Ethics Service Committee for the East Midlands, UK. Informed consent was obtained either before surgery or soon after in accordance with the Code of Practice for Research issued by the Human Tissue Authority. Consent and ethical approval for internationally obtained samples was obtained at the exporting centres. Multi-region sampling with or without 5-ALA administration was conducted on patients with suspected GBM based on clinical history and a whole batch of MRI sequences, including T1-weighted, T2-weighted, fluid-attenuated inversion recovery (FLAIR), T1-postcontrast (gadolinium), diffusion weighted, diffusion tensor imaging, perfusion imaging, and magnetic resonance spectroscopy. Intraoperative neuronavigation was conducted using T1-postcontrast scans but target selection utilised information from all other sequences. Tissue surplus to pathological confirmation of diagnosis was immediately frozen in liquid nitrogen and stored at -80°C or fixed in paraformaldehyde for research use. Clinical information pertinent to the patients utilised in this study is detailed in Table 3.1.

2.2. Tumour tissue sample preparation for LC-MS

Tumour tissue obtained from patients was initially divided into fragments using a scalpel. The cutting surface was in direct contact with a bed of dry ice to prevent tissue from thawing, a process which would allow enzymatic reactions to occur and alter/degrade metabolomic and lipidomic profiles. The wet weight of each tumour fragment was measured prior to metabolite extraction. Disruption of tissue in 100 µL of ice-cold (4°C) methanol (MeOH) of high-performance liquid chromatography (HPLC)-grade was performed using a

handheld homogeniser (Bibby Scientific Stuart; SHM1) until the disappearance of visible clumps. 300 µL of ice-cold HPLC-grade chloroform was then added to each sample and vortexed well, followed by the administration of 100 µL ice-cold HPLC-grade water and further vortexing. These steps were carried out using autoclaved 2 mL Eppendorf tubes with rounded bottoms for ease of use with the homogeniser. Samples were then centrifugated for 10 min at 13,000 x g at 4°C to separate the two phases of the extraction procedure. The upper phases containing polar metabolites were transferred into new Eppendorf tubes and stored at -80°C. By carefully displacing the protein sediments occupying the separation point between the two phases, the lower phases were transferred into fresh tubes and stored at -80°C. Since the total volume of the lower phases exceeded 200 µL, samples were dried down using a vacuum evaporator (SpeedVac; ThermoFisher Scientific) set to room temperature, followed by reconstitution in 100 µL isopropanol. Samples were then centrifugated for 10 min at 13,000 x g at a temperature of 4°C. Supernatants were carefully removed and stored in MS vials at -80°C. Prior to LC-MS analysis, MeOH/H_2O extracts were transferred into MS vials and quality controls (QCs) were prepared by pooling 5 µL from each sample.

2.3. Liquid chromatography-non-tandem mass spectrometry

The LC-MS metabolomics analysis of prepared tumour samples was conducted by Dr Dong-Hyun Kim. Metabolites in the upper phase were separated using a zwitterionic-hydrophilic interaction liquid chromatography (ZIC-pHILIC) column (150 x 4.6 mm^2, 5 µm) maintained at 45°C in a ThermoFisher Dionex UltiMate 3000 LC system (Thermo Fisher Scientific, Hemel Hampstead, UK). A linear LC gradient from 80% B to 5% B was used over 15 min followed by a 5 min wash with 5% B and 7 min re-equilibration with 80% B at a flow rate of 300 µL/min, where B was 100% acetonitrile and A was 20 mM ammonium carbonate in 18.2 MΩ water (Elga Maxima; Elga LabWater). Injection volume was set to 10 µL and samples were maintained at 4°C. MS was performed using an Orbitrap Exactive (Thermo Fisher Scientific, Hemel Hampstead, UK) with a HESI-II probe operated in a polarity switching mode and using the following settings: resolution 50,000,

AGC target: balanced, *m/z* range 70-1,400, sheath gas 40, auxiliary gas 5, sweep gas 1, probe temperature 150°C, and capillary temperature 275°C. For positive mode ionisation: source voltage +4.5 kV, capillary voltage +40 V, tube voltage +70 V, skimmer voltage +20 V. For negative mode ionisation: source voltage -3.5 kV, capillary voltage -30 kV, tube voltage -70 kV, skimmer voltage -18 kV. Mass calibration was performed before each batch. The mass range was extended to cover small metabolites by inclusion of low-mass ions to the standard Thermo calmix masses (below *m/z* 1400), $C_2H_6NO_2$ (*m/z* 76.0393) for ESI+ and $C_3H_5O_3$ (*m/z* 89.0244) for ESI-.

The LC-MS lipidomics analysis of prepared tumour samples was conducted by Dr Catherine Ortori. Lipids extracts from patient tumour tissue was initially separated using a reverse phase ACE Excel 2 C18 column 50 x 2.1 mm column equipped with the appropriate guard column and held at 50°C in an Acella modular system (ThermoFisher Scientific, Hemel Hempsted, UK) with cooled autosampler, column oven and quaternary pumps. The injection volume was set to 10 µL, with samples held at 10°C. LC mobile phases consisted of A [60% of 0.1% MS-grade ammonium acetate (final volume) in 18.2 MΩ water (Elga Maxima; Elga LabWater) with 40% acetonitrile] and B [10% of 0.1% MS-grade ammonium acetate (final concentration) in 18.2 MΩ water (Elga Maxima; Elga LabWater) with 10% acetonitrile and 80% isopropanol (MS-grade, VWR, UK]. The gradient adopted is displayed in Table 2.1. MS was performed using an Exactive Orbital ion-trap mass spectrometer (ThermoFisher Scientific, Hemel Hampstead, UK) acquiring data simultaneously in full scan ion mode (*m/z* 100-1900; resolution 25,000) in both positive and negative polarity switching modes. The flow rates of sheath gas, desolvation gas and sweep gas were 30, 15 and 5 units, respectively. The capillary and desolvation heater temperatures were set to 250°C and 300°C, respectively. The spray voltage was set to 4000 V. Local control of the LC system was conducted using Xcalibre 2.0.7, which was also used for MS control and data acquisition.

Table 2.1. Mobile phase gradient setting for the tumour tissue lipidomics experiment

Time (min)	B%	Flow rate (µL/min)
0	32	450
1	70	450
4	85	450
5	100	600
10	100	600
11	32	600
12	32	450

2.4. Metabolomics and lipidomics data pre-processing

Raw LC–MS data were processed with XCMS for untargeted peak-picking (Tautenhahn, Böttcher and Neumann, 2008) and mzMatch for alignment and annotation of related peaks (Scheltema *et al.*, 2011). IDEOM software was used for noise filtering and putative metabolite identification, as shown previously (Creek *et al.*, 2011). Metabolite identification was performed by matching accurate masses and retention times of authentic standards [Level 1 metabolite identification according to the metabolomics standards initiative (Sumner *et al.*, 2007, 2014)], but when standards were not available, predicted retention times were employed, hence these identifications should be considered as putative (Level 2 identification).

Lipidomics data was pre-processed by Dr Catherine Ortori using Progenesis Comet. Database searches for lipid was conducted using HMDB, Lipid Maps and Metlin at an accuracy of 5 parts per million (ppm). LC-MS chromatograms were viewed and displayed using Xcalibre 3.0.63.

2.5. Metabolomics and lipidomics data analysis

Metabolomics QC and data analysis was performed using the free online MetaboAnalyst 4.0 tool (Ritchie *et al.*, 2015). Using either the metabolite set enrichment analysis (MSEA) or pathway analysis suite, metabolites with non-human putative identifications were removed from the set of variables. Data analysis was then performed according to the protocol outlined by Xia and Wishart (2011). Briefly, peak intensity values for each identified metabolite was uploaded followed by the removable of variables with >50% missing values and

imputation of remaining zero values with half of the minimum positive value. Filters were then applied to remove features if their relative standard deviations (RSDs) were >30% in the QC samples. Sample normalisation based on total ion count was performed using IDEOM software. Therefore, only log transformation of the data sets was applied. For univariate analysis, no data scaling was applied, whereas Pareto scaling was applied prior to multivariate analysis. Univariate models were conducted with a *p*-value cut-off of 0.05 following correction for multiple comparison based on false discovery rate (FDR). In two-sample *t*-test comparisons, variances were not assumed to be equal between groups. Other features of MetaboAnalyst 4.0 were used to generate heatmaps and dendrograms, featuring hierarchical clustering of samples and metabolites, as well as principle components analysis (PCA) and correlation analysis. Lists of metabolites identified as significant were compared against pathway-associated metabolite sets within the MSEA suite or analysed for pathway impact within the pathway analysis suite of MetaboAnalyst. Orthogonal partial least squares-discriminant analysis (OPLS-DA) of metabolomics and lipidomics data was conducted using Umetrics SIMCA-P 13 software.

2.6. Cell culture

The aGBM U87 cell line was cultured in Dulbecco's Modified Eagle Medium (DMEM; Gibco) supplemented with 10% foetal bovine serum (FBS; HyClone), non-essential amino acids (NEAAs; HyClone/Gibco), and Penicillin/ Streptomycin (P/S; Sigma). The paediatric glioma cell lines Res186, Res259, UW479, KNS42, and SF188 were initially cultured in DMEM/F-12 (Gibco) supplemented with 10% FBS, L-glutamine, NEAAs and P/S. Later experiments required conditioning of paediatric glioma cell lines to culture in DMEM with NEAAs and P/S. The recurrent ependymoma cell line BXD-1425EPN cell line was cultured in DMEM supplemented with 10% FBS, NEAAs, and P/S. All cell lines were cultured at 37°C in a 5% CO_2 incubator. Cells cultured under lipoprotein-deficient conditions were grown in media containing lipoprotein deficient serum from foetal calf (LD-FBS; Sigma) in place of FBS. Due to availability issues,

later experiments were performed using lipoprotein deficient bovine calf serum (LD-BCS; Bioquote) as a replacement product for LD-FBS.

2.7. Cellular viability assays

Cells were grown in 48-well plates at appropriate seeding densities. Growth under lipoprotein-replete or -deplete conditions was assessed by staining cells with a 0.2% crystal violet (Sigma; C6158) solution for 30 min followed by a series of washes with distilled water to remove excess stain. Crystal violet was solubilised with a 1% sodium dodecyl sulfate (MP Biomedicals) solution before absorbance was measured at 570 nm using a FLUOstar Omega microplate reader (BMG LABTECH). The procedure was repeated with empty wells as controls to remove any background signal.

Cellular viability was also assessed using the resazurin-based PrestoBlue assay (ThermoFisher Scientific; A13261). The PrestoBlue substrate reagent was added at a 1:10 dilution to the culture medium and left to incubate at 37°C for 30 min. 100µl from each well was transferred to black-bottomed 96-well plates and fluorescence measured using 544-nm excitation and 590-nm emission settings on the FLUOstar Omega microplate reader (BMG LABTECH). Medium only controls were included to remove background fluorescence.

2.8. Spheroid culture and image processing

All cell lines were seeded into ultra-low attachment (ULA) 96-well plates at various seeding densities (total volume 200 µL of culture medium) and maintained at 37°C in a 5% CO_2 incubator for 4 days to allow aggregation of single cells into spheroids. From this timepoint (now referred to as day 0), a 50% medium change was performed every three days. Special attention was given to day 0 spheroids allocated for lipoprotein deprivation with a 50% medium change conducted thrice to reduce the initial lipoprotein-replete medium by one-eight. Brightfield images were taken every three days which coincided with medium changes. Medium changes were conducted prior to

image capture to wash away debris surrounding the spheroids and provide clearer demarcation of the spheroid circumference. Images were taken using a Canon camera attached to a brightfield microscope set with a 10x or 20x magnification lens. Spheroid growth assessment was performed by import of images into ImageJ (FiJi version) and using a macro developed by Ivanov *et al.*, 2014 to measure spheroid area through demarcation of the spheroid boundary. For failed automatic measurements, manual demarcation of the spheroid boundary was conducted.

2.9. Exogenous cholesterol and fatty acid rescue

0.641 g of palmitic acid (PA) was saponified in 10 mL of 300 mM sodium chloride (NaCl) in aqueous solution warmed to 70°C. 66.6 µL of this 250 mM PA/NaCl solution was then added to 5 mL of 10% fatty acid-free bovine serum albumin (BSA) in Dulbecco's phosphate buffered solution (Sigma; A1595) pre-warmed to 37°C. This mixture was incubated for 1 hr at 37°C and stirred frequently to facilitate fatty acid conjugation to BSA. The final palmitic acid concentration was 3.33 mM, which was roughly equivalent to the concentrations of Oleic Acid (OA)-Albumin (3.28 mM) and Linoleic Acid (LA)-Albumin (3.35 mM) purchased from Sigma (O3008 and L9530, respectively). Exogenous fatty acids were added to culture medium to a final concentration of 300 µM, based on values used by Griffiths *et al.*, 2013. Due to the ability of BSA to quench fluorescent signals, the BSA content within treated and non-treated cells was made equal. Cells were cultured under lipoprotein-deplete conditions for 72 hr with or without the addition of exogenous fatty acid prior to cellular viability assessment using the PrestoBlue assay as outlined in section 2.7.

30 mg of methyl-β-cyclodextrin (MβCD)-cholesterol (Sigma; C4591) was dissolved in 5.35 mL of double distilled water (ddH_2O) to generate a 13.7 mM solution that was filter-sterilised and stored as aliquots at -20°C. Exogenous addition of cholesterol was conducted by diluting the 13.7 mM MβCD-cholesterol solution in medium lacking lipoproteins or containing LXR agonists in solution. Final concentrations used were 2.5, 5, 10, and 20 µM. Cellular

viability assessment after 72 hr was performed using the PrestoBlue assay as outlined in section 2.7.

2.10. Flow cytometric cell cycle analysis

Cells were seeded in T25 flasks at an appropriate density to generate ~1 million cells at 70-90% confluency after 5 days of growth. Seeded cells were left overnight in lipoprotein-replete medium to ensure attachment prior to replacement of culture medium with either fresh lipoprotein-replete or -deplete medium (0 hr timepoint). At the 72 hr timepoint, culture medium containing floating cells was collected and adherent cells were washed twice with Hanks' balanced salt solution, trypsinised and neutralised with medium. The two cell fractions were combined and spun down in a centrifuge at 300 x g for 5 min. The supernatant was removed followed by suspension of the pellet as single cells by pipetting action in 0.5 mL phosphate buffered saline (PBS). Fixation of this cell suspension by the addition of 4.5 mL 70% ethanol was conducted for at least 2 hr at 4°C. Ethanol was removed by pelleting cells at 300 x g for 5 min and repeated with a PBS wash step. The resulting cell pellet was then resuspended in 0.5 mL propidium iodide (PI) staining solution [0.1% (v/v) Triton X-100, 10 µg/mL PI, and 100 µg/mL DNase-free RNase A in PBS] and kept in the dark at room temperature for 30 min. PI binding to DNA was measured using the Beckman Coulter FC500 flow cytometer with excitation and emission wavelengths set to 536 and 617 nm, respectively. Cell cycle analysis of the raw data was conducted using Weasel software after the initial application of gates to select single cells.

2.11. RNA extraction

RNA extraction from either tumour tissue or cells was performed using the mirVana miRNA isolation kit (ThermoFisher Scientific; AM1561), consisting of lysis/binding buffer, miRNA homogenate additive, wash solutions 1 and 2/3, and filter cartridges with collection tubes. For RNA extraction from tumour tissue, initial homogenisation of tumour tissue in 500 µL of lysis/binding buffer

(approximately 10x the volume of tumour tissue) was conducted until all clumps were no longer visible. 50 µL (10% v/v) of miRNA homogenate additive was added to the lysate, vortexed and then kept on ice for 10 min. 500 µL of acid-phenol:chloroform (ThermoFisher Scientific; AM9722) was added to the lysate equal to the volume of lysis/binding buffer that was initially added. The mixture was vortexed for 60 sec followed by centrifugation at 10,000 x g for 5 min for phase separation. The aqueous upper phase was transferred to a fresh tube with an approximate volume of 500 µL. 625 µL of absolute ethanol, equating to 1.25x the volume of the of the aqueous upper phase, was added and the mixture transferred into filter cartridges with collection tubes. RNA was isolated from the liquid phase by centrifugation for 15 sec at 10,000 x g, followed by wash steps using 700 µL of wash solution 1 and 500 µL of wash solution 2/3 conducted twice. Washes were conducted by centrifugation for 10 sec at 10,000 x g. Residual liquid was discarded trough centrifugation for 1 min at 10,000 x g prior to the application of 100 uL of nuclease-free water (ThermoFisher Scientific; BP2484) pre-heated to 95°C. RNA was eluted through a 30 sec centrifugation step at 10,000 x g and assessed for purity at the absorbance ratio 260nm/280nm (~2.0) and the presence of contaminants at the absorbance ratio 260nm/230nm (ranging between 2.0-2.2) using a NanoDrop spectrophotometer (ThermoFisher Scientific). For RNA extraction from cell pellets, the same protocol was adopted using 300 µL of lysis/binding buffer and appropriate volumes of other reagents within the kit and eluted in 50 µL of nuclease-free water (ThermoFisher Scientific; BP2484) to increase the concentration of RNA. Samples were stored at -80° and subjected to minimal freeze-thaw cycles to prevent degradation.

2.12. DNase treatment

DNase treatment of RNA samples was performed since the mirVana RNA extraction method does not fully remove contaminating genomic DNA. The TURBO DNA-free kit (ThermoFisher Scientific; AM1907) was used, consisting of TURBO DNase (2 units/µL), 10x TURBO DNase buffer, DNase inactivation reagent and nuclease-free water (ThermoFisher Scientific; BP2484). 25 µL

reaction volumes were set up consisting of 21.5 µL of RNA, 0.5 µL TURBO DNase and 0.5 uL RiboLock RNase inhibitor (ThermoFisher Scientific; EO0381). Mixtures were incubated at 37°C for 20 min followed by the addition of 2.5 µL DNase inactivation reagent and incubation at 22°C for 5 min to terminate the reaction. Removal of the DNase inactivation reagent was conducted by centrifugation at 10,000 x g for 1.5 min and transfer of the supernatant containing RNA into fresh tubes. RNA purity and contamination were assessed using a NanoDrop spectrophotometer as discussed above.

2.13. Transcriptomics

RNA extracts prepared from either tumour tissue or pelleted cells were first diluted in nuclease-free water (ThermoFisher Scientific; BP2484) to produce 10 µL samples containing 1000 ng of RNA, equating to a concentration of 100 ng/µL. RNA samples were sent to the Nottingham Arabidopsis Stock Centre headed by Prof Sean May and managed by Dr Marcos Castellanos-Uribe. Initial quality assessment of the RNA samples was performed using an Agilent RNA 6000 Nano kit (to produce a gel) run on an Agilent Bioanalyzer 2100 instrument to determine signs of degradation based on the ratio of the 18S and 28S ribosomal bands, quantitatively summarised as a RNA Integrity Number (RIN). RNA samples with RIN scores less than 7 were re-extracted from surplus tumour tissue and re-evaluated for integrity. Following the quality assessment phase, RNA samples approved for downstream transcriptomics analysis were assessed using Affymetrix Human Gene ST2.1 Strips. Briefly, the Affymetrix GeneChip WT PLUS Reagent Kit was used to create double-stranded cDNA from the RNA template, from which cRNA was produced as a template for a second round of cDNA synthesis. The resultant single-stranded cDNA library was fragmented, terminally labelled and hybridised to the strips using the Affymetric GeneAtlas Hybridisation, Wash, and Stain Kit for WT Array Strips. Prior to downstream differential expression analysis, evaluation of array hybridisation was conducted using the Partek Genomics Suite to identify artefacts on the chip that would generate spurious results.

2.14. Transcriptomics analysis

For the multi-region sampled HGG metabolomics study, multilevel linear modelling was conducted by Dr Anbarasu Lourdusamy. A separate but complementary analysis was conducted in collaboration with Dr Tahseen Jilani and Dr Tom Giles associated with the Advanced Data Analysis Centre within the University of Nottingham. For the lipoprotein and LXR agonist studies, the differential gene expression analysis using R software was conducted independently. Briefly, raw data was pre-processed with the *oligo* package (Carvalho and Irizarry, 2010) to mediate quantile normalisation using the Robust Multi-array Average (RMA) method. Assessment of two QC metrics of the data was performed by visualising Relative Log Expression (RLE) [compares the expression level of one probeset against the median expression of the same probeset across samples] and Normalised Unscaled Standard Errors (NUSE) [standardises standard error estimates across arrays so that the median standard error for the probeset is 1 across all arrays]. Low variance genes were then removed using the *genefilter* package (Bourgon, Gentleman and Huber, 2010) prior to differential gene expression analysis using the *limma* package (Ritchie *et al.*, 2015). The significance of differentially expressed genes (DEGs) was determined using a 0.05 *p*-value cut-off after correction for multiple comparisons using the Benjamini-Hochberg (BH) method. Gene ontology (GO) enrichment analysis of DEGs was conducted using the *topGO* package by applying statistical tests based on either gene counts (Fisher's exact test) or gene scores (Kolmogorov-Smirnov-like test) to different algorithms. The 'classic' algorithm tests each GO term independently, therefore not taking the GO hierarchy into account. The 'weight01' algorithm is a mixture of the 'elim' [traverses the GO hierarchy from bottom to top, discarding any genes that annotated with significantly enriched descendant GO terms] and 'weight' [connected nodes are compared to detect the most locally significant GO terms] algorithms introduced by Alexa, Rahnenführer and Lengauer (2006). The parentChild algorithm was introduced by Grossmann *et al.*, 2007 to consider the annotation of terms to the current term's parents and, in doing so, reduce the number of false positives due to the inheritance problem of annotations

from more specific descendent terms. Generation of transcriptional networks was conducted using NetworkAnalyst (Xia, Benner and Hancock, 2014). Lists of DEGs along with log2 expression values were inputted into the online interface and assessed using either of the curated databases IMEx (Breuer *et al.*, 2013) or String (Szklarczyk *et al.*, 2015) with a confidence score cut-off of 900 and the requirement of experimental evidence to validate. The complexity of the initially identified first-order networks was reduced by evaluating zero-order networks, which only outlines seed proteins that directly interact with each other.

2.15. Sample preparation for cell-based metabolomics and lipidomics

For the optimisation of metabolite extraction methods, the appropriate number of cells was seeded into T25 flasks to reach 70-80% confluency after a 5-day culture period. After removal of the culture medium, cells were rinsed briefly with PBS warmed to 37°C, which was then discarded from the flask. Cellular metabolism was then quenched by the addition of 400 µL of HPLC-grade MeOH kept on dry ice. Whilst keeping the flask on ice, cells were scraped off the growing surface and transferred into pre-cooled Eppendorf tubes. Extracts were shaken at 4°C for 30 min to facilitate cell lysis. Bi-phasic extraction was conducted through the addition of 1200 µL ice-cold HPLC-grade chloroform and 400 µL of ice-cold HPLC-grade water, leading to a 1:3:1 ratio of MeOH:chloroform:water. Mixtures were vortexed well prior to centrifugation at max speed for 10 min at 4°C. Supernatants were then transferred into fresh pre-cooled Eppendorf tubes and stored at -80°C prior to LC-MS analysis. In protocols including a drying step to concentrate metabolites, MeOH/chloroform solvent evaporation was conducted using a Jouan vacuum evaporator set to room temperature and with pulsed ventilation. Polar and non-polar metabolites were reconstituted in 70 or 100 µL of HPLC-grade MeOH or isopropanol, respectively. Samples were then spun down at 13,000 x g to remove debris and the supernatants placed in MS vials prior to analysis. For experiments using T75 flasks or petri dishes, solvents were scaled up so that 700 µL MeOH was added to quench metabolism followed by the addition of

2100 and 700 µL of chloroform and water, respectively, according to the steps outlined above. To maintain consistency during the bi-phasic extraction, 1400 µL of the upper polar phase and 1900 µL of the lower non-polar phase were collected. In all experimental set-ups, QCs were prepared by pooling 10 µL from each sample.

2.16. Spent medium analysis

For the analysis of spent medium metabolites, 1 mL of culture medium was removed at the 72 hr timepoint and transferred into an Eppendorf tube for centrifugation at 10,000 rpm for 5 min. The supernatant was transferred into a fresh Eppendorf tube for storage at. -80°C. Prior to storage, 250 µL was removed to which 750 µL of HPLC-grade MeOH pre-cooled to -20°C was added and vortexed to precipitate proteins. Mixtures were incubated at -20°C for 20 min before vortexing for 15 sec and centrifuging at 17,000 rpm for 10 min at 4°C. The supernatant was then removed and transferred into a fresh Eppendorf tube for storage at -80°C.

2.17. Liquid chromatography mass spectrometry analysis of cell-based metabolites and lipids

The LC-MS metabolomics analysis of prepared cell-based samples was conducted by Dr Salah Abdelrazig primarily and Sergey Evseev, using the same protocol outlined in 1.2. The LC-MS lipidomics analysis of prepared cell-based samples was conducted by Dr Catherine Ortori. Lipidomics of cell-based lipids consisted of initial lipid separation using a reverse phase ACE Excel 2 C18 column (50 x 2.1 mm) with guard column and Krudcatcher maintained at 50°C in a ThermoFisher Dionex UltiMate 3000 LC system (Thermo Fisher Scientific, Hemel Hampstead, UK). The injection volume was set to 10 µL, with samples held at 10°C. LC mobile phases consisted of A [60% of 0.1% MS-grade ammonium acetate (final volume) in 18.2 MΩ water (Elga Maxima; Elga LabWater) with 40% acetonitrile] and B [10% of 0.1% MS-grade ammonium acetate (final concentration) in 18.2 MΩ water (Elga Maxima; Elga LabWater)

with 10% acetonitrile and 80% isopropanol (MS-grade, VWR, UK]. The gradient adopted is displayed in Table 2.2. MS was performed using a Q-Exactive Plus Orbital ion-trap mass spectrometer (ThermoFisher Scientific, Hemel Hampstead, UK) acquiring data simultaneously in full scan ion mode (*m/z* 200-2000; resolution 70,000) in both positive and negative polarity switching modes. Tandem MS/MS spectra were produced on the 5 most intense ions at any one time at a resolution of 17,500. The flow rates of sheath gas, desolvation gas and sweep gas were 47.5, 11.25 and 2.25 units, respectively. The capillary and desolvation heater temperatures were set to 256°C and 412°C, respectively. The spray voltage was set to 3500V. Local control of the LC system used Chromeleon Express as well Xcalibre 3.0.63, which was also used for MS control and data acquisition.

Table 2.2. Mobile phase gradient setting for the cell-based lipidomics experiment

Time (min)	B%	Flow rate (µL/min)
0	30	400
1	35	300
7	100	500
11	100	500
12	20	500
15	20	500

2.18. Cell-based metabolomics and lipidomics data pre-processing

Pre-processing of metabolomics data and lipidomics data was performed according to the methodology outlined in sections 2.4 and 2.5. Univariate analysis of lipidomics data was conducted by Dr Catherine Ortori using LipidSearch software.

2.19. Amplex Red cholesterol assay

Cholesterol levels within cell-based lipid extracts were assayed using the Amplex Red Cholesterol Assay Kit (Invitrogen, A12216). This kit contained Amplex Red reagent, dimethyl sulfoxide (DMSO), 200 U/mL horseradish

peroxidase (HRP), ~3% hydrogen peroxide (H_2O_2) stock solution, 5x reaction buffer, 200 U/mL cholesterol oxidase, 200 U/mL cholesterol esterase, and 2 mg/mL cholesterol reference standard. A 1x reaction buffer was prepared by adding 2.5 mL of 5x reaction buffer to 10 mL of ddH_2O. A series of cholesterol standards ranging between 0 to 20 µg/mL were generated from the cholesterol reference standard in 1x reaction buffer and pipetted in 40 µL volumes (3 technical replicates) into a black-walled, black-bottomed 96-well plate. For each sample, 35 µL of 1x reaction buffer was pipetted into the 96-well plate to which 5 µL of sample was added. This was repeated for isopropanol only controls. A 200 U/mL catalase solution was prepared by dissolving 1 mg of catalase (Sigma; C1345) in 25 mL of PBS. 10 µL of catalase solution was added to the wells containing either cholesterol standards, samples, or isopropanol only and negative (1x reaction buffer) controls, based on the recommendations of Robinet *et al.* (2010). The plate was then incubated at 37°C for 15 min. A positive control was prepared by preparing a 20 mM H_2O_2 working solution by diluting the stock in ddH_2O, which was further diluted in 1x reaction buffer to a final concentration of 10 µM for use in the assay. 1 mg of the Amplex Red reagent was dissolved in 200 µL DMSO. A working solution of 300 µM Amplex Red reagent was then prepared by adding 75 µL Amplex Red reagent stock solution, 50 µL of 200 U/mL HRP, 50 µL of 200 U/mL cholesterol oxidase solution, and 5 µL of 200 U/mL cholesterol esterase to 4.82 mL of 1x reaction buffer (sufficient for ~100 assays). This mixture was used to measure total cholesterol levels, whereas excluding cholesterol esterase from the mix enabled free cholesterol levels to be measured. Reactions were started by adding 50 µL of the Amplex Red reagent working solution containing the added constituents detailed above to each cholesterol standard, sample and controls. The plate was incubated at 37°C for 30 min whilst protected from light. Fluorescence was then measured using a FLUOstar Omega microplate reader (BMG LABTECH) set to 544-nm excitation and 590-nm emission.

2.20. Liver X receptor agonist treatment

5 mg of GW3965 HCl (Selleckchem; S2630) was dissolved in 808.4 µL of DMSO to generate a 10 mM stock solution. 10 mg of LXR-623 was dissolved in 473.1 µL of DMSO to generate a 50 mM stock solution. Cells to be treated were initially seeded in medium containing 10% FBS and left to attach overnight. The next day medium was replaced with medium containing 0.5% FBS. After 24 hr, medium was exchanged with medium containing 1% FBS and LXR agonists at concentrations ranging between 5 and ~50 µM. Cells were then incubated at 37°C in a 5% CO_2 environment. Low serum conditions were used to prevent lipoproteins present in FBS from rescuing growth during the 72 hr LXR agonist treatment. Controls containing vehicle only were included to account for DMSO toxicity. However, drug concentrations were chosen so that the DMSO concentration was <0.3%. Cells were then either harvested for RNA/protein extraction, flow cytometric analysis as described in section 2.10, or assessed for cellular viability in the presence or absence of exogenous cholesterol. The latter was performed using the PrestoBlue assay as outlined in section 2.7 with the FLUOstar Omega microplate reader (BMG LABTECH) set to 544-nm excitation and 590-nm emission. Medium only controls were included to remove background fluorescence.

2.21. Protein extraction

Cell pellets were lysed with RadioImmunoPrecipitation Assay (RIPA) buffer consisting of 150 mM NaCl, 1% Triton X-100, 0.5% sodium deoxycholate, 0.1% sodium dodecyl sulfate (SDS), and 50 mM Tris solution adjusted to pH 8.0. Prior to lysis, cOmplete™ protease inhibitor cocktail (Sigma) and PhosStop (Sigma) stock solutions (25x and 20x concentrations, respectively) were diluted in the RIPA buffer to a 1x final concentration. 25 µL of this mixture was then used to lyse cell pellets through incubation on ice for 30 min and vortexing of samples every 10 min. At the end of the incubation period, lysates were spun down at 14,000 x g for 15 min with the centrifuge set to 4°C, followed by the transfer of supernatants into fresh Eppendorf tubes for storage at -80°C.

2.22. Protein quantification by Bradford assay

A series of standard dilutions between 0 to 500 µg/mL was prepared from a 1 mg/mL BSA stock solution dissolved in ddH_2O. 10 µL of each standard solution was pipetted in triplicate into a 96-well plate. Protein samples to be assayed were prepared by a 1:40 dilution in ddH_2O performed in duplicate, of which 10 µL of each duplicate was transferred to a 96-well plate. Bio-Rad protein assay dye reagent was diluted in a 1:4 ratio with ddH_2O. 200 µL of the dye reagent was added to all the standards and samples in the 96-well plate and left to incubate for 5 min. Absorbance at 595 nm was then measured using the FLUOstar Omega microplate reader (BMG LABTECH). Standard curves were drawn using Microsoft Excel from which sample protein concentrations were determined.

2.23. Sodium dodecyl sulfate-polyacrylamide gel electrophoresis

Samples were prepared by dilution to either 1 or 1.5 µg/µL with RIPA lysis buffer and 4x SDS sample buffer (1x final concentration). SDS sample buffer consists of 40% glycerol, 240 mM Tris/hydrochloric acid (HCl) pH6.8, 8% SDS, and 0.04% bromophenol blue. 5% β-mercaptoethanol was added fresh to the sample buffer each time. Diluted samples were then boiled at 95°C for 7 min to denaturise protein structures, followed by downstream use or storage at -20°C. SDS-gels of were prepared to mediate protein separation using the Mini-PROTEAN Tetra cell (Bio-Rad). Lower (resolving) gels were prepared with varying acrylamide percentages (7%, 10% or 13%) within a mixture of buffer [1.5 M Tris/HCl pH8.8 and 0.4% SDS], ddH_2O, 0.6% of 10% aqueous ammonium persulfate (APS) and 0.08% tetramethylethylenediamine (TEMED). Upper (stacking) gels containing 4% acrylamide were prepared with buffer [0.5 M Tris/HCl pH 6.7 and 0.4% SDS], ddH_2O, 0.5% of 10% APS and 0.1% TEMED. Combs were inserted into the upper gel to form wells upon polymerisation. Gels were placed into SDS-polyacrylamide gel electrophoresis (PAGE) tanks containing electrode buffer [25 mM Tris and 193 mM glycine dissolved in ddH_2O with a 1% final concentration of SDS]. Combs were removed from the upper

(stacking) gel and the appropriate volume of each sample and Amersham ECL Rainbow Marker (GE Healthcare) pipetted into the wells. Proteins were run through the stacking gel at 80V (40 mA) for ~30 min and then at 140V (100 mA) for ~60 min through the resolving gel.

2.24. Protein transfer and Western blotting

After separating proteins by SDS-PAGE, the stacking gel was removed from the resolving gel and placed into contact with polyvinylidene difluoride (PVDF) membranes. PVDF membranes were initially activated by submersion in MeOH for 30 sec and hydrated by soaking in ddH_2O for 3 min and transfer buffer for 10 min. Transfer buffer was prepared as follows: 25 mM Tris and 193 mM glycine dissolved in ddH_2O containing a final v/v MeOH content of 20%. The gel and PVDF membrane were sandwiched in cassettes between two pieces of filter paper and a sponge (all pre-wetted in transfer buffer) on each side, ensuring the removal of any air bubbles. Cassettes were placed in tanks filled with transfer buffer and incorporating an ice pack to maintain low temperatures. Western blot transfer was conducted at 100V (350 mA) for 60 min with the tank placed inside a fridge. The successful transfer of proteins was then determined through Ponceau staining, followed by a series of washes in ddH_2O and transfer buffer to remove the stain. At this point, membranes were cut to allow assessment of multiple proteins with different molecular weights. Preparation of membranes for Western blotting was conducted by blocking for 60 min with either milk or BSA dissolved to a 5% w/v concentration in Tris buffered saline-Tween 20 (TBST) [2 mM Tris/HCl pH 7.6, 13.5 mM NaCl, and 0.1% Tween-20]. After washing thrice with TBST for 10 min each, membranes were exposed for 60 min to primary antibodies diluted in either 5% milk- or BSA-TBST. The following antibodies were used at the following concentrations and diluted in either 5% milk- or BSA-TBST in accordance with the manufacturer's instructions: 1:500 ABCA1 (Abcam; ab18180), 1:1000 ABCG1 (Abcam; ab52617); 1:1000 AKT (Cell Signalling; #2920); 1:1000 Caspase-3 (Cell Signalling; #9662), 1:1,000 GAPDH (Cell Signalling; #5174), 1:1000 LC3B (Cell Signalling; #3868), 1:1000 LDLR (Abcam; ab52818), 1:1000 p21 (Cell Signalling;

#2947), 1:1000 p27 (Cell Signalling; #3686), 1:1000 p-AKT (Cell Signalling; #4058), 1:3000 p-AKT substrates (Cell Signalling; #3179), and 1:1000 SKP2 (Cell Signalling; #2652). Another round of 3x 10 min TBST washes was proceeded by a 60 min incubation of the membranes with the appropriate horseradish peroxidase-linked secondary antibody (rabbit or mouse) diluted 1:2000 in either 5% milk- or BSA-TBST. Antibody binding was assessed through chemiluminescent measurement upon 3 min incubation with ECL (ThermoFisher Scientific) after equilibration to room temperature. Bands were detected using photographic film in a dark room. Membranes were stored over a short time period in TBST. Re-probing of the same membrane was conducted by first stripping previously applied antibodies for 15 min using ReBlot Plus Mild Antibody Stripping Solution (Millipore), washing twice with TBST for 2 min, and repeating the Western blotting procedure from the blocking state as outlined above.

Chapter 3

Investigating intratumour metabolic heterogeneity in adult GBM

3. Investigating intratumour metabolic heterogeneity in adult GBM

A key feature of gliomagenesis is the development of ITH which allows evolutionary adaptation to selective pressures within the tumour microenvironment. However, less is understood about the impact of ITH on the metabolic landscape. We performed LC-MS on GBM intratumour fragments taken from four to five different regions selected by pre- and intra-operative neuro-navigation using StealthStation™ (Figure 3.1) and by 5-ALA-based isolation of invasive margin tissue (Figure 3.2A). Target selection was made using information from a whole batch of MRI sequences as detailed in section 2.1. This surgical sampling scheme aimed to determine if the heterogeneity observed at the genomic level manifests phenotypically as intratumour metabolic heterogeneity within the global metabolite (metabolome) and lipid (lipidome) spheres (Figure 3.2B).

Bulk tumour tissue from core regions has historically been used for molecular and cellular neuro-oncological research. However, the spatiotemporal aspects of ITH means that research based on tissue from one tumour region is too reductionist and fails to characterise the entire heterogeneous genomic landscape, likely contributing to the consistent lack of efficacy in phase II clinical trials using single agents targeting aberrant biological mechanisms prevalent in the surgically-resected tumour core. Staining of tumour fragments using haematoxylin and eosin (Figure 3.3) or Ki67 (Figure 3.4) confirmed the heterogenous nature of HGG at a cellular level regarding density, morphology and proliferative potential. This work conducted by Dr Saachi Chhaya BMBS also demonstrated the merit of surgical sampling as a method to study intratumour heterogeneity. We therefore adopted a multi-region sampling approach (Figure 3.2A) as pioneered by Prof. Colin Watts' group in which several tumour fragments are taken during standard surgical treatment for GBM (Sottoriva et al., 2013). Mass spectrometric analysis of tumour fragments generated a spatial and quantitative output that was used to test the following hypotheses: 1) GBMs harbour a heterogeneous metabolic landscape featuring niches delineated by distinct metabolomic and lipidomic profiles; 2) The therapy-

relevant invasive margin is characterised by a distinct metabolomic and lipidomic signature that may be amenable to metabolism-based therapeutic intervention; 3) Metabolic and lipid profiles functionally represent underlying genomic heterogeneity in metabolism-related genes.

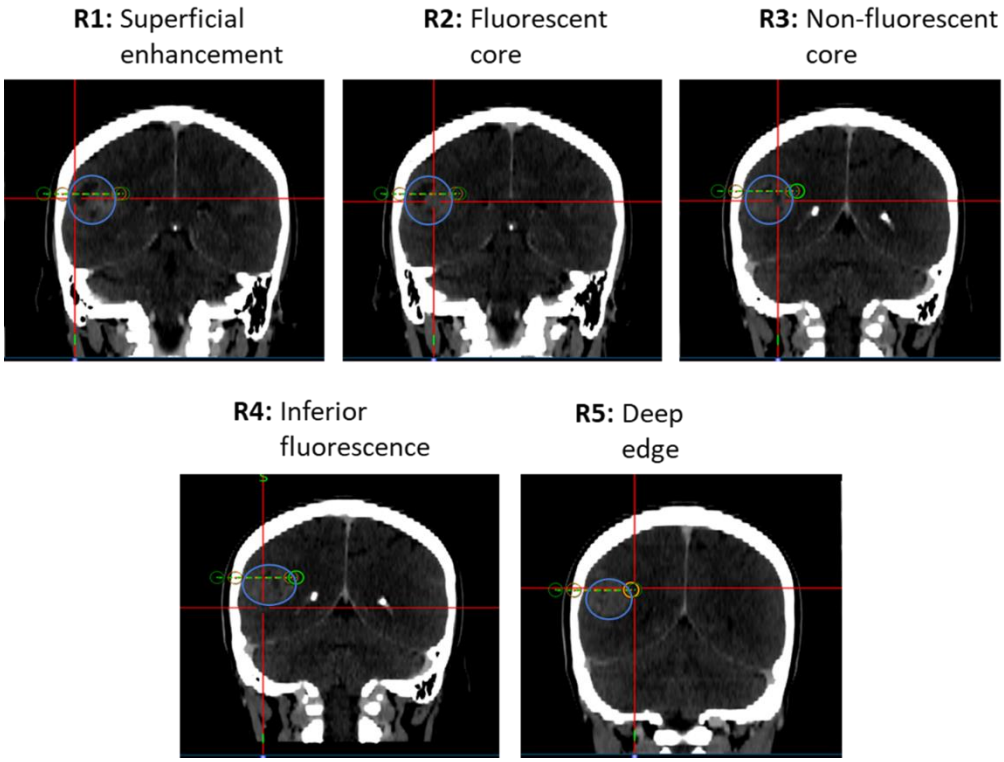

Figure 3.1. Stereotactic neuronavigation using CT scans of patient 9. Stereotactic CT images of patient 9 are displayed as an example of the use to the StealthStation™ neuro-navigation tool. The outline of the tumour mass is indicated by the blue circle. However, it is important to remember that the white areas indicating the tumour mass represent areas of blood-brain barrier breakdown, with the true edge of the tumour extending beyond the contrasted area but undefinable. Target selection was conducted utilising information from a whole batch of MRI sequences. Region (symbol R) designations are labelled within the figure. Locations of each region are depicted by the red cursor.

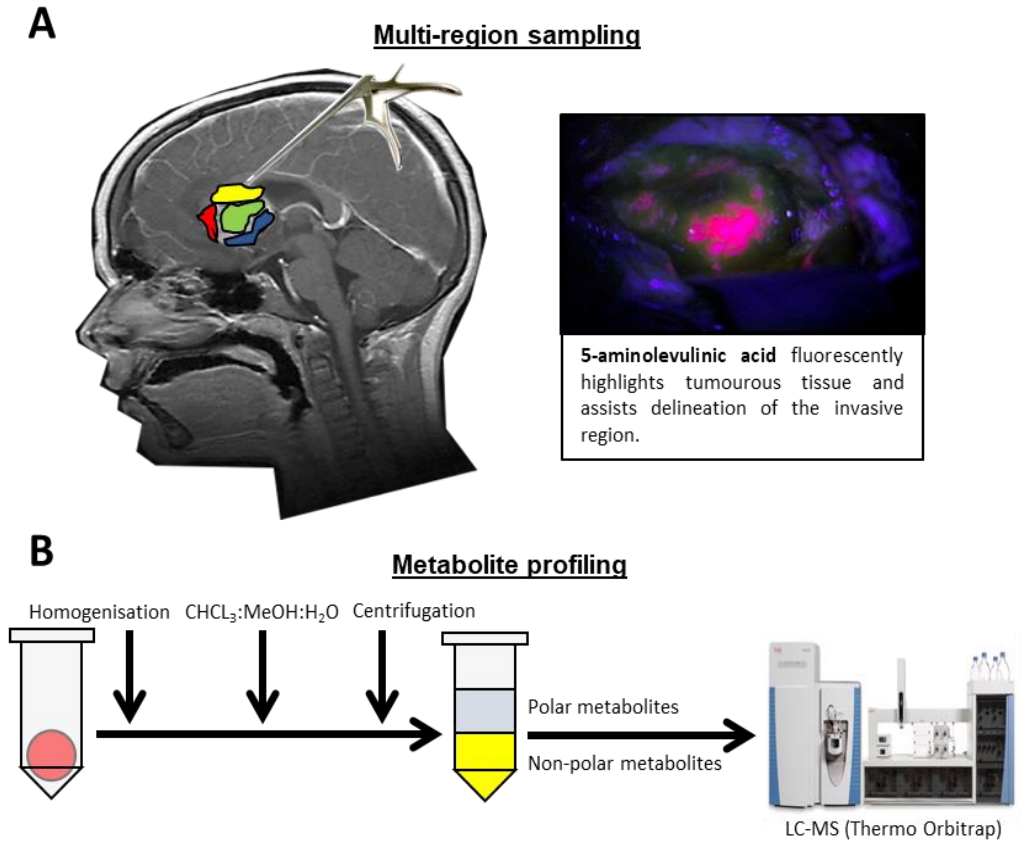

Figure 3.2. Schematic representation of the methodology used to profile intratumour metabolic heterogeneity in HGG. (A) Sampling of multiple tumour regions (4-5 per patient) during standard surgical treatment (left). Administration of 5-aminolevulinic acid (5-ALA) assists surgical excision of minimal disease beyond the main tumour mass (right). (B) Biphasic extraction of both polar and non-polar metabolites from each tumour fragment for LC-MS-based metabolomic and lipidomic analyses.

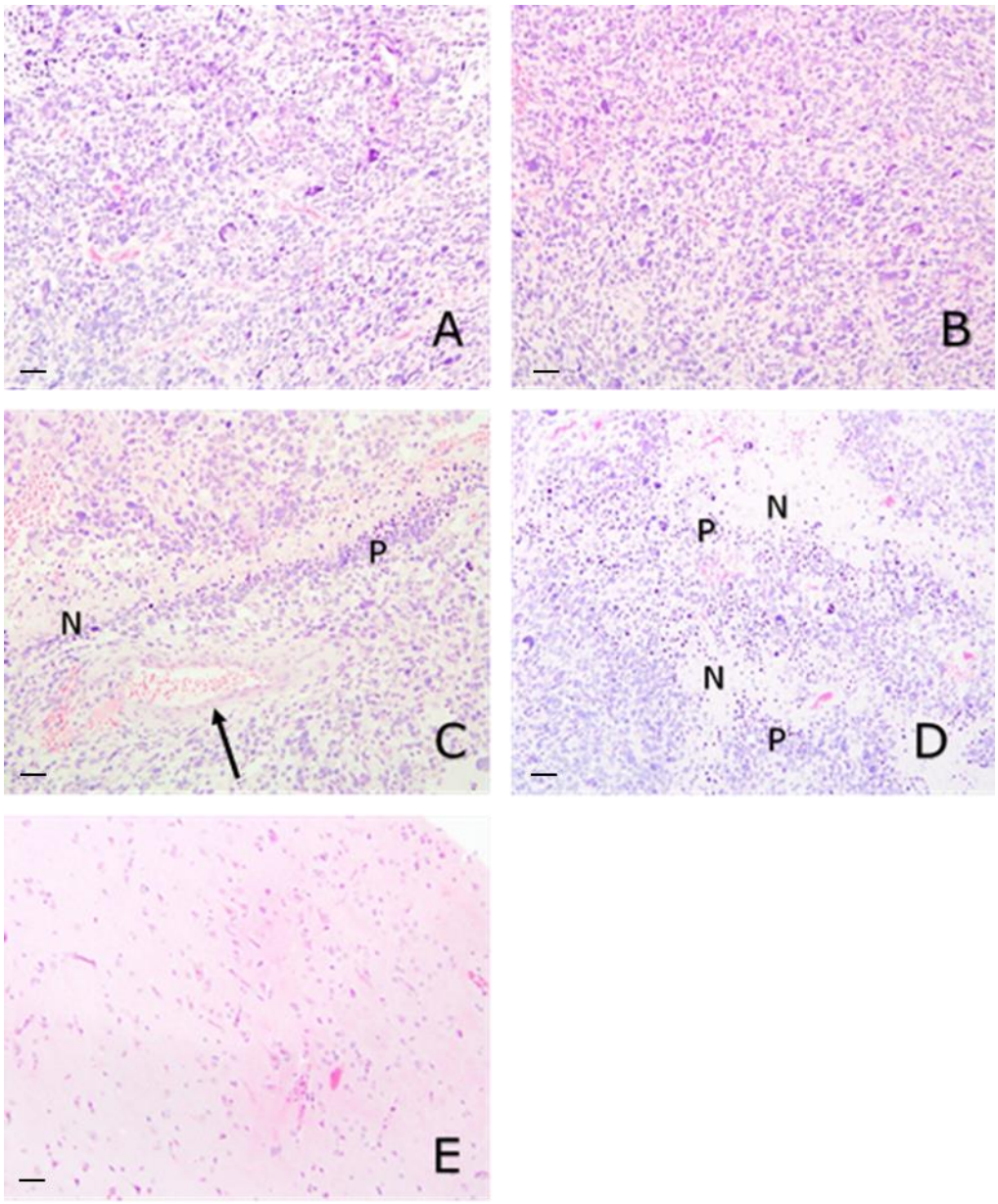

Figure 3.3. Representative example of haematoxylin and eosin staining of tumour fragments sampled from patient 15. This work was produced by Dr Saachi Chhaya BMBS. (A) Tissue sampled from the lateral temporal region demonstrates high cellularity, anaplasia, nuclear pleomorphism, and a mixture of dark nuclei suggesting hyperchromatism. (B) Anterior region tissue exhibits features of anaplasia, nuclear pleomorphism and hyperchromatism. (C) Tissue from the core region shows the highest cell density and evidence of mitoses. An area of necrosis (N) is observed and is lined with pseudopalisading cells (P). A blood vessel can an also be seen (arrow), reflecting the highly vascular tumour core. (D) Posterior temporal region tissue contains a large section of necrotic tissue (N) and palisading cells (P), as well as features indicative of hyperchromatism. (E) The invasive margin has a low nuclear to cytoplasmic ratio and the tissue is not as anaplastic in comparison to other regions. Brightfield images were taken at 10x magnification. Scale bars represent 100 μm in length.

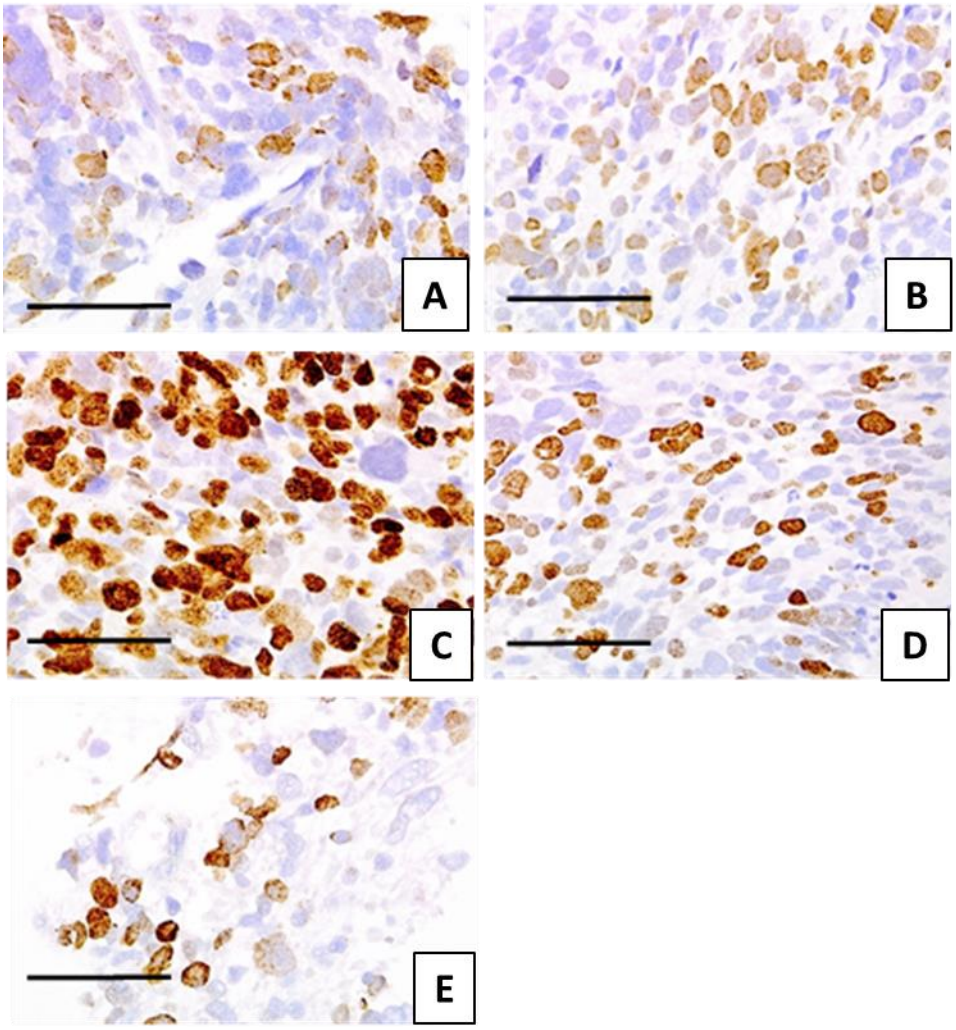

Figure 3.4. Representative example of a Ki67 immunohistochemical staining of tumour fragments sampled from patient 15. This work was produced by Dr Saachi Chhaya BMBS. (A, B and D) Immunohistochemistry was performed using Ki-67 at a dilution of 1:50. Almost a third of cells are stained positive for Ki67 in the lateral temporal, anterior and posterior temporal regions. (C) Strong staining within the central core indicates that this is the most proliferative region. (E) The invasive margin is the least proliferative with minimal staining of cells. Tumour images were taken at x40 magnification. Scale bars represent 10μm in length.

3.1. Patient information and tumour fragment details

Multi-region sampling was conducted on five patients with pathology-confirmed diagnoses of HGG. Four patients (6, 8, 9, and 15) had typical GBMs whereas one patient (14) had a malignant glioneuronal tumour (MGNT), a HGG with neuronal characteristics. Of the four GBMs, three were identified as *IDH1* wildtype (6, 8, and 9), whereas patient 15 expressed the mutant R132H variant. Prior to surgery, patients 6, 9 and 14 were administered 5-ALA to facilitate

complete resection of residual disease within the invasive margin, designated by the surgeon as the most likely region to contain infiltrating tumour cells and residing in close proximity to micro deposits of neoplastic cells which will ultimately generate the recurrent tumour. Four to five tumour regions were removed from each patient. However, different numbers of fragments were obtained depending on the size of each tumour region (ranging from 2-6 replicates). Stereotactic registration of each tumour region using the StealthStation™ pre/peri-operative imaging tool provided positional information within the tumour mass, as depicted on computer tomography images (Figure 3.1). Prior to LC-MS analysis, the minimal wet tissue weight required to obtain sufficient metabolome coverage and signal from low abundance metabolites was optimised using grey and white temporal lobe tissue fragments ranging from 15 to 40 mg in weight (section 8.1 in the Appendix). 20 mg of tissue was determined to be the minimum required to produce strong signals across the metabolome, although an optimum weight of 30-35 mg was recommended to enable identification of low concentration metabolites. Based on the available tissue, replicates of ~20 mg were produced for patients 6, 8, 9, and 14, whereas surplus tissue from patient 15 allowed replicates of ~30 mg. Of note, replicates as low as 10 mg were produced from patient 6 due to the small amount of available tissue for some tumour regions from which to sample. Table 3.1 summarises the clinical characteristics of the patients utilised in this study. Additional details about the tumour regions obtained during surgery are provided in Table 3.2.

Table 3.1. Clinical information for the five patients chosen for the intra-tumour metabolic heterogeneity study.

Patient number	Sex	Age	Histology	*IDH1* status	Tumour site	5-ALA adminisation	Resection status (%)	Survival (months)	Treatment RT/CT	TMZ response	Comments
6	Male	53	GBM	WT	Left occipital	Yes	100	29.1	60/TMZ	Good	
8	Female	54	GBM	WT	Left frontal	No	90	5.1	60/TMZ	Poor	Very bloody/vascular
9	Male	48	GBM	WT	Left frontal, intrinsic	Yes	100	17.2	60/TMZ	Good	
14	Female	39	MGNT	WT	Left temporal	Yes	100	Alive	60/TMZ	Good	BRAF V600E negative
15	Female	33	GBM	R132H	Right temporal	No	100	25.7	60/TMZ	Good	Moderate MGMT methylation

Details are provided about the histological diagnosis (GBM: glioblastoma multiforme; MGNT: malignant glioneuronal tumour), *IDH1* status (WT: wildtype), 5-amino-levulinic acid (5-ALA) administration, radiotherapy (RT) in Gray units, chemotherapy (CT), and response to temozolomide (TMZ).

Table 3.2. Sample information for the five patients chosen for the intra-tumour metabolic heterogeneity study.

Patient number	Sample ID	Region ID	Region (clinical description)	Region type	Fragment weight range (mg)
6	6.1	R1	Superficial fluorescence	Non-invasive	11-22
	6.2	R2	Core, mild fluorescence	Non-invasive	
	6.3	R3	Inferior fluorescence	Non-invasive	
	6.4	R4	Medial edge, mild fluorescence	Invasive	
8	8.1	R1	Superficial medial	Non-invasive	16-26
	8.2	R2	Anterior medial	Non-invasive	
	8.3	R3	Deep edge	Non-invasive	
	8.4	R4	Medial front	Invasive	
9	9.1	R1	Superficial enhancement	Non-invasive	20-28
	9.2	R2	Core enhancement	Non-invasive	
	9.3	R3	Inferior fluorescence	Non-invasive	
	9.4	R4	Anterior enhancement	Non-invasive	
	9.5	R5	Invasive margin, fluorescence	Invasive	
14	14.1	R1	Superficial enhancement	Non-invasive	18-28
	14.2	R2	Fluorescent core	Non-invasive	
	14.3	R3	Non-fluorescent core	Non-invasive	
	14.4	R4	Inferior fluorescence	Non-invasive	
	14.5	R5	Deep edge	Invasive	
15	15.1	R1	Lateral temporal	Non-invasive	27-39
	15.2	R2	Anterior	Non-invasive	
	15.3	R3	Core	Non-invasive	
	15.4	R4	Posterior temporal	Non-invasive	
	15.5	R5	Lateral edge	Invasive	

3.2. LC-MS based metabolite profiling of HGG metabolism

Briefly, polar and non-polar compounds were extracted from each tumour fragment using a biphasic extraction procedure (methanol:water:chloroform) to enable analysis of both the metabolome and lipidome from the same sample. All samples were analysed by LC-MS within the same batch to avoid variation introduced by running samples at different time points (batch-to-batch variation). Pooled quality control samples were included to analyse instrument stability over the 48-hour run period, allowing removal of ions with high relative standard deviations (RSDs). Raw LC-MS data was pre-processed by peak identification, alignment, annotation, noise filtering, and putative identification of metabolites. Peak intensities were then normalised to total ion count to account for differences in tissue weight and metabolite content. Non-human metabolites were removed from the data to yield 503 human metabolites with putative identifications. The following subsections detail the results of univariate and multivariate analyses characterising intratumour metabolic heterogeneity. Patients 6 and 15 will be discussed in the main text to cover IDH-wildtype and -mutant GBM, with the remaining patients summarised in sections 8.2, 8.3 and 8.4 in the Appendix.

3.3. HGGs display intratumour metabolic heterogeneity

Principle component(s) analysis of metabolomic profiles revealed regional heterogeneity as well as overlap between some regions with similar metabolic activity. In patient 6, the first principle component largely separated each tumour region, accounting for 45.5% of the variation in the data (Figure 3.5A). The horizontal plane indicated that regions 6_2 and 6_3 are more similar in comparison to regions 6_1 and 6_4, as supported by hierarchical clustering of the samples (Figure 3.5B). Clustering of the samples also demonstrated a shorter distance measure between replicate 4 of region 6_3 (designated as 6_3_4) and fragments from region 6.2, supported by metabolomic similarities as depicted in the heatmap overview (Figure 3.5C). Since these regions were located adjacent to each other within the original tumour mass, it is possible

that fragment 6_3_4 was derived from the same metabolic niche containing region 6_2. However, this is highly speculative and given that 6_3_4 was taken from the same tissue sample as the other region 6_3 fragments, the designation of 6_3_4 as a replicate from region 6_3 was retained.

In patient 15, separation of samples along the first component demonstrated that most of the variation occurred between region 15_5 and all other regions collectively (Figure 3.6A), supported by low dissimilarity between regions 15_1, 15_2, 15_3 and 15_4 and clustering of fragments from these regions (Figure 3.6B). The heatmap overview of patient 15's metabolome (Figure 3.6C) highlighted a largely homogenous metabolic landscape within the non-invasive regions compared to patient 6. Interestingly, both patients showed separation and clustering of the invasive margin from non-invasive regions in support of our hypothesis that the invasive margin displays a distinct metabolomic signature.

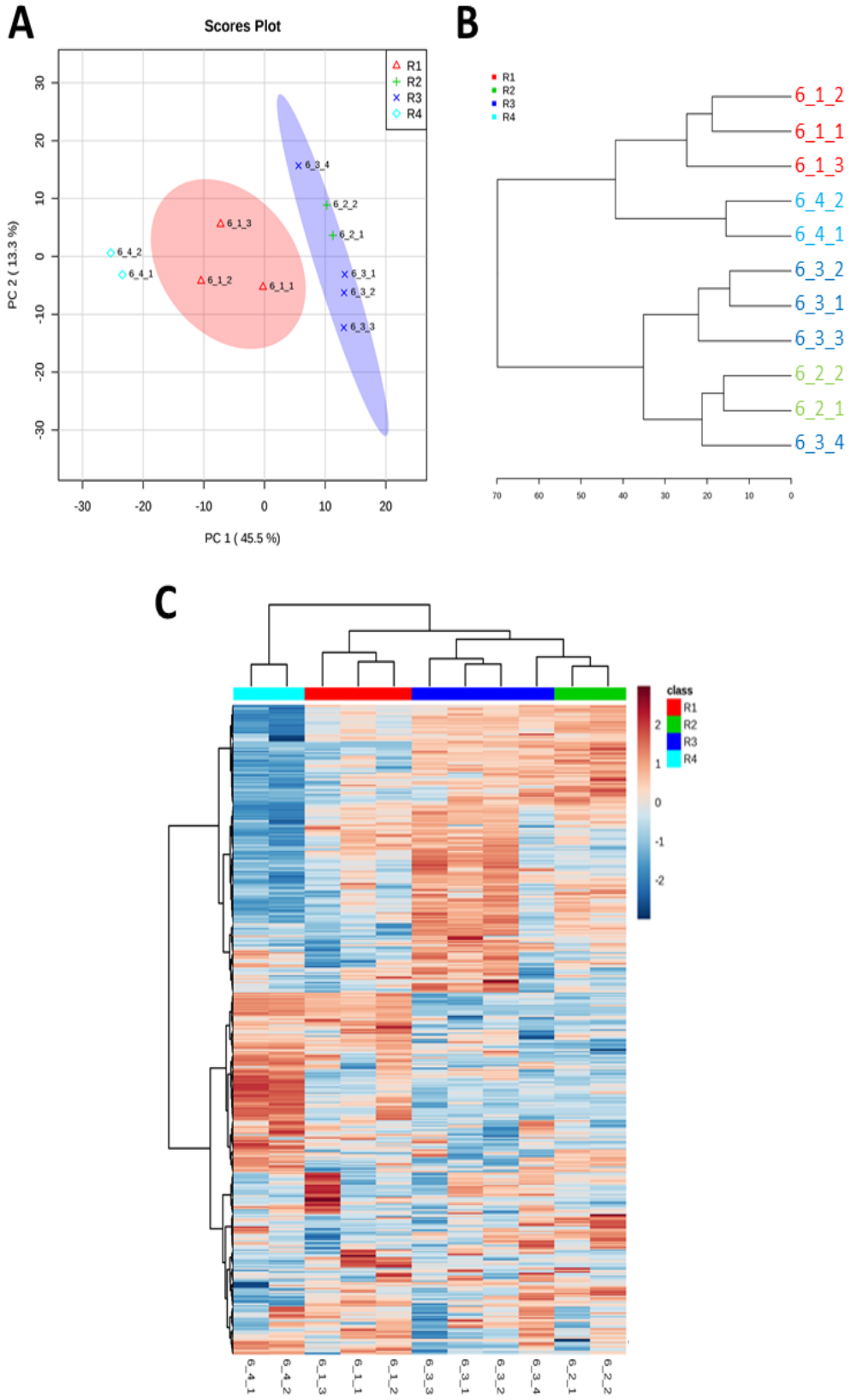

Figure 3.5. Diagnostic plots for patient 6 metabolomics data. (A) Dimensional reduction through principle components analysis and visualisation of sample variation. (B) Hierarchical clustering analysis measuring dissimilarity between samples. (C) Heatmap overview of the metabolome. Sample IDs delineate the patient, region (symbol R), and replicate numbers, respectively.

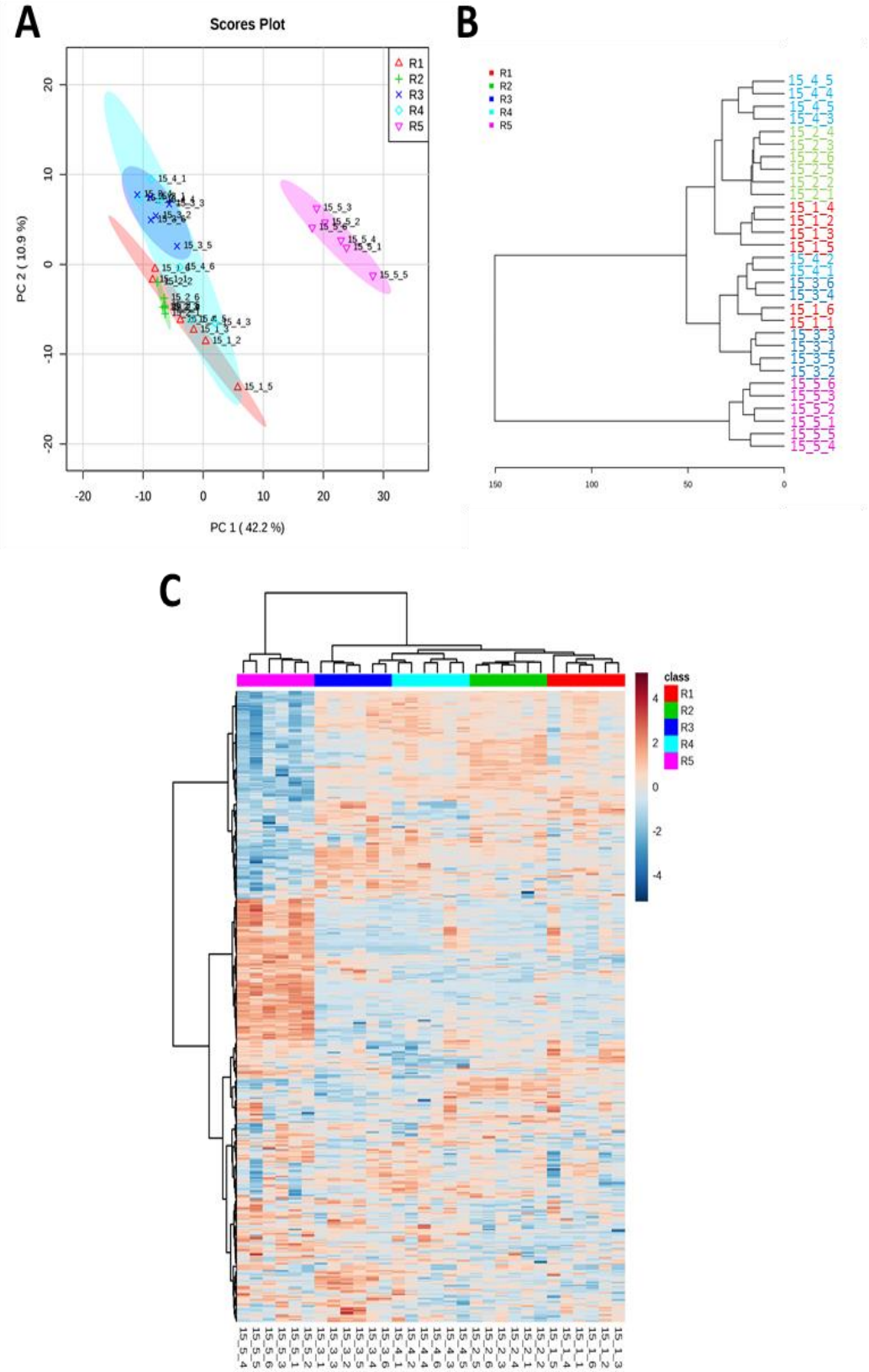

Figure 3.6. Diagnostic plots for patient 15 metabolomics data. (A) Dimensional reduction through PCA and visualisation of sample variation. (B) Hierarchical clustering analysis measuring dissimilarity between samples. (C) Heatmap overview of the metabolome. Sample IDs delineate the patient, region (symbol R), and replicate numbers, respectively.

3.4. Metabolites differ in extent of heterogeneity across HGG regions

Multivariate analysis of the HGG metabolome revealed a more heterogeneous metabolic landscape in patient 6 compared to patient 15. To determine metabolites with significant variation across regions, a one-way analysis of variance (ANOVA) test was performed to select for variables with a false discovery rate (FDR)-corrected *p*-value of less than 0.05. A greater number of significant metabolites was identified in patient 15 (151) compared to patient 6 (307), which was unexpected considering the homogenous nature of patient 15 but is likely explained by the highly distinct invasive margin, the higher number of replicates per region, and the balanced nature of the data set (i.e. same number of replicates for each region). Heatmaps displaying the top 50 significant metabolites confirmed the findings of the multivariate analysis above, highlighting the relative similarity between regions 6_2 and 6_3 (Figure 3.7), and the stark contrast between the invasion margin and non-invasive regions of patient 15 (Figure 3.8). Table 3.3 lists metabolites that were identified in all five patients to be significantly variant across regions.

Each list of significant metabolites was imported into the MSEA suite of the online MetaboAnalyst metabolomics data analysis tool to determine if heterogeneity was confined to specific metabolic pathways. A significant score for *glucose-alanine cycle* (raw *p*-value=0.013) was obtained in patient 6 (Table 3.4). In patient 15, significance was reached for the metabolite sets *phosphatidylethanolamine biosynthesis* (raw *p*-value=0.012), *cardiolipin biosynthesis* (raw *p*-value=0.029), *pyrimidine metabolism* (raw *p*-value=0.031), and *phosphatidylcholine biosynthesis* (raw *p*-value=0.032) (Table 3.5). In the other patients, no metabolite set was significantly enriched in patient 8 (Table 8.1 in the Appendix); *phenylacetate metabolism* (raw *p*-value=0.030) and *glycolysis* (raw *p*-value=0.045) were enriched in patient 9 (Table 8.5 in the Appendix); and *phosphatidylethanolamine biosynthesis* (raw *p*-value=0.025) were enriched in patient 14 (Table 8.9 in the Appendix). In no patient did the MSEA reach significance following correction for multiple comparisons using either the Holm or FDR methods. Coupled with low fold enrichment scores,

solid conclusions could not be made regarding the elucidation of metabolic pathways displaying the highest heterogeneity.

Table 3.3. List of metabolites commonly identified across all five patients as significantly variant using a one-way ANOVA model.

Metabolite	ID confidence
Alpha-ketoisovaleric acid	10
L-Ornithine	10
Glycerophosphocholine	10
N-Acetylglutamine	9
(S)-2,3,4,5-Tetrahydropyridine-2-carboxylate	8
2-Dehydro-3-deoxy-L-rhamnonate	8
3-Sulfinoalanine	8
4-Guanidinobutanoic acid	8
Anserine	8
Carnosine	8
D-Glucose	8
D-Proline	8
N-Acetyl-L-aspartate	8
(S)-3-Methyl-2-oxopentanoic acid	8
1-(beta-D-Ribofuranosyl)-1,4-dihydronicotinamide	7
Asn-Lys-Asn-Pro	7
Cystenyl-Serine	7
Glutamylleucine	7
Glu-Phe-Asn-Arg	7
Leucyl-Lysine	7
Leucyl-Threonine	7
Maleamate	7
Met-Ala-Ser	7
Met-Gly-Ser	7
N-Acetylaspartylglutamate	7
4-Pyridoxic acid	6
L-Methionine S-oxide	6
1-Pyrroline-5-carboxylate	6
Glycerophosphoethanolamine	6
2-Octenoylcarnitine	5
Ala-Ala-Ala	5
Asp-Thr-Thr-Asp	5
Glu-Thr-Thr	5
Methionyl-Asparatate	5

ID confidence scores delineate the confidence of the putative metabolite identification.

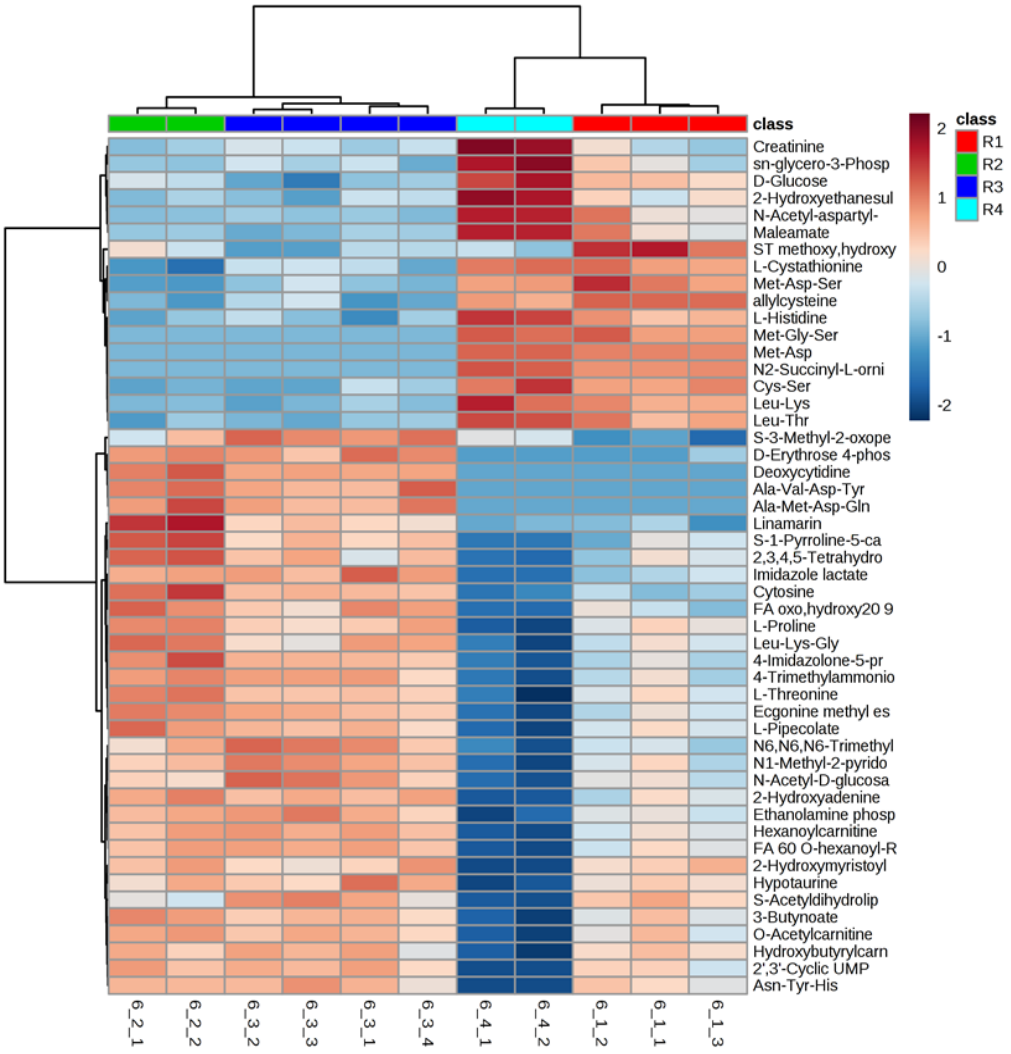

Figure 3.7. Identification of regionally variant metabolites in patients 6. One-way ANOVA was conducted on the metabolomic profiles from patients 6. Only the top 50 significant metabolites are displayed in the heatmaps. Sample IDs (bottom) delineate the patient, region (symbol R), and replicate numbers, respectively.

Table 3.4. Metabolite set enrichment analysis of metabolites in patient 6 identified as significant using one-way ANOVA.

Metabolite Set	Total	Expected	Hits	Raw p	Holm p	FDR
Glucose-Alanine Cycle	13	1.56	5	0.0134	1	1
Histidine Metabolism	43	5.17	9	0.0623	1	1
Glycine and Serine Metabolism	59	7.09	11	0.0847	1	1
Malate-Aspartate Shuttle	10	1.2	3	0.108	1	1
Carnitine Synthesis	22	2.64	5	0.113	1	1

The table details the top five enriched metabolite sets based on significantly differentially abundant metabolites with log2 fold-change >0.58 or < -0.58. Significant raw *p*-values (Raw p) for enriched metabolite sets were adjusted for multiple comparisons using the Holm (Holm p) or false-discovery rate (FDR) method.

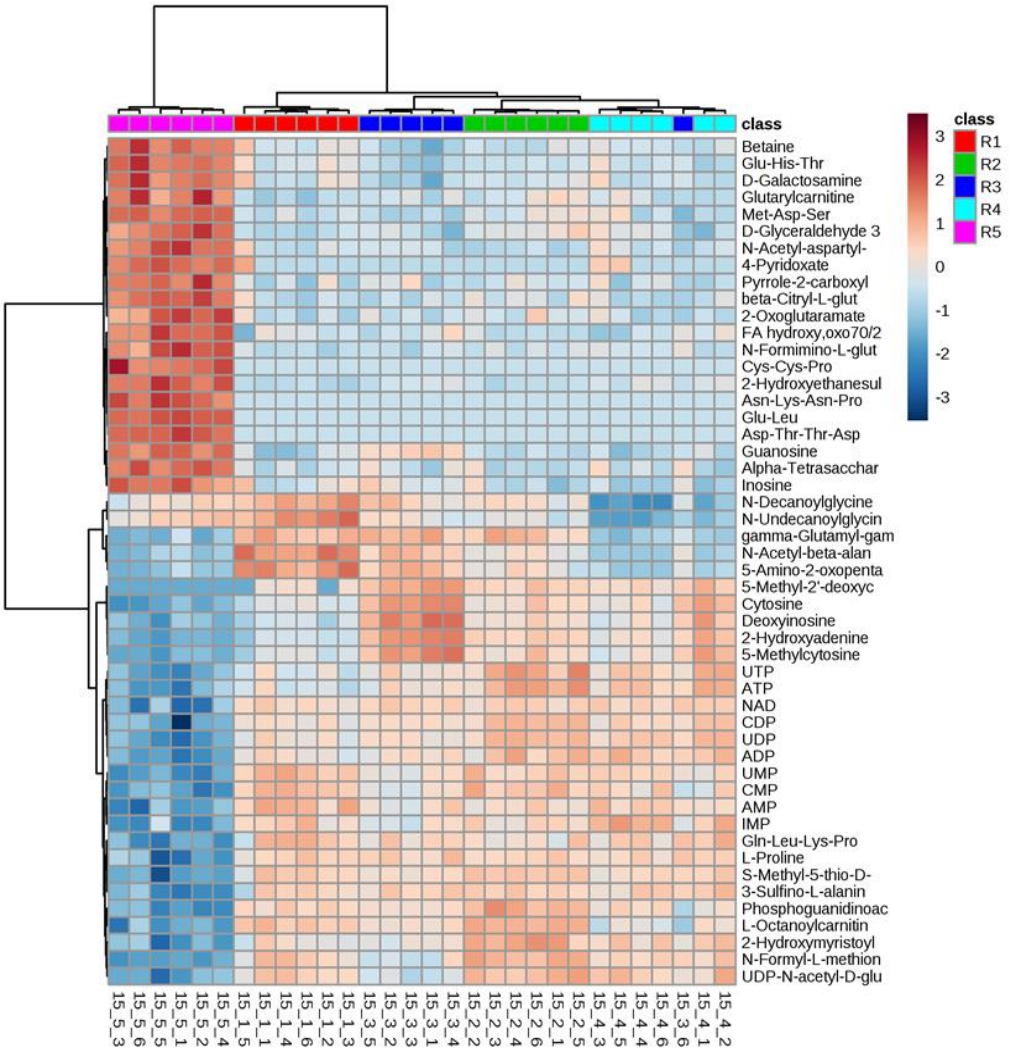

Figure 3.8. Identification of regionally variant metabolites in patients 15. One-way ANOVA was conducted on the metabolomic profiles from patients 15. Only the top 50 significant metabolites are displayed in the heatmaps. Sample IDs (bottom) delineate the patient, region (symbol R), and replicate numbers, respectively.

Table 3.5. Metabolite set enrichment analysis of metabolites in patient 15 identified as significant using one-way ANOVA.

Metabolite Set	Total	Expected	Hits	Raw p	Holm p	FDR
Phosphatidylethanolamine Biosynthesis	12	2.92	7	0.0117	1	0.789
Cardiolipin Biosynthesis	11	2.67	6	0.0294	1	0.789
Pyrimidine Metabolism	59	14.3	21	0.0305	1	0.789
Phosphatidylcholine Biosynthesis	14	3.4	7	0.0322	1	0.789
Arginine and Proline Metabolism	53	12.9	18	0.0681	1	0.947

The table details the top five enriched metabolite sets based on significantly differentially abundant metabolites with log2 fold-change >0.58 or < -0.58. Significant raw *p*-values (Raw p) for enriched metabolite sets were adjusted for multiple comparisons using the Holm (Holm p) or false-discovery rate (FDR) method.

Following the difficulties above with the MSEA, a biased approach was adopted to determine the regional distribution of metabolites belonging to the glycolysis pathway and TCA cycle. An indication as to the functional effect of these pathways was determined through assessment of several species involved in energetics, including ATP and NADH. Given the importance of amino acids to normal cellular function, essential, conditional, and non-essential amino acids were also assessed. L-glutamate, L-serine and glycine feed into the one-carbon metabolic pathway, featuring the folate and methionine cycles. These metabolic pathways were also analysed since they feed intermediates into nucleotide and glutathione synthesis (Yang and Vousden, 2016).

The heatmaps in Figure 3.9 highlighted regional heterogeneity in metabolites related to glycolysis, TCA cycle, and energetics in patient 6. Within the glycolysis pathway, only D-glucose had a significant ANOVA score (FDR<0.01) in reflection of regional heterogeneity and higher metabolite abundance of the metabolite within the invasive margin compared to the non-invasive regions (2.36-fold increase) (Figure 3.9A). Significant scores for citrate and isocitrate were also obtained between the non-invasive regions and the invasive margin (Figure 3.9B), perhaps reflecting differences in mitochondrial activity and lipid synthesis. Regional heterogeneity was observed for several energetic species, including ATP, creatine, and NADH (Figure 3.9C). Interestingly, regions 6_2 and 6_3 demonstrated an above median abundance of NAD+, as observed for its reduced equivalent NADH. Both these metabolites demonstrated a significant ANOVA score, but only NAD+ levels within the invasive margin were significantly different to non-invasive regions (FDR<0.01). A similar pattern of differences confined between non-invasive and invasive regions was identified for most amino acids apart from L-glutamine, which demonstrated homogeneity across all regions that was not reflected in its immediate downstream product, L-glutamate (Figure 3.10A, B, and C). Although L-serine and L-glycine showed non-significant heterogeneity between regions, this did not translate into significantly variable glutathione levels (Figure 3.11A and B). Table 3.6 summarises the biased analysis of intratumour metabolic

heterogeneity across all regions and between non-invasive and invasive regions in patient 6.

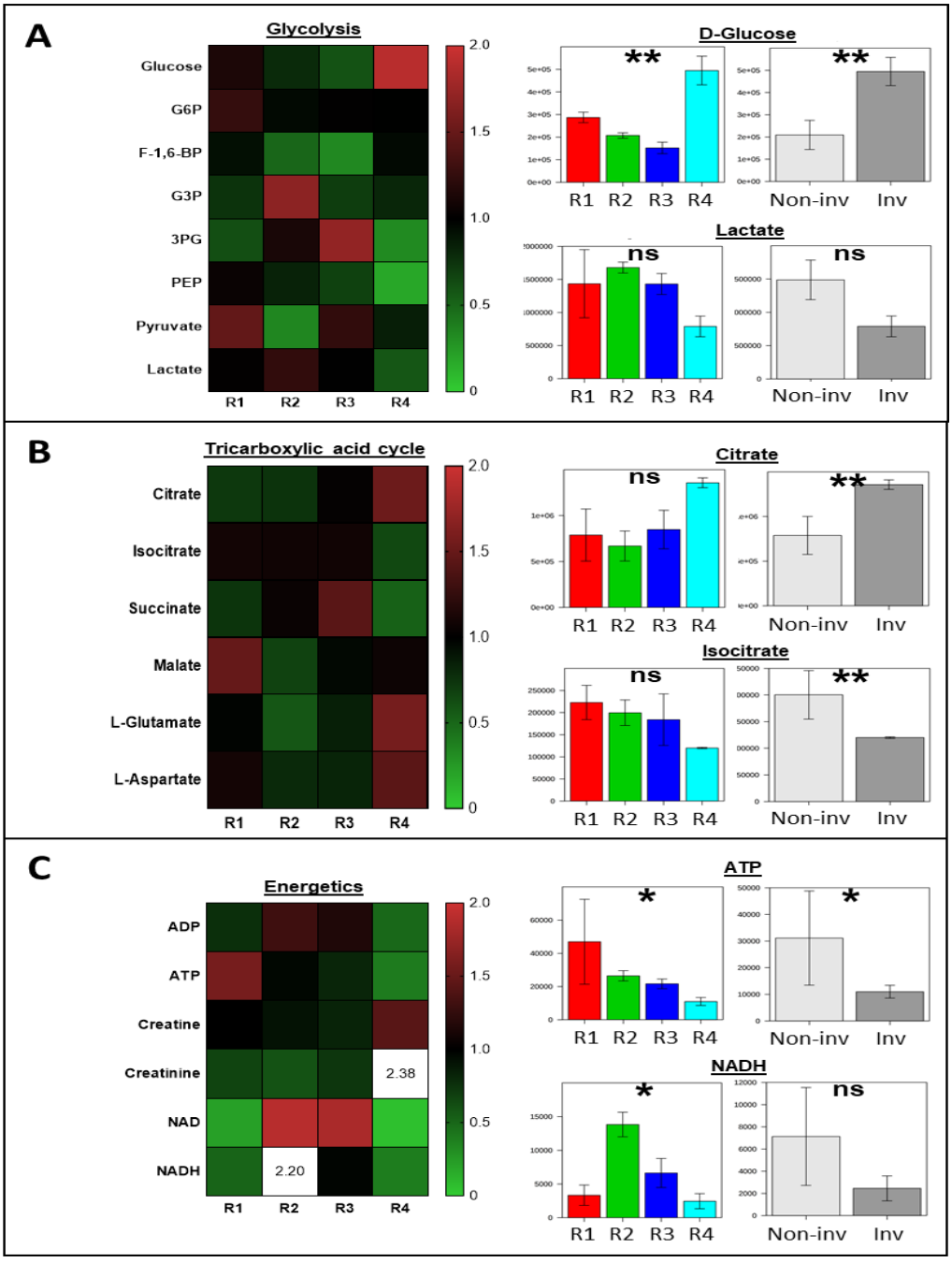

Figure 3.9. Regional variation in patient 6 of metabolites generated within the glycolysis pathway, tricarboxylic acid cycle, and energetics. Heatmaps display median replicate values of mean-centred peak intensities for metabolites generated within glycolysis (A), TCA cycle (B), and energetics (C). Scale bars depict the grading of colours for fold changes ranging between 0 and 2. Fold changes above 2 are numbered. Peak intensities for metabolites of interest across regions (symbol R; left bar plot) and between region types (right bar plot) are displayed in each panel. Statistical evaluation of regional variation was conducted using a one-way ANOVA model and two-sample t-test, respectively. Abbreviations: Non-inv – non-invasive (light grey); Inv – invasive (dark grey). ns = not significant; * = $p<0.05$; ** = $p<0.01$; *** = $p<0.001$; **** = $p<0.0001$.

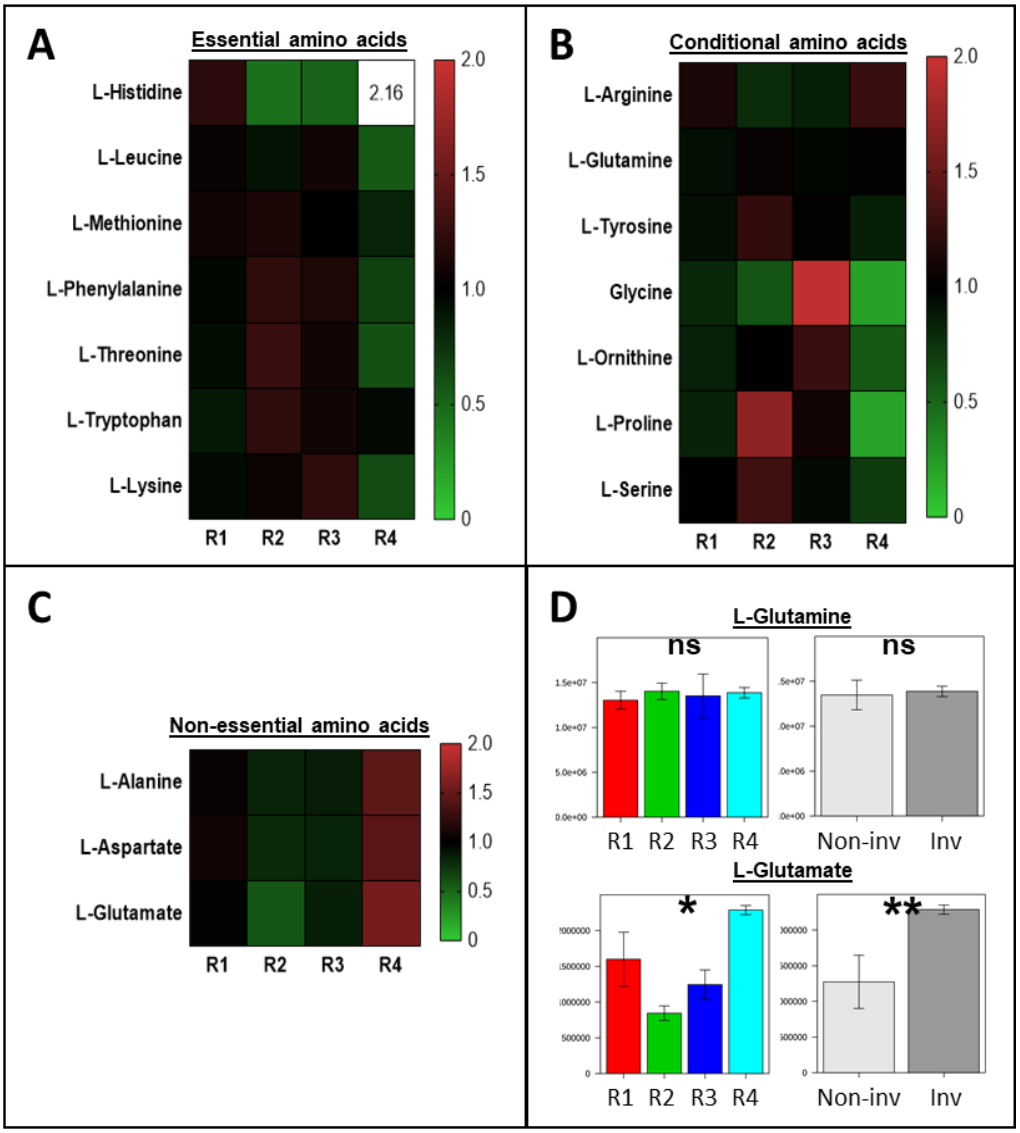

Figure 3.10. Regional variation in patient 6 of essential conditional and non-essential amino acids. Heatmaps display median replicate values of mean-centred peak intensities for essential (A), conditional (B), and non-essential (C) amino acids. Scale bars depict the grading of colours for fold changes ranging between 0 and 2. Fold changes above 2 are numbered. Peak intensities for metabolites of interest across regions (symbol R; left bar plot) and between region types (right bar plot) are displayed in (D).

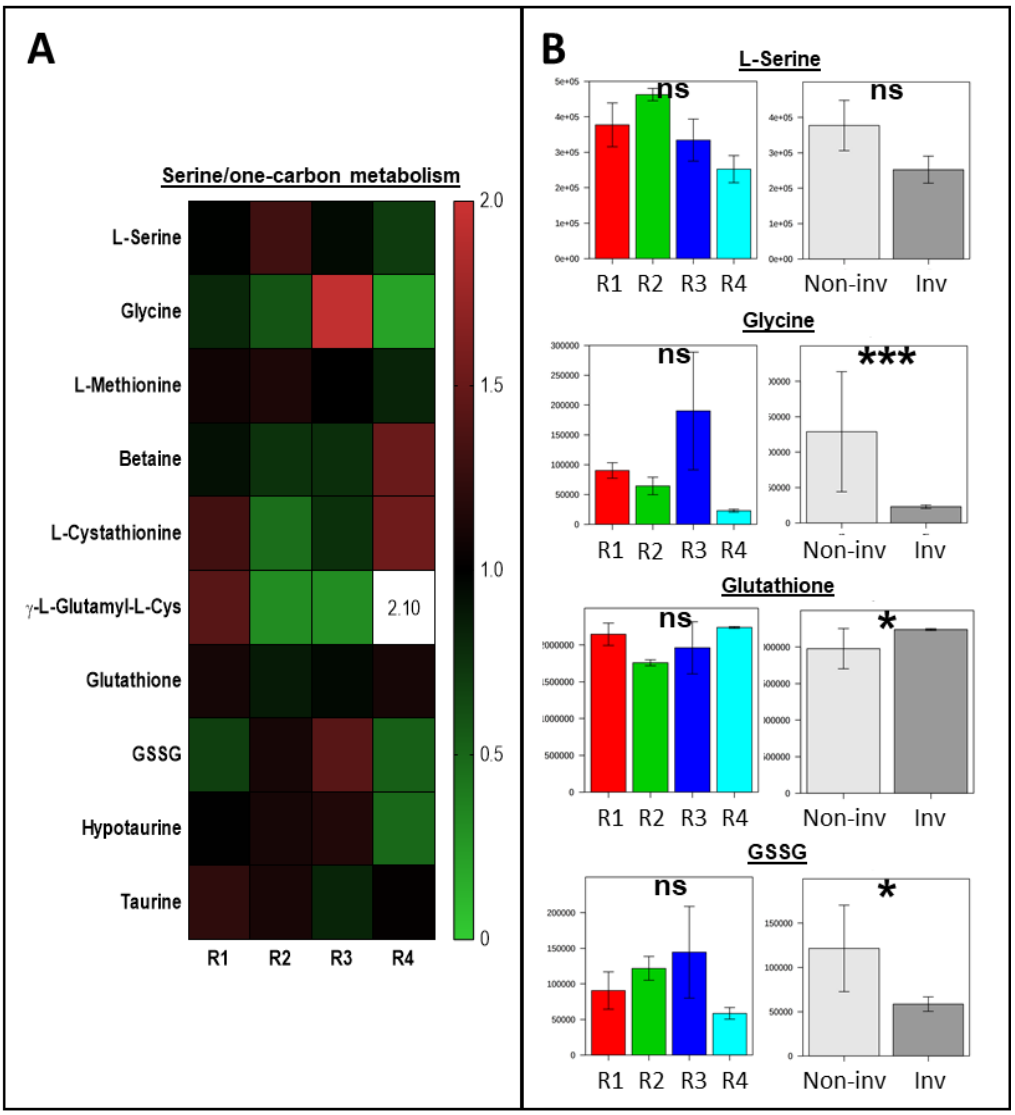

Figure 3.11. Regional variation in patient 6 of metabolites belonging to the serine/one-carbon metabolic pathway. Heatmaps display median replicate values of mean-centred peak intensities for metabolites generated within serine/one-carbon metabolism (A). Scale bars depict the grading of colours for fold changes ranging between 0 and 2. Fold changes above 2 are numbered. Peak intensities for metabolites of interest across regions (symbol R; left bar plot) and between region types (right bar plot) are displayed in (B). Statistical evaluation of regional variation was conducted using a one-way ANOVA model and two-sample *t*-test, respectively. Abbreviations: Non-inv – non-invasive (light grey); Inv – invasive (dark grey). ns = not significant; * = $p<0.05$; ** = $p<0.01$; *** = $p<0.001$; **** = $p<0.0001$.

Table 3.6. Metabolic variation across region and region types in patient 6.

Metabolite	ID confidence	Across regions		Invasive vs non-invasive regions		
		FDR	Significant	log2FC	FDR	Significant
Glycolysis						
D-Glucose	8	1.45E-03	**	1.24	6.72E-03	**
D-Glucose 6-phosphate	10	8.06E-01	ns	-0.01	8.78E-01	ns
D-Fructose-1,6-bisphosphate	10	1.48E-01	ns	-0.09	2.73E-01	ns
D-Glyceraldehyde 3-phosphate	10	4.08E-01	ns	-0.36	7.05E-01	ns
3-Phospho-D-glycerate	10	1.55E-01	ns	-1.84	1.82E-01	ns
Phosphoenolpyruvate	10	1.29E-01	ns	-2.69	8.28E-02	ns
Pyruvate	10	2.18E-01	ns	-0.28	9.85E-01	ns
Lactate	10	9.48E-02	ns	-0.91	1.42E-01	ns
Tricarboxylic acid cycle						
Citrate	8	2.02E-01	ns	0.78	1.21E-03	**
Isocitrate	8	2.59E-01	ns	-0.74	3.41E-03	**
Succinate	10	2.36E-01	ns	-1.08	4.11E-03	**
Malate	10	2.41E-01	ns	0.11	4.35E-01	ns
Energetics						
ADP	10	2.10E-01	ns	-1.18	2.48E-02	*
ATP	8	4.98E-02	*	-1.50	3.85E-02	*
Creatine	10	9.10E-03	**	0.66	5.11E-05	****
Creatinine	10	1.22E-03	**	1.78	1.36E-04	***
NAD+	10	8.87E-03	**	-4.27	4.53E-03	**
NADH	10	2.50E-02	*	-1.54	2.16E-01	ns
Essential amino acids						
L-Histidine	10	1.77E-03	**	1.54	7.51E-04	***
L-Leucine	10	4.12E-02	*	-0.97	7.64E-02	ns
L-Lysine	8	4.59E-02	*	-0.79	2.29E-01	ns
L-Methionine	10	2.17E-01	ns	-0.33	6.53E-02	ns
L-Phenylalanine	8	3.27E-02	*	-0.64	1.47E-01	ns
L-Threonine	10	8.88E-04	***	-0.85	1.31E-01	ns
L-Tryptophan	10	2.60E-01	ns	-0.08	8.17E-01	ns
Conditional amino acids						
L-Arginine	10	1.44E-01	ns	0.44	1.34E-01	ns
L-Glutamine	10	9.17E-01	ns	0.04	5.99E-01	ns
L-Tyrosine	10	3.47E-01	ns	-0.29	2.29E-01	ns
Glycine	10	5.38E-02	ns	-2.49	5.92E-04	***
L-Ornithine	10	4.52E-02	*	-0.97	2.43E-01	ns
L-Proline	10	6.51E-04	***	-2.57	2.78E-04	***
L-Serine	10	7.29E-02	ns	-0.58	1.61E-01	ns
Non-essential amino acids						
L-Alanine	10	1.02E-02	*	0.68	8.22E-05	****
L-Aspartate	10	1.17E-01	ns	0.67	9.86E-04	***
L-Glutamate	10	1.51E-02	*	0.84	1.11E-03	**
Serine/one-carbon metabolism						
Betaine	10	4.27E-02	*	0.77	2.52E-02	*
L-Cystathionine	10	1.34E-03	**	0.80	9.28E-03	**
γ-L-Glutamyl-L-cysteine	8	2.05E-01	ns	1.47	7.38E-03	**
Glutathione	10	3.52E-01	ns	0.18	4.48E-02	*
Glutathione disulfide	10	2.86E-01	ns	-1.05	2.11E-02	*
Hypotaurine	8	1.72E-03	**	-1.19	5.36E-05	****
Taurine	10	3.89E-01	ns	0.03	6.96E-01	ns

Metabolites highlighted in red showed RSD values >30% in QC samples. ID confidence scores delineate the confidence of the putative metabolite identification. Fold changes are invasive to non-invasive comparisons and are displayed as logarithms to the base 2 (log2FC). Fold changes >0.58 or < -0.58 are depicted in red and green, respectively. Statistical evaluation of variation between regions and region types was performed using a one-way ANOVA model and two-sample *t*-test, respectively. Significance scores were corrected for multiple comparisons using false discovery rate (FDR). ns = not significant; * = $p<0.05$; ** = $p<0.01$; *** = $p<0.001$; **** = $p<0.0001$.

Patient 15 demonstrated a relatively homogenous non-invasive metabolomic profile in terms of glycolysis (Figure 3.12), TCA cycle (Figure 3.13), and amino acid metabolism (Figure 3.14). Heterogeneous levels of ADP, ATP ($p< 0.0001$), NAD+ and NADH (FDR<0.05) were observed in support of regional differences in energetics (Figure 3.12C). Consistent with previous analyses, heterogeneity predominantly occurred between the non-invasive and invasive regions, with significant scores for most essential and conditional amino acids (Figure 3.13A, B, and C). Of note, several glycolytic intermediates were lower in abundance in the non-invasive regions, indicative of increased glycolytic activity leading to greater ATP levels (Figure 3.12A). Surprisingly, lactate levels were increased in the invasive region despite hypothesised increased relative glycolytic activity within the non-invasive regions. We hypothesise that the high lactate levels within the invasive region may be derived from infiltrating tumour cells since glioma cell invasion is dependent upon lactate efflux (Colen *et al.*, 2011). Lactate may also enhance tumour cell motility, as seen in head and neck carcinoma cell lines, whilst reducing migration of immune cells (Goetze *et al.*, 2011). Lactate within the invasive region may therefore be a biomarker of tumour invasion and immune evasion to be investigated in a larger cohort.

Citrate and isocitrate levels were reduced in the non-invasive regions (Figure 3.12B), related perhaps to reduced TCA anapleurosis or shuttling of carbon atoms into lipid synthesis. Indeed, levels of the L-glutamate and its precursor, L-glutamine, were relatively unchanged across all regions (Figure 3.13D), indicating a lack of anapleurotic activity. No significant scores for glutathione in oxidised or reduced form were observed (Figure 3.14B), suggestive of sustained synthesis to replenish metabolite pools. Table 3.7 summarises the biased analysis of intratumour metabolic heterogeneity across all regions and between non-invasive and invasive regions in patient 15. Collectively, both patients 6 and 15 highlighted the different extents of heterogeneity within several metabolic pathways that was particularly evident between the non-invasive and invasive regions.

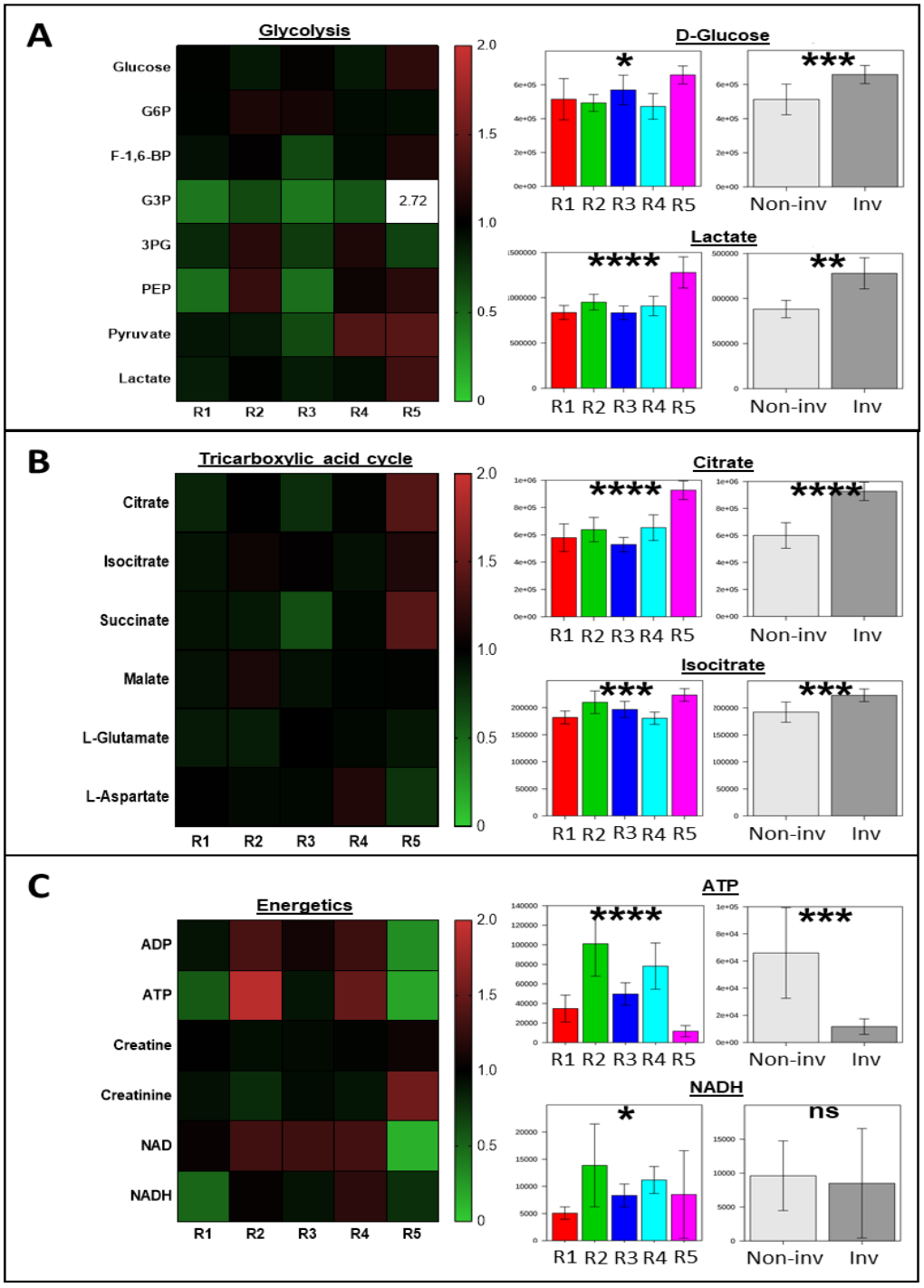

Figure 3.12. Regional variation in patient 15 of metabolites generated within the glycolysis pathway, tricarboxylic acid cycle, and energetics. Heatmaps display median replicate values of mean-centred peak intensities for metabolites generated within glycolysis (A), TCA cycle (B), and energetics (C). Scale bars depict the grading of colours for fold changes ranging between 0 and 2. Fold changes above 2 are numbered. Peak intensities for metabolites of interest across regions (symbol R; left bar plot) and between region types (right bar plot) are displayed in each panel. Statistical evaluation of regional variation was conducted using a one-way ANOVA model and two-sample t-test, respectively. Abbreviations: Non-inv – non-invasive (light grey); Inv – invasive (dark grey). ns = not significant; * = $p<0.05$; ** = $p<0.01$; *** = $p<0.001$; **** = $p<0.0001$.

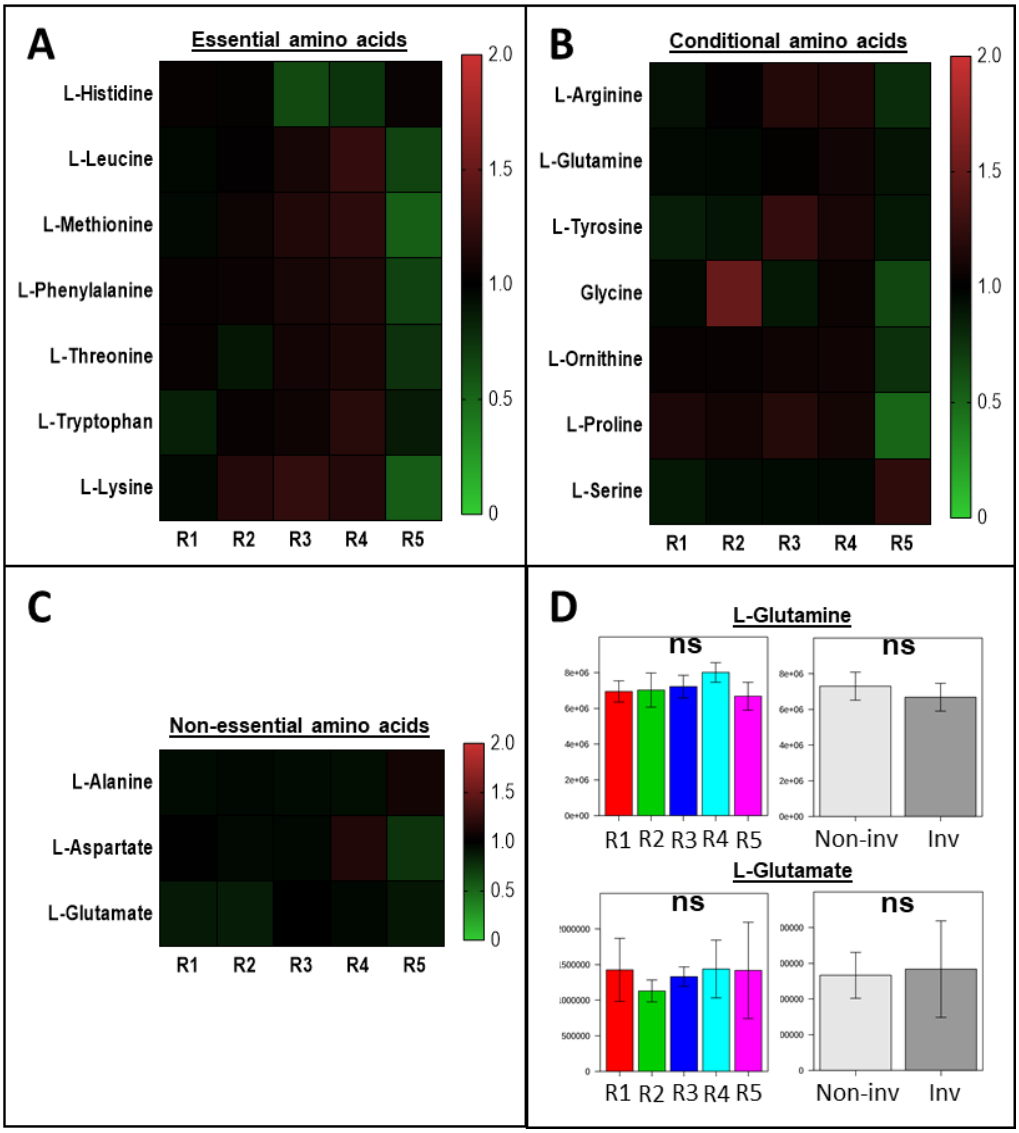

Figure 3.13. Regional variation in patient 15 of essential, conditional, and non-essential amino acids. Heatmaps display median replicate values of mean-centred peak intensities for essential (A), conditional (B), and non-essential (C) amino acids. Scale bars depict the grading of colours for fold changes ranging between 0 and 2. Fold changes above 2 are numbered. Peak intensities for metabolites of interest across regions (symbol R; left bar plot) and between region types (right bar plot) are displayed in (D). Statistical evaluation of regional variation was conducted using a one-way ANOVA model and two-sample *t*-test, respectively. Abbreviations: Non-inv – non-invasive (light grey); Inv – invasive (dark grey). ns = not significant; * = $p<0.05$; ** = $p<0.01$; *** = $p<0.001$; **** = $p<0.0001$.

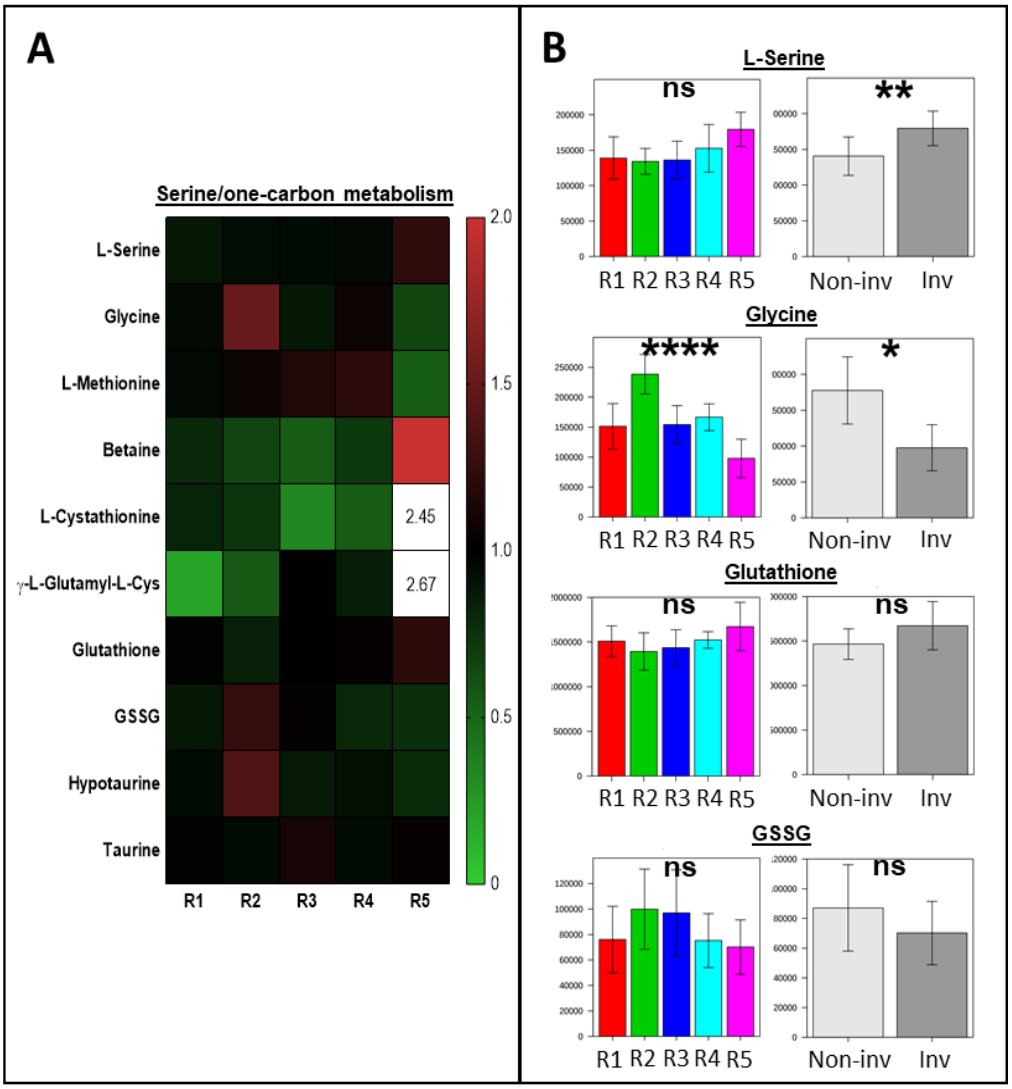

Figure 3.14. Regional variation in patient 15 of metabolites belonging to the serine/one-carbon metabolic pathway. Heatmaps display median replicate values of mean-centred peak intensities for metabolites generated within serine/one-carbon metabolism (A). Scale bars depict the grading of colours for fold changes ranging between 0 and 2. Fold changes above 2 are numbered. Peak intensities for metabolites of interest across regions (symbol R; left bar plot) and between region types (right bar plot) are displayed in (B). Statistical evaluation of regional variation was conducted using a one-way ANOVA model and two-sample *t*-test, respectively. Abbreviations: Non-inv – non-invasive (light grey); Inv – invasive (dark grey). ns = not significant; * = $p<0.05$; ** = $p<0.01$; *** = $p<0.001$; **** = $p<0.0001$.

Table 3.7. Metabolic variation across region and region types in patient 15.

Metabolite	ID confidenc	Across regions		Invasive vs non-invasive regions		
		FDR	Significant	log2FC	FDR	Significant
Glycolysis						
D-Glucose	8	1.90E-02	*	0.36	2.55E-04	***
D-Glucose 6-phosphate	10	9.57E-02	ns	-0.16	9.45E-02	ns
D-Fructose-1,6-bisphosphate	10	8.55E-02	ns	0.56	1.33E-01	ns
D-Glyceraldehyde 3-phosphate	10	9.90E-09	****	2.42	4.69E-05	****
3-Phospho-D-glycerate	10	1.31E-01	ns	-0.53	2.72E-01	ns
Phosphoenolpyruvate	10	1.98E-02	*	0.74	3.02E-01	ns
Pyruvate	10	5.96E-01	ns	0.23	7.43E-01	ns
Lactate	10	3.08E-06	****	0.54	1.26E-03	**
Tricarboxylic acid cycle						
Citrate	8	4.42E-06	****	0.63	1.22E-07	****
Isocitrate	8	2.64E-04	***	0.22	5.27E-04	***
Succinate	10	6.49E-06	****	0.77	6.03E-05	****
Malate	10	1.12E-02	*	0.07	5.53E-01	ns
Energetics						
ADP	10	8.08E-11	****	-1.96	1.90E-05	****
ATP	8	1.72E-08	****	-2.51	5.14E-04	***
Creatine	10	2.48E-01	ns	0.14	2.94E-01	ns
Creatinine	10	1.07E-06	****	0.80	6.37E-03	**
NAD+	10	7.60E-09	****	-2.82	3.49E-03	**
NADH	10	3.46E-02	*	-0.18	4.63E-01	ns
Essential amino acids						
L-Histidine	10	3.86E-01	ns	0.18	1.71E-01	ns
L-Leucine	10	6.65E-08	****	-0.74	1.23E-03	**
L-Lysine	8	5.69E-05	****	-1.08	9.21E-03	**
L-Methionine	10	1.78E-07	****	-0.93	2.33E-03	**
L-Phenylalanine	8	6.74E-06	****	-0.71	2.05E-03	**
L-Threonine	10	2.97E-06	****	-0.51	4.82E-03	**
L-Tryptophan	10	3.81E-04	***	-0.31	4.78E-02	*
Conditional amino acids						
L-Arginine	10	3.31E-02	*	-0.30	6.34E-02	ns
L-Glutamine	10	5.33E-02	ns	-0.13	1.58E-01	ns
L-Tyrosine	10	1.42E-04	***	-0.19	1.59E-01	*
Glycine	10	8.29E-05	****	-0.86	1.99E-02	*
L-Ornithine	10	2.43E-03	**	-0.55	3.09E-02	*
L-Proline	10	1.05E-08	****	-1.12	3.36E-03	**
L-Serine	10	5.91E-02	ns	0.35	8.03E-03	**
Non-essential amino acids						
L-Alanine	10	4.43E-01	ns	0.17	4.50E-02	*
L-Aspartate	10	5.66E-01	ns	-0.08	5.06E-01	ns
L-Glutamate	10	6.23E-01	ns	0.09	9.79E-01	ns
Serine/one-carbon metabolism						
Betaine	10	2.50E-10	****	1.65	1.18E-05	****
L-Cystathionine	10	2.56E-06	****	1.92	1.27E-08	****
γ-L-Glutamyl-L-cysteine	8	1.97E-03	**	1.93	3.58E-05	****
Glutathione	10	2.29E-01	ns	0.19	1.89E-01	ns
Glutathione disulfide	10	2.55E-01	ns	-0.31	1.99E-01	ns
Hypotaurine	8	3.34E-04	***	-0.33	1.49E-01	ns
Taurine	10	3.59E-02	*	0.07	4.32E-01	ns

Metabolites highlighted in red showed RSD values >30% in QC samples. ID confidence scores delineate the confidence of the putative metabolite identification. Fold changes are invasive to non-invasive comparisons and are displayed as logarithms to the base 2 (log2FC). Fold changes >0.58 or < -0.58 are depicted in red and green, respectively. Statistical evaluation of variation between regions and region types was performed using a one-way ANOVA model and two-sample *t*-test, respectively. Significance scores were corrected for multiple comparisons using false discovery rate (FDR). ns = not significant; * = $p<0.05$; ** = $p<0.01$; *** = $p<0.001$; **** = $p<0.0001$.

3.5. Lipid heterogeneity within and between HGG patients

The heterogeneity observed within metabolomic profiles in relation to regional variation between invasive and non-invasive regions were largely replicated within lipidomic profiles. PCA of all patients revealed spread between tumour fragments in patients 6, 8 and 9 (Figure 3.15B). Samples from patients 14 and 15 were more clustered in comparison to the other patients (Figure 3.15B). Interestingly, patient 15 was slightly segregated from the other patients, suggestive of a distinct lipidomic signature. This is likely due to the *IDH1* mutation in patient 15 influencing the lipid signature displayed by this tumour. All QC samples apart from one showed strong clustering, indicating minimal shift during the experiment duration (Figure 3.15A). From Figure 3.15B, it was evident that some samples from different tumours demonstrated a similar lipidomic profile that segregated from the main cluster of samples. Analysing the region type revealed most of these samples to be derived from the invasive margin (Figure 3.15C). Sample 9_5_2 from the invasive region of patient 9 did not cluster with all other invasive region profiles and may therefore be an outlier. Collectively, this supported the notion of a highly distinct lipidomic signature within the invasive margin compared to non-invasive regions.

Multivariate analysis based on class discrimination using an OPLS-DA model confirmed the clustering and separation of invasive region lipidomic profiles, although some non-invasive region samples were co-segregated (Figure 3.16A). The strength of the model was only moderate with R2Y=0.662 and Q=0.56, with R2X=0.414. The R2X value indicates the predictive and orthogonal variation in X (data matrix) explained by the model, whereas the R2Y value indicates the total sum of variation in Y (class discrimination) explained by the model. The Q2 value depicts the goodness of prediction of the model and to identify overfitting. The most important lipid species distinguishing the invasive and non-invasive regions were sphingolipids and fatty acids, respectively (Figure 3.16B), which may represent biomarkers for further evaluation. A few lysophospholipid species were also associated with the invasive margin (Figure 3.16B). Hypoxic and Ras-transformed cells have been shown to scavenge

exogenous lipids (Kamphorst *et al.*, 2013). Therefore, differences between the non-invasive and invasive regions in terms of lysophospholipid species may reflect differences in lipid scavenging potential. However, lipid classes were identified for only a small fraction of lipids since tandem MS/MS was not conducted in the methodology. Therefore, the differences observed may not reflect the full complement of lipids classes that are altered within and between patients.

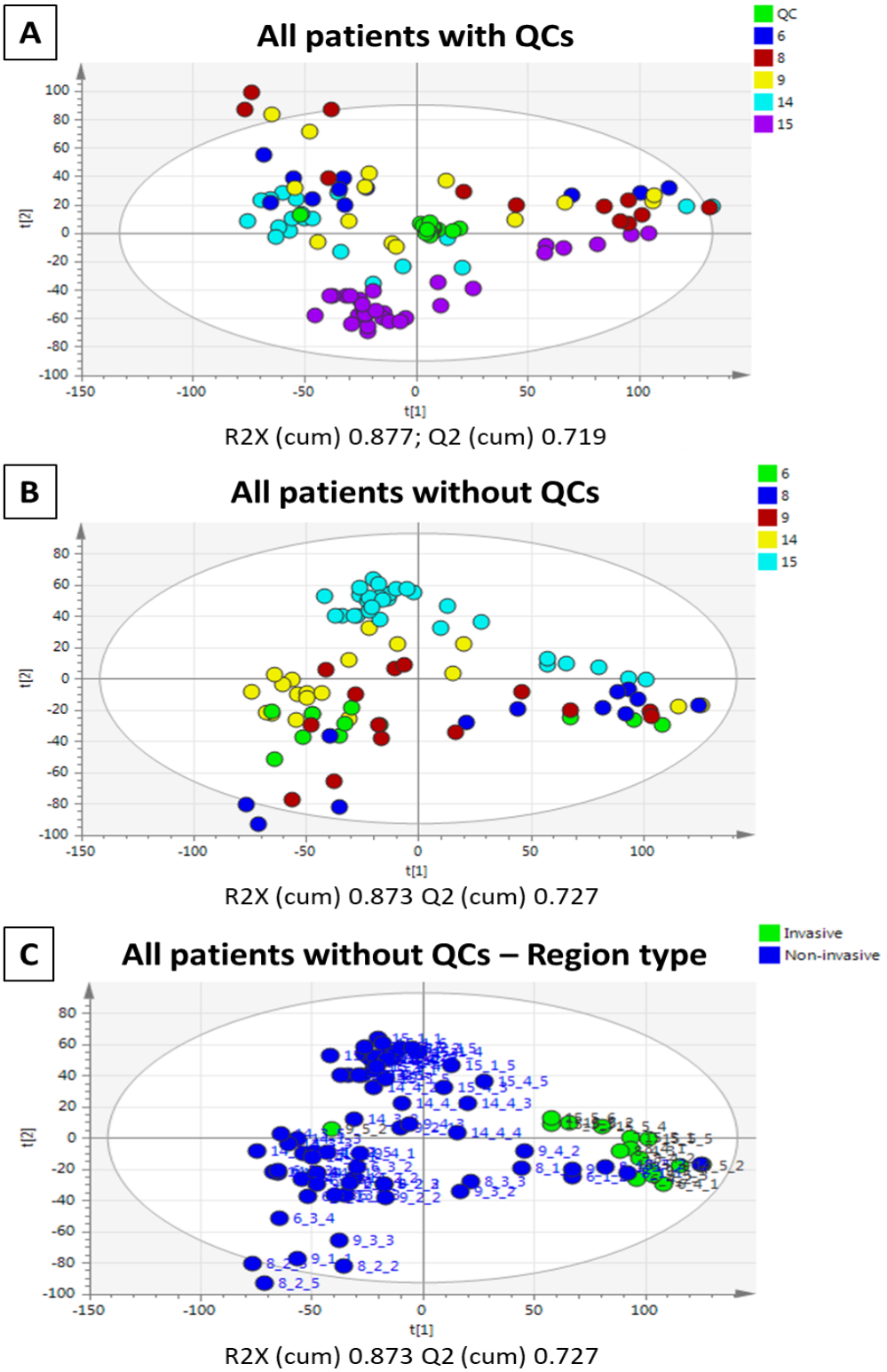

Figure 3.15. PCA of lipidomic profiles from all five patients. The position of tumour fragments from each patient are positioned in the model plane formed by the first two principle components in the presence (A) or absence (B and C) of the QC samples. Figure legends (top right) delineate colour choices for patient number (A and B) and region type (C). R2X (cum) and Q2 (cum) values quantitatively depict the amount of explained (goodness of fit) and predicted (goodness of prediction) variation accounted for by the fitted model, respectively. Hotelling's T^2 calculated at 95% confidence level is depicted as an ellipse within each figure.

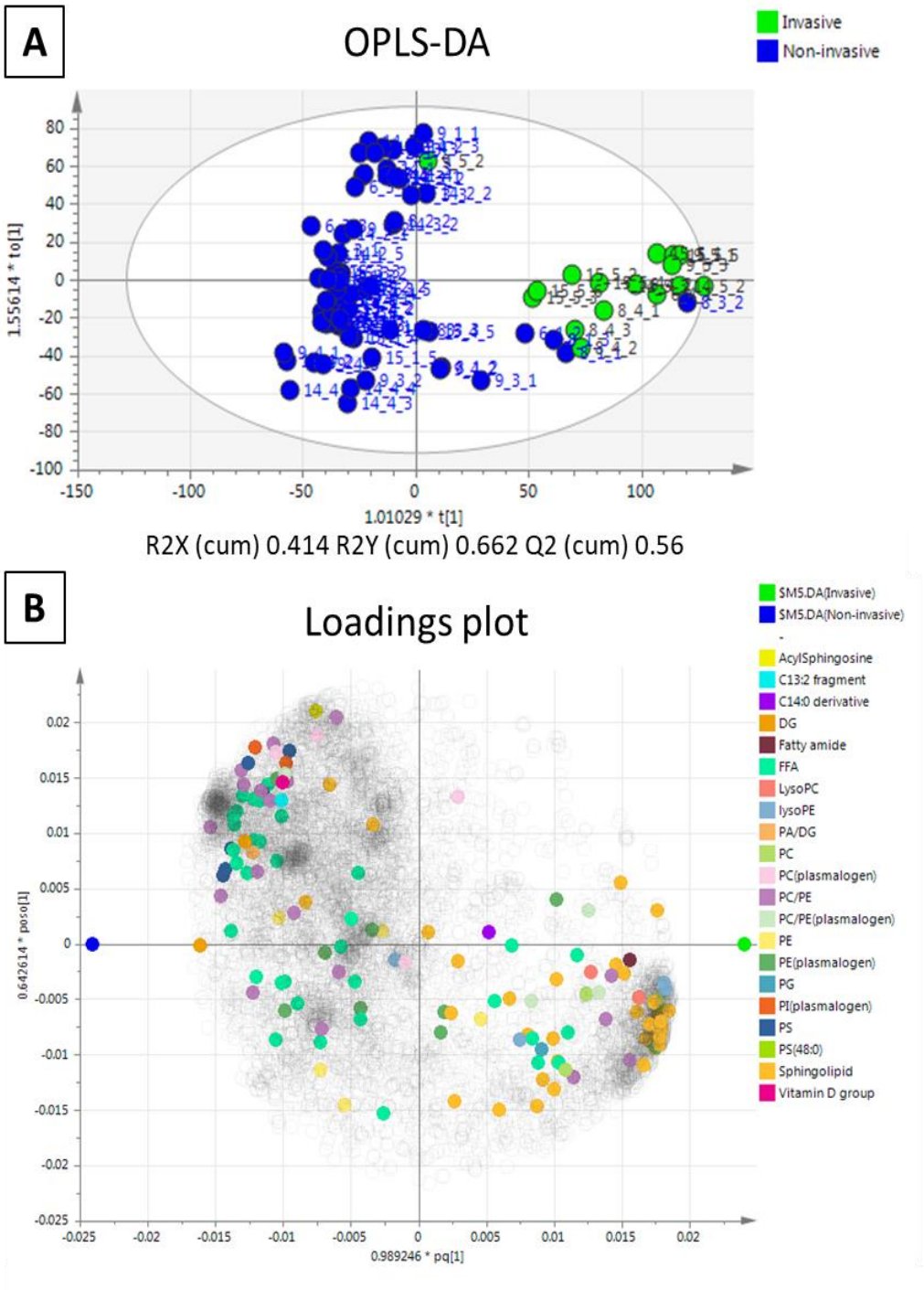

Figure 3.16. OPLS-DA of lipidomic profiles from all five patients. (A) The position of tumour fragments from each patient are positioned in the model plane formed by the predictive (Y) and orthogonal components (X). R2X (cum) accounts for the predictive and orthogonal variation in X. R2Y (cum) is the total sum of variation in Y explained by the model. Q2 (cum) depicts the amount of predicted (goodness of prediction) variation accounted for by the model. The loadings for each variable derived from the OPLS-DA analysis are displayed in (B). Figure legends (top right) delineate the colour choices for region type (A) and lipid species (B). Hotelling's T^2 calculated at 95% confidence level is depicted as an ellipse in (A).

3.6. Multilevel modelling identifies differentially abundant metabolites between the non-invasive and invasive regions

In order to identify common changes across several patients, multilevel modelling was performed on patients 9, 14, and 15, covering *IDH1* wildtype GBM, *IDH1* mutant GBM, and MGNT tumour types. A multilevel model was applied since it is not statistically appropriate to treat samples from the same patient as independent. Table 3.8 confirms the significance of several metabolites associated with glycolysis, TCA cycle, energetics, amino acid synthesis and glutathione metabolism. The model emphasises the higher abundance of several amino acids, including L-proline, in the non-invasive regions compared to the invasive margin. The two metabolites with the highest fold changes, N-acetyl-L-aspartate (NAA) and N-acetyl-aspartyl-glutamate (NAAG), are neuronal markers, indicating that tissue from the invasive margin is not solely constituted of tumour cells. MSEA of metabolites with a fold change > 1.5 or < -0.67 showed significant enrichment of *nucleotide sugars metabolism*, *starch and sucrose metabolism* and *phosphatidylcholine biosynthesis*, with respective raw *p*-values of 0.012, 0.017 and 0.031 (Table 3.9). Pathway analysis of the same list of differentially abundant metabolites revealed significant impact to several pathways, including *lysine degradation*, *pyrimidine metabolism* and *arginine and proline metabolism*, with impact scores of 0.33, 0.36 and 0.32, respectively (Table 3.10).

Table 3.8. Metabolites of differential abundance between non-invasive and invasive regions using a multilevel linear model.

Metabolite	ID confidence	log2FC	FDR	Significant	Higher abundance
N-Acetyl-aspartyl-glutamate	7	3.70	0.00E+00	****	Invasive
N-Acetyl-L-aspartate	8	1.77	5.65E-06	****	Invasive
D-Glyceraldehyde 3-phosphate	10	1.50	5.42E-05	****	Invasive
Creatinine	10	0.89	5.07E-05	****	Invasive
L-Cystathionine	10	0.88	5.07E-03	**	Invasive
Betaine	10	0.66	2.55E-02	*	Invasive
L-Histidine	10	0.52	1.03E-02	*	Invasive
Glutathione	10	0.37	5.37E-03	**	Invasive
D-Glucose 6-phosphate	10	0.36	3.17E-02	*	Invasive
Citrate	8	0.32	2.46E-02	*	Invasive
Creatine	10	0.26	7.84E-04	***	Invasive
L-Alanine	8	0.23	8.45E-03	**	Invasive
L-Aspartate	10	-0.17	3.88E-02	*	Non-invasive
Isocitrate	8	-0.23	4.52E-02	*	Non-invasive
L-Tryptophan	10	-0.29	3.40E-02	*	Non-invasive
Glutathione disulfide	10	-0.54	2.77E-02	*	Non-invasive
Choline phosphate	10	-0.64	5.51E-04	***	Non-invasive
L-Threonine	10	-0.65	0.00E+00	****	Non-invasive
L-Phenylalanine	8	-0.72	2.58E-04	***	Non-invasive
L-Ornithine	10	-0.90	1.60E-05	****	Non-invasive
UDP-N-acetyl-D-glucosamine	6	-0.90	5.65E-06	****	Non-invasive
L-Leucine	10	-0.92	1.40E-03	**	Non-invasive
Ethanolamine phosphate	10	-1.04	8.01E-03	**	Non-invasive
NADH	10	-1.06	1.17E-02	*	Non-invasive
L-Kynurenine	8	-1.17	3.60E-03	**	Non-invasive
L-Lysine	8	-1.35	1.23E-02	*	Non-invasive
Glycine	10	-1.39	1.08E-02	*	Non-invasive
(S)-1-Pyrroline-5-carboxylate	6	-1.66	0.00E+00	****	Non-invasive
L-Proline	10	-1.70	2.33E-05	****	Non-invasive
ATP	8	-1.92	2.14E-04	***	Non-invasive
NAD+	10	-2.15	3.15E-03	**	Non-invasive
5-Methylcytosine	8	-2.53	5.87E-04	***	Non-invasive
2-Hydroxyadenine	7	-2.82	1.75E-03	**	Non-invasive

Metabolites highlighted in red showed RSD values >30% in QC samples. ID confidence scores delineate the confidence of the putative metabolite identification. Fold changes are displayed as logarithms to the base 2 (log2FC). Fold changes >0.58 or < -0.58 are depicted in red and green, respectively. The region type with the higher peak intensity is indicated. Significance scores were FDR-corrected for multiple comparisons. ns = not significant; * = $p<0.05$; ** = $p<0.01$; *** = $p<0.001$; **** = $p<0.0001$.

Table 3.9. Metabolite set enrichment analysis of metabolites identified as differentially abundant based on a multilevel linear model.

Metabolite Set	Total	Expected	Hits	Raw p	Holm p	FDR
Nucleotide Sugars Metabolism	20	2.71	7	0.0122	1	0.847
Starch and Sucrose Metabolism	31	4.21	9	0.0173	1	0.847
Phosphatidylcholine Biosynthesis	14	1.9	5	0.0309	1	0.986
Lactose Synthesis	20	2.71	6	0.0428	1	0.986
Carnitine Synthesis	22	2.99	6	0.0656	1	0.986

The table details the top five enriched metabolite sets based on significantly differentially abundant metabolites with log2 fold-change >0.58 or < -0.58. Significant raw *p*-values (Raw p) for enriched metabolite sets were adjusted for multiple comparisons using the Holm (Holm p) or false-discovery rate (FDR) method.

Table 3.10. Pathway analysis of metabolites identified as differentially abundant based on a multilevel linear model.

Metabolic Pathway	Total	Expected	Hits	Raw p	Holm p	FDR	Impact
Lysine degradation	47	2.1674	12	6.85E-07	5.48E-05	5.48E-05	0.33359
Pyrimidine metabolism	60	2.7669	13	1.76E-06	0.000139	7.05E-05	0.35932
Arginine and proline metabolism	77	3.5509	14	6.33E-06	0.000494	0.000169	0.32182
Valine, leucine and isoleucine biosynthesis	27	1.2451	6	0.001124	0.086543	0.022479	0.32856
Glycine, serine and threonine metabolism	48	2.2135	7	0.005628	0.42769	0.09004	0.33636

The table details the top five impacted metabolic pathways based on significantly differentially abundant metabolites with log2 fold-change >0.58 or < -0.58. Significant raw *p*-values (Raw p) for enriched metabolite sets were adjusted for multiple comparisons using the Holm (Holm p) or false-discovery rate (FDR) method. Impact scores range between 0 and 1.

Collective analysis of differentially abundant metabolites between the non-invasive and invasive regions of patients 9, 14, and 15 demonstrated significant enrichment of several metabolic pathways. However, to determine if these pathways were also enriched at the individual level, each patient was assessed independently through statistical evaluation of differentially abundant metabolites between the non-invasive and invasive regions using a t-test. Heatmaps for patients 6 (Figure 3.17A) and 15 (Figure 3.17B) demonstrated the capacity of several metabolites to distinguish non-invasive from invasive regions. MSEA of differentially abundant metabolites in patient 6 revealed significant enrichment of glutathione metabolism (raw p-value=0.033) (Table 3.11), whereas pathway analysis identified significant scores for arginine and proline metabolism (raw p-value=2.78E-07), histidine metabolism (raw p-value=7.20E-05), and pyrimidine metabolism (raw p-value=0.00025) (Table 3.12). However, pathway impact scores were low (0.26, 0.24 and 0.23, respectively). In patient 15, MSEA showed significant enrichment for phosphatidylethanolamine synthesis (raw p-value=0.030), purine metabolism (raw p-value=0.036), and pyrimidine metabolism (raw p-value=0.038) (Table 3.13). Pathway analysis identified significant impact on several pathways, including pyrimidine metabolism (raw p-value=7.07E-11), arginine and proline metabolism (raw p-value=1.72E-06), and purine metabolism (raw p-value=4.46E-06), with modest impact scores of 0.54, 0.25 and 0.38, respectively (Table 3.14). Similar analyses in the other patients revealed patient-specific enrichment in certain metabolic sets, including *de novo* triacylglycerol

biosynthesis (raw p-value=0.102), glycolysis (raw p-value=0.00043) and phosphatidylethanolamine biosynthesis (raw p-value=0.0025) in patients 8, 9 and 14, respectively. However, arginine and proline metabolism were consistently observed to be significantly impacted in patients 8, 9 and 14. Along with the data from patients 6 and 15, this analysis indicated that non-invasive and invasive regions differ metabolically in terms of arginine and proline metabolism. This analysis also highlighted inter-patient heterogeneity indicating that there are not only metabolites commonly altered between patients (Table 3.15), but also some metabolites that are altered in some patients and not others.

Table 3.11. Metabolite set enrichment analysis of metabolites in patient 6 identified as significant using *t*-test.

Metabolite Set	Total	Expected	Hits	Raw p	Holm p	FDR
Glutathione Metabolism	21	3.26	7	0.0326	1	0.966
Phosphatidylcholine Biosynthesis	14	2.17	5	0.052	1	0.966
Glutamate Metabolism	49	7.61	12	0.0635	1	0.966
Lactose Synthesis	20	3.11	6	0.0753	1	0.966
Nucleotide Sugars Metabolism	20	3.11	6	0.0753	1	0.966

The table details the top five enriched metabolite sets based on significantly differentially abundant metabolites with log2 fold-change >0.58 or < -0.58. Significant raw *p*-values (Raw p) for enriched metabolite sets were adjusted for multiple comparisons using the Holm (Holm p) or false-discovery rate (FDR) method.

Table 3.12. Pathway analysis of metabolites in patient 6 identified as significant using *t*-test.

Metabolic Pathway	Total	Expected	Hits	Raw p	Holm p	FDR	Impact
Arginine and proline metabolism	77	4.1267	17	2.78E-07	2.22E-05	2.22E-05	0.25857
Histidine metabolism	44	2.3581	10	7.20E-05	0.005687	0.002879	0.24098
Pyrimidine metabolism	60	3.2156	11	0.000246	0.019209	0.006567	0.23188
Taurine and hypotaurine metabolism	20	1.0719	6	0.000439	0.033819	0.008784	0.1241
beta-Alanine metabolism	28	1.5006	6	0.002994	0.22753	0.047901	0.18935

The table details the top five impacted metabolic pathways based on significantly differentially abundant metabolites with log2 fold-change >0.58 or < -0.58. Significant raw *p*-values (Raw p) for enriched metabolite sets were adjusted for multiple comparisons using the Holm (Holm p) or false-discovery rate (FDR) method. Impact scores range between 0 and 1.

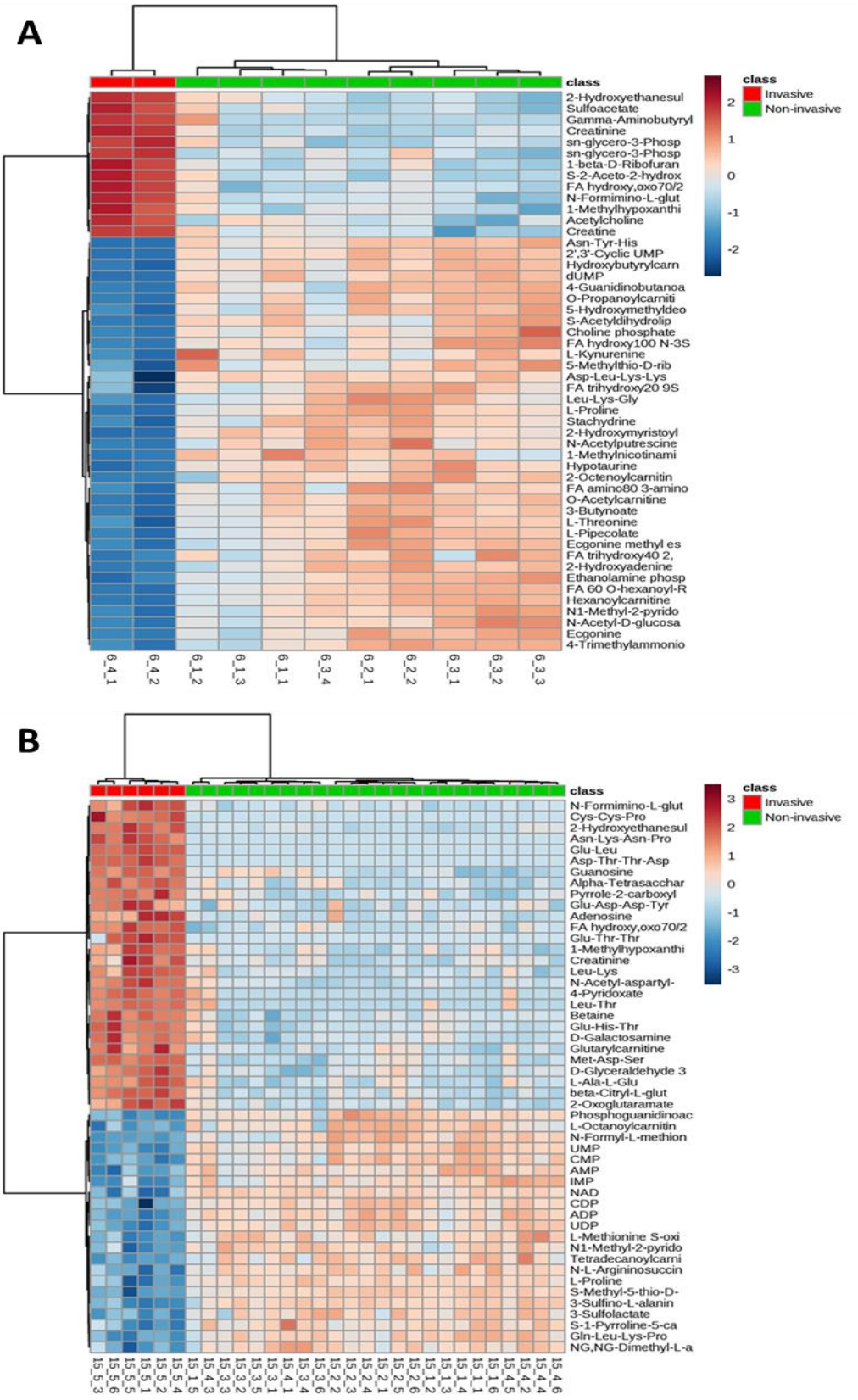

Figure 3.17. Identification of differentially abundant metabolites between non-invasive and invasive regions in patients 6 and 15. *t*-test was conducted on the metabolomic profiles from patients 6 (A) and 15 (B). Only the top 50 significant metabolites are displayed in the heatmaps. Sample IDs delineate the patient, region (symbol R), and replicate numbers, respectively.

Table 3.13. Metabolite set enrichment analysis of metabolites in patient 15 identified as significant using *t*-test.

Metabolite Set	Total	Expected	Hits	Raw p	Holm p	FDR
Phosphatidylethanolamine Biosynthesis	12	1.92	5	0.0302	1	1
Purine Metabolism	74	11.9	18	0.0362	1	1
Pyrimidine Metabolism	59	9.45	15	0.0377	1	1
Phosphatidylcholine Biosynthesis	14	2.24	5	0.0584	1	1
Arginine and Proline Metabolism	53	8.49	13	0.0666	1	1

The table details the top five enriched metabolite sets based on significantly differentially abundant metabolites with log2 fold-change >0.58 or < -0.58. Significant raw *p*-values (Raw p) for enriched metabolite sets were adjusted for multiple comparisons using the Holm (Holm p) or false-discovery rate (FDR) method.

Table 3.14. Pathway analysis of metabolites in patient 15 identified as significant using *t*-test.

Metabolic Pathway	Total	Expected	Hits	Raw p	Holm p	FDR	Impact
Pyrimidine metabolism	60	3.2405	19	7.07E-11	5.65E-09	5.65E-09	0.53745
Arginine and proline metabolism	77	4.1587	16	1.72E-06	0.000136	6.87E-05	0.24659
Purine metabolism	92	4.9688	17	4.46E-06	0.000348	0.000119	0.37727
Lysine degradation	47	2.5384	9	0.0007	0.053937	0.01401	0.14851
Alanine, aspartate and glutamate metabolism	24	1.2962	6	0.00133	0.10107	0.021277	0.02849

The table details the top five impacted metabolic pathways based on significantly differentially abundant metabolites with log2 fold-change >0.58 or < -0.58. Significant raw *p*-values (Raw p) for enriched metabolite sets were adjusted for multiple comparisons using the Holm (Holm p) or false-discovery rate (FDR) method. Impact scores range between 0 and 1.

Table 3.15. List of metabolites commonly identified across all five patients as significantly variant between invasive and non-invasive regions using *t*-test

Metabolite	ID confidence	Average peak intensity	Patient				
			6	8	9	14	15
sn-glycero-3-Phosphocholine	10	2.01E+07	1.32163	1.1026	0.93661	1.6265	-0.3168
N-Acetyl-L-aspartate	8	1.65E+06	2.15628	2.10291	1.60199	2.08613	1.24566
Homocarnosine	6	2.73E+05	2.41363	1.93713	1.37063	2.04648	0.59055
N-Acetyl-aspartyl-glutamate	7	1.66E+05	3.64803	1.95495	4.04411	4.06921	3.52785
2,3,4,5-Tetrahydropyridine-2-carboxylate	8	1.25E+05	-1.7871	-3.5246	-2.5618	-3.7791	-1.2785
Maleamate	7	6.25E+04	3.24738	2.90692	2.31301	2.67203	2.05577
Ala-Ala-Ala	5	4.80E+04	2.3148	1.36601	1.76856	2.62921	2.78769
S-1-Pyrroline-5-carboxylate	6	4.14E+04	-1.4469	-3.2917	-2.2616	-2.4104	-1.275
2-Isopropylmaleate	6	2.25E+04	-0.9595	-0.7886	-0.6838	-2.1438	-0.5317
Met-Ala-Ser	7	1.23E+04	2.09761	1.08513	2.04076	2.89598	4.58719
3-Sulfino-L-alanine	8	1.20E+04	-3.3058	-2.6808	-3.8994	-5.8419	-3.0084
Leu-Thr	7	1.03E+04	2.07401	1.65745	2.18098	2.52069	4.24157
4-Acetamidobutanoate	6	1.01E+04	1.34468	0.51766	0.62217	0.17144	1.47682
Val-His	7	6.59E+03	2.59782	1.41798	1.95411	1.2418	1.22726
[FA trihydroxy(2:0)] N-(9S,11R,15S-trihydroxy-5Z,13E-prostadienoyl)-ethanolamine	5	3.64E+03	-2.9215	-2.8365	-2.1006	-1.7412	0.64971
Met-Gly-Ser	7	2.12E+03	1.91114	1.26447	1.74245	2.29838	3.94019
4-Pyridoxate	6	9.78E+02	2.60845	1.4386	2.89125	1.95445	4.64427

Metabolites highlighted in red showed RSD values >30% in QC samples. ID confidence scores delineate the confidence of the putative metabolite identification. Fold changes in metabolite peak intensities between the invasive and non-invasive regions are displayed as logarithms to the base 2 (log2FC). Fold changes >0.58 or < -0.58 are depicted in red and green, respectively.

3.7. Non-invasive regions exhibit (or are characterised by) high proline levels

These findings revealed that metabolomic heterogeneity was largely confined between non-invasive and invasive regions. Of particular interest was the observation of consistently higher levels of L-proline within non-invasive regions compared to invasive margin in all five patients (Figure 3.18), indicating that increased synthesis or reduced catabolism of L-proline is important to tumour growth. Increased abundance of L-proline co-occurred with a similar increase in its catabolic breakdown product, 1-pyrroline-5-carboxylate (P5C). Indeed, the pattern finder feature of MetaboAnalyst indicated that L-proline and P5C were strongly correlated with a highly significant ($p<0.01$) score of 0.8 and above, across all patients (Table 3.16). L-glutamate 5-semialdehyde (GSA), another product of proline catabolism, showed a positive correlation with L-proline in four patients (Table 3.16). Transfer of the amino group from L-glutamate to GSA yields L-ornithine, which is part of the urea cycle. In all patients, L-ornithine was positively and significantly correlated with L-proline (Table 3.16). Only in patients 8, 14 and 15 was L-proline significantly correlated with two other members of the urea cycle, L-argininosuccinate and L-arginine (Table 3.16). From these findings, proline metabolism and associated metabolic pathways appear important to HGG growth. However, since the LC-MS analysis represents a single time-point, it is not possible to determine whether increased synthesis or reduced degradation of L-proline is the contributing factor, thus requiring further study.

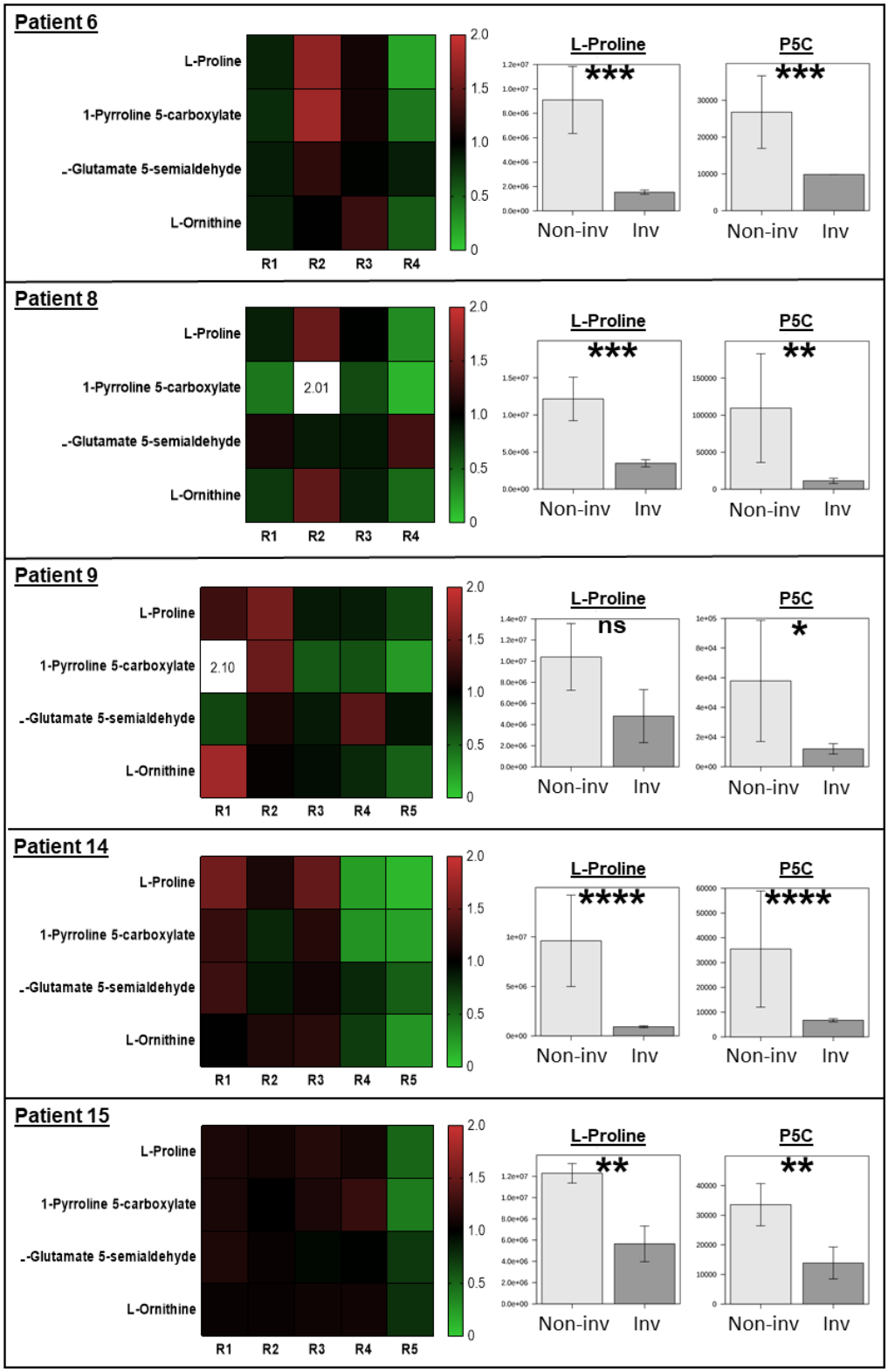

Figure 3.18. Regional variation in all five patients of metabolites belonging to the proline metabolism pathway. Heatmaps display the median replicate value of mean-centred metabolite peak intensities. Fold changes above 2 are numbered. Peak intensities for L-proline and P5C within the non-invasive and invasive regions are displayed in each panel. Statistical evaluation of was performed using a two-sample t-test, respectively. Abbreviations: Non-inv – non-invasive (light grey); Inv – invasive (dark grey). ns = not significant; * = $p<0.05$; ** = $p<0.01$; *** = $p<0.001$; **** = $p<0.0001$.

Table 3.16. Regional comparison of metabolites associated with proline metabolism and correlation with L-proline.

Metabolite	ID confidenc	Invasive vs non-invasive			Correlation analysis		
		log2FC	FDR	Significant	Correlation	FDR	Significant
Patient 6							
L-Proline	10	-2.57	2.78E-04	***	N/A		
1-Pyrroline-5-carboxylate	6	-1.45	5.92E-04	***	0.91	1.42E-03	**
L-Glutamate 5-semialdehyde	8	-0.27	2.67E-01	ns	0.53	1.77E-01	ns
L-Glutamate	10	0.84	1.11E-03	**	-0.88	2.85E-03	**
L-Ornithine	10	-0.97	2.43E-01	ns	0.75	2.42E-02	*
L-Argininosuccinate	8	0.59	8.26E-02	ns	-0.48	2.40E-01	ns
L-Arginine	10	0.44	1.34E-01	ns	-0.64	8.11E-02	ns
Patient 8							
L-Proline	10	-1.81	7.30E-04	***	N/A		
1-Pyrroline-5-carboxylate	6	-3.29	1.14E-03	**	0.96	3.79E-06	****
L-Glutamate 5-semialdehyde	8	0.50	2.28E-03	**	-0.80	3.35E-03	**
L-Glutamate	10	0.37	1.73E-01	ns	-0.58	5.34E-02	ns
L-Ornithine	10	-1.12	4.72E-03	**	0.92	9.72E-05	****
L-Argininosuccinate	8	-0.22	9.50E-01	ns	-0.29	3.81E-01	ns
L-Arginine	10	-0.92	1.43E-02	*	0.87	5.63E-04	***
Patient 9							
L-Proline	10	-1.12	3.46E-01	ns	N/A		
1-Pyrroline-5-carboxylate	6	-2.26	1.17E-02	*	0.88	3.92E-04	***
L-Glutamate 5-semialdehyde	8	-0.37	4.87E-01	ns	0.21	5.79E-01	ns
L-Glutamate	10	0.05	8.64E-01	ns	-0.13	7.40E-01	ns
L-Ornithine	10	-1.20	4.80E-02	*	0.83	1.69E-03	**
L-Argininosuccinate	8	-0.82	2.04E-01	ns	0.47	1.80E-01	ns
L-Arginine	10	-0.12	8.67E-01	ns	0.48	1.74E-01	ns
Patient 14							
L-Proline	10	-3.39	9.82E-09	****	N/A		
1-Pyrroline-5-carboxylate	6	-2.41	8.95E-07	****	0.91	4.39E-08	****
L-Glutamate 5-semialdehyde	8	-1.00	6.16E-05	****	0.85	3.07E-06	****
L-Glutamate	10	0.34	6.74E-04	***	0.18	4.99E-01	ns
L-Ornithine	10	-1.85	3.95E-02	*	0.84	4.42E-06	****
L-Argininosuccinate	8	-2.70	2.04E-03	**	0.94	1.65E-09	****
L-Arginine	10	-0.34	3.01E-01	ns	0.74	2.40E-04	***
Patient 15							
L-Proline	10	-1.12	3.36E-03	**	N/A		
1-Pyrroline-5-carboxylate	6	-1.27	3.34E-03	**	0.91	1.22E-10	****
L-Glutamate 5-semialdehyde	8	-0.60	3.41E-03	**	0.74	1.19E-05	****
L-Glutamate	10	0.09	9.79E-01	ns	-0.23	2.82E-01	ns
L-Ornithine	10	-0.55	3.09E-02	*	0.84	4.14E-08	****
L-Argininosuccinate	8	-1.00	1.43E-03	**	0.90	2.23E-10	****
L-Arginine	10	-0.30	6.34E-02	ns	0.54	4.47E-03	**

ID confidence scores delineate the confidence of the putative metabolite identification. Fold changes are displayed as logarithms to the base 2 (log2FC). Fold changes >0.58 or < -0.58 are depicted in red and green, respectively. Significance scores were FDR-corrected for multiple comparisons. ns = not significant; * = $p<0.05$; ** = $p<0.01$; *** = $p<0.001$; **** = $p<0.0001$.

3.8. Regional heterogeneity in metabolism-associated gene expression

To determine if the basis of metabolic heterogeneity was due to an underlying heterogeneous transcriptomic profile, a multilevel model was applied to identify genes that were upregulated in the invasive margin, as these transcripts were hypothesised to be the most likely to influence the metabolomic profile displayed by this region. Only a few metabolism-related genes were identified (*LRP2*, *PDK4*) (Table 3.17), indicating that metabolic transcripts were largely uniform between non-invasive and invasive regions. It is also possible that other upregulated genes have an as yet unidentified role in tumour metabolism, either directly or indirectly. Integration of the upregulated genes in the invasive margin with metabolomic data through canonical correlation analysis identified strong correlation scores for creatinine and L-ornithine (Figure 3.19). However, the biological significance of this remains to be elucidated through in vitro functional models.

Table 3.17. Significantly upregulated genes within the invasive margin determined using a multilevel linear model

Gene	log2FC	FDR		cont….		
ERMN	3.648	0.015239954		*PEX5L*	2.481	0.013573742
MAG	3.412	0.006896786		*HHATL*	2.458	0.007283041
MOBP	3.255	0.006896786		*HAPLN2*	2.438	0.006896786
MAL	3.216	0.009637143		*CD22*	2.407	0.009637143
ENPP2	3.161	0.04896076		*HHIP*	2.407	0.017447666
MOG	3.153	0.038164656		*MAP7*	2.386	0.043909255
SLC5A11	2.887	0.006926583		*CLCA4*	2.322	0.000479084
KLK6	2.851	0.02148992		*LGI3*	2.313	0.02148992
CNTNAP4	2.847	0.015198309		*TMEM144*	2.308	0.038846488
LRP2	2.789	0.002497308		*SLCO1A2*	2.302	0.006896786
DOCK5	2.789	0.02148992		*PIP4K2A*	2.267	0.017447666
EDIL3	2.770	0.038169065		*SEPT4*	2.236	0.006926583
NKAIN2	2.762	0.023627392		*RAPGEF5*	2.228	0.023627392
OPALIN	2.760	0.000479084		*GRM3*	2.209	0.009192237
FA2H	2.688	0.009192237		*MYRF*	2.180	0.000902181
BCAS1	2.658	0.042333074		*TPPP*	2.148	0.038033482
PLEKHH1	2.626	0.00074939		*NKX6-2*	2.145	0.00438546
CAPN3	2.605	0.026137615		*CARNS1*	2.117	0.009637143
CTNNA3	2.561	0.042333074		*PDK4*	2.092	0.02148992
PLCL1	2.484	0.007283041		*C10orf90*	2.058	0.041754283

The top 40 significantly upregulated genes within the invasive margin compared to the non-invasive regions are displayed. Genes are ordered according to fold changes to the logarithm of base 2 (log2FC). False discovery rate (FDR)-corrected *p*-values were calculated using a multilevel linear model.

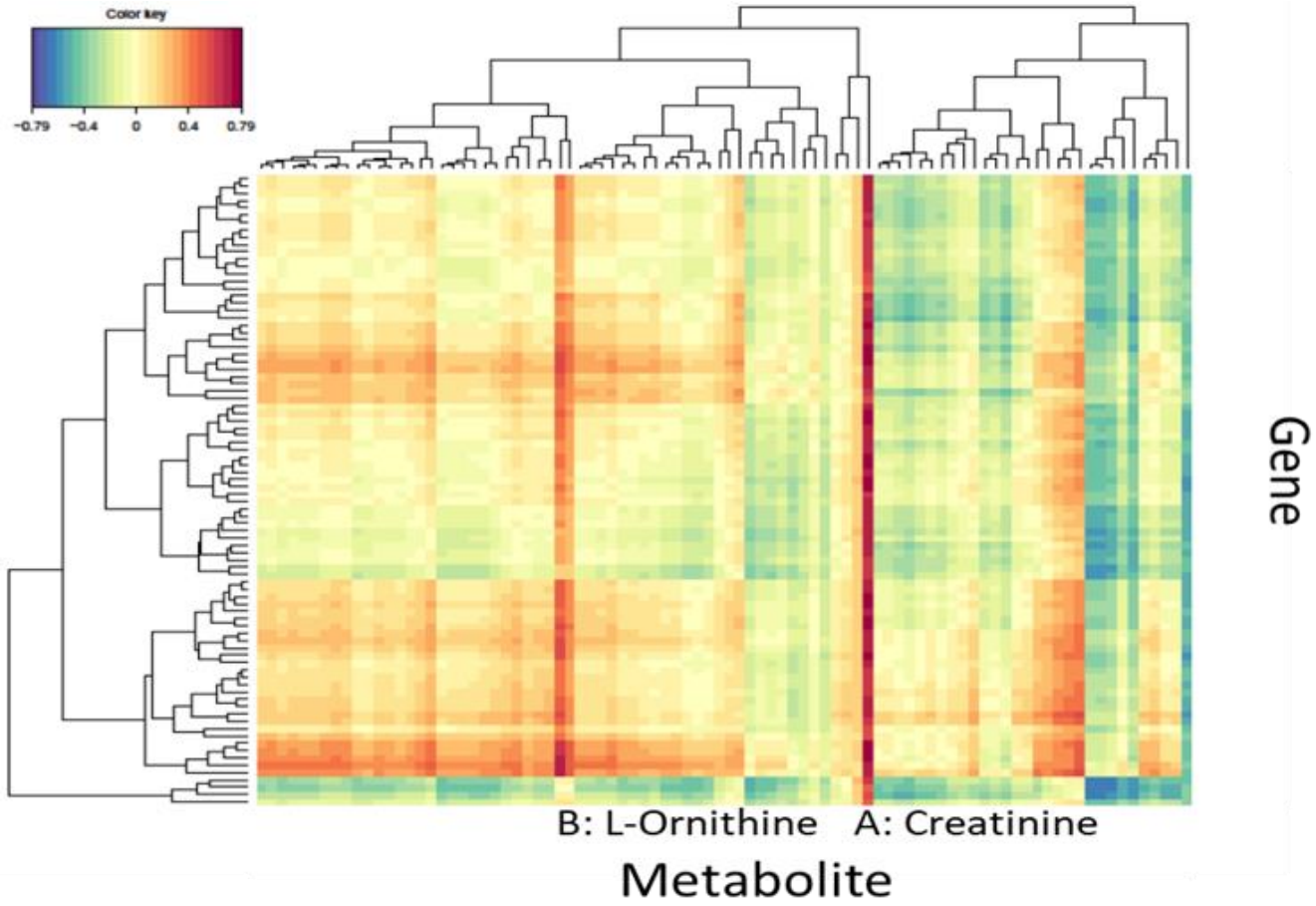

Figure 3.19. Canonical correlation analysis identifying gene-metabolite associations. Canonical correlation analysis between upregulated genes in the invasive margin and differentially abundant metabolites between the non-invasive and invasive regions. The positions of creatinine (A) and L-ornithine (B) with the strongest positive correlations are identified within the figure.

Since only a few metabolism-related genes were identified as differentially expressed between invasive and non-invasive regions, the expression of genes encoding enzymes within glycolysis, PPP, TCA cycle, glutamine, serine/one-carbon, and lipid metabolism were examined to determine evidence of regionally heterogeneous expression. Most genes demonstrated minimal variation (maximum fold change of ~2) across regions in patients 9 (Figure 3.20), 14 (Figure 3.21) and 15 (Figure 3.22). Interestingly, in all three patients the expression of *PDK4* (Figure 3.20A, 3.21A and 3.22A) and *LRP2* (Figure 3.20G, 3.21G and 3.22G) were higher in the invasive region (R5) compared to non-invasive regions, confirming the combined analyses presented in Table 3.17. These findings indicate that ITH in GBM does not extend to most metabolism-related genes, possibly accounting for the relative homogeneity observed for some metabolites across all regions. Therefore, screens will be required to determine which enzymes represent synthetic lethal partners to commonly observed GBM mutations. Ideally, enzymes essential for cancer survival but expressed at a low level would be ideal candidates since relatively low drug concentrations would be required to achieve therapeutic efficacy. For metabolites that do demonstrate regional variation, it is possible that there is gene-protein mismatch, which describes the non-correlation that can occur between transcript levels and protein expression or activity due to post-transcriptional or post-translational regulation, respectively. Combined transcriptomic/ metabolomic studies may therefore benefit from the addition of (phospho)proteomic or reverse-phase protein array (Creighton and Huang, 2015) data to examine protein levels, and isotopically labelled substrates to examine protein activity.

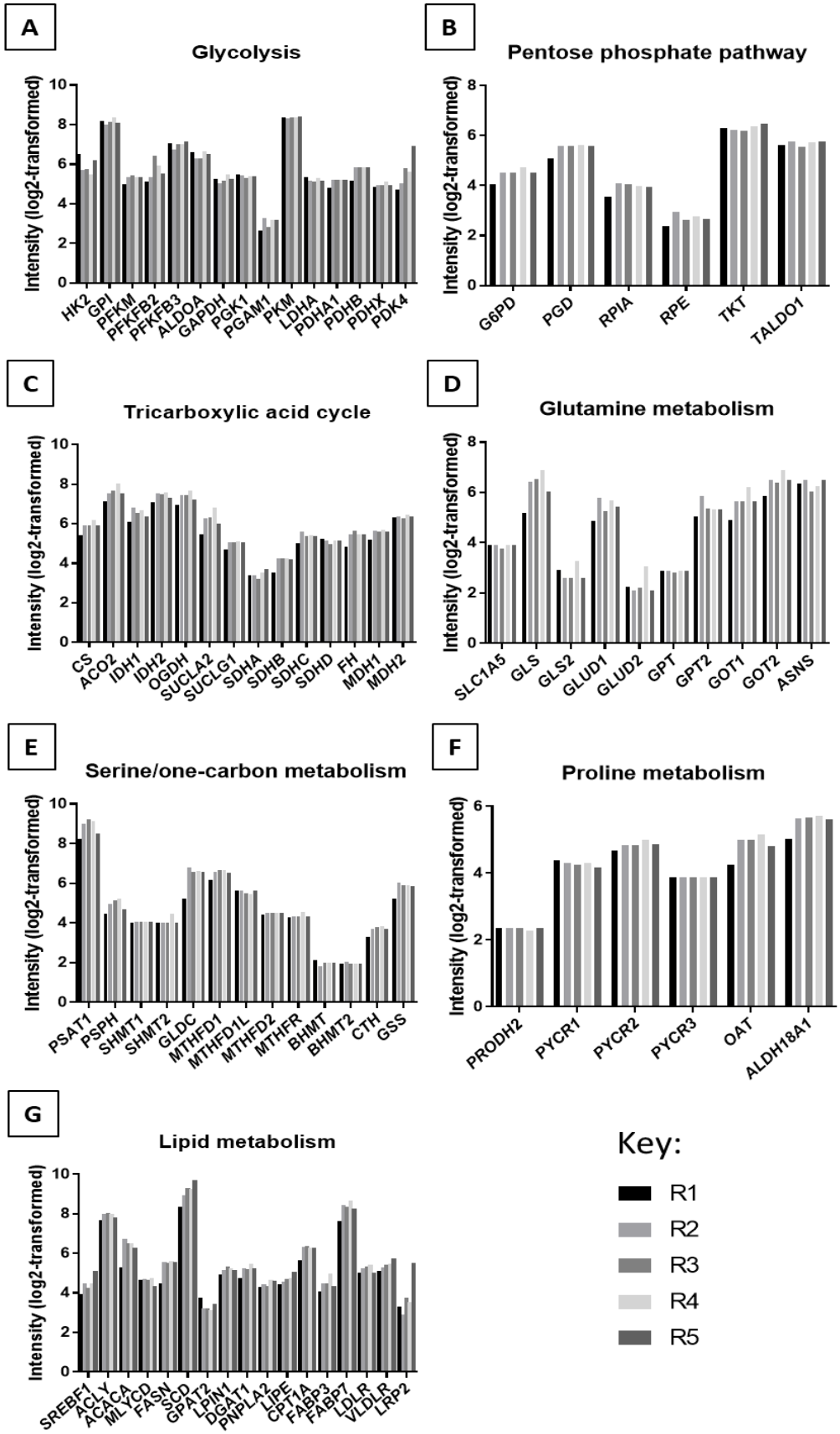

Figure 3.20. Regional expression of metabolism-related genes in patient 9. The expression of genes encoding enzymes within the metabolic pathways in A-G are displayed as log2-transformed intensity values. Variation across regions (symbol R) are shown for patient 9.

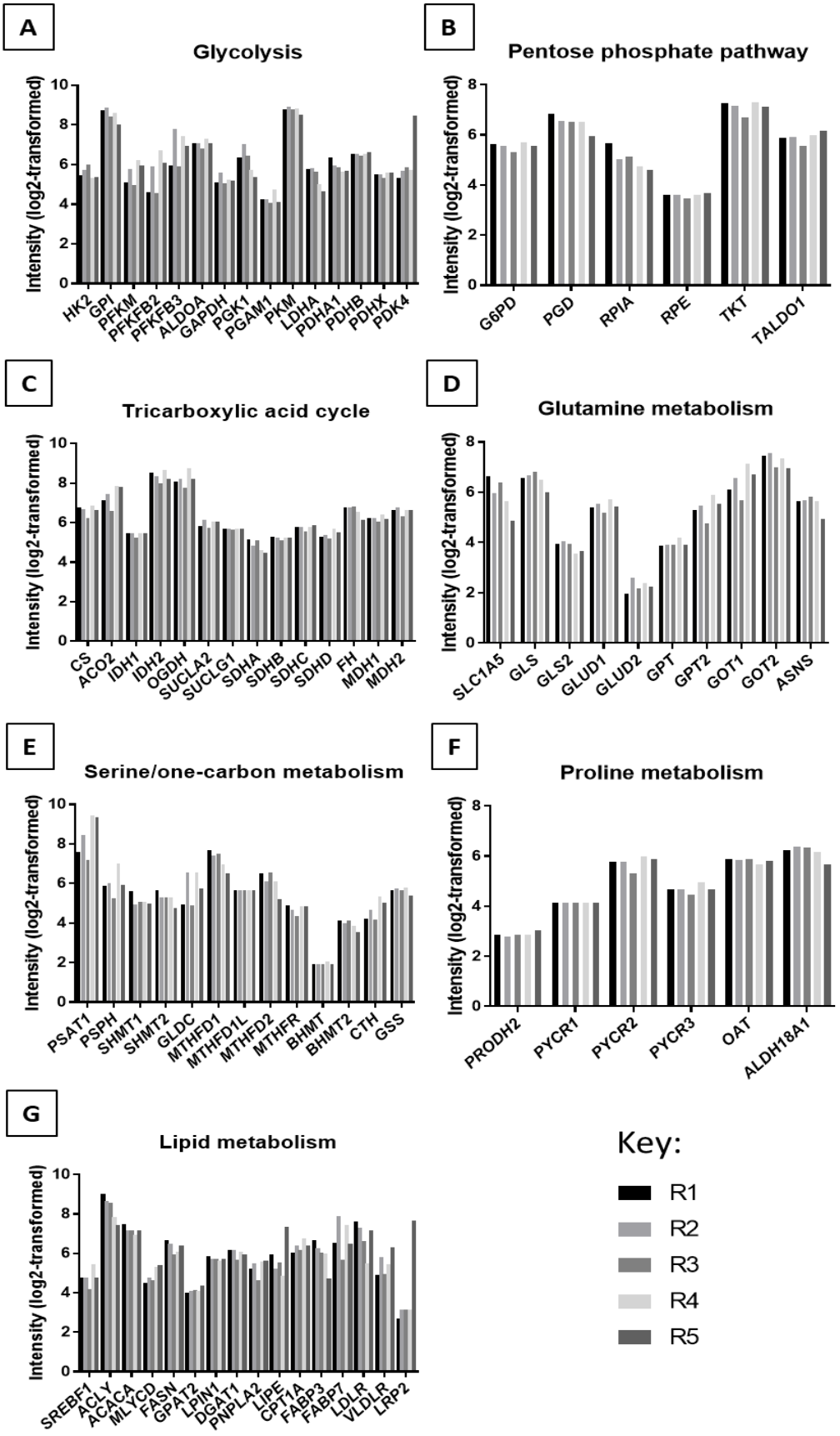

Figure 3.21. Regional expression of metabolism-related genes in patient 14. The expression of genes encoding enzymes within the metabolic pathways in A-G are displayed as log2-transformed intensity values. Variation across regions (symbol R) are shown for patient 14.

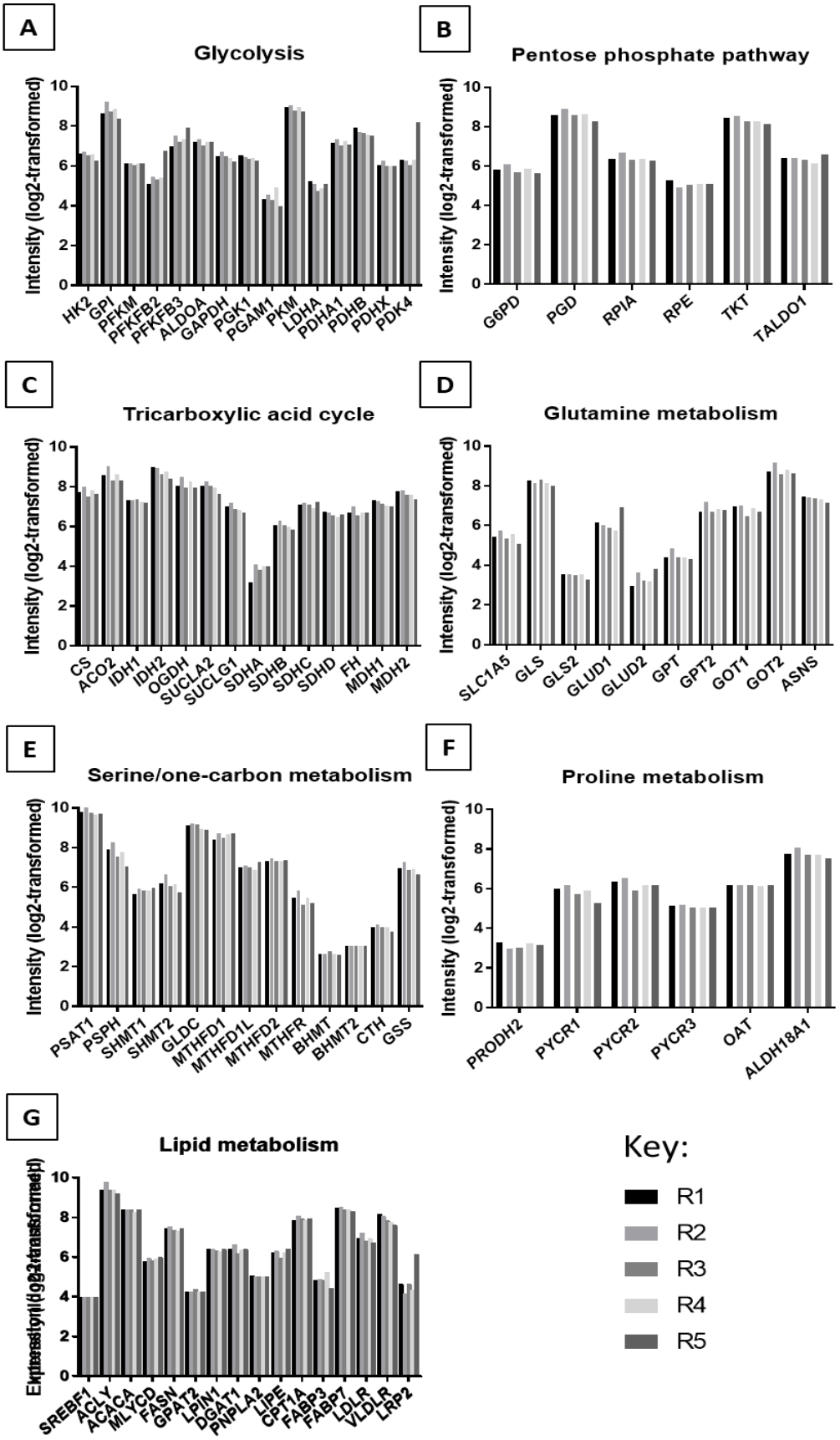

Figure 3.22. Regional expression of metabolism-related genes in patient 15. The expression of genes encoding enzymes within the metabolic pathways in A-G are displayed as log2-transformed intensity values. Variation across regions (symbol R) are shown for patient 15.

3.9. Normal brain component within the invasive margin

Surgical removal of tissue from the invasive margins aims to collect tumour cells that have invaded into the surrounding normal brain parenchyma. Therefore, invasive margin tissue consists predominantly of normal brain cell types with low tumour cell content and possible recruitment of various immune cells within the microenvironment. MRS studies use several metabolic markers to distinguish tumour from normal tissue including NAA, which is a marker of neuron integrity and viability. A 2.4- to 4.5-fold increase in NAA levels was measured across all patients (Table 3.18). This was matched by its hydrolysis product, NAAG, which modulates glutamate release and may have a role in neuroprotection and synaptic plasticity. Levels of creatine, a marker of energetic potential, are reduced in GBM relative to normal brain tissue in MRS studies, consistent with higher energy consumption within tumour tissue. Comparison of invasive versus non-invasive regions revealed a minor increase in creatine levels ranging from 1.10- to 1.58-fold, which was significant in patients 6, 8, and 14 (Table 3.18). The proliferative activity of tumours results in high membrane turnover and increased choline levels for membrane lipid synthesis. Interestingly, MRS studies have demonstrated that choline levels maintain elevation beyond the margins of contrast enhancement due to tumour cell infiltration (Horská and Barker, 2010). Consistent with this, choline levels were relatively unchanged between non-invasive and invasive regions in patients 6, 8, and 9 (Table 3.18). In patient 14, choline levels within the invasive margin were reduced by more than half compared to the non-invasive regions, perhaps reflecting lower tumour cell content compared to invasive region tissue from the other patients. In contrast to all other patients, choline levels in patient 15 demonstrated a 1.85-fold increase in invasive margin compared to non-invasive regions. Further evidence of a normal brain component within the invasive margin was supported by the observation of reduced levels of 5-ALA (Table 3.18), Interestingly, patients 6, 9, and 14, who were administered 5-ALA, demonstrated higher fold changes in 5-ALA levels between invasive and non-invasive regions compared to patients 8 and 15. Multilevel modelling using transcriptomic profiles from patients 9, 14 and 15 from section 3.8 identified

92 upregulated genes in the invasive margin enriched for *positive regulation of nervous system development* (GO: 0051962; raw *p*-value=7.68E-04). Overall, these findings indicate that invasive margin tissue contains low tumour cell content. Therefore, the distinct metabolomic profile of the invasive margin may largely be due to the normal brain component that features neurons as well as other cell types.

Table 3.18. Regional comparison of metabolites indicative of a normal brain component within the invasive region

Metabolite	ID confidence	Invasive vs non-invasive			Higher abundance
		log2FC	FDR	Significant	
Patient 6					
N-Acetyl-L-aspartate	10	2.16	2.67E-04	***	Invasive
N-Acetyl-aspartyl-glutamate	6	3.65	1.54E-04	***	Invasive
Creatine	8	0.66	5.11E-05	****	Invasive
Choline	10	-0.09	7.26E-01	ns	Non-invasive
5-Aminolevulinic acid	10	-4.27	2.67E-04	***	Non-invasive
Patient 8					
N-Acetyl-L-aspartate	10	2.10	3.57E-03	**	Invasive
N-Acetyl-aspartyl-glutamate	6	1.95	8.86E-03	**	Invasive
Creatine	8	0.56	3.91E-02	*	Invasive
Choline	10	-0.04	9.91E-01	ns	Non-invasive
5-Aminolevulinic acid	10	-0.89	1.28E-01	ns	Non-invasive
Patient 9					
N-Acetyl-L-aspartate	10	1.60	1.03E-02	*	Invasive
N-Acetyl-aspartyl-glutamate	6	4.04	2.40E-03	**	Invasive
Creatine	8	0.30	4.41E-01	ns	Invasive
Choline	10	-0.28	4.87E-01	ns	Non-invasive
5-Aminolevulinic acid	10	-1.93	1.83E-02	*	Non-invasive
Patient 14					
N-Acetyl-L-aspartate	10	2.09	1.13E-03	**	Invasive
N-Acetyl-aspartyl-glutamate	6	4.07	6.59E-10	****	Invasive
Creatine	8	0.35	1.50E-04	***	Invasive
Choline	10	-1.27	4.34E-02	*	Non-invasive
5-Aminolevulinic acid	10	-1.81	2.66E-05	****	Non-invasive
Patient 15					
N-Acetyl-L-aspartate	10	1.25	1.43E-03	**	Invasive
N-Acetyl-aspartyl-glutamate	6	3.53	4.57E-05	****	Invasive
Creatine	8	0.14	2.94E-01	ns	Invasive
Choline	10	0.89	4.60E-03	**	Invasive
5-Aminolevulinic acid	10	-0.31	6.92E-03	**	Non-invasive

Metabolites highlighted in red showed RSD values >30% in QC samples. ID confidence scores delineate the confidence of the putative metabolite identification. Fold changes are displayed as logarithms to the base 2 (log2FC). Fold changes >0.58 or < -0.58 are depicted in red and green, respectively. Significance scores were FDR-corrected for multiple comparisons. ns = not significant; * = p<0.05; ** = p<0.01; *** = p<0.001; **** = p<0.0001.

3.10. Chapter discussion

The subclonal nature of GBM has been demonstrated through a range of techniques, including genome-wide copy number analysis, single-cell transcriptomics, and protein-level expression of RTKs (Snuderl *et al.*, 2011; Sottoriva *et al.*, 2013; Patel *et al.*, 2014). Given the intimate association between gene expression and metabolism, it is of scientific interest to determine whether the genetic heterogeneity observed within GBM manifests phenotypically as a patchwork landscape of metabolically distinct niches, however inter-convertible or transient. Genetic heterogeneity often occurs within redundant signalling pathways that converge to regulate metabolic pathways required to generate energy and biomass for sustained cancer cell proliferation. It is therefore equally plausible that the metabolic landscape is largely flat in reflection of a minimum set of critical metabolic requirements. Metabolic heterogeneity within gliomas has been shown across tumour grades (Chinnaiyan *et al.*, 2012), but has only been investigated in the context of a single tumour in cancers of the lung (Hensley *et al.*, 2016) and kidney (Okegawa *et al.*, 2017). We performed multi-region sampling in five HGG patients to profile intratumour metabolic heterogeneity following successful implementation of this technique in characterising genetic variation within a spatial context (Sottoriva *et al.*, 2013). Combined with LC-MS, metabolomic and lipidomic profiles were obtained from four to five tumour regions per patient; to our knowledge, this is the first instance where intratumour GBM metabolomics has been conducted. The extent of heterogeneity varied between patients and at the individual level. For instance, several metabolites within the glycolysis pathway showed regional variation in patient 6, in contrast to the relatively invariant profile in patient 15. Overlap of metabolomic profiles from different regions provided evidence of metabolic niches. The existence of metabolic niches may be related to the ability of the tumour vasculature to perfuse the oncogenic mass, as has been demonstrated through combined dynamic contrast-enhanced MRI (DCE-MRI) and ^{13}C-isotopic analysis of lung cancer metabolic heterogeneity (Hensley *et al.*, 2016). The relatively homogenous metabolomic profile of *IDH1* mutant patient 15 is of note since

genetic lesions within *IDH1* affect both gene expression and metabolism (Reitman *et al.*, 2011; Tönjes *et al.*, 2013). With a larger cohort, it can be investigated if mutant *IDH1* expression results in a more metabolically homogenous tumour given the strength of this oncogenic lesion in driving tumourigenesis and metabolic reprogramming, in contrast to *IDH1* wildtype GBMs that are characterised by several oncogenic lesions, including chromosome $7^{-}/10^{+}$, *CDKN2A* deletion, and amplification of *EGFR* and *PDGFRA* (Sturm *et al.*, 2012). However, *IDH1* mutations have been demonstrated to be subclonal in 20% of GBMs (McGranahan *et al.*, 2015), meaning that the extent of metabolic heterogeneity may be influenced by the dominance of *IDH1* mutations within the tumour hierarchy.

Complicating the phenomenon of genetically induced metabolic re-programming is the capacity of cancer cells to undergo metabolic plasticity within a low nutrient or oxygen tumour microenvironment. Kucharzewska and colleagues highlighted several metabolic changes in GBM cells cultured in hypoxic conditions (Kucharzewska, Christianson and Belting, 2015). Stochastic determination of metabolic phenotypes is also observed since isogenic glioma stem-like cells (GSCs) can adopt either a glycolytic profile or utilise oxidative phosphorylation to generate energy. In each GSC subtype, hypoxic stress increased the expression of glycolysis-related genes and promoted lactate production (Shibao *et al.*, 2017). We hypothesised that hypoxic niches would shape the metabolomic landscape by inducing a glycolytic phenotype. Patient 6 demonstrated evidence of a glycolytic phenotype in non-invasive regions compared to the invasive margin. Heterogeneity in several glycolytic intermediates, including G3P and pyruvate, was observed that might reflect differences in pentose phosphate pathway flux and pyruvate kinase activity, respectively. Hypoxia has been demonstrated to reduce pentose phosphate pathway activity and upregulate glycolytic enzymes leading to a “go” instead of “grow” phenotype (Kathagen *et al.*, 2013; Kathagen-Buhmann *et al.*, 2016). Patient 15 demonstrated a reduction in G3P levels in non-invasive regions, perhaps reflective of a proliferative response, whereas a higher abundance of

G3P was observed in the invasive margin. However, the expression of several glycolytic and PPP enzymes was largely homogenous across all regions, conflicting with hypotheses based on current understanding of associations between metabolism and invasion/proliferation.

Heterogeneity was also observed in TCA cycle metabolites that may reflect dynamic flux changes within connected metabolic pathways. Citrate, which is consumed in *de novo* fatty acid synthesis (Currie *et al.*, 2013), was present at lower levels in the non-invasive regions of patients 6 and 15. Hypoxia induces reductive metabolism of glutamine to generate citrate for lipid synthesis via wildtype and mutant IDH1 (Metallo *et al.*, 2011; Reitman *et al.*, 2011). Evidence of this process within patient 6 and 15 was not immediately obvious, since glutamine and isocitrate levels were relatively uniform and citrate pools were reduced within non-invasive regions. Collectively, the findings from patient 15 hint at the lack of a hypoxia-induced metabolic phenotype, supporting the observations of Kickingereder and colleagues of strong inhibition of *HIF1A* and decreased expression of HIF1α target genes in *IDH1* mutant gliomas (Kickingereder *et al.*, 2015). Patient 15 also featured glucose levels that were only moderately reduced and lower lactate levels in non-invasive regions compared to the invasive margin, both of which do not strongly support induction of a glycolytic phenotype to due to the development of hypoxia.

Santandreu and colleagues provided evidence of intratumour metabolic heterogeneity at the mitochondrial level following identification of a higher respiratory rate and fewer antioxidant systems within the periphery compared to the centre of the tumour (Santandreu *et al.*, 2008). This phenotypic spectrum is likely influenced by the development of hypoxia, often within the centre of solid cancers, which increases ROS production (Tafani *et al.*, 2016). Glycolytic regions within patient 6 showed increased levels of oxidised glutathione. The abundance of reduced glutathione was consistent across regions in patients 6 and 15 that may be supplemented by serine and glycine incorporation into one-carbon metabolism (Yang and Vousden, 2016) and conversion of ɣ-glutamyl-

cysteine into glutathione, as supported by decreased levels of ɣ-glutamyl-cysteine within non-invasive regions. Patient 6 and 15 also demonstrated increased levels of most essential, conditional and non-essential amino acids within non-invasive regions compared to the invasive margin. It is possible that the higher cellularity of the non-invasive regions could be a confounding factor. However, increased amino acid uptake and synthesis may reflect the need of building blocks for protein synthesis. Of therapeutic interest was the increased concentrations of L-proline and its strong correlation with its immediate breakdown product P5C in non-invasive regions. Proline biosynthesis is documented to support redox homeostasis in IDH1-mutant glioma by reducing the NADH/NAD+ ratio via PYCR1 activity, which enables continuation of TCA cycle activity when flux through the electron transport chain is limiting as seen in hypoxic conditions (Hollinshead *et al.*, 2018). In line with this, Liu and colleagues showed that cycling between the two metabolites recycles NAD+ units for use in glycolysis and the pentose phosphate pathway (Liu *et al.*, 2015). In contrast, proline catabolism via *Prodh* was shown to support spheroidal breast cancer growth via ATP production and was also found to be increased in lung metastases compared to primary breast cancer tumours using $^{13}C_6$-glucose as a tracer (Elia *et al.*, 2017). GBM cells that have infiltrated normal brain show increased gene expression of *PRODH* compared to tumour cells derived from the core, calling for further study into the role of proline in tumour metabolism (Darmanis *et al.*, 2017).

Recently, Heiland and colleagues utilised 1D-NMR spectroscopy on 33 patients and identified 46 metabolites. Despite image-guided tumour sampling and 5-ALA administration, the group could not characterise metabolic heterogeneity. Moreover, this study utilised single region biopsies from the contrast-enhanced tumour core only and so could only reveal data on inter-tumour heterogeneity, in contrast to multi-region surgical sampling method (Heiland *et al.*, 2017). We measured the levels of 503 metabolites across four to five regions covering several metabolic pathways, including glycolysis, TCA cycle, amino acid metabolism, and redox metabolism. Despite greater coverage, some

metabolites of importance to tumour metabolism were not detected, including αKG and 2HG that have important consequences on cancer cell proliferation. However, Heiland and colleagues also performed transcriptomics on 48 patents covering the four Verhaak expression subgroups and integrated the data with metabolomic profiles (Heiland *et al.*, 2017). We attempted to integrate transcriptomic and metabolomic data to determine associations between genetic and metabolic heterogeneity. However, genes that were upregulated between the invasive and non-invasive regions were largely associated with neuronal myelin sheath processes and therefore did not provide useful information pertaining to gene-metabolite interactions within a spatial context. Similarly, a lack of enrichment for metabolic processes was observed in the multi-region transcriptomics analysis conducted by Sottoriva and colleagues (Sottoriva *et al.*, 2013). However, it is possible that the different metabolomic profiles observed between non-invasive and invasive regions reflects regulation of metabolism at the posttranslational level as opposed to the transcriptional level. The activity of several enzymes is regulated through phosphorylation or binding of metabolites to allosteric sites. Moreover, regulatory proteins or metabolic enzymes may demonstrate altered protein turnover. Future investigations involving stable isotopes and protein immunoblotting may elucidate heterogeneity between the non-invasive and invasive regions accounting for the observed metabolic differences.

Our experimental design can be improved by obtaining at least three replicates from each region for transcriptomic profiling providing that at least 30 mg of tissue is left over from what is required for metabolomics analysis. Additionally, dual metabolite/RNA extraction methods currently in development in the laboratory could be used to permit more accurate integration of data from the same tumour cell population. In a larger cohort of patients, the identification of consistent metabolomic alterations can be investigated as biomarkers of invasion alongside histopathological and MRI data, and correlated with survival to identify metabolic factors associated with either a better or worse prognosis. Other limitations to the study are inherent to the chosen methodology. LC-MS

analysis of quenched metabolism cannot provide information on dynamic flux through pathways, making interpretation of metabolic phenotypes a difficult task. To overcome this, ^{13}C-isotope-labelled substrates have been implemented to great effect to study substrate utilisation and the destination of carbon units, as shown by the usage of 1,2-^{13}C-acetate in GBM and brain metastases (Mashimo *et al.*, 2014). Moreover, the presence of a normal brain component within the invasive margin precludes the identification of metabolic markers for invading cells. At the time of writing, isolation techniques pioneered in our laboratory have been successfully optimised to permit fluorescence-activated cell sorting to isolate and purify infiltrating tumour cells on the basis of persistent 5-ALA fluorescence post-surgery (Rahman et al., manuscript in preparation). Such an approach is directly amenable to metabolomic analysis in a future study, where a pure, tumour-rich invasive margin profile is elucidated for the first time.

Chapter 4

Assessing the dependency of adult and paediatric GBM cells on lipoproteins for metabolic viability and growth

4. Assessing the dependency of adult and paediatric GBM cells on lipoproteins for metabolic viability and growth

Lipoproteins are multi-molecular assemblies consisting of proteins as well as cholesterol and lipid species. They function to transport nutrients from the gut and liver to the periphery (Tulenko and Sumner, 2002). Although the BBB blocks the passage of LDLs, small HDLs can traverse into the CNS. Independent of the blood supply, apolipoprotein E-containing lipoproteins are generated by astrocytes and are taken up by neurons and astrocytes via receptors of the LDLR family (Wang and Eckel, 2014). The role of lipoproteins within the CNS is to transfer phospholipids and cholesterol between cells but they are also implicated in the pathogenesis of Alzheimer's disease (Vance and Hayashi, 2010). Interestingly, recent work has demonstrated the dependency of U87 GBM cells and Ras-transformed astrocytes on lipoproteins for sustained tumour growth (Ríos *et al.*, 2014). This has been corroborated within an *in vivo* mouse model of aGBM highlighting a non-oncogene addiction to lipoproteins for the maintenance of cholesterol homeostasis and tumour growth (Villa *et al.*, 2016). We investigated whether the lipoprotein dependency observed in aGBM models is also a feature of pGBM and hypothesised that biological differences between the two age groups at the genetic level would lead to distinct metabolic responses to lipoprotein deprivation.

4.1. Adult and paediatric GBM cells are dependent on lipoproteins for growth in monolayer models

Several cells lines were evaluated to investigate lipoprotein dependency between age groups and between grades within pGBM. U87 cells were utilised to model aGBM, whereas KNS42 and SF188 were included to assess the pGBM response. UW479, Res259 and Res186 were also investigated to compare outcomes in paediatric gliomas of grade III, II and I, respectively. All cell lines were grown in basal media with the addition of either FBS or LD-FBS to simulate lipoprotein-replete and -deplete conditions, respectively. Assessment of GBM cell viability over 7 days of culture revealed a relative increase in viability in

KNS42 and SF188 cells cultured under lipoprotein-deplete compared to -replete conditions (Figure 4.1B and C). The observed increase in relative viability was significant (p<0.05) in SF188 cells after 5 days and the growth curve implied an increased growth rate (Figure 4.1C). Although not significant in the KNS42 cell line, cellular viability was consistently higher under lipoprotein-deplete conditions relative to -deplete conditions across the 7-day period (Figure 4.1B). In contrast, U87 cellular viability was maintained until day 3, after which the growth plateaued leading to significant (p<0.05) differences in comparison to the growth of control cells (Figure 4.1A). However, microscopic observations were not concordant with the higher cellular viability of pGBM cells as suggested by the PrestoBlue cell viability assay (section 8.5 in the Appendix). Therefore, a crystal violet assay was conducted alongside to assess the validity of the observations made using the PrestoBlue assay. As shown in Figure 4.1, the crystal violet assay revealed a relative reduction in cell number starting at day 5 that was significant (p<0.05) at day 7 in KNS42 and SF188 cells. These results indicated that growth under lipoprotein-deplete conditions induced functional responses within the pGBM cell lines which were generating an artefactual readout from the PrestoBlue assay. This was not observed for the U87 cell line that displayed similar results from both assays (Figure 4.1A), in support of different metabolic responses between adult and paediatric GBM cells to the removal of lipoproteins from the growth medium.

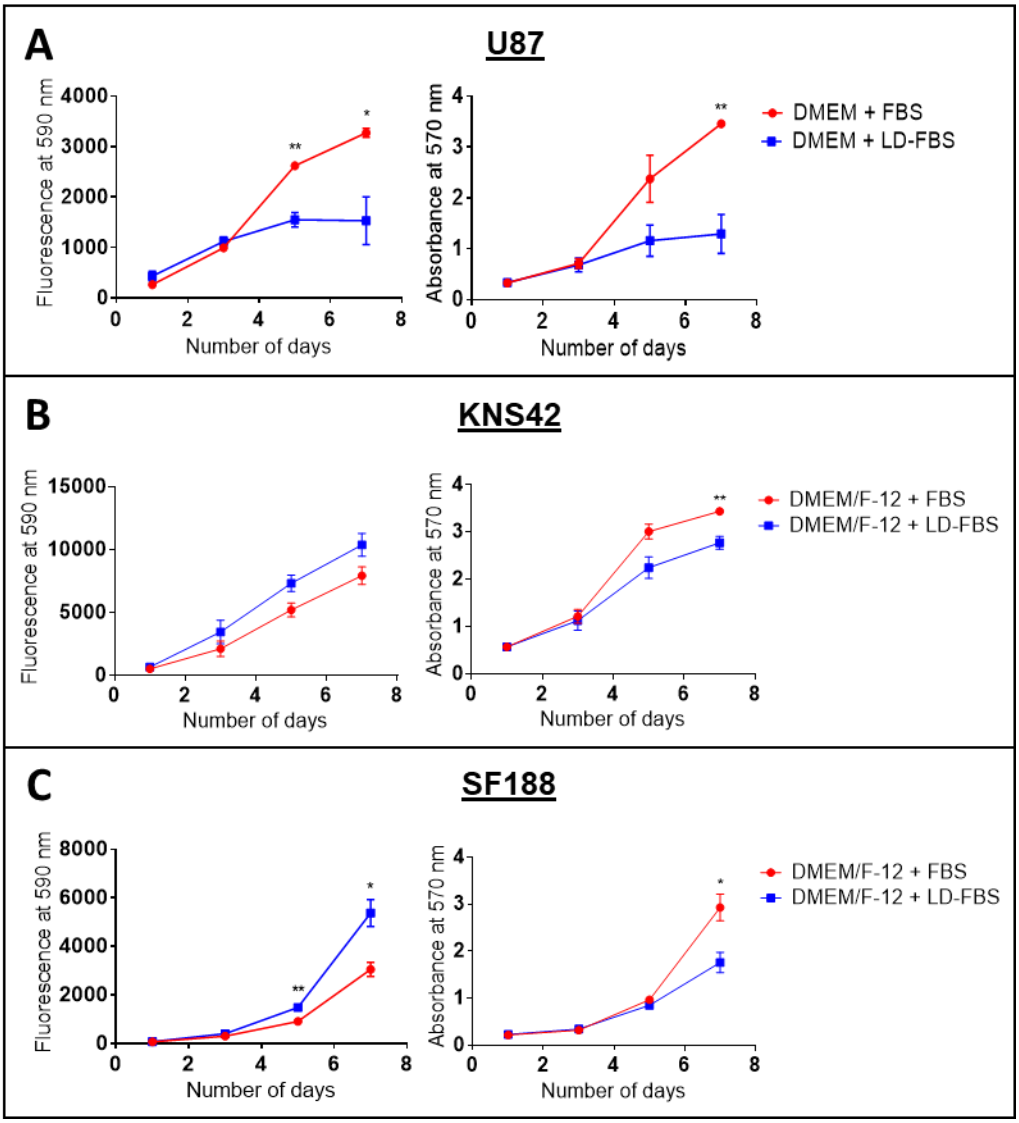

Figure 4.1. Cell viability assessment of adult and paediatric GBM cells cultured under lipoprotein-deplete or -replete conditions. Adult (U87) or paediatric (KNS42, SF188) GBM cells were cultured in the presence (red) or absence (blue) of lipoproteins within the culture medium. Each panel displays readouts of cellular viability using either the PrestoBlue (left) or crystal violet (right) reagents. Fluorescence and absorbance was measured at 590 nm and 570 nm wavelengths, respectively. Error bars represent the SEM of n=3 experiments performed in triplicate. Significance was measured at each timepoint using the student *t*-test: * $p<0.05$; ** $p<0.01$; *** $p<0.001$.

Three lower-grade paediatric gliomas were also assessed to determine if the metabolic responses observed replicate those seen in the pGBM cell lines. Growth of the grade III UW479 and grade II Res259 cell lines under lipoprotein-deplete conditions resulted in a higher PrestoBlue readout compared to control cells that was significant at day 7 in both cases ($p<0.05$) (Figure 4.2A and B). As observed for the GBM cell lines, cell viability assessment using the crystal violet assay showed the opposite result with reduced viability over time. In both cell lines, the difference in viability was significant at day 7 but was more prominent in the UW479 cell line compared to the Res259 cell line (Figure 4.2A and B). Out of all six cell lines tested, Res186 demonstrated the largest response to growth under lipoprotein deficient conditions in both the PrestoBlue and crystal violet assays (Figure 4.2C). Control Res186 cells demonstrated a normal growth curve whereas cells deprived of lipoproteins showed a minimal increase in growth. The effect of removing lipoproteins from the medium was likely cytostatic considering that Res186 cells were still present within wells without any overt morphological indications of apoptosis induction (Figure 4.3). However, lipoprotein-starved Res186 cells did appear morphologically different compared to control cells, characterised by an elongated phenotype. This was also observed in the U87 cell line along with additional cell shrinkage indicative of apoptosis induction (Figure 4.3).

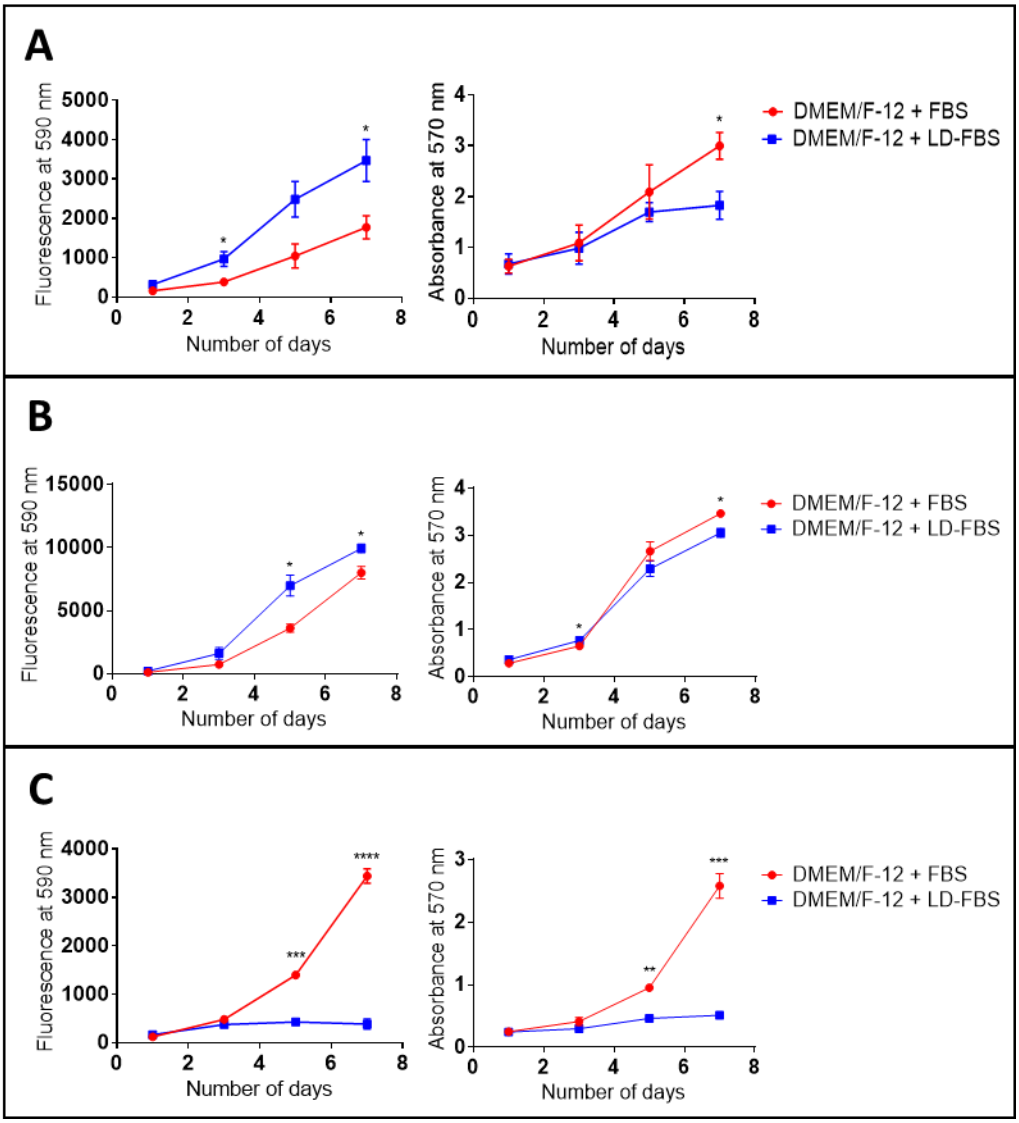

Figure 4.2. Cell viability assessment of paediatric glioma grades I, II and III cells cultured under lipoprotein-deplete or -replete conditions. UW479 (grade III), Res259 (grade II) and Res186 (grade I) cells were cultured in the presence (red) or absence (blue) of lipoproteins within the culture medium. Each panel displays readouts of cellular viability using either the PrestoBlue (left) or crystal violet (right) reagents. Fluorescence and absorbance was measured at 590 nm and 570 nm wavelengths, respectively. Error bars represent the SEM of n=3 experiments performed in triplicate. Significance was measured at each timepoint using the student t-test: * $p<0.05$; ** $p<0.01$; *** $p<0.001$.

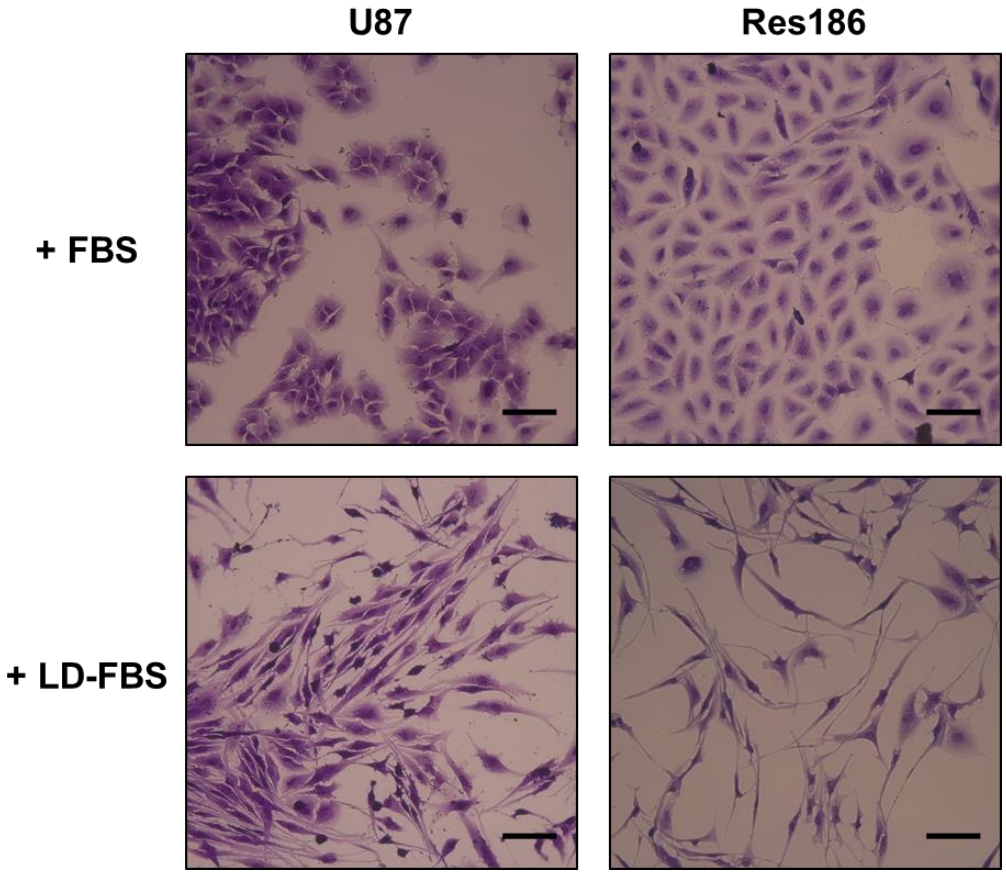

Figure 4.3. Crystal violet staining of U87 and Res186 cells cultured in the presence or absence of lipoproteins. Cells were cultured in the presence (+ FBS) or absence (+ LD-FBS) of lipoproteins for 5 days. Images were taken using a camera attached to a brightfield microscope and are representative of n=3 experiments. Scale bars represent 100 μm in length.

The findings above indicated a higher capacity of pGBM cell lines compared to their adult counterpart to increase reducing potential following metabolic stress, as indicated by the PrestoBlue assay. A possible explanation for these differences may be accounted for in the underlying tumour biology between age groups as represented by these cell lines. However, we explored the contribution of the basal medium to the differential responses since pGBM cells were cultured in DMEM/F-12 with 4.5 g/L glucose compared to DMEM with 1 g/L glucose medium for aGBM cells. Indeed, upon conditioning the pGBM cells to growth in DMEM with 1 g/L glucose the increased PrestoBlue output was no longer observed (Figure 4.4B and C). This was not attributable to lower glucose levels as a compensatory response was not identified using DMEM with 4.5 g/L glucose under lipoprotein-deficient conditions. We therefore modified our hypothesis investigating the metabolic differences between adult and paediatric glioma cells to an alternate hypothesis exploring the metabolic vulnerability underlying growth under lipoprotein deficient conditions for GBM cells within both age groups. To this end, the following experiments were conducted using DMEM with 1 g/L glucose as the basal medium since this concentration of glucose more closely resembles physiological levels compared to the 4.5 g/L glucose within DMEM/F-12.

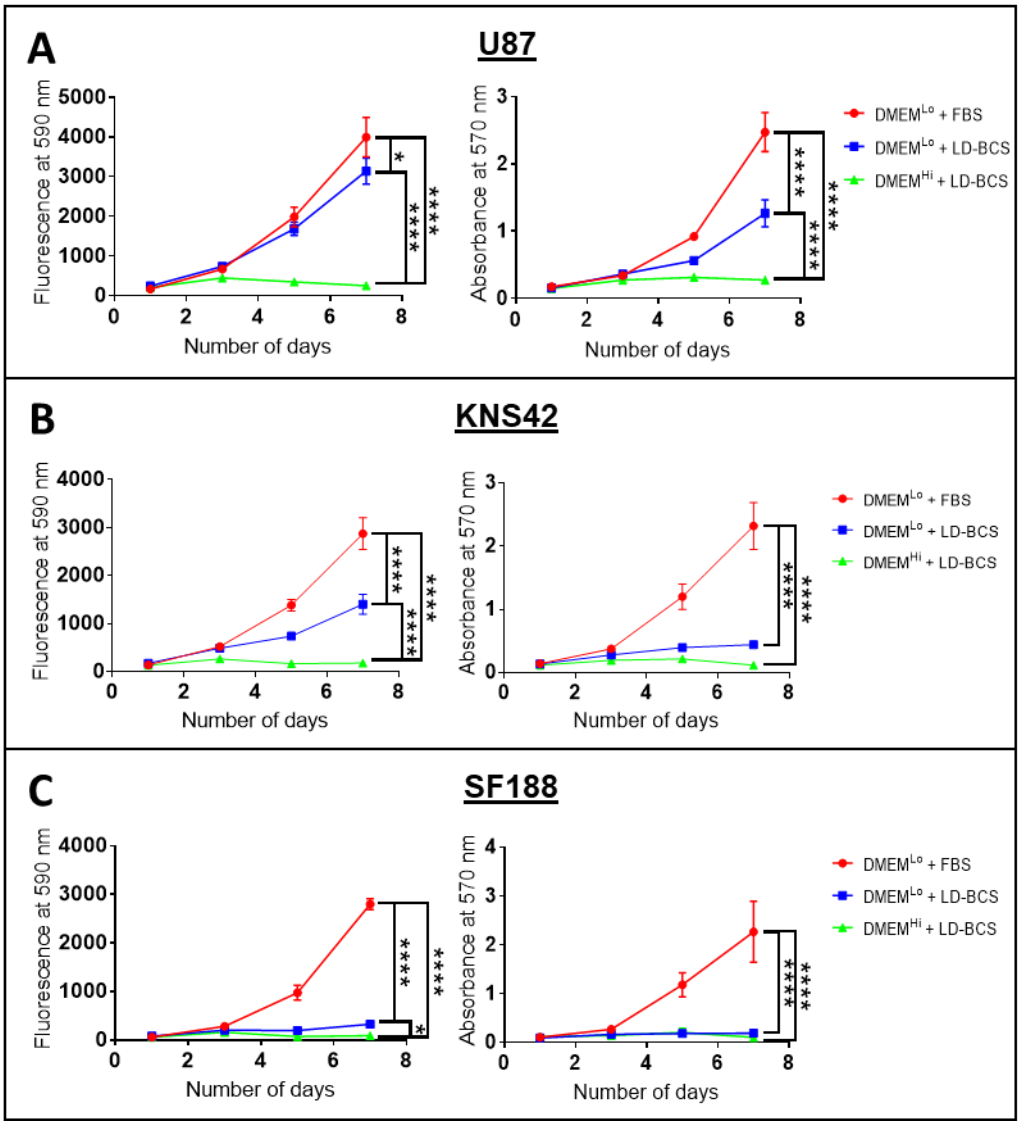

Figure 4.4. Lipoprotein dependency of adult and paediatric GBM cells under standardised conditions. Adult (U87) or paediatric (KNS42, SF188) GBM cells were cultured in the presence (red) or absence (blue) of lipoproteins within the same basal culture medium (DMEM), containing either 1 g/L (red and blue) or 4 g/L glucose (green). Each panel displays readouts of cellular viability using either the PrestoBlue (left) or crystal violet (right) reagents. Fluorescence and absorbance was measured at 590 nm and 570 nm wavelengths, respectively. Error bars represent the SEM of n=3 experiments performed in triplicate. Significance was measured using the *t*-test: * $p<0.05$; ** $p<0.01$; *** $p<0.001$. Abbreviations: BCS – bovine calf serum.

4.2. Adult and paediatric GBM cells are dependent on lipoproteins for growth in spheroid models

Adult and paediatric GBM cells grown as monolayers demonstrated a metabolic vulnerability to growth under lipoprotein deficient conditions. Evidence in the literature indicates differences in metabolic gene expression in spheroid models compared to cells grown as monolayers (Smith *et al.*, 2012; Takahashi *et al.*, 2015). We hypothesised that adult and paediatric GBM cells would demonstrate increased relative resistance to growth in the absence of lipoproteins when cultured as spheroids as opposed to monolayers. Cell numbers for the U87, KNS42 and SF188 cell lines were optimised to generate spheroids of approximately 300 µm in diameter 4 days after seeding as single cells in ULA plates. U87 spheroids were compact and rounded at all seeding densities tested, with 5000 cells generating the required spheroid size upon day 4 (Figure 4.5A and B). In contrast, KNS42 spheroids were more loosely aggregated and only became rounded at seeding densities of 2500 cells and above (Figure 4.6A). KNS42 spheroids were often surrounded by debris that could be washed away. This indicated that compared to the U87 cell line, KNS42 cells were not fully viable when grown as spheroids, perhaps due to the use of DMEM with 1 g/L glucose instead of DMEM/F-12 with 4.5 g/L glucose. Seeding 5000 KNS42 cells produced spheroids that were just below 300 µm in diameter (Figure 4.6B). SF188 clustered to form tight, rounded spheroids with minimal debris indicative of cell death (Figure 4.7A). In contrast to KNS42 spheroids which displayed a plateau in size at increasing cell densities, SF188 spheroids steadily increased in size but were associated with greater variability at higher seeding densities. Although 2500 cells would have been sufficient to produce spheroids of 300 µm in diameter (Figure 4.7B), a seeding density of 5000 SF188 cells was adopted for consistency with the U87 and KNS42 cell lines.

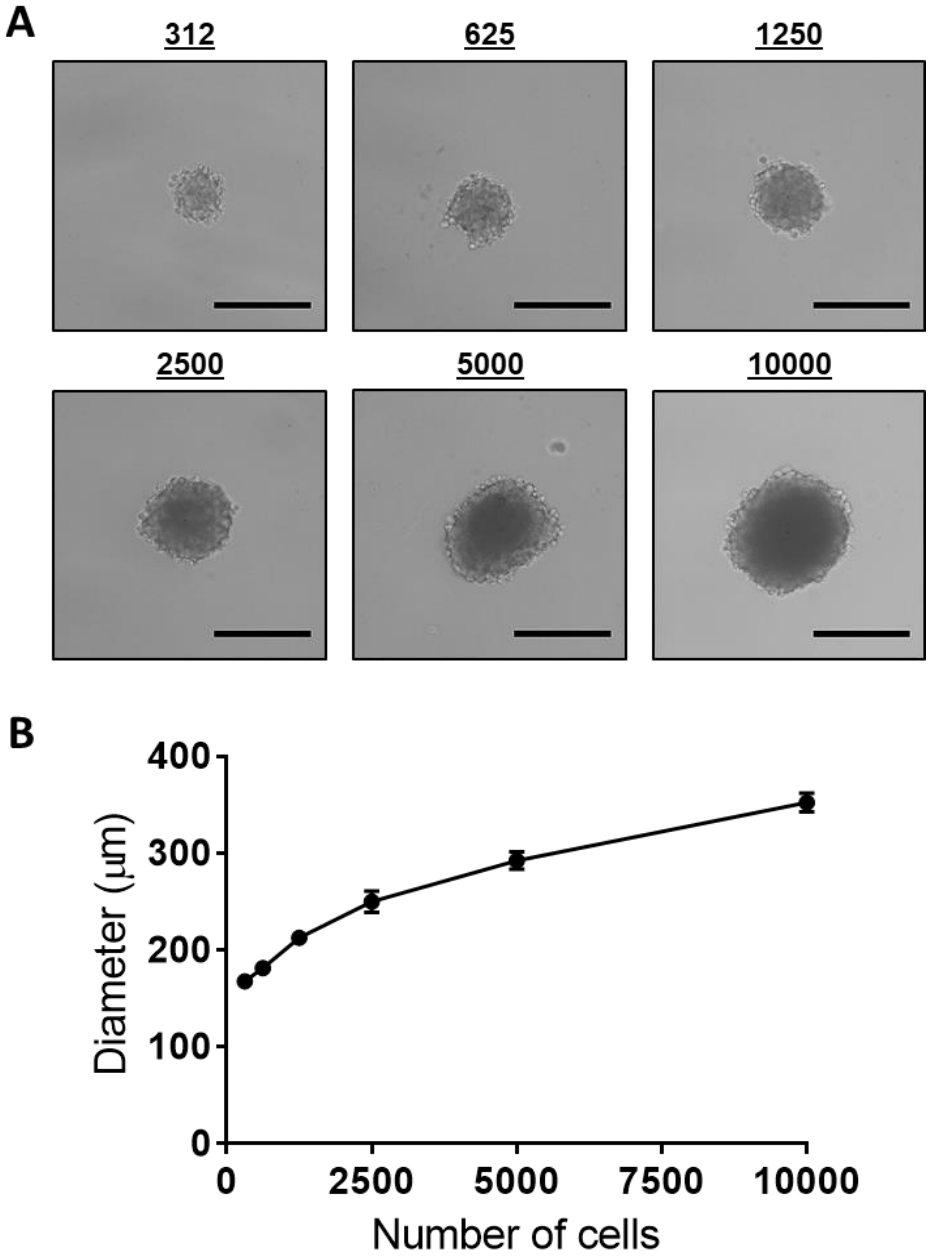

Figure 4.5. Optimisation of cell numbers for U87 spheroid generation. (A) Brightfield images of spheroids 4 days after seeding the number of cells indicated. Images are representative of n=3 experiments. Black bars (bottom right) depict 300 µm in scaled length. (B) Relationship between seeding density and the diameter (µm) of spheroids after 4 days growth. Error bars represent the SEM of n=3 experiments performed with six replicates.

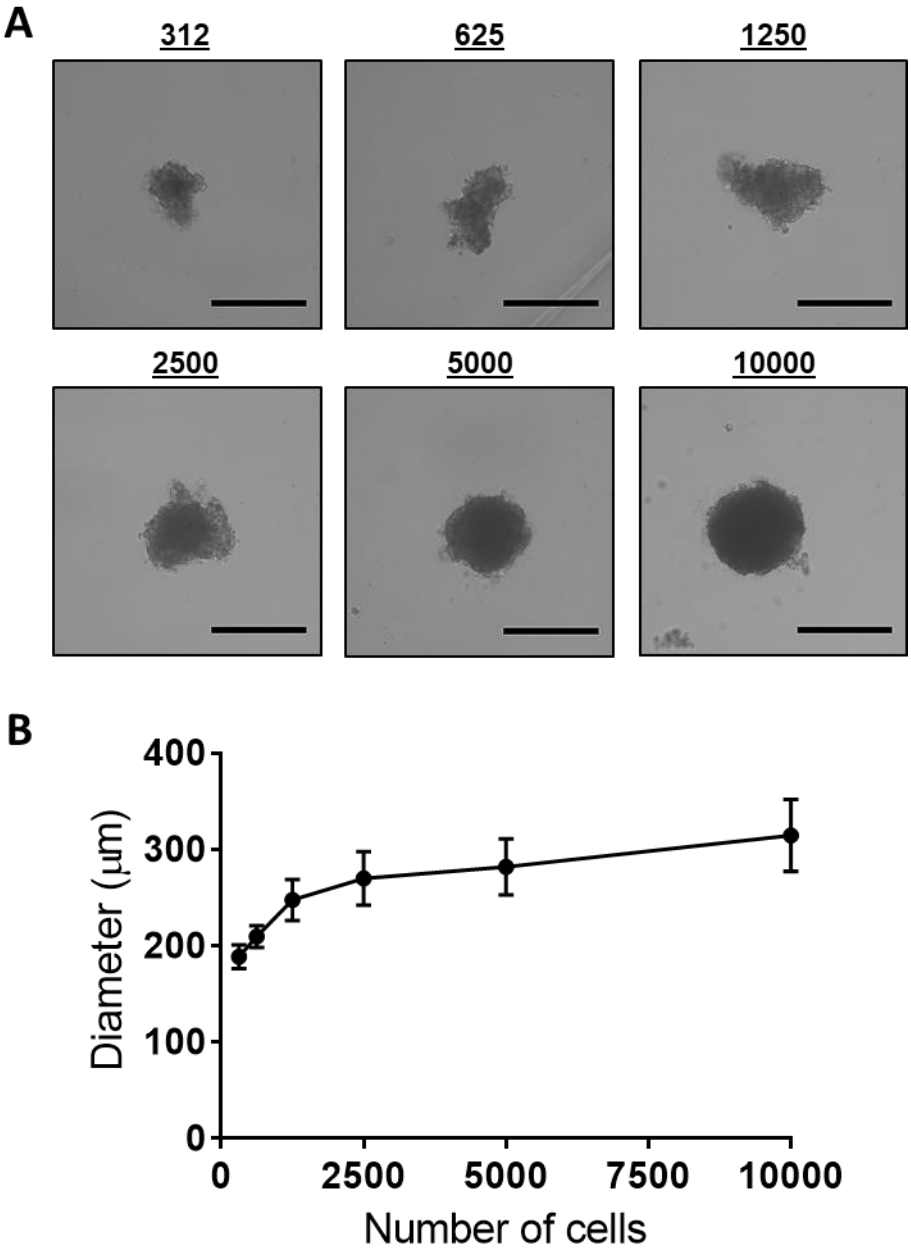

Figure 4.6. Optimisation of cell numbers for KNS42 spheroid generation. (A) Brightfield images of spheroids 4 days after seeding the number of cells indicated. Images are representative of n=3 experiments. Black bars (bottom right) depict 300 µm in scaled length. (B) Relationship between seeding density and the diameter (µm) of spheroids after 4 days growth. Error bars represent the SEM of n=3 experiments performed with six replicates.

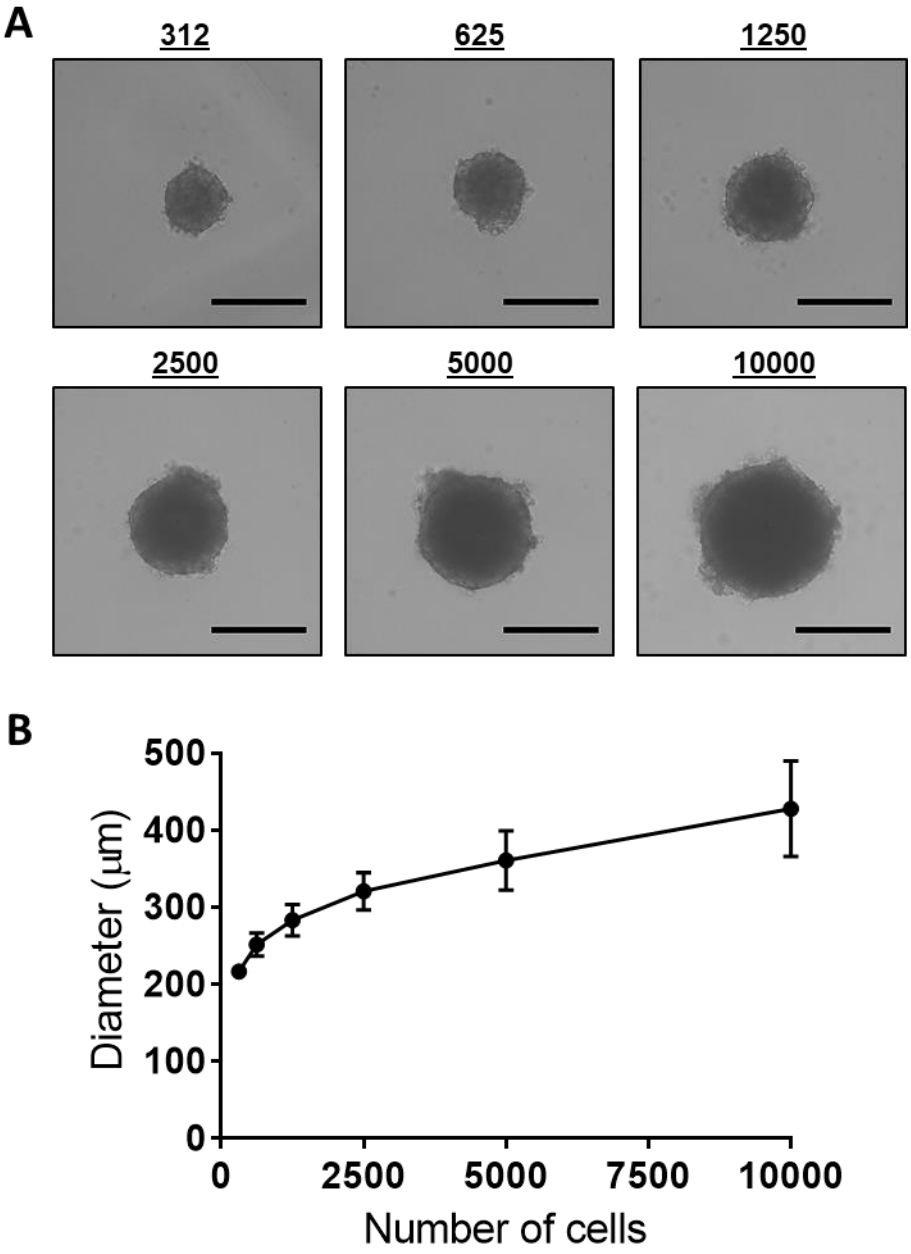

Figure 4.7. Optimisation of cell numbers for SF188 spheroid generation. (A) Brightfield images of spheroids 4 days after seeding the number of cells indicated. Images are representative of n=3 experiments. Black bars (bottom right) depict 300 µm in scaled length. (B) Relationship between seeding density and the diameter (µm) of spheroids after 4 days growth. Error bars represent the SEM of n=3 experiments performed with six replicates.

Following optimisation of spheroid seeding densities for the U87, KNS42 and SF188 cell lines, spheroid growth was assessed under lipoprotein-replete or -deplete conditions over a 14-day period. Control U87 spheroids steadily increased in diameter from 340 to 450 µm over 14 days (Figure 4.8A). The pattern of growth was largely matched by spheroids deprived of lipoproteins leading to non-significant differences in size despite consistently lower diameters compared to the control spheroids. The differences were accounted for by an initial decline in spheroid size at day 3 immediately following removal of lipoproteins, which might indicate that the cells were adapting to the metabolic stress during this period. Interestingly, from day 6 onwards small groups of cells were breaking off from control spheroids to give the appearance of migration despite the use of ULA plates (Figure 4.8B). This phenotype was not observed in the lipoprotein-deprived spheroids. In contrast to U87 cells, KNS42 and SF188 spheroids cultured under lipoprotein deficient conditions demonstrated stark differences compared to control spheroids, with significant differences in size observed from 9 days onwards in both paediatric cell lines (Figure 4.9A and Figure 4.10A). Reduced growth of KNS42 and SF188 spheroids appeared to be cytostatic with no overt indications of extensive apoptosis induction (Figure 4.9B and Figure 4.10B). In conclusion, growth in spheroid format indicated an increased capacity of U87 cells to deal with the metabolic stresses associated with lipoprotein deprivation, whereas the findings from KNS42 and SF188 spheroids corroborated with the initial results from monolayer models.

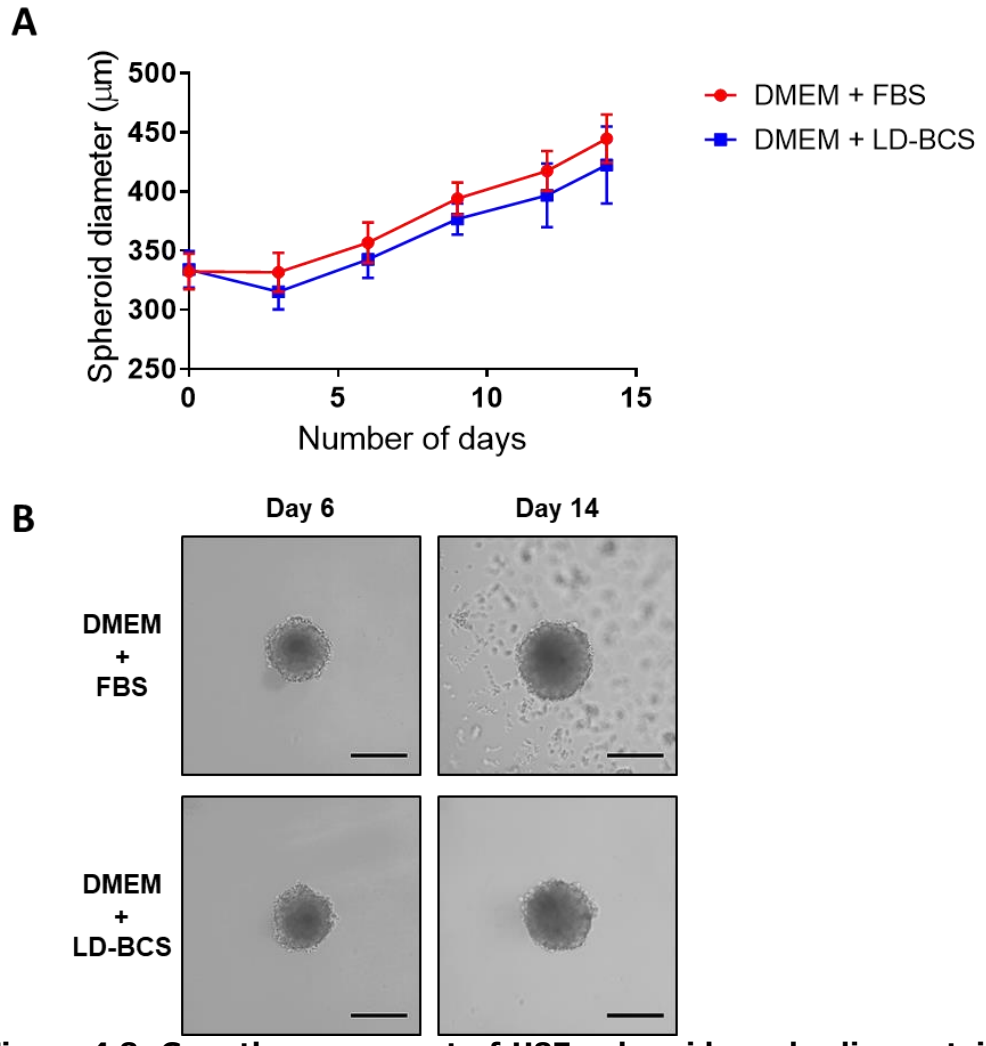

Figure 4.8. Growth assessment of U87 spheroids under lipoprotein deficient conditions. (A) Spheroid diameter (µm) was measured over a 14-day period in the presence (red) or absence (blue) of lipoproteins within the culture medium. Error bars represent the SEM of at least n=3 experiments performed with six replicates. (B) Representative brightfield images of spheroids at day 6 and 14. Black bars (bottom right) depict 300 µm in scaled length. Significance was measured at each timepoint using the *t*-test: * $p<0.05$; ** $p<0.01$; *** $p<0.001$.

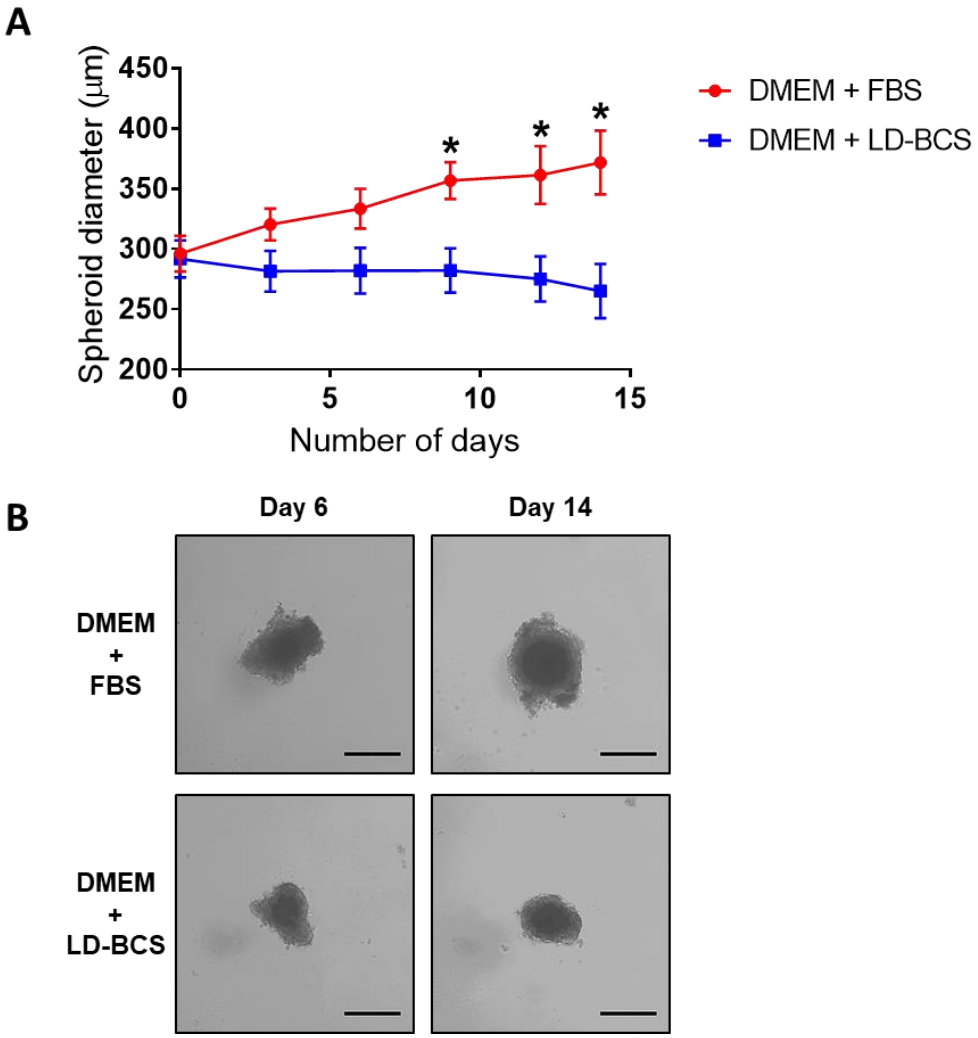

Figure 4.9. Growth assessment of KNS42 spheroids under lipoprotein deficient conditions. (A) Spheroid diameter (µm) was measured over a 14-day period in the presence (red) or absence (blue) of lipoproteins within the culture medium. Error bars represent the SEM of at least n=3 experiments performed with six replicates. (B) Representative brightfield images of spheroids at day 6 and 14. Black bars (bottom right) depict 300 µm in scaled length. Significance was measured at each timepoint using the *t*-test: * $p<0.05$; ** $p<0.01$; *** $p<0.001$.

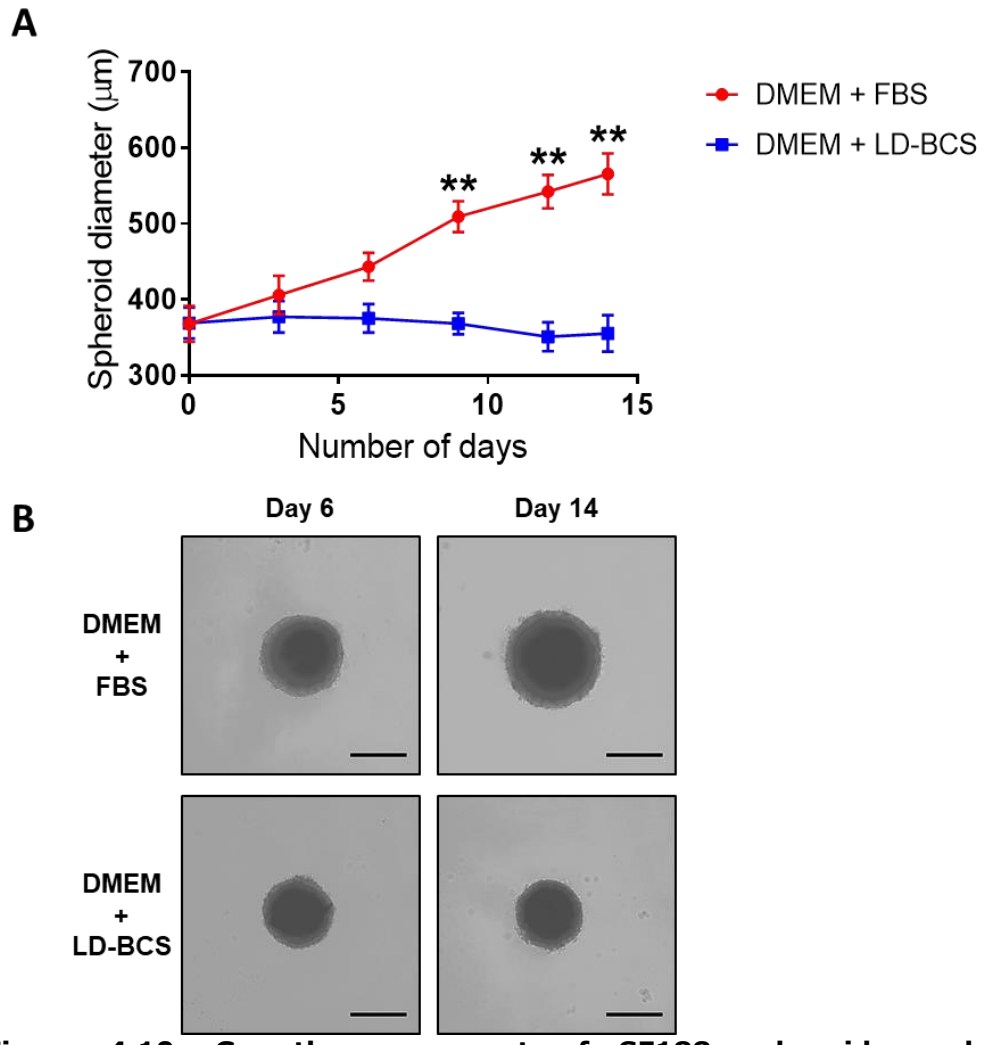

Figure 4.10. Growth assessment of SF188 spheroids under lipoprotein deficient conditions. (A) Spheroid diameter (µm) was measured over a 14-day period in the presence (red) or absence (blue) of lipoproteins within the culture medium. Error bars represent the SEM of at least n=3 experiments performed with six replicates. (B) Representative brightfield images of spheroids at day 6 and 14. Black bars (bottom right) depict 300 µm in scaled length. Significance was measured at each timepoint using the *t*-test: * $p<0.05$; ** $p<0.01$; *** $p<0.001$.

4.3. Lipoprotein deprived adult GBM cells respond to the addition of exogenous fatty acids or cholesterol

The cell viability experiments above highlighted a metabolic vulnerability to lipoprotein deprivation in both adult and paediatric HGG cells cultured as monolayers. Since lipoproteins contain several lipid and cholesterol species, we hypothesised that the addition of exogenous fatty acids or cholesterol may rescue the growth defect imposed by removal of lipoproteins within the growth media. Palmitic acid (18:0), oleic acid (18:1) and linoleic (18:2) acid were chosen to represent saturated, mono- and poly-unsaturated fatty acids, respectively. Maintenance of a specific ratio of saturated to unsaturated fatty acids is essential to maintain cellular viability and deviation from the homeostatic state can lead to metabolic stress and the induction of cell death (Griffiths *et al.*, 2013; Young *et al.*, 2013). U87 cells cultured in lipoprotein deficient medium (LPDM) demonstrated significantly improved viability upon addition of either oleic acid or linoleic acid, whereas exogenous palmitic acid did not rescue growth (Figure 4.11A). In both KNS42 and SF188 cell lines, addition of either saturated or unsaturated fatty acids did not significantly improve viability in the absence of lipoproteins (Figure 4.11B and C). These results indicate that the removal of lipoproteins from the growth medium caused either 1) an increase in the saturated-to-unsaturated fatty acid ratio in U87 cells, hence the rescue in viability upon addition of mono-unsaturated oleic acid and poly-unsaturated linoleic acid, whereas fatty acid homeostasis was maintained in the paediatric cells; or 2) U87 cells have a higher capacity for fatty acid uptake from the extracellular environment compared to KNS42 and SF188 cells.

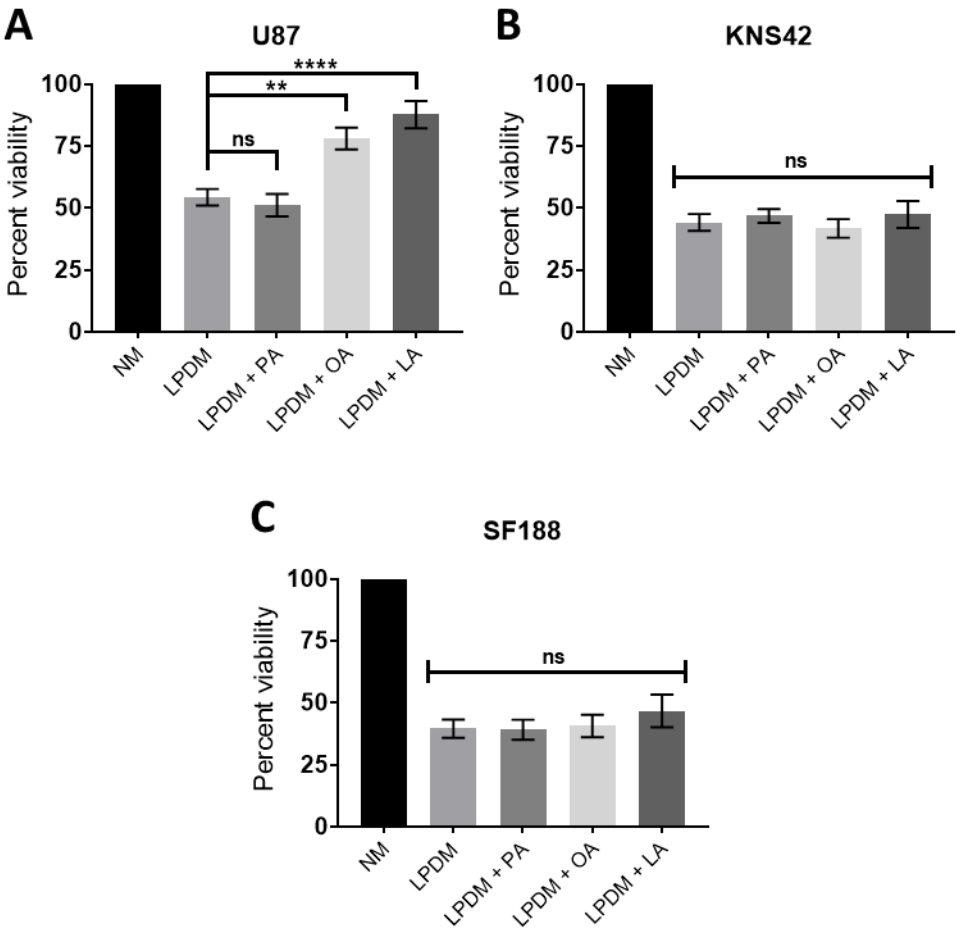

Figure 4.11. Rescue of lipoprotein-deprived adult and paediatric GBM cells with exogenous fatty acids. Adult U87 (A) and paediatric KNS42 (B) and SF188 (C) cells were cultured for three days in either normal medium containing lipoproteins or lipoprotein deprived medium (LPDM) supplemented with either palmitic acid (PA), oleic acid (OA), or linoleic acid (LA). Viability was assessed using the PrestoBlue assay and expressed as a percentage of the control condition with normal media (NM). Error bars represent the SEM of at least n=3 experiments performed in triplicate. Significance was measured using the *t*-test: ns not significant; * $p<0.05$; ** $p<0.01$; *** $p<0.001$.

Sterols form a large component of lipoproteins and have been demonstrated to promote aberrant tumour growth. To determine if the reduced viability under lipoprotein deficient conditions is due to reduced cholesterol content, a series of cholesterol concentrations were added to the growth medium. Cholesterol was complexed with MβCD which assists solubility in water. Addition of 2.5 to 10 µM MβCD-cholesterol significantly improved the viability of U87 cells deprived of lipoproteins but did not rescue growth completely relative to control cells (Figure 4.12A). KNS42 cells demonstrated a similar trend in response to MβCD-cholesterol but was not significant across the range of concentrations used (Figure 4.12B). In SF188 cells, significant improvements in cellular viability was achieved upon supplementation of LPDM with 5 or 10 µM MβCD-cholesterol (Figure 4.12C). However, the improvement was only marginal, consisting of only 10% increase in viability. In combination with the fatty acid experiments above, these results indicated that addition of either fatty acids or MβCD-cholesterol was not sufficient to completely rescue growth under lipoprotein deficient conditions, with the exception of linoleic acid supplementation in U87 cells. Considering that lipoproteins consist of both lipid and sterol species, combined deficiency of fatty acids and cholesterol may be necessary and sufficient to underlie the growth defect demonstrated by adult and paediatric GBM cells.

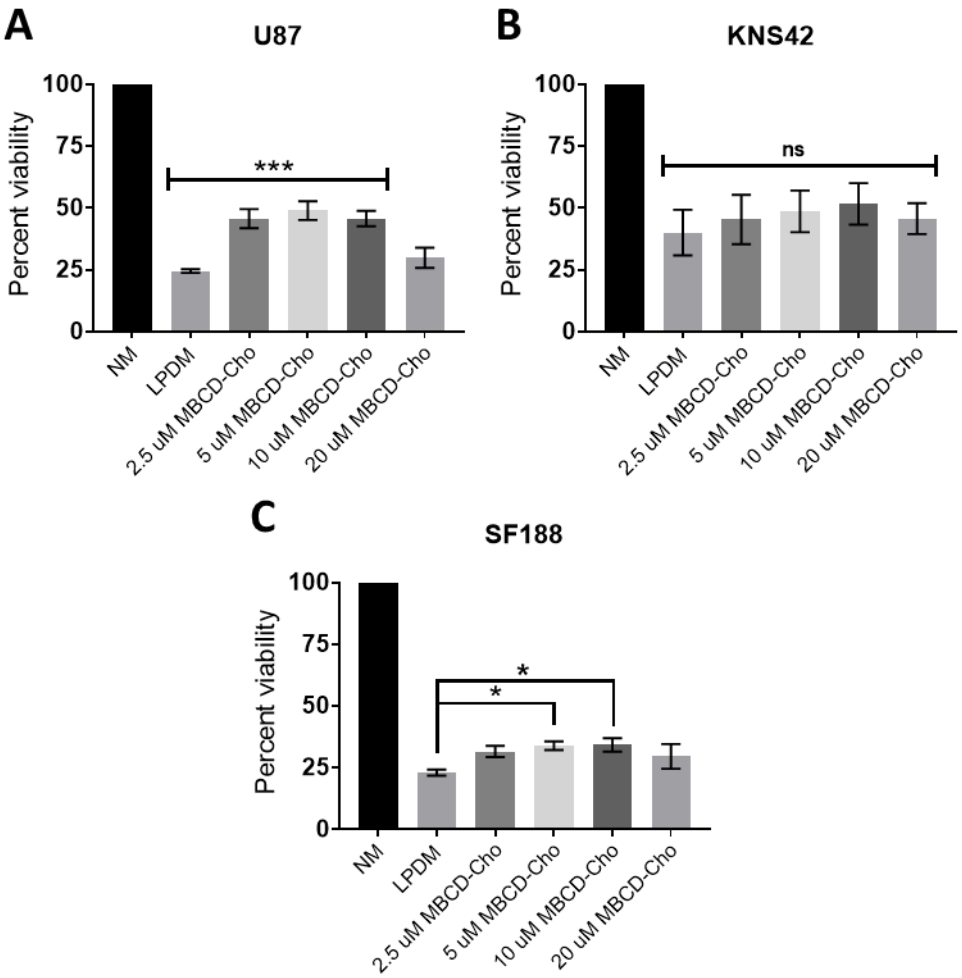

Figure 4.12. Rescue of lipoprotein-deprived adult and paediatric GBM cells with exogenous cholesterol. Adult U87 (A) and paediatric KNS42 (B) and SF188 (C) cells were cultured for three days in either normal medium containing lipoproteins or lipoprotein deprived medium (LPDM) supplemented with various concentrations of cholesterol complexed to methyl-β-cyclodextrin (MβCD-Cho). Viability was assessed using the PrestoBlue assay and expressed as a percentage of the control condition (NM). Error bars represent the SEM of at least n=3 experiments performed in triplicate. Significance was measured using the *t*-test: ns not significant; * $p<0.05$; ** $p<0.01$; *** $p<0.001$.

4.4. Growth under lipoprotein-deplete conditions induced cell cycle arrest in paediatric GBM cells

Assessment of paediatric GBM cells under lipoprotein deficient conditions revealed a cytostatic phenotype with no overt indications of apoptosis induction. Therefore, cell cycle analysis through flow cytometry was performed on PI-stained cells that were cultured under lipoprotein-replete or -deplete conditions for 3 days prior to fixation. This timepoint was chosen since the divergence of viability curves at this point implies that molecular changes in response to lipoprotein deficiency have occurred. Cell cycle analysis of U87 cells was consistent with the greater resistance displayed by this cell line to metabolic stress (Figure 4.13). No significant changes to all four phases of the cell cycle was observed for the U87 cell line (Figure 4.13A), in contrast to the KNS42 and SF188 cell lines that displayed a significant decrease and increase of the percentage of cells in G0 and S phases, respectively (Figure 4.13B and C). Additionally, the KNS42 cell line demonstrated a significant decrease in the G2 phase and a minor increase in the sub G0 phase (Figure 4.13B). These results indicate that after 3 days culture under lipoprotein deficient conditions, U87 cells demonstrated no alterations to cell cycle dynamics, whereas KNS42 and SF188 paediatric cells demonstrated G1/S transition in association with an elongation of S phase. This phenotype may have manifested due to stalled replication forks following DNA damage or deficiencies in metabolites required for DNA synthesis and replication, potentially highlighting differences in DNA repair capacity between the adult and paediatric GBM cell lines.

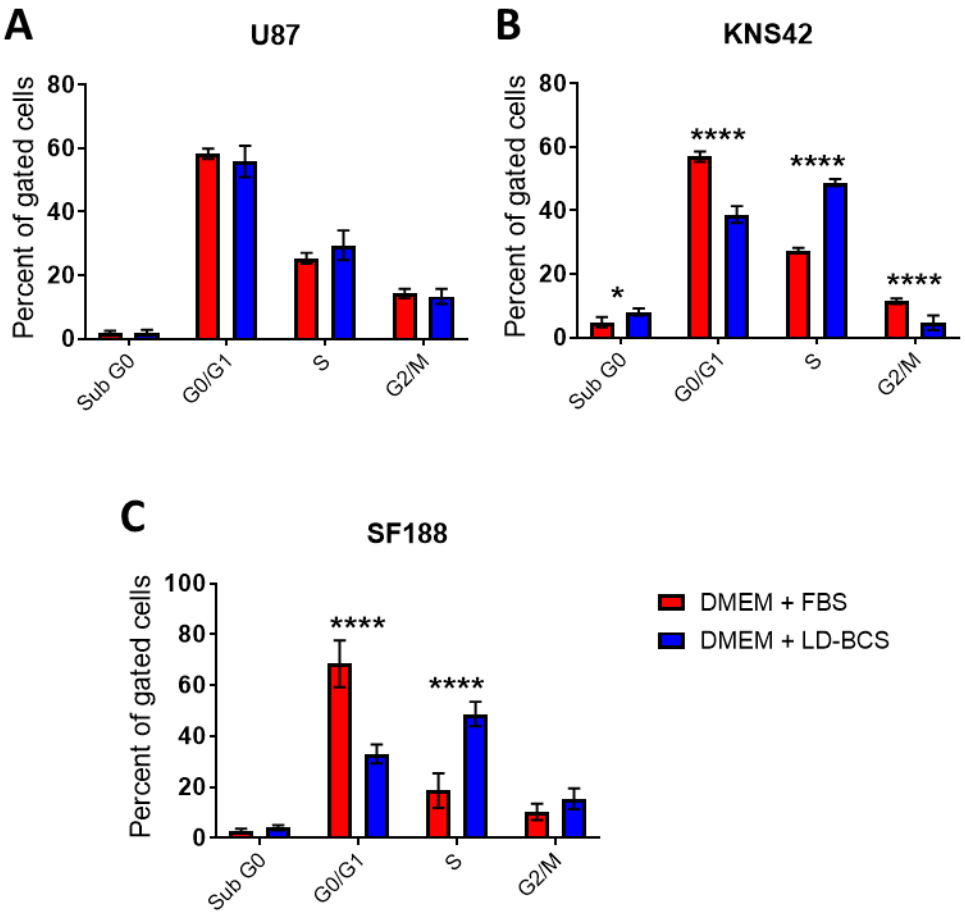

Figure 4.13. Flow cytometric analysis of adult and paediatric GBM cells deprived of lipoproteins. Adult U87 (A) and paediatric KNS42 (B) and SF188 (C) cells were cultured for three days in the presence (red) or absence (blue) of lipoproteins. Error bars represent the SEM of at least n=3 experiments performed in triplicate. Significance was measured using the t-test: * $p<0.05$; ** $p<0.01$; *** $p<0.001$.

4.5. Distinct transcriptomic responses are displayed between lipoprotein-deprived adult and paediatric GBM cells

Analysis of the effects of depriving GBM cells of lipoproteins has shown that measurable phenotypic responses are observed from day 3 onwards. We therefore aimed to elucidate the underlying genetic basis for these differences as well as decipher the mechanisms leading to cytostatic growth through application of transcriptomics via gene expression microarrays. RNA was extracted from GBM cells cultured in either lipoprotein-replete or -deplete conditions for 3 days. In U87 cells, 51 genes were identified as significantly differentially expressed after correction for multiple testing (Table 4.1). The

highest upregulated transcript with known function was *STC2*, which encodes a secreted glycoprotein that has either oncogenic or tumour suppressor properties depending on the tumour type (Law and Wong, 2010; Hou *et al.*, 2015). Interestingly, gene ontology (GO) enrichment analysis identified *cellular response to hypoxia* as the top enriched category within the U87 transcriptome, despite being cultured under normoxic conditions (Table 4.2). Other transcripts upregulated within this GO category were *CA9*, *BNIP3*, *VEGFRA*, and *NDNF*. Metabolic stress associated with growth under lipoprotein deficient conditions thus appeared to stimulate a hypoxic response in U87 cells, perhaps reflective of induced transcriptional programs following ROS generation. Possibly orchestrating these responses was the observed upregulation of *AK4*, which can stabilise HIF1α through ROS production and enable cells to avoid the AMPK-mediated metabolic checkpoint (Jan *et al.*, 2017). Evidence of a cellular response to lipoprotein deficiency was demonstrated by upregulation of *LIPG*, an extracellular enzyme that releases lipids from HDLs and facilitates lipoprotein uptake (Slebe *et al.*, 2016). Increased transcript levels of *RDH10* further supported this by implicating alterations to lipid droplets (Jiang and Napoli, 2013). Nutrient deprivation has been shown to stimulate lipolysis in conjunction with autophagy (Jaishy and Abel, 2016). The observation of increased *BNIP3* expression supports this functional mechanism (Bellot *et al.*, 2009). However, decreased expression of *DIRAS3* implied suppression of autophagic processes (Lu *et al.*, 2014), meaning that it was unclear what the autophagic response was under lipoprotein deficient conditions. To identify protein-protein interactions within the list of differentially expressed genes, network analysis was performed using NetworkAnalyst (Xia, Benner and Hancock, 2014). The list of significant genes uploaded into the online tool was extended to cover genes with an unadjusted *p*-value of 0.05 (total of 547 genes) for the U87 cell line, since only 51 genes were significant after correction for multiple comparisons. Identified networks were associated with secreted factors (Figure 4.14A), differentiation (Figure 4.14B), and fatty acid/sterol-related metabolism (Figure 4.14C and D).

Table 4.1. List of the most differentially expressed genes in U87 cells deprived of lipoproteins for 3 days.

Symbol	Name	log2FC	AveExpr	adj.P.Val	B
C5orf46	chromosome 5 open reading frame 46	2.128	3.929	5.32E-22	46.00
LOC154761	family with sequence similarity 115, member C pseudogene	1.478	5.693	1.30E-09	19.11
STC2	stanniocalcin 2	1.268	5.682	6.01E-07	12.51
CP	ceruloplasmin	1.196	5.200	4.91E-06	10.46
TXNIP	thioredoxin interacting protein	1.100	6.602	6.11E-05	7.95
LOX	lysyl oxidase	1.066	6.597	1.41E-04	7.10
CA9	carbonic anhydrase 9	1.055	5.430	1.72E-04	6.83
BNIP3	BCL2 interacting protein 3	1.040	10.236	2.18E-04	6.48
AK4	adenylate kinase 4	1.033	6.938	2.44E-04	6.31
LIPG	lipase G, endothelial type	1.030	5.773	2.44E-04	6.24
ERVK-7	endogenous retrovirus group K member 7	1.025	5.507	2.60E-04	6.12
VEGFA	vascular endothelial growth factor A	1.021	6.432	2.60E-04	6.02
RDH10	retinol dehydrogenase 10	1.010	8.498	3.11E-04	5.77
DIRAS3	DIRAS family GTPase 3	-1.018	5.515	2.65E-04	5.96
MT1F	metallothionein 1F	-1.022	7.425	2.60E-04	6.05
LOC105372733	uncharacterized LOC105372733	-1.040	3.996	2.18E-04	6.48
PSG5	pregnancy specific beta-1-glycoprotein 5	-1.100	4.563	6.11E-05	7.95
USP17L5	ubiquitin specific peptidase 17-like family member 5	-1.278	7.035	5.23E-07	12.80
ABCA1	ATP binding cassette subfamily A member 1	-1.325	5.823	1.40E-07	14.20
ZNF595	zinc finger protein 595	-1.435	6.229	4.17E-09	17.67

Statistical evaluation of differentially expressed genes was performed by implementing a Bayesian linear model using the R package *limma*. Fold changes between lipoprotein-replete and -deplete conditions are expressed as logarithms to the base of 2 (log2FC) alongside average expression values (AveExpr). Genes that are upregulated under lipoprotein-deplete conditions have log2FC values in red, whereas downregulated genes are in green. *P*-values were adjusted for multiple comparisons using the Bonferonni-Holm method. B-statistics (B) indicate the log odds that a gene is differentially expressed.

Table 4.2. Gene ontology analysis of genes differentially expressed in U87, KNS42 and SF188 cells deprived of lipoproteins.

GO.ID	Term	Annotated	Significant	Expected	classicFisher	classicKS	weight01KS	parentchildFis	Genes
U87									
GO:0071456	cellular response to hypoxia	98	5	0.53	1.70E-04	5.80E-03	8.80E-04	3.50E-04	*STC2, CA9, BNIP3, VEGFA, NDNF*
GO:0032376	positive regulation of cholesterol trans...	11	2	0.06	1.52E-03	2.99E-02	2.69E-02	8.73E-02	*ABCA1, LIPG*
GO:0030823	regulation of cGMP metabolic process	12	2	0.06	1.82E-03	1.01E-01	3.50E-02	2.80E-02	*VEGFA, PDE5A*
GO:0030199	collagen fibril organization	15	3	0.08	6.40E-05	4.81E-02	4.81E-02	1.30E-04	*LOX, LUM, P4HA1*
KNS42									
GO:0060337	type I interferon signaling pathway	52	16	0.99	8.00E-16	4.90E-08	2.10E-09	1.00E-08	*IFI6, OAS2, IRF7, OAS1, MX1, XAF1, IFI35, IFITM1, IRF9, IFI27, USP18, OAS3, ISG15, STAT2, IFIT3, IFIT2*
GO:0051607	defense response to virus	107	17	2.05	1.30E-11	2.80E-07	2.00E-05	1.50E-08	*DDIT4, OAS2, IRF7, OAS1, IFI44L, MX1, IFITM1, IRF9, OAS3, ISG15, IFNE, CXCL10, STAT2, HTRA1, IFIT3, IFIT2, MICA*
GO:0006695	cholesterol biosynthetic process	42	15	0.8	5.10E-16	1.60E-09	8.00E-03	3.54E-02	*INSIG1, HMGCS1, MSMO1, DHCR24, MVK, DHCR7, NSDHL, ACAT2, SQLE, MVD, SC5D, EBP, IDI1, TM7SF2, HMGCR*
SF188									
GO:0060337	type I interferon signaling pathway	55	20	3.08	4.90E-12	3.50E-08	1.30E-09	1.80E-05	*IFI6, IFIT1, OAS2, XAF1, STAT2, MX1, IFIT2, IFIT3, IRF7, IRF9, MIR21, USP18, OAS3, ISG15, WNT5A, IFITM1, STAT1, SAMHD1, OASL, IFI35*
GO:0045540	regulation of cholesterol biosynthetic p...	27	14	1.51	2.50E-11	1.10E-07	1.10E-07	8.85E-03	*HMGCS1, MVK, SC5D, TM7SF2, DHCR7, MVD, SQLE, CYP51A1, IDI1, LSS, SCD, HMGCR, FDPS, FASN*
GO:0051607	defense response to virus	111	28	6.22	7.30E-12	1.90E-08	1.80E-06	2.00E-07	*IFIH1, IFIT1, OAS2, IL1B, STAT2, MX1, IFIT2, IFIT3, IL6, IRF7, IFI44L, PML, IRF9, HERC5, DDX58, OAS3, MICA, ISG15, GBP3, CXCL10, IFITM1, TNFAIP3, STAT1, HTRA1, SAMHD1, PARP9, OASL, EXOSC5*
GO:0006695	cholesterol biosynthetic process	41	20	2.3	5.40E-15	1.40E-09	2.80E-03	2.18E-03	*INSIG1, HMGCS1, MSMO1, MVK, ACAT2, SC5D, TM7SF2, EBP, DHCR7, MVD, SQLE, CYP51A1, DHCR24, IDI1, LSS, SCD, HMGCR, NSDHL, FDPS, FASN*
GO:0016126	sterol biosynthetic process	43	21	2.41	1.10E-15	1.90E-10	3.10E-02	8.90E-07	*INSIG1, HMGCS1, MSMO1, MVK, ACAT2, SC5D, TM7SF2, EBP, DHCR7, MVD, SQLE, CYP51A1, DHCR24, IDI1, LSS, CYB5R2, SCD, HMGCR, NSDHL, FDPS, FASN*

Statistical evaluation of gene ontology (GO) categories based of the number of significant-to-expected observations using either Fisher's exact test (Fis) or Kolmogorov-Smirnov test (KS). Different algorithms were utilised to take account of the GO hierarchy, including classic, weight01, and parentchild. Genes that are upregulated and downregulated under lipoprotein-deplete conditions are highlighted in red and green, respectively.

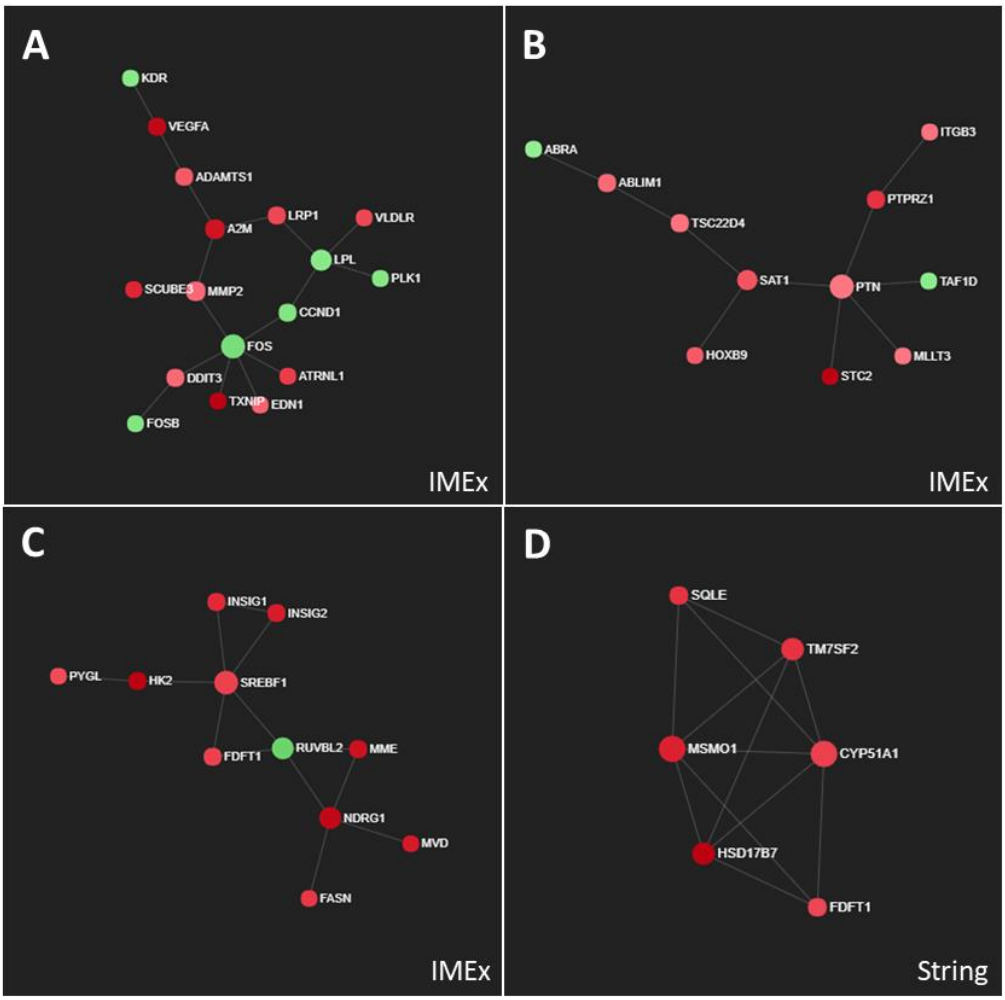

Figure 4.14. Network analysis of differentially expressed genes in U87 cells cultured under lipoprotein deficient conditions. Genes that are upregulated and downregulated following culture under lipoprotein deficient conditions for 72 hr are highlighted in red and green, respectively. The curated database utilised to generate the networks is displayed in the bottom right corner of each panel.

KNS42 cells cultured under lipoprotein deficient conditions demonstrated transcriptomic changes indicative of an inflammatory response as evidenced by enrichment of the GO processes *type I interferon signalling pathway* and *defence to virus* (Table 4.2). Several upregulated genes were associated with stress responses, including *SESN2*, *DDIT4*, and *SLC6A9* (GLYT1) (Table 4.3). *SESN2* is a tumour suppressor that limits ER stress (Ro *et al.*, 2016), inhibits mTORC1 signalling (Parmigiani *et al.*, 2014), and protects cells from glucose-starvation induced cell death via regulation of mitochondrial homeostasis (Ding *et al.*, 2016). Interestingly, *SESN2* upregulation implicates reduced mTORC1-

dependent expression of lipid genes (Byun *et al.*, 2017), possibly to conserve ATP and NADH under metabolic stress. Increased expression of *DDIT4* supports this stress response by its role in inhibiting mTORC1 (Tirado-Hurtado, Fajardo and Pinto, 2018), and has been associated with a worse prognosis in GBM (Pinto *et al.*, 2017). Several of the upregulated genes were ATF4 target genes, including *SLC6A9* (*GLYT1*), *CHAC1*, and *ASNS*, implicating the induction of ER stress and the UPR. *SLC6A9* (*GLYT1*) is a glycine transporter that increases glycine uptake required for glutathione synthesis under cellular stress (Howard and Hirst, 2011). Additional evidence of metabolic dysregulation due to growth under lipoprotein deficient conditions included increased expression of *DHRS3*, a p53-induced ER protein that is associated with lipid droplet accumulation (Deisenroth *et al.*, 2011), and *ALD1L2*, which stimulates ATP production (Kang *et al.*, 2016) and distributes one-carbon units between the cytosol and mitochondria (Krupenko *et al.*, 2010). Interestingly, the most upregulated gene in KNS42 cells deprived of lipoproteins, *GDF15*, is an anti-inflammatory cytokine and is implicated in cellular stress protection (Li *et al.*, 2017). Network analysis of differentially expressed genes in KNS42 cells highlighted *STAT1*, *STAT2*, *IRF9* and *ISG15* as a key node in the network (Figure 4.15B). In section 4.3, it was shown that the administration of exogenous cholesterol was not sufficient to rescue KNS42 cellular viability under lipoprotein deficient conditions. Transcriptomics analysis identified upregulation of 15 genes associated with the GO *cholesterol biosynthetic process*, including *HMGCS1*, *HMGCR*, and *MVK* in the early stages of cholesterol synthesis, and *DHCR24* and *DHCR7* in the latter. This supports our hypothesis that growth under lipoprotein deficient conditions leads to reduced intracellular cholesterol levels and the induction of cholesterol synthetic processes, features that were not apparent in the GO analysis of the U87 cell line.

Table 4.3. List of the most differentially expressed genes in KNS42 cells deprived of lipoproteins for 3 days.

Symbol	Name	log2FC	AveExpr	adj.P.Val	B
GDF15	growth differentiation factor 15	2.280	6.314	7.98E-21	44.98
ALDH1L2	aldehyde dehydrogenase 1 family member L2	2.180	5.681	2.89E-19	40.57
SLC6A9	solute carrier family 6 member 9	2.178	5.585	2.89E-19	40.50
NUPR1	nuclear protein 1, transcriptional regulator	2.058	5.727	4.05E-17	35.50
SESN2	sestrin 2	2.039	6.040	7.49E-17	34.70
ASNS	asparagine synthetase (glutamine-hydrolyzing)	1.925	7.879	6.57E-15	30.26
CTH	cystathionine gamma-lyase	1.874	3.680	4.12E-14	28.37
IFI6	interferon alpha inducible protein 6	1.840	8.499	1.36E-13	27.11
SEL1L3	SEL1L family member 3	1.795	6.776	6.51E-13	25.50
ULBP1	UL16 binding protein 1	1.768	4.232	1.59E-12	24.56
DDIT4	DNA damage inducible transcript 4	1.763	5.244	1.76E-12	24.37
CHAC1	ChaC glutathione specific gamma-glutamylcyclotransferase 1	1.721	7.487	7.37E-12	22.93
SLC1A4	solute carrier family 1 member 4	1.706	5.595	1.14E-11	22.44
INSIG1	insulin induced gene 1	1.694	8.330	1.60E-11	22.05
DHRS3	dehydrogenase/reductase 3	1.650	4.519	7.00E-11	20.58
HMGCS1	3-hydroxy-3-methylglutaryl-CoA synthase 1	1.592	6.774	4.68E-10	18.72
TMEM154	transmembrane protein 154	1.578	3.900	6.94E-10	18.29
MMP9	matrix metallopeptidase 9	-1.057	8.488	3.86E-04	4.77
ZNF595	zinc finger protein 595	-1.063	5.305	3.48E-04	4.88
HNRNPU	heterogeneous nuclear ribonucleoprotein U	-1.083	6.526	2.42E-04	5.31
MAP1LC3C	microtubule associated protein 1 light chain 3 gamma	-1.565	6.029	1.00E-09	17.88

Statistical evaluation of differentially expressed genes was performed by implementing a Bayesian linear model using the R package *limma*. Fold changes between lipoprotein-replete and -deplete conditions are expressed as logarithms to the base of 2 (log2FC) alongside average expression values (AveExpr). Genes that are upregulated under lipoprotein-deplete conditions have log2FC values in red, whereas downregulated genes are in green. *P*-values were adjusted for multiple comparisons using the Bonferonni-Holm method. B-statistics (B) indicate the log odds that a gene is differentially expressed.

The transcriptomic response of SF188 cells was more akin to KNS42 rather than the U87 cell line, possibly reflecting differences between adult and paediatric GBM. However, there were more differentially expressed genes with roles in metabolism (Table 4.4). *FABP3* is induced under hypoxia and mediates lipid droplet accumulation independent of *de novo* synthesis (Bensaad *et al.*, 2014). Although cultured under normoxia, SF188 cells demonstrated an upregulation of *FABP3*. Cholesterol dysregulation was also observed with increased gene expression of *INSIG1* and *HMGCS1*, indicating reduced cellular sterol levels under lipoprotein deficient conditions. This was supported by enrichment of the GO *cholesterol biosynthetic process* and *sterol biosynthetic process* due to

upregulation of several cholesterol synthesis genes, including *HMGCS1*, *HMGCR*, *MVK*, *DHCR24* and *DHCR7*. Evidence of cellular stress was indicated by enrichment of the GO processes *type I interferon signalling pathway* and *defence response to virus* (Table 4.2), as supported by increased expression of *NUPR1* (Emma *et al.*, 2016) and *PTGS2* (COX2), which mediates several inflammatory responses (Stasinopoulos *et al.*, 2013). Network analysis highlighted interferon-stimulated gene 15 (*ISG15*) as a key node in the network (Figure 4.15B). ISG15 is a ubiquitin-like protein that can conjugate with intracellular proteins (ISGylation) and is induced by type I interferons (IFNs), viral and bacterial infection, lipopolysaccharide, retinoic acid, or genotoxic stress-inducing agents (Villarroya-Beltri, Guerra and Sánchez-Madrid, 2017). Another upregulated gene, the E3 ligase *HERC6*, mediates ISGylation in which ISG15 is conjugated to proteins in a process similar to ubiquitination (Oudshoorn *et al.*, 2012). ISGylation is involved in several cellular processes, including DNA repair, autophagy, protein translation and exosome secretion (Segatto *et al.*, 2014). Interestingly, several miRNAs were downregulated in SF188 cells starved of lipoproteins; MiR-548c impairs migration and invasion (Sun *et al.*, 2016), whilst MiR-1299 suppresses cell proliferation by targeting CDK6 (Zhu *et al.*, 2016) and is a negative regulator of STAT3 (Wang *et al.*, 2017). Downregulation of these miRNAs is likely a cellular mechanism to maintain tumourigenic properties. However, counteracting these effects was the observed downregulation of MiR-21, which is an oncogenic miRNA that confers invasive properties in tumours (Bornachea *et al.*, 2012).

Table 4.4. List of the most differentially expressed genes in SF188 cells deprived of lipoproteins for 3 days.

Symbol	Name	logFC	AveExpr	adj.P.Val	B
NUPR1	nuclear protein 1, transcriptional regulator	2.572	7.542	1.83E-04	5.91
IFI6	interferon alpha inducible protein 6	2.427	7.142	2.44E-07	15.56
FLG	filaggrin	2.100	5.876	1.12E-06	12.30
FABP3	fatty acid binding protein 3	2.003	5.011	2.44E-07	14.62
SAMD9L	sterile alpha motif domain containing 9 like	1.971	5.388	2.44E-07	14.86
INSIG1	insulin induced gene 1	1.840	8.715	2.82E-07	14.18
LOC101927880	uncharacterized LOC101927880	1.817	6.444	2.04E-06	11.41
ULBP1	UL16 binding protein 1	1.801	5.090	2.26E-02	-0.60
PTGS2	prostaglandin-endoperoxide synthase 2	1.797	6.402	1.64E-06	11.81
EDN1	endothelin 1	1.783	7.359	2.44E-07	14.52
HERC6	HECT and RLD domain containing E3 ubiquitin protein ligase family member 6	1.773	5.193	3.72E-07	13.76
IFIT1	interferon induced protein with tetratricopeptide repeats 1	1.714	4.080	2.02E-06	11.54
LUM	lumican	1.684	7.660	1.23E-05	9.15
OAS2	2'-5'-oligoadenylate synthetase 2	1.681	4.425	1.27E-05	9.05
DHRS3	dehydrogenase/reductase 3	1.674	4.232	1.23E-05	9.11
LOC105375440	uncharacterized LOC105375440	1.637	4.585	1.11E-06	12.48
CXCL11	C-X-C motif chemokine ligand 11	1.626	5.183	1.12E-06	12.26
HTR1D	5-hydroxytryptamine receptor 1D	1.625	5.967	3.94E-06	10.64
KCNN3	potassium calcium-activated channel subfamily N member 3	1.598	4.995	9.32E-05	6.85
IFIH1	interferon induced with helicase C domain 1	1.590	4.192	9.55E-07	12.74
TMEM52B	transmembrane protein 52B	1.580	7.110	3.77E-06	10.74
HSD17B2	hydroxysteroid 17-beta dehydrogenase 2	1.529	7.007	3.94E-06	10.59
OR2B6	olfactory receptor family 2 subfamily B member 6	1.523	3.850	8.52E-06	9.71
SAMD9	sterile alpha motif domain containing 9	1.514	6.478	2.04E-06	11.38
HMGCS1	3-hydroxy-3-methylglutaryl-CoA synthase 1	1.502	7.247	7.42E-06	9.88
ERMARD	ER membrane associated RNA degradation	-1.008	6.074	4.40E-03	1.65
HIST1H1D	histone cluster 1 H1 family member d	-1.012	3.539	2.32E-03	2.47
SNORD88B	small nucleolar RNA, C/D box 88B	-1.025	6.884	1.12E-03	3.56
SNORD65	small nucleolar RNA, C/D box 65	-1.048	6.082	4.08E-03	1.76
MT1X	metallothionein 1X	-1.054	8.729	5.35E-04	4.57
FRG1HP	FSHD region gene 1 family member H, pseudogene	-1.082	4.775	1.31E-03	3.33
MIR1299	microRNA 1299	-1.085	5.416	6.64E-03	1.07
HIST1H1B	histone cluster 1 H1 family member b	-1.091	9.173	4.18E-03	1.71
MIR548C	microRNA 548c	-1.094	2.881	4.08E-03	1.76
SNORD12	small nucleolar RNA, C/D box 12	-1.095	6.914	6.33E-04	4.32
HIST1H3I	histone cluster 1 H3 family member i	-1.112	10.648	4.50E-04	4.82
MIR21	microRNA 21	-1.130	6.335	4.07E-03	1.78
SNORD4A	small nucleolar RNA, C/D box 4A	-1.150	4.684	1.54E-03	3.09
SFXN2	sideroflexin 2	-1.166	5.392	4.62E-04	4.73
HIST1H3F	histone cluster 1 H3 family member f	-1.389	8.786	2.66E-05	8.24
MAP1LC3C	microtubule associated protein 1 light chain 3 gamma	-1.436	6.065	1.83E-04	5.87
HIST1H2BI	histone cluster 1 H2B family member i	-1.436	4.193	5.70E-04	4.49

Statistical evaluation of differentially expressed genes was performed by implementing a Bayesian linear model using the R package *limma*. Fold changes between lipoprotein-replete and -deplete conditions are expressed as logarithms to the base of 2 (log2FC) alongside average expression values (AveExpr). Genes that are upregulated under lipoprotein-deplete conditions have log2FC values in red, whereas downregulated genes are in green. *P*-values were adjusted for multiple comparisons using the Bonferonni-Holm method. B-statistics (B) indicate the log odds that a gene is differentially expressed.

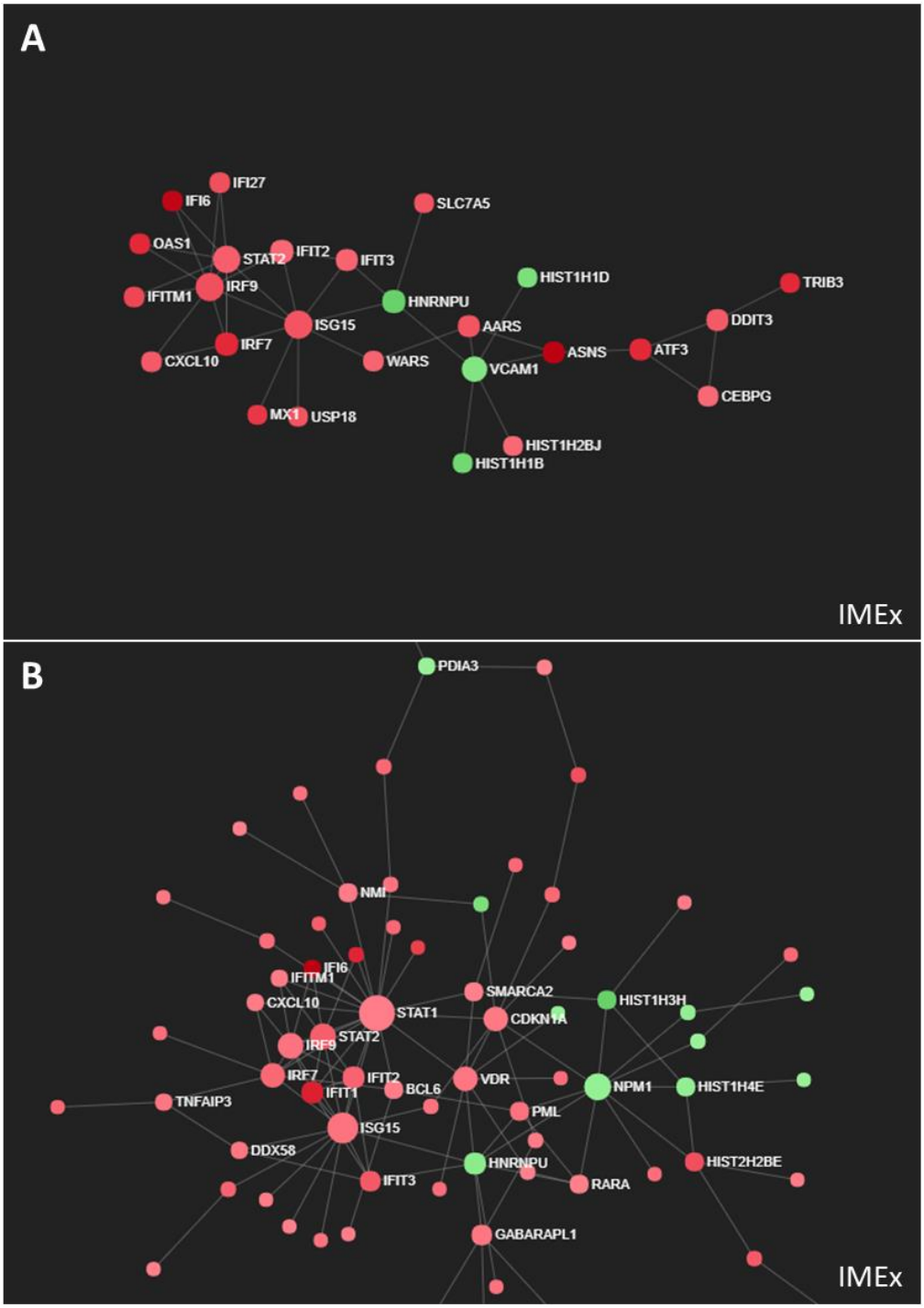

Figure 4.15. Network analysis of differentially expressed genes in KNS42 and SF188 cells cultured under lipoprotein deficient conditions. Genes that are upregulated and downregulated following culture under lipoprotein deficient conditions for 72 hr in KNS42 (A) and SF188 (B) are highlighted in red and green, respectively. The curated database utilised to generate the networks is displayed in the bottom right corner of each panel.

It was particularly evident from the transcriptomics data that upregulation of a cholesterol biosynthetic response was a key feature of pGBM cells under lipoprotein deficient conditions. Examination of the changes in expression of several genes involved in cholesterol regulation, synthesis, export, import and storage (Table 4.5) revealed different responses between the adult U87 and the paediatric KNS42 and SF188 cell lines. pGBM cell lines demonstrated a positive log2 fold change in most genes involved in regulation, synthesis, import and storage of cholesterol under lipoprotein deficient conditions (Figure 4.16). For most genes, a positive log2 fold change was also identified for the U87 cell line but was less in magnitude compared to the pGBM response (Figure 4.16). Interestingly, the negative log2 fold change in ABCA1 was much greater in magnitude in the U87 cell line compared to the pGBM cell lines (Figure 4.16), suggesting that reduced export is the primary mechanism by which U87 cells maintain cholesterol homeostasis under lipoprotein deficient conditions. These results support inherent differences in response to metabolic stress due to lipoprotein deficiency between U87 and pGBM cell lines, which may be a reflection of the different genetic pathologies underlying adult and paediatric GBM.

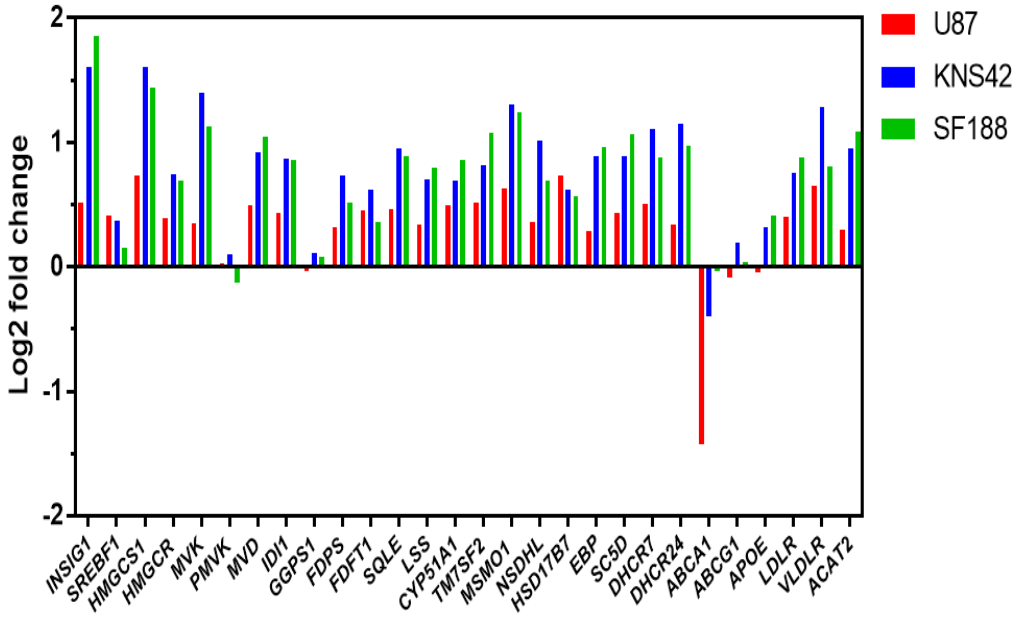

Figure 4.16. Differential expression of cholesterol-related genes under lipoprotein deficient conditions in U87, KNS42 and SF188 cells. Log2 fold changes under lipoprotein deficient conditions of genes involved in cholesterol regulation, synthesis, export, import and storage are displayed for U87 (red), KNS42 (blue) and SF188 (green).

Table 4.5. Statistical analysis of cholesterol-related genes in U87, KNS42 and SF188 cells under lipoprotein deficient conditions

Gene	log2FC			*F*	adj.P.Val	Significance
	U87	KNS42	SF188			
Regulation						
INSIG1	0.519	1.606	1.850	75.145	3.34E-06	****
SREBF1	0.417	0.369	0.158	3.441	0.244454	ns
Synthesis						
HMGCS1	0.731	1.606	1.444	54.104	1.58E-05	****
HMGCR	0.390	0.741	0.697	23.191	0.001054	**
MVK	0.348	1.394	1.131	43.358	3.85E-05	****
PMVK	0.031	0.105	-0.131	0.430	0.904111	ns
MVD	0.493	0.920	1.046	15.620	0.004692	**
IDI1	0.434	0.866	0.859	23.316	0.001054	**
GGPS1	-0.031	0.109	0.077	0.237	0.952797	ns
FDPS	0.318	0.736	0.518	12.283	0.009993	**
FDFT1	0.456	0.616	0.360	14.573	0.005714	**
SQLE	0.462	0.952	0.888	37.873	7.61E-05	****
LSS	0.337	0.704	0.798	16.085	0.00427	**
CYP51A1	0.498	0.694	0.862	30.918	0.000248	***
TM7SF2	0.519	0.814	1.079	14.709	0.005648	**
MSMO1	0.631	1.301	1.243	43.729	3.85E-05	****
NSDHL	0.358	1.011	0.689	21.010	0.001641	**
HSD17B7	0.734	0.620	0.569	8.248	0.037001	*
EBP	0.289	0.891	0.962	22.392	0.001206	**
SC5D	0.437	0.893	1.069	43.746	3.85E-05	****
DHCR7	0.507	1.112	0.875	32.783	0.000188	***
DHCR24	0.340	1.148	0.973	22.194	0.001239	**
Efflux						
ABCA1	-1.427	-0.399	-0.038	14.518	0.005714	**
ABCG1	-0.08855	0.19242	-0.00503	1.008	0.877179	ns
APOE	-0.041	0.324	0.415	3.827	0.204333	ns
Uptake						
LDLR	0.400	0.756	0.884	16.970	0.00373	**
VLDLR	0.654	1.282	0.803	12.039	0.010708	*
Storage						
ACAT2	0.299	0.957	1.082	22.893	0.001111	**

Fold changes between lipoprotein-replete and -deplete conditions are expressed as logarithms to the base of 2 (log2FC). Analysis of variance (ANOVA) using the R package *limma* was performed to determine if the if the log2FC values differ significantly from zero based on the *F* statistic. *P*-values were adjusted for multiple comparisons (adj.P.Val) using the Bonferonni-Holm method. ns = not significant; * = p<0.05; ** = p<0.01; *** = p<0.001; **** = p<0.0001.

4.6. Chapter discussion

Lipoproteins function to deliver lipid and sterol species from the liver to peripheral organs (Tulenko and Sumner, 2002). HDLs are the only class of lipoproteins capable of penetrating the BBB, although a fraction of lipoproteins within the CNS are synthesised by astrocytes and to a lesser extent by neurons. CNS lipoproteins are hypothesised to maintain homeostasis through distribution of lipid and sterol species throughout the brain (Wang and Eckel, 2014). However, the association between apolipoprotein variants and the pathogenesis of Alzheimer's disease implicates other biological roles besides lipid/sterol delivery (Vance and Hayashi, 2010). In cancer, lipoproteins have

been demonstrated to be an essential component of the growth medium for the maintenance of cellular viability of Ras-transformed astrocytes and the U87 cell line (Ríos *et al.*, 2014). We initially identified a different response to lipoprotein deprivation in pGBM cells, characterised by increased cellular viability by the PrestoBlue assay. However, this was deemed artefactual following observations made using the crystal violet assay, which is a triarylmethane dye that can bind to ribose type molecules such as DNA in nuclei and thus give a readout of cell number. The basis of the PrestoBlue assay is the reduction of the active resazurin reagent into resorufin by reductants in viable mitochondria. Therefore, drug treatment or culture under different conditions may influence redox/mitochondrial metabolism but not the rate of proliferation, resulting in incorrect conclusions being drawn from the PrestoBlue assay. Additional components within the DMEM/F-12 basal medium, such as lipoic acid (cofactor for the pyruvate dehydrogenase complex and α-ketoglutarate dehydrogenase), most likely maintained redox/ mitochondrial metabolism in pGBM cells cultured under lipoprotein-deplete conditions, which did not translate into increased cell numbers as determined using the crystal violet assay. Using the same basal medium for both adult and paediatric GBM cells, a greater vulnerability to lipoprotein deprivation was observed in pGBM cells compared to their adult counterpart in both monolayer and spheroid models. Impairment of cellular viability was not observed to be a HGG-specific phenomena, as grade-specific responses were seen with the grade II paediatric Res259 glioma cell line demonstrating resilience to the removal of lipoproteins, whereas a cytostatic response was observed in the grade I paediatric Res186 cell line accompanied with morphological changes reminiscent of elongation. This change in morphology was also identified in U87 cells, and the underlying cause may be due to altered membrane dynamics or induction of epithelial-mesenchymal transition (EMT). Interestingly, growth of U87 cells within spheroids led to a resistant phenotype, which was not seen in the pGBM cell lines. Previous research has demonstrated the differential effects of culturing cells in spheroid format on metabolism (Smith *et al.*, 2012). These results highlight the importance of lipoproteins to the maintenance of

GBM cell line growth, particularly within paediatric models. The importance of lipoproteins within an *in vivo* setting has indirectly been demonstrated through inhibition of lipoprotein uptake using LXR agonists (Villa *et al.*, 2016).

The findings from monolayer and spheroid experiments indicated that the removal of lipoproteins is cytostatic. Flow cytometric analysis revealed a significant increase in the percentage of pGBM cells in S phase. Combined with the reduced growth rates, this alluded to the induction of S phase arrest, a phenomenon previously observed in response to nucleoside analogues (Shi *et al.*, 2001). U87 cells demonstrated an unaltered profile due to minimal viability differences at this timepoint. Since major differences in viability were only observed from day 3 onwards, we hypothesised that any transcriptomic response underlying the phenotypic changes following lipoprotein deprivation would be secondary or tertiary in nature. Transcriptomics was therefore applied to cells deprived of lipoproteins for 3 days. The data analysis hinted at stress induction with several genes implicated in ER stress and autophagy. ATF4, a key mediator of the ER stress response, was upregulated in KNS42 cells but was only significant when the *p*-value was unadjusted for multiple comparisons. It is possible that significant induction of such keys drivers of stress responses occurred within 24 hours of the induction of stress and that turnover of the transcripts reduced significance at day 3. Interestingly, the U87 cell line demonstrated upregulation of several genes associated with a hypoxic response, whereas pGBM cell lines demonstrated transcriptomic signatures associated with inflammatory signalling and cholesterol biosynthesis. Both pGBM cell lines demonstrated a stark induction of genes associated with cholesterol homeostasis in comparison to the U87 cell line, which may highlight a pGBM-specific tumour biology for further study using patient tissue. It is unclear as to why a hypoxic response was initiated considering that U87 cells were cultured in normoxia. However, it is possible that increased ROS production due to metabolic stress led to the stabilisation and activity of HIFα, hypotheses that can be tested through measurement of protein levels and cellular localisation via Western blotting and confocal microscopy, respectively.

Changes in membrane lipid composition can lead to the induction of ER stress and the unfolded protein response (UPR) (Volmer and Ron, 2015). The induction of cholesterol synthetic genes under lipoprotein-derived conditions implicates reduced cholesterol levels. Cholesterol is required in the ER membrane to maintain the lateral mobility of transmembrane proteins, and its depletion is correlated with impaired ER-to-Golgi transport and ultimately protein section (Ridsdale *et al.*, 2006). Low cholesterol levels in the ER membrane may therefore initiate an ER stress response, a hypothesis that could be tested by examining ER ultrastructure under lipoprotein deficient conditions in the presence or absence of exogenous cholesterol. Cholesterol depletion may also account for the inflammatory responses observed in the pGBM cell lines since limiting cholesterol synthesis induces a type I IFN response. Network analysis highlighted the centrality of STAT2 and IRF9 within both KNS42 and SF188 cell lines deprived of lipoproteins. IFN-β increases STAT2 and IRF9 expression which drive IL-6 expression via NFκB (Nan *et al.*, 2018), which is also involved in mediating ER stress-driven inflammatory responses. Significant upregulation of IL-6 was observed in KNS42 and SF188 cells under lipoprotein deficient conditions, but this was only significant when unadjusted for multiple comparisons in the KNS42 cell line. Prolonged activation of IRF9 in complex with STATs 1 and 2 following continuous exposure to low-level IFN-β mediates resistance to DNA damage (Cheon *et al.*, 2013).

The transcriptomics data showed few significant responses from genes associated with lipid or cholesterol metabolism. Decreased expression of *ABCA1* in U87 cells hinted at cellular responses due to low sterol levels. Although increased expression of cholesterol related genes, including *SREBF1*, *INSIG1*, *INSIG2*, *STARD4*, *MVD*, *SQLE*, *LRP1*, and *VLDLR*, was observed in U87 cells, *p*-values were not significant following adjustment for multiple comparisons. In contrast, several of these genes were significantly upregulated in pGBM cells, implicating dysregulated cholesterol metabolism due to deprivation of lipoproteins as a paediatric biology-specific phenomenon. This was met by upregulation of *VLDLR* and/or *LDLR* to increase lipoprotein uptake.

Surprisingly, addition of exogenous cholesterol could not rescue the growth defect, indicating other roles provided for by lipoproteins. There is evidence to suggest that HDLs function as mitogens. Using a fibroblast model, Angius and colleagues demonstrated that cell transition from G0 to G1/S required HDL uptake to increase cholesterol ester levels, with a concomitant increase in pAKT via SR-BI (Angius *et al.*, 2015). This may provide some explanation as to the cytostatic observations following lipoprotein deprivation. Indeed, supplementation of lipoprotein deficient medium with HDL rescued the growth of transformed astrocytes (Ríos *et al.*, 2014). HDLs are similar in saturated lipid, cholesterol and sphingolipid composition to lipid rafts, with lipid exchange occurring between lipid rafts and HDLs (Sorci-Thomas *et al.*, 2012). Therefore, future studies could examine lipid raft dynamics that may be adversely affected by deprivation of lipoproteins, with implications on raft-localised signalling proteins.

Chapter 5

Determining the metabolic changes associated with growth under lipoprotein deficient conditions in adult and paediatric GBM cells

5. Determining the metabolic changes associated with growth under lipoprotein deficient conditions in adult and paediatric GBM cells

In the previous chapter, adult and paediatric GBM cells were shown to exhibit a similar dependency on lipoproteins for the maintenance of cellular viability and proliferation. Lipoproteins consist of several cholesterol and lipid species, including triglycerides and phospholipids (Wasan *et al.*, 2008). Cholesterol and lipids are important components of the plasma membrane and must accumulate in biomass to enable cell division (Simons and Toomre, 2000). Lipids are also utilised as substrates to produce energy through β-oxidation or as building blocks in the generation of secondary signalling molecules (Currie *et al.*, 2013). We therefore hypothesised that depriving GBM cells of lipoproteins would alter the lipidome and allow the identification of lipid species whose abundance is highly dependent upon lipoprotein uptake. Since several metabolites associated with carbon metabolism feed into the lipid synthesis pathway, we envisaged a compensatory response in several metabolic pathways to maintain a lipogenic phenotype, a feature highly characteristic of the latter malignant stages of tumour progression (Menendez and Lupu, 2007). In this endeavour, we utilised LC-MS as an analytical technique to profile both polar (metabolites) and non-polar (lipid) compounds from adult and paediatric glioma cells cultured under lipoprotein-replete or -deplete conditions.

5.1. Optimisation of cell numbers and metabolite extraction methods for LC-MS sample generation

Six glioma cell lines were chosen to study lipoprotein dependence across age group as well as tumour grade: U87 (adult grade IV), KNS42 (paediatric grade IV), SF188 (paediatric grade IV), UW479 (paediatric grade III), Res259 (paediatric grade II), and Res186 (paediatric grade I). All cell lines under review were cultured in the same medium consisting of 1 g/L glucose DMEM with 10% FBS, P/S, and NEAAs representing normal medium (NM). Growth under lipoprotein-deplete conditions was mediated through replacement of the FBS

component in NM with lipoprotein-deficient calf serum (LPDM). Based on the cellular viability assays discussed previously, a 72 hr timepoint was chosen for the metabolomics and lipidomics analysis since *in vitro* phenotypic alterations manifested at or after this timepoint under lipoprotein deficient conditions. Simultaneous extraction of both polar metabolites and non-polar lipids through a bi-phasic extraction procedure was conducted to enable combined metabolomics and lipidomics analyses. The metabolite extraction procedure was optimised using the U87 cell line grown in T25 flasks to compare two different methods: 1) methanol extraction and 2) bi-phasic extraction using a 1:3:1 ratio of methanol:chloroform:water. 154 metabolites with putative identifications were commonly identified between the two extraction procedures, which was lower than the expected number of approximately 700 metabolites, typically identified using LC-MS. This was attributed to there being too few cells in a T25 flask from which metabolites were extracted. An arbitrary fold change threshold of 0.8 was chosen to compare the extraction efficiencies of the two extraction procedures. Out of the 154 metabolites, 123 metabolites demonstrated a fold change ≥0.8 when comparing the bi-phasic to the methanol extraction procedure. Several metabolites demonstrated higher peak intensities following bi-phasic extraction compared to methanol alone, perhaps reflecting increased cell lysis due to the addition of chloroform (Table 5.1). To improve the strength of the LC-MS signal, we increased the number of cells being extracted from by using petri dishes and T75 flasks and included a drying step to concentrate the metabolites. Analysis of the peak intensity signal from a T75 flask (1.06E8) and two petri dishes combined (1.12E8) indicated that the number of cells from a T75 flask was sufficient to generate a strong LC-MS signal for metabolomics and lipidomics analysis with the incorporation of a drying step into the biphasic extraction procedure.

Table 5.1. Metabolite peak intensities and fold change differences between two metabolite extraction protocols.

Putative metabolite	MeOH extraction	Bi-phasic extraction	Fold change (Bi:MeOH)
[FA methyl(6:0)] 2-methyl-hexanoic acid	2657	128870	48.49
Butanal	2442	83555	34.22
[FA (10:1/2:0)] 2E-Decenedioic acid	2444	56210	23.00
[FA hydroxy(9:0)] 2-hydroxy-nonanoic acid	928	12410	13.38
2,5-Dioxopentanoate	6367	75050	11.79
N4-(Acetyl-beta-D-glucosaminyl)asparagine	6855	1587	0.23
Octadecanamide	51249	10847	0.21
Linoleate	13642	2451	0.18
(L-Seryl)adenylate	18624	2181	0.12
di-n-Undecylamine	607623	22290	0.04

Ten representative metabolites with putative identifications are displayed derived from methanol (MeOH) or bi-phasic (methanol:chloroform:water) extraction of cellular metabolites. Fold changes represent the ratio of peak intensities between the bi-phasic and MeOH extraction procedures (Bi:MeOH).

5.2. Determination of doubling times under lipoprotein-replete and -deplete conditions

A preliminary experiment examining the metabolome of the U87 cell line under lipoprotein-replete and –deplete conditions was performed using n=3 replicates. This experiment highlighted issues associated with different growth rates under the two experimental conditions. As growth rate was reduced under lipoprotein-deficient conditions, seeding the same number of cells at 0 hr led to different numbers of cells at the 72 hr timepoint. Therefore, to examine the same number of cells at the 72 hr timepoint, we measured the doubling time of each cell line under the two experimental conditions using the exponential growth equation to calculate doubling times and *k* values (Table 5.2). This had the added benefit of preventing the need for an extensive normalisation procedure to account for differing cell numbers.

Table 5.2. Doubling times of adult and paediatric glioma cells under lipoprotein-replete and -deplete conditions

Parameter	U87		KNS42		SF188		UW479		Res259		Res186	
	NM	LPDM	NM	LPDM	NM	LPDM	NM	LPDM	NM	LPDM	NM	LPDM
k	0.0214	0.0129	0.0136	0.0096	0.0230	0.0110	0.0201	0.0159	0.0274	0.0138	0.0271	0.0173
DT (hr)	32.38	53.75	51.16	72.29	30.09	63.09	34.56	43.64	25.28	50.34	25.57	40.19

The parameter *k* represents the rate constant in the growth equation $N = N_0 \times e^{kt}$, where *N* is the number of cells at *t* time (hr) after the start of an experiment seeded with N_0 cells. The doubling time DT is calculated as $\ln(2)/k$.

5.3. Metabolomics of adult and paediatric GBM cells cultured under lipoprotein-replete and -deplete conditions

Following the optimisation of cell numbers and metabolite extraction procedures, the metabolomic profiles of all six cell lines cultured under lipoprotein-replete or -deplete conditions was assessed through LC-MS-based metabolite profiling. A total of 604 human metabolites with putative identifications were obtained from the LC-MS analysis of cellular metabolites, referred to as the 'metabolomic fingerprint'. Analysis of culture medium components to determine changes in nutrient levels following metabolite exchange between cells and the microenvironment was also conducted. This is referred to as the 'metabolomic footprint', of which 150 human metabolites were identified putatively. The data was mined for canonical metabolites within classic well characterised metabolic pathways, including glycolysis and the TCA cycle. Growth under lipoprotein-deprived conditions resulted in cell-specific glycolytic responses generally characterised by reduced glycolytic intermediates (Figure 5.1), indicative of increased metabolic flux. In U87 and Res186 cells, this was associated with increased lactate levels (Figure 5.1A and F), perhaps reflecting an amplified Warburg effect. Interestingly, the pGBM KNS42 cell line demonstrated minimal changes to early glycolytic intermediates that was not observed for the other pGBM cell line, SF188 (Figure 5.1B and C). Several paediatric glioma cell lines demonstrated reduced pyruvate levels, reaching significance in the KNS42, SF188, Res259, and Res186 cell lines (Table 5.3). Reduced levels of pyruvate likely indicate increased shuttling of this metabolite into the TCA cycle to maintain energy production as well as supply carbon units for lipid synthesis, as hypothesised under lipoprotein deficient conditions.

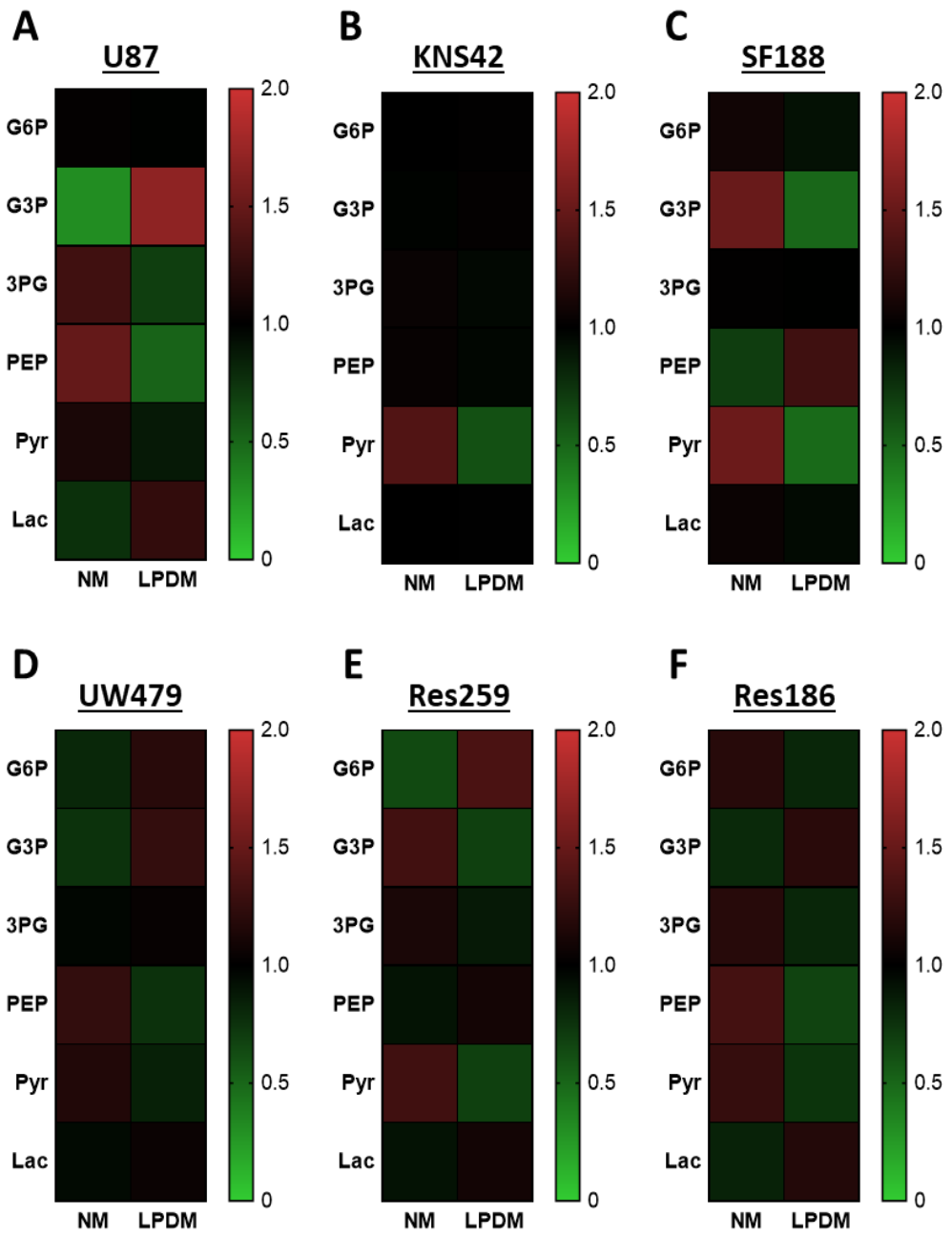

Figure 5.1. Heatmap representation of glycolysis metabolites under lipoprotein-replete or -deplete conditions. (A-F) Mean peak intensities for glycolysis metabolites identified from six glioma cell lines cultured under lipoprotein-replete (NM) or -deplete (LPDM) conditions were centred using the grand mean. Scale bars depict the grading of colours for fold changes ranging between 0 and 2. Abbreviations: G6P – glucose 6-phosphate; G3P – glyceraldehyde 3-phosphate; 3PG – 3-phospho-glycerate; PEP – phosphoenolpyruvate; Pyr – pyruvate; Lac – lactate.

Table 5.3. Fold change differences for metabolites within the glycolysis pathway and tricarboxylic acid cycle under lipoprotein-replete relative to lipoprotein-deplete conditions.

Metabolite	ID confidence	U87		KNS42		SF188		UW479		Res259		Res186	
		log2FC	FDR	log2FC	FDR	log2FC	FDR	log2FC	FDR	log2FC	FDR	log2FC	FDR
Glycolysis													
D-Glucose 6-phosphate	10	-0.04	9.20E-01	0.01	9.99E-01	-0.24	4.83E-01	0.57	4.66E-01	**1.08**	**6.03E-03**	-0.55	9.98E-02
D-Glyceraldehyde 3-phosphate	8	**2.45**	**2.12E-05**	0.06	9.95E-01	-1.60	5.22E-02	**0.72**	**1.69E-02**	-0.94	1.41E-01	0.59	9.98E-02
3-Phospho-D-glycerate	8	-0.92	8.53E-02	-0.12	8.93E-01	-0.01	4.94E-01	0.09	9.48E-01	-0.36	4.08E-01	-0.55	2.16E-01
Phosphoenolpyruvate	8	**-1.53**	**2.06E-02**	-0.09	9.97E-01	0.90	2.16E-01	-0.71	1.78E-01	0.28	7.16E-01	-0.99	9.30E-02
Pyruvate	8	-0.36	3.28E-01	**-1.20**	**2.00E-02**	**-1.66**	**5.10E-03**	-0.46	1.24E-01	**-0.93**	**1.17E-02**	**-0.76**	**1.87E-02**
Lactate	10	0.70	7.73E-02	0.01	9.91E-01	-0.15	6.45E-01	0.14	9.00E-01	0.26	5.13E-01	0.49	7.60E-02
Tricarboxylic acid cycle													
Citrate	8	0.50	8.52E-02	**0.35**	**3.62E-02**	0.38	5.82E-02	0.47	7.05E-02	0.20	2.91E-01	0.08	6.67E-01
Succinate	10	**-1.63**	**6.11E-05**	**-0.79**	**1.58E-02**	0.20	1.11E-01	**-0.79**	**9.47E-03**	**-0.40**	**4.95E-02**	**-2.16**	**3.02E-07**
Malate	10	-0.10	6.78E-01	**-0.34**	**2.56E-02**	**-0.66**	**2.43E-04**	-0.49	1.92E-01	-0.04	8.69E-01	-0.30	7.89E-02
Energetics													
ADP	10	0.21	7.36E-01	0.24	7.33E-01	0.12	7.58E-01	0.22	8.62E-01	0.30	7.98E-01	-0.26	6.17E-01
ATP	8	**0.80**	**4.17E-02**	-0.05	9.72E-01	0.38	4.14E-01	0.43	4.12E-01	0.20	5.64E-01	-0.24	5.20E-01
Creatine	10	**-1.38**	**5.27E-03**	**-0.84**	**1.09E-03**	**-1.13**	**1.05E-05**	**-2.60**	**3.67E-04**	**-1.41**	**5.64E-05**	**-1.59**	**3.02E-07**
Creatinine	10	**-3.42**	**1.40E-04**	**-2.63**	**8.45E-05**	**-2.97**	**9.10E-06**	**-4.71**	**4.97E-05**	**-3.68**	**5.54E-07**	**-2.85**	**1.50E-06**
NAD+	8	0.57	3.22E-01	0.17	6.44E-01	0.28	1.92E-01	0.18	5.61E-01	0.40	1.67E-01	0.31	2.69E-01
NADH	8	-0.04	9.98E-01	-0.28	2.84E-01	-0.28	5.32E-02	0.14	5.35E-01	0.23	4.79E-01	0.44	7.89E-02
NADPH	8	0.21	7.25E-01	-0.05	8.45E-01	-0.30	5.29E-01	0.50	5.43E-01	0.22	5.56E-01	0.10	7.72E-01

Metabolites highlighted in red showed RSD values >30% in QC samples. Fold change differences are given to the base of 2 (log2FC) where green and red represent significantly reduced or elevated metabolite levels under lipoprotein-deplete conditions relative to lipoprotein-replete. Statistical evaluation was performed using a *t* test and *p*-values were corrected for multiple comparisons using the false discovery rate (FDR). Abbreviations: ADP – adenine diphosphate; ATP – adenine triphosphate; NAD(P)+ – nicotinamide adenine dinucleotide (phosphate); NAD(P)H – reduced NAD+/NADP+.

Analysis of TCA cycle metabolites provided evidence of dysregulated mitochondrial metabolism following significantly reduced succinate levels in all cell lines barring SF188 (Figure 5.2 and 5.3). However, lipoprotein-deprived SF188 cells demonstrated significantly reduced malate levels as was also observed for KNS42 cells (Figure 5.2), consistent with the incomplete shuttling of carbon atoms around the TCA cycle. In all cell lines, citrate levels showed an increasing trend, reaching significance in KNS42 cells (Figure 5.2 and 5.3). As summarised in Table 5.3, a prevailing picture emerged of reduced TCA cycle flux possibly in association with shuttling of citrate carbon into lipid synthesis pathways. Reductive carboxylation of glutamine is a means by which cells with dysfunctional mitochondria or under hypoxic stress can generate lipids for normal cellular function (Metallo *et al.*, 2011; Mullen *et al.*, 2011). Surprisingly, significantly increased instead of decreased levels of glutamine were observed in KNS42 and SF188 cells, which was associated with higher levels of glutamate in the SF188 cell line (Figure 5.2). Glutamine and glutamate levels were largely unchanged in the other cells lines (Figure 5.2 and 5.3), indicating that glutamine was not used as a TCA anapleurotic or anabolic substrate within the experimental conditions.

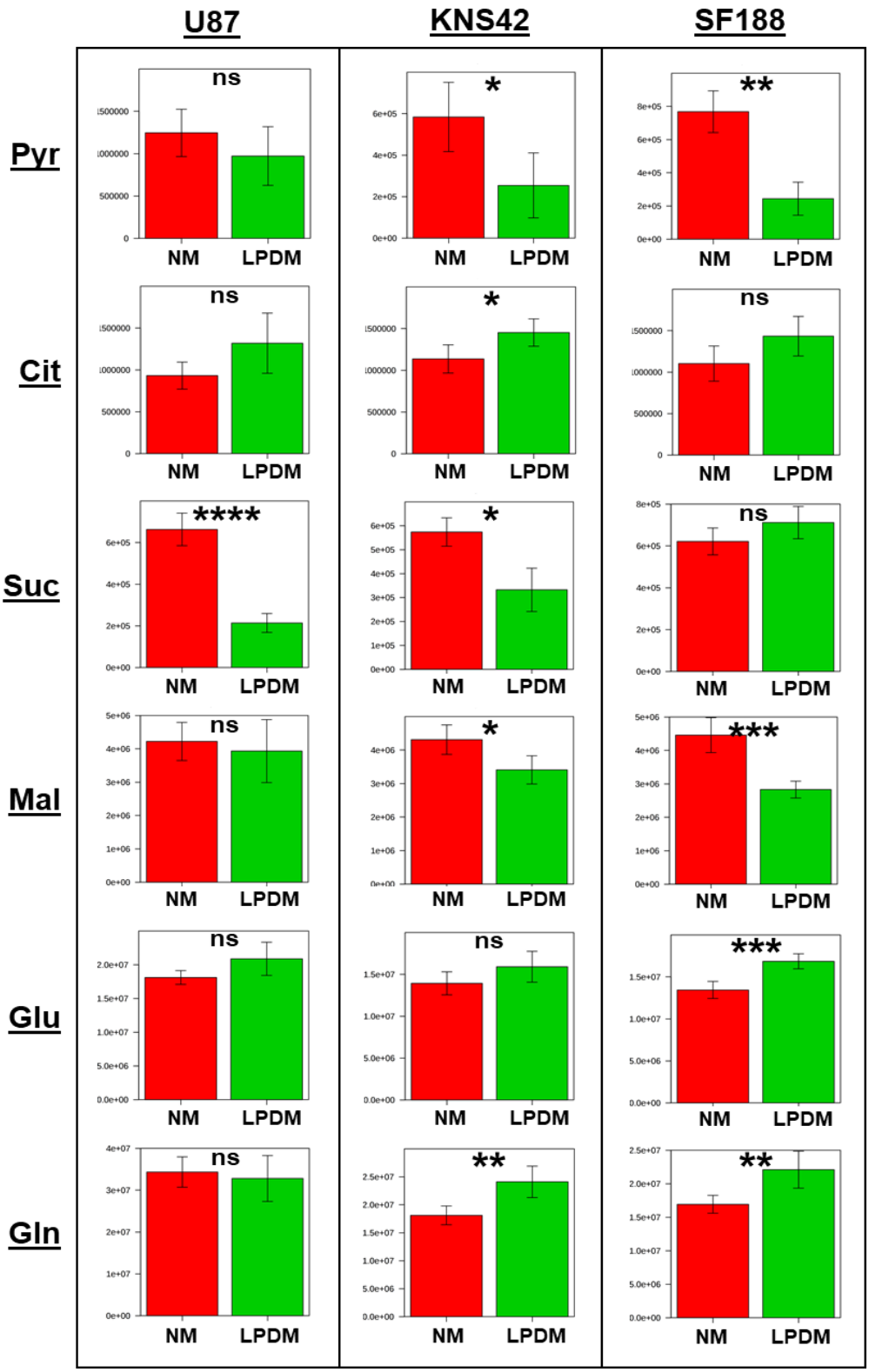

Figure 5.2. Peak intensities of tricarboxylic acid cycle-related metabolites in U87, KNS42 and SF188 cultured under lipoprotein-replete or -deplete conditions. Mean peak intensities are displayed for TCA cycle-related metabolites under lipoprotein-replete (NM; red) or -deplete (LPDM; green) conditions Abbreviations: Pyr – pyruvate; Cit – citrate; Suc – succinate; Mal – malate; Glu – glutamate; Gln – glutamine. Statistical evaluation was performed using a two-sample *t*-test: ns = not significant; * = $p<0.05$; ** = $p<0.01$; *** = $p<0.001$; **** = $p<0.0001$.

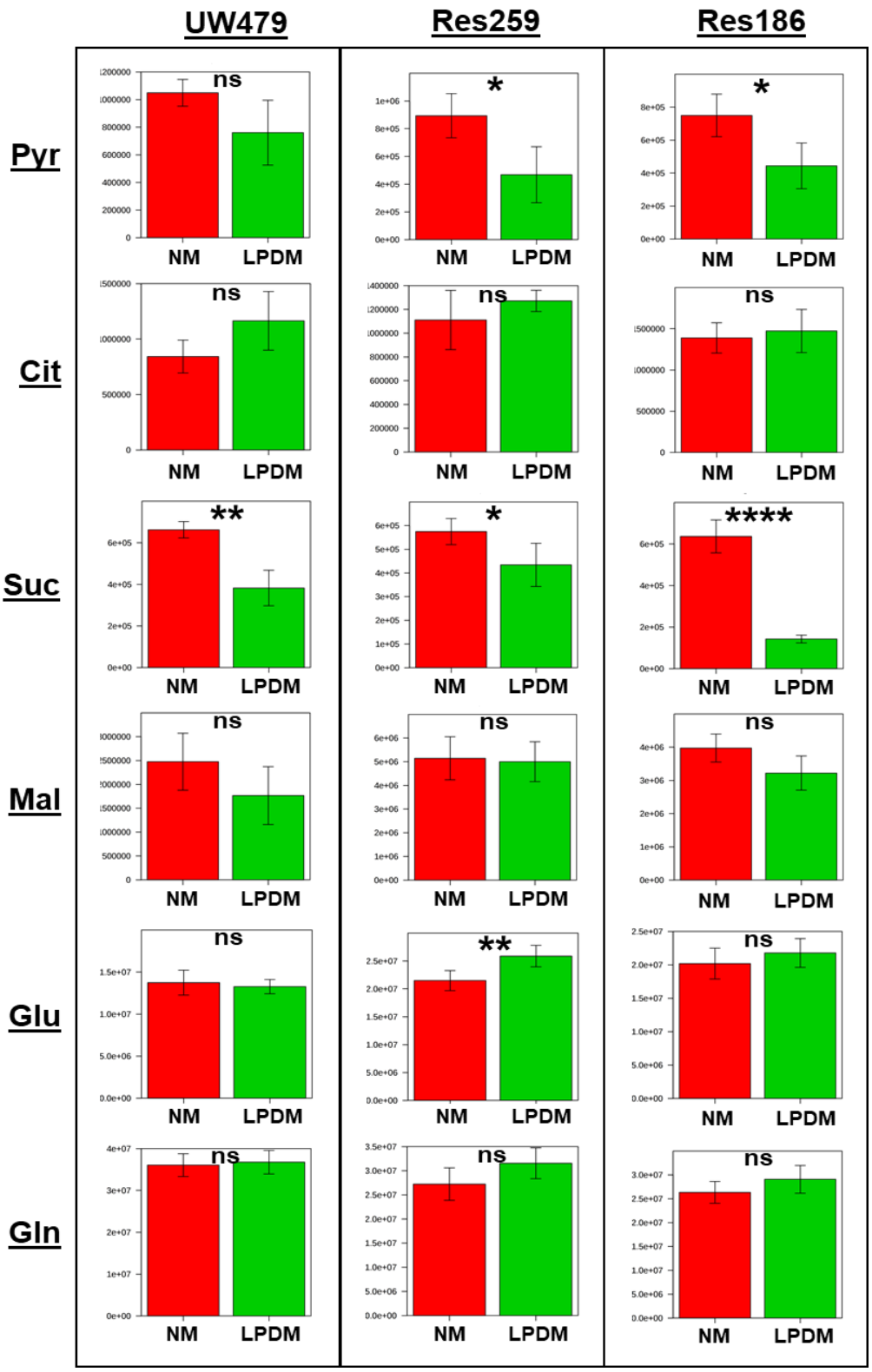

Figure 5.3. Peak intensities of tricarboxylic acid cycle-related metabolites in UW479, Res259 and Res186 cultured under lipoprotein-replete or -deplete conditions. Mean peak intensities are displayed for TCA cycle-related metabolites under lipoprotein-replete (NM; red) or -deplete (LPDM; green) conditions Abbreviations: Pyr – pyruvate; Cit – citrate; Suc – succinate; Mal – malate; Glu – glutamate; Gln – glutamine. Statistical evaluation was performed using a two-sample *t*-test: ns = not significant; * = $p<0.05$; ** = $p<0.01$; *** = $p<0.001$; **** = $p<0.0001$.

The analysis above indicated that growth under lipoprotein deficient conditions resulted in increased glycolysis and decreased flux within the TCA cycle. Given that ATP is produced in the biosynthesis of succinate and reduced FAD is generated in the conversion of succinate to fumarate for utilisation in oxidative phosphorylation, we hypothesised that energetic substrates would be altered under lipoprotein deficient conditions. However, levels of ADP and ATP were largely unchanged in all cells lines (Figure 5.4), apart from a significant increase in ATP levels in U87 cells in line with evidence of increased glycolysis (Table 5.3). Interestingly, although we concluded the possibility of increased lipid synthesis based on reduced TCA flux and increased citrate levels, the levels of the essential cofactor in lipid synthesis, NADPH, were not significantly altered under lipoprotein deficient conditions (Table 5.3). This was also the case for NAD and NADH which are essential reducing equivalents in several metabolic pathways (Table 5.3). As summarised in Figure 5.4, these results indicate that energetics is largely unaffected by the removal of lipoproteins from the growth medium.

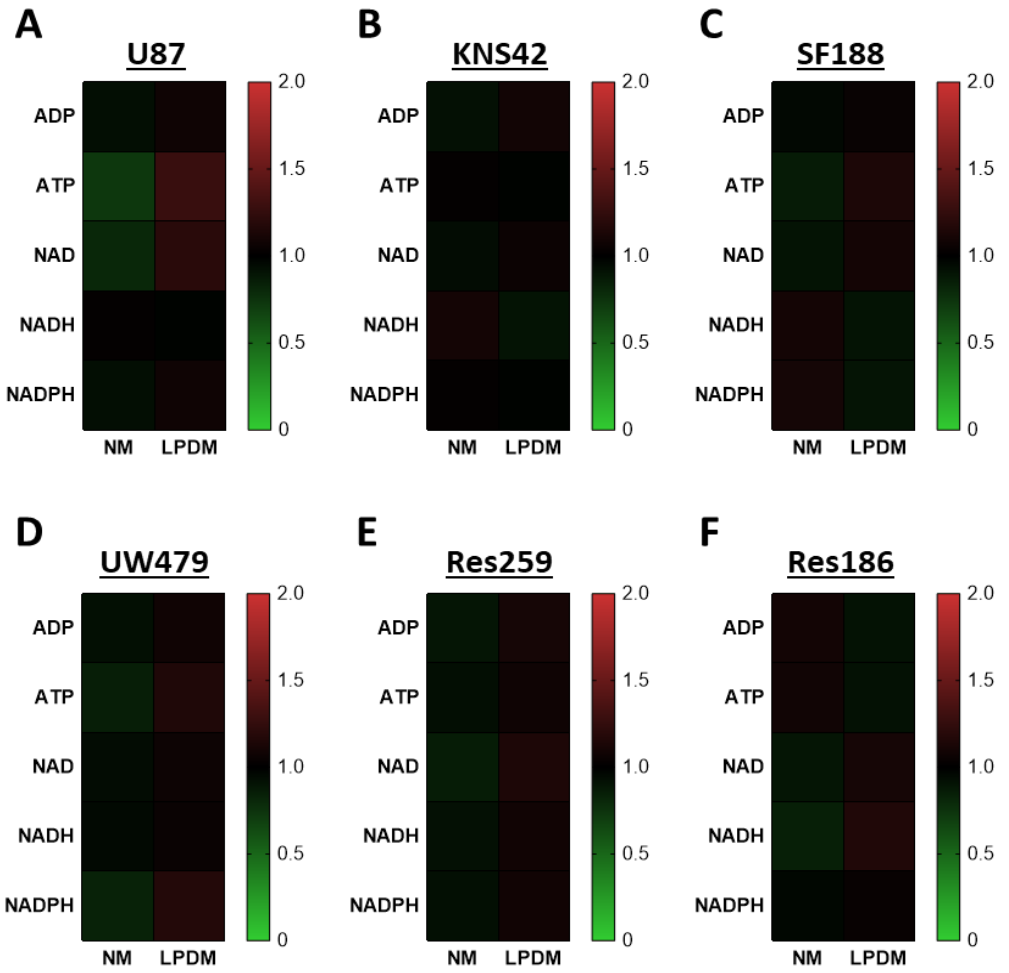

Figure 5.4. Heatmap representation of energetic metabolites under lipoprotein-replete or -deplete conditions. (A-F) Mean peak intensities for energetic metabolites identified from six glioma cell lines cultured under lipoprotein-replete (NM) or -deplete (LPDM) conditions were centred using the grand mean. Scale bars depict the grading of colours for fold changes ranging between 0 and 2. Abbreviations: ADP – adenine diphosphate; ATP – adenine triphosphate; NAD(P)+ – nicotinamide adenine dinucleotide (phosphate); NAD(P)H – reduced NAD+/NADP+.

The culture of adult and paediatric glioma cells under lipoprotein deficient conditions caused minimal changes to amino acid metabolism, as summarised in Table 5.4. Although several amino acids demonstrated a significant change within cell lines, fold changes were not consistent with a marked metabolic response following lipoprotein deprivation. Exceptions to this included serine, glycine, and alanine (Table 5.4). Serine and glycine are important metabolites for growth (Jain *et al.*, 2012; Labuschagne *et al.*, 2014). Although significantly reduced serine levels were observed within the fingerprint of all cell lines

(Figure 5.5A, B and C; Figure 5.6A, B and C), this is likely attributed to the significantly lower serine component within LPDM compared to NM (Figure 5.5D and Figure 5.6D). In contrast, there was a general increase in fingerprint glycine levels that was significant in SF188, UW479 and Res259, which was not due to different levels between NM and LPDM (Figure 5.7and Figure 5.8). Fingerprint alanine levels were significantly reduced in LPDM compared to NM in all cell lines, with the exception of the U87 cell line (Figure 5.9 and Figure 5.10). This could be attributed to significantly lower levels of alanine in LPDM compared to NM (Figure 5.9D and Figure 5.10D). It is interesting to note the highly significant release of alanine from U87, KNS42, SF188 and Res186 cells deprived of external lipoproteins to the extent that there are non-significant differences between footprints in NM and LPDM, despite lower levels in LDPM compared to NM to begin with (Figure 5.9D and Figure 5.10D). We hypothesise that the increased alanine release is due to increased synthesis via alanine transaminase, which converts pyruvate and glutamine into αKG and alanine, thus potentially contributing to TCA anapleurosis. Alternatively, lipoprotein starvation may induce autophagy to obtain amino acids from protein catabolism for use as energetic substrates, with release of alanine as a byproduct. However, it must be stressed that the observations made for alanine within the footprint and medium controls are to be interpreted with caution since alanine obtained a very low identification confidence score (Table 5.5). Serine and glycine both feed into the methionine cycle which is directly associated with glutathione synthesis. Within this pathway, only cystathionine demonstrated a significant reduction in U87, KNS42, SF188, and Res186 cells (Table 5.6). Reduced glutathione levels were not significantly lower in LPDM compared to NM, indicating that acute lipoprotein-deprivation does not induce stress associated with increased ROS production, within the context of this experiment.

Table 5.4. Fold change differences for amino acid metabolites under lipoprotein-replete relative to lipoprotein-deplete conditions.

Metabolite	ID confidence	U87		KNS42		SF188		UW479		Res259		Res186	
		log2FC	FDR	log2FC	FDR	log2FC	FDR	log2FC	FDR	log2FC	FDR	log2FC	FDR
Essential amino acids													
L-Histidine	10	0.11	4.60E-01	0.28	5.01E-02	**0.44**	**2.72E-03**	0.12	1.07E-01	**0.31**	**1.51E-02**	**0.38**	**8.72E-03**
L-Isoleucine	10	0.13	1.15E-01	0.11	2.56E-01	**0.31**	**1.89E-03**	0.03	6.81E-01	**0.26**	**2.36E-02**	0.26	1.29E-01
L-Lysine	8	0.27	4.42E-01	0.14	8.04E-01	0.23	5.22E-01	-0.19	5.61E-01	0.17	4.80E-01	0.18	5.13E-01
L-Methionine	10	0.08	1.88E-01	0.13	1.25E-01	**0.31**	**8.67E-05**	-0.09	4.61E-01	**0.40**	**2.36E-03**	0.29	9.07E-01
L-Threonine	10	**0.21**	**3.47E-02**	**0.28**	**5.71E-04**	**0.24**	**1.14E-03**	-0.11	2.47E-01	**0.40**	**1.08E-05**	0.11	3.92E-01
L-Tryptophan	10	0.16	2.03E-01	**0.23**	**1.20E-02**	**0.36**	**2.13E-04**	-0.07	6.37E-01	**0.50**	**6.69E-04**	0.38	1.72E-01
L-Valine	8	0.06	5.87E-01	0.18	7.20E-02	**0.33**	**9.60E-04**	-0.02	8.01E-01	**0.25**	**2.18E-02**	0.19	2.69E-01
Conditional amino acids													
L-Arginine	10	-0.03	9.20E-01	-0.09	6.40E-01	0.18	3.47E-01	-0.15	4.68E-01	-0.08	6.21E-01	0.11	4.26E-01
L-Cysteine	8	-0.16	8.82E-01	0.70	1.67E-01	0.42	3.37E-01	-0.80	2.85E-01	0.27	6.59E-01	0.04	6.63E-01
L-Glutamine	10	-0.07	7.31E-01	**0.41**	**6.39E-03**	**0.38**	**7.99E-03**	0.03	8.39E-01	0.21	1.03E-01	0.14	2.25E-01
L-Tyrosine	10	**0.28**	**3.15E-02**	**0.45**	**1.00E-03**	**0.62**	**1.33E-04**	0.04	7.69E-01	**0.70**	**4.99E-05**	**0.49**	**2.35E-02**
Glycine	10	0.40	7.84E-02	0.36	9.47E-02	**0.84**	**9.84E-04**	**0.35**	**8.89E-03**	**0.60**	**1.15E-03**	0.25	1.72E-01
L-Proline	10	**0.29**	**2.89E-02**	0.21	6.99E-02	**0.48**	**7.22E-04**	-0.06	3.24E-01	**0.28**	**3.54E-03**	0.34	2.31E-01
L-Serine	10	**-0.54**	**1.12E-02**	**-0.53**	**3.48E-04**	**-0.55**	**1.46E-03**	**-0.82**	**2.08E-05**	**-0.56**	**1.95E-03**	**-0.82**	**1.09E-04**
Non-essential amino acids													
L-Alanine	8	-0.37	9.35E-02	**-0.73**	**4.16E-04**	**-0.76**	**2.10E-05**	**-0.93**	**2.37E-03**	**-0.34**	**1.07E-02**	**-1.46**	**3.65E-06**
L-Asparagine	10	-0.14	1.65E-01	**0.42**	**6.84E-03**	**0.72**	**4.14E-04**	-0.02	8.39E-01	**0.45**	**1.11E-02**	-0.03	7.72E-01
L-Aspartate	10	-0.12	3.44E-01	0.25	1.65E-01	0.22	5.32E-02	-0.18	2.05E-01	**0.39**	**3.67E-02**	**-0.48**	**3.65E-03**
L-Glutamate	10	0.21	8.98E-02	0.19	1.64E-01	**0.33**	**8.38E-04**	-0.05	7.69E-01	**0.27**	**9.74E-03**	0.11	4.24E-01

Fold change differences are given to the base of 2 (log2FC) where green and red represent significantly reduced or elevated metabolite levels under lipoprotein-deplete conditions relative to lipoprotein-replete. Statistical evaluation was performed using a *t* test and *p*-values were corrected for multiple comparisons using the false discovery rate (FDR).

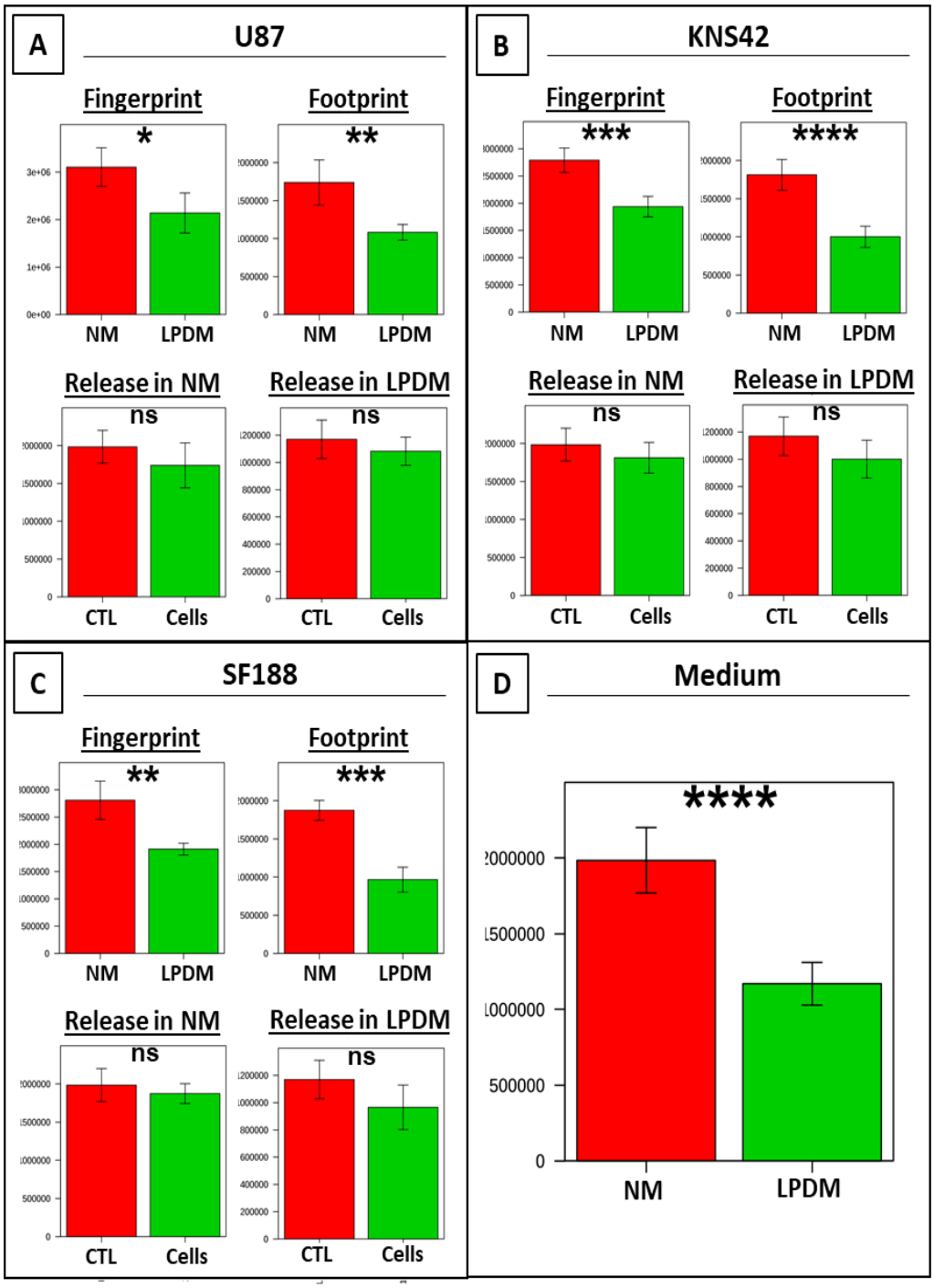

Figure 5.5. Peak intensities of serine in U87, KNS42 and SF188 cells cultured under lipoprotein-replete or -deplete conditions. Peak intensities for serine are displayed following extraction from (A) U87, (B) KNS42 and (C) SF188 cells (fingerprint; top left in each panel) or cultured medium (footprint; top right in each panel) under lipoprotein-replete (red) or -deplete (green) conditions. Comparisons between either NM or LPDM in the presence or absence (CTL) of cells are included (bottom left and bottom right in each panel, respectively). Serine levels within NM and LPDM in the absence of cells are compared in (D). Statistical evaluation was performed using a two-sample *t*-test: ns = not significant; * = $p<0.05$; ** = $p<0.01$; *** = $p<0.001$; **** = $p<0.0001$.

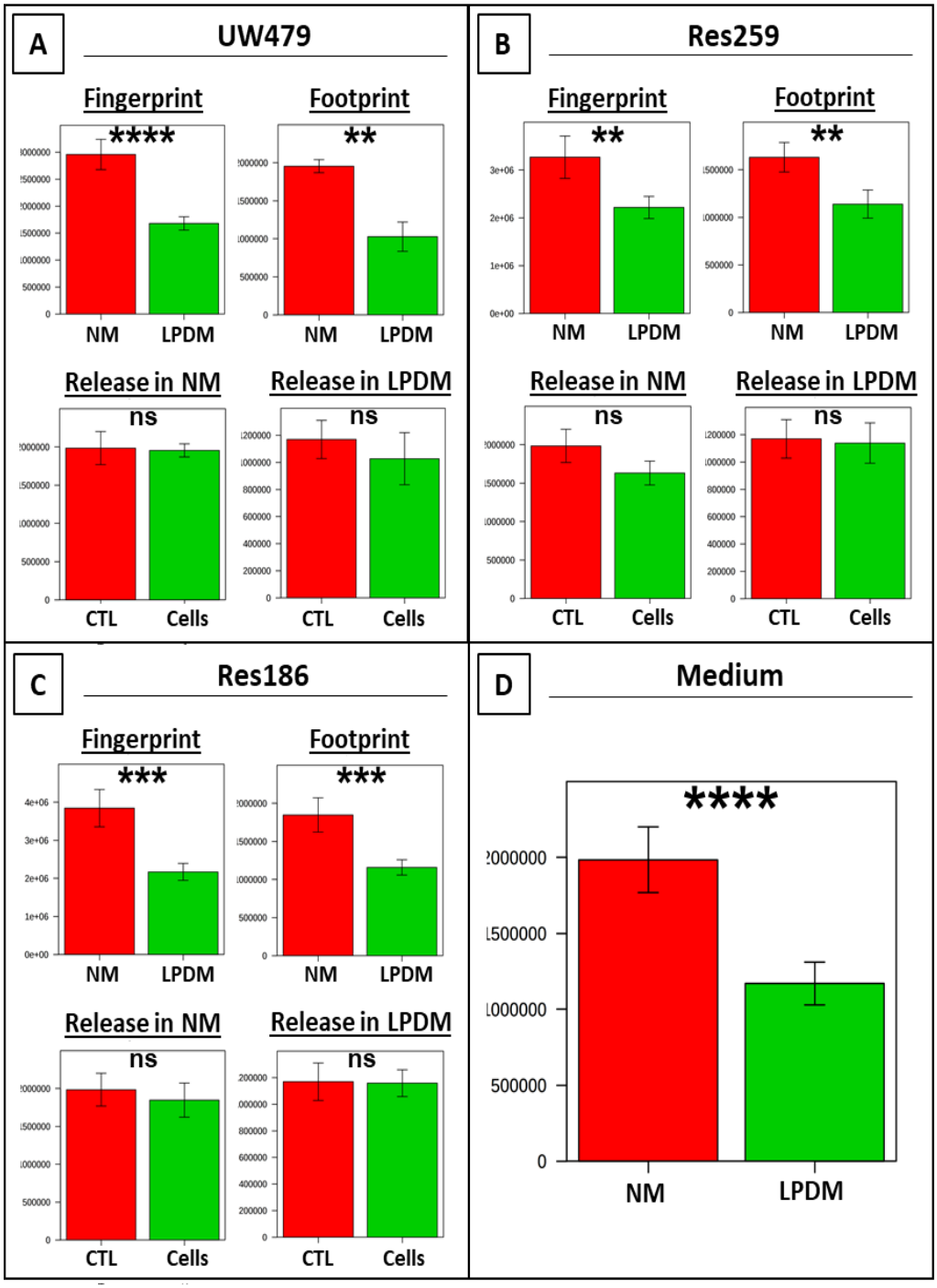

Figure 5.6. Peak intensities of serine in UW479, Res259 and Res186 cells cultured under lipoprotein-replete or -deplete conditions. Peak intensities for serine are displayed following extraction from (A) U8479, (B) Res259 and (C) Res186 cells (fingerprint; top left in each panel) or cultured medium (footprint; top right in each panel) under lipoprotein-replete (red) or -deplete (green) conditions. Comparisons between either NM or LPDM in the presence or absence (CTL) of cells are included (bottom left and bottom right in each panel, respectively). Serine levels within NM and LPDM in the absence of cells are compared in (D). Statistical evaluation was performed using a two-sample *t*-test: ns = not significant; * = $p<0.05$; ** = $p<0.01$; *** = $p<0.001$; **** = $p<0.0001$.

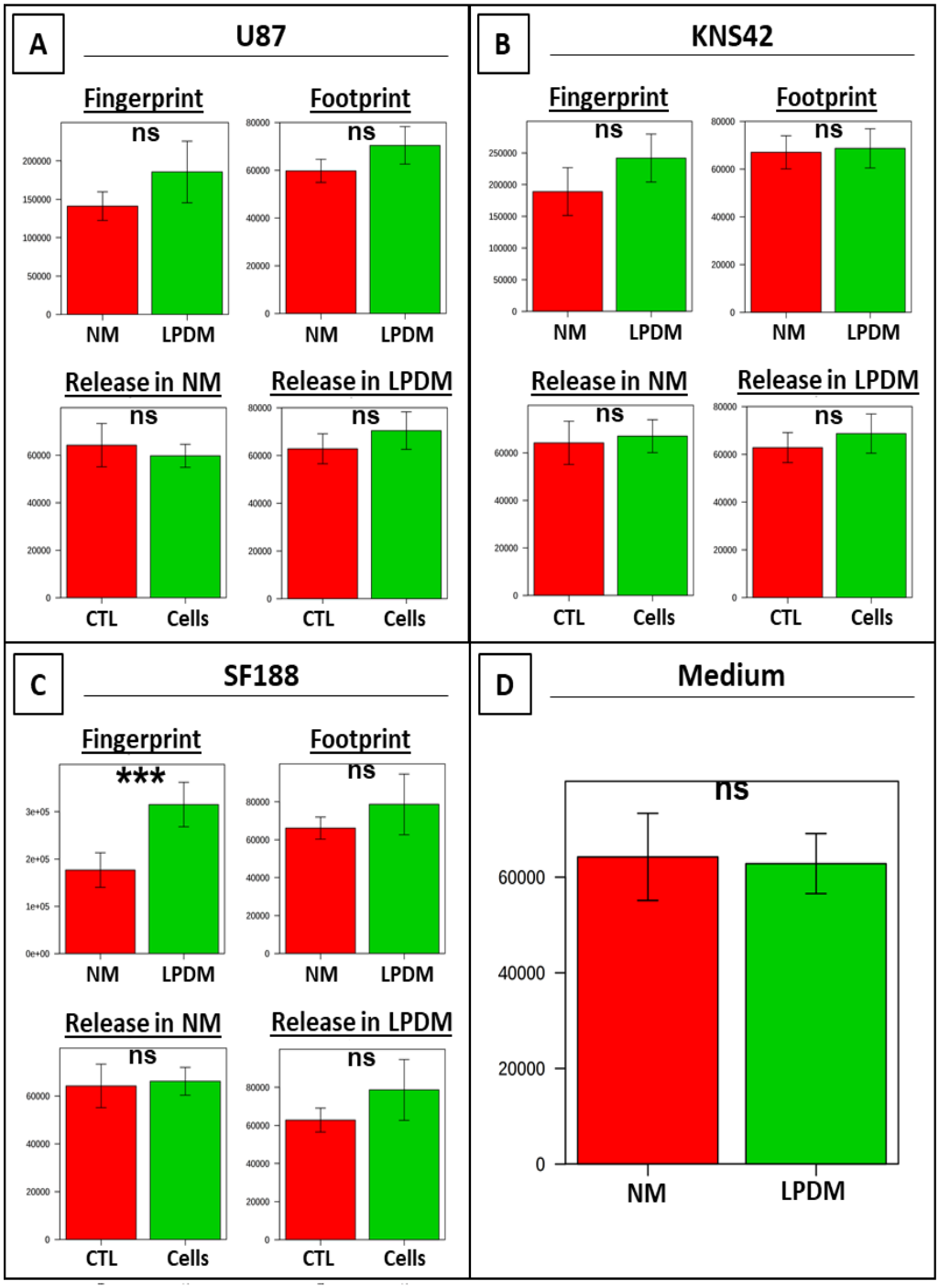

Figure 5.7. Peak intensities of glycine in U87, KNS42 and SF188 cells cultured under lipoprotein-replete or -deplete conditions. Peak intensities for glycine are displayed following extraction from (A) U87, (B) KNS42 and (C) SF188 cells (fingerprint; top left in each panel) or cultured medium (footprint; top right in each panel) under lipoprotein-replete (red) or -deplete (green) conditions Comparisons between either NM or LPDM in the presence or absence (CTL) of cells are included (bottom left and bottom right in each panel, respectively). Glycine levels within NM and LPDM in the absence of cells are compared in (D). Statistical evaluation was performed using a two-sample *t*-test: ns = not significant; * = $p<0.05$; ** = $p<0.01$; *** = $p<0.001$; **** = $p<0.0001$.

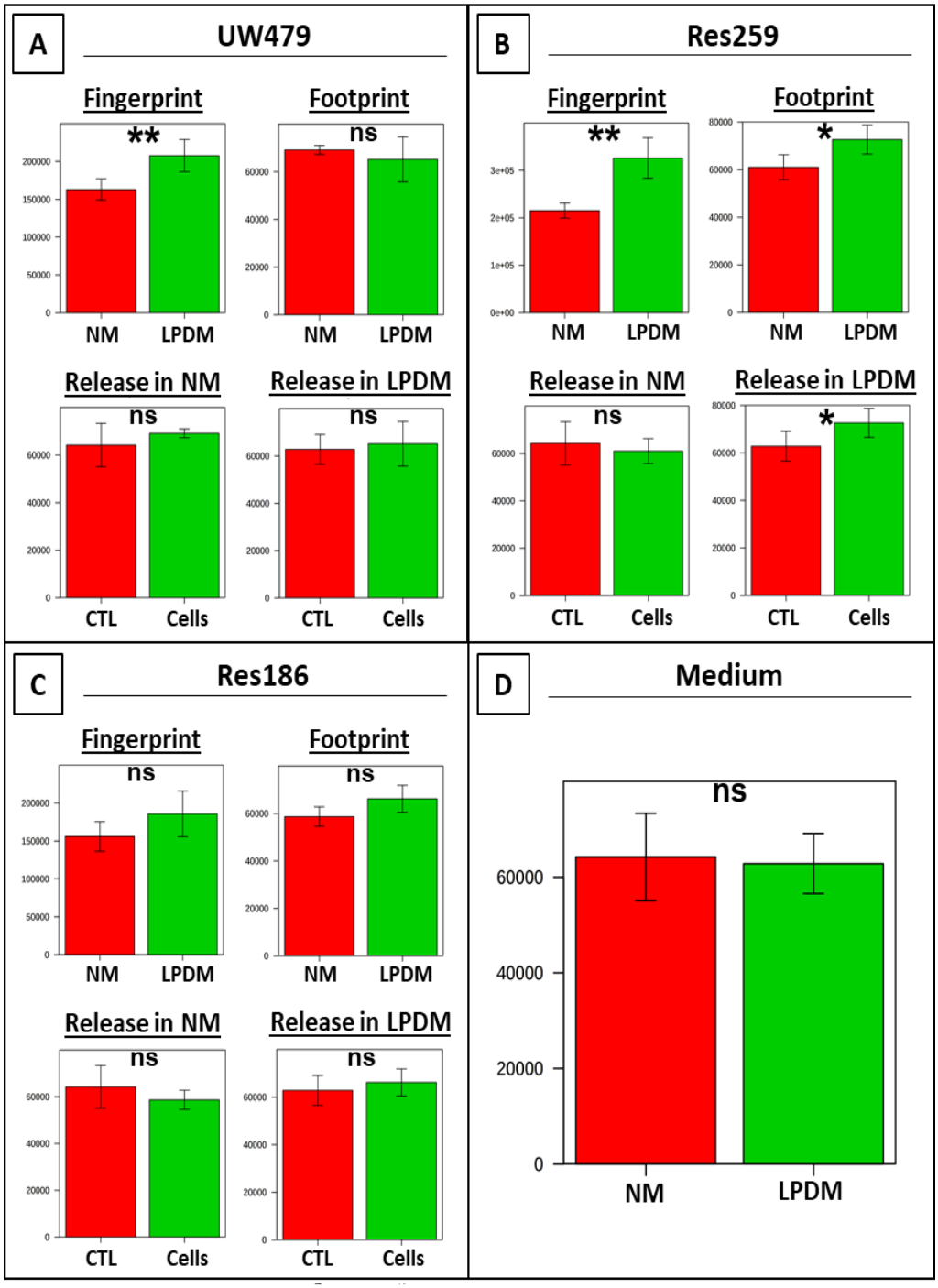

Figure 5.8. Peak intensities of glycine in UW479, Res259 and Res186 cells cultured under lipoprotein-replete or -deplete conditions. Peak intensities for glycine are displayed following extraction from (A) U8479, (B) Res259 and (C) Res186 cells (fingerprint; top left in each panel) or cultured medium (footprint; top right in each panel) under lipoprotein-replete (red) or -deplete (green) conditions. Comparisons between either NM or LPDM in the presence or absence (CTL) of cells are included (bottom left and bottom right in each panel, respectively). Glycine levels within NM and LPDM in the absence of cells are compared in (D). Statistical evaluation was performed using a two-sample *t*-test: ns = not significant; * = $p<0.05$; ** = $p<0.01$; *** = $p<0.001$; **** = $p<0.0001$.

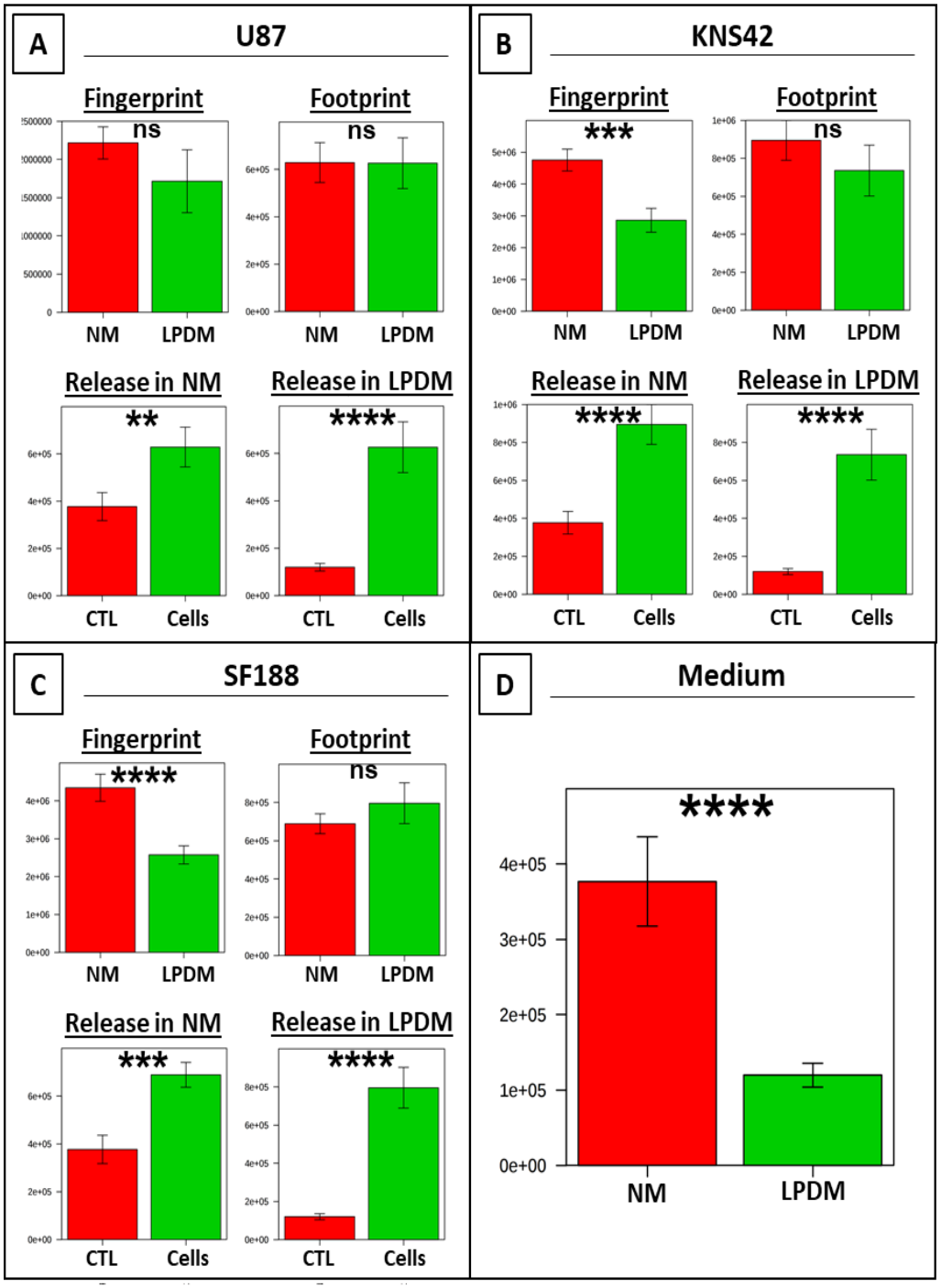

Figure 5.9. Peak intensities of alanine in U87, KNS42 and SF188 cells cultured under lipoprotein-replete or -deplete conditions. Peak intensities for alanine are displayed following extraction from (A) U87, (B) KNS42 and (C) SF188 cells (fingerprint; top left in each panel) or cultured medium (footprint; top right in each panel) under lipoprotein-replete (red) or -deplete (green) conditions. Comparisons between either NM or LPDM in the presence or absence (CTL) of cells are included (bottom left and bottom right in each panel, respectively). Glycine levels within NM and LPDM in the absence of cells are compared in (D). Statistical evaluation was performed using a two-sample *t*-test: ns = not significant; * = $p<0.05$; ** = $p<0.01$; *** = $p<0.001$; **** = $p<0.0001$.

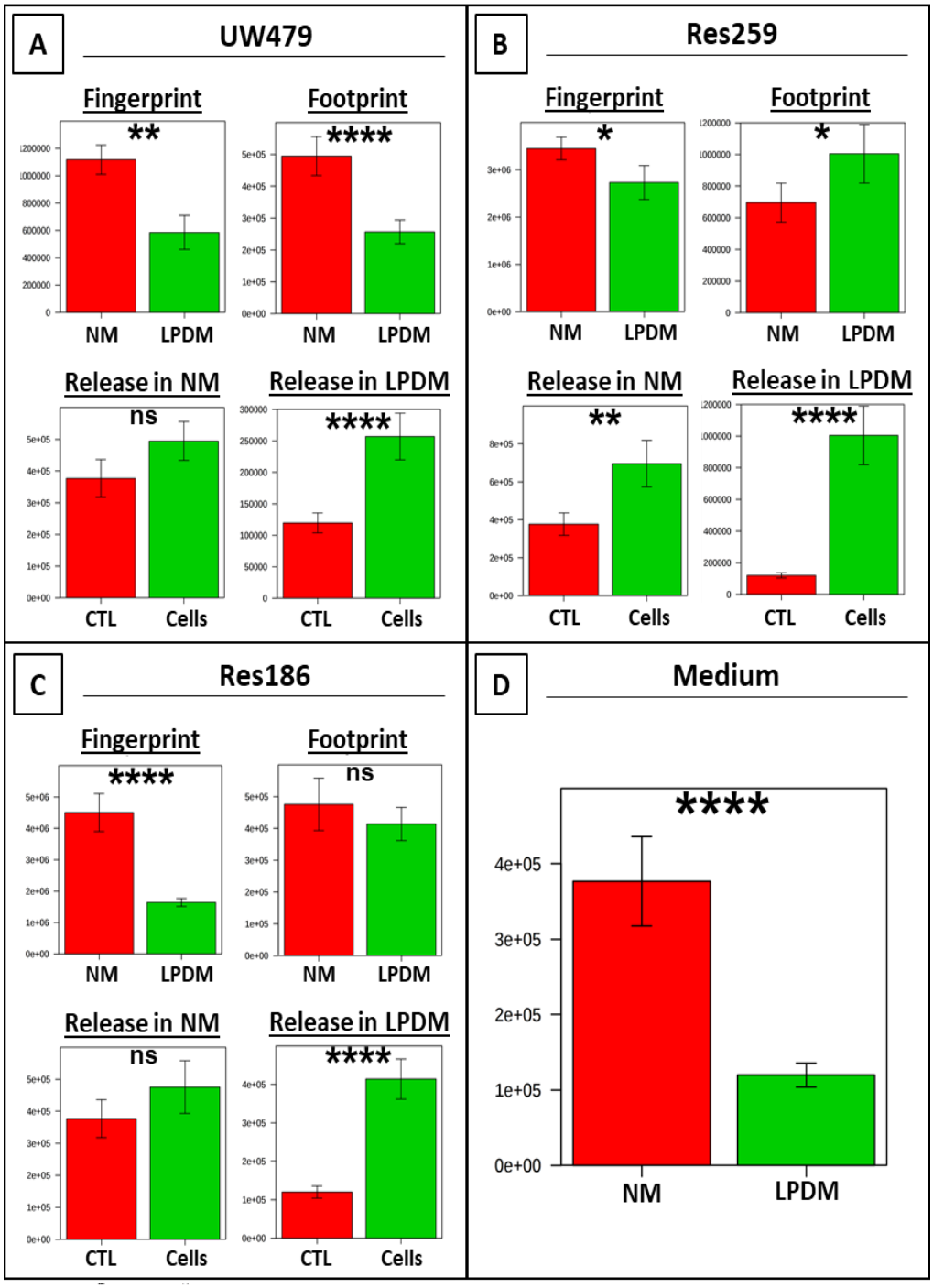

Figure 5.10. Peak intensities of alanine in UW479, Res259 and Res186 cells cultured under lipoprotein-replete or -deplete conditions. Peak intensities for alanine are displayed following extraction from (A) U8479, (B) Res259 and (C) Res186 cells (fingerprint; top left in each panel) or cultured medium (footprint; top right in each panel) under lipoprotein-replete (red) or -deplete (green) conditions. Comparisons between either NM or LPDM in the presence or absence (CTL) of cells are included (bottom left and bottom right in each panel, respectively). Glycine levels within NM and LPDM in the absence of cells are compared in (D). Statistical evaluation was performed using a two-sample *t*-test: ns = not significant; * = $p<0.05$; ** = $p<0.01$; *** = $p<0.001$; **** = $p<0.0001$.

Table 5.5. Identification confidence scores for metabolites detected within the footprint of cultured glioma cells and medium only controls.

Footprint/medium metabolite	ID confidence
Serine	8
Glycine	8
Alanine	4
Glutamate 5-semialdehyde	8
Proline	4
1-Pyrroline 5-carboxylate	8
Choline phosphate	4

Table 5.6. Fold change differences for metabolites related to one carbon metabolism under lipoprotein-replete relative to lipoprotein -deplete conditions.

Metabolite	ID confidence	U87		KNS42		SF188		UW479		Res259		Res186	
		log2FC	FDR	log2FC	FDR	log2FC	FDR	log2FC	FDR	log2FC	FDR	log2FC	FDR
L-Serine	10	**-0.54**	**1.12E-02**	**-0.53**	**3.48E-04**	**-0.55**	**1.46E-03**	**-0.82**	**2.08E-05**	**-0.56**	**1.95E-03**	**-0.82**	**1.09E-04**
Glycine	10	0.40	7.84E-02	0.36	9.47E-02	**0.84**	**9.84E-04**	**0.35**	**8.89E-03**	**0.60**	**1.15E-03**	0.25	1.72E-01
L-Methionine	10	0.08	1.88E-01	0.13	1.25E-01	**0.31**	**5.60E-02**	-0.09	4.61E-01	**0.40**	**2.36E-03**	0.29	3.46E-01
S-Adenosyl-L-methionine	8	0.43	7.05E-01	0.10	9.42E-01	-0.19	8.94E-01	-1.12	4.32E-01	0.61	3.27E-01	-0.63	3.44E-01
S-Adenosyl-L-homocysteine	8	-0.14	9.02E-01	-0.09	8.41E-01	0.39	4.35E-01	0.15	8.39E-01	-0.06	7.42E-01	-0.51	9.56E-01
L-Cystathionine	10	**-1.02**	**9.66E-03**	**-0.78**	**5.32E-04**	**-0.92**	**7.75E-03**	-0.67	5.97E-02	-0.21	5.13E-01	**-1.65**	**6.81E-05**
Glutathione	8	0.16	9.44E-01	-0.35	4.40E-01	-0.74	5.98E-02	0.17	8.18E-01	-0.29	2.62E-01	0.21	5.82E-01
Glutathione disulfide	10	0.55	2.25E-01	0.14	6.09E-01	0.13	7.75E-01	0.11	8.39E-01	0.39	6.58E-02	0.90	5.71E-02

Fold change differences are given to the base of 2 (log2FC) where green and red represent significantly reduced or elevated metabolite levels under lipoprotein-deplete conditions relative to lipoprotein-replete. Statistical evaluation was performed using a *t* test and *p*-values were corrected for multiple comparisons using the false discovery rate (FDR).

The online Metaboanalyst metabolomics analysis tool was used to identify metabolites that were significantly altered between NM and LPDM using a statistical *t*-test for each cell line. The results from this analysis were then fed into the metabolite set enrichment suite and pathway analysis to determine significantly affected metabolic pathways following lipoprotein deprivation. *Taurine and hypotaurine* metabolism was the only metabolite set enriched, reaching significance at the raw *p*-value level in the KNS42, SF188 and UW479 cell lines (Table 5.7). Pathway analysis supported this observation but also revealed significant alterations to *arginine and proline* metabolism across all cell lines. However, the pathway impact was less than 0.15 indicating minimal metabolic alterations (Table 5.7). Within the taurine biosynthesis pathway, cysteine sulfonate, hypotaurine and taurine were consistently reduced to a significant level across all cell lines (Figure 5.11 and Figure 5.12), highlighting the detrimental impact of lipoprotein deprivation on taurine metabolism. However, since these metabolites were not identified in the footprint, it is possible that the observations may reflect differences in medium composition. This is seen for the proline metabolism pathway in which significantly reduced GSA levels were observed across all cell lines (Figure 5.13 and Figure 5.14). However, examination of the footprint indicated that GSA levels were low in LPDM to begin with (Figure 5.13D and Figure 5.14D). Fingerprint proline levels were significantly increased in lipoprotein deficient conditions in U87, SF188 and Res259 cells and were not significantly altered in the remaining cell lines (Figure 5.15 and Figure 5.16), despite reduced proline levels in LPDM compared to NM (Figure 5.15D and Figure 5.16D). Several cell lines demonstrated significant release of proline in LPDM, suggesting proline synthesis within lipoprotein deprived conditions. This is supported by increased P5C levels within the fingerprint and footprint of most cell lines (Figure 5.17 and Figure 5.18). All cell lines demonstrated significant release of proline from cells compared to medium alone but the release within LPDM was greater in many cases leading to higher footprint levels in LPDM compared to NM (Figure 5.15 and Figure 5.16). However, as was the case with alanine, interpretations of

proline levels within the footprint and medium controls are tentatively made since proline obtained a very low identification confidence score (Table 5.5).

Table 5.7. Metabolite set enrichment analysis and pathway analysis results for taurine and hypotaurine metabolism and arginine and proline metabolism between lipoprotein-replete and -deplete conditions.

Cell line	Taurine and hypotaurine metabolism			Arginine and proline metabolism		
	MSEA	Pathway analysis	Pathway impact	MSEA	Pathway analysis	Pathway impact
U87	2.62E-01	**2.12E-03**	0.34173	2.72E-01	**4.60E-05**	0.11358
KNS42	**6.87E-03**	**2.52E-07**	0.54676	1.54E-01	**1.29E-05**	0.12731
SF188	**2.22E-02**	**1.41E-07**	0.54676	2.45E-01	**4.92E-05**	0.13751
UW479	**4.63E-02**	**7.37E-05**	0.45504	1.62E-01	**7.97E-06**	0.13326
Res259	1.01E-01	**3.13E-04**	0.44425	2.45E-01	**4.71E-07**	0.14892
Res186	2.80E-01	**2.43E-04**	0.39568	3.10E-01	**7.57E-05**	0.14094

Values represent raw *p*-values following metabolite set enrichment analysis (MSEA) and pathway analysis. Significant scores ($p<0.05$) are highlighted in bold. Pathway impact scores range between 0 and 1.

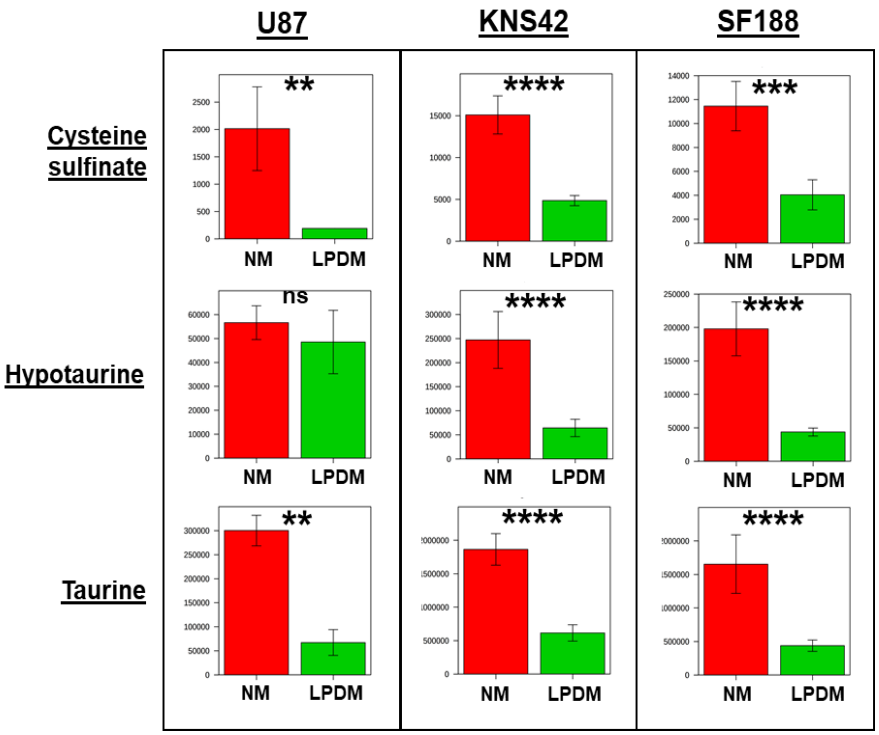

Figure 5.11. Peak intensities of taurine-related metabolites in U87, KNS42 and SF188 cultured under lipoprotein-replete or -deplete conditions. Mean peak intensities are displayed for taurine-related metabolites under lipoprotein-replete (NM; red) or -deplete (LPDM; green) conditions Statistical evaluation was performed using a two-sample t-test: ns = not significant; * = p<0.05; ** = p<0.01; *** = p<0.001; **** = p<0.0001.

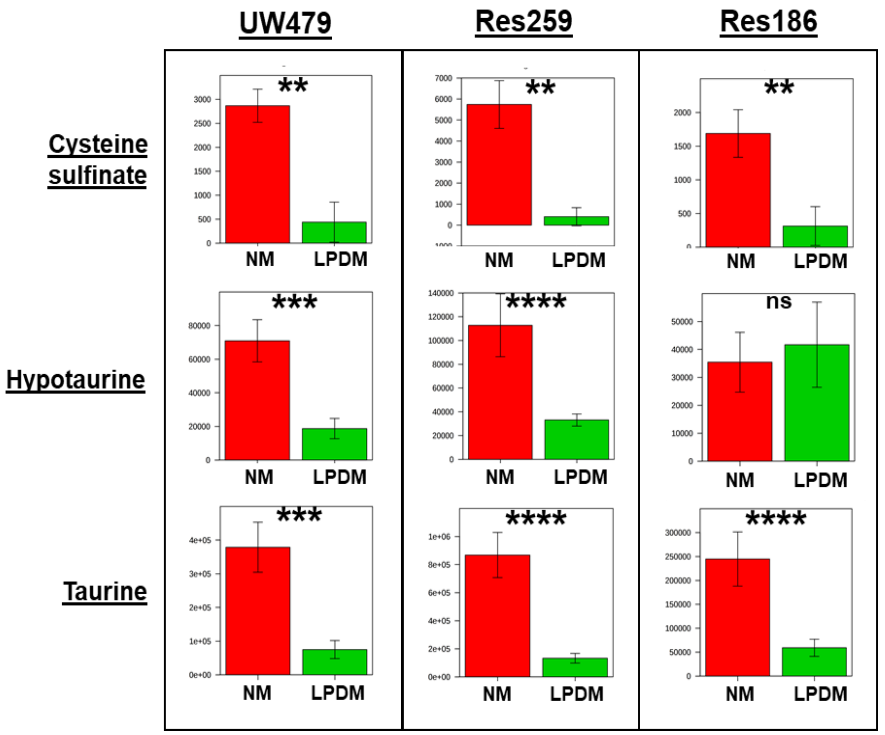

Figure 5.12. Peak intensities of taurine-related metabolites in UW479, Res259 and Res186 cultured under lipoprotein-replete or -deplete conditions. Mean peak intensities are displayed for taurine-related metabolites under lipoprotein-replete (NM; red) or -deplete (LPDM; green) conditions Statistical evaluation was performed using a two-sample t-test: ns = not significant; * = p<0.05; ** = p<0.01; *** = p<0.001; **** = p<0.0001.

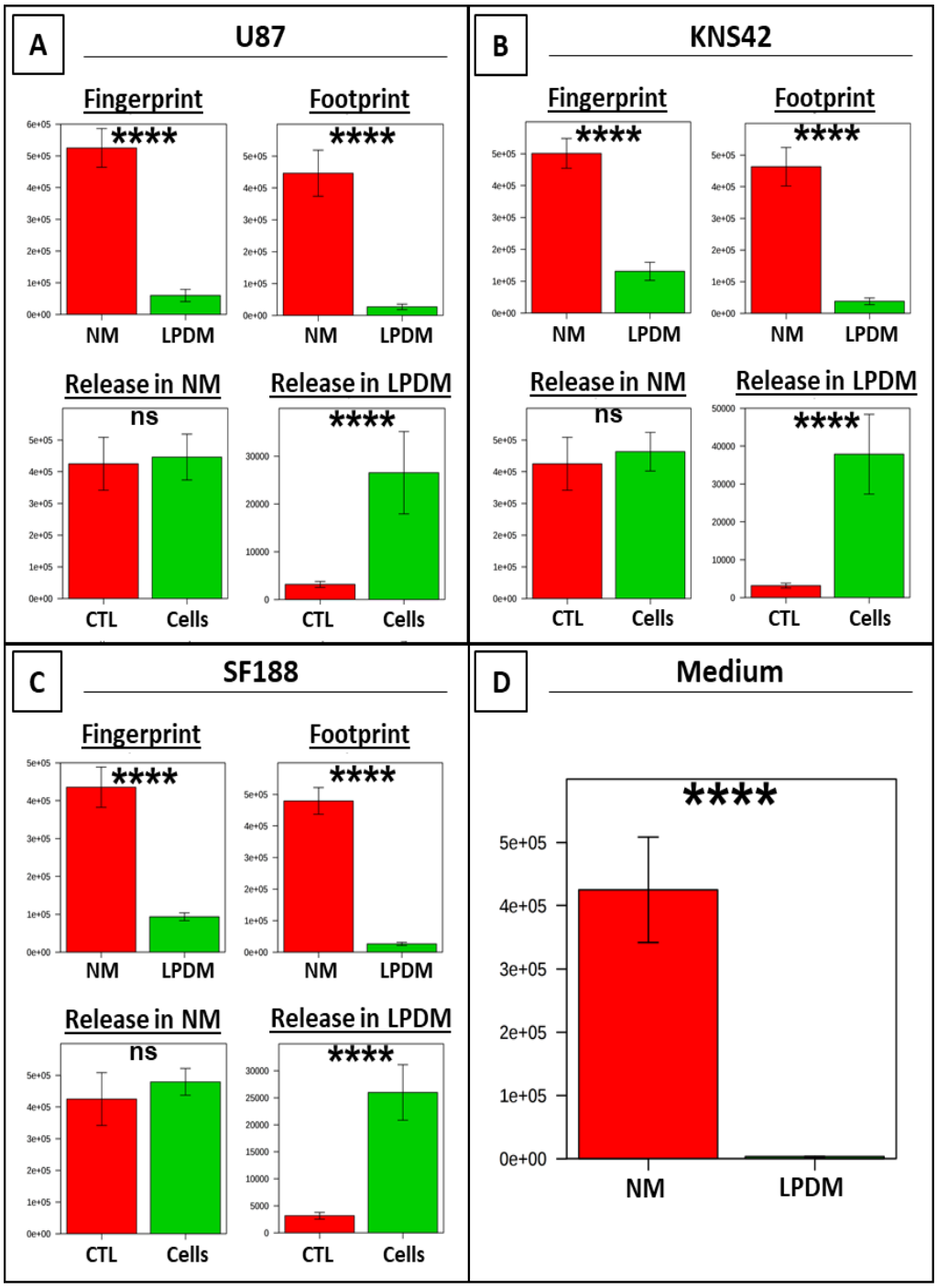

Figure 5.13. Peak intensities of glutamate 5-semialdehyde in U87, KNS42 and SF188 cells cultured under lipoprotein-replete or -deplete conditions. Peak intensities for glutamate 5-semialdehyde (GSA) are displayed following extraction from (A) U87, (B) KNS42 and (C) SF188 cells (fingerprint; top left in each panel) or cultured medium (footprint; top right in each panel) under lipoprotein-replete (red) or -deplete (green) conditions. Comparisons between either NM or LPDM in the presence or absence (CTL) of cells are included (bottom left and bottom right in each panel, respectively). GSA levels within NM and LPDM in the absence of cells are compared in (D). Statistical evaluation was performed using a two-sample *t*-test: ns = not significant; * = $p<0.05$; ** = $p<0.01$; *** = $p<0.001$; **** = $p<0.0001$.

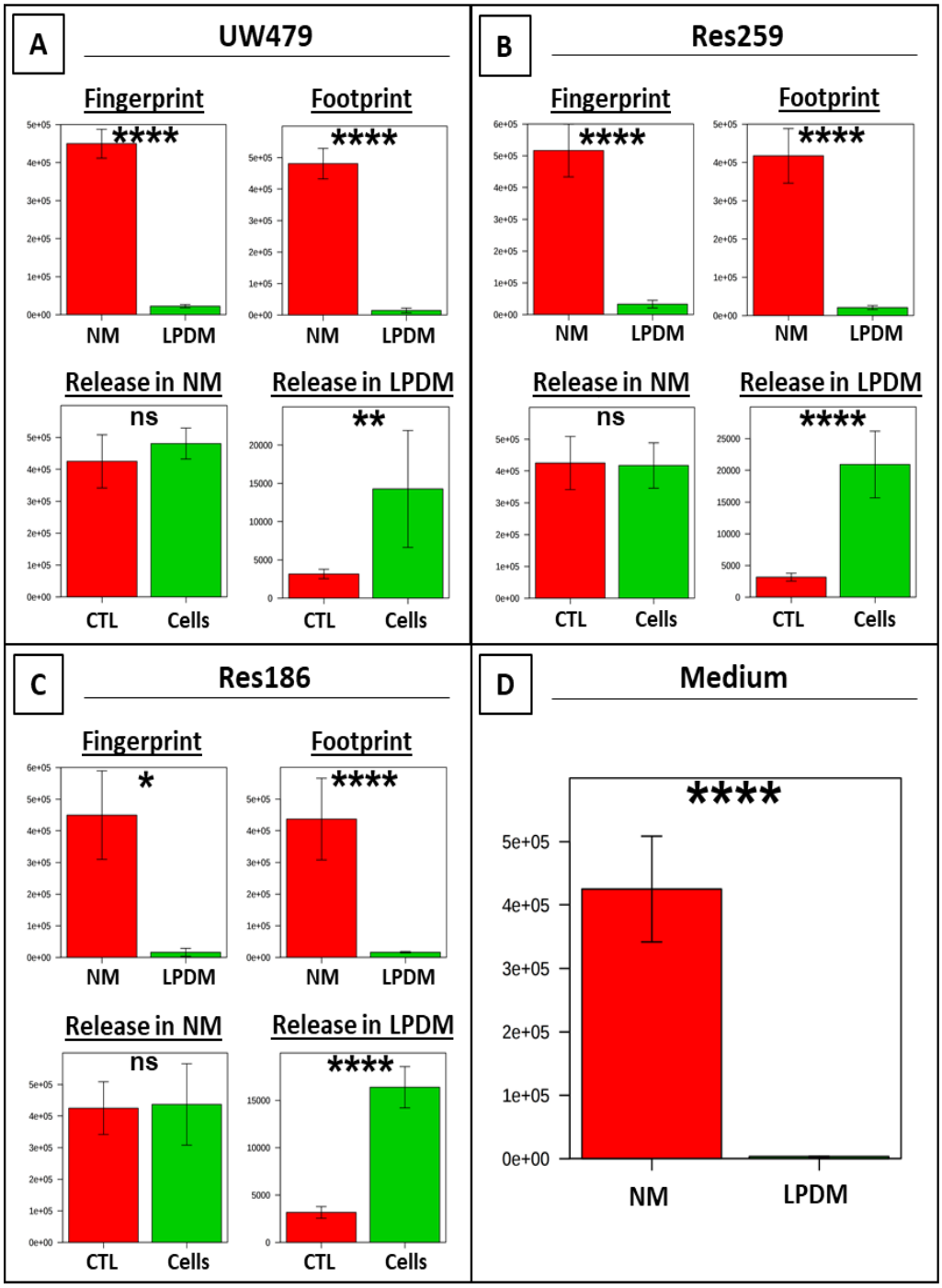

Figure 5.14. Peak intensities of glutamate 5-semialdehyde in UW479, Res259 and Res186 cells cultured under lipoprotein-replete or -deplete conditions. Peak intensities for glutamate 5-semialdehyde (GSA) are displayed following extraction (A) U8479, (B) Res259 and (C) Res186 from cells (fingerprint; top left in each panel) or cultured medium (footprint; top right in each panel) under lipoprotein-replete (red) or -deplete (green) conditions. Comparisons between either NM or LPDM in the presence or absence (CTL) of cells are included (bottom left and bottom right in each panel, respectively). GSA levels within NM and LPDM in the absence of cells are compared in (D). Statistical evaluation was performed using a two-sample *t*-test: ns = not significant; * = $p<0.05$; ** = $p<0.01$; *** = $p<0.001$; **** = $p<0.0001$.

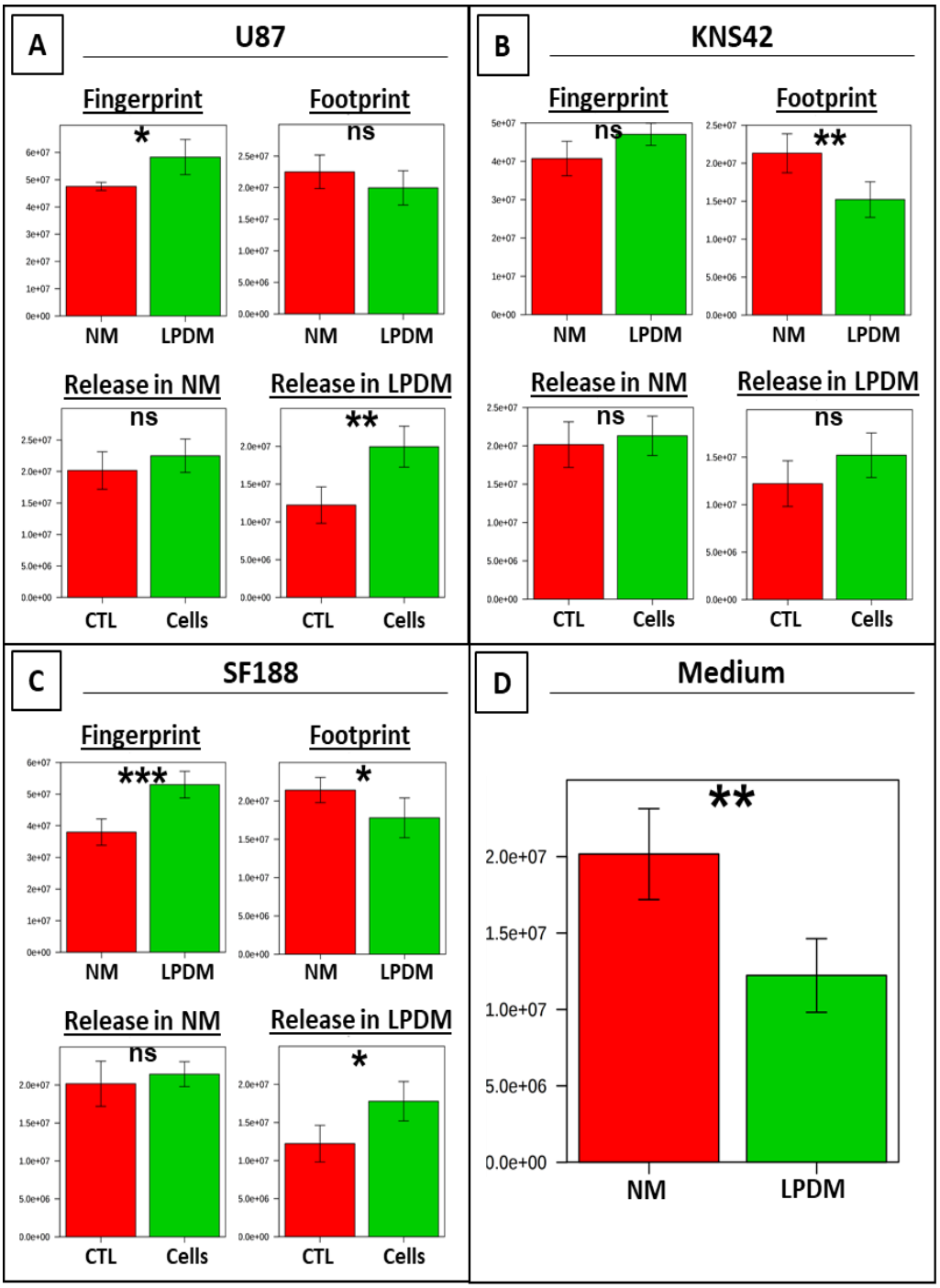

Figure 5.15. Peak intensities of proline in U87, KNS42 and SF188 cells cultured under lipoprotein-replete or -deplete conditions. Peak intensities for proline are displayed following extraction from (A) U87, (B) KNS42 and (C) SF188 cells (fingerprint; top left in each panel) or cultured medium (footprint; top right in each panel) under lipoprotein-replete (red) or -deplete (green) conditions. Comparisons between either NM or LPDM in the presence or absence (CTL) of cells are included (bottom left and bottom right in each panel, respectively). Proline levels within NM and LPDM in the absence of cells are compared in (D). Statistical evaluation was performed using a two-sample *t*-test: ns = not significant; * = $p<0.05$; ** = $p<0.01$; *** = $p<0.001$; **** = $p<0.0001$.

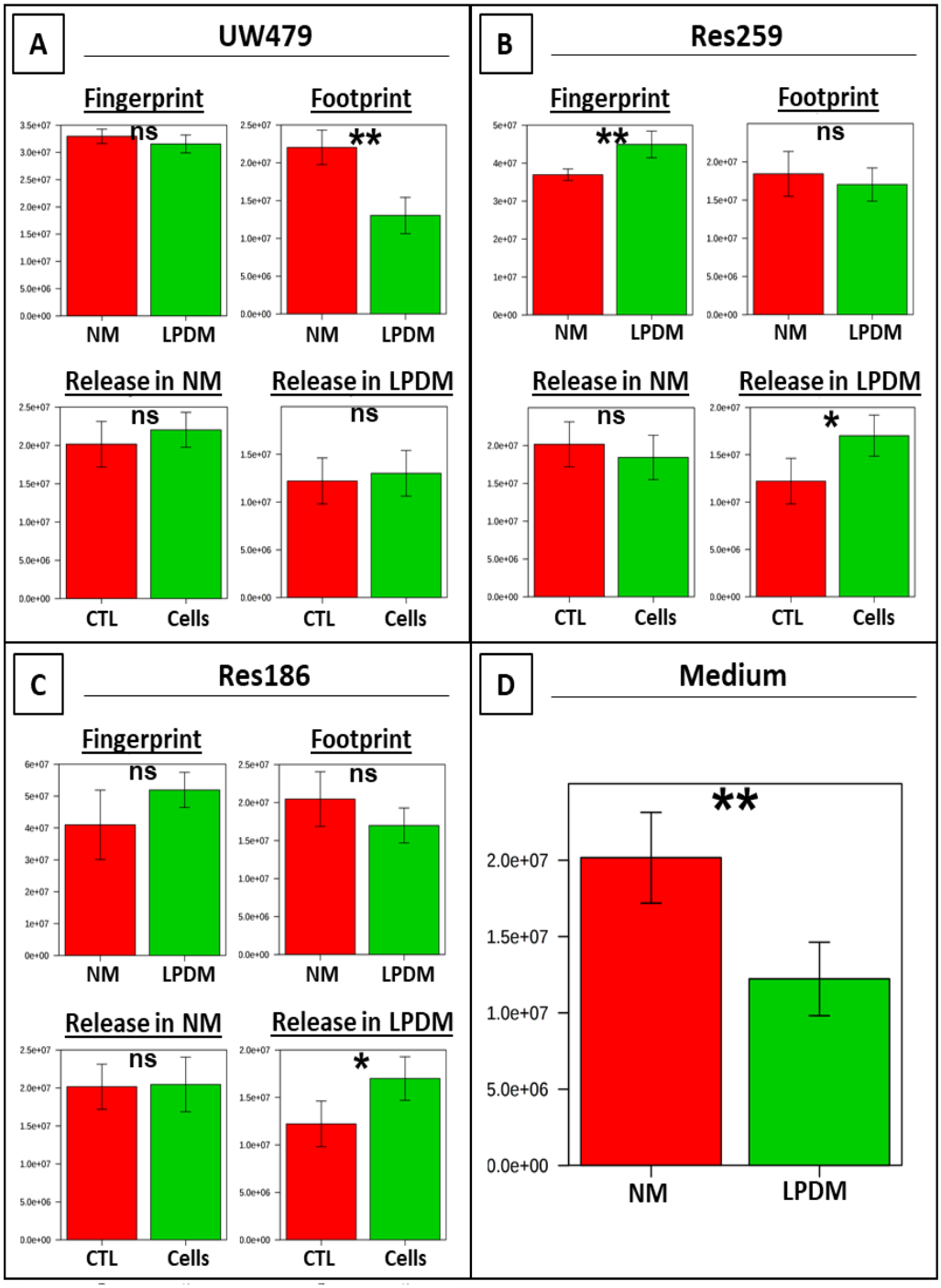

Figure 5.16. Peak intensities of proline in UW479, Res259 and Res186 cells cultured under lipoprotein-replete or -deplete conditions. Peak intensities for proline are displayed following extraction from (A) U8479, (B) Res259 and (C) Res186 cells (fingerprint; top left in each panel) or cultured medium (footprint; top right in each panel) under lipoprotein-replete (red) or -deplete (green) conditions. Comparisons between either NM or LPDM in the presence or absence (CTL) of cells are included (bottom left and bottom right in each panel, respectively). Proline levels within NM and LPDM in the absence of cells are compared in (D). Statistical evaluation was performed using a two-sample *t*-test: ns = not significant; * = $p<0.05$; ** = $p<0.01$; *** = $p<0.001$; **** = $p<0.0001$.

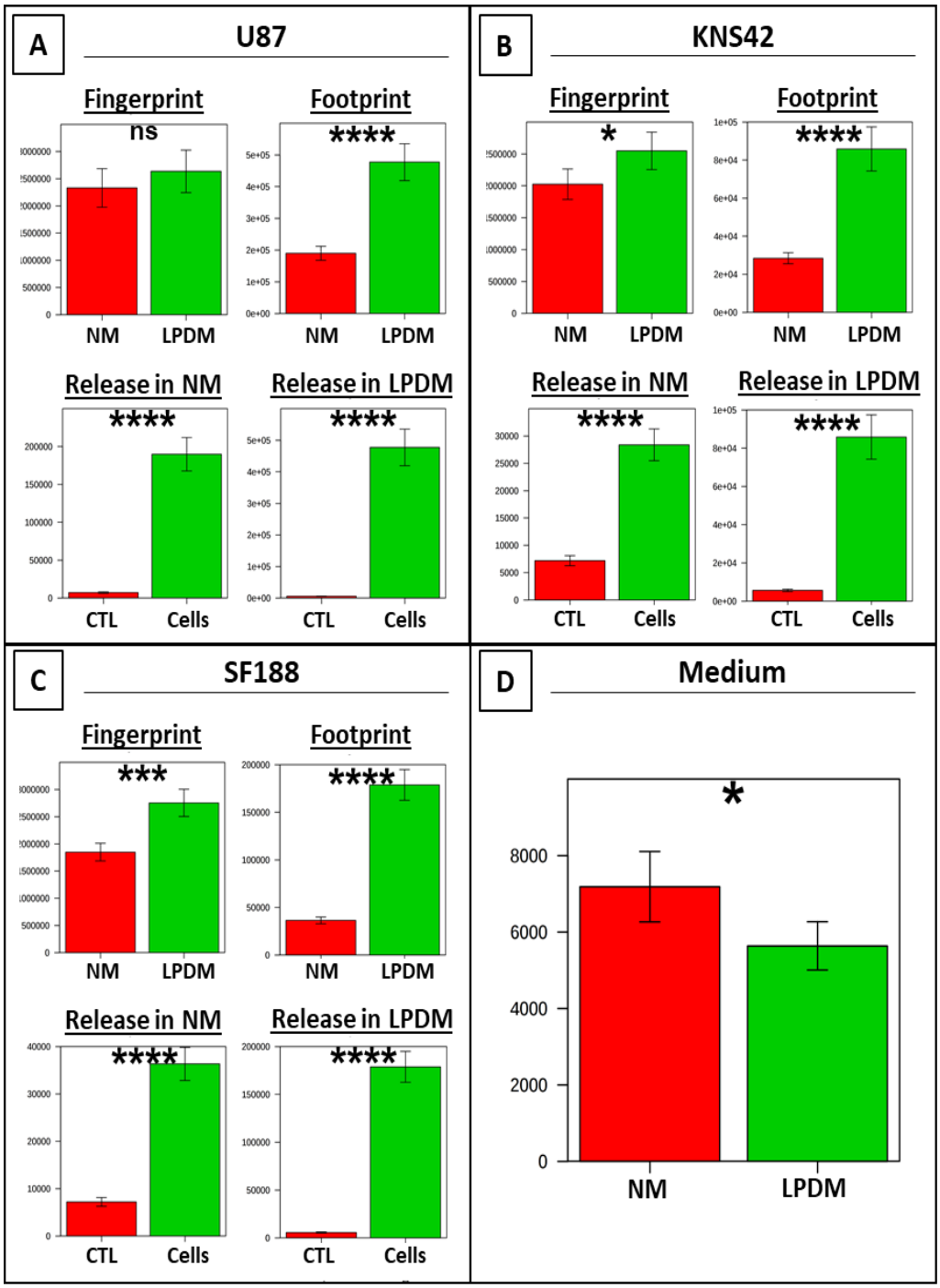

Figure 5.17. Peak intensities of 1-pyrroline 5-carboxylate in U87, KNS42 and SF188 cells cultured under lipoprotein-replete or -deplete conditions. Peak intensities for 1-pyrroline 5-carboxylate (P5C) are displayed following extraction from (A) U87, (B) KNS42 and (C) SF188 cells (fingerprint; top left in each panel) or cultured medium (footprint; top right in each panel) under lipoprotein-replete (red) or -deplete (green) conditions. Comparisons between either NM or LPDM in the presence or absence (CTL) of cells are included (bottom left and bottom right in each panel, respectively). P5C levels within NM and LPDM in the absence of cells are compared in (D). Statistical evaluation was performed using a two-sample *t*-test: ns = not significant; * = $p<0.05$; ** = $p<0.01$; *** = $p<0.001$; **** = $p<0.0001$.

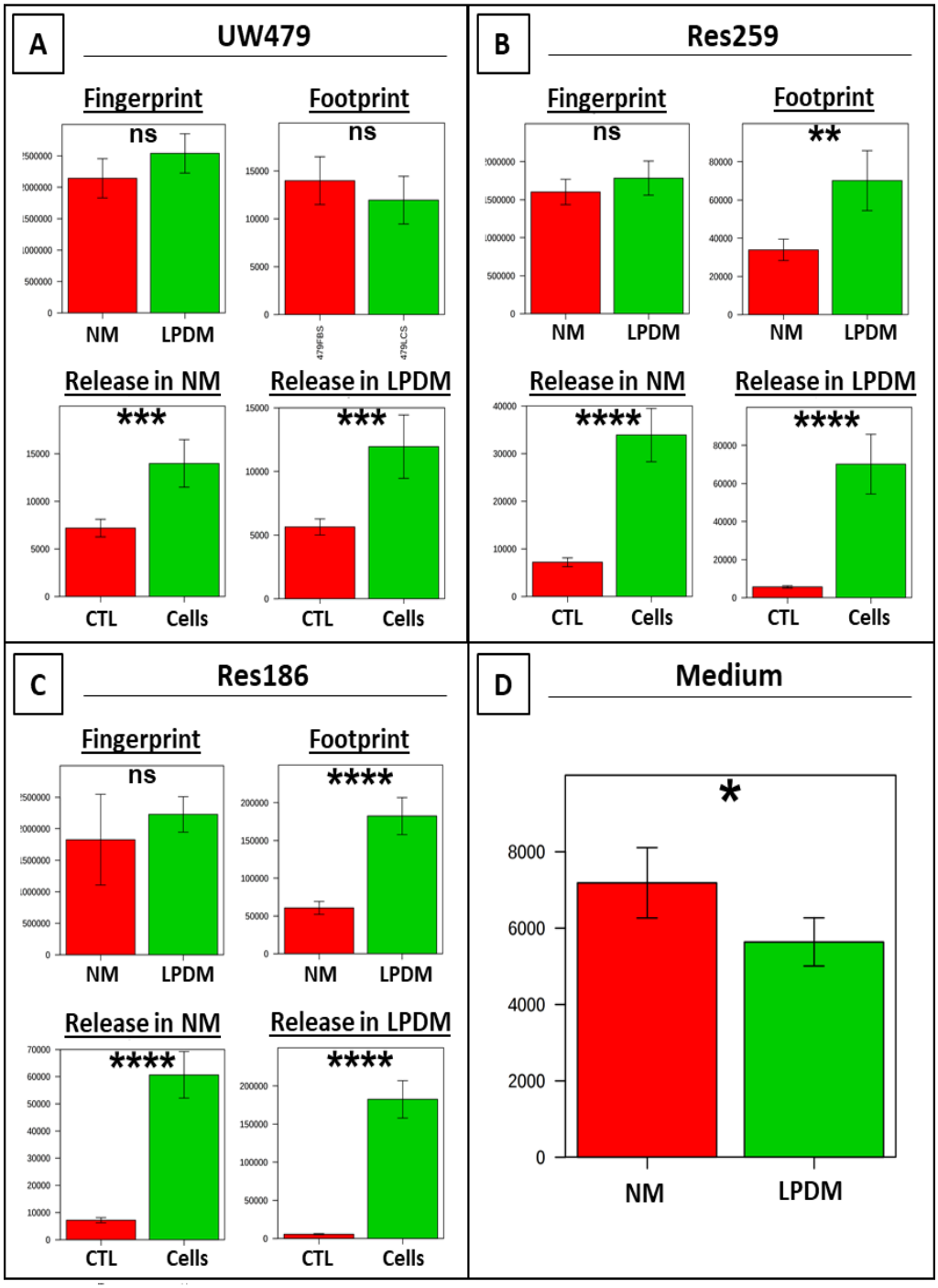

Figure 5.18. Peak intensities of 1-pyrroline 5-carboxylate in UW479, Res259 and Res186 cells cultured under lipoprotein-replete or -deplete conditions. Peak intensities for 1-pyrroline 5-carboxylate (P5C) are displayed following extraction from (A) U8479, (B) Res259 and (C) Res186 cells (fingerprint; top left in each panel) or cultured medium (footprint; top right in each panel) under lipoprotein-replete (red) or -deplete (green) conditions. Comparisons between either NM or LPDM in the presence or absence (CTL) of cells are included (bottom left and bottom right in each panel, respectively). P5C levels within NM and LPDM in the absence of cells are compared in (D). Statistical evaluation was performed using a two-sample *t*-test: ns = not significant; * = $p<0.05$; ** = $p<0.01$; *** = $p<0.001$; **** = $p<0.0001$.

The choline synthesis pathway is important for the synthesis of the membrane lipid phosphatidylcholine. Choline levels were consistently reduced in all cell lines to a significant level, but only translated into significantly reduced choline phosphate levels in U87 and Res186 cells (Figure 5.19 and Figure 5.20). Assessment of choline phosphate levels within the footprint and medium controls indicated greater release under lipoprotein-deplete compared to -replete conditions, which was significant in all cell lines with the exception of UW479 cells. (Figure 5.21 and Figure 5.22). However, the identification confidence score for choline phosphate was very low meaning that the findings made for the footprint and medium controls must be interpreted with caution (Table 5.5). Interestingly, CDP-choline levels were significantly increased in lipoprotein-starved KNS42, SF188 and Res259 cells (Figure 5.19 and Figure 5.20). Overall, these findings support increased activity within the phosphatidylcholine synthesis pathway under lipoprotein deficient conditions in order to meet membrane lipid requirements for cancer cell proliferation, which otherwise would have been obtained through lipoprotein uptake.

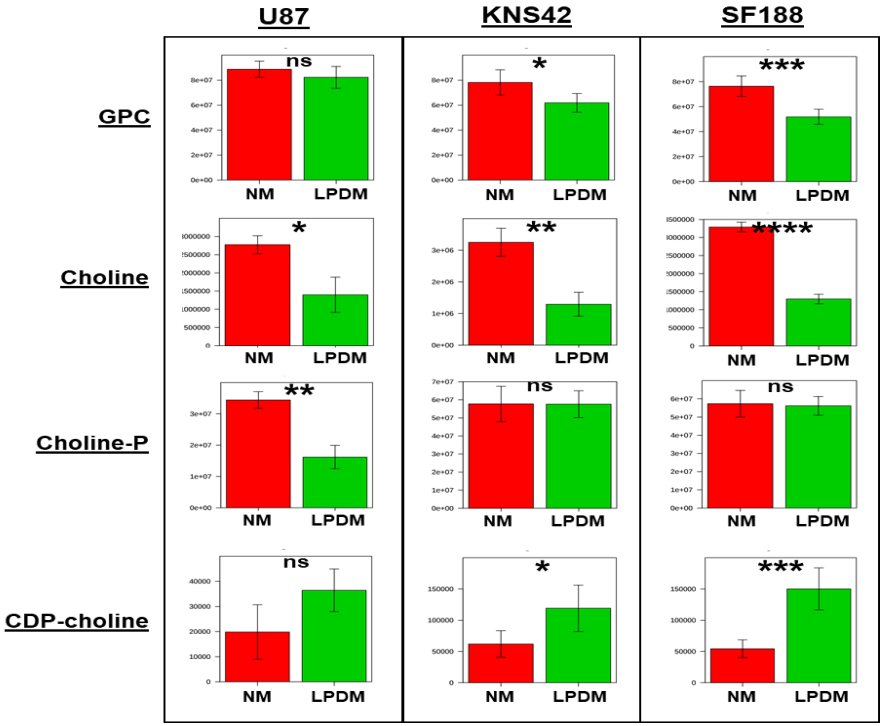

Figure 5.19. Peak intensities of choline-related metabolites in U87, KNS42 and SF188 cultured under lipoprotein-replete or -deplete conditions. Mean peak intensities are displayed for choline-related metabolites under lipoprotein-replete (NM; red) or -deplete (LPDM; green) conditions Statistical evaluation was performed using a two-sample t-test: ns = not significant; * = p<0.05; ** = p<0.01; *** = p<0.001; **** = p<0.0001.

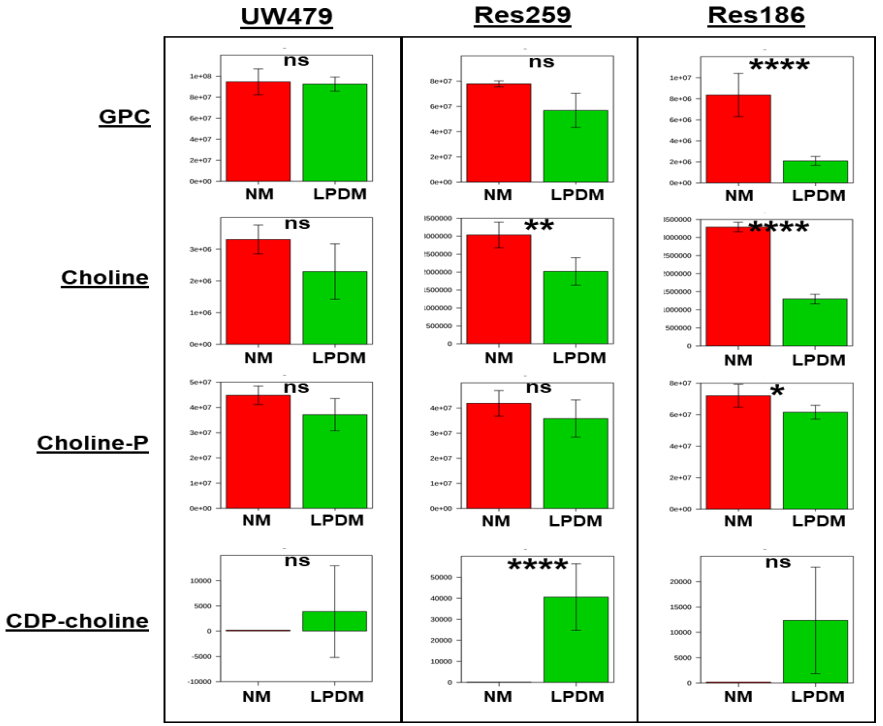

Figure 5.20. Peak intensities of choline-related metabolites in UW479, Res259 and Res189 cultured under lipoprotein-replete or -deplete conditions. Mean peak intensities are displayed for choline-related metabolites under lipoprotein-replete (NM; red) or -deplete (LPDM; green) conditions Statistical evaluation was performed using a two-sample t-test: ns = not significant; * = p<0.05; ** = p<0.01; *** = p<0.001; **** = p<0.0001.

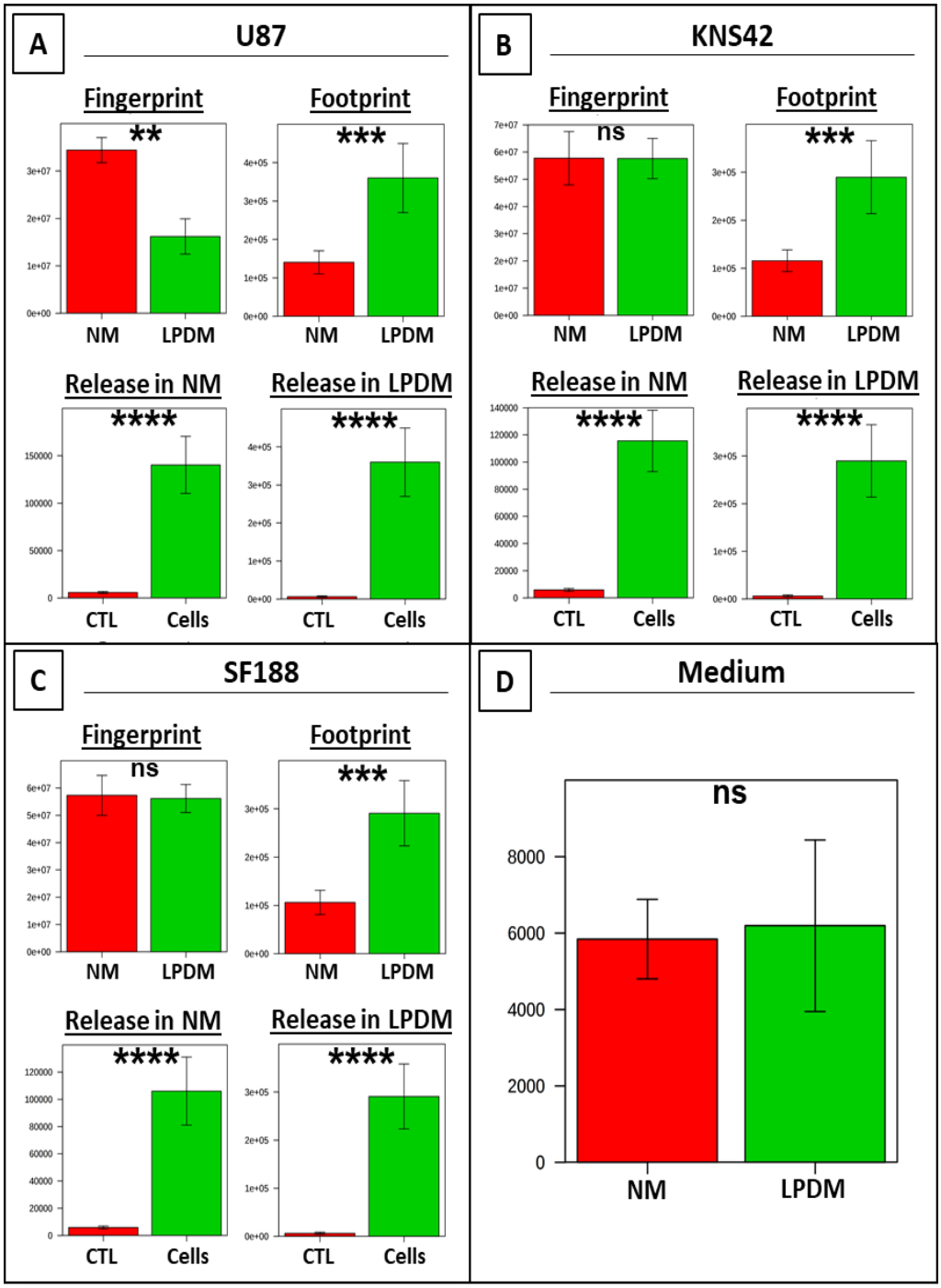

Figure 5.21. Peak intensities of choline phosphate in U87, KNS42 and SF188 cells cultured under lipoprotein-replete or -deplete conditions. Peak intensities for choline phosphate are displayed following extraction from (A) U87, (B) KNS42 and (C) SF188 cells (fingerprint; top left in each panel) or cultured medium (footprint; top right in each panel) under lipoprotein-replete (red) or -deplete (green) conditions. Comparisons between either NM or LPDM in the presence or absence (CTL) of cells are included (bottom left and bottom right in each panel, respectively). Choline phosphate levels within NM and LPDM in the absence of cells are compared in (D). Statistical evaluation was performed using a two-sample *t*-test: ns = not significant; * = $p<0.05$; ** = $p<0.01$; *** = $p<0.001$; **** = $p<0.0001$.

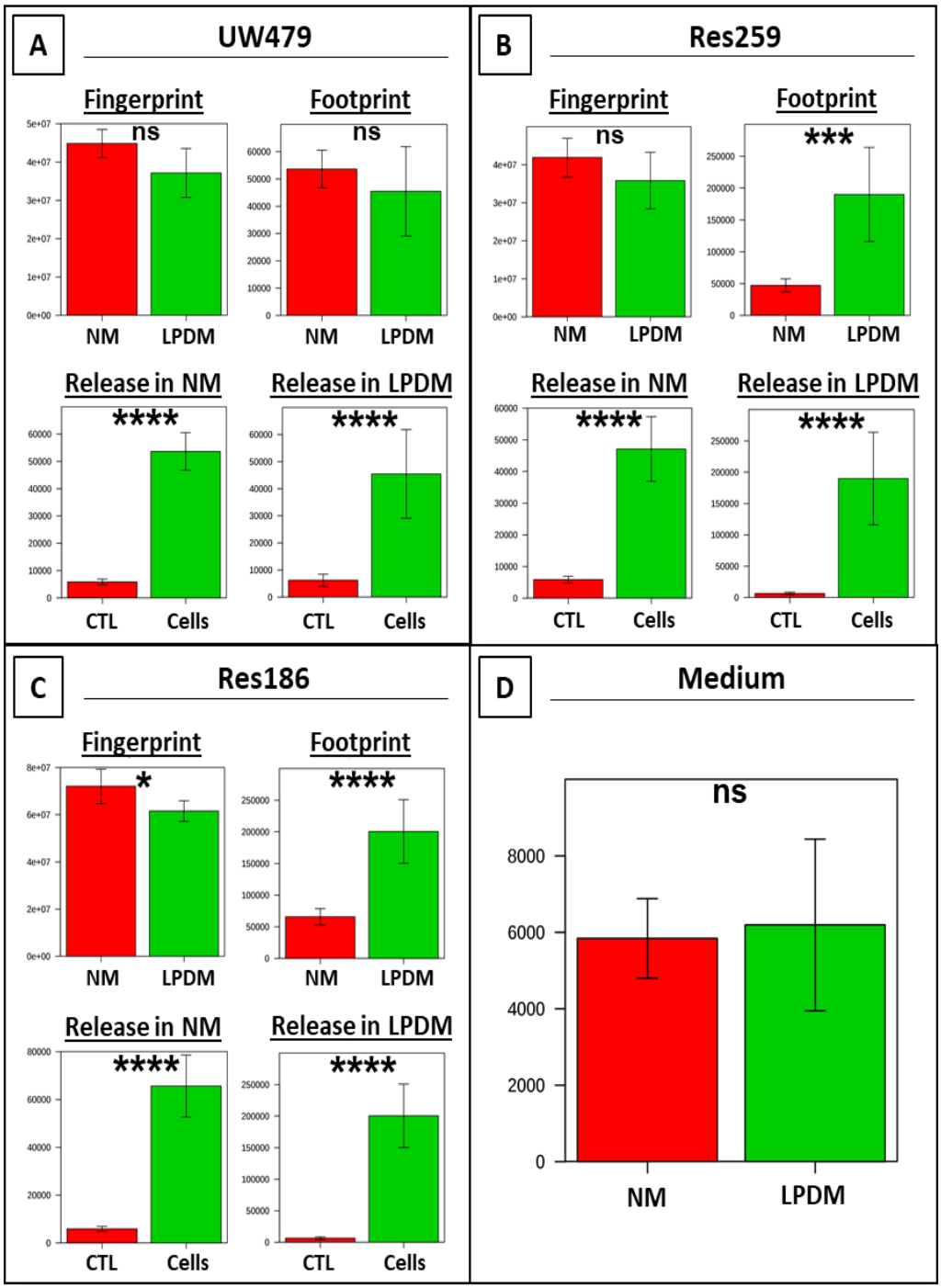

Figure 5.22. Peak intensities of choline phosphate in UW479, Res259 and Res186 cells cultured under lipoprotein-replete or -deplete conditions. Peak intensities for choline phosphate are displayed following extraction from (A) U8479, (B) Res259 and (C) Res186 cells (fingerprint; top left in each panel) or cultured medium (footprint; top right in each panel) under lipoprotein-replete (red) or -deplete (green) conditions. Comparisons between either NM or LPDM in the presence or absence (CTL) of cells are included (bottom left and bottom right in each panel, respectively). Choline phosphate levels within NM and LPDM in the absence of cells are compared in (D). Statistical evaluation was performed using a two-sample *t*-test: ns = not significant; * = $p<0.05$; ** = $p<0.01$; *** = $p<0.001$; **** = $p<0.0001$.

5.4. Lipidomics of adult and paediatric GBM cells cultured under lipoprotein deficient conditions

The metabolomics analysis previously generated suggested evidence of carbon shuttling into lipid synthesis. We therefore performed lipidomics analysis to determine if the removal of lipoproteins as a source of lipids caused alterations to the intracellular lipid profile. OPLS-DA analysis of lipidomic profiles taken in either the positive or negative mode highlighted the lipidomic similarities between KNS42 and SF188 cells and between U87, Res259 and Res186 cells, with UW479 demonstrating a distinct lipid signature (Figure 5.23). For each cell line, samples were segregated according to culture condition (lipoprotein-replete or -deplete). The OPLS-DA model in Figure 5.23A indicated that the classes weakly delineated the variation in the data, with R2Y and Q2 values of 0.533 and 0.343, respectively. The strength of the OPLS-DA model in the negative mode was moderate, with R2Y and Q2 values of 0.884 and 0.656, respectively. Classifying samples according to culture condition alone generated very strong OPLS-DA models with goodness of prediction (Q2) values of 0.939 and 0.925, respectively (Figure 5.24).

Despite identification of thousands of lipid ion species, putative identifications for just over 300 lipid species were obtained using LipidSearch due to the inherent complexity of lipid structures. Different grades of identification were obtained for lipids based on the confidence of lipid class and fatty acid structure. Lipids with grade C identification and above as well as significant fold change (>1.50 or <0.67) were grouped into lipid classes to determine the major lipid species altered under lipoprotein deficient conditions (Figure 5.25 and Figure 5.26). Cell-line specific responses were observed, including the reduction of several triglycerides and a few diacylglycerol species in KNS42, SF188, and UW479 (Figure 5.25B and C; Figure 5.26A), implicating a lipid droplet response to lipoprotein deprivation in pHGG cells. Interestingly, triglycerides were increased in U87, Res259, and Res186 cells (Figure 5.25A; Figure 5.26B and C), indicating that lipid droplet dynamics in aGBM and paediatric LGG may differ in comparison to the pHGG cell lines. A number of lysophosphatidylcholine

species, which have been demonstrated previously to be utilised as an external source of lipids by cancer cells, were reduced across all cell lines (Figure 5.25 and Figure 5.26). Consistent with the CDP-choline findings from the metabolomics analysis, several phosphatidylcholine species were increased under lipoprotein deficient conditions (Figure 5.25 and Figure 5.26). This was also largely replicated by other membrane lipids, including phosphatidylethanolamine and phosphatidylglycerol to a lesser extent (Figure 5.25 and Figure 5.26). A small number of phosphatidylserine and sphingomyelin species were also altered, but not with a consistent pattern across all cell lines (Figure 5.25 and Figure 5.26). Differences in the direction of change of lipid species may reflect compartment-specific perturbation resulting from lipoprotein deprivation. Increased levels of specific phosphatidylcholine, -ethanolamine, and -serine species could be a response to a change in membrane dynamics, and may be a downstream response to stress within the ER, the initial site of phospholipid synthesis. In contrast, the observed reduction in several triglyceride in KNS42 and SF188 cells support a hypothesis of altered lipid droplet dynamics due to lipoprotein deprivation, possibly due to an induction in fatty acid oxidation processes to maintain ATP levels.

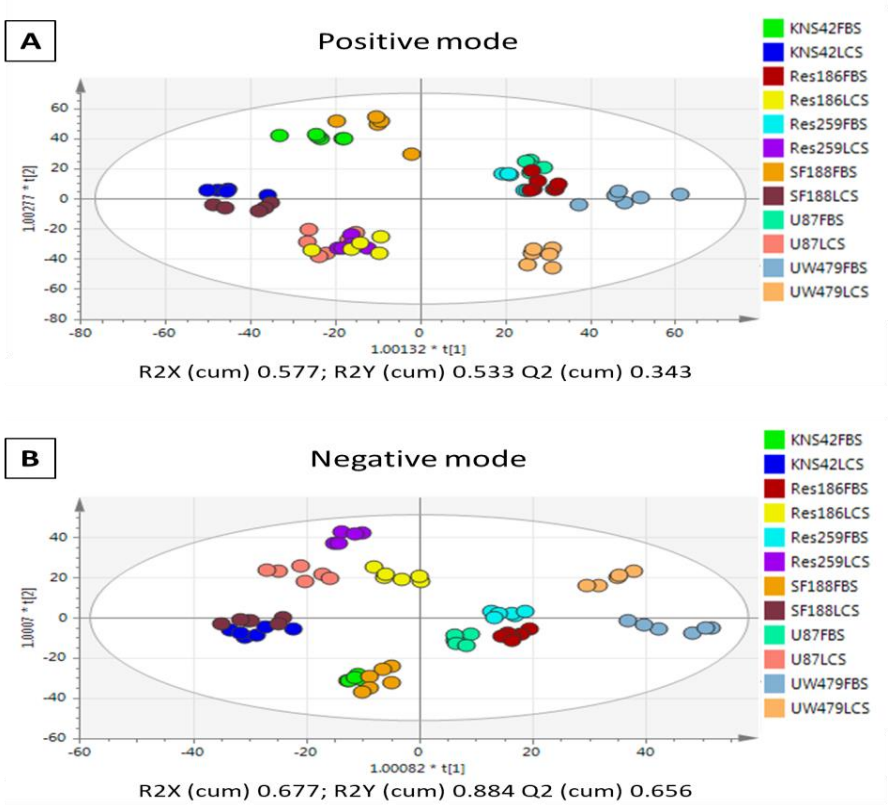

Figure 5.23. OPLS-DA of lipidomic profiles from adult and paediatric glioma cells classified according to cell line and culture conditions. Glioma cells cultured under lipoprotein-replete or -deplete conditions are indicated by the suffixes FBS and LCS, respectively. OPLS-DA was performed on lipidomics data obtained in the positive (A) and negative (B) mode.

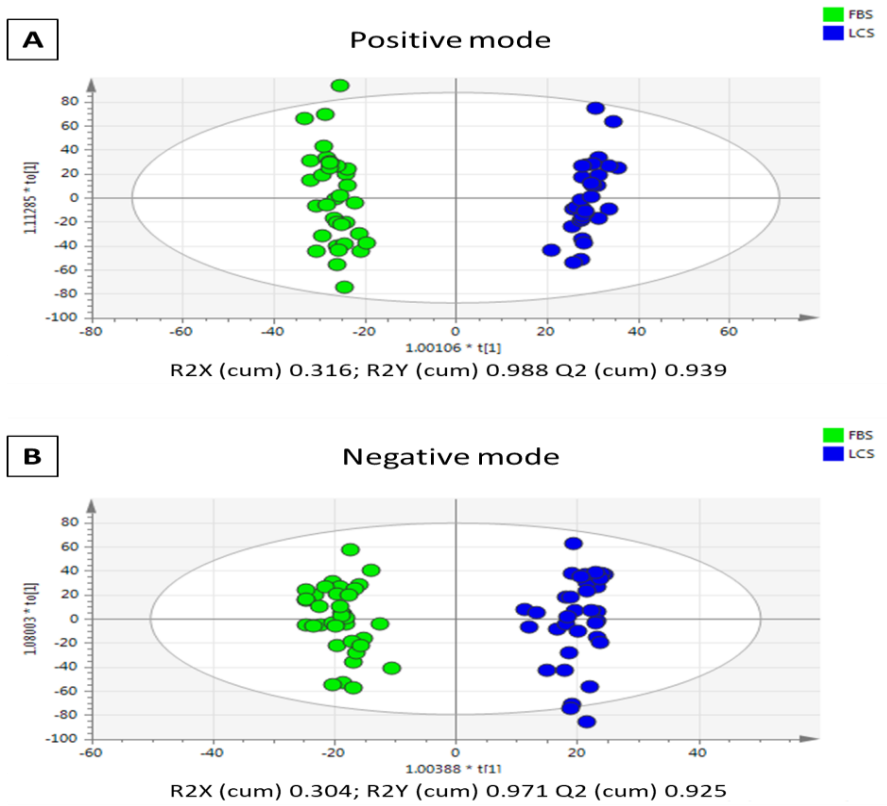

Figure 5.24. OPLS-DA of lipidomic profiles from adult and paediatric glioma cells classified according to culture condition only. Glioma cells were cultured under lipoprotein-replete (FBS; green) or -deplete conditions (LCS; blue). OPLS-DA was performed on lipidomics data obtained in the positive (A) and negative (B) mode.

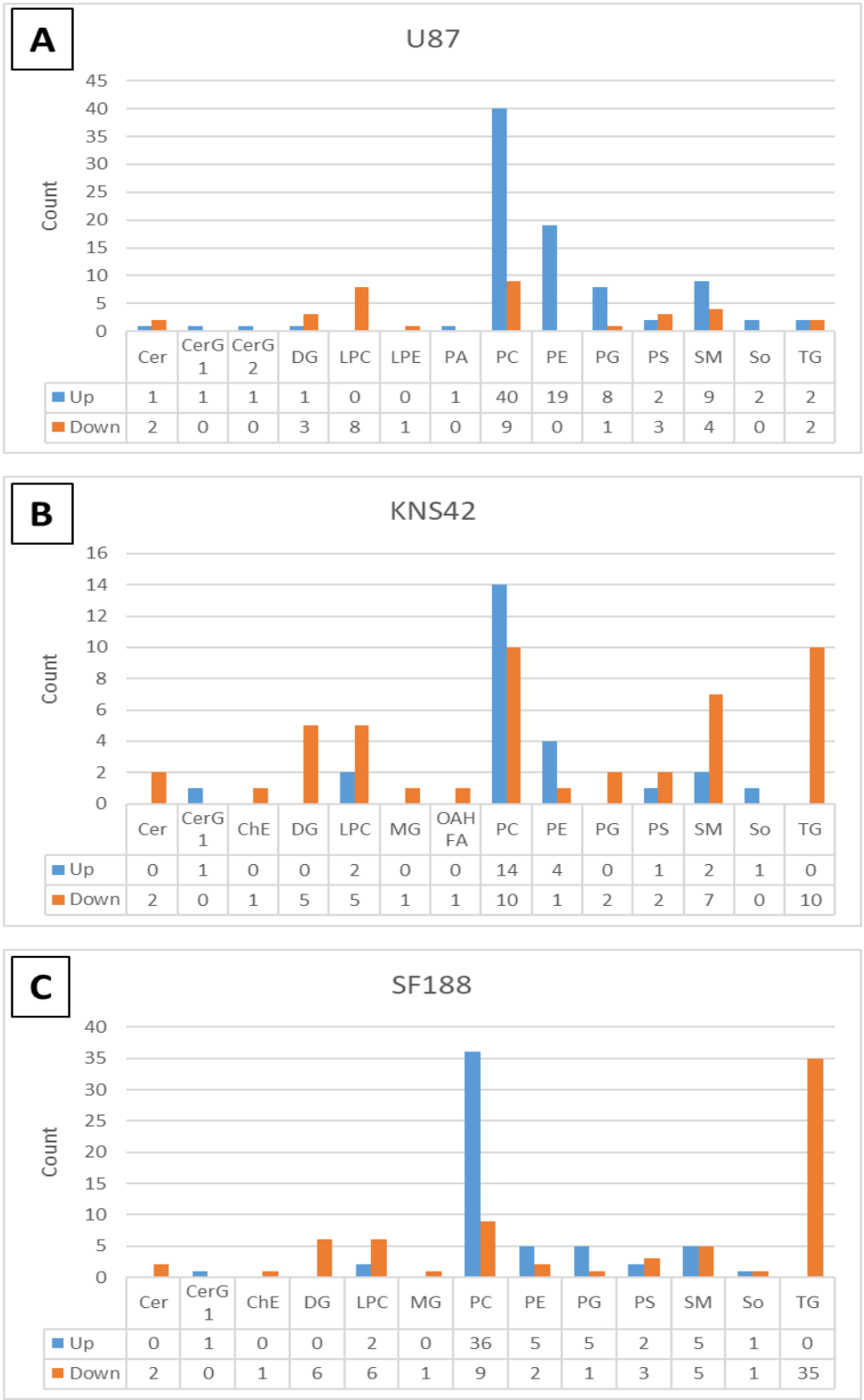

Figure 5.25. Lipid classes of significantly differentially abundant lipids in adult and paediatric GBM cells cultured under lipoprotein - deplete conditions. The number of each lipid species increased or decreased in abundance under lipoprotein deficient conditions is displayed in blue and orange, respectively. Abbreviations: Cer – ceramide; DG – diacylglycerol; LPC – lysophosphatidylcholine; LPE – lysophosphatidyl-ethanolamine; PA – phosphatidic acid; PC – phosphatidylcholine; PE – phosphatidylethanolamine; PG – phosphatidylglycerol; PS – phosphatidyl-serine; SM – sphingomyelin; So – sphingosine; TG – triglyceride.

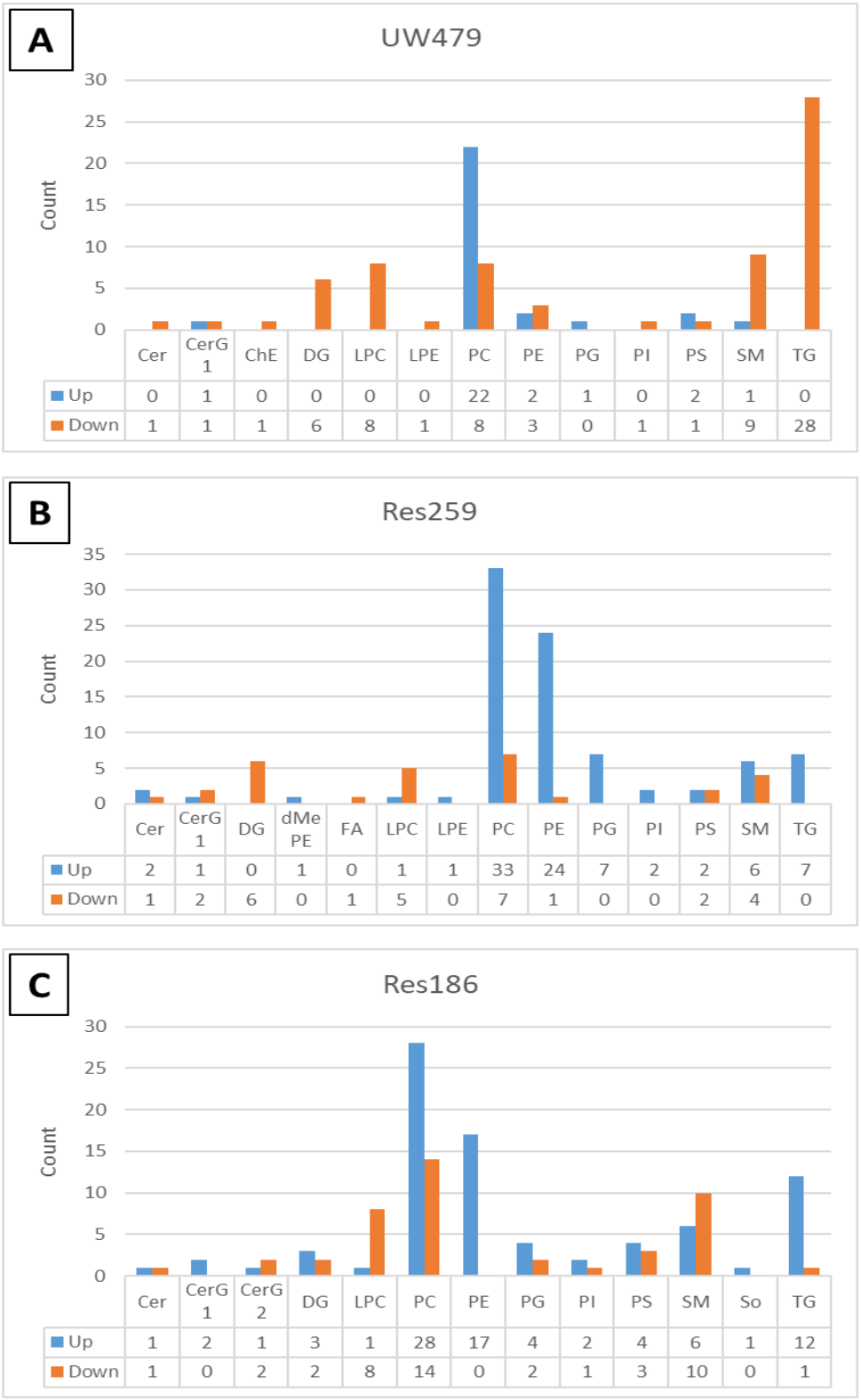

Figure 5.26. Lipid classes of significantly differentially abundant lipids in paediatric glioma cells cultured under lipoprotein -deplete conditions. The number of each lipid species increased or decreased in abundance under lipoprotein deficient conditions is displayed in blue and orange, respectively. Abbreviations: Cer – ceramide; DG – diacylglycerol; LPC – lysophosphatidylcholine; LPE – lysophosphatidylethanolamine; PA – phosphatidic acid; PC – phosphatidylcholine; PE – phosphatidyl-ethanolamine; PG – phosphatidylglycerol; PS – phosphatidyl-serine; SM – sphingomyelin; So – sphingosine; TG – triglyceride.

5.5. Cholesterol levels in adult and paediatric GBM cells cultured under lipoprotein deficient conditions

The findings from the metabolomics and lipidomics analysis demonstrated evidence of metabolic perturbations within central carbon metabolism as well as lipid synthesis. Following the findings from the transcriptomics analysis reported previously in chapter 2 relating to the upregulation of several genes involved in cholesterol regulation and synthesis, we hypothesised that removing lipoproteins from the growth medium has a detrimental impact on cellular cholesterol content. Cellular cholesterol is either in free form or esterified for storage within lipid droplets. We performed an assay to measure total cholesterol and cholesterol ester levels using the Amplex Red assay. In all glioma cell lines, the total cholesterol levels were significantly reduced upon lipoprotein starvation (Figure 5.27A and B). Total cholesterol levels encompasses both the free cholesterol and cholesterol in esterified form. Free cholesterol levels were significantly reduced only in the KNS42 and Res186 cell lines (Figure 5.27C and D). Calculating the change in cholesterol ester levels between lipoprotein-replete and -deplete conditions revealed a significant reduction in all glioma cell lines (Figure 5.27E and F). The change in total cholesterol was largely determined by the cholesterol ester component, with the exception of the Res186 cell line which demonstrated a larger reduction of free cholesterol compared to cholesterol in esterified form (Figure 5.27). These results supported our hypothesis that the removal of lipoproteins leads to depletion of total cholesterol and is suggestive of altered lipid droplet dynamics.

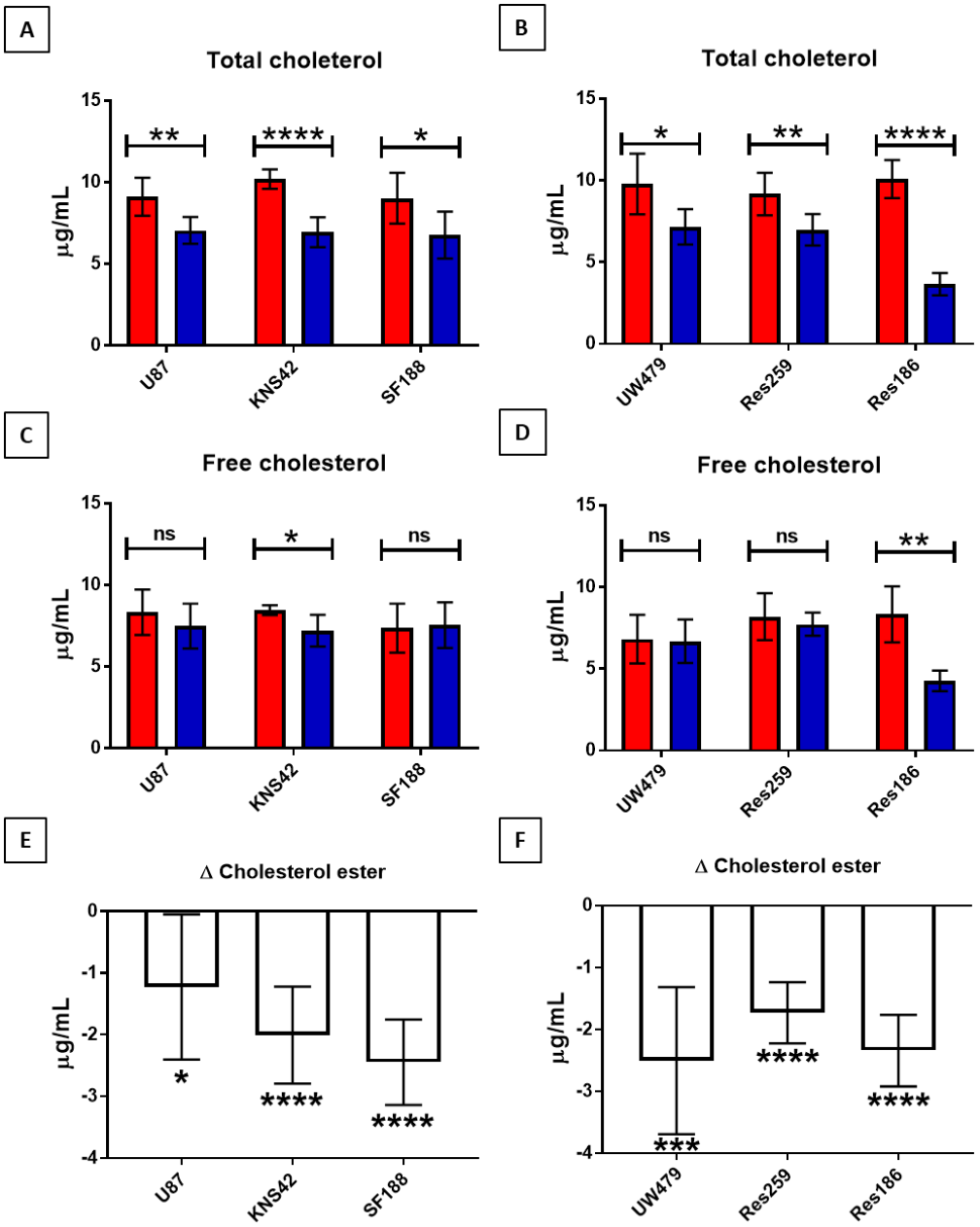

Figure 5.27. Change in total cholesterol, free cholesterol and cholesterol ester levels in adult and paediatric glioma cells cultured under lipoprotein-deplete conditions. (A) Total cholesterol levels in U87, KNS42 and SF188 cells were measured under lipoprotein-replete (red) and -deplete (blue) conditions. (B) Total cholesterol levels in UW479, Res259, and Res186 cells. (C) Free cholesterol levels in in U87, KNS42 and SF188 cells. (D) Free cholesterol levels in UW479, Res259, and Res186 cells. (E) Change in cholesterol ester levels between lipoprotein-replete and -deplete conditions in U87, KNS42, and SF188 cells. (F) Change in cholesterol ester levels between lipoprotein-replete and -deplete conditions in UW479, Res259, and Res186 cells. Total and free cholesterol levels were measured using the Amplex Red assay at emission wavelength of 590 nm. Results are the mean ± SD for n=6 independent replicates. Statistical evaluation was performed using a *t*-test: ns = not significant; * = $p<0.05$; ** = $p<0.01$; *** = $p<0.001$; **** = $p<0.0001$.

5.6. Chapter discussion

We previously showed that the culture of both adult and paediatric glioma cells in acute lipoprotein-deficient conditions reduced growth rates with concordant effects on cell cycle. Given the lipid and sterol constituents that make up lipoproteins, we hypothesised that their removal from the growth medium would alter the cellular metabolome and lipidome to account for the metabolic and proliferative deficiency. *De novo* synthesis of fatty acids is mediated via the shuttling of acetyl-CoA carbon units derived from citrate of the TCA cycle. Reduced levels of succinate were consistently observed across all cell lines with the exception of SF188, which demonstrated reduced malate levels. Cells overexpressing MYC demonstrate altered metabolomic profiles due to direct and indirect regulation of metabolic transcripts by MYC (Dang, Le and Gao, 2009). These results are suggestive of reduced flux within the later stages of the TCA cycle. A general trend in higher levels of citrate was observed across all cell lines, which was significant for the KNS42 cell line. However, it is not possible to make the assertion that citrate levels are being maintained to supplement lipid synthesis. Direct analysis of lipid synthesis rates would be required to determine the validity of this assertion. Considering the reduced levels of succinate, it would be consistent with known metabolic responses that glutamine would mediate TCA cycle anapleurosis via conversion of its downstream product glutamate into αKG. Instead, levels of glutamine and glutamate were either unchanged or increased. This suggests that glutamine does not play a significant role in mediating the metabolic stress response to lipoprotein deficiency in the glioma lines studied here, despite previously being shown to undergo reductive carboxylation to supplement lipid synthesis in cells with dysfunctional mitochondria or exposed to hypoxic conditions (Metallo *et al.*, 2011; Mullen *et al.*, 2011).

The demonstration of reduced levels of succinate hint at dysfunctional oxidative phosphorylation under lipoprotein conditions. However, ATP levels were not significantly altered apart from an increase in the U87 cell line. Lipoprotein-deprived U87 cells demonstrated reduced glycolytic intermediates,

including phosphoenolpyruvate, which might indicate increased glycolysis leading to higher lactate levels. It was not particularly evident from the other cell lines that glycolysis was induced under lipoprotein deprived conditions. However, pyruvate levels were consistently reduced indicating either increased shuttling into the TCA cycle or reduced cycling from malate. Apart from ATP, levels of the energetic cofactors NAD, NADH and NADPH were largely unaltered with only minimal fold changes between NM and LPDM. NAPDH is an essential cofactor for lipid synthesis. Therefore, the unaltered levels of NADPH provided evidence against induced *de novo* synthesis following metabolic stress. This is contradictory to increased levels of CDP-choline and decreased choline levels that are suggestive of phosphatidylcholine biosynthesis. Given the potential alterations to glycolysis and TCA cycle, it was surprising that ATP and NADH levels were unaltered. Perhaps mediating this homeostatic state is activity within the proline biosynthesis pathway. Previous research has demonstrated the importance of the proline biosynthesis pathway to the maintenance of cancer cell survival by ensuring recycling between NAD(P) and NAD(P)H (Liu *et al.*, 2015). Most cell lines demonstrated increased proline levels accompanied by increased levels of its immediate precursor metabolite, P5C, within KNS42 and SF188 pGBM cells. In all cell lines, removal of lipoproteins resulted in a significantly higher release of proline into LPDM compared to NM. This is despite significantly lower levels of GSA, which spontaneously dehydrates into P5C. In plants, osmotic stress leads to proline accumulation (Miller *et al.*, 2009); possibly indicative of deregulated regulation of osmolarity was the observation of reduced taurine levels across all cell lines. Taurine maintains osmolarity, is a neuroprotective antioxidant, and is an inhibitory neurotransmitter (Wu and Prentice, 2010). This may also partially explain the relative increase in several amino acids to maintain osmolarity. Taurine also has a role stimulating lipoprotein uptake via LDLR (Stephan, Lindsey and Hayes, 1987; Murakami *et al.*, 2002) and regulates lipid and sterol levels in HepG2 cells (Yanagita *et al.*, 2008), and can regulate neuroinflammatory processes (Agca *et al.*, 2014; Gebara *et al.*, 2015). Endogenous synthesis of taurine is mediated by astrocytes (Choe, Olson and Bourque, 2012). However, further research will be required

to identify whether taurine biosynthesis is reduced following lipoprotein deprivation or that LPDM contains reduced amounts of taurine.

Lipidomic analysis highlighted differences between cell lines cultured under lipoprotein replete or deplete conditions. The lipidomic profile of KNS42 cells was similar to SF188 cells, whereas U87, Res259 and Res186 clustered separately, indicating a pGBM-specific effect. UW479 demonstrated a unique profile that was separated from the other cell lines. This might also underlie different genetic control of metabolism across cell lines. Identifying the class to which differentially abundant lipids belong to was concordant with the groupings identified from the OPLS-DA analysis. Specifically, KNS42, SF188 and UW479 cells were characterised by a decrease in several triglycerides and diacyglycerols upon depletion of lipoproteins from the growth medium, indicative of a pHGG-specific phenomena. A possible explanation for these observations is the mobilisation of lipid droplets leading to the conversion of triglyceride stores into diacyglycerol which are utilised to synthesise phospholipids. This is consistent with the large number of phosphatidylcholine and to a lesser extent phosphatidylethanolamine species that are upregulated under lipoprotein deficient conditions as well as the increase in CDP-choline as observed from the metabolomics analysis. However, evidence from the transcriptomics analysis as well as the identification of a significant reduction in a particular cholesterol ester species in KNS42 and SF188 cells suggested dysregulated cholesterol metabolism as a consequence of lipoprotein deprivation. Assessment of cholesterol levels using the Amplex red assay revealed a general reduction in total cholesterol that was significant in all paediatric glioma cell lines. This was mainly attributed to a reduction in cholesterol esters, apart from Res186 cells in which the effect on free cholesterol levels was greater compared to the esterified form. These results support our hypothesis that the removal of lipoproteins leads to dysregulated cholesterol metabolism, consistent with the potential role of lipoproteins as distributers of cholesterol and lipid species within the CNS.

LC-MS-based metabolite profiling enabled widespread coverage of the metabolome, detecting 604 metabolites. However, some metabolites from key pathways were not identified, making biological interpretation of peak intensity differences difficult. Comparative methods of analysing the metabolome such as ^{1}H-NMR can distinguish metabolic subtypes within GBM cell lines (Cuperlovic-Culf *et al.*, 2012) and demonstration of preferential metabolism of glucose and acetate in the neuronal and glial compartments, respectively (Deelchand *et al.*, 2009). In another study, evidence of β-oxidation was seen upon [2,4,6,8-$^{13}C_4$]octanoate administration in mice specific to the astrocytic compartment and accounted for 20% of oxidative metabolism in the brain (Ebert, Haller and Walton, 2003). However, these methods cover a smaller proportion of the metabolome but do identify metabolites from key pathways within central carbon metabolism. Complementing NMR techniques is the use of ^{13}C-labelled isotopes to conduct metabolic flux analysis (MFA), which is amenable for the study of cells growing at different proliferation rates since metabolic fluxes (units of nmol/10^6 cells/hr) are calculated using the growth rate parameter and external rates – the uptake of nutrients and secretion of metabolic byproducts – inferred through metabolomic footprinting (Antoniewicz, 2018). Utilisation of ^{13}C-MFA would have accounted for the different growth rates observed between GBM cell cultured under lipoprotein-replete and -deplete conditions, as well as informing on metabolic fluxes through glycolysis and the TCA cycle in response to lipoprotein starvation. Nevertheless, we have demonstrated that LC-MS analysis of adult and paediatric glioma cell lines has generated evidence of altered metabolic pathways under lipoprotein-deplete conditions.

Chapter 6

Evaluating the therapeutic potential of LXR agonists in adult and paediatric GBM cells

6. Evaluating the therapeutic potential of LXR agonists in adult and paediatric GBM cells

The culture of adult and paediatric GBM cells under lipoprotein-deplete conditions was shown previously to reduce total cholesterol levels, predominantly of the esterified form of cholesterol. Associated with reduced total cholesterol levels was the increased expression of genes associated with cholesterol regulation and synthesis, including *INSIG1*, *INSIG2*, *HMGCR*, *HMGCS1*, and *MVK*. These results in addition to the reduced growth rate following prolonged lipoprotein deprivation indicate that cholesterol regulation and metabolism represents a metabolic vulnerability within adult and paediatric GBM cells. Pharmacological methods of depriving cells of lipoproteins can be achieved through the use of LXR agonists, which were initially developed to reduce cardiovascular diseases (Lin and Gustafsson, 2015). LXR agonists prevent lipoprotein uptake by inducing the expression of *MYLIP* (which encodes IDOL), an E3 ubiquitin ligase that mediates the degradation of LDLR (Zelcer *et al.*, 2009) and VLDLR (Hong *et al.*, 2010). This prevents cells from utilising external sources of cholesterol pools. However, intracellular cholesterol levels are further depleted upon LXR agonist treatment due to upregulation of cholesterol exporters at the plasma membrane, including ABCA1 and ABCG1 (Bovenga, Sabbà and Moschetta, 2015). The therapeutic potential of LXR agonists has already been demonstrated in U87 cells expressing the EGFRvIII mutant variant within in vitro and in vivo models (D. Guo *et al.*, 2011; Villa *et al.*, 2016). We therefore endeavoured to further characterise the therapeutic action of LXR agonists within adult U87 cells and hypothesised that treatment of pGBM cells would similarly result in reduced cellular viability. Two LXR agonists were evaluated: 1) GW3965, a full LXRα/full LXRβ agonist; and 2) LXR-623, a partial LXRα/full LXRβ agonist.

6.1. LXR agonists reduce cellular viability in adult and paediatric GBM cells

In order to evaluate the potency of the LXR agonists GW3965 and LXR-623, dose-response curves were determined for the adult U87 and the paediatric

KNS42 and SF188 cell lines. Cell viability with respect to vehicle (DMSO) alone was chosen as the response factor. Sigmoidal curves were obtained for both drugs in all cell lines (Figure 6.1). In the U87 cell line, 72 hr of GW3965 treatment reduced viability at concentrations of 2.5 µM and above with an IC_{50} value of 8.30 µM (Figure 6.1A). Concentrations above 5 µM reduced viability in KNS42 and SF188 cells with IC_{50} values of 12.96 and 12.29, respectively (Figure 6.1A). For LXR-623, concentrations above 1 µM reduced U87 viability with an IC_{50} value of 8.50 µM (Figure 6.1B). Drug responses in KNS42 and SF188 were observed at concentrations above 10 and 5 µM, with IC_{50} values of 27.51 and 22.49 µM, respectively (Figure 6.1B). These results indicate that paediatric KNS42 and SF188 cells, whilst comparably sensitive within a micromolar range, are relatively less susceptible to LXR agonist treatment compared to adult U87 cells.

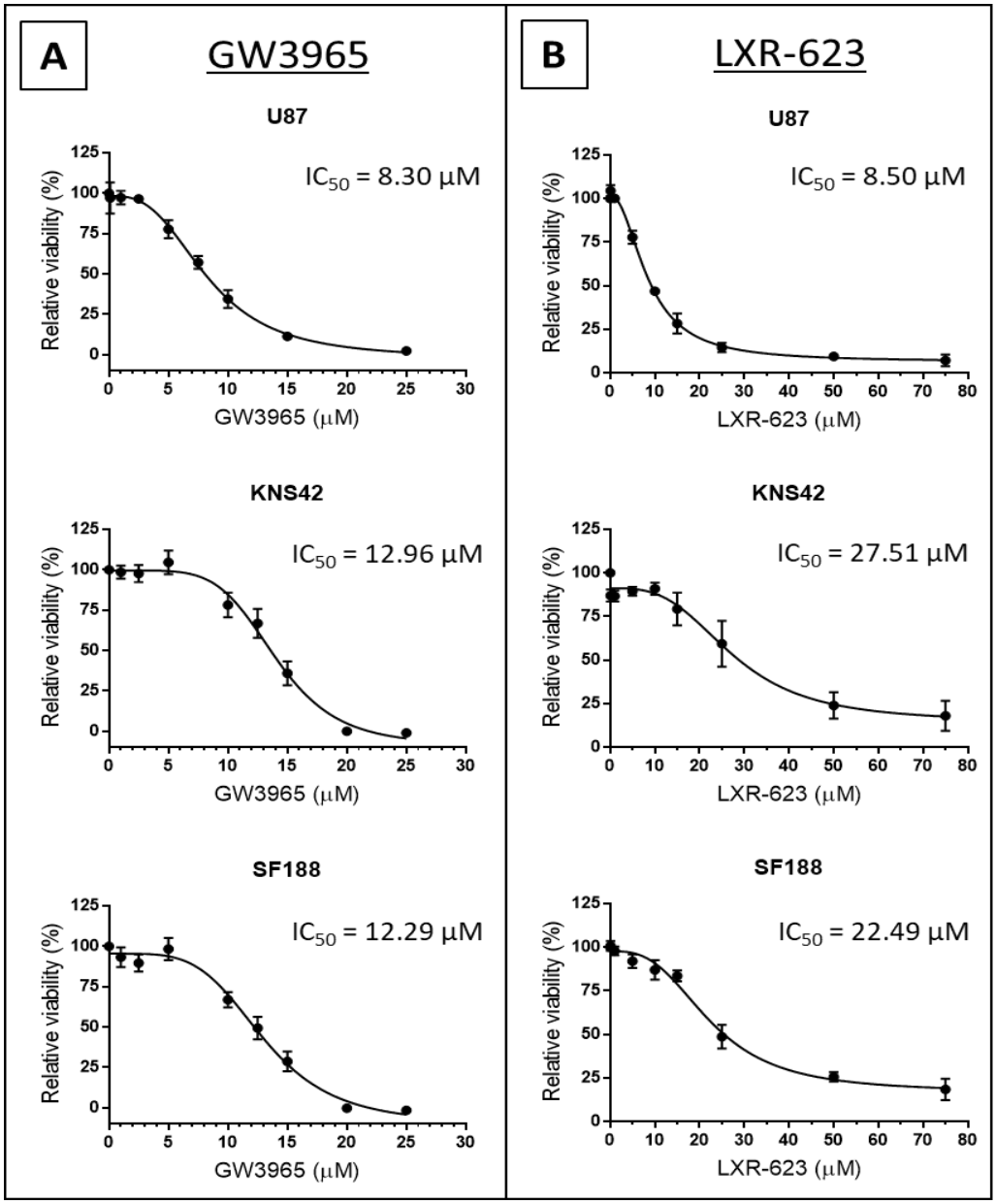

Figure 6.1. Determination of IC_{50} values for GW3965 and LXR-623 in adult and paediatric GBM cells. Dose response curves for U87, KNS42 and SF188 following exposure to either GW3965 (A) or LXR-623 (B) for 72 hrs. Cell viability assessment was performed using the PrestoBlue assay and expressed as a percentage of the vehicle only control. Error bars represent the SEM of n=3 independent experiments conducted in triplicate.

To explore the effect of LXR agonist treatment over the 72-hr period, cell viability was measured every 24 hrs at three different concentrations encompassing the IC_{50} value for each LXR agonist and across all three cell lines. For GW3965, these concentrations were 5, 10 and 20 µM. For LXR-623, these concentrations were 7.5, 15 and 30 µM. Large differences in U87 viability were

observed from 24 hrs onwards at GW3965 concentrations of 10 and 20 µM (Figure 6.2A). For KNS42 and SF188, 10 µM GW3965 treatment did not change viability compared to vehicle only, requiring concentrations of 20 µM to reduce viability after 24 hrs (Figure 6.2B and C). LXR-632 concentrations of 7.5, 15 and 30 µM reduced U87 viability compared to vehicle only after 48 hrs, whereas 15 and 30 µM LXR-623 showed large differences in viability after 24 hrs (Figure 6.3A). For both pGBM cell lines, changes in cellular viability were observed after 24 hrs at concentrations of 15 and 30 µM for KNS42 and 30 µM for SF188 cells (Figure 6.3B and C). These results indicate that the detrimental effects of LXR agonist treatment manifest as reduced cellular viability following at least 48 hrs exposure.

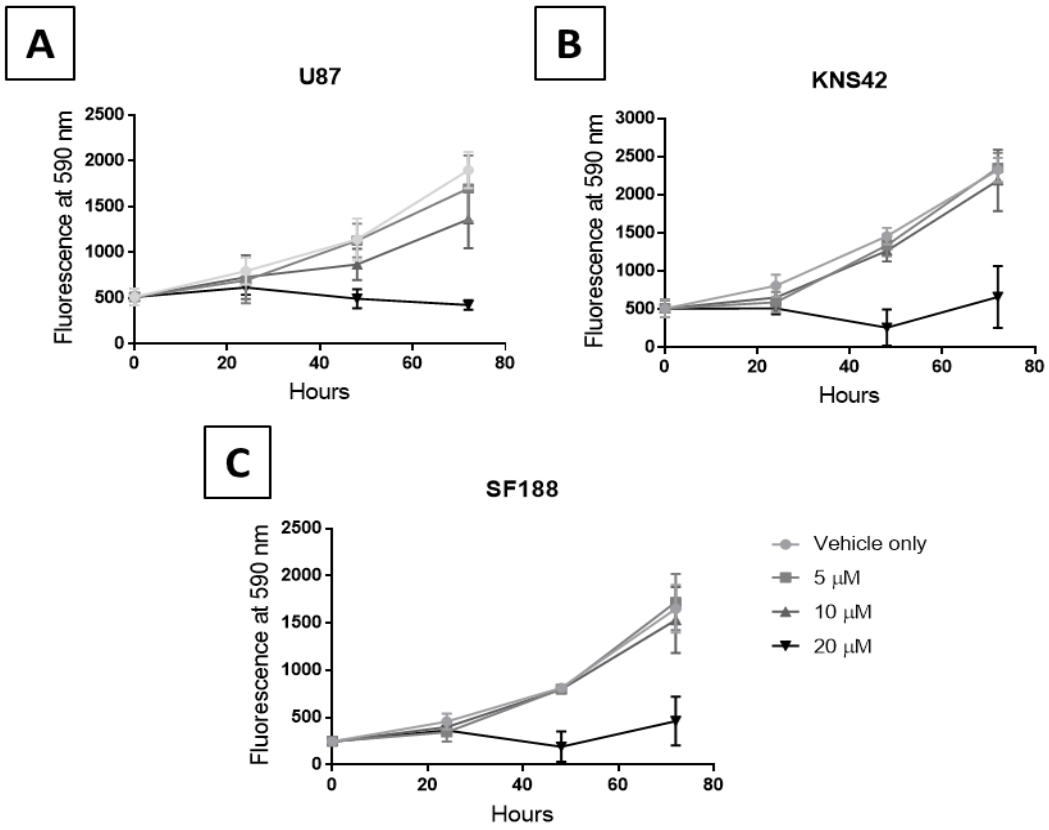

Figure 6.2. Cell viability assessment of adult and paediatric GBM cells exposed to GW3965. U87 (A), KNS42 (B) and SF188 (C) cells were treated over a 72-hr period. Cell viability was measured using the PrestoBlue assay, measured at a wavelength of 590 nm. Error bars represent the SEM of n=3 independent experiments conducted in triplicate.

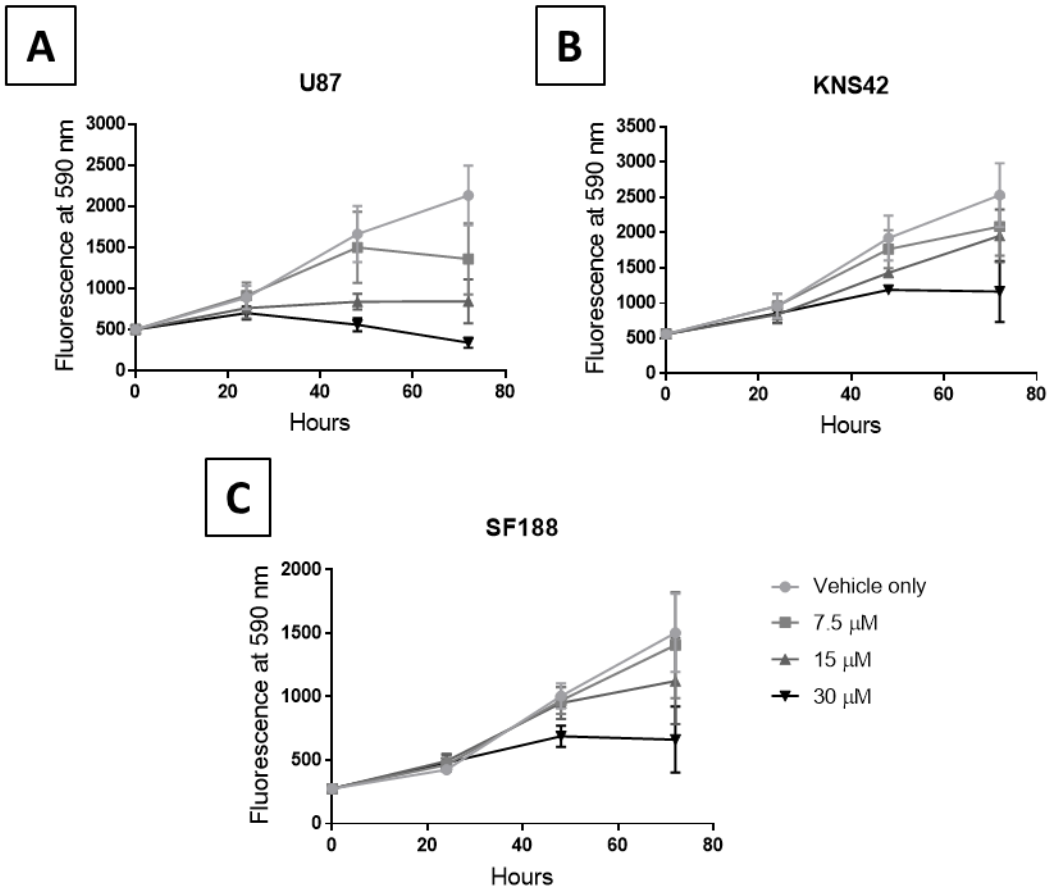

Figure 6.3. Cell viability assessment of adult and paediatric GBM cells exposed to LXR-623. U87 (A), KNS42 (B) and SF188 (C) cells were treated over a 72-hr period. Cell viability was measured using the PrestoBlue assay, measured at a wavelength of 590 nm. Error bars represent the SEM of n=3 independent experiments conducted in triplicate.

According to the literature, ligand-mediated activation of LXRs increases the expression of genes, such as *ABCA1* and *ABCG1*, leading to reduced intracellular cholesterol levels (Lin and Gustafsson, 2015). We therefore investigated whether the addition of exogenous cholesterol would rescue the reduction in cellular viability. In GW3965-treated U87 cells, there was a trend in increased viability in the presence of increasing concentrations of MβCD-cholesterol up to 10 µM (Figure 6.4A). Similar observations were made for U87 cells treated with LXR-623, reaching significance for 5 to 10 µM MβCD-cholesterol (Figure 6.4B). In contrast, addition of MβCD-cholesterol did not rescue the cellular viability of KNS42 or SF188 cells treated with either GW3965 or LXR-623 (Figure 6.4). Interestingly, in all cell lines and under both treatments, the addition of 20

µM MβCD-cholesterol to the growth medium caused a significant reduction in cellular viability (Figure 6.4). These results highlight the essential requirement for cholesterol homeostasis in the proper functioning of cells, as well as differences between adult and paediatric GBM cells in terms of processing exogenous cholesterol.

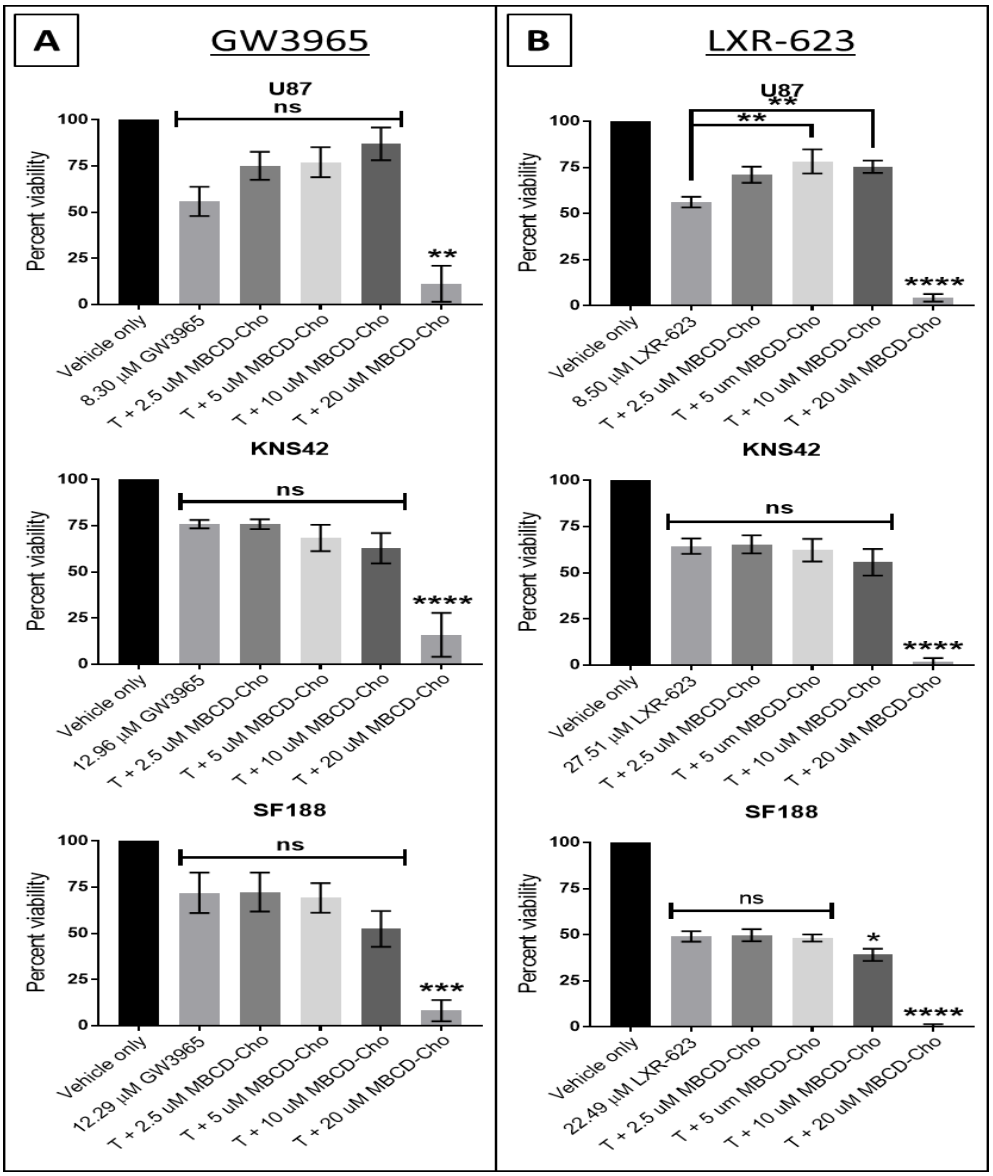

Figure 6.4. Rescue of LXR agonist-treated adult and paediatric GBM cells with exogenous cholesterol. U87, KNS42 and SF188 cells were exposed to IC_{50} concentrations of either GW3965 (A) or LXR-623 (B) for 72 hr. Various concentrations of water-soluble MβCD-cholesterol were added in combination with the treatment (T). Cell viability was measured using the PrestoBlue assay, measured at a wavelength of 590 nm, and expressed as a percentage of the vehicle only control. Error bars represent the SEM of n=3 independent experiments conducted in triplicate. Statistical *t*-tests were performed relative to the treatment only condition: ns = not significant; * = $p<0.05$; ** = $p<0.01$; *** = $p<0.001$; **** = $p<0.0001$.

6.2. Flow cytometric analysis of LXR agonist treatment

The treatment of adult and paediatric GBM cells with LXR agonists was demonstrated to reduce cellular viability after 72 hr exposure. However, it was not discernible whether the effect on cellular viability was the product of a cytotoxic or cytostatic response. We therefore performed flow cytometric analysis of LXR-treated cell lines to determine if LXR agonist treatment causes cell cycle arrest and/or increases the apoptotic fraction. Previous research in ovarian cancer has demonstrated that LXR agonists induce cell cycle arrest in G0/G1 phase (Rough *et al.*, 2010). We therefore hypothesised that LXR agonist treatment would induce G0/G1 phase cell cycle arrest in U87, KNS42 and SF188 cells. For each LXR agonist, flow cytometric analysis was conducted on cells treated with the respective IC_{50} concentration in addition to a higher concentration shown to reduce viability by 75% based on dose-response curves (Table 6.1).

Table 6.1. Drugs concentrations used in the therapeutic evaluation of LXR agonists.

Cell line	GW3965		LXR-623	
	IC_{50} (µM)	Higher conc. (µM)	IC_{50} (µM)	Higher conc. (µM)
U87	8.30	11.80	8.50	16.80
KNS42	12.96	14.50	27.51	51.00
SF188	12.29	14.40	22.49	49.00

Treatment of U87 cells with the IC_{50} concentration of GW3965 only resulted in a significant reduction of cells within the G2/M phase (Figure 6.5A). In contrast, treatment of U87 cells with 11.8 µM GW3965 caused a significant increase in the percentage of cells in G0/G1 phase and reduced the number of cells in both S and G2/M phases with respect to vehicle only-treated cells (Figure 6.5A). GW3965 at a concentration of 11.8 µM also led to a significant increase in the sub G0 fraction in comparison to cells treated with the IC_{50} concentration (Figure 6.5A). However, the effect was minimal with only a ~5% increase. Treatment of KNS42 and SF188 cells with respective IC_{50} concentrations of GW3965 did not induce significant alterations to any cell cycle phase (Figure 6.5B and C). Higher concentrations of GW3965 caused a significant increase in the sub G0 fraction in KNS42 cells and led to a reduced percentage of cells in the S and G2/M phases in SF188 cells (Figure 6.5B and C). This equated to a ~15% and ~10% increase in the sub G0 fraction in KNS42 and SF188 cells, respectively.

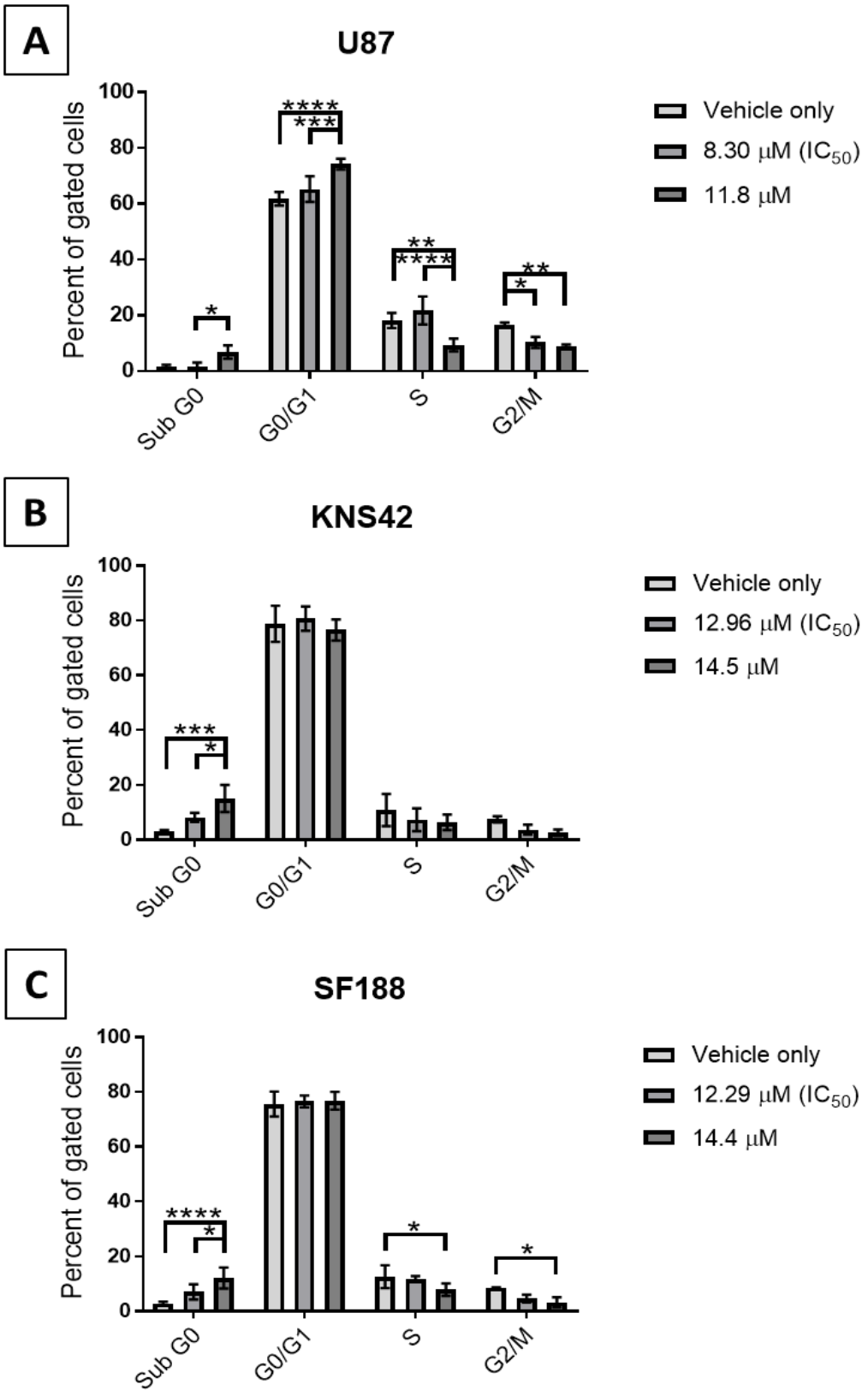

Figure 6.5. Flow cytometric analysis of adult and paediatric GBM cells following treatment with GW3965. U87 (A), KNS42 (B) and SF188 (C) cells were exposed to two concentrations of drug for 72 hr. Error bars represent the SD of at least n=3 experiments. Statistical evaluation was conducted using a two-way ANOVA: ns = not significant; * = $p<0.05$; ** = $p<0.01$; *** = $p<0.001$; **** = $p<0.0001$.

For LXR-623, treatment of U87 cells with either the IC_{50} concentration or 16.8 µM resulted in a significant increase and decrease in the percentages of cells within S and G2/M phases, respectively (Figure 6.6A). In KNS42 and SF188 cells, treatment with either the IC_{50} concentration or ~50 µM caused a significant increase and decrease in the percentages of cells within the sub G0 and G0/G1 phases, respectively (Figure 6.6B and C). The increase in the sub G0 fraction ranged from ~5% at the IC_{50} concentration to ~15% at the higher concentration. The number of cells in S and G2/M phases were unaffected in both pGBM cell lines at either of the LXR-623 concentrations tested (Figure 6.6B and C). The flow cytometric analysis of adult and pGBM cells indicated that LXR-623 caused cell line-specific effects, with a predominantly S phase and G0/G1 phase response in U87 and pGBM cells, respectively. In contrast, GW3965 demonstrated a significant G0/G1 response in U87 cells that was not observed with LXR-623. For both LXR agonists, pGBM cells showed minimal responses in S and G2/M phases apart from significant minimal reductions in GW3965-treated SF188 cells.

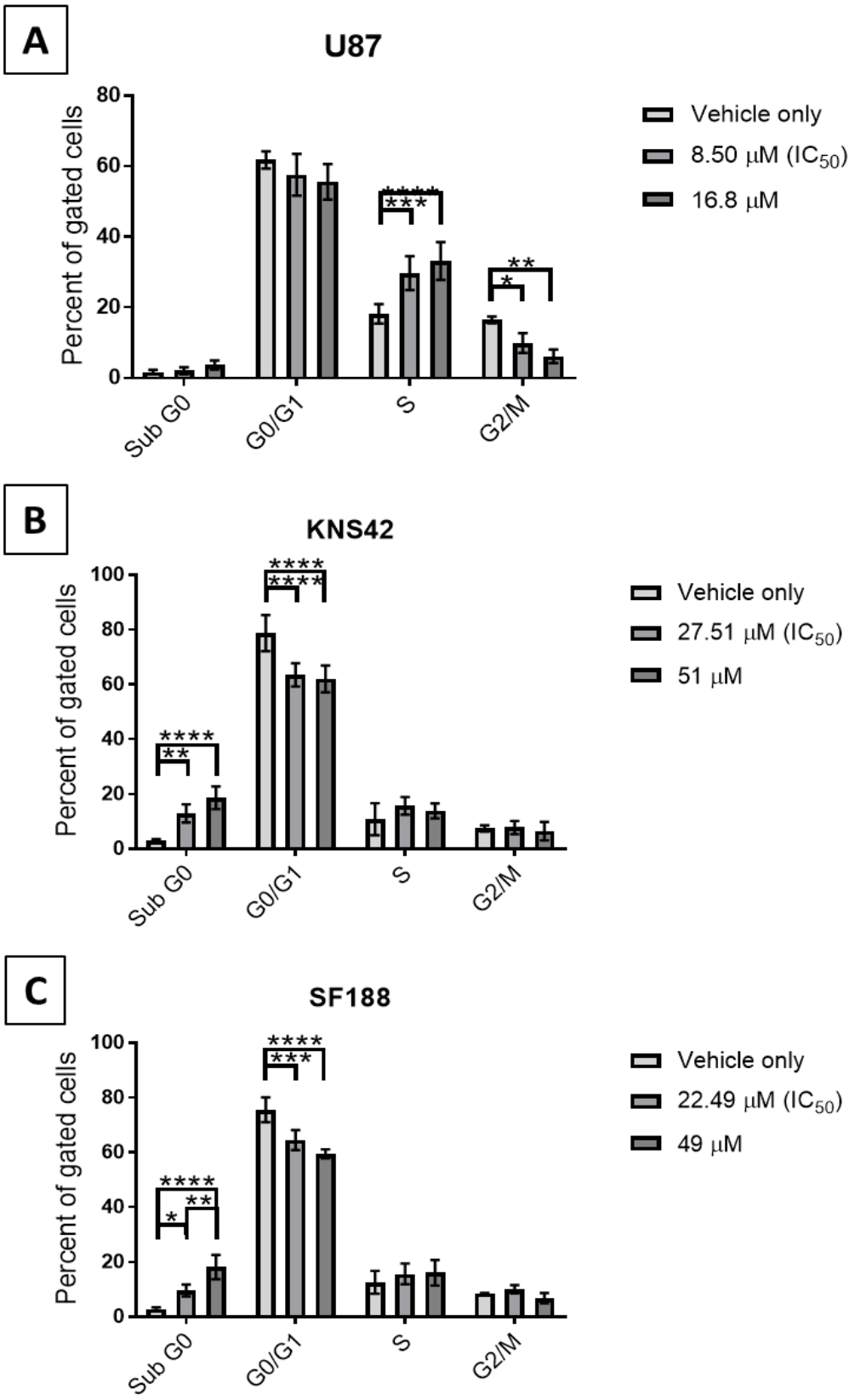

Figure 6.6. Flow cytometric analysis of adult and paediatric GBM cells following treatment with LXR-623. U87 (A), KNS42 (B) and SF188 (C) cells were exposed to two concentrations of drug for 72 hr. Error bars represent the SD of at least n=3 experiments. Statistical evaluation was conducted using a two-way ANOVA: ns = not significant; * = $p<0.05$; ** = $p<0.01$; *** = $p<0.001$; **** = $p<0.0001$.

6.3. Transcriptomic analysis of LXR agonist-treated adult and paediatric GBM cells

Pharmacological activation of LXR activity in adult and paediatric GBM cells has been demonstrated to have a detrimental effect on cellular viability. In U87 cells, the addition of exogenous cholesterol rescued cellular viability indicating that reduced intracellular cholesterol levels was part of the underlying cause of LXR agonist toxicity. However, exogenous cholesterol administration could not rescue KNS42 and SF188 cells treated with LXR agonists. To identify other factors involved in the therapeutic action of LXR agonists, we performed genome-wide gene expression analysis of U87, KNS42 and SF188 cells treated with IC_{50} concentrations of either GW3965 or LXR-623 for 72 hrs. GO analysis of GW3965-treated U87 cells revealed significant enrichment of *regulation of cholesterol biosynthetic processes*, *reverse cholesterol transport* and *phospholipoid homeostasis*, due to upregulation of *ABCA1*, *ABCG1*, *LIPG*, *LSS* and *MVD* (Table 6.2). Increased expression of *FABP3*, *FASN* and *SREBF1* within these gene ontologies also indicated differential regulation of fatty acid processes. Transcriptomics analysis also hinted at a potential mechanism of reduced cellular viability associated with enrichment of genes within the *PERK-mediated unfolded protein response*, *negative regulation of ERK1 and ERK2 cascades*, and *negative regulation of TORC1 signalling* (Table 6.2). In contrast, treatment of U87 cells with LXR-623 enriched GO categories associated with cellular signalling, proliferation and apoptosis (Table 6.3). Notable expression changes included upregulation of *VEGFA*, *MYC* and *NAMPT*, and downregulation of *PDGFRB*. GO analysis of KNS42 and SF188 cells treated with either GW3965 or LXR-623 resulted in the common enrichment of processes associated with *DNA replication*, *cell division* and *cell cycle* (Table 6.4, Table 6.5, Table 6.6 and Table 6.7). Genes of interest that were downregulated included *BUB1*, *AURKB*, *PLK1*, *CCNA2*, *CCNB1*, *CCNB2*, and *CCNE1*, *BMP4* and *SKP2*; upregulated genes included *EREG*, *ASNS*, and *VEGFA*, *DDIT3*, *NUPR1* and *CDKN2B*.

Table 6.2. Gene ontology analysis of significantly differentially expressed genes in GW3965-treated U87 cells.

GO.ID	Term	Annotated	Significant	Expected	classicFisher	classicKS	weight01KS	parentchildFis	Genes
GO:0036499	PERK-mediated unfolded protein response	15	4	0.3	1.90E-04	1.90E-03	3.70E-05	4.06E-02	*ASNS*, *CXCL8*, *DDIT3*, *ATF3*
GO:0071456	cellular response to hypoxia	141	11	2.85	1.30E-04	5.60E-03	4.40E-04	2.84E-03	*STC2*, *VEGFA*, *CA9*, *NDRG1*, *STC1*, *ICAM1*, *RGCC*, *S100B*, *ERO1A*, *PTN*, *EPAS1*
GO:0060712	spongiotrophoblast layer development	7	3	0.14	2.70E-04	5.10E-03	5.13E-03	1.33E-03	*LIF*, *ADM*, *PHLDA2*
GO:0055091	phospholipid homeostasis	7	4	0.14	5.40E-06	6.00E-03	6.05E-03	4.89E-03	*ABCA1*, *ABCG1*, *LIPG*, *FABP3*
GO:0070373	negative regulation of ERK1 and ERK2 cas...	39	5	0.79	1.06E-03	1.06E-02	1.06E-02	1.34E-02	*LIF*, *SPRY1*, *ATF3*, *SPRY2*, *GBP1*
GO:0045540	regulation of cholesterol biosynthetic p...	31	5	0.63	3.60E-04	1.10E-02	1.10E-02	3.40E-01	*SREBF1*, *ABCG1*, *FASN*, *LSS*, *MVD*
GO:1904262	negative regulation of TORC1 signaling	8	3	0.16	4.20E-04	2.20E-02	2.20E-02	3.02E-02	*SESN2*, *SPAAR*, *SESN3*
GO:0032868	response to insulin	151	11	3.05	2.40E-04	2.90E-05	2.34E-02	2.92E-02	*SREBF1*, *SESN2*, *ADM*, *TRIB3*, *NUCKS1*, *INSIG2*, *ICAM1*, *FABP3*, *SESN3*, *LPIN1*, *TNFSF10*
GO:0030324	lung development	103	11	2.08	6.90E-06	4.71E-02	2.79E-02	6.30E-04	*NOG*, *SREBF1*, *LIF*, *PDGFRA*, *VEGFA*, *CHI3L*, *ID1*, *SPRY1*, *PTN*, *SPRY2*, *EPAS1*
GO:0043691	reverse cholesterol transport	9	3	0.18	6.30E-04	4.08E-02	4.08E-02	1.07E-01	*ABCA1*, *ABCG1*, *LIPG*

Statistical evaluation of gene ontology (GO) terms based of the number of significant-to-expected observations using either Fisher's exact test (Fis) or Kolmogorov-Smirnov test (KS). Different algorithms were utilised to take account of the GO hierarchy, including classic, weight01, and parentchild. GO terms were ranked according to *p*-values obtained using the weight01KS algorithm and test. Genes that were upregulated and downregulated following GW3965 exposure for 72 hr are highlighted in red and green, respectively.

Table 6.3. Gene ontology analysis of significantly differentially expressed genes in LXR-623-treated U87 cells.

GO.ID	Term	Annotated	Significant	Expected	classicFisher	classicKS	weight01KS	parentchildFis	Genes
GO:0006915	apoptotic process	1100	103	49.63	8.80E-14	5.60E-08	8.80E-03	1.27E-02	*NOG*, *VEGFA*, *GDF15*, *CSF2*, *ID3*, *ADM*, *CHAC1*, *EDNRB*, *NDRG1*, *ASNS*, *DDIT3*, *TAF9B*, *ID1*, *MT3*, *PPP1R15A*, *CNR1*, *PHLDA2*, *IER3*, *PDGFRB*, *TBX3*, *F3*, *IRS2*, *ICAM1*, *CTH*, *USP53*, *MKNK2*, *MYC*, *KITLG*, *FAM162A*, *TRIB3*
GO:0042127	regulation of cell proliferation	903	92	40.74	1.80E-14	8.90E-07	1.93E-02	2.70E-11	*NOG*, *VEGFA*, *CSF2*, *CXCL8*, *ADM*, *EDNRB*, *PDGFRA*, *NDRG1*, *LIF*, *ID1*, *E2F7*, *PHLDA2*, *PDGFRB*, *TBX3*, *MXI1*, *F3*, *IRS2*, *ADAMTS1*, *MYC*, *KITLG*, *NAMPT*, *TXNIP*, *ARHGEF2*, *CEBPB*, *SPRY2*, *HMOX1*, *S100B*, *ASPM*, *PDE5A*
GO:0008283	cell proliferation	1124	107	50.71	7.70E-15	2.70E-08	2.02E-02	7.70E-15	*NOG*, *VEGFA*, *CSF2*, *CXCL8*, *ADM*, *EDNRB*, *PDGFRA*, *NDRG1*, *LIF*, *LGR4*, *ID1*, *NDP*, *MT3*, *E2F7*, *PHLDA2*, *PDGFRB*, *TBX3*, *MXI1*, *F3*, *IRS2*, *ADAMTS1*, *MYC*, *KITLG*, *NAMPT*, *TXNIP*, *ARHGEF2*, *CEBPB*, *SPRY2*, *HMOX1*, *S100B*
GO:0042325	regulation of phosphorylation	843	85	38.03	4.20E-13	2.50E-05	3.93E-02	4.90E-04	*NOG*, *VEGFA*, *GDF15*, *CSF2*, *EDNRB*, *PDGFRA*, *LIF*, *ID1*, *MT3*, *DUSP5*, *PIK3R3*, *PPP1R15A*, *SESN2*, *SRPX2*, *PDGFRB*, *SPINK1*, *IRS2*, *SEMA7A*, *ICAM1*, *MYC*, *KITLG*, *TRIB3*, *ARHGEF2*, *SPRY2*, *GPRC5A*, *PDE5A*, *DDIT4*, *TNFRSF10B*, CENPE, *SPRY4*
GO:0035556	intracellular signal transduction	1501	133	67.72	3.90E-16	6.90E-07	1.53E-01	7.30E-06	*ABCA1*, *VEGFA*, *GDF15*, *CSF2*, *CXCL8*, *ADM*, *CHAC1*, *EDNRB*, *PDGFRA*, *NDRG1*, *SESN3*, *LIF*, *RND3*, *DDIT3*, *TAF9B*, *ID1*, *LPAR4*, *EIF4EBP1*, *MT3*, *E2F7*, *DUSP5*, *PPP1R15A*, *SESN2*, *IER3*, *PDGFRB*, *SPAAR*, *SPINK1*, *F3*, *IRS2*, *SEMA7A*

Statistical evaluation of gene ontology (GO) terms based of the number of significant-to-expected observations using either Fisher's exact test (Fis) or Kolmogorov-Smirnov test (KS). Different algorithms were utilised to take account of the GO hierarchy, including classic, weight01, and parentchild. GO terms were ranked according to *p*-values obtained using the weight01KS algorithm and test. Genes that were upregulated and downregulated following LXR-623 exposure for 72 hr are highlighted in red and green, respectively.

Table 6.4. Gene ontology analysis of significantly differentially expressed genes in GW3965-treated KNS42 cells.

GO.ID	Term	Annotated	Significant	Expected	classicFisher	classicKS	weight01KS	parentchildFis	Genes
GO:0051301	cell division	395	125	41.42	< 1e-30	3.20E-17	2.60E-17	< 1e-30	*CCNE2, VEGFA, OIP5, KIF11, SPC25, ASPM, KIF20B, NCAPG, KIF20A, CDC6, DSN1, ANLN, HELLS, KIF4A, CENPE, BIRC5, SKA3, NUSAP1, CCNA2, SGO1, KNL1, CDC25A, BUB1, KIFC1, MASTL, MAD2L1, SPAG5, ARHGEF2, NCAPH, SMC2*
GO:0000278	mitotic cell cycle	719	209	75.39	< 1e-30	< 1e-30	2.70E-07	5.00E-05	*CLSPN, CCNE2, ASNS, ORC1, DLGAP5, MCM10, TYMS, KIF11, GINS2, SPC25, PBK, KIF20B, NCAPG, CDKN2B, KIF20A, GINS1, CDC6, DSN1, ANLN, MYBL2, DTL, KIF4A, ATAD5, CENPE, BIRC5, PLK4, SKA3, NUSAP1, MCM3, CCNA2*
GO:0006260	DNA replication	211	88	22.12	< 1e-30	4.50E-23	7.60E-06	7.30E-27	*CLSPN, CCNE2, ORC1, MCM10, GINS2, GINS1, PCLAF, CDC6, DTL, FEN1, MCM3, GMNN, BMP4, EXO1, CDC25A, PCNA, TICRR, RRM2, BRIP1, ORC6, RFC2, POLQ, BRCA2, DSCC1, POLA2, MCM4, RFWD3, DNA2, PRIM1, MCM8*
GO:0000070	mitotic sister chromatid segregation	110	54	11.53	1.00E-24	2.00E-18	0.0015	6.20E-05	*DLGAP5, NCAPG, CDC6, DSN1, KIF4A, CENPE, NUSAP1, SGO1, BUB1, KIFC1, MAD2L1, SPAG5, NCAPH, SMC2, AURKB, KIF14, CCNB1, NDC80, TTK, DSCC1, PRC1, TRIP13, CHMP4C, SLF1, KIF18A, NCAPD3, GEN1, TACC3, CENPF, KIF22*
GO:0044770	cell cycle phase transition	422	124	44.25	2.10E-28	2.10E-22	0.0165	0.25792	*CLSPN, CCNE2, ORC1, DLGAP5, MCM10, TYMS, CDKN2B, CDC6, ANLN, DTL, ATAD5, CENPE, PLK4, MCM3, CCNA2, CDC25A, BUB1, PCNA, MASTL, TICRR, HMMR, MAD2L1, RRM2, AURKB, KIF14, FAM83D, CCNB1, ORC6, E2F1, NDC80*

Statistical evaluation of gene ontology (GO) terms based of the number of significant-to-expected observations using either Fisher's exact test (Fis) or Kolmogorov-Smirnov test (KS). Different algorithms were utilised to take account of the GO hierarchy, including classic, weight01, and parentchild. GO terms were ranked according to *p*-values obtained using the weight01KS algorithm and test. Genes that were upregulated and downregulated following GW3965 exposure for 72 hr are highlighted in red and green, respectively.

Table 6.5. Gene ontology analysis of significantly differentially expressed genes in LXR-623-treated KNS42 cells.

GO.ID	Term	Annotated	Significant	Expected	classicFisher	classicKS	weight01KS	parentchildFis	Genes
GO:0007062	sister chromatid cohesion	113	65	23.04	3.70E-18	1.30E-20	1.70E-16	2.30E-09	*NDC80*, *CENPI*, *CENPE*, *SKA2*, *TNKS*, *ZWILCH*, *BIRC5*, *SPC24*, *KNTC1*, *FEN1*, *KIF18A*, *KNL1*, *AURKB*, *CENPK*, *CENPU*, *BUB1*, *CENPL*, *SPC25*, *MAD2L1*, *MIS12*, *DSN1*, *SGO1*, *CDCA8*, *CHTF8*, *CENPM*, *POGZ*, *CENPC*, *SLF1*, *CENPF*, *DSCC1*
GO:0051301	cell division	434	165	88.51	4.50E-18	2.90E-15	1.90E-15	2.90E-17	*HMCN1*, *CCNE2*, *NDC80*, *KIF11*, *CENPE*, *CCNA2*, *BRIP1*, *ASPM*, *NUSAP1*, *NCAPG*, *HELLS*, *BRCA2*, *KIF20A*, *CDC6*, *OIP5*, *SKA2*, *ANLN*, *SMC2*, *TNKS*, *ZWILCH*, *SKA3*, *BIRC5*, *SPAG5*, *SPC24*, *KNTC1*, *KIF4A*, *TPX2*, *TOP2A*, *CCNB1*, *CDCA2*
GO:0006260	DNA replication	239	101	48.74	6.80E-15	7.10E-14	5.30E-05	2.00E-12	*CLSPN*, *CCNE2*, *GINS2*, *RFWD3*, *BMP4*, *POLQ*, *RMI1*, *BRIP1*, *DTL*, *TICRR*, *BRCA2*, *CDC6*, *ORC1*, *PCLAF*, *MCM8*, *GMNN*, *RRM2*, *MCM10*, *GINS1*, *CHAF1B*, *CHEK1*, *EXO1*, *POLA2*, *DNA2*, *FEN1*, *RRM1*, *PCNA*, *ESCO2*, *CDC7*, *POLA1*
GO:0007049	cell cycle	1372	450	279.8	< 1e-30	< 1e-30	0.00025	1.40E-29	*SKP2*, *HMCN1*, *CLSPN*, *DLGAP5*, *CCNE2*, *GINS2*, *NDC80*, *KIF11*, *STIL*, *CENPI*, *RFWD3*, *DIRAS3*, *BMP4*, *RBL1*, *CENPE*, *MKI67*, *WDR76*, *CCNA2*, *PDGFRB*, *BRIP1*, *ASPM*, *NUSAP1*, *HMMR*, *NCAPG*, *DTL*, *FANCI*, *TICRR*, *HELLS*, *BRCA2*, *MYBL2*
GO:0000070	mitotic sister chromatid segregation	120	62	24.47	2.20E-14	1.50E-13	0.00055	0.00052	*DLGAP5*, *NDC80*, *CENPE*, *NUSAP1*, *NCAPG*, *CDC6*, *SMC2*, *TNKS*, *SPAG5*, *KIF4A*, *KIF18A*, *CCNB1*, *AURKB*, *NCAPD3*, *BUB1*, *MAD2L1*, *MIS12*, *GEN1*, *DSN1*, *SGO1*, *KIF14*, *KIF18B*, *CDCA8*, *CHTF8*, *POGZ*, *KIFC1*, *NCAPH*, *CENPC*, *SLF1*, *CDC23*

Statistical evaluation of gene ontology (GO) terms based of the number of significant-to-expected observations using either Fisher's exact test (Fis) or Kolmogorov-Smirnov test (KS). Different algorithms were utilised to take account of the GO hierarchy, including classic, weight01, and parentchild. GO terms were ranked according to *p*-values obtained using the weight01KS algorithm and test. Genes that were upregulated and downregulated following LXR-623 exposure for 72 hr are highlighted in red and green, respectively.

Table 6.6. Gene ontology analysis of significantly differentially expressed genes in GW3965-treated SF188 cells.

GO.ID	Term	Annotated	Significant	Expected	classicFisher	classicKS	weight01KS	parentchildFis	Genes
GO:0051301	cell division	398	120	41.93	2.10E-28	2.20E-15	5.90E-14	1.50E-27	*SPC24*, *OIP5*, *CCNF*, *EREG*, *VEGFA*, *SPAG5*, *BUB1*, *PLK1*, *SPC25*, *NCAPH*, *KIF20A*, *SKA3*, *ESPL1*, *AURKB*, *CDCA8*, *CENPE*, *E2F8*, *SGO1*, *NEK2*, *CENPA*, *KIF11*, *CCNA2*, *NUSAP1*, *BIRC5*, *NDC80*, *ASPM*, *CCNB1*, *CDC25C*, *FAM83D*, *CCNB2*
GO:0007062	sister chromatid cohesion	101	49	10.64	3.90E-22	2.50E-15	6.90E-14	9.50E-10	*SPC24*, *BUB1*, *PLK1*, *SPC25*, *ESPL1*, *AURKB*, *CDCA8*, *CENPE*, *SGO1*, *CENPA*, *BIRC5*, *NDC80*, *KIF22*, *DSCC1*, *KNL1*, *CDC20*, *CENPF*, *INCENP*, *KIF18A*, *FEN1*, *KIF2C*, *DSN1*, *ZWINT*, *SKA2*, *MAD2L1*, *CENPI*, *CENPQ*, *ZWILCH*, *CENPM*, *SGO2*
GO:0006260	DNA replication	208	87	21.91	< 1e-30	1.00E-20	7.20E-07	5.20E-29	*EREG*, *ESCO2*, *E2F8*, *CHAF1B*, *CDC25C*, *PCLAF*, *DSCC1*, *GINS2*, *CDK1*, *MCM5*, *GINS4*, *POLE2*, *RRM2*, *EXO1*, *CLSPN*, *ORC1*, *RFC2*, *PRIM1*, *RFC5*, *CDC25A*, *RMI1*, *CCNE2*, *DTL*, *CDK2*, *MCM10*, *GINS1*, *MCM7*, *PCNA*, *NASP*, *CDC45*
GO:0000070	mitotic sister chromatid segregation	110	50	11.59	5.50E-21	3.00E-13	1.20E-05	0.00017	*DLGAP5*, *SPAG5*, *BUB1*, *PLK1*, *NCAPH*, *ESPL1*, *AURKB*, *CDCA8*, *CENPE*, *SGO1*, *NEK2*, *NUSAP1*, *NDC80*, *CCNB1*, *KIF22*, *DSCC1*, *NCAPG*, *KIF18B*, *KIF4A*, *CDC20*, *CENPF*, *PRC1*, *KIF18A*, *KIF14*, *KIF2C*, *DSN1*, *ZWINT*, *MAD2L1*, *NCAPD2*, *KIFC1*
GO:0000278	mitotic cell cycle	727	198	76.59	< 1e-30	< 1e-30	6.50E-05	0.00023	*ASNS*, *EREG*, *DLGAP5*, *SPAG5*, *BUB1*, *PLK1*, *SPC25*, *TYMS*, *NCAPH*, *KIF20A*, *GTSE1*, *SKA3*, *MKI67*, *ESPL1*, *AURKB*, *CDCA8*, *CENPE*, *E2F8*, *SGO1*, *NEK2*, *CENPA*, *KIF11*, *CCNA2*, *NUSAP1*, *BIRC5*, *NDC80*, *PBK*, *CCNB1*, *CDC25C*, *CCNB2*

Statistical evaluation of gene ontology (GO) terms based of the number of significant-to-expected observations using either Fisher's exact test (Fis) or Kolmogorov-Smirnov test (KS). Different algorithms were utilised to take account of the GO hierarchy, including classic, weight01, and parentchild. GO terms were ranked according to *p*-values obtained using the weight01KS algorithm and test. Genes that were upregulated and downregulated following GW3965 exposure for 72 hr are highlighted in red and green, respectively.

Table 6.7. Gene ontology analysis of significantly differentially expressed genes in LXR-623-treated SF188 cells.

GO.ID	Term	Annotated	Significant	Expected	classicFisher	classicKS	weight01KS	parentchildFis	Genes
GO:0051301	cell division	368	154	83.85	7.20E-17	2.20E-13	1.80E-09	6.40E-16	*CCNF*, *SPC25*, *KIF20A*, *HELLS*, *VEGFA*, *CCNA2*, *KIF11*, *CCNE2*, *NCAPG*, *FAM83D*, *BRIP1*, *SKA3*, *BUB1*, *EREG*, *NUSAP1*, *CENPE*, *ASPM*, *PLK1*, *ANLN*, *CDCA2*, *NDC80*, *ESPL1*, *OIP5*, *NCAPH*, *SPC24*, *CDK2*, *CCNB1*, *SKA2*, *TOP2A*, *BRCC3*, *CDC7*
GO:0006260	DNA replication	206	105	46.94	4.30E-19	1.10E-16	4.70E-05	2.20E-16	*PCLAF*, *ESCO2*, *CHAF1B*, *CCNE2*, *BMP4*, *CLSPN*, *MCM10*, *BRIP1*, *EREG*, *DTL*, *GINS3*, *GINS2*, *RMI1*, *MCM5*, *EXO1*, *RRM2*, *GINS1*, *CDK2*, *TICRR*, *MCM3*, *PCNA*, *RFC5*, *CDC7*, *CDC25C*, *CCNE1*, *E2F8*, *DNA2*, *GINS4*, *CDC25A*, *NASP*
GO:0000278	mitotic cell cycle	685	275	156.08	2.50E-26	2.50E-21	7.30E-05	0.00529	*SKP2*, *MKI67*, *SPC25*, *ASNS*, *KIF20A*, *EDN1*, *DLGAP5*, *CCNA2*, *KIF11*, *CCNE2*, *NCAPG*, *PDGFRB*, *CDKN2B*, *BMP4*, *CLSPN*, *MCM10*, *GTSE1*, *SKA3*, *BUB1*, *EREG*, *NUSAP1*, *CENPE*, *PLK1*, *ANLN*, *DTL*, *GINS2*, *NDC80*, *MCM5*, *MYBL2*, *ESPL1*
GO:0007049	cell cycle	1186	439	270.24	< 1e-30	7.10E-30	0.00013	1.30E-30	*SKP2*, *DDIT3*, *NUPR1*, *MKI67*, *PCLAF*, *CCNF*, *SPC25*, *ASNS*, *KIF20A*, *PTGS2*, *EDN1*, *CENPI*, *DLGAP5*, *ESCO2*, *HELLS*, *CHAF1B*, *WDR76*, *CCNA2*, *KIF11*, *CCNE2*, *NCAPG*, *FAM83D*, *PDGFRB*, *CDKN2B*, *BMP4*, *CLSPN*, *MCM10*, *BRIP1*, *GTSE1*, *SKA3*
GO:0051726	regulation of cell cycle	762	261	173.63	3.10E-14	7.60E-14	0.0013	1.30E-10	*SKP2*, *DDIT3*, *NUPR1*, *MKI67*, *PCLAF*, *CCNF*, *ASNS*, *PTGS2*, *EDN1*, *DLGAP5*, *WDR76*, *CCNA2*, *KIF11*, *CCNE2*, *FAM83D*, *PDGFRB*, *CDKN2B*, *BMP4*, *CLSPN*, *BRIP1*, *GTSE1*, *BUB1*, *EREG*, *NUSAP1*, *CENPE*, *ASPM*, *PLK1*, *ANLN*, *LIF*, *DTL*

Statistical evaluation of gene ontology (GO) terms based of the number of significant-to-expected observations using either Fisher's exact test (Fis) or Kolmogorov-Smirnov test (KS). Different algorithms were utilised to take account of the GO hierarchy, including classic, weight01, and parentchild. GO terms were ranked according to *p*-values obtained using the weight01KS algorithm and test. Genes that were upregulated and downregulated following LXR-623 exposure for 72 hr are highlighted in red and green, respectively.

In order to obtain greater understanding of the biological processes involved following exposure to LXR agonists, network analysis was conducted on each list of significantly differentially expressed genes to generate a visual representation of protein-to-protein interactions. Analysis of GW3965-treated U87 cells identified networks associated with lipoprotein uptake and fatty acid/sterol synthesis (Figure 6.7A and B). Increased expression of *INSIG1* is consistent with upregulation of *SREBF1*, which has been shown to be a target of LXR activity (Rong *et al.*, 2017). Surprisingly, increased expressed of *MYLIP*, which encodes the E3 ubiquitin ligase *IDOL*, was associated with upregulation of *LDLR*. Lipogenesis is a non-desirable side-effect of LXR agonist use precluding therapeutic use (Lin and Gustafsson, 2015). Increased expression of *FASN* in treated U87 cells confirms that this is an issue with the pharmacologic action of GW3965 (Figure 6.7B). Evidence of ER stress was observed within a network featuring upregulated expression of *ATF3*, *DDIT3* and *TRIB3* (Figure 6.7C). Other networks included reduced RTK signalling (Figure 6.7D), increased expression of angiogenic genes (Figure 6.7E) and decreased transcription of histone proteins (Figure 6.7F). The same analysis conducted following treatment of U87 cells with LXR-623 identified hubs centred on *CEBPB*, *DDIT3*, *MYC*, *SMAD3*, *CCNB1* and *PDGFRB* (Figure 6.8A and B). Within the positive gene network in Figure 6.9A, several genes involved in stress responses were present. The negative network in Figure 6.9B demonstrated reduced expression of mitosis-related genes, including *PRC1*, *PLK1*, *BUB1*, *CCNA2*, *CCNE2*, and *CENPE*. Moreover, cell signalling associated with TGFβ (Figure 6.9C), PDGFR (Figure 6.9C and D), KIT (Figure 6.9D) and PI/calcium (Figure 6.9E) was predominantly negatively affected by LXR agonist treatment. An interesting network was observed involved in upregulation of amino acid transporters (Figure 6.9G), as well as a trio of genes centred on SOX2 involved in differentiation (Figure 6.9H).

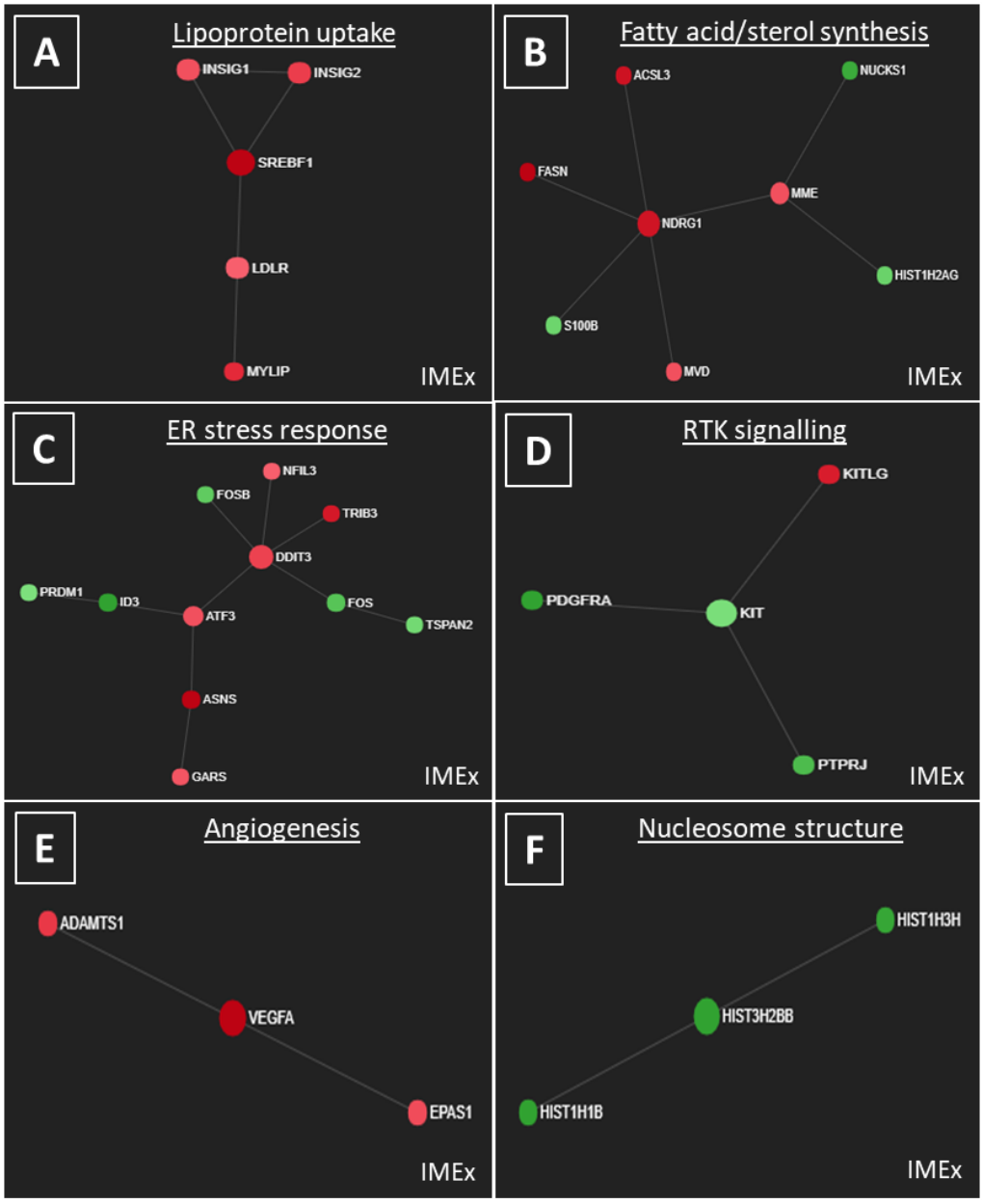

Figure 6.7. Network analysis of significantly differentially expressed genes in GW3965-treated U87 cells. Genes that are upregulated and downregulated following drug exposure for 72 hr are highlighted in red and green, respectively. The curated database utilised to generate the networks is displayed in the bottom right corner.

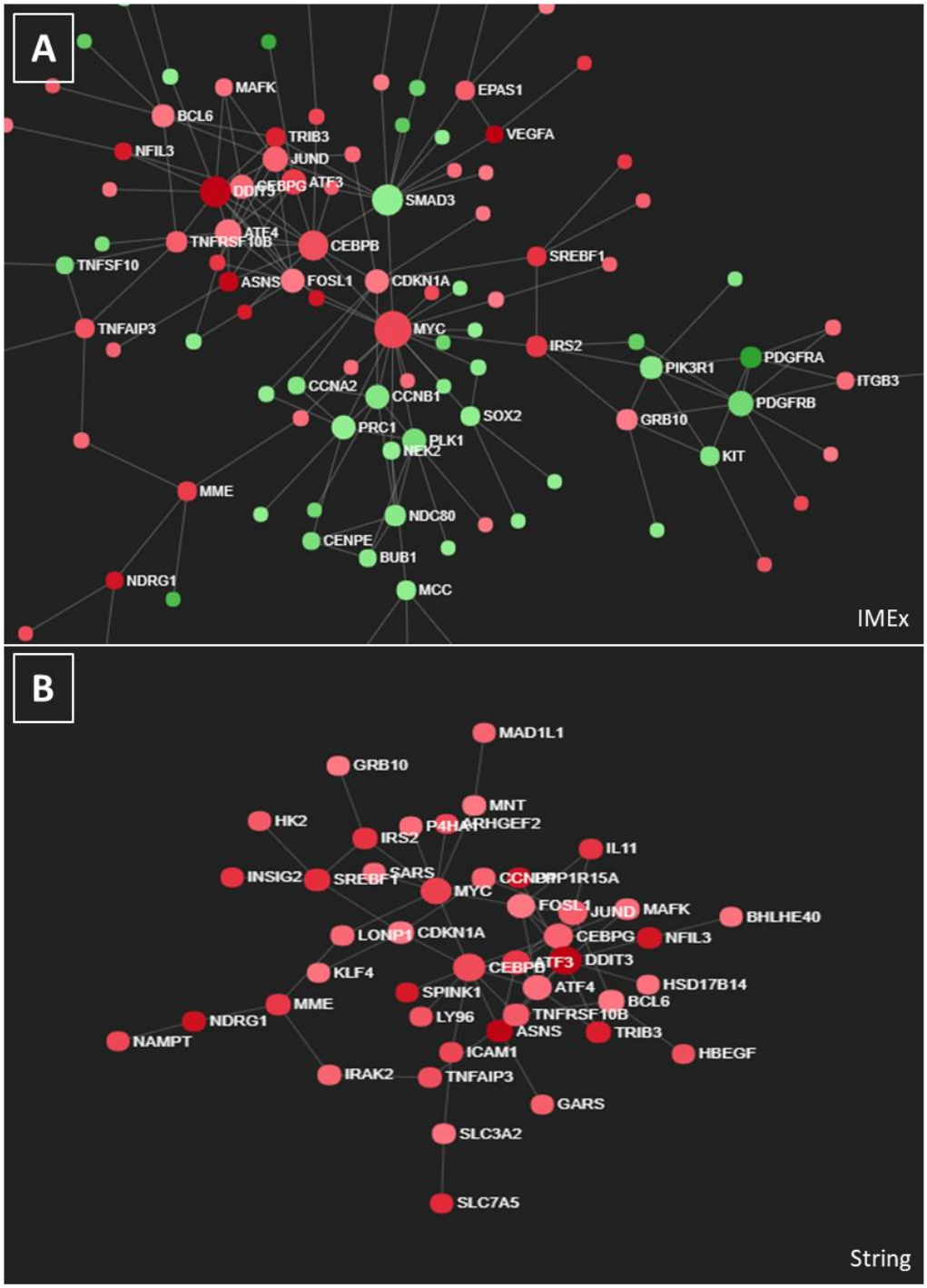

Figure 6.8. Large networks of significantly differentially expressed genes in LXR-623-treated U87 cells. Genes that are upregulated and downregulated following drug exposure for 72 hr are highlighted in red and green, respectively. The curated database utilised to generate the networks is displayed in the bottom right corner.

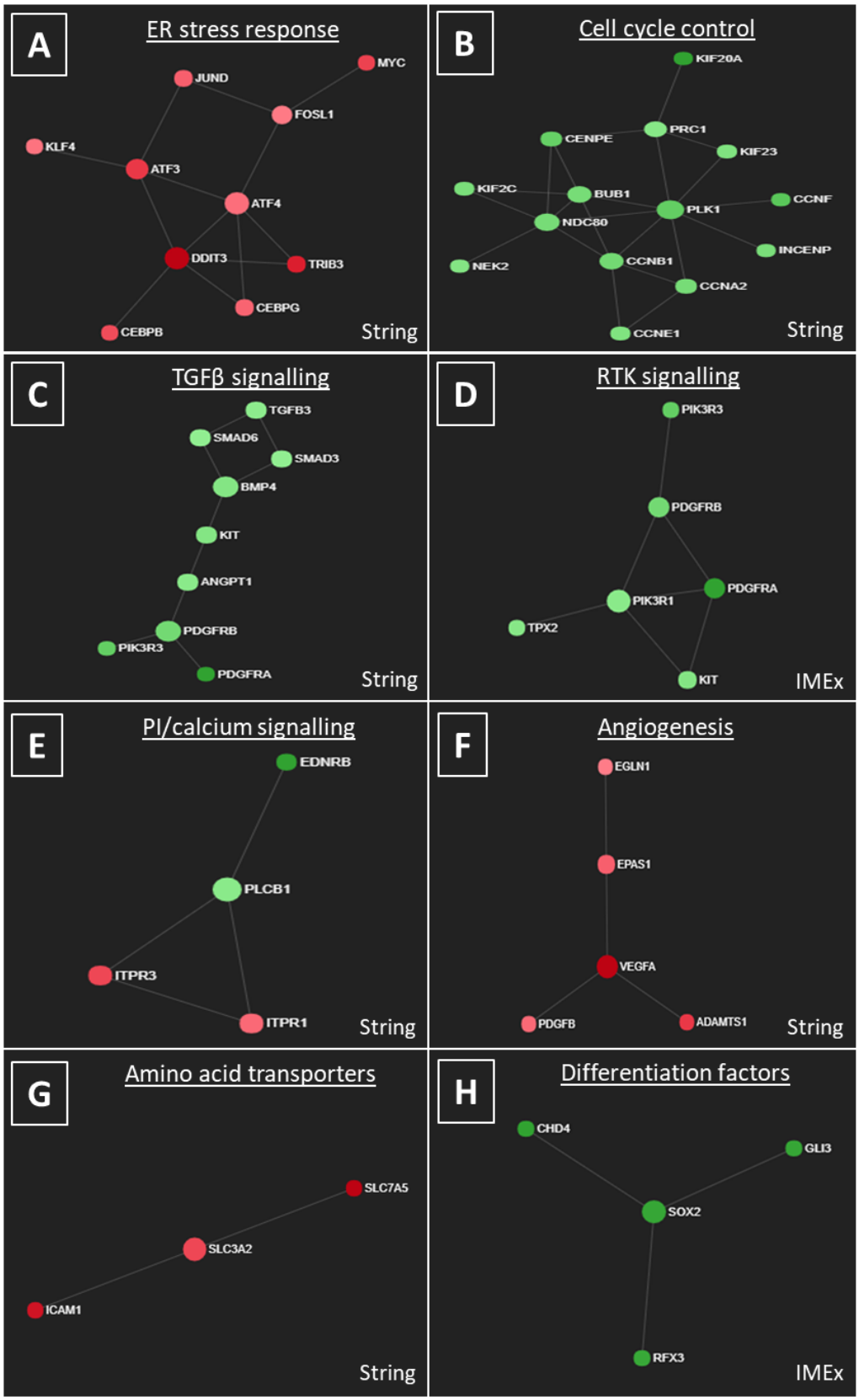

Figure 6.9. Small networks of significantly differentially expressed genes in LXR-623-treated U87 cells. Genes that are upregulated and downregulated following drug exposure for 72 hr are highlighted in red and green, respectively. The curated database utilised to generate the networks is displayed in the bottom right corner.

In KNS42, network analysis of upregulated genes highlighted the importance of *EGR1*, *MYC*, *EGFR* and *CEBPB* (Figure 6.10A). The downregulated network identified several cyclins and regulatory proteins involved in DNA replication (Figure 6.10B). Inspection of smaller networks again identified gene groups associated with lipoprotein uptake (Figure 6.11A), ER stress response (Figure 6.11B), and amino acid transporters (Figure 6.11G). However, additional biological processes were observed compared to the U87 cell line. The stress associated with GW3965 not only appeared to affect ER homeostasis but also caused upregulation of several genes involved in mitochondrial protein folding (Figure 6.11C). This suggests that sustained high-level LXR activation may be detrimental to mitochondrial activity with therapeutic implications in terms of efficacy and side-effects. Additional networks highlighted the mixed effects on cell cycle control and cell signalling, with upregulation of genes with either a positive or negative regulatory effect (Figure 6.11D). Within the cell signalling network, one arm depicts the increased expression of urokinase plasmologen activated receptor (Figure 6.11E), a GPI-anchored cell surface receptor with oncogenic activity (Di Mauro *et al.*, 2017). This provides evidence that exposure to LXR agonists not only engages antiproliferative responses but can also either directly or indirectly induce malignant activity. Interestingly, GW3965 treatment upregulated several genes associated with serine/folate metabolism (Figure 6.11F). This metabolic pathway generates intermediates that are shuttled towards purine and glutathione synthesis and can generate NADH for use in redox reactions (Yang and Vousden, 2016). A novel network was identified featuring genes encoding tRNA synthetases (Figure 6.11H). Associated with these genes was *EPRS* that is part of the GAIT complex involved in regulating inflammatory mRNA translation following stimulation by IFN-ɣ (Mukhopadhyay *et al.*, 2009). The positive and negative networks generated from LXR-623 treatment of KNS42 cells (Figure 6.12A and B) largely replicated the finding observed for GW3965, with smaller networks associated with ER stress response (Figure 6.13A), mitochondrial protein homeostasis (Figure 6.13C), serine/folate metabolism (Figure 6.13G), and tRNA synthetases/GAIT complex (Figure 6.13H). However, the involvement of additional biological

processes was observed including peroxisome biogenesis (Figure 6.13B), antagonistic TGFβ signalling (Figure 6.13D), Hippo signalling (Figure 6.13E), and genome maintenance (Figure 6.13F). Considering that peroxisomes are derived from ER and mitochondrial components, it is plausible that the stress associated with the ER and mitochondria would have downstream consequences on peroxisome function (Sugiura *et al.*, 2017). As seen for GW3965, undesirable tumour-promoting effects were observed in direct or indirect consequence of LXR-623 administration. Downregulation of *MOB1A* and *SAV1* within the Hippo signalling pathway may remove downstream inhibition of TEAD target gene expression resulting in proliferation and the prevention of apoptosis (Meng, Moroishi and Guan, 2016). Interestingly, within the genome maintenance network (Figure 6.13F), SMC5 is a component of a complex involved in DNA double strand break repair by homologous recombination (Menolfi *et al.*, 2015). Observed downregulation of this component may therefore increase the risk of further oncogenic DNA lesions.

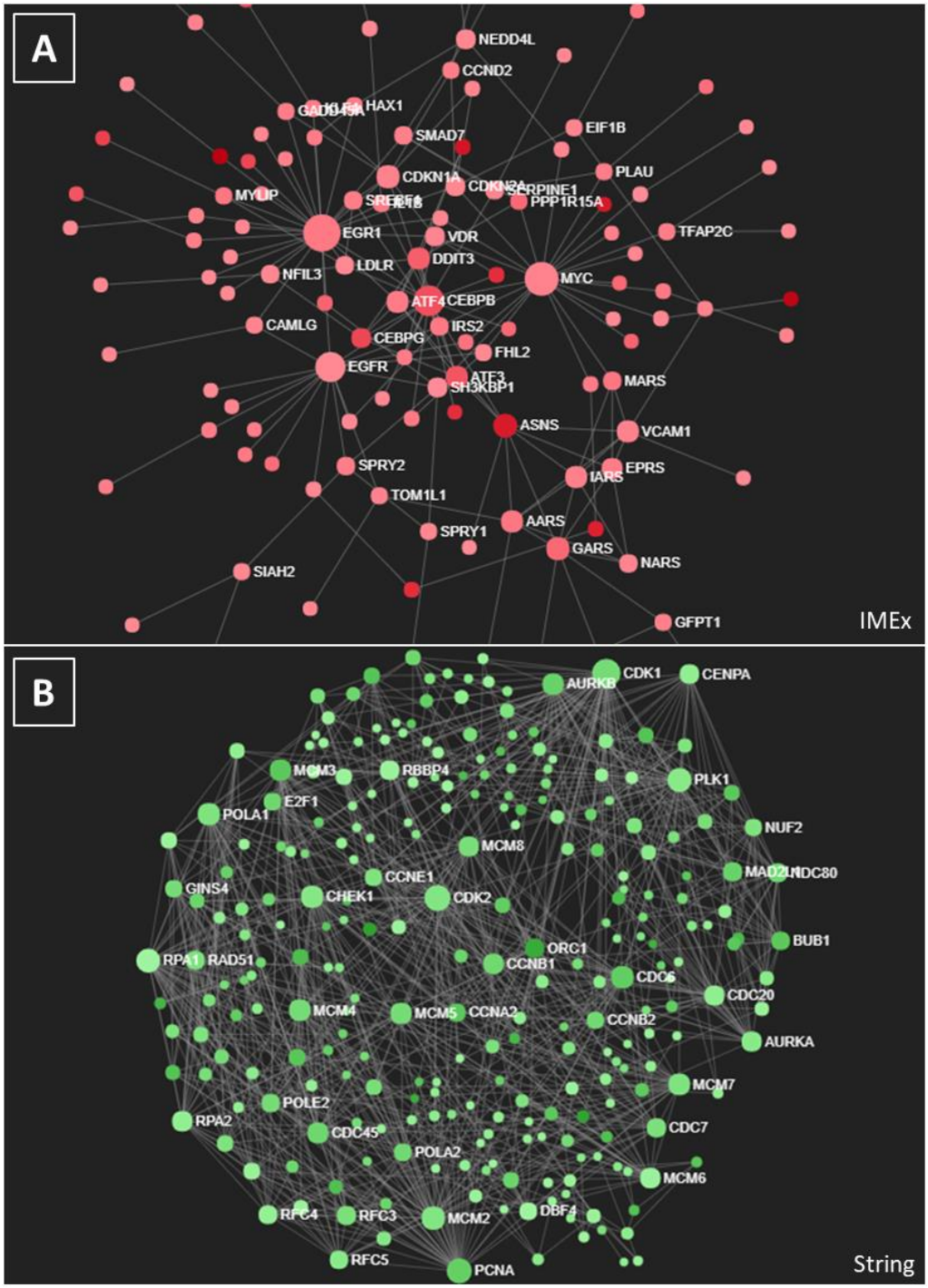

Figure 6.10. Large networks of significantly differentially expressed genes in GW3965-treated KNS42 cells. Genes that are upregulated and downregulated following drug exposure for 72 hr are highlighted in red and green, respectively. The curated database utilised to generate the networks is displayed in the bottom right corner.

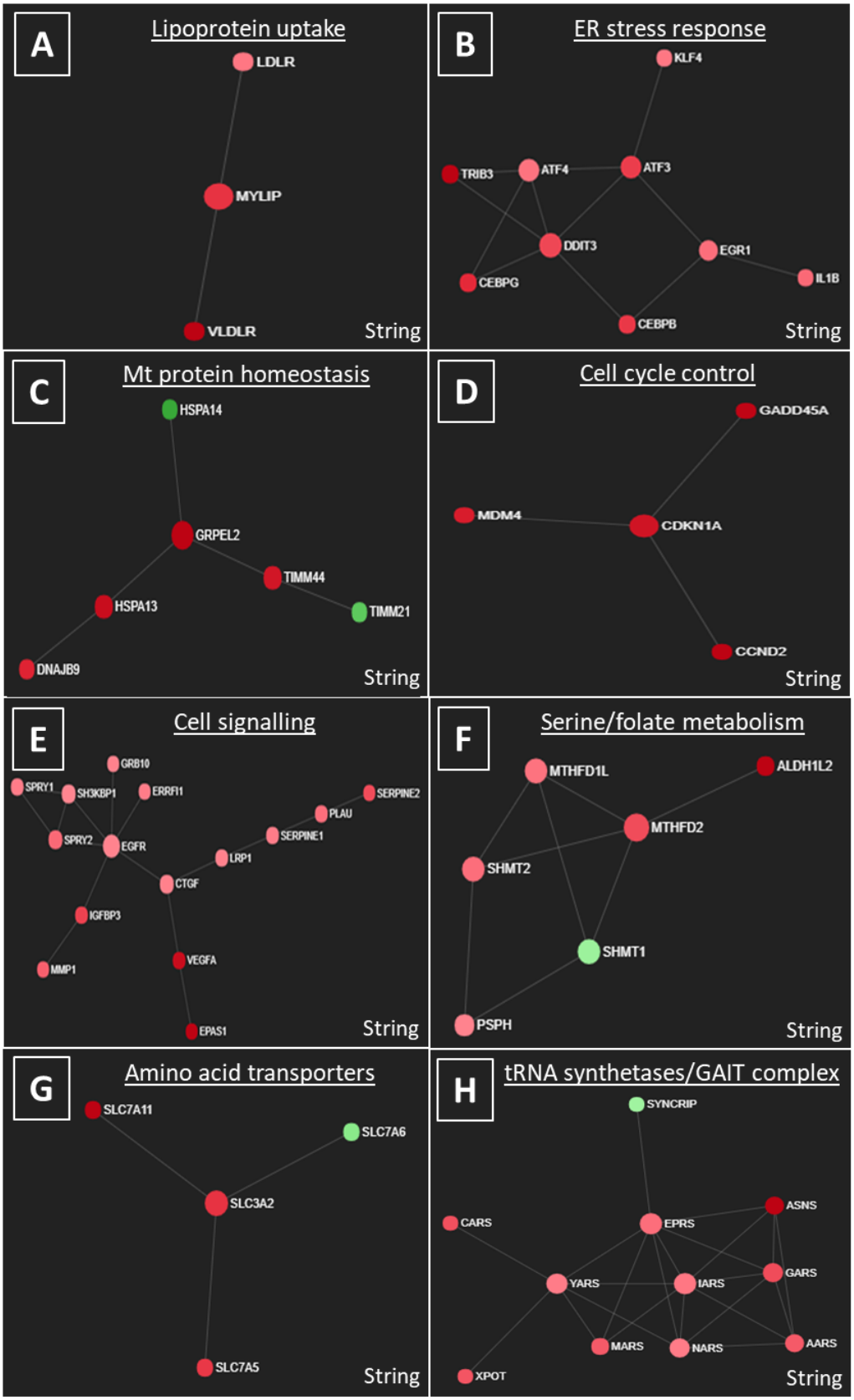

Figure 6.11. Small networks of significantly differentially expressed genes in GW3965-treated KNS42 cells. Genes that are upregulated and downregulated following drug exposure for 72 hr are highlighted in red and green, respectively. The curated database utilised to generate the networks is displayed in the bottom right corner.

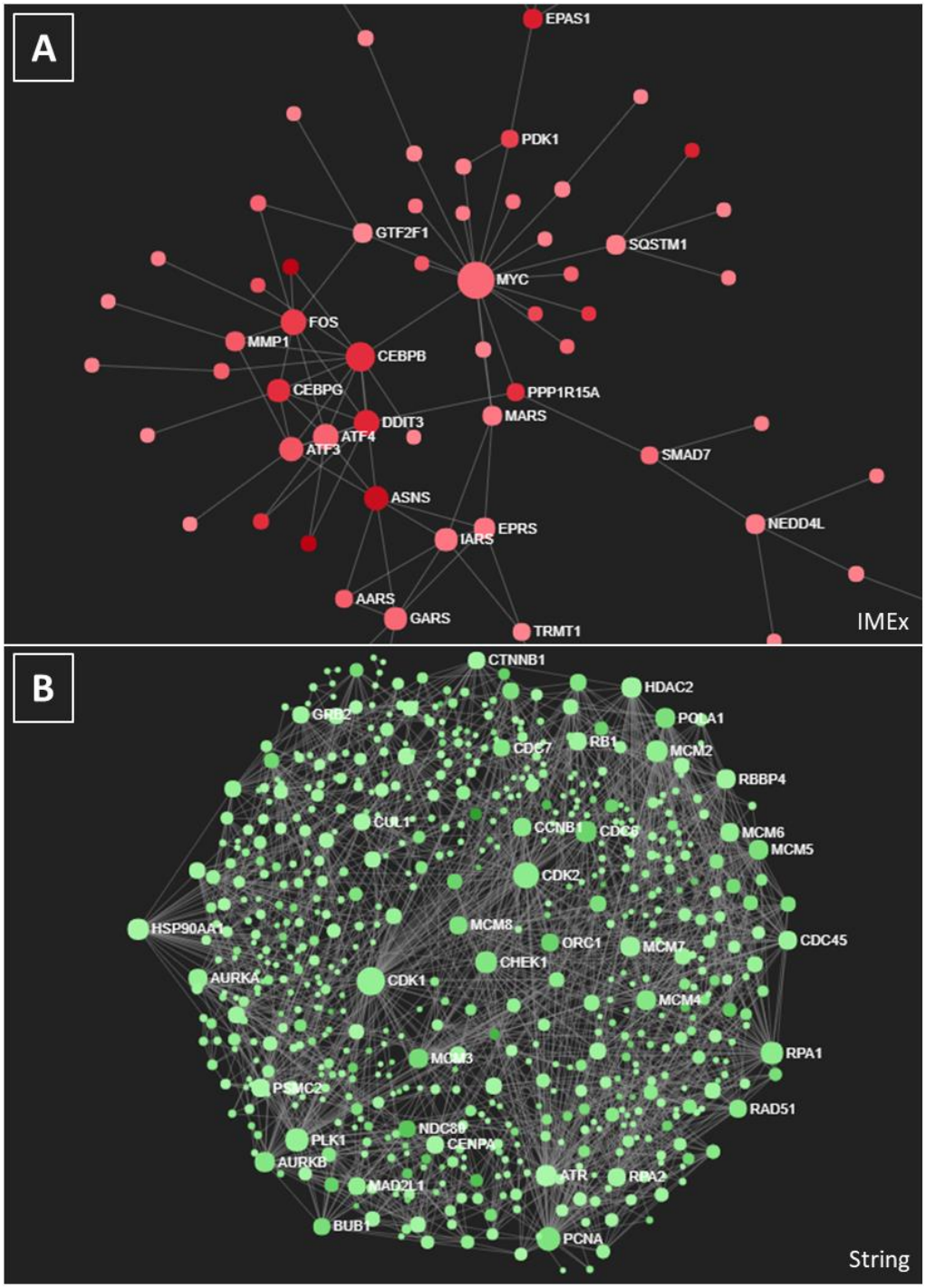

Figure 6.12. Large networks of significantly differentially expressed genes in LXR-623-treated KNS42 cells. Genes that are upregulated and downregulated following drug exposure for 72 hr are highlighted in red and green, respectively. The curated database utilised to generate the networks is displayed in the bottom right corner.

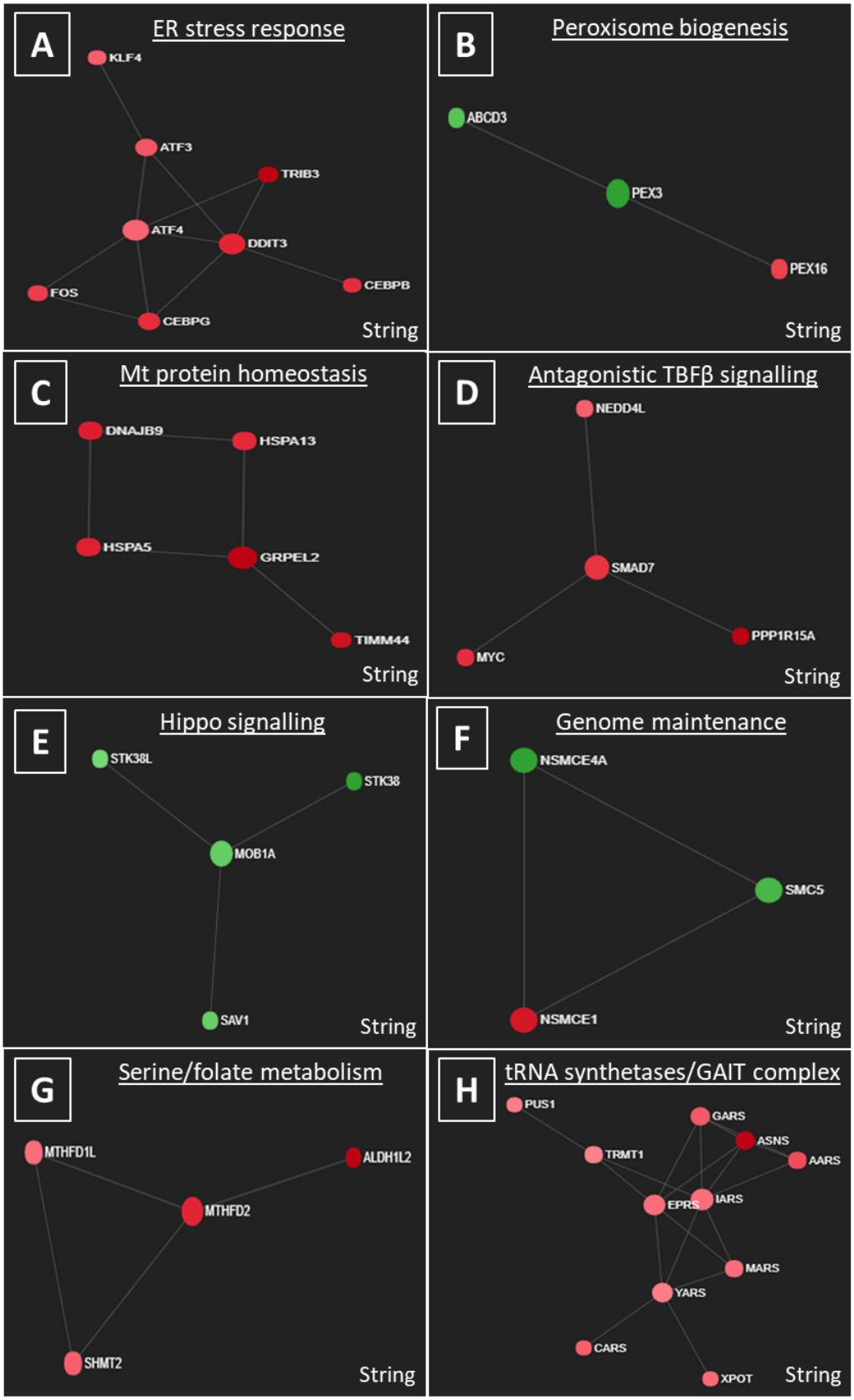

Figure 6.13. Small networks of significantly differentially expressed genes in LXR-623-treated KNS42 cells. Genes that are upregulated and downregulated following drug exposure for 72 hr are highlighted in red and green, respectively. The curated database utilised to generate the networks is displayed in the bottom right corner

Treatment of SF188 with either GW3965 or LXR-623 produced similar results as observed for KNS42 cells exposed to the same compound (Figure 6.14 and Figure 6.16). Analysis of protein-to-protein interactions encoded by significantly differentially expressed genes in GW3965-treated SF188 cells revealed networks associated with lipoprotein uptake (Figure 6.15A), ER stress/inflammation (Figure 6.15B), ER stress/mitochondrial protein homeostasis (Figure 6.15C), uPA signalling (Figure 6.15E), serine/folate metabolism (Figure 6.15F), amino acid transporters (Figure 6.15G), and tRNA synthetases/GAIT complex (Figure 6.15H). Consistent with aberrant mitochondrial function, decreased expression of four genes formed a network indicating dysfunctional protein translocation across the outer and inner mitochondrial membranes (Figure 6.15D).

LXR-623-treated SF188 cells also displayed several of the networks observed following GW3965 exposure, including lipoprotein uptake (Figure 6.17A) and ER stress/cell cycle control (Figure 6.17B). The mitochondrial protein homeostasis network was associated with genes with roles in endoplasmic reticulum-associated protein degradation (ERAD) (Figure 6.17C), a stress response to mediate the degradation of misfolded proteins (Ruggiano, Foresti and Carvalho, 2014). Interestingly, increased expression of *ATG4A* and *MAP1LC3B* (Figure 6.17D) implicates an autophagic response, which under stress conditions promotes survival by degrading defective mitochondria and other organelles and releasing metabolic constituents to support growth (J. Y. Guo *et al.*, 2011). Several networks indicated altered activity of additional membrane compartments, including the Golgi apparatus (Figure 6.17G) and multivesicular bodies (Figure 6.17H), as well as the proteins involved in cargo transport between the ER and the Golgi apparatus (Figure 6.17E and F). In addition to altered Hippo signalling (Figure 6.17J), increased and decreased expression was observed for MYC (Figure 6.17I) and WNT signalling (Figure 6.17K), respectively. Novel downregulation of a network of genes associated with ECM modelling was identified following LXR-623 exposure (Figure 6.17L). Finally, increased expression of ACSS1 is suggestive of acetate utilisation as a

metabolic substrate to supplement acetyl-CoA metabolite pools (Figure 6.17M).

These results highlighted cell-specific responses to pharmacological activation of LXR transcriptional activity, as well as sets of genes commonly altered irrespective of cell line or drug used. These common responses may support activation of a number of transcriptions factors following LXR agonist treatment in all three cell lines. Transcriptional networks identified amongst DEGs often featured centrally located transcription factors connected to multiple genes. This included *MYC* (proliferation and metabolism), *DDIT3* (ER stress), *ATF3* (ER stress), and *E2F1* (cell cycle control). Future work could perform bioinformatics analysis of DEGs to identify common transcription factor binding regions in order to highlight transcription factors highly involved in the response to LXR-agonist treatment. However, gene expression responses for the pGBM cell lines were more similar compared to the adult U87 cell line. Whether this is a product U87 cells being exposed to lower concentrations of drug or is due to underlying genetic differences between adult and paediatric GBM cells requires further study.

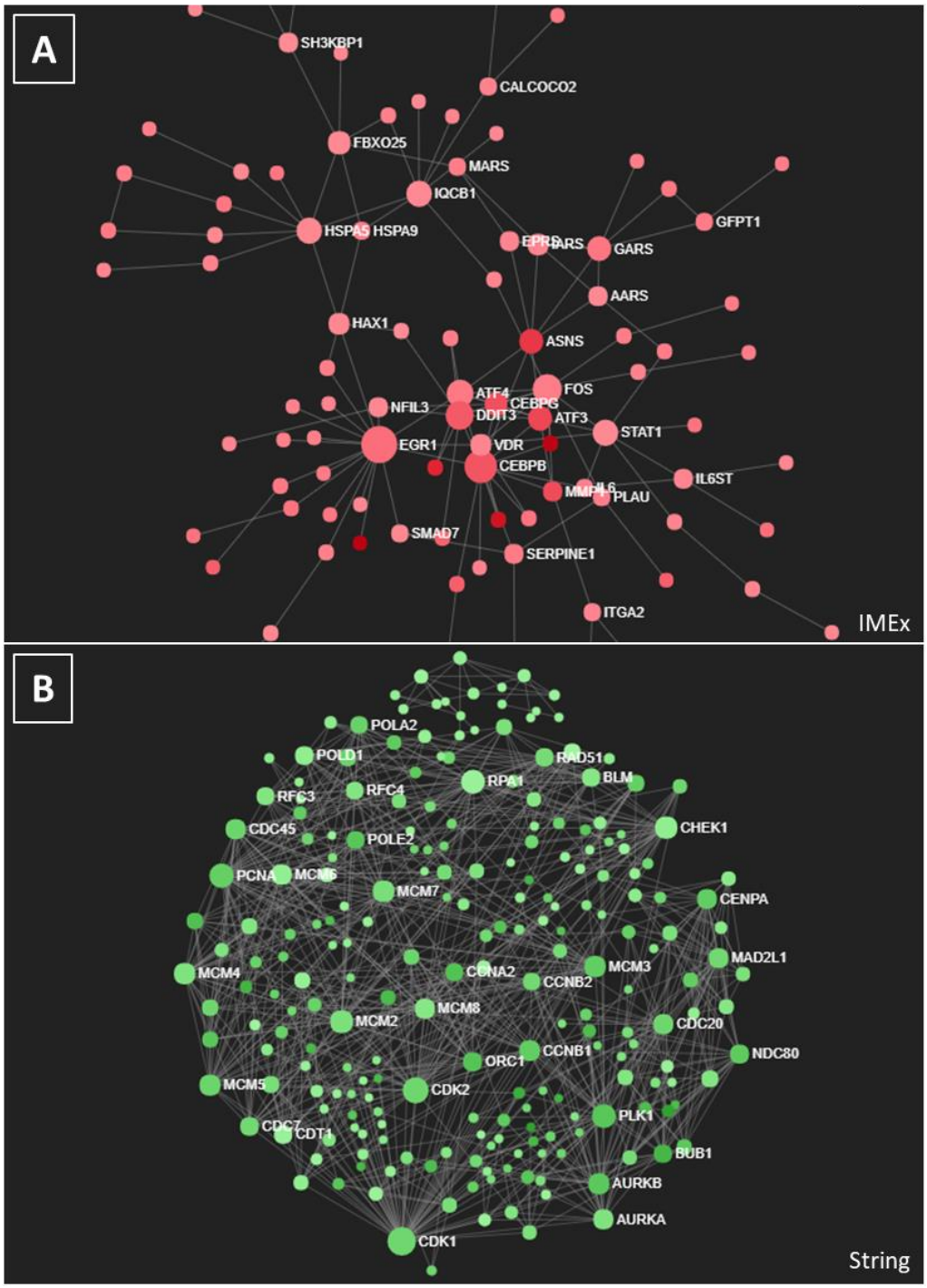

Figure 6.14. Large networks of significantly differentially expressed genes in GW3965-treated SF188 cells. Genes that are upregulated and downregulated following drug exposure for 72 hr are highlighted in red and green, respectively. The curated database utilised to generate the networks is displayed in the bottom right corner.

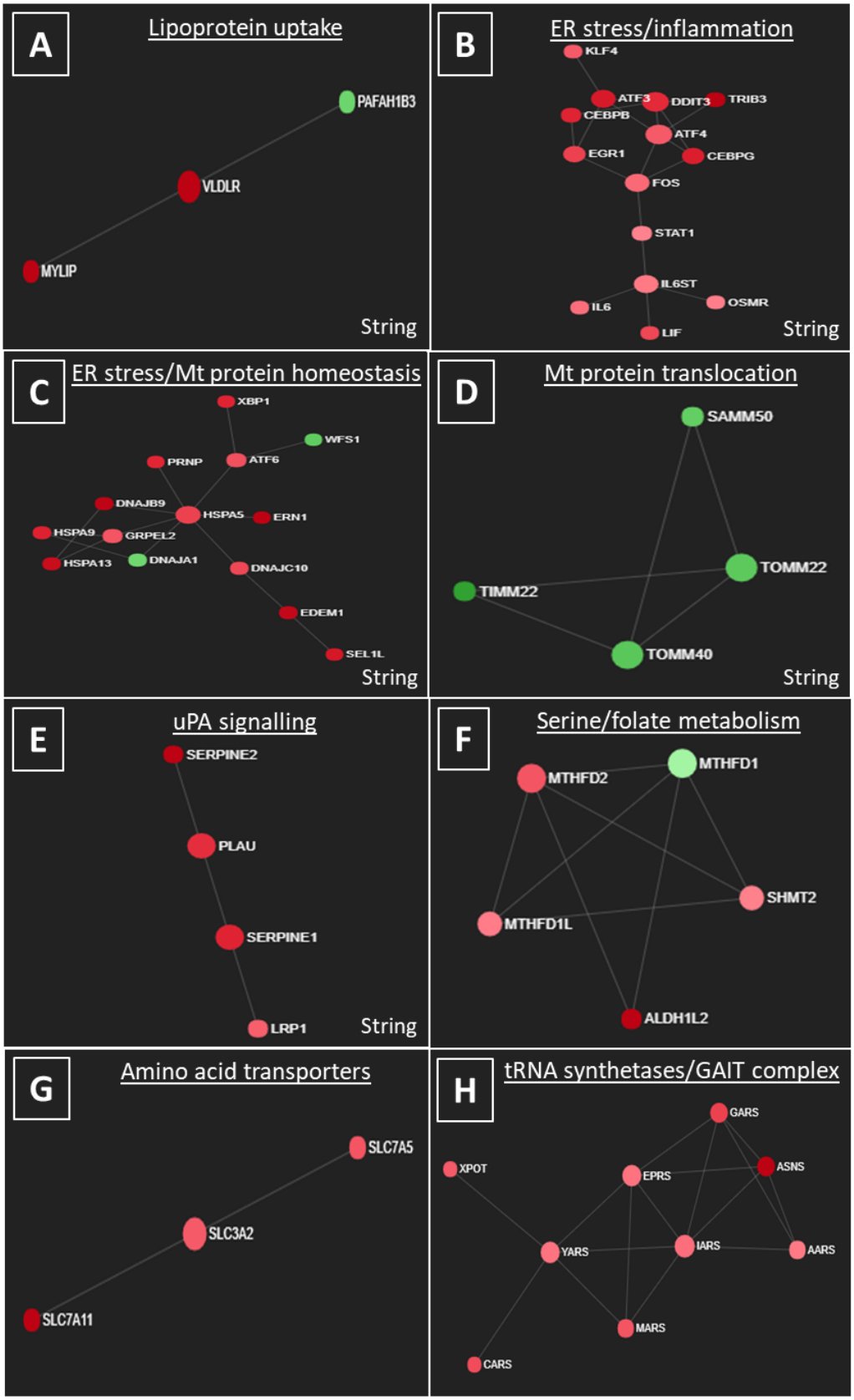

Figure 6.15. Small networks of significantly differentially expressed genes in GW3965-treated SF188 cells. Genes that are upregulated and downregulated following drug exposure for 72 hr are highlighted in red and green, respectively. The curated database utilised to generate the networks is displayed in the bottom right corner.

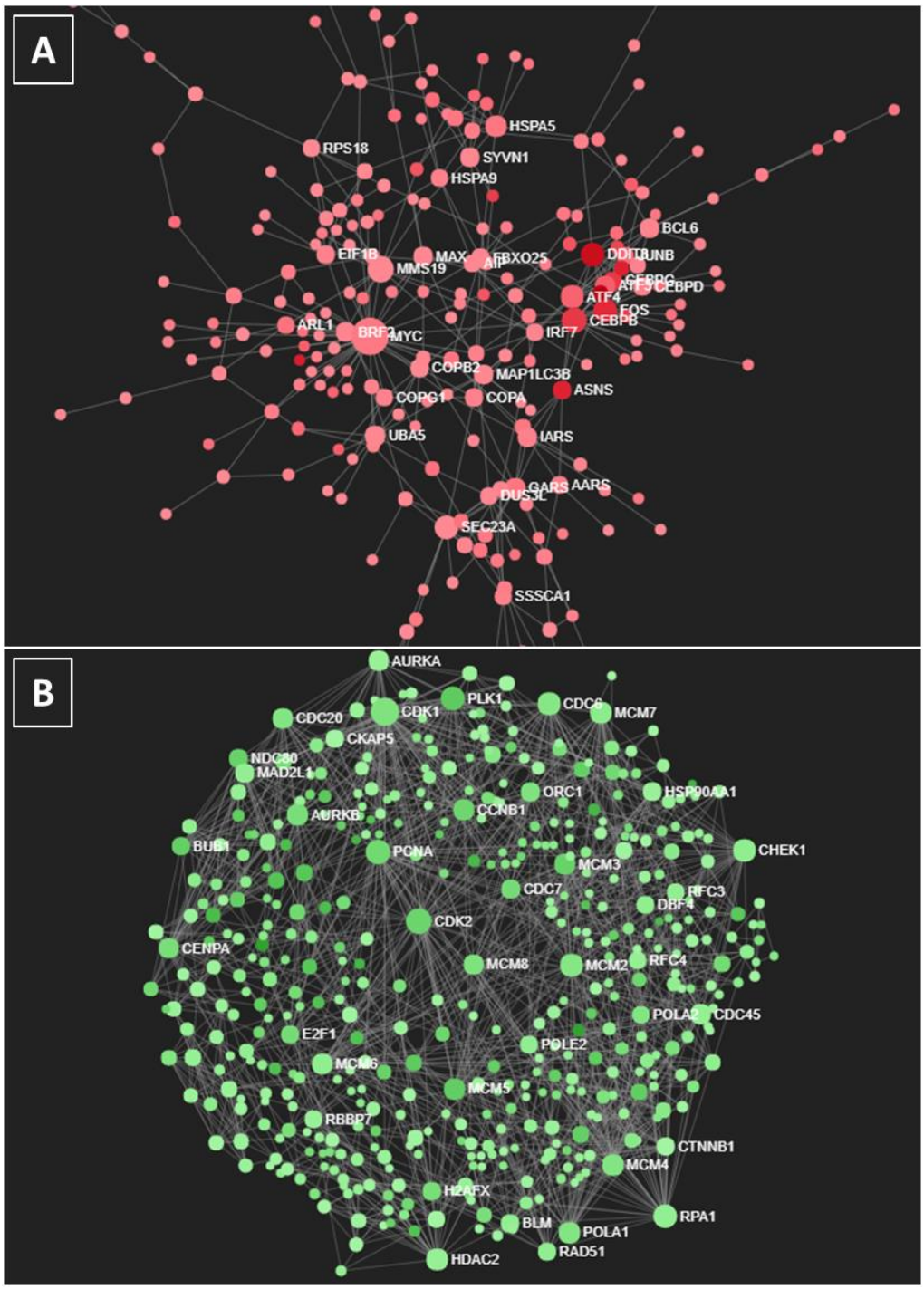

Figure 6.16. Large networks of significantly differentially expressed genes in LXR-623-treated SF188 cells. Genes that are upregulated and downregulated following drug exposure for 72 hr are highlighted in red and green, respectively. The curated database utilised to generate the networks is displayed in the bottom right corner.

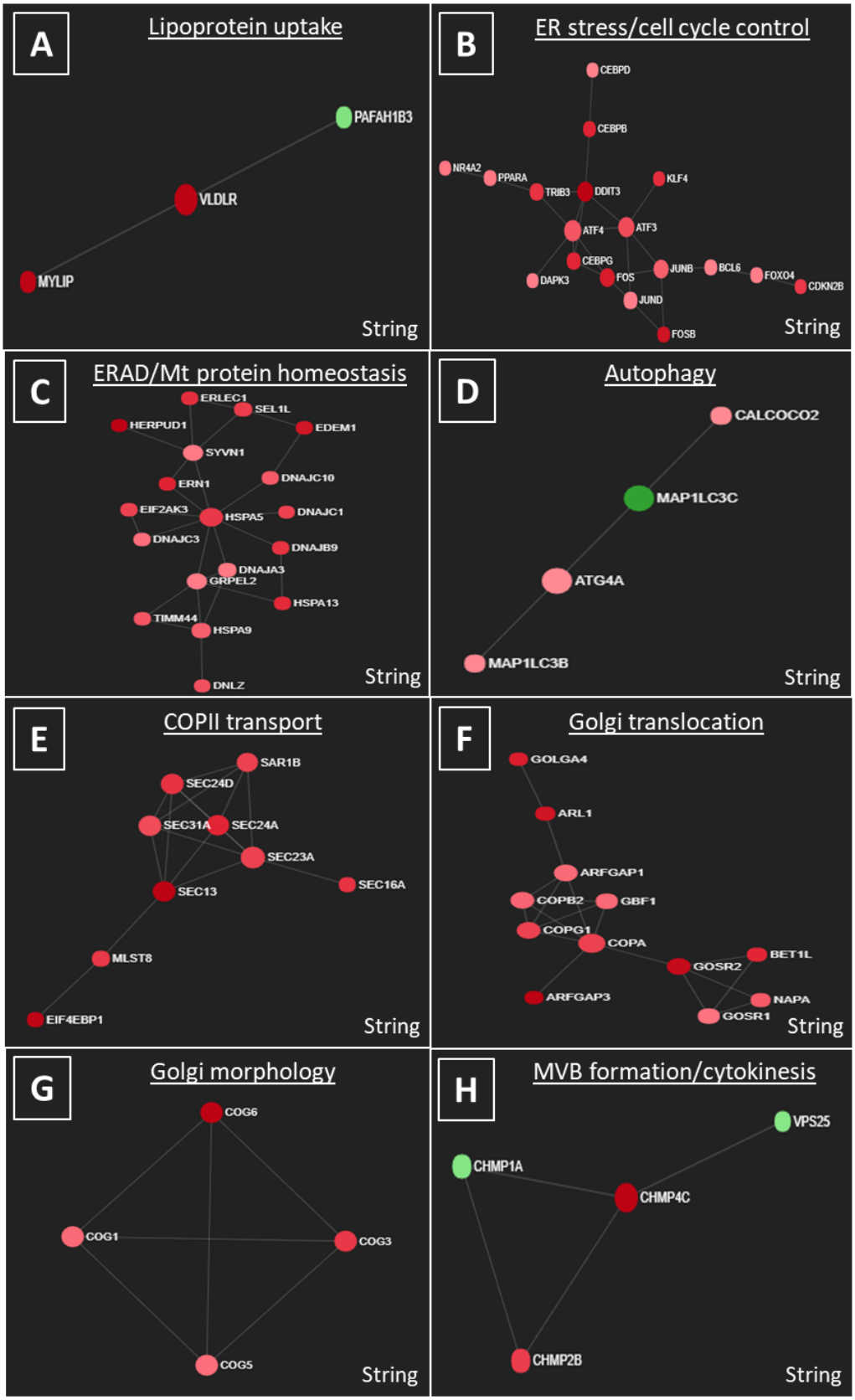

Figure 6.17. Small networks of significantly differentially expressed genes in LXR-623-treated SF188 cells. Genes that are upregulated and downregulated following drug exposure for 72 hr are highlighted in red and green, respectively. The curated database utilised to generate the networks is displayed in the bottom right corner.

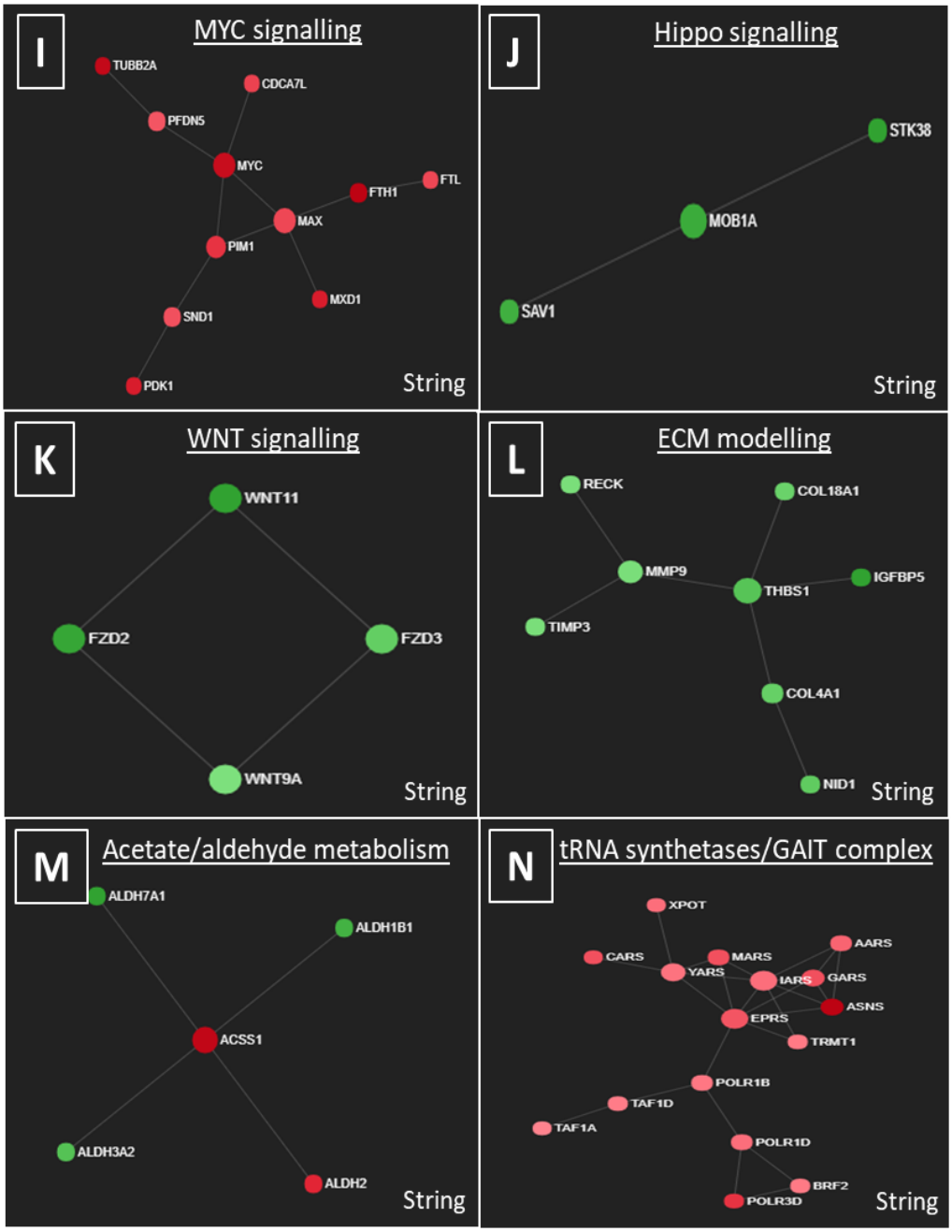

Figure 6.17 continued...

6.4. Western blot analysis of LXR agonist-treated adult and paediatric GBM cells

Previous research into the therapeutic application of LXR agonists uncovered reduced AKT phosphorylation, increased protein levels of cell cycle regulators, including p21, p27 and SKP2, and cleavage of caspase-3 following induction of apoptosis (Lin and Gustafsson, 2015). However, the responses were cell line-specific responses indicating that only some or all of these processes may be

involved in the response of adult and paediatric GBM cells to LXR agonists. We therefore assessed the expression of these protein markers through Western blotting to determine if the findings from prostate cancer and ovarian carcinoma models are also replicated within cell lines of astrocytic lineage. Initially, protein levels of ABCA1, ABCG1 and LDLR were assessed to illustrate LXR activation and downstream activity. Drug-induced activation of LXR increased target gene expression of ABCA1 all cell lines, whereas ABCG1 levels were unchanged (Figure 6.18). Evaluation of LDLR levels was precluded by the identification of four bands. The top two bands likely represent the mature (higher molecular weight) and precursor LDLR proteins, with the lower two bands depicting non-specific binding products of the antibody used. These upper bands were largely unchanged in all cell lines, with the exception of LXR-623-treated SF188 cells that demonstrated reduced levels (Figure 6.18C). This protein level data is concordant with the observed upregulation of the LDLR transcript observed in the gene expression analyses above. Despite these observations for LDLR, the increased protein levels of ABCA1 is supportive of LXR activity (Figure 6.18).

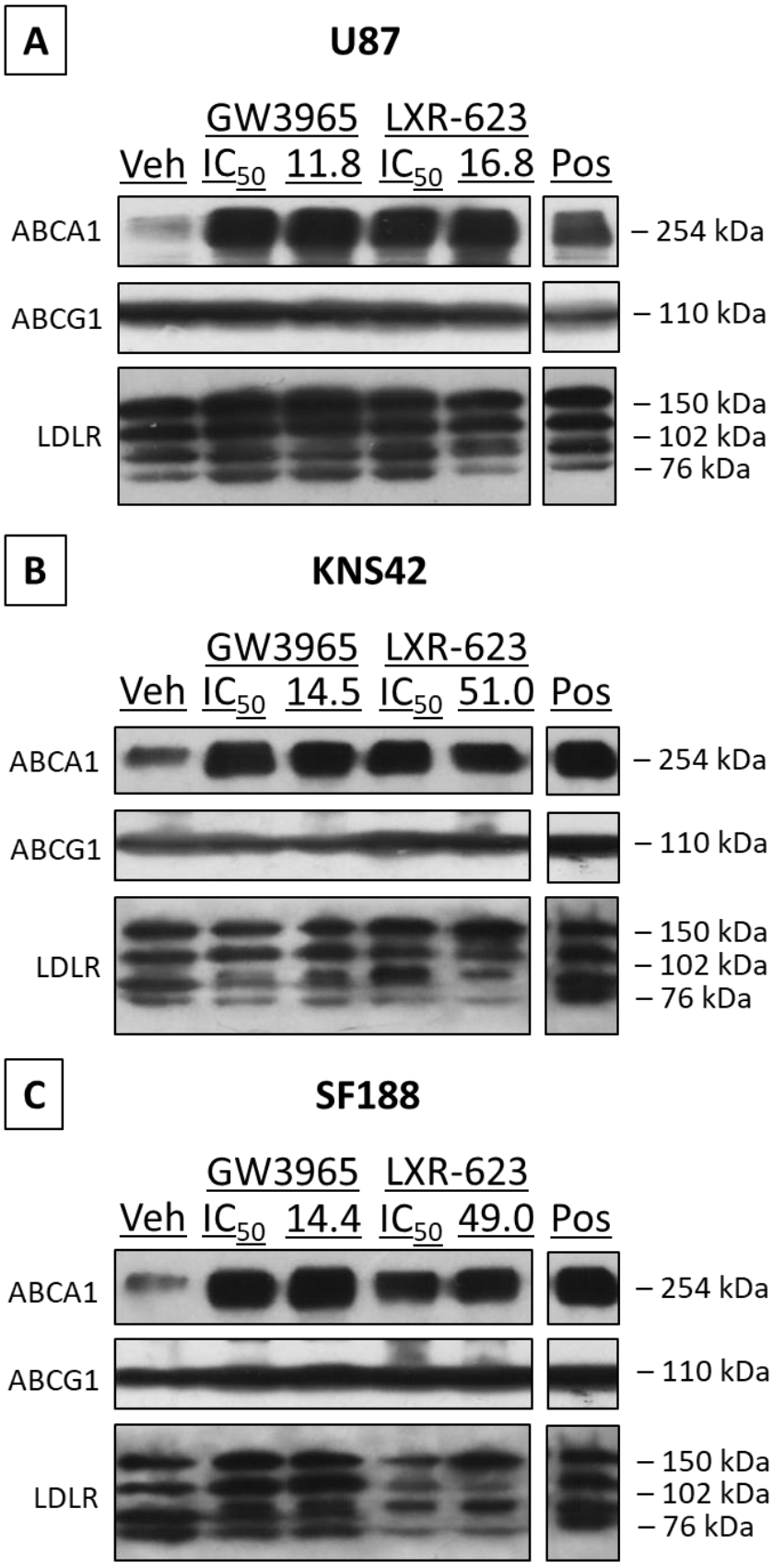

Figure 6.18. Protein levels of ABCA1, ABCG1 and LDLR in adult and paediatric GBM cells treated with either GW3965 or LXR-623. U87 (A), KNS42 (B) and SF188 (C) cells were treated with drug for 72 hr at the IC_{50} value or indicated concentration (μM). Images depict the results of an n=1 experiment.

Examination of AKT phosphorylation and downstream consequences on p-AKT substrates indicated no response in U87 and KNS42 cells (Figure 6.19A and B). Similar observations were made for the SF188 cell line apart from the lack of p-AKT in the vehicle only control implying an increase in AKT phosphorylation upon LXR agonist treatment (Figure 6.19C). Further study is required to determine if this is an artefact or represents reduced upstream pathway activation due to culture under low serum conditions (1% FBS). However, since the phosphorylation status of downstream p-AKT substrates was consistent with the treated cell lines (Figure 6.19), this indicated that the lack of AKT phosphorylation was an artefact. We therefore concluded that LXR agonist treatment had no effect of the AKT pathway following exposure to drug for 72 hr. It is possible that an effect may have manifested within 24 to 48 hr and recovered to normal basal levels due to feedback mechanisms.

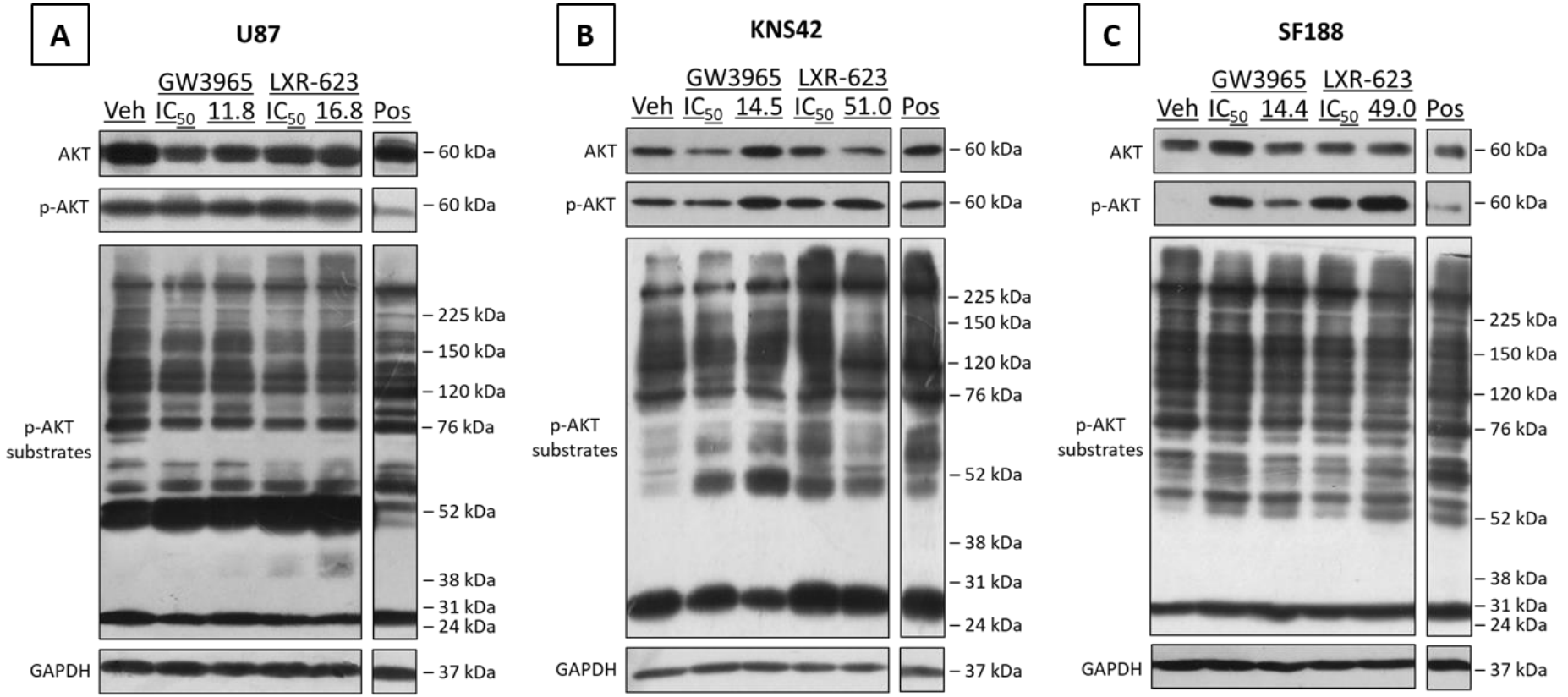

Figure 6.19. Protein levels of AKT, p-AKT and p-AKT substrates in adult and paediatric GBM cells treated with either GW3965 or LXR-623. U87 (A), KNS42 (B) and SF188 (C) cells were treated with drug for 72 hr at the IC_{50} value or indicated concentration (μM). Images depict the results of an n=2 experiment.

We next explored the expression of markers of cell cycle control (p21, p27, and SKP2) and apoptosis (caspase-3). In all cell lines, SKP2 protein levels were reduced following treatment with either GW3965 or LXR-623, predominantly at concentrations above the IC50 concentrations (Figure 6.20). However, despite an established role for SKP2 in inhibiting p21 and p27, only a minor increase in p21 protein levels was observed across all cell lines exposed to either of the two LXR agonists, with p27 protein remaining consistent between conditions. Levels of cleaved caspase-3 were increased in all LXR agonist-treated cells (Figure 6.20). However, the intensity was not comparable to the positive control in which apoptosis was induced by exposure to temozolomide. This suggests that only a small apoptotic response was induced, consistent with the small increase in the sub G0 fraction from the flow cytometric analysis above. Possibly confounding these results is the observation of cleaved caspase-3 within the vehicle only control of the pGBM cell lines (Figure 6.20B and C), which may be derived from cellular stress following growth under low serum conditions for 72 hr. Despite this, LXR agonist treatment increased cleaved caspase-3 levels relative to vehicle only controls in support of apoptosis induction in pGBM cell lines as a mechanism underlying reduced viability (Figure 6.20B and C).

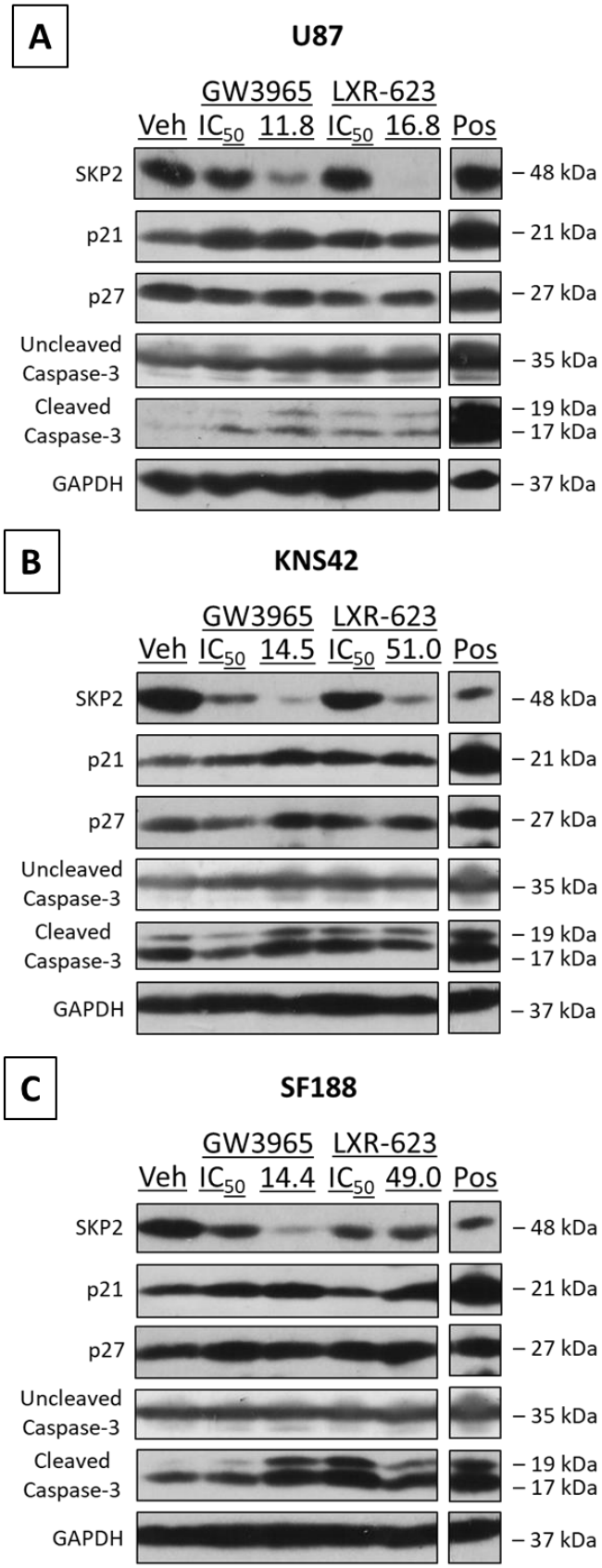

Figure 6.20. Protein levels of cell cycle and apoptosis markers in adult and paediatric GBM cells treated with either GW3965 or LXR-623. U87 (A), KNS42 (B) and SF188 (C) cells were treated with drug for 72 hr at the IC_{50} value or indicated concentration (μM). Images depict the results of an n=1 experiment.

Transcriptomic analysis of treated cell lines suggested induction of ER stress and dysfunctional mitochondrial activity. We therefore hypothesised that LXR agonist treatment would upregulate autophagic stress responses to obtain nutrients and remove defective organelles. Examination of increased LC3B-II levels was suggestive of autophagic processes following pharmacological activation of LXR activity (Figure 6.21). However, p62 showed increased protein levels following GW3965 administration. LXR-623 had differential effects causing a minor increase in p62 levels in U87 cells (Figure 6.21A), whereas levels were unchanged or reduced in KNS42 and SF188 cells (Figure 6.21A and B), respectively. Due to the complexities associated with the study of autophagy, it is not possible to make solid conclusions from these results apart from a suggestive impact on normal autophagic processes. It is also notable that LC3B-II levels were high within the vehicle only control of KNS42 and SF188 cells indicating that these paediatric GBM cells lines fare worse under low serum conditions compared to the U87 cell line (Figure 6.21).

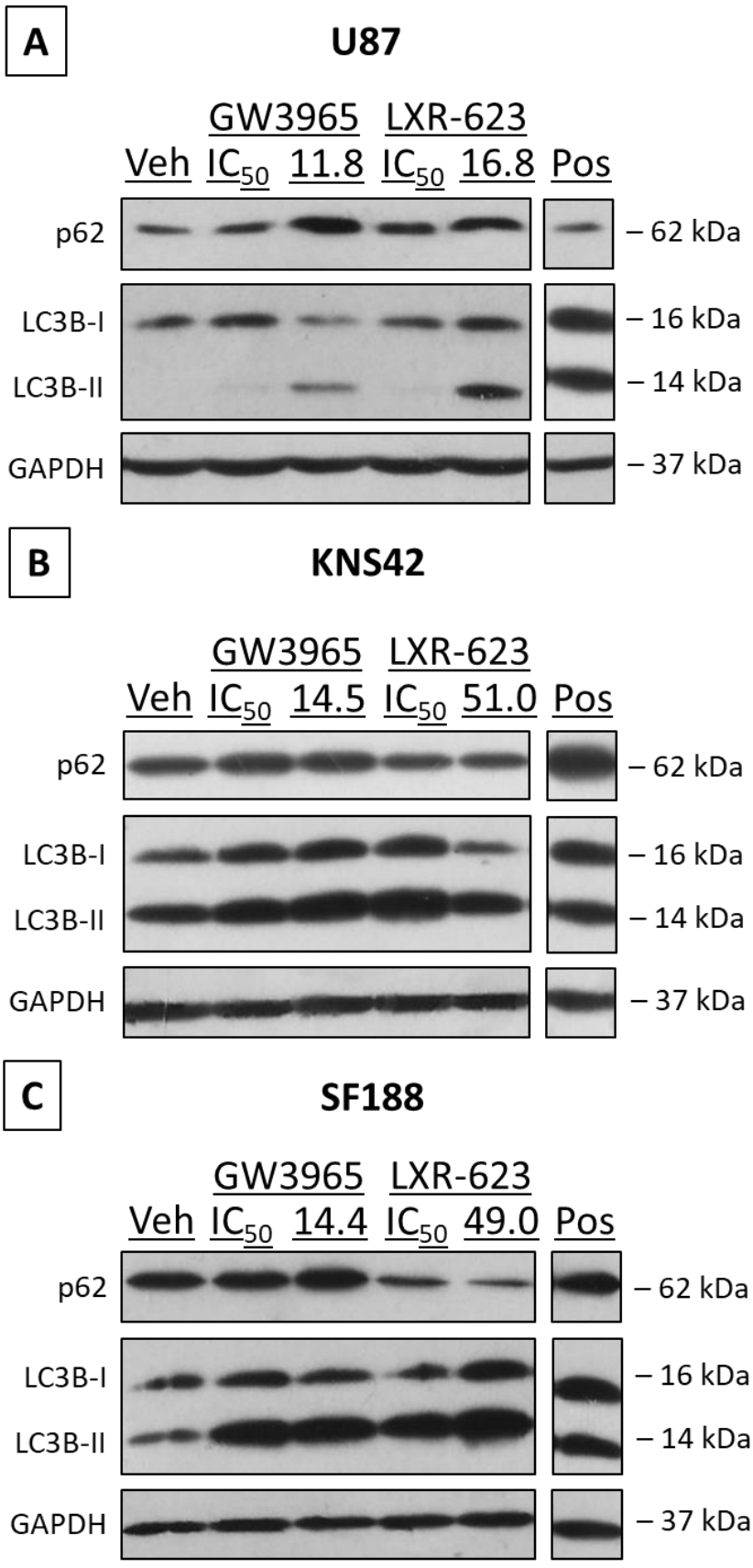

Figure 6.21. Protein levels of autophagy markers in adult and paediatric GBM cells treated with either GW3965 or LXR-623. U87 (A), KNS42 (B) and SF188 (C) cells were treated with drug for 72 hr at the IC_{50} value or indicated concentration (μM). Images depict the results of an n=1 experiment.

6.5. Chapter discussion

The rationale behind the therapeutic assessment of LXR agonists followed the identification of adult and paediatric GBM vulnerability to the removal of lipoproteins and consequent reduction in intracellular cholesterol levels. LXR agonists replicate lipoprotein deficiency by inducing the expression of IDOL, an E3 ubiquitin ligase which mediates the degradation of LDLR (Zelcer *et al.*, 2009) and VLDLR (Hong *et al.*, 2010). This has the effect of reducing cholesterol import via uptake from the external milieu. LXR agonists further reduce intracellular cholesterol levels through transcriptional induction of ABCA1 and ABCG1, plasma membrane proteins involved in reverse cholesterol transport (Bovenga, Sabbà and Moschetta, 2015). Other means of reducing intracellular cholesterol levels can be achieved using statins. However, conflicting evidence surrounds the therapeutic efficacy of statins, with potential resistance mechanisms associated with differential expression of cholesterol synthetic genes, as well as scavenging of cholesterol from external sources (Clendening and Penn, 2012). LXR agonists therefore have the added benefit over statins by stimulating cholesterol export and reducing cholesterol import, although *de novo* synthesis is not inhibited.

We hypothesised that LXR agonists would be toxic to adult and paediatric GBM *in vitro* models. Cellular viability assessment of cells exposed to LXR agonists over 72 hr identified a dose-dependent response. IC_{50} values for each LXR agonist were lower in U87 cells compared to the two paediatric GBM cell lines. However, the mechanism underlying this increased susceptibility remains to be elucidated. Potential reasons include differential basal protein levels of LXRα/β isoforms or expression levels of cholesterol *de novo* biosynthesis genes. Indeed, previous research has identified variable susceptibility to statins based on differential *HMGCS1* and *HMGCR* transcript levels, indicating that some cells can meet cholesterol demands through *de novo* synthesis whereas others are reliant on external sources (Clendening, Pandyra, Li, *et al.*, 2010). The measurement of cellular viability following exposure to LXR agonists also highlighted the micromolar concentrations required over the relatively long

period of 72 hr. Mice treated with 400 mg/kg LXR-623 via oral gavage achieved concentrations ranging between 1.75 to 7.76 µM in intracranial tumours (Villa *et al.*, 2016). In human subjects, oral treatment with a single dose of 300 mg achieved a peak plasma concentration of 4.56 µM, which was associated with adverse neurological events in all six patients within this dosage group (Katz *et al.*, 2009), even though brain concentrations of LXR-623 are likely lower than observed in the plasma. Other chemotherapeutic drugs display cytotoxic activity within the nanomolar range and can induce significant cell death *in vitro* over a shorter time scale of 24 to 48 hrs (e.g. temozolomide). This indicates that LXR agonists are not particularly potent inducers of cytotoxicity, requiring processes that take over 24 hrs to develop, thus presenting a pharmacological challenge to achieve and maintain therapeutic doses within patients. However, other drug response variables, distinct from cellular viability chosen in this study, may have elucidated ligand induced effects at lower concentrations of LXR-623. Drug variables that could be used in future investigations could include cell death/membrane integrity (trypan blue exclusion assay), lipoprotein uptake (confocal microscopy), cholesterol levels and distribution, and immunoblotting of cholesterol synthesis and transport proteins. Alternatively, downstream investigations into LXR-623 could be conducted using the minimal concentration required to induce drug-specific targets, including such as *ABCA1*.

The concentrations required and the time taken by LXR agonists to reduce cellular viability implicates either secondary or tertiary gene expression processes that may be induced following the initial insult, as has been suggested (Candelaria *et al.*, 2014). We obtained evidence of this through network analysis of differentially expressed genes identifying ER stress and mitochondrial protein homeostatic responses in most cell lines and treatment conditions. LXR agonists have been demonstrated to affect plasma membrane dynamics leading to a reduction in the height and width of lipids rafts in prostate cancer cells (Pommier *et al.*, 2010). It is feasible that cholesterol dynamics are affected within different compartments throughout the cell,

including the ER, leading to stress responses. This could be assessed in future studies through confocal microscopy of cholesterol labelled with either filipin or BODIPY. Additionally, ER stress may be initiated via upregulated expression of FASN and consequent accumulation of lipids leading to lipotoxicity, as supported by increased expression of *SREBF1* and *FASN* in GW3965-treated U87 cells. This highlights a drawback to the use of LXR agonists in therapeutic applications due to adverse side effects associated with hepatic steatosis. Moreover, CNS-related adverse events have been observed in human subjects in a phase I trial of LXR-623 (Katz *et al.*, 2009), thus requiring further chemical engineering to improve the drug design and its pharmacologic mode of action (Viennois *et al.*, 2012). However, as tools to examine LXR targeting, GW3965 and LXR-623 demonstrated regulation of diverse gene sets, encompassing lipoprotein regulation, stress responses, cell signalling, cell cycle control, cell division, DNA replication, and metabolism. Considering that the exposure period was 72 hrs, it is unclear whether some of these gene expression changes are a direct consequence of LXR activity or are an indirect consequence due to stress from the initial insult. Examination of transcriptomic profiles at different time points or chromatin immunoprecipitation (ChIP) analysis would be required to elucidate this. Interestingly, some of the networks consisted solely of, or featured a mix of genes with either tumour suppressive or oncogenic properties. The induction of oncogenic genes may not be a product of LXR activation but may represent stress responses inherent to the GBM cell lines. However, given the purported role of LXRs predominantly in the regulation of glucose (Anthonisen *et al.*, 2010), cholesterol and fatty acid homeostasis (Lin and Gustafsson, 2015), it is particularly interesting to observe the diverse sets of genes affected, including serine/folate metabolism, Hippo signalling, amino acid transporters, and tRNA synthetases.

Serine/folate metabolism is important for the generation of purine nucleotides, NADH and αKG (Yang and Vousden, 2016). Upregulation of several genes within this pathway may represent a compensatory response to maintain TCA cycle activity within mitochondria as well as producing NADH to allow redox

reactions within other metabolic pathways. The folate cycle also feeds into the methionine cycle which generates glutathione (Yang and Vousden, 2016). Therefore, insult from ROS generation may be ablated by the increased expression of mitochondrial *SHMT2* and *MTHFD2*. Correlation analysis to identify metabolic enzymes associated with high proliferation in 60 cell lines identified *SHMT2*, *MTHFD2* and *MTHFD1L* with an essential role in supporting cancer growth (Jain *et al.*, 2012). Upregulation of the membrane transporter *SLC7A5* (LAT1) and its chaperone *SLC3A2* (CD98) is suggestive of altered exchange of essential amino acids between the intracellular and extracellular environments. The stability and transporter activity of the LAT1 transporter has been demonstrated to be modulated by cholesterol (Dickens *et al.*, 2017). Therefore, reduced cholesterol levels may have a positive effect by inhibiting SLC7A5 (LAT1), which is highly expressed in several human cancers (Zhao, Wang and Pan, 2015). High intensity staining of SLC7A5 (LAT1) has been observed to be specific to infiltrating glioma cells in contrast to cells within the centre of the tumour (Nawashiro *et al.*, 2005). Collectively, these novel gene expression changes may be exploited to overcome adaptive responses to stress and may inform on the future development of combined therapeutic regimens.

Similar work conducted by Guo and colleagues identified a reduction in growth rates following activation of LXR by GW3965 (D. Guo *et al.*, 2011). In concordance with our data, large differences in proliferative capacity were observed after the 24 hr timepoint. A concentration of 5 µM had more impact in the study by Guo and colleagues in contrast to our observations of ~10 µM required to reduce cellular viability. This disparity in findings may be accounted for by the use of 1% LD-FBS medium in their study compared to 1% FBS in our study, which may supply sufficient amounts of lipoprotein to increase resistance to LXR agonists. Indeed, Guo and colleagues went on to show the rescue of cell viability by addition of LDLs within the culture medium (D. Guo *et al.*, 2011). We demonstrated rescue of U87 cells upon addition of MβCD-cholesterol, which was significant for LXR-623 but not GW3965. Moreover, Guo and colleagues identified increased expression of *ABCA1* and *MYLIP* (encodes

IDOL) that was observed within 24 hr, leading to high protein levels of ABCA1, as well as a reduction in mature LDLR protein starting at 8 hr and lasting to 48 hr (D. Guo *et al.*, 2011). We observed a similar increase in ABCA1 levels but did not identify reduced levels of LDLR, apart from decreased expression in LXR-623-treated SF188 cells. Surprisingly, LDLR transcript levels were consistently overexpressed following drug treatment and translated into slightly increased protein levels in GW3965-treated U87 and SF188 cells. The mechanisms underlying this discrepancy are unclear but may relate to the length of agonist exposure (72 hr versus 48 hr), meaning that feedback regulation may increase LDLR expression despite upregulation of *MYLIP* (encodes IDOL).

Investigations conducted by Pommier and colleagues using the LXR agonist T0901317 revealed caspase-3 cleavage after 48hr, associated with reduced AKT phosphorylation (Pommier *et al.*, 2010). We observed caspase-3 cleavage in all cell lines and treatments at the 72-hr period, which was more prominent in the KNS42 and SF188 lines. However, cleavage of caspase-3 was observed in the vehicle only control for KNS42 and SF188, indicating that growth under low serum conditions was already having a negative impact on cellular viability of the pGBM cell lines. Moreover, p-AKT phosphorylation was largely unaffected by either GW3965 or LXR-623 across all cell lines. However, T0901317 also targets FXR and PXR (Lin and Gustafsson, 2015) and is therefore not amenable for comparison with GW3965 and LXR-623. Research conducted by Derangère and colleagues identified a non-caspase-3-dependent mechanism of cell death involving caspase-1 called pyroptosis induced by T0901317 (Derangère *et al.*, 2014). Future research should determine the full complement of LXR agonist-induced responses leading to cell death in cancerous cell lines of astrocytic origin, with emphasis on the examination of ER stress and morphology (via electron microscopy), mitochondrial viability, autophagy, lipotoxicity, and membrane dynamics.

Chapter 7

Discussion

7. Discussion

7.1. Intratumour metabolic heterogeneity within HGGs

The recently elucidated existence of ITH within GBM provided a strong rationale to investigate the hypothesis of regional differences in metabolism. At the point of writing, studies concerning GBM metabolism have focused primarily on metabolomic reprogramming as grade increases (Chinnaiyan *et al.*, 2012) and in response to oncogenic drivers of gliomagenesis, such as EGFR/EGFRvIII (Guo *et al.*, 2009; Inda *et al.*, 2010; D. Guo *et al.*, 2011), MYC (Wise *et al.*, 2008), and IDH1/2 mutations (Reitman *et al.*, 2011). Associations between oncogenes and metabolic pathways, as observed between MYC and glutamine (DeBerardinis and Cheng, 2010), suggest that variations within the genetic landscape would manifest at the metabolic level, with major implications on therapeutic strategies targeting only one metabolic pathway, which are likely to be redundant. Metabolic stresses within the tumour microenvironment are also capable of selecting for cancer cells with gene expression patterns or genetic mutations that promote survival, as observed under glucose-deprived conditions (Yun *et al.*, 2009).

We profiled the metabolomic and lipidomic landscapes of HGGs through LC-MS-based analysis of multi-region surgically-resected primary tumour fragments. Although multi-region sampling has been conducted before to investigate ITH in GBM (Sottoriva *et al.*, 2013), the methodology had yet to be applied to determine regional metabolic heterogeneity. The primary aim of this study was to determine if intratumour metabolic heterogeneity is a biological attribute of HGGs, with characterisation of the metabolism of infiltrating tumour cells secondary to this objective. Most patients demonstrated heterogeneity at the metabolomic level, although several patients (particularly patients 9, 14, and 15) featured overlapping metabolomic profiles derived from non-invasive regions, indicating similarities in terms of overall metabolism. However, it was evident in all patients that the metabolomic profile within the invasive margin was distinct compared to that

observed for the non-invasive regions, except for patient 8 whose profile was skewed by the very bloody/vascular region 2.

Heterogeneity in canonical metabolites belonging to well described pathways, including glycolysis, TCA cycle, energetics, and amino acid metabolism was observed in all patients but to different extents: patient 6 (18 out of 42 significantly variant by ANOVA), patient 8 (39/42), patient 9 (10/42), patient 14 (39/42), and patient 15 (29/42). Only the canonical metabolites D-glucose and L-ornithine demonstrated significant regional heterogeneity across all patients, indicating that intratumour metabolic heterogeneity is patient-specific. Moreover, as observed for patients 14 and 15, regional heterogeneity was more pronounced between invasive and non-invasive regions, with less heterogeneity between non-invasive regions. Lipidomic profiling also demonstrated considerable overlap between non-invasive profiles, with most invasive region samples segregating and clustering apart from non-invasive region samples across all patients. The identification of a distinct metabolomic and lipidomic profile within the invasive margin is of therapeutic significance since this region harbours tumour cells that have infiltrated normal brain parenchyma and will ultimately seed recurrent, treatment-refractory tumours. Therefore, understanding the metabolomic and lipidomic profiles of the invasive region is paramount to the tailoring of therapeutic strategies aimed at inhibiting aberrant cancer metabolic activity which may be critical for rapid re-growth of tumour from residual, infiltrative neoplastic cells.

In patients displaying a degree of metabolomic homogeneity across non-invasive regions, it is possible that the sampling procedure may have failed to detect micro-niches of altered metabolism. Indeed, metabolic differences at the single-cell level has been demonstrated between GSCs and differentiated glioma cells (Shibao *et al.*, 2017), reflecting inherent differences in metabolism between cell cycle states (Agathocleous and Harris, 2013). Since GSCs are purported to account for only a small percentage of the tumour cell population, their metabolic differences are potentially masked by the metabolism of non-

tumour propagating cells. Metabolic heterogeneity may therefore only be present between stem-like and non-tumourigenic tumour cells, but this will require validation through isolation and study of metabolic heterogeneity in non-tumourigenic tumour cell populations only. Another potential explanation for metabolic homogeneity within some patients may reflect the basic metabolic requirements of proliferating cells to accumulate energy and biomass. This is supported by the convergence of several signalling pathways involved in cancer on a few key metabolic pathways, such as glycolysis, TCA cycle, and lipid metabolism (Cairns, Harris and Mak, 2011). ITH may therefore result in relatively homogenous metabolomic and lipidomic profiles and may only be influenced by substrate utilisation as suggested in previous studies (Hensley *et al.*, 2016). Consistent with this, most patients demonstrated significant variation in glucose, serine, glycine and lactate. Future studies should develop methods of delineating limiting substrates within HGGs as these will be particularly therapeutically relevant considering that they may represent non-oncogene addictions, which describes pathways that are not driving tumourigenesis but are relied upon to maintain tumour viability, such as stress responses (Nagel, Semenova and Berns, 2016). It is important to appreciate that metabolic pathways which are highly active across non-invasive and invasive regions, may represent an alternative therapeutic strategy which circumvents genetic intra-tumour heterogeneity; the presumption here is that such aberrantly active pathways must be critical for tumour viability and which potentially represents more ubiquitous therapy avenues than precision medicine approaches, which may not in reality be as practical as hoped, for sufficiently divergent tumours.

Overall, there are two therapeutic implications with regards to the identification of metabolic heterogeneity: 1) significantly varying metabolic substrates (e.g. glucose, serine, glycine, etc) may represent nutrients that are limiting for tumour growth due to non-oncogene addictions; therefore, further reduction through pharmacological means may facilitate tumour growth reduction. 2) metabolites that are minimally variant across regions and patients

(e.g. glutamine) may be amenable for therapeutic targeting in the majority of HGG patients, irrespective of genetic subgrouping. Both hypotheses can be tested in larger cohorts, which was a limitation of our study. Moreover, it can be determined in larger cohorts if different gene expression subtypes of GBM or IDH mutant status influence the extent of regional heterogeneity, and whether the degree of metabolic intratumour heterogeneity influences overall survival. The identification of metabolism-based prognostic signatures will enable clinical stratification of patients, as has been conducted for breast (Haukaas *et al.*, 2016; Cappelletti *et al.*, 2017), kidney (Hakimi *et al.*, 2016) and cervical cancer (Yang *et al.*, 2017), and will be facilitated by progress made to translate MS-based diagnostics to the clinic (Shushan, 2010).

The results drawn using the chosen methodology of analysing multi-region sampled tumour fragments through LC-MS are further confounded by the lack of data delineating the contribution of non-tumour or stromal cells, including immune cells, neurons, and endothelial cells, to the metabolomes within the non-invasive and invasive regions. Metabolic coupling is a key feature between cell types, such as the glutamine-glutamate cycle between astrocytes and neurons (Schousboe *et al.*, 2014), and MS-based analysis of tumour fragments fails to identify such interactions. Several studies have demonstrated evidence highlighting the importance of stromal compartments within the tumour microenvironment to tumour progression in terms of the growth-promoting cytokines, ligand-receptor interactions, and metabolic coupling involving lactate, amino acids and fatty acids (Lyssiotis and Kimmelman, 2017; Quail and Joyce, 2017). Secreted metabolites from tumour cells can also impact stroma cells as observed in IDH mutant acute myeloid leukaemia in which the oncometabolite 2HG induced NFκB activation in bone marrow stromal cells, leading to reduced chemotherapy-induced apoptosis (Chen *et al.*, 2016). Combined with the metabolic plasticity of cancer cells, effective treatment of cancer therefore likely requires targeting of metabolic vulnerabilities in reprogrammed cancer cells as well as the metabolic co-dependencies present

between cancer cells and stromal cells, thus requiring future investigation of the contribution of the tumour microenvironment to the tumour metabolome.

Future attempts to fully characterise intratumour metabolic heterogeneity should also utilise single-cell isolation strategies as exemplified by Darmanis, in conjunction with developments within the metabolomics and lipidomics fields in relation to single-cell applications (Rubakhin, Lanni and Sweedler, 2013; Zenobi, 2013). In this regard, our laboratory has developed a method to purify GBM invasive margin cells from normal brain parenchyma by utilising the post-operative fluorescence signal from 5-ALA-guided surgical resections and application of dissociated invasive margin cells to fluorescence-activated cell sorting (FACS) (Smith et al, manuscript in preparation for PNAS). This will enable the metabolomic and lipidomic readout of pure invasive margin cells to be determined, without the confounding factor of normal brain signals.

7.2. LC-MS-based characterisation of metabolic intratumour heterogeneity

LC-MS was the methodology chosen to profile metabolites and lipids due to greater coverage of the metabolome and lipidome compared to other analytical methods, such as ^{1}H-NMR (~10x greater coverage by LC-MS compared to ^{1}H-NMR). Application of a similar multi-region sampling technique followed by gas chromatography-MS was successfully implemented by Okegawa and colleagues to investigate metabolism in kidney tumours (Okegawa *et al.*, 2017). We successfully identified peak intensity values for ~500 metabolites informing on several metabolic pathways, including glycolysis, TCA cycle, and the metabolism of glutamine, serine, and other amino acids. Analysis of the LC-MS data using univariate and multivariate methods enabled identification of significantly varying metabolites, as well as the clustering of replicates from the same tumour fragment in support of regional heterogeneity. Alterations to specific metabolic pathways could be deduced but was precluded by the absence of identification for some key metabolites,

such as oxaloacetate within the TCA cycle. This may be due to limiting amounts of tissue available from which to sample, with weights as low as ~15 mg being assessed. Due to the nature of the project, this was an unavoidable consequence and also prevented the assessment of n=6 replicates for each category, which is an accepted standard within the metabolomics community. Future application of this method must therefore carefully balance the need for several replicates with the need to have sufficient material to obtain good LC-MS signal strength and pick up low concentration metabolites.

Metabolite profiling by LC-MS is a useful tool to assess the global metabolome and is therefore amenable for the identification of biomarkers. For instance, we identified proline pathway metabolites as distinguishing features of invasive and non-invasive regions. However, our LC-MS method provided only a snapshot of metabolism and did not inform on dynamic metabolic flux. Incorporation of stable isotopic tracers into the LC-MS methodology *ex vivo* would identify changes to metabolic flux and inform on metabolic enzymes with potentially different activity between tumourous and normal brain tissue. A successful implementation of this approach was conducted by Okegawa and colleagues who performed an *ex vivo* stable isotopic tracer experiment on tumour and adjacent normal kidney tissue slices producing results suggestive of different PDH and PC activity (Okegawa *et al.*, 2017). Combined with our 5-ALA-based sorting of infiltrating tumour cells in development, such a study could be extended to investigate the metabolic changes driving infiltrating tumour cells compared to non-infiltrating tumour cells. This would enable us to investigate the conflicting evidence by Kathagen-Buhmann and colleagues, who demonstrated a dichotomy between glycolysis and PPP activity at the gene expression level associated with migratory or proliferative phenotypes, respectively (Kathagen-Buhmann *et al.*, 2016), and our observations of regional homogeneity in the expression of glycolysis and PPP enzymes between invasive and non-invasive regions. Furthermore, incorporation of other multi-modality imaging strategies, such as DCE-MRI, to the LC-MS methodology will proffer more regional biological information in association with metabolomic and

lipidomic profiles, as exemplified by Hensley and colleagues in their *ex vivo* identification of heterogenous glucose metabolism and its relation to the extent of regional perfusion in lung cancer (Hensley *et al.*, 2016).

7.3. Integration of metabolomic and transcriptomic data

The project hypothesis required integration of metabolomics and transcriptomics data to investigate whether underlying heterogeneity in gene expression would manifest at the metabolic level. Multilevel modelling was performed to identify DEGs between the invasive and non-invasive regions. However, only a few metabolism-related genes were identified indicating relatively minimal regional metabolic heterogeneity, compared to previously reported genetic and genomic GBM ITH. Analysis of genes encoding enzymes within canonical metabolic pathways also demonstrated regional homogeneity, supporting the findings from the multilevel modelling approach. This precluded the integration of metabolomics and transcriptomics data to elucidate gene-metabolite associations. A limitation of the study was the evaluation of only n=1 gene expression profiles per region due to lack of material remaining following metabolomics and lipidomics analyses from the same tissue samples, meaning that statistical evaluation of regional genetic variation within single patients could not be assessed. Improved methodology involving the simultaneous extraction of metabolites, lipids and RNA are currently in development within our laboratory to obtain as much omics information from the little tissue available. Heiland and colleagues successfully integrated ^{1}H-NMR metabolomics data with transcriptomics data, establishing links between GBM gene expression signatures and metabolites. However, this study did not take into account regional heterogeneity at the genetic and metabolic level (Heiland *et al.*, 2017). Okegawa and colleagues sequenced 23 metabolism genes associated with kidney cancer but could not correlate gene clusters with metabolic groupings (Okegawa *et al.*, 2017), in line with the findings of Hakimi and colleagues indicating that metabolic alterations are not necessarily correlated with metabolic enzyme gene expression (Hakimi *et al.*, 2016). The proposed link is to non-canonical metabolic flux, gene-protein level

mismatch, or cofactor levels affecting enzyme activity. However, evidence to the contrary was obtained in a GBM study of differential fluorescence intensity following 5-ALA administration which was attributed to regional heterogeneity of glutaminase 2 (GLS2) expression and its effects on NADPH production (Kim *et al.*, 2017). As mentioned above, isotopic tracer studies may help elucidate metabolic enzyme activity or alternatively, metabolomics/transcriptomics studies could be combined with proteomics data to overcome the gene-protein level mismatch (Meierhofer, Weidner and Sauer, 2014).

7.4. Normal brain component within the invasive region

A caveat associated with our investigation of metabolism within the invasive margin is the low tumour cell content (~5%, as determined by 5-ALA FACS-purified quantitative data, Smith et al, manuscript in preparation). The invasive region demarks the location of normal brain-infiltrating tumour cells that will ultimately seed recurrent tumours in other local and distal brain locations. Delineation of the invasive region was based on the surgeon's experience of spread of disease along white matter tracts, consistent with research demonstrating tumour cell invasion along white matter tracts and blood vessels. Given the nature of the invasive region, the normal brain component making up most of the tissue is a confounding factor when trying to make assertions regarding the metabolism of infiltrating tumour cells compared to core tumour cells. Normal brain controls from the same neuro-anatomical region could have been included to remove the metabolic signature of normal brain from the invasive region profile. However, metabolic signatures have been shown to differ across different brain regions in mouse models (Ivanisevic *et al.*, 2014). Therefore, use of human normal brain tissue from temporal lobe, for example, may not be representative of metabolism within the vicinity of the tumour, which could be in a different brain region.

The identification of reduced proline pathway metabolites within the invasive region may therefore reflect normal brain metabolism as opposed to a metabolic attribute of infiltrating tumour cells. However, consistent reduction

in proline pathway metabolites and significant impact to arginine and proline metabolism across all five patients, supports a functional role of altered proline metabolism within the invasive margin. Indeed, recent RNA-sequencing of infiltrating tumour cells isolated from the invasive region revealed increased expression of *PRODH*, implicating proline metabolism as functionally relevant to invasive tumour cells and calling for further study (Darmanis *et al.*, 2017). This can be conclusively determined through analysis of proline pathway metabolites in FACS-isolated invasive region tissue, obtaining both a 5-ALA-positive infiltrating tumour and 5-ALA-negative normal brain component. This methodology would provide the perfect internal normal brain control, avoiding the confounding factor due to different metabolic profiles associated with different brain regions. *In vitro* studies examining tumour cell migration/invasion can also investigate the effect of knockdown of proline pathway enzymes, including *PRODH*, *PYCR*s, *P5CHD* and *P5CS*, or the effect of adding exogenous proline pathway metabolites, to test the hypothesis that ATP production derived from proline catabolism increases migratory/invasive potential. Finally, ^{15}N-labelled proline may be used to examine metabolic flux differences between infiltrating tumour cells and normal brain cells and can be associated with proline pathway enzyme activities. The reverse hypothesis that proline synthesis within non-invasive regions promotes tumour growth should also be investigated through isotopic evaluation of glutamine metabolism, following the identification of proline synthesis maintaining cellular viability in MYC-overexpressing tumour cells (Liu *et al.*, 2012).

7.5. Adult and paediatric GBM dependency on lipoproteins for survival

Our investigations into lipoprotein dependency revealed a requirement for lipoproteins within the culture medium to sustain tumour growth rates. Metabolomics analysis demonstrated minimal alterations to canonical metabolic pathways, whereas lipidomics analysis revealed alteration to several lipid species, including reduced levels of triglyceride species within the pGBM cell lines that was not observed for the adult U87 cell line. This provided evidence of lipid droplet involvement in the pGBM cell lines maintaining the

levels of other lipid species besides triglycerides, a hypothesis which can be tested using basic Nile Red staining to more complex Raman spectroscopy. Interestingly, combined with the demonstration of different responses to exogenous fatty acid supplementation, adult and paediatric GBM cells might maintain lipid homeostasis through alternate means, with the former scavenging from external sources and the latter utilising *de novo* synthesis, hypotheses that can be tested through assessment of fatty acid-binding proteins and lipid synthesis rates. Transcriptomics analysis also highlighted differential enrichment of GO processes in pGBM cells compared to U87 cells, related to defence/stress and hypoxia responses, respectively. Combined with different cell cycle responses, these results collectively indicate differences in terms of lipoprotein metabolism between adult and paediatric GBM cells. However, a common feature of lipoprotein deficiency across all cell lines was a reduction in total cholesterol levels, particularly in terms of cholesterol esters. Several genes involved in cholesterol synthesis were upregulated in both U87 and pGBM cells but were upregulated to a greater extent in the latter. These differences may be due to the presence of *TP53* mutants in the KNS42 and SF188 cells compared to wildtype p53 in U87 cells. In breast cancer, mutant p53 has been demonstrated to induce the expression of seven genes within the mevalonate pathway, including *HMGCR*, *MVK*, *MVD*, *FDPS*, *SQLE*, *LSS*, *and DHCR7*, by interaction with SREBPs at gene promoters, attributing a metabolic vulnerability to statins (Freed-Pastor *et al.*, 2012).

The increased expression of cholesterol synthesis genes indicates that GBM cells can upregulate *de novo* synthesis of cholesterol in the absence of lipoprotein uptake. However, prolonged deprivation of lipoproteins is eventually detrimental to monolayer cultures of U87 and pGBM cell lines, likely related to the inability to rescue cholesterol ester levels despite increased *de novo* synthesis, or is related to the mitogenic properties of lipoproteins (Angius *et al.*, 2015). Interestingly, U87 spheroids demonstrated unperturbed growth under lipoprotein deficient conditions, in contrast to the pGBM spheroids which were cytostatic. Growth of U87 cells in 3D format may therefore alter

the gene expression profile favourably to accommodate metabolic stress, a hypothesis which can be tested through transcriptomic analysis of monolayer and spheroid models of U87 cells cultured under lipoprotein-replete or -deplete conditions. Caveats of the analyses conducted above include metabolite differences observed between medium supplemented with either FBS or LCS, as well as the different origins of the supplements (foetal calf vs. calf) that may expose cells to different complements of growth factors.

Overall, these results highlight the importance of lipoproteins to tumour cell growth in terms of supplying nutrients. However, the importance of lipoproteins within the brain *in situ* and during tumour progression is less clear and future experiments will need to fully elucidate if tumours are more dependent on lipoprotein compared to normal brain, as suggested by higher LDLR expression (Rudling *et al.*, 1990), rather than an artefact of *in vitro* culture. Knockout studies in mice indicate that LDLR is not essential for the maintenance of brain cholesterol levels (Osono *et al.*, 1995; Taha *et al.*, 2009) but negatively impacts lysine metabolism and carnitine synthesis (Lee *et al.*, 2016). Conclusive evaluation of the importance of lipoproteins to GBM growth can be achieved through immunohistochemical evaluation of LDLR levels and measurement of lipoprotein uptake. Villa and colleagues performed the latter and demonstrated increased uptake (Villa *et al.*, 2016). If confirmed, brain tumour cells may be selectively vulnerable to LDLR-ablation therapies or strategies taking advantage of high tumour LDLR expression, such as liposomal delivery of drugs (Zhang *et al.*, 2013; Liu *et al.*, 2014) or LDLR-targeting peptide vectors (Molino *et al.*, 2017). Moreover, engineering tumour cells to mediate shRNA-induced silencing of LDLR following chemical induction of transcription will allow *in vivo* assessment of lipoprotein dependency in orthotopic mouse models.

7.6. Ligand activation of LXR in adult and paediatric GBM

The antitumour properties of LXR agonists have previously been shown in several tumour types, including prostate, colon, and breast cancer (Lin and Gustafsson, 2015). Within GBM, LXR agonists reduce tumour xenograft growth in orthotopic mouse models due to reduced cholesterol uptake, increased export and lack of *de novo* synthesis (Villa *et al.*, 2016). We demonstrated reduced cellular viability in both adult and paediatric GBM models following treatment with either GW3965 or LXR-623. Evidence of a caspase-3-dependent mechanism of cell death was demonstrated. However, other mechanisms of reduced cellular viability may be in effect and transcriptomic analysis following LXR agonist treatment revealed evidence of ER stress and the unfolded protein response. Interestingly, several genes involved in mitochondrial protein folding were upregulated. Through high-resolution confocal microscopy assessment, it can be determined if mitochondrial networks are negatively impacted by LXR agonist treatment. Other mechanisms of reduced cellular viability investigated in other tumour types include caspase-1-dependent pyroptosis (Derangère *et al.*, 2014), inhibition of Hedgehog signalling (Agarwal *et al.*, 2014), and altered lipid membrane dynamics (Pommier *et al.*, 2010). However, these may represent tissue specific responses, indicating that the genetic and epigenetic features of a cell may influence the response to LXR agonists. In support of this, addition of exogenous cholesterol only partially rescued cellular viability within U87 cells following LXR agonist treatment, whereas no benefit was observed in the pGBM cell lines. Collectively, these results suggest other effects in addition to cholesterol depletion underlie toxicity to LXR agonists and that endogenous cholesterol production may be necessary but not sufficient to sustain HGG growth. For instance, the pGBM cell lines demonstrated downregulation of several genes involved in cell cycle control and division, in contrast to U87 cells which showed upregulation of genes related to cell signalling and proliferation. This again highlights the similarities between the two pGBM cells lines and the distinct biological response displayed by U87 cells, which might be indicative of differences between adult and paediatric GBM. Whether these enriched processes are secondary to cholesterol depletion-mediated induction of cell

death or activation of other processes related to LXR transcriptional activation requires transcriptome assessment at earlier timepoints and knowledge of LXR target genes in astrocytes, as has been conducted through ChIP in mouse liver (Boergesen *et al.*, 2012), foam cells (Feldmann *et al.*, 2013), and macrophages (Pehkonen *et al.*, 2012).

Despite demonstrating therapeutic efficacy against several cancer types, the identification of elevated plasma triglyceride levels and steatosis via the SREBP1-mediated upregulation of lipogenic genes, including FASN, ACC, SCD-1 and phosphoethanolamine cytidyltransferase, in the livers in mouse subjects has precluded further clinical testing of LXR agonists (Schultz *et al.*, 2000; Collins *et al.*, 2002; Joseph, Laffitte, *et al.*, 2002). This has been attributed largely to activation of LXRα in liver and adipose tissue (Schultz *et al.*, 2000; Joseph, Laffitte, *et al.*, 2002; Joseph, McKilligin, *et al.*, 2002; Bradley *et al.*, 2007). Pharmaceutical development for LXRβ-selective agonists may circumvent undesirable side effects. Indeed, the LXRα-partial/LXRβ-full agonist LXR-623 does not activate hepatic lipogenesis due to a unique transcriptional cofactor recruitment profile (Wrobel *et al.*, 2008; Quinet *et al.*, 2009). However, neurological indications were observed in human subjects in a Phase I trial of LXR-623. Paradoxically, LXR agonists show beneficial effects in models of Alzheimer's disease (Koldamova *et al.*, 2005; Zelcer *et al.*, 2007; Fitz *et al.*, 2010; Terwel *et al.*, 2011), in which dysregulated control of cholesterol homeostasis has been attributed to the pathogenic mechanism (Arenas, Garcia-Ruiz and Fernandez-Checa, 2017). However, overexpression of LDLR, which is pharmacologically reduced upon LXR activation, has been shown to be beneficial in removing protein plaques associated with Alzheimer's disease (Kim *et al.*, 2009; Castellano *et al.*, 2012). Therefore, future assessment of LXR agonists must determine the context-dependent consequences of supraphysiological LXR activation on the health of all brain cell types. Despite these barriers to progress, there is still a strong rationale to investigate the therapeutic efficacy of LXR agonists in GBM, since mice with knockdown of LXRb demonstrate increased numbers and proliferation of astrocytes.

7.7. Identifying a metabolic 'Achilles heel'

One of the main objectives of this project was the identification of a metabolic 'Achilles heel' in adult and paediatric GBM. Multi-region sampling of aGBM revealed enrichment of *arginine and proline metabolism*, with reduced levels of several proline-related metabolites observed within the invasive margin compared to non-invasive regions. The significance of this remains unclear due to the caveat of a potential normal brain component within invasive margin tissue. However, observation of increased *PRODH* expression in infiltrating tumour cells (Darmanis *et al.*, 2017) provides a strong rationale for further study of the importance of proline to GBM involving knockdown experiments and invasion assays. The LC-MS-based analysis also revealed metabolic homogeneity in some tumours compared to others. If such homogeneity can be confirmed in a larger cohort of tumours, this subset may show a strong response to single agents targeting a particular metabolic pathway following identification of substrate preference (i.e. glucose, glutamine, acetate, etc). This could initially be tested *in vitro* using spheroid culture models of heterogeneous subclonal populations, as has been conducted for the study of subclonal interactions (Inda *et al.*, 2010; Marusyk *et al.*, 2014). It is important to state that such a ubiquitous, single-agent therapeutic strategy, necessitates a description of intra-tumour metabolism within distinct regions and differs from the 'magic bullet' single agent approach which relies on data from single tumour regions and which has consistently resulted in lack of Phase II clinical trials in HGG.

Studies into tumour metabolism have primarily investigated the use of glucose or glutamine to sustain growth by generating energy and supplying carbon atoms for the synthesis of more complex molecules, such as lipids and sterols. However, cancer cells can also meet metabolic needs through scavenging of nutrients from the extracellular environment, either through receptor-mediated uptake or micropinocytosis (Commisso *et al.*, 2013). In GBM, Villa and colleagues identified a non-oncogene addiction to lipoprotein uptake due to reduced *de novo* synthesis of cholesterol and decreased capacity to produce

endogenous LXR ligands (Villa *et al.*, 2016). Our investigations into lipoproteins highlighted cholesterol as the critical ingredient for growth, as was particularly evident in the U87 cell line. 26 NAPDH molecules are consumed in *de novo* synthesis of cholesterol (Lunt and Vander Heiden, 2011). Therefore, exogenous uptake may enable GBM cells to redirect NADPH into other reducing reactions (Vander Heiden, Cantley and Thompson, 2009; Pavlova and Thompson, 2016). GBMs may therefore be particularly susceptible to cholesterol-lowering drugs, including statins and LXR agonists.

Cholesterol-rich diets have been shown to increase cancer predisposition, and the administration of statins to reduce cellular cholesterol levels has been observed to lower incidence rates (Hu *et al.*, 2012). In support of this, statin use has been shown to lower the risk of glioma (Gaist *et al.*, 2013). These studies indicate that cholesterol is a major nutrient for tumourigenesis. We chose to investigate LXR agonists because cholesterol levels were lowered by two mechanisms: reduced uptake and increased export. Although therapeutic efficacy was observed, the concentrations required were relatively high compared to standard cytotoxic compounds, meaning that combination strategies may be more efficacious and less likely to cause side-effects. This has been demonstrated for statins in combination with either temozolomide or gefitinib (Cemeus *et al.*, 2008; Oliveira *et al.*, 2018). Based on this, future assessment of cholesterol depletion using either statins or LXR agonists can investigate the additive effects with standard chemo- and/or radiotherapy therapeutic regimen. Indeed, the identification of an elongated S phase supporting stalled DNA replication in lipoprotein-starved paediatric cells may reveal a vulnerability to drugs and radiation that induce further DNA damage. However, ongoing investigations into LXR agonist must also explore biological responses in all cell types found within the tumour microenvironment, including immune cells, stromal cells, and endothelial cells. This can be achieved through functional assessment of immortalised cell lines of each cell type to determine effects on normal function, or through transcriptional analysis of LXR agonist-treated tumour and surrounding tissue in mouse models

following single-cell sorting of individual cell types, as demonstrated by Darmanis and colleagues (Darmanis *et al.*, 2017).

Through our metabolic investigations of *in vitro* cultures, we identified difference between adult and paediatric GBM cell lines following lipoprotein starvation and treatment with LXR agonists. Metabolomics analysis highlighted a significant reduction in the levels of pyruvate and malate within the pGBM cell lines compared to the adult U87 cell line under lipoprotein-deplete conditions. This alluded to potentially inherent differences in metabolism within adult and paediatric GBM. Supporting this was the identification of a higher number of significantly reduced triglyceride species in the pGBM cell lines compared to the adult U87 cell line. These findings may be explained by differences in genetic and epigenetic traits related to the cell-of-origin and tumourigenesis. Added to this is the possible misrepresentation of the chosen cell lines for the study of metabolism in adult and paediatric GBM given the clonal nature of the disease. For instance, the presence of mutant p53 in KNS42 and SF188 cells may account for the differences in transcriptomic response to lipoprotein starvation, as well as the higher dosage of LXR-623 required to induce the same reduction in cellular viability as for the adult U87 cell line. However, *TP53* mutations are also a feature of adult GBM, highlighting again the possible misrepresentation of the *in vivo* situation using these cell lines. Caution must therefore be exercised in ascribing metabolic differences to the factor of age alone in exclusion of the underlying genetic basis. Future analysis of bulk tissue from paediatric patients, containing the full complement of tumour subclones, will statistically highlight metabolic similarities or differences in large cohorts of adult and paediatric GBM, and thus inform on the possibility of personalising therapeutic regimens according to age group.

The identification of a metabolic 'Achilles heel' remains elusive due to the essential requirement for the normal functioning of all metabolic pathways. However, inroads into the identification of metabolic co-dependencies associated with particular oncogenes will allow synergistic combination of

standard chemotherapeutic agents with metabolism-targeting therapies, since inhibition of two independent hallmarks of cancer will reduce the probability of surviving tumour subclones demonstrating resistance to one therapeutic agent. The impetus behind this body of work is the dismal outcomes for both adult and paediatric GBM patients. Downstream investigation of conclusions drawn from this body of work will hopefully help tailor effective therapeutic strategies leading to better patient outcomes and quality of life in the future.

Chapter 8

Appendix

8. Appendix

8.1. Tissue weight optimisation

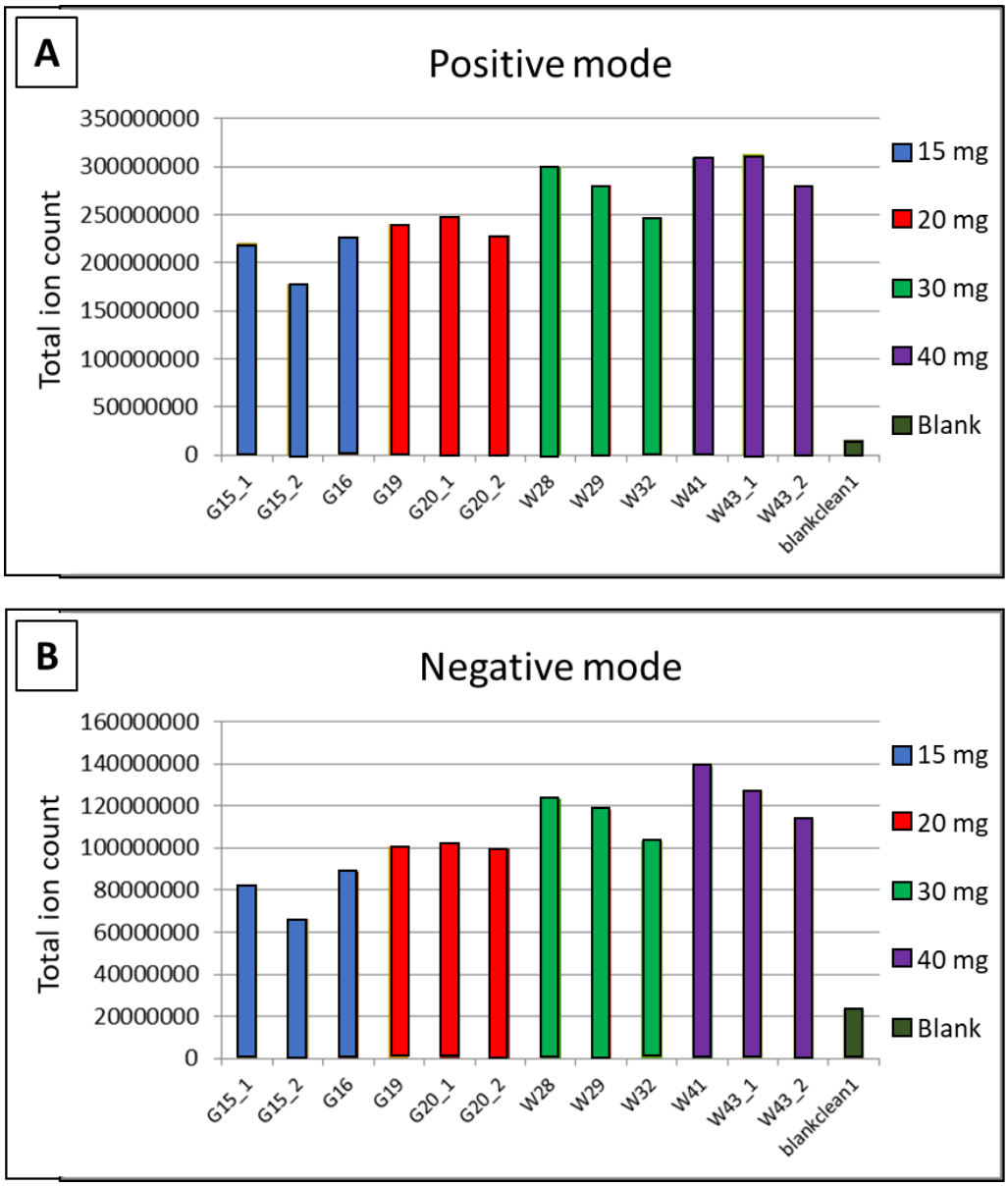

Figure 8.1. Tissue weight optimisation based on total ion counts. LC-MS-based metabolite analysis of tissue weights approximating the categories in the figure legend. Total ion counts in the positive and negative mode are displayed in A and B, respectively. Samples starting with G and W represent grey and white brain matter, respectively, with the blank sample consisting of methanol alone.

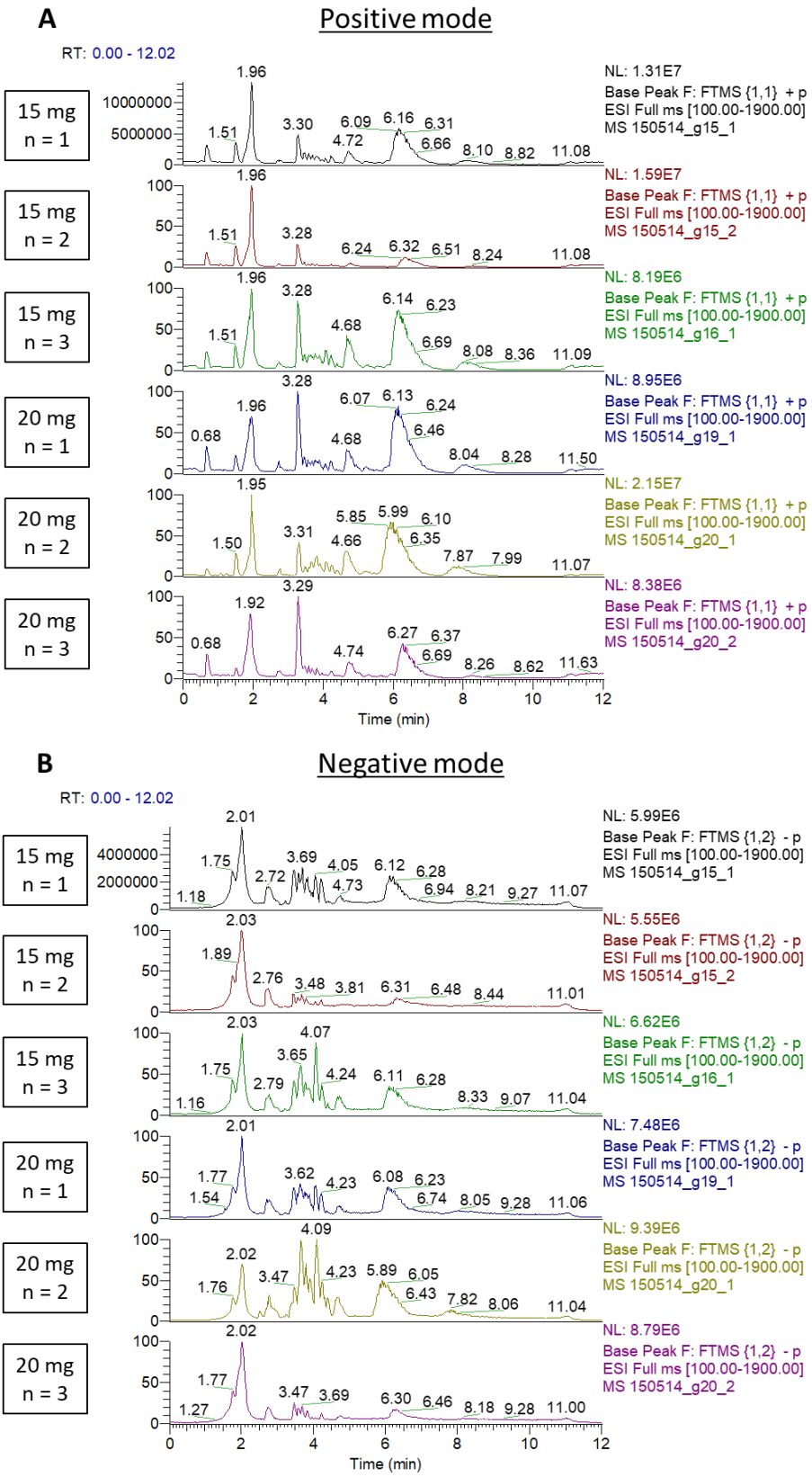

Figure 8.2. Ion chromatograms of grey matter analysed by LC-MS. Spectra in the positive and negative modes are displayed in A and B, respectively. Weights used for tissue weight optimisation are displayed to the left of each chromatogram. Maximum peak intensities are displayed at the top of the information to the right of each chromatogram.

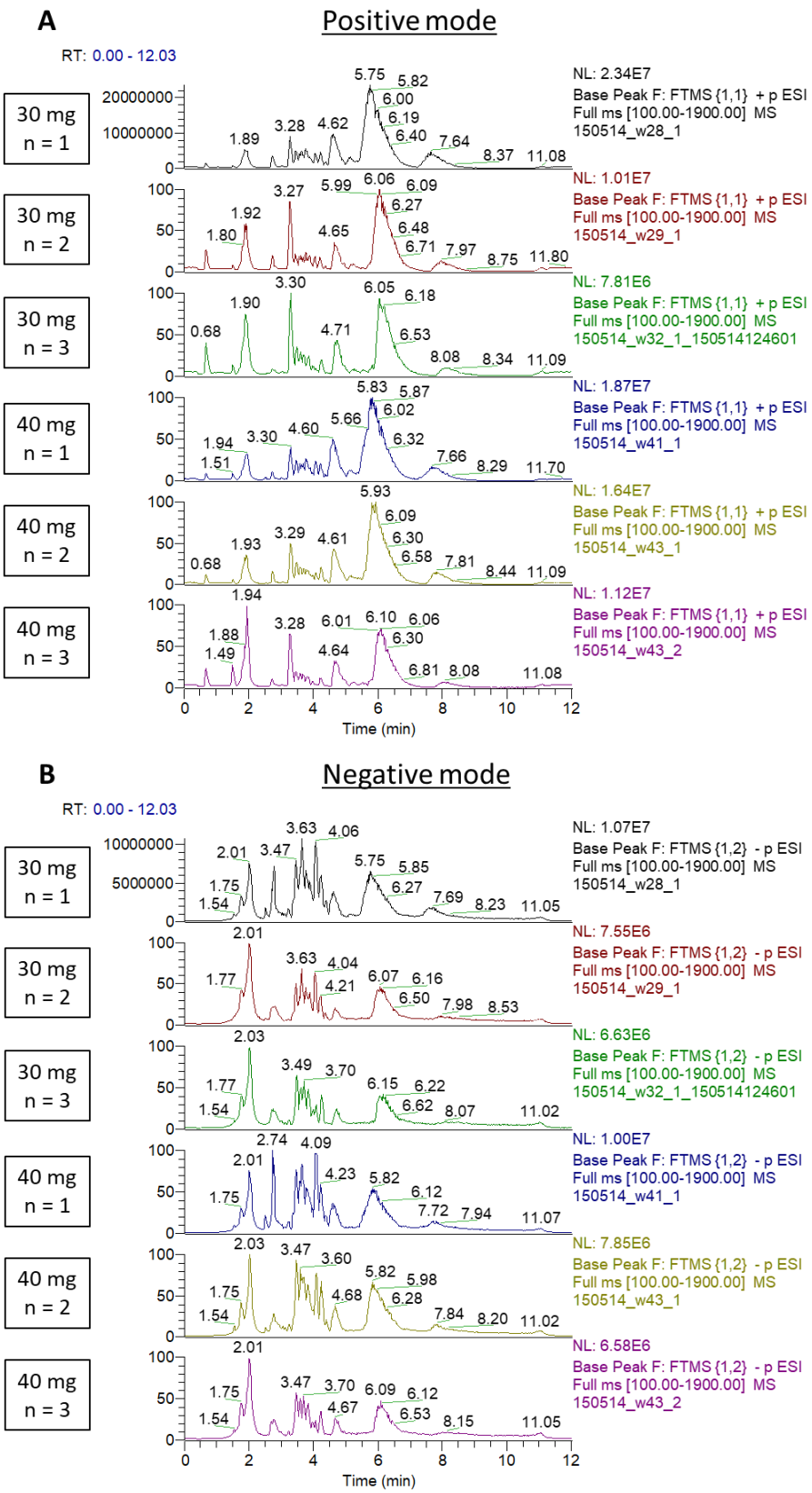

Figure 8.3. Ion chromatograms of white matter analysed by LC-MS. Spectra in the positive and negative modes are displayed in A and B, respectively. Weights used for tissue weight optimisation are displayed to the left of each chromatogram. Maximum peak intensities are displayed at the top of the information to the right of each chromatogram.

8.2. Patient 8 metabolomics summary

PCA analysis of patient 8 highlighted clustering of samples from each region and emphasised the unique metabolome demonstrated by region 8_2 (Figure 8.4A), as supported by hierarchical analysis (Figure 8.4B) and unique heatmap signature (Figure 8.4C). In line with this, analysis of regional variation using a one-way ANOVA model revealed metabolite variation to occur predominantly due to region 8_2, with the other regions demonstrating similar metabolomic profiles (data not shown). MSEA of significantly varying metabolites revealed no significant enrichment of any metabolite set (Table 8.1). Inspection of metabolites pertaining to glycolysis, TCA cycle and energetics highlighted the distinction of region 8_2 generally characterised by lower peak intensities in comparison to other regions, with the exception of higher levels of pyruvate, lactate and creatinine (data not shown). The invasive region demonstrated increased levels of early glycolytic intermediates as well TCA-related metabolites, possibly leading to increased ATP and creatine levels as observed. Regional variation in essential, conditional and non-essential amino acids further distinguished region 8_2 (data not shown). However, region 8_3 demonstrated increased levels of several amino acids relative to other regions, including glycine and l-glutamate (Table 8.2). Comparison of non-invasive and invasive regions revealed a general decease in essential and conditional amino acids that reached significance in most cases (Table 8.2). Significant heterogeneity between regions was observed across regions in terms of serine/one-carbon metabolism, leading to significant variation in glutathione and glutathione disulphide levels (data not shown). Metabolites varying significantly between non-invasive and invasive regions were assessed for enriched metabolite sets but generated no significant results (Table 8.3). Pathway analysis identified significant impact on several pathways, including *arginine and proline metabolism* (raw *p*-value=1.41E-05; impact=0.43) (Table 8.4).

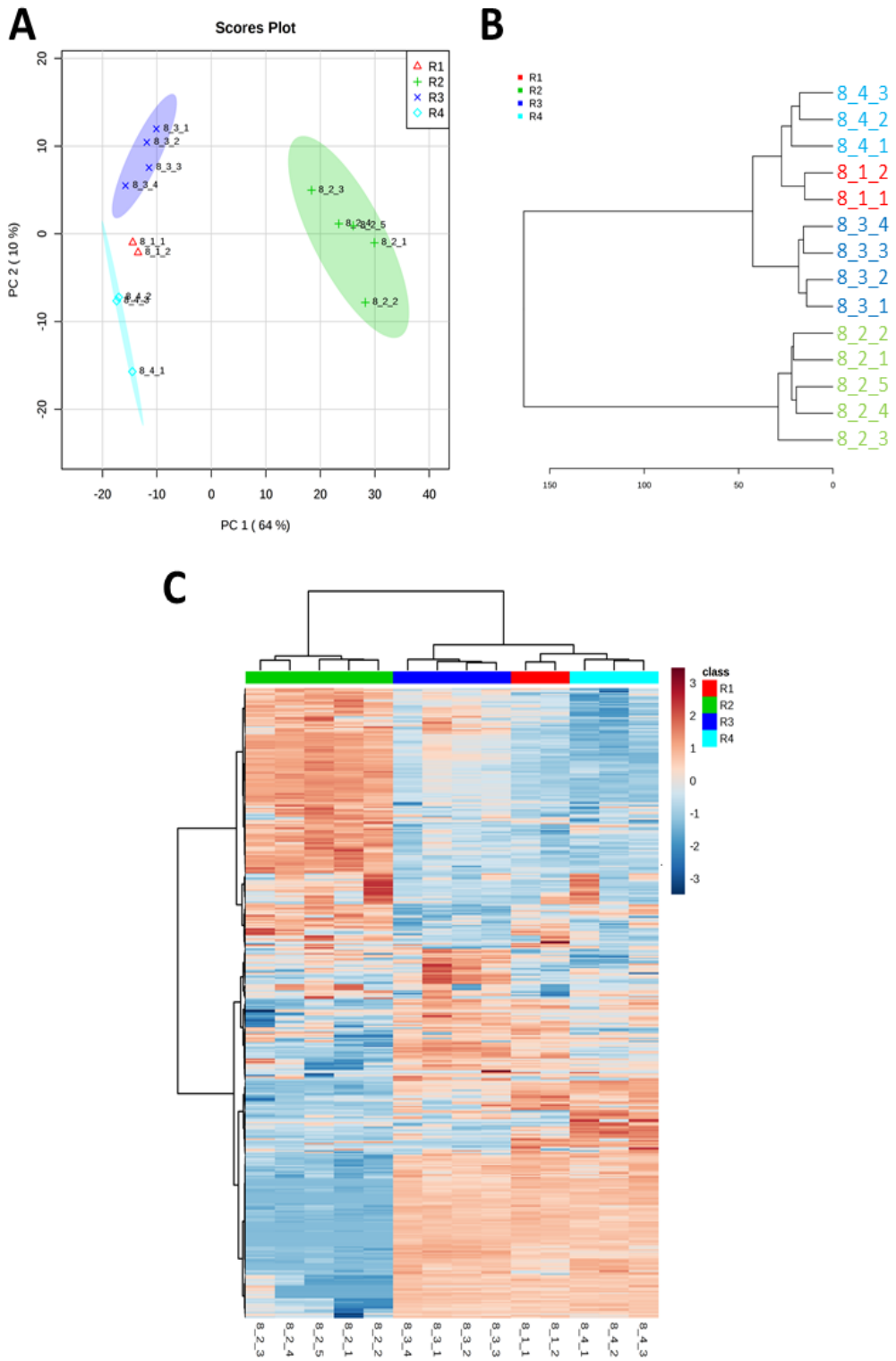

Figure 8.4. Diagnostic plots for patient 8 metabolomics data. (A) Dimensional reduction through PCA and visualisation of sample variation. (B) Hierarchical clustering analysis measuring dissimilarity between samples. (C) Heatmap overview of the metabolome. Sample IDs delineate the patient, region (symbol R), and replicate numbers, respectively.

Table 8.1. Metabolite set enrichment analysis of metabolites in patient 8 identified as significant using one-way ANOVA.

Metabolite Set	Total	Expected	Hits	Raw p	Holm p	FDR
Glutamate Metabolism	49	13.7	19	0.0631	1	1
Phosphatidylethanolamine Biosynthesis	12	3.36	6	0.0878	1	1
Aspartate Metabolism	35	9.81	13	0.152	1	1
Urea Cycle	29	8.13	11	0.16	1	1
Cardiolipin Biosynthesis	11	3.08	5	0.168	1	1

The table details the top five enriched metabolite sets based on significantly differentially abundant metabolites with log2 fold-change >0.58 or < -0.58. Significant raw *p*-values (Raw p) for enriched metabolite sets were adjusted for multiple comparisons using the Holm (Holm p) or false-discovery rate (FDR) method.

Table 8.2. Metabolic variation across region and region types in patient 8.

Metabolite	ID confidence	Across regions		Invasive vs non-invasive regions		
		FDR	Significant	log2FC	FDR	Significant
Glycolysis						
D-Glucose	8	5.15E-08	****	0.66	5.77E-02	ns
D-Glucose 6-phosphate	10	3.69E-02	*	0.81	8.44E-02	ns
D-Fructose-1,6-bisphosphate	10	3.27E-05	****	1.78	2.47E-02	*
D-Glyceraldehyde 3-phosphate	10	8.03E-06	****	1.42	2.53E-02	*
3-Phospho-D-glycerate	10	6.34E-04	***	-1.15	9.38E-01	ns
Phosphoenolpyruvate	10	2.71E-03	**	-0.43	8.14E-01	ns
Pyruvate	10	1.66E-04	***	-1.21	3.33E-01	ns
Lactate	10	1.70E-03	**	-0.01	8.51E-01	ns
Tricarboxylic acid cycle						
Citrate	8	6.19E-03	**	0.09	6.06E-01	ns
Isocitrate	8	1.76E-07	****	1.15	2.48E-02	*
Succinate	10	2.21E-07	****	0.43	1.54E-01	ns
Malate	10	6.54E-04	***	0.32	1.17E-01	ns
Energetic and redox species						
ADP	10	6.26E-03	**	0.84	6.60E-02	ns
ATP	8	3.61E-01	ns	0.30	2.84E-01	ns
Creatine	10	8.91E-07	****	0.56	3.91E-02	*
Creatinine	10	2.39E-05	****	-0.49	3.32E-01	ns
NAD+	10	2.33E-01	ns	-0.41	6.02E-01	ns
NADH	10	1.34E-03	**	-0.02	2.26E-01	ns
Essential amino acids						
L-Histidine	10	4.65E-03	**	-0.28	2.31E-01	ns
L-Leucine	10	2.64E-06	****	-1.49	1.14E-03	**
L-Lysine	8	4.84E-07	****	-2.14	1.71E-02	**
L-Methionine	10	7.53E-07	****	-1.44	9.32E-04	***
L-Phenylalanine	8	2.50E-06	****	-1.45	1.67E-03	**
L-Threonine	10	4.55E-04	***	-0.42	1.37E-01	ns
L-Tryptophan	10	1.12E-07	****	-1.46	2.41E-03	**
Conditional amino acids						
L-Arginine	10	3.18E-05	****	-0.92	1.43E-02	**
L-Glutamine	10	1.46E-07	****	-0.49	2.70E-02	**
L-Tyrosine	10	1.84E-06	****	-1.50	1.21E-02	**
Glycine	10	1.05E-07	****	-0.68	1.87E-01	ns
L-Ornithine	10	1.70E-06	****	-1.12	4.72E-03	**
L-Proline	10	1.96E-07	****	-1.81	7.30E-04	***
L-Serine	10	3.01E-03	**	-0.59	1.44E-01	ns
Non-essential amino acids						
L-Alanine	10	6.14E-04	***	0.30	3.06E-01	ns
L-Aspartate	10	1.45E-02	*	0.61	1.08E-01	ns
L-Glutamate	10	2.41E-06	****	0.37	1.73E-01	ns
Serine/one-carbon metabolism						
Betaine	10	5.84E-03	**	0.03	9.07E-01	ns
L-Cystathionine	10	1.30E-07	****	0.88	4.97E-02	*
γ-L-Glutamyl-L-cysteine	8	7.24E-03	**	0.86	5.38E-02	ns
Glutathione	10	3.71E-03	**	0.85	4.99E-02	*
Glutathione disulfide	10	2.64E-03	**	-0.26	7.49E-01	ns
Hypotaurine	8	7.89E-07	****	-1.31	1.01E-01	ns
Taurine	10	5.35E-01	ns	-0.02	8.56E-01	ns

Metabolites highlighted in red showed RSD values >30% in QC samples. ID confidence scores delineate the confidence of the putative metabolite identification. Fold changes are invasive to non-invasive comparisons and are displayed as logarithms to the base 2 (log2FC). Fold changes >0.58 or < -0.58 are depicted in red and green, respectively. Statistical evaluation of variation between regions and region types was performed using a one-way ANOVA model and two-sample t-test, respectively. Significance scores were corrected for multiple comparisons using false discovery rate (FDR). ns = not significant; * = $p<0.05$; ** = $p<0.01$; *** = $p<0.001$; **** = $p<0.0001$.

Table 8.3. Metabolite set enrichment analysis of metabolites in patient 8 identified as significant using t-test.

Metabolite Set	Total	Expected	Hits	Raw p	Holm p	FDR
De Novo Triacylglycerol Biosynthesis	9	1.18	3	0.102	1	1
Cardiolipin Biosynthesis	11	1.44	3	0.165	1	1
Aspartate Metabolism	35	4.58	6	0.303	1	1
Phenylacetate Metabolism	9	1.18	2	0.334	1	1
Citric Acid Cycle	32	4.19	5	0.41	1	1

The table details the top five enriched metabolite sets based on significantly differentially abundant metabolites with log2 fold-change >0.58 or < -0.58. Significant raw *p*-values (Raw p) for enriched metabolite sets were adjusted for multiple comparisons using the Holm (Holm p) or false-discovery rate (FDR) method.

Table 8.4. Pathway analysis of metabolites in patient 8 identified as significant using t-test.

Metabolic Pathway	Total	Expected	Hits	Raw p	Holm p	FDR	Impact
Arginine and proline metabolism	77	3.295	13	1.41E-05	0.001129	0.001129	0.43153
Cysteine and methionine metabolism	56	2.3963	8	0.002202	0.17396	0.08808	0.20986
D-Arginine and D-ornithine metabolism	8	0.34233	3	0.003643	0.28418	0.097154	0
Valine, leucine and isoleucine biosynthesis	27	1.1554	4	0.025991	1	0.51981	0.18283
Aminoacyl-tRNA biosynthesis	75	3.2094	7	0.038896	1	0.54406	0

The table details the top five impacted metabolic pathways based on significantly differentially abundant metabolites with log2 fold-change >0.58 or < -0.58. Significant raw *p*-values (Raw p) for enriched metabolite sets were adjusted for multiple comparisons using the Holm (Holm p) or false-discovery rate (FDR) method. Impact scores range between 0 and 1.

8.3. Patient 9 metabolomics summary

PCA analysis of patient 9 highlighted overlapping metabolomic signatures between regions 9_2, 9_3, 9_4 and 9_5 (Figure 8.5A). Region 9_1 demonstrated a distinct metabolome as supported by hierarchical analysis (Figure 8.5A). Replicates 9_1_1 and 9_1_3 were particularly distinct, whereas 9_1_2 displayed similarities to replicates from region 9_2 (Figure 8.5B and C). Analysis of regional variation using a one-way ANOVA model revealed little variation between regions 9_2 and 9_3, with distinct heatmap signatures displayed by regions 9_1 and 9_5 (data not shown). MSEA of significantly varying metabolites revealed significant enrichment of *phenylacetate metabolism* (raw p-value=0.030) and *glycolysis* (raw p-value=0.045) (Table 8.5). Inspection of metabolites pertaining to glycolysis, TCA cycle and energetics highlighted high variability in glycolytic and energetic intermediates, with less variation demonstrated by TCA cycle-related metabolites (data not shown). The invasive region demonstrated increased levels of early glycolytic intermediates, but this was associated with decreased levels of ATP and NADH compared to non-invasive regions (Table 8.6). Regional variation in essential, conditional and non-essential amino acids distinguished region 9_1, characterised by higher metabolite peak intensities compared to the other regions (data not shown). Despite significant variation in L-serine and glycine levels across regions, regional variation in metabolites pertaining to serine/one-carbon metabolism was not significant (data not shown). Metabolites varying significantly between non-invasive and invasive regions were assessed for enriched metabolite sets, identifying significant enrichment of *glycolysis* (raw *p*-value=0.00043), *gluconeogenesis* (raw *p*-value=0.0028), and *mitochondrial electron transport train* (raw *p*-value=0.0072) (Table 8.7). Pathway analysis identified significant impact on arginine and proline metabolism (raw *p*-value=0.00080; impact=0.15) (Table 8.8).

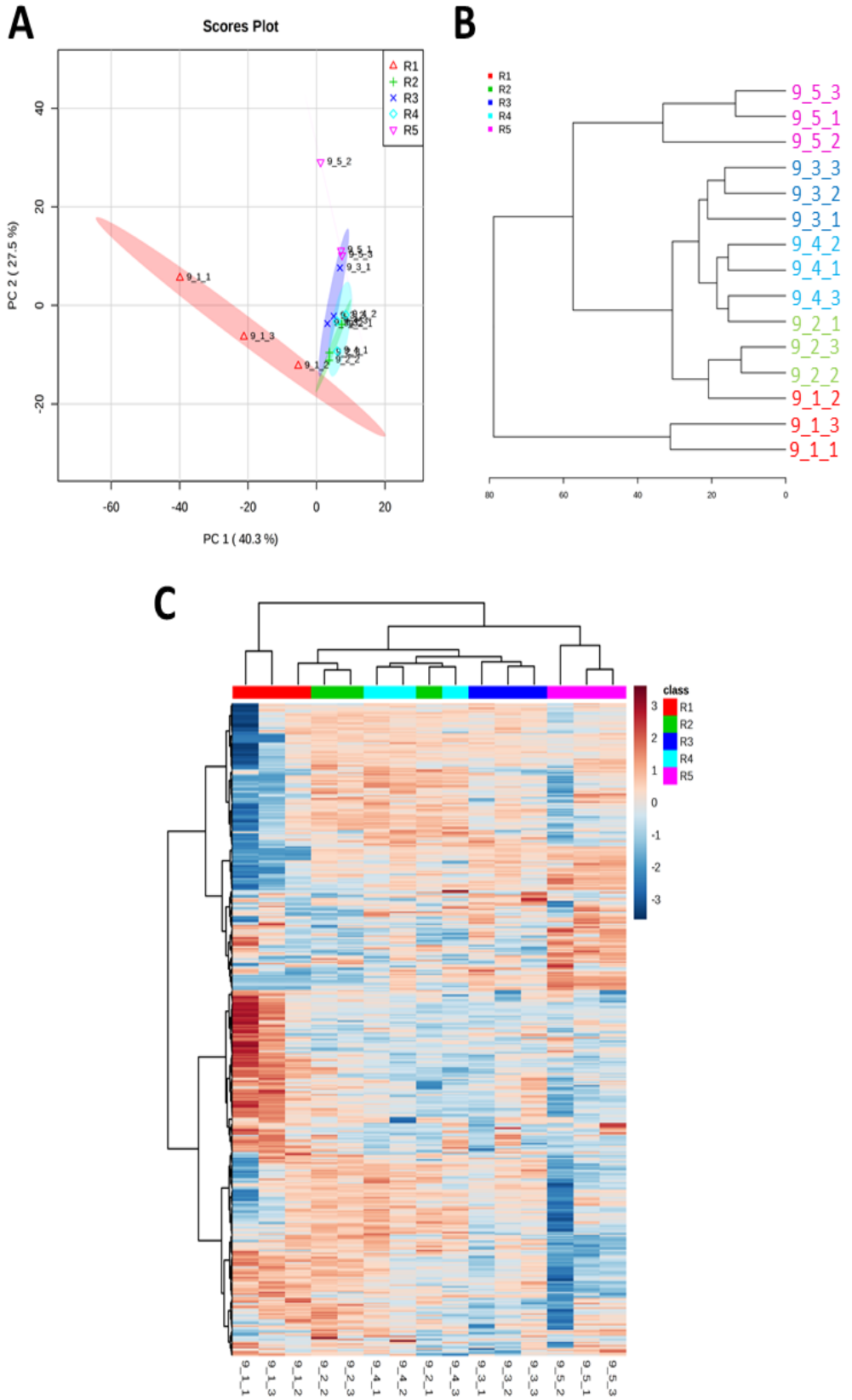

Figure 8.5. Diagnostic plots for patient 9 metabolomics data. (A) Dimensional reduction through PCA and visualisation of sample variation. (B) Hierarchical clustering analysis measuring dissimilarity between samples. (C) Heatmap overview of the metabolome. Sample IDs delineate the patient, region (symbol R), and replicate numbers, respectively.

Table 8.5. Metabolite set enrichment analysis of metabolites in patient 9 identified as significant using one-way ANOVA.

Metabolite Set	Total	Expected	Hits	Raw p	Holm p	FDR
Phenylacetate Metabolism	9	0.729	3	0.0302	1	1
Glycolysis	25	2.03	5	0.0452	1	1
Arginine and Proline Metabolism	53	4.3	8	0.0574	1	1
Glutathione Metabolism	21	1.7	4	0.083	1	1
Glutamate Metabolism	49	3.97	7	0.0936	1	1

The table details the top five enriched metabolite sets based on significantly differentially abundant metabolites with log2 fold-change >0.58 or < -0.58. Significant raw *p*-values (Raw p) for enriched metabolite sets were adjusted for multiple comparisons using the Holm (Holm p) or false-discovery rate (FDR) method.

Table 8.6. Metabolic variation across region and region types in patient 9.

Metabolite	ID confidence	Across regions		Invasive vs non-invasive regions		
		FDR	Significant	log2FC	FDR	Significant
Glycolysis						
D-Glucose	8	3.42E-02	*	0.73	1.03E-02	*
D-Glucose 6-phosphate	10	1.17E-01	ns	0.77	2.27E-01	ns
D-Fructose-1,6-bisphosphate	10	4.45E-02	*	1.09	2.56E-01	ns
D-Glyceraldehyde 3-phosphate	10	1.60E-01	ns	0.97	2.27E-02	*
3-Phospho-D-glycerate	10	3.59E-02	*	-3.93	2.39E-05	****
Phosphoenolpyruvate	10	2.89E-01	ns	-1.47	4.22E-01	ns
Pyruvate	10	8.96E-01	ns	0.14	9.36E-01	ns
Lactate	10	4.09E-01	ns	-0.15	7.38E-01	ns
Tricarboxylic acid cycle						
Citrate	8	5.34E-01	ns	-0.08	8.02E-01	ns
Isocitrate	8	2.48E-01	ns	-0.18	7.05E-01	ns
Succinate	10	2.16E-01	ns	-0.08	9.57E-01	ns
Malate	10	1.95E-01	ns	-0.22	6.25E-01	ns
Energetic and redox species						
ADP	10	9.61E-02	ns	-1.57	8.64E-02	ns
ATP	8	4.62E-02	*	-2.73	6.87E-03	**
Creatine	10	3.96E-01	ns	0.30	4.41E-01	ns
Creatinine	10	1.22E-01	ns	0.68	2.08E-01	ns
NAD+	10	3.51E-02	*	-3.67	6.24E-05	****
NADH	10	1.59E-01	ns	-2.35	4.19E-02	*
Essential amino acids						
L-Histidine	10	1.43E-01	ns	0.60	1.01E-01	ns
L-Leucine	10	1.82E-01	ns	-0.60	4.87E-01	ns
L-Lysine	8	3.21E-01	ns	-1.07	4.84E-01	ns
L-Methionine	10	5.99E-02	ns	-0.53	3.28E-01	ns
L-Phenylalanine	8	7.05E-02	ns	-0.62	3.03E-01	ns
L-Threonine	10	6.28E-02	ns	-0.68	3.28E-01	ns
L-Tryptophan	10	1.67E-01	ns	-0.34	4.02E-01	ns
Conditional amino acids						
L-Arginine	10	3.96E-01	ns	-0.12	8.67E-01	ns
L-Glutamine	10	8.43E-03	**	-0.27	2.20E-01	ns
L-Tyrosine	10	1.16E-01	ns	-0.08	8.95E-01	ns
Glycine	10	4.63E-02	*	-0.93	5.19E-02	ns
L-Ornithine	10	4.99E-03	**	-1.20	4.80E-02	*
L-Proline	10	1.06E-01	ns	-1.12	3.46E-01	ns
L-Serine	10	9.86E-03	**	-1.34	5.34E-02	ns
Non-essential amino acids						
L-Alanine	10	6.85E-01	ns	0.26	6.12E-01	ns
L-Aspartate	10	1.94E-01	ns	-0.20	6.54E-01	ns
L-Glutamate	10	1.97E-01	ns	0.05	8.64E-01	ns
Serine/one-carbon metabolism						
Betaine	10	1.91E-01	ns	0.43	5.34E-01	ns
L-Cystathionine	10	1.13E-01	ns	-0.09	9.33E-01	ns
ɣ-L-Glutamyl-L-cysteine	8	2.95E-01	ns	0.72	3.03E-01	ns
Glutathione	10	3.42E-02	*	0.50	7.76E-02	ns
GSSG	10	6.83E-01	ns	-0.48	4.65E-01	ns
Hypotaurine	8	5.46E-02	ns	-1.16	3.03E-01	ns
Taurine	10	1.84E-01	ns	0.03	8.55E-01	ns

Metabolites highlighted in red showed RSD values >30% in QC samples. ID confidence scores delineate the confidence of the putative metabolite identification. Fold changes are invasive to non-invasive comparisons and are displayed as logarithms to the base 2 (log2FC). Fold changes >0.58 or < -0.58 are depicted in red and green, respectively. Statistical evaluation of variation between regions and region types was performed using a one-way ANOVA model and two-sample *t*-test, respectively. Significance scores were corrected for multiple comparisons using false discovery rate (FDR). ns = not significant; * = $p<0.05$; ** = $p<0.01$; *** = $p<0.001$; **** = $p<0.0001$.

Table 8.7. Metabolite set enrichment analysis of metabolites in patient 9 identified as significant using t-test.

Metabolite Set	Total	Expected	Hits	Raw p	Holm p	FDR
Glycolysis	25	1.07	6	0.000427	0.0418	0.0418
Gluconeogenesis	35	1.5	6	0.00282	0.274	0.138
Mitochondrial Electron Transport Chain	19	0.816	4	0.00718	0.689	0.188
Starch and Sucrose Metabolism	31	1.33	5	0.00857	0.814	0.188
Glycerol Phosphate Shuttle	11	0.473	3	0.0096	0.902	0.188

The table details the top five enriched metabolite sets based on significantly differentially abundant metabolites with log2 fold-change >0.58 or < -0.58. Significant raw *p*-values (Raw p) for enriched metabolite sets were adjusted for multiple comparisons using the Holm (Holm p) or false-discovery rate (FDR) method.

Table 8.8. Pathway analysis of metabolites in patient 9 identified as significant using t-test.

Metabolic Pathway	Total	Expected	Hits	Raw p	Holm p	FDR	Impact
Arginine and proline metabolism	77	1.1516	6	0.000798	0.063868	0.063868	0.14868
Pentose phosphate pathway	32	0.4786	2	0.081536	1	1	0.04289
D-Arginine and D-ornithine metabolism	8	0.11965	1	0.11373	1	1	0
Histidine metabolism	44	0.65808	2	0.13934	1	1	0.0247
Nicotinate and nicotinamide metabolism	44	0.65808	2	0.13934	1	1	0.08015

The table details the top five impacted metabolic pathways based on significantly differentially abundant metabolites with log2 fold-change >0.58 or < -0.58. Significant raw *p*-values (Raw p) for enriched metabolite sets were adjusted for multiple comparisons using the Holm (Holm p) or false-discovery rate (FDR) method. Impact scores range between 0 and 1.

8.4. Patient 14 metabolomics summary

PCA analysis of patient 14 demonstrated overlap between regions 14_1, 14_2 and 14_3 with separation of regions 14_4 and 14_5 from the main cluster (Figure 8.6A), as reflected through hierarchical analysis (Figure 8.6B). Replicates from other regions were interspersed in line with the overlapping metabolomics profiles as emphasised by heatmap signatures (Figure 8.6C). Analysis of regional variation using a one-way ANOVA model revealed little variation between regions 14_1, 14_2 and 14_3, with distinct heatmap signatures displayed by regions 14_4 and 14_5 (data not shown). MSEA of significantly varying metabolites revealed significant enrichment of *phosphatidylethanolamine biosynthesis* (raw p-value=0.025) (Table 8.9). Inspection of metabolites pertaining to glycolysis, TCA cycle and energetics highlighted significant variability in all three pathways (data not shown). The invasive region demonstrated increased levels of early glycolytic intermediates, but this was associated with decreased levels of ATP and NADH compared to non-invasive regions (Table 8.10). Regional variation in essential, conditional and non-essential amino acids largely discriminated between regions 14_1, 14_2 and 14_3 and regions 14_4 and 14_5, collectively (data not shown). Significant reduction in several essential and conditional amino acids was observed in the invasive margin compared to non-invasive regions (Table 8.10). Regional variation for several metabolites within to serine/one-carbon metabolism was significant, leading to significantly varying glutathione levels (data not shown). MSEA of metabolites varying significantly between non-invasive and invasive regions identified significant enrichment of *phosphatidylethanolamine biosynthesis* (raw *p*-value=0.025) and *phosphatidylcholine biosynthesis* (raw *p*-value=0.0077) (Table 8.11). Pathway analysis identified significant impact on *pyrimidine metabolism* (raw *p*-value=1.35E-08; impact=0.54) and *arginine and proline metabolism* (raw *p*-value=9.05E-07; impact=0.35) (Table 8.12).

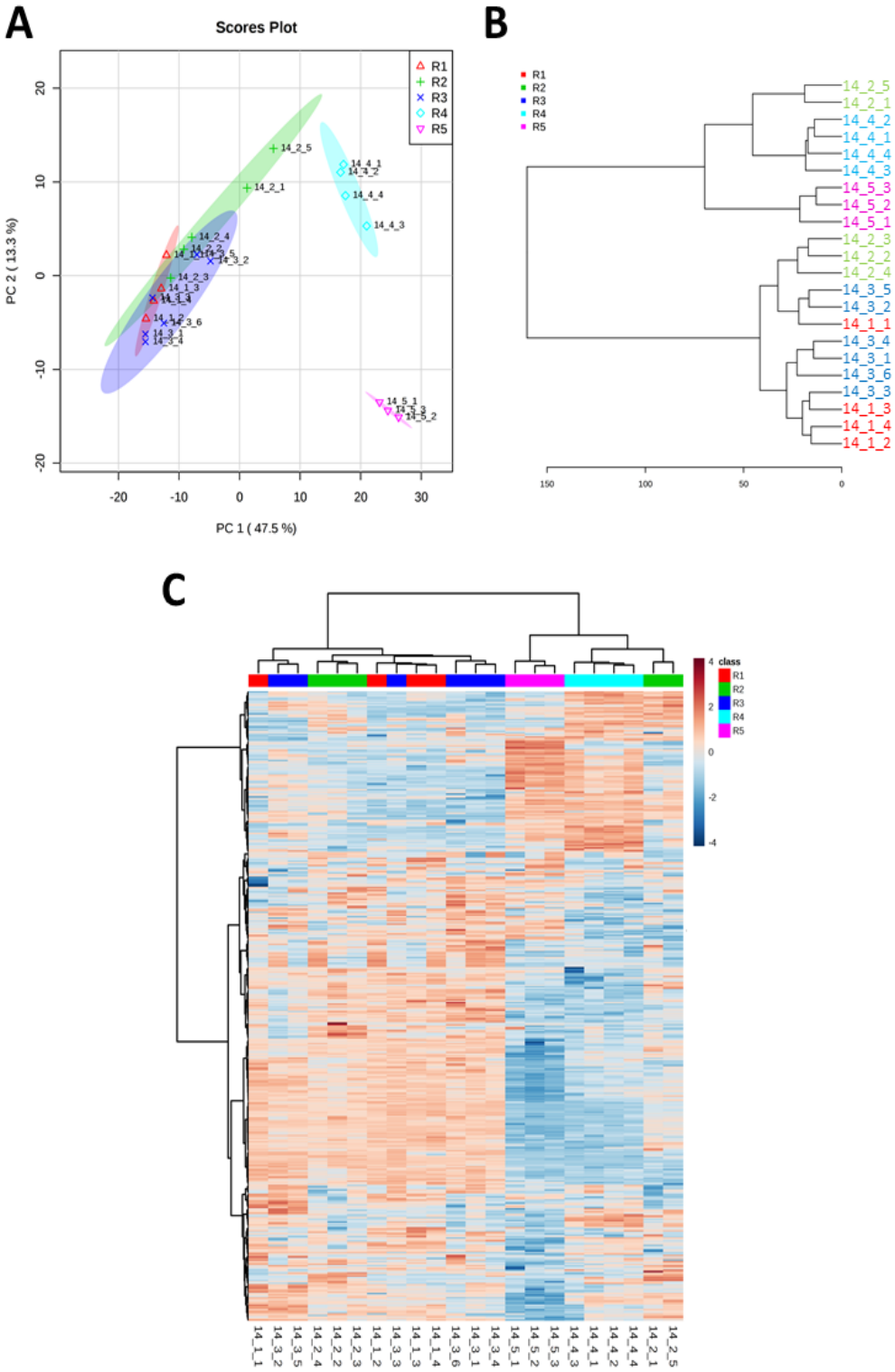

Figure 8.6. Diagnostic plots for patient 14 metabolomics data. (A) Dimensional reduction through PCA and visualisation of sample variation. (B) Hierarchical clustering analysis measuring dissimilarity between samples. (C) Heatmap overview of the metabolome. Sample IDs delineate the patient, region (symbol R), and replicate numbers, respectively.

Table 8.9. Metabolite set enrichment analysis of metabolites in patient 14 identified as significant using one-way ANOVA.

Metabolite Set	Total	Expected	Hits	Raw p	Holm p	FDR
Phosphatidylethanolamine Biosynthesis	12	3.33	7	0.0246	1	0.989
Cardiolipin Biosynthesis	11	3.05	6	0.0543	1	0.989
Phosphatidylcholine Biosynthesis	14	3.88	7	0.0629	1	0.989
Arginine and Proline Metabolism	53	14.7	20	0.068	1	0.989
De Novo Triacylglycerol Biosynthesis	9	2.5	5	0.0725	1	0.989

The table details the top five enriched metabolite sets based on significantly differentially abundant metabolites with log2 fold-change >0.58 or < -0.58. Significant raw *p*-values (Raw p) for enriched metabolite sets were adjusted for multiple comparisons using the Holm (Holm p) or false-discovery rate (FDR) method.

Table 8.10. Metabolic variation across region and region types in patient 14.

Metabolite	ID confidence	Across regions		Invasive vs non-invasive regions		
		FDR	Significant	log2FC	FDR	Significant
Glycolysis						
D-Glucose	8	4.29E-04	***	0.81	5.40E-03	**
D-Glucose 6-phosphate	10	3.11E-02	*	0.91	3.11E-01	ns
D-Fructose-1,6-bisphosphate	10	1.19E-03	**	0.95	4.99E-03	**
D-Glyceraldehyde 3-phosphate	10	2.50E-04	***	1.07	7.18E-05	****
3-Phospho-D-glycerate	10	3.60E-04	***	-2.75	6.62E-03	**
Phosphoenolpyruvate	10	1.98E-02	*	-1.71	1.20E-01	ns
Pyruvate	10	5.96E-01	ns	-0.47	8.73E-01	ns
Lactate	10	1.04E-03	**	-0.22	3.65E-02	*
Tricarboxylic acid cycle						
Citrate	8	3.04E-02	*	0.07	2.44E-01	ns
Isocitrate	8	4.51E-05	****	-1.00	4.70E-03	**
Succinate	10	6.21E-03	**	-0.21	5.25E-01	ns
Malate	10	1.28E-05	****	-1.13	1.94E-02	*
Energetic and redox species						
ADP	10	2.06E-02	*	-1.33	1.09E-01	ns
ATP	8	8.58E-03	**	-2.61	1.24E-03	**
Creatine	10	6.83E-03	**	0.35	1.50E-04	***
Creatinine	10	4.93E-07	****	1.30	8.15E-06	****
NAD+	10	5.65E-05	****	-3.14	2.62E-01	ns
NADH	10	4.95E-03	**	-1.89	6.44E-08	****
Essential amino acids						
L-Histidine	10	2.84E-02	*	0.57	3.56E-01	ns
L-Leucine	10	1.18E-08	****	-2.05	1.09E-04	***
L-Lysine	8	2.00E-08	****	-2.95	4.46E-03	**
L-Methionine	10	2.45E-08	****	-1.59	1.94E-04	***
L-Phenylalanine	8	4.89E-07	****	-1.17	7.34E-04	***
L-Threonine	10	1.58E-07	****	-0.96	8.63E-07	****
L-Tryptophan	10	1.30E-04	***	-0.34	1.24E-01	ns
Conditional amino acids						
L-Arginine	10	3.30E-04	***	-0.34	3.01E-01	ns
L-Glutamine	10	1.46E-04	***	0.05	5.20E-01	ns
L-Tyrosine	10	5.92E-03	**	-0.42	3.71E-02	*
Glycine	10	5.81E-10	****	-3.17	2.67E-05	****
L-Ornithine	10	2.20E-06	****	-1.85	3.95E-02	*
L-Proline	10	3.67E-12	****	-3.39	9.82E-09	****
L-Serine	10	8.06E-08	****	-1.39	1.16E-02	*
Non-essential amino acids						
L-Alanine	10	3.90E-01	ns	0.22	6.20E-02	ns
L-Aspartate	10	1.86E-05	****	-1.11	7.65E-02	ns
L-Glutamate	10	5.32E-03	**	0.34	6.74E-04	***
Serine/one-carbon metabolism						
Betaine	10	5.42E-03	**	-0.77	1.88E-02	*
L-Cystathionine	10	2.13E-02	*	0.01	3.69E-01	ns
γ-L-Glutamyl-L-cysteine	8	7.77E-02	ns	1.34	2.29E-03	**
Glutathione	10	1.03E-04	***	-1.26	1.48E-09	****
GSSG	10	1.86E-05	****	0.74	4.01E-04	***
Hypotaurine	8	1.81E-10	****	-4.16	1.15E-04	***
Taurine	10	2.39E-02	*	-0.36	1.04E-01	ns

Metabolites highlighted in red showed RSD values >30% in QC samples. ID confidence scores delineate the confidence of the putative metabolite identification. Fold changes are invasive to non-invasive comparisons and are displayed as logarithms to the base 2 (log2FC). Fold changes >0.58 or < -0.58 are depicted in red and green, respectively. Statistical evaluation of variation between regions and region types was performed using a one-way ANOVA model and two-sample t-test, respectively. Significance scores were corrected for multiple comparisons using false discovery rate (FDR). ns = not significant; * = $p<0.05$; ** = $p<0.01$; *** = $p<0.001$; **** = $p<0.0001$.

Table 8.11. Metabolite set enrichment analysis of metabolites in patient 14 identified as significant using t-test.

Metabolite Set	Total	Expected	Hits	Raw p	Holm p	FDR
Phosphatidylethanolamine Biosynthesis	12	2.25	7	0.00249	0.244	0.244
Phosphatidylcholine Biosynthesis	14	2.62	7	0.00766	0.743	0.376
Cardiolipin Biosynthesis	11	2.06	4	0.133	1	1
Glutathione Metabolism	21	3.94	6	0.185	1	1
Carnitine Synthesis	22	4.12	6	0.217	1	1

The table details the top five enriched metabolite sets based on significantly differentially abundant metabolites with log2 fold-change >0.58 or < -0.58. Significant raw *p*-values (Raw p) for enriched metabolite sets were adjusted for multiple comparisons using the Holm (Holm p) or false-discovery rate (FDR) method.

Table 8.12. Pathway analysis of metabolites in patient 14 identified as significant using t-test.

Metabolic Pathway	Total	Expected	Hits	Raw p	Holm p	FDR	Impact
Pyrimidine metabolism	60	3.8887	18	1.35E-08	1.08E-06	1.08E-06	0.5381
Arginine and proline metabolism	77	4.9904	18	9.05E-07	7.15E-05	3.62E-05	0.34536
Histidine metabolism	44	2.8517	11	7.07E-05	0.005511	0.001884	0.15953
Lysine degradation	47	3.0461	10	0.000629	0.048405	0.011098	0.12758
Cysteine and methionine metabolism	56	3.6294	11	0.000694	0.052718	0.011098	0.21888

The table details the top five impacted metabolic pathways based on significantly differentially abundant metabolites with log2 fold-change >0.58 or < -0.58. Significant raw *p*-values (Raw p) for enriched metabolite sets were adjusted for multiple comparisons using the Holm (Holm p) or false-discovery rate (FDR) method. Impact scores range between 0 and 1.

8.5. Crystal violet staining of adult and paediatric cells cultured under lipoprotein-replete or -deplete conditions

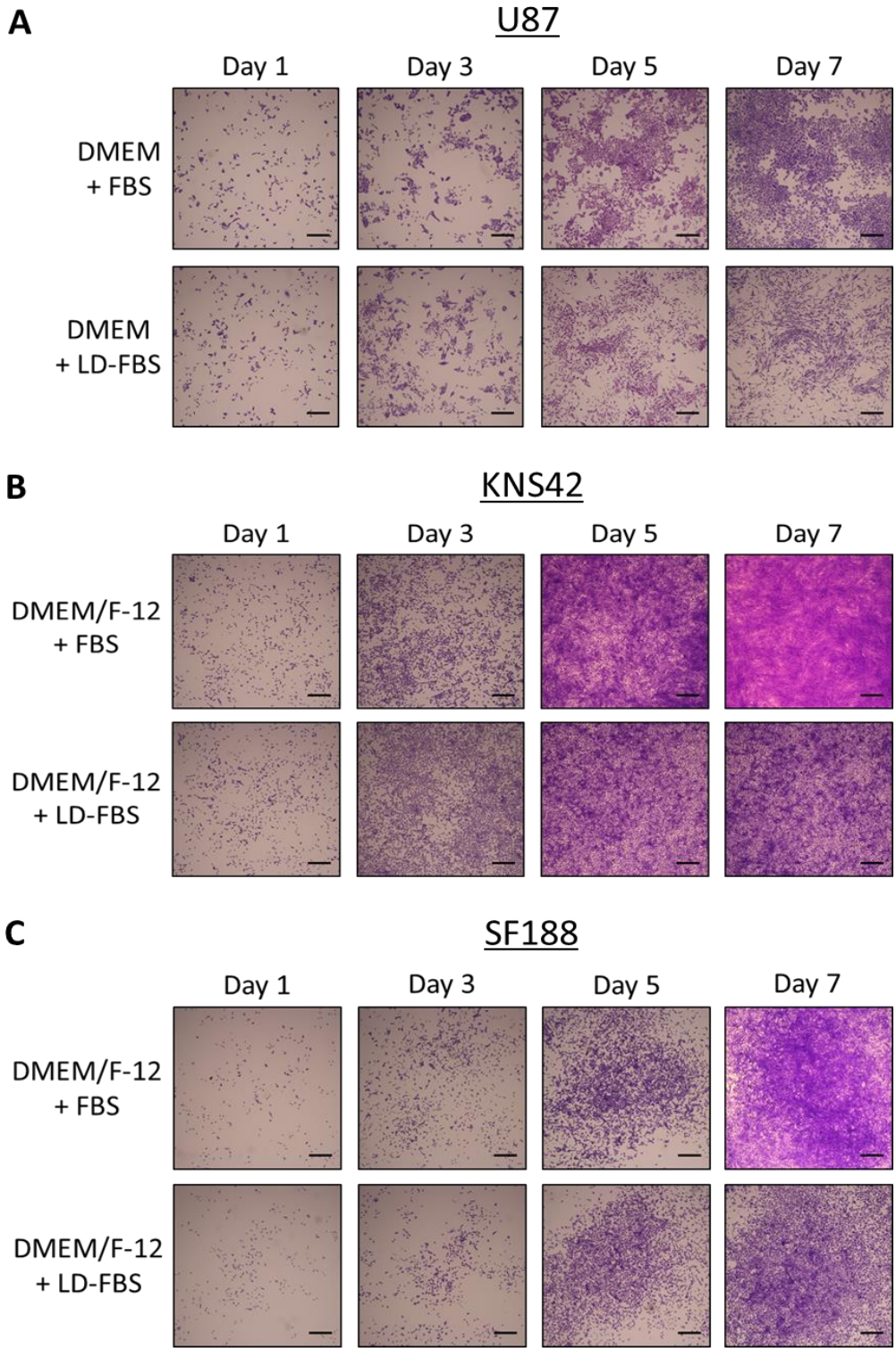

Figure 8.7. Crystal violet staining of adult and paediatric GBM cells cultured under lipoprotein-replete or -deplete conditions. Adult U87 (A) and paediatric KNS42 (B) and SF188 (C) cells were cultured in medium in either the presence (+FBS) or absence of lipoproteins (+LD-FBS) over 7 days. Scale bars represent 500 μm in length.

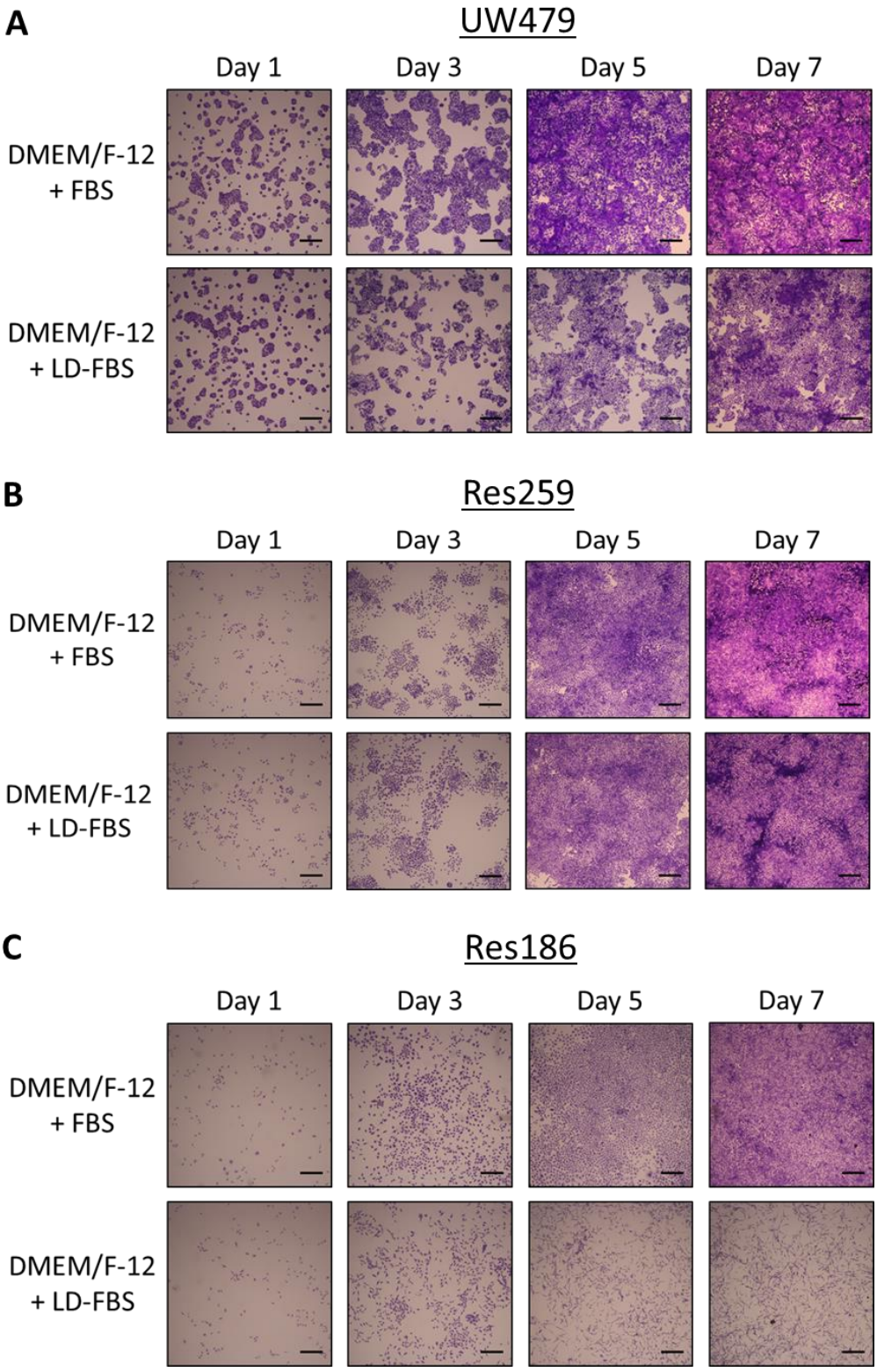

Figure 8.8. Crystal violet staining of adult and paediatric GBM cells cultured under lipoprotein-replete or -deplete conditions. Adult U87 (A) and paediatric KNS42 (B) and SF188 (C) cells were cultured in medium in either the presence (+FBS) or absence of lipoproteins (+LD-FBS) over 7 days. Scale bars represent 500 μm in length.

8.6. Outputs

Abstracts, Posters and Oral Presentations

November 2017 Society of Neuro-Oncology, San Francisco Poster presentation: "An integrated multi-omics approach identifies gene-metabolite associations within the invasive region of high-grade gliomas".

September 2017 Glioma Club, London Oral presentation: "Multi-omic characterisation of the high-grade glioma invasive margin reveals a region-specific genetic and metabolic profile".

June 2017 British Neuro-Oncology Society, Edinburgh Discussed poster presentation: "A GBM invasive region expression profile identified through a multi-region sampling approach".

October 2016 European Association of Neuro-Oncology, Mannheim Poster presentations: 1) "LC-MS-based genome-wide profiling of glioblastoma multiforme reveals distinct metabolism within the invasive margin". 2) "Adult and paediatric GBM cells show differential phenotypic responses to external lipoprotein deprivation".

June 2016 British Neuro-Oncology Society, Leeds Poster presentation: "Limitations of external lipid sources induces differential proliferative and morphological responses in adult and paediatric GBM cells".

June 2016 International Symposium on Paediatric Neuro-Oncology, Liverpool: Poster presentation: "Paediatric GBM cells demonstrate metabolic resilience to growth under lipoprotein deficient conditions".

December 2015 Metabomeeting, Cambridge Poster presentation: "The metabolic classification of intratumour heterogeneity in glioblastoma multiforme using LC-MS-based metabolite profiling".

October 2015 Glioma Club, London Oral presentation: "Molecular characterisation of intratumoural metabolic heterogeneity in paediatric and adult glioblastoma multiforme".

July 2015 British Neuro-Oncology Society, Nottingham Poster presentation: "Characterising intratumour heterogeneity in paediatric glioblastoma multiforme using a novel advanced mass spectrometry technique".

Publications

Preliminary title: "Metabolomic and lipidomic study of glioblastoma multiforme highlights intratumour metabolic heterogeneity". Pending for publication in winter 2018.

Preliminary title: "Adult and paediatric GBM cells are dependent on lipoproteins for growth and metabolic homeostasis". Pending for publication in winter 2018.

Grants Awarded

December 2016 – November 2017 Children's Cancer and Leukaemia Group/Little Princess Trust (£24,806) Co-applicant on proposal titled "Identifying the metabolic 'Achilles hell' of childhood brain cancers".

Chapter 9

References

9. References

Ackerman, J. J. *et al.* (1987) 'Deuterium nuclear magnetic resonance measurements of blood flow and tissue perfusion employing 2H2O as a freely diffusible tracer.', *Proceedings of the National Academy of Sciences of the United States of America*, 84(12), pp. 4099–102.

Agarwal, J. R. *et al.* (2014) 'Activation of liver X receptors inhibits hedgehog signaling, clonogenic growth, and self-renewal in multiple myeloma.', *Molecular cancer therapeutics*, 13(7), pp. 1873–81.

Agathocleous, M. and Harris, W. A. (2013) 'Metabolism in physiological cell proliferation and differentiation.', *Trends in cell biology*, 23(10), pp. 484–92.

Agca, C. A. *et al.* (2014) 'Taurine ameliorates neuropathy via regulating NF-κB and Nrf2/HO-1 signaling cascades in diabetic rats.', *Food and chemical toxicology : an international journal published for the British Industrial Biological Research Association*, 71, pp. 116–21.

Ahmed, R. *et al.* (2014) 'Malignant gliomas: current perspectives in diagnosis, treatment, and early response assessment using advanced quantitative imaging methods.', *Cancer management and research*, 6, pp. 149–70.

Akhavan, D. *et al.* (2013) 'De-repression of PDGFRβ transcription promotes acquired resistance to EGFR tyrosine kinase inhibitors in glioblastoma patients', *Cancer Discovery*, 3(5), pp. 534–547.

Alberghina, L. and Gaglio, D. (2014) 'Redox control of glutamine utilization in cancer.', *Cell death & disease*, 5(12), p. e1561.

Alexa, A., Rahnenführer, J. and Lengauer, T. (2006) 'Improved scoring of functional groups from gene expression data by decorrelating GO graph structure.', *Bioinformatics (Oxford, England)*, 22(13), pp. 1600–7.

Allwood, J. W. and Goodacre, R. (2010) 'An introduction to liquid chromatography-mass spectrometry instrumentation applied in plant metabolomic analyses', *Phytochemical Analysis*, 21(1), pp. 33–47.

Amelio, I. *et al.* (2014) 'Serine and glycine metabolism in cancer.', *Trends in biochemical sciences*, 39(4), pp. 191–8.

Angius, F. *et al.* (2015) 'High-density lipoprotein contribute to G0-G1/S transition in Swiss NIH/3T3 fibroblasts.', *Scientific reports*, 5, p. 17812.

Anthonisen, E. H. *et al.* (2010) 'Nuclear receptor liver X receptor is O-GlcNAc-modified in response to glucose.', *The Journal of biological chemistry*, 285(3), pp. 1607–15.

Antoniewicz, M. R. (2018) 'A guide to 13C metabolic flux analysis for the cancer biologist.', *Experimental & molecular medicine*, 50(4), p. 19.

Apfel, R. *et al.* (1994) 'A novel orphan receptor specific for a subset of thyroid hormone-responsive elements and its interaction with the retinoid/thyroid hormone receptor subfamily.', *Molecular and cellular biology*, 14(10), pp. 7025–35.

Arenas, F., Garcia-Ruiz, C. and Fernandez-Checa, J. C. (2017) 'Intracellular Cholesterol Trafficking and Impact in Neurodegeneration.', *Frontiers in molecular neuroscience*, 10(November), p. 382.

Awad, H., Khamis, M. M. and El-Aneed, A. (2015) 'Mass spectrometry, review of the basics: Ionization', *Applied Spectroscopy Reviews*, 50(2), pp. 158–175.

Bababeygy, S. R. *et al.* (2009) 'HMG-CoA reductase inhibition causes increased necrosis and apoptosis in an in vivo mouse glioblastoma multiforme model', *Anticancer Research*, 29(12), pp. 4901–4908.

Banks, W. A. (2016) 'From blood-brain barrier to blood-brain interface: New opportunities for CNS drug delivery', *Nature Reviews Drug Discovery*, 15(4), pp. 275–292.

Bastawrous, M. *et al.* (2018) 'In-vivo NMR spectroscopy: A powerful and complimentary tool for understanding environmental toxicity.', *Metabolites*, 8(2).

Bastien, J. I. L., McNeill, K. a. and Fine, H. a. (2015) 'Molecular characterizations of glioblastoma, targeted therapy, and clinical results to date.', *Cancer*, 121(4), pp. 502–16.

Bauer, D. E. *et al.* (2005) 'ATP citrate lyase is an important component of cell growth and transformation.', *Oncogene*, 24(41), pp. 6314–6322.

Bax, D. A. *et al.* (2009) 'EGFRvIII deletion mutations in pediatric high-grade glioma and response to targeted therapy in pediatric glioma cell lines', *Clinical Cancer Research*, 15(18), pp. 5753–5761.

Bax, D. A. *et al.* (2010) 'A distinct spectrum of copy number aberrations in

pediatric high-grade gliomas', *Clinical Cancer Research*, 16(13), pp. 3368–3377.

Behin, A. *et al.* (2003) 'Primary brain tumours in adults.', *Lancet*, 361(9354), pp. 323–331.

Bellot, G. *et al.* (2009) 'Hypoxia-induced autophagy is mediated through hypoxia-inducible factor induction of BNIP3 and BNIP3L via their BH3 domains', *Molecular and Cellular Biology*, 29(10), pp. 2570–2581.

Bender, S. *et al.* (2013) 'Reduced H3K27me3 and DNA hypomethylation are major drivers of gene expression in K27M mutant pediatric high-grade gliomas', *Cancer Cell*, 24(5), pp. 660–672.

Bensaad, K. *et al.* (2014) 'Fatty acid uptake and lipid storage induced by HIF-1α contribute to cell growth and survival after hypoxia-reoxygenation.', *Cell reports*, 9(1), pp. 349–65.

Bhat, K. P. L. P. L. *et al.* (2013) 'Mesenchymal differentiation mediated by NF-κB promotes radiation resistance in glioblastoma', *Cancer Cell*, 24(3), pp. 331–346.

Bjerke, L. *et al.* (2013) 'Histone H3.3. mutations drive pediatric glioblastoma through upregulation of MYCN.', *Cancer discovery*, 3(5), pp. 512–9.

Blom, T., Somerharju, P. and Ikonen, E. (2011) 'Synthesis and biosynthetic trafficking of membrane lipids.', *Cold Spring Harbor perspectives in biology*, 3(8), p. a004713.

Boergesen, M. *et al.* (2012) 'Genome-wide profiling of liver X receptor, retinoid X receptor, and peroxisome proliferator-activated receptor α in mouse liver reveals extensive sharing of binding sites.', *Molecular and cellular biology*, 32(4), pp. 852–67.

Bonavia, R. *et al.* (2011) 'Heterogeneity maintenance in glioblastoma: a social network.', *Cancer research*, 71(12), pp. 4055–60.

Bornachea, O. *et al.* (2012) 'EMT and induction of miR-21 mediate metastasis development in Trp53-deficient tumours', *Scientific Reports*, 2, pp. 1–12.

Boroughs, L. K. and DeBerardinis, R. J. (2015) 'Metabolic pathways promoting cancer cell survival and growth.', *Nature cell biology*, 17(4), pp. 351–359.

Bothwell, J. H. F. and Griffin, J. L. (2011) 'An introduction to biological nuclear magnetic resonance spectroscopy.', *Biological reviews of the Cambridge*

Philosophical Society, 86(2), pp. 493–510.

Bourgon, R., Gentleman, R. and Huber, W. (2010) 'Independent filtering increases detection power for high-throughput experiments.', *Proceedings of the National Academy of Sciences of the United States of America*, 107(21), pp. 9546–51.

Bovenga, F., Sabbà, C. and Moschetta, A. (2015) 'Uncoupling nuclear receptor LXR and cholesterol metabolism in cancer', *Cell Metabolism*, 21(4), pp. 517–526.

Bozdag, S. *et al.* (2013) 'Age-specific signatures of glioblastoma at the genomic, genetic, and epigenetic levels.', *PloS one*, 8(4), p. e62982.

Bozza, P. T. and Viola, J. P. B. (2010) 'Lipid droplets in inflammation and cancer.', *Prostaglandins, leukotrienes, and essential fatty acids*, 82(4–6), pp. 243–250.

Bradley, M. N. *et al.* (2007) 'Ligand activation of LXR beta reverses atherosclerosis and cellular cholesterol overload in mice lacking LXR alpha and apoE.', *The Journal of clinical investigation*, 117(8), pp. 2337–46.

Brennan, C. W. *et al.* (2013) 'The somatic genomic landscape of glioblastoma.', *Cell*, 155(2), pp. 462–77.

Breuer, K. *et al.* (2013) 'InnateDB: Systems biology of innate immunity and beyond - Recent updates and continuing curation', *Nucleic Acids Research*, 41(D1), pp. 1228–1233.

Brown, M. S. and Goldstein, J. L. (1986) 'A receptor-mediated pathway for cholesterol homeostasis.', *Science (New York, N.Y.)*, 232(4746), pp. 34–47.

Brown, M. S. and Goldstein, J. L. (1997) 'The SREBP pathway: regulation of cholesterol metabolism by proteolysis of a membrane-bound transcription factor.', *Cell*, 89(3), pp. 331–40.

Brown, M. S. and Goldstein, J. L. (1999) 'A proteolytic pathway that controls the cholesterol content of membranes, cells, and blood', *Proceedings of the National Academy of Sciences*, 96(20), pp. 11041–11048.

Bruntz, R. C. *et al.* (2017) 'Exploring cancer metabolism using stable isotope-resolved metabolomics (SIRM).', *The Journal of biological chemistry*, 292(28), pp. 11601–11609.

Bulik, M. *et al.* (2013) 'Potential of MR spectroscopy for assessment of glioma

grading', *Clinical Neurology and Neurosurgery*, 115(2), pp. 146–153.

Bulstrode, H. *et al.* (2017) 'Elevated FOXG1 and SOX2 in glioblastoma enforces neural stem cell identity through transcriptional control of cell cycle and epigenetic regulators.', *Genes & development*, 31(8), pp. 757–773.

Byun, J. K. *et al.* (2017) 'A positive feedback loop between Sestrin2 and mTORC2 is required for the survival of glutamine-depleted lung cancer cells', *Cell Reports*, 20(3), pp. 586–599.

Cairns, R. a, Harris, I. S. and Mak, T. W. (2011) 'Regulation of cancer cell metabolism.', *Nature reviews. Cancer*, 11(2), pp. 85–95.

Candelaria, N. R. *et al.* (2014) 'Antiproliferative effects and mechanisms of liver X receptor ligands in pancreatic ductal adenocarcinoma cells.', *PloS one*, 9(9), p. e106289.

Cappelletti, V. *et al.* (2017) 'Metabolic footprints and molecular subtypes in breast cancer.', *Disease markers*, 2017, p. 7687851.

Caro, P. *et al.* (2012) 'Metabolic signatures uncover distinct targets in molecular subsets of diffuse large B cell lymphoma.', *Cancer cell*, 22(4), pp. 547–60.

Carvalho, B. S. and Irizarry, R. A. (2010) 'A framework for oligonucleotide microarray preprocessing', *Bioinformatics*, 26(19), pp. 2363–2367.

Castellano, J. M. *et al.* (2012) 'Low-density lipoprotein receptor overexpression enhances the rate of brain-to-blood Aβ clearance in a mouse model of β-amyloidosis.', *Proceedings of the National Academy of Sciences of the United States of America*, 109(38), pp. 15502–7.

Castillo, M., Smith, J. K. and Kwock, L. (2000) 'Correlation of myo-inositol levels and grading of cerebral astrocytomas', *American Journal of Neuroradiology*, 21(9), pp. 1645–1649.

Cemeus, C. *et al.* (2008) 'Lovastatin enhances gefitinib activity in glioblastoma cells irrespective of EGFRvIII and PTEN status', *Journal of Neuro-Oncology*, 90(1), pp. 9–17.

Cesare, A. J. and Reddel, R. R. (2010) 'Alternative lengthening of telomeres: Models, mechanisms and implications', *Nature Reviews Genetics*, 11(5), pp. 319–330.

Chen, J.-Y. *et al.* (2016) 'The oncometabolite R-2-hydroxyglutarate activates NF-

κB-dependent tumor-promoting stromal niche for acute myeloid leukemia cells.', *Scientific reports*, 6, p. 32428.

Chen, W. *et al.* (2007) 'Enzymatic reduction of oxysterols impairs LXR signaling in cultured cells and the livers of mice.', *Cell metabolism*, 5(1), pp. 73–9.

Cheon, H. *et al.* (2013) 'IFNβ-dependent increases in STAT1, STAT2, and IRF9 mediate resistance to viruses and DNA damage', *EMBO Journal*, 32(20), pp. 2751–2763.

Chinnaiyan, P. *et al.* (2012) 'The metabolomic signature of malignant glioma reflects accelerated anabolic metabolism.', *Cancer research*, 72(22), pp. 5878–88.

Cho, J. *et al.* (2011) 'Glioblastoma-derived epidermal growth factor receptor carboxyl-terminal deletion mutants are transforming and are sensitive to EGFR-directed therapies', *Cancer Research*, 71(24), pp. 7587–7596.

Choe, K. Y., Olson, J. E. and Bourque, C. W. (2012) 'Taurine release by astrocytes modulates osmosensitive glycine receptor tone and excitability in the adult supraoptic nucleus.', *The Journal of neuroscience : the official journal of the Society for Neuroscience*, 32(36), pp. 12518–27.

Chu, K. *et al.* (2006) 'Stearoyl-coenzyme A desaturase 1 deficiency protects against hypertriglyceridemia and increases plasma high-density lipoprotein cholesterol induced by liver X receptor activation.', *Molecular and cellular biology*, 26(18), pp. 6786–98.

Clendening, J. W., Pandyra, A., Boutros, P. C., *et al.* (2010) 'Dysregulation of the mevalonate pathway promotes transformation', *Proceedings of the National Academy of Sciences*, 107(34), pp. 15051–15056.

Clendening, J. W., Pandyra, A., Li, Z., *et al.* (2010) 'Exploiting the mevalonate pathway to distinguish statin-sensitive multiple myeloma.', *Blood*, 115(23), pp. 4787–97.

Clendening, J. W. and Penn, L. Z. (2012) 'Targeting tumor cell metabolism with statins.', *Oncogene*, 31(48), pp. 4967–78.

Colen, C. B. *et al.* (2011) 'Metabolic targeting of lactate efflux by malignant glioma inhibits invasiveness and induces necrosis: an in vivo study.', *Neoplasia (New York, N.Y.)*, 13(7), pp. 620–32.

Collins, J. L. *et al.* (2002) 'Identification of a nonsteroidal liver X receptor agonist through parallel array synthesis of tertiary amines', *Journal of Medicinal Chemistry*, 45(10), pp. 1963–1966.

Commisso, C. *et al.* (2013) 'Macropinocytosis of protein is an amino acid supply route in Ras-transformed cells.', *Nature*, 497(7451), pp. 633–7.

Cowin, G. J. *et al.* (1996) 'Serine isotopmer analysis by 13C-NMR defines glycine-serine interconversion in situ in the renal proximal tubule.', *Biochimica et biophysica acta*, 1310(1), pp. 32–40.

Creek, D. J. *et al.* (2011) 'Toward global metabolomics analysis with hydrophilic interaction liquid chromatography-mass spectrometry: Improved metabolite identification by retention time prediction', *Analytical Chemistry*, 83(22), pp. 8703–8710.

Creighton, C. J. and Huang, S. (2015) 'Reverse phase protein arrays in signaling pathways: A data integration perspective', *Drug Design, Development and Therapy*, 9, pp. 3519–3527.

Cuperlovic-Culf, M. *et al.* (2012) '1H NMR metabolomics analysis of glioblastoma subtypes: Correlation between metabolomics and gene expression characteristics', *Journal of Biological Chemistry*, 287(24), pp. 20164–20175.

Currie, E. *et al.* (2013) 'Cellular fatty acid metabolism and cancer.', *Cell Metabolism*, 18(2), pp. 153–161.

Dang, C. V., Le, A. and Gao, P. (2009) 'MYC-induced cancer cell energy metabolism and therapeutic opportunities', *Clinical Cancer Research*, 15(21), pp. 6479–6483.

Daniëls, V. W. *et al.* (2014) 'Cancer cells differentially activate and thrive on de novo lipid synthesis pathways in a low-lipid environment', *PLoS ONE*, 9(9), pp. 13–19.

Darmanis, S. *et al.* (2017) 'Single-Cell RNA-Seq Analysis of Infiltrating Neoplastic Cells at the Migrating Front of Human Glioblastoma', *Cell Reports*, 21(5), pp. 1399–1410.

Davidson, S. M. *et al.* (2016) 'Environment impacts the metabolic dependencies of ras-driven non-small cell lung cancer', *Cell Metabolism*, 23(3), pp. 517–528.

DeBerardinis, R. J. *et al.* (2007) 'Beyond aerobic glycolysis: transformed cells can engage in glutamine metabolism that exceeds the requirement for protein and nucleotide synthesis.', *Proceedings of the National Academy of Sciences of the United States of America*, 104(49), pp. 19345–19350.

DeBerardinis, R. J. and Cheng, T. (2010) 'Q's next: the diverse functions of glutamine in metabolism, cell biology and cancer.', *Oncogene*, 29(3), pp. 313–24.

DeBose-Boyd, R. A. (2008) 'Feedback regulation of cholesterol synthesis: Sterol-accelerated ubiquitination and degradation of HMG CoA reductase', *Cell Research*, 18(6), pp. 609–621.

Deelchand, D. K. *et al.* (2009) 'Simultaneous measurement of neuronal and glial metabolism in rat brain in vivo using co-infusion of [1,6-13C2]glucose and [1,2-13C2]acetate', *Journal of Magnetic Resonance*, 196(2), pp. 157–163.

Deisenroth, C. *et al.* (2011) 'p53-inducible DHRS3 is an endoplasmic reticulum protein associated with lipid droplet accumulation', *Journal of Biological Chemistry*, 286(32), pp. 28343–28356.

Derangère, V. *et al.* (2014) 'Liver X receptor β activation induces pyroptosis of human and murine colon cancer cells', *Cell Death and Differentiation*, 21(12), pp. 1914–1924.

Dickens, D. *et al.* (2017) 'Modulation of LAT1 (SLC7A5) transporter activity and stability by membrane cholesterol', *Scientific Reports*, 7(January), pp. 1–13.

Ding, B. *et al.* (2016) 'Sestrin2 is induced by glucose starvation via the unfolded protein response and protects cells from non-canonical necroptotic cell death', *Scientific Reports*, 6(February), pp. 1–14.

Ding, L. *et al.* (2012) 'Clonal evolution in relapsed acute myeloid leukaemia revealed by whole-genome sequencing.', *Nature*, 481(7382), pp. 506–10.

Du, X., Pham, Y. H. and Brown, A. J. (2004) 'Effects of 25-hydroxycholesterol on cholesterol esterification and sterol regulatory element-binding protein processing are dissociable: Implications for cholesterol movement to the regulatory pool in the endoplasmic reticulum', *Journal of Biological Chemistry*, 279(45), pp. 47010–47016.

Dufour, C. *et al.* (2006) 'High-grade glioma in children under 5 years of age: A

chemotherapy only approach with the BBSFOP protocol', *European Journal of Cancer*, 42(17), pp. 2939–2945.

Eberlin, L. S. *et al.* (2012) 'Classifying human brain tumors by lipid imaging with mass spectrometry.', *Cancer research*, 72(3), pp. 645–54.

Eberlin, L. S. *et al.* (2013) 'Ambient mass spectrometry for the intraoperative molecular diagnosis of human brain tumors.', *Proceedings of the National Academy of Sciences of the United States of America*, 110(5), pp. 1611–6.

Ebert, D., Haller, R. G. and Walton, M. E. (2003) 'Energy contribution of octanoate to intact rat brain metabolism measured by 13C nuclear magnetic resonance spectroscopy.', *The Journal of neuroscience : the official journal of the Society for Neuroscience*, 23(13), pp. 5928–5935.

Egozi, D. *et al.* (2007) 'Regulation of the cell cycle inhibitor p27 and its ubiquitin ligase Skp2 in differentiation of human embryonic stem cells', *The FASEB Journal*, 21(11), pp. 2807–2817.

Elegbede, J. A. *et al.* (1986) 'Increasing the thermosensitivity of a mammary tumor (CA755) through dietary modification.', *European journal of cancer & clinical oncology*, 22(5), pp. 607–15.

Elia, I. *et al.* (2017) 'Proline metabolism supports metastasis formation and could be inhibited to selectively target metastasizing cancer cells.', *Nature communications*, 8, p. 15267.

Ellis, H. P. *et al.* (2015) 'Current Challenges in Glioblastoma: Intratumour Heterogeneity, Residual Disease, and Models to Predict Disease Recurrence.', *Frontiers in oncology*, 5(November), p. 251.

Emma, M. R. *et al.* (2016) 'NUPR1, a new target in liver cancer: implication in controlling cell growth, migration, invasion and sorafenib resistance', *Cell death & disease*, 7(6), p. e2269.

Endo, A. (1992) 'The discovery and development of HMG-CoA reductase inhibitors.', *Journal of lipid research*, 33(11), pp. 1569–82.

Endo, A., Kuroda, M. and Tanzawa, K. (1976) 'Competitive inhibition of 3-hydroxy-3-methylglutaryl coenzyme a reductase by ML-236A and ML-236B fungal metabolites, having hypocholesterolemic activity', *FEBS Letters*, 72(2), pp. 323–326.

Fan, J. *et al.* (2014) 'Quantitative flux analysis reveals folate-dependent NADPH production.', *Nature*, 510(7504), pp. 298–302.

Fan, Q.-W. *et al.* (2013) 'EGFR phosphorylates tumor-derived EGFRvIII driving STAT3/5 and progression in glioblastoma.', *Cancer cell*, 24(4), pp. 438–49.

Fangusaro, J. (2012) 'Pediatric high grade glioma: a review and update on tumor clinical characteristics and biology.', *Frontiers in Oncology*, 2(August), pp. 1–10.

Faubert, B. *et al.* (2013) 'AMPK is a negative regulator of the warburg effect and suppresses tumor growth in vivo', *Cell Metabolism*, 17(1), pp. 113–124.

Faury, D. *et al.* (2007) 'Molecular profiling identifies prognostic subgroups of pediatric glioblastoma and shows increased YB-1 expression in tumors.', *Journal of clinical oncology : official journal of the American Society of Clinical Oncology*, 25(10), pp. 1196–208.

Feldmann, R. *et al.* (2013) 'Genome-wide analysis of LXRα activation reveals new transcriptional networks in human atherosclerotic foam cells.', *Nucleic acids research*, 41(6), pp. 3518–31.

Finlay, J. L. *et al.* (1995) 'Randomized phase III trial in childhood high-grade astrocytoma comparing vincristine, lomustine, and prednisone with the eight-drugs-in-1-day regimen', *Journal of Clinical Oncology*, 13(1), pp. 112–123.

Fitz, N. F. *et al.* (2010) 'Liver X receptor agonist treatment ameliorates amyloid pathology and memory deficits caused by high-fat diet in APP23 mice.', *The Journal of neuroscience : the official journal of the Society for Neuroscience*, 30(20), pp. 6862–72.

Florian, C. L. *et al.* (1995) 'Characteristic metabolic profiles revealed by 1H NMR spectroscopy for three types of human brain and nervous system tumours.', *NMR in biomedicine*, 8(6), pp. 253–264.

Fontebasso, A. M. *et al.* (2013) 'Mutations in SETD2 and genes affecting histone H3K36 methylation target hemispheric high-grade gliomas.', *Acta neuropathologica*, 125(5), pp. 659–69.

Fontebasso, A. M. *et al.* (2014) 'Recurrent somatic mutations in ACVR1 in pediatric midline high-grade astrocytoma.', *Nature genetics*, 46(5), pp. 462–6.

La Fougère, C. *et al.* (2011) 'Molecular imaging of gliomas with PET: Opportunities and limitations', *Neuro-Oncology*, 13(8), pp. 806–819.

Freed-Pastor, W. A. *et al.* (2012) 'Mutant p53 disrupts mammary tissue architecture via the mevalonate pathway.', *Cell*, 148(1–2), pp. 244–58.

Freije, W. a *et al.* (2004) 'Gene expression profiling of gliomas strongly predicts survival.', *Cancer research*, 64(18), pp. 6503–10.

Fukuchi, J. *et al.* (2004) 'Antiproliferative effect of liver X receptor agonists on LNCaP human prostate cancer cells.', *Cancer research*, 64(21), pp. 7686–7689.

Gaist, D. *et al.* (2013) 'Use of statins and risk of glioma: a nationwide case–control study in Denmark', *British Journal of Cancer*, 108(3), pp. 715–720.

Gao, P. *et al.* (2009) 'c-Myc suppression of miR-23a/b enhances mitochondrial glutaminase expression and glutamine metabolism.', *Nature*, 458(7239), pp. 762–765.

Gaskell, S. J. (1997) 'Electrospray : Principles and practice', *Journal of Mass Spectrometry*, 32(April), pp. 677–688.

Gatenby, R. a *et al.* (2009) 'Adaptive therapy.', *Cancer research*, 69(11), pp. 4894–903.

Gebara, E. *et al.* (2015) 'Taurine increases hippocampal neurogenesis in aging mice.', *Stem cell research*, 14(3), pp. 369–79.

Geng, F. *et al.* (2016) 'Inhibition of SOAT1 suppresses glioblastoma growth via blocking SREBP-1-mediated lipogenesis.', *Clinical cancer research : an official journal of the American Association for Cancer Research*, 22(21), pp. 5337–5348.

Gerlinger, M. *et al.* (2012) 'Intratumor heterogeneity and branched evolution revealed by multiregion sequencing.', *The New England journal of medicine*, 366(10), pp. 883–92.

Gill, B. J. *et al.* (2014) 'MRI-localized biopsies reveal subtype-specific differences in molecular and cellular composition at the margins of glioblastoma.', *Proceedings of the National Academy of Sciences of the United States of America*, 111(34), pp. 12550–5.

Gillies, R. J., Verduzco, D. and Gatenby, R. a. (2012) 'Evolutionary dynamics of carcinogenesis and why targeted therapy does not work.', *Nature reviews. Cancer*, 12(7), pp. 487–93.

Godard, S. *et al.* (2003) 'Classification of human astrocytic gliomas on the basis

of gene expression: a correlated group of genes with angiogenic activity emerges as a strong predictor of subtypes.', *Cancer research*, 63(20), pp. 6613–25.

Goebell, E. *et al.* (2006) 'Disarrangement of fiber tracts and decline of neuronal density correlate in glioma patients - A combined diffusion tensor imaging and1H-MR spectroscopy study', *American Journal of Neuroradiology*, 27(7), pp. 1426–1431.

Goetze, K. *et al.* (2011) 'Lactate enhances motility of tumor cells and inhibits monocyte migration and cytokine release.', *International journal of oncology*, 39(2), pp. 453–63.

Goldstein, J. L. and Brown, M. S. (1990) 'Regulation of the mevalonate pathway.', *Nature*, 343(6257), pp. 425–430.

Goldstein, J. L. and Brown, M. S. (2009) 'The LDL receptor', *Arteriosclerosis, Thrombosis, and Vascular Biology*, 29(4), pp. 431–438.

Goldstein, J. L., DeBose-Boyd, R. A. and Brown, M. S. (2006) 'Protein sensors for membrane sterols', *Cell*, 124(1), pp. 35–36.

de Gonzalo-Calvo, D. *et al.* (2015) 'Intratumor cholesteryl ester accumulation is associated with human breast cancer proliferation and aggressive potential: a molecular and clinicopathological study', *BMC cancer*. BMC Cancer, 15, p. 460.

Gravendeel, L. A. M. *et al.* (2009) 'Intrinsic gene expression profiles of gliomas are a better predictor of survival than histology', *Cancer Research*, 69(23), pp. 9065–9072.

Griffiths, B. *et al.* (2013) 'Sterol regulatory element binding protein-dependent regulation of lipid synthesis supports cell survival and tumor growth.', *Cancer & metabolism*, 1(1), p. 3.

Grossmann, S. *et al.* (2007) 'Improved detection of overrepresentation of Gene-Ontology annotations with parent-child analysis', *Bioinformatics*, 23(22), pp. 3024–3031.

Grube, S. *et al.* (2014) 'Overexpression of fatty acid synthase in human gliomas correlates with the WHO tumor grade and inhibition with Orlistat reduces cell viability and triggers apoptosis.', *Journal of neuro-oncology*, 118(2), pp. 277–87.

Grundy, R. G. *et al.* (2007) 'Primary postoperative chemotherapy without radiotherapy for intracranial ependymoma in children: the UKCCSG/SIOP prospective study.', *The Lancet. Oncology*, 8(8), pp. 696–705.

Grundy, R. G. *et al.* (2010) 'Primary postoperative chemotherapy without radiotherapy for treatment of brain tumours other than ependymoma in children under 3 years: results of the first UKCCSG/SIOP CNS 9204 trial.', *European journal of cancer (Oxford, England : 1990)*, 46(1), pp. 120–33.

Guilhaus, M., Mlynski, V. and Selby, D. (1997) 'Perfect Timing: Time-of-flight Mass Spectrometry', *Rapid Communications in Mass Spectrometry*, 11(9), pp. 951–962.

Guo, D. *et al.* (2009) 'EGFR Signaling Through an Akt-SREBP-1-Dependent, Rapamycin-Resistant Pathway Sensitizes Glioblastomas to Antilipogenic Therapy', *Science Signaling*, 2(101), pp. ra82-ra82.

Guo, D. *et al.* (2011) 'An LXR agonist promotes glioblastoma cell death through inhibition of an EGFR/AKT/SREBP-1/LDLR-dependent pathway.', *Cancer discovery*, 1(5), pp. 442–56.

Guo, J. Y. *et al.* (2011) 'Activated Ras requires autophagy to maintain oxidative metabolism and tumorigenesis', *Genes and Development*, 25(5), pp. 460–470.

Guo, J. Y. *et al.* (2013) 'Autophagy suppresses progression of K-ras-induced lung tumors to oncocytomas and maintains lipid homeostasis', *Genes and Development*, 27(13), pp. 1447–1461.

Hakimi, A. A. *et al.* (2016) 'An Integrated Metabolic Atlas of Clear Cell Renal Cell Carcinoma.', *Cancer cell*, 29(1), pp. 104–116.

Hanahan, D. and Weinberg, R. a (2011) 'Hallmarks of cancer: the next generation.', *Cell*, 144(5), pp. 646–74.

Hao, B. *et al.* (2005) 'Structural basis of the Cks1-dependent recognition of p27 Kip1 by the SCF Skp2 ubiquitin ligase', *Molecular Cell*, 20(1), pp. 9–19.

Haque, T. *et al.* (2007) 'Gene expression profiling from formalin-fixed paraffin-embedded tumors of pediatric glioblastoma.', *Clinical cancer research : an official journal of the American Association for Cancer Research*, 13(21), pp. 6284–92.

Hatzivassiliou, G. *et al.* (2005) 'ATP citrate lyase inhibition can suppress tumor

cell growth.', *Cancer Cell*, 8(4), pp. 311–321.

Haukaas, T. H. *et al.* (2016) 'Metabolic clusters of breast cancer in relation to gene- and protein expression subtypes.', *Cancer & metabolism*, 4, p. 12.

Vander Heiden, M. G., Cantley, L. C. and Thompson, C. B. (2009) 'Understanding the Warburg effect: the metabolic requirements of cell proliferation.', *Science (New York, N.Y.)*, 324(5930), pp. 1029–33.

Heiland, D. H. *et al.* (2017) 'The integrative metabolomic-transcriptomic landscape of glioblastome multiforme.', *Oncotarget*, 8(30), pp. 49178–49190.

Hensley, C. T. *et al.* (2016) 'Metabolic heterogeneity in human lung tumors.', *Cell*, 164(4), pp. 681–94.

Ho, Y. K. *et al.* (1978) 'Low-density lipoprotein (LDL) receptor activity in human acute myelogenous leukemia cells.', *Blood*, 52(6), pp. 1099–114.

Hollinshead, K. E. R. *et al.* (2018) 'Oncogenic IDH1 Mutations Promote Enhanced Proline Synthesis through PYCR1 to Support the Maintenance of Mitochondrial Redox Homeostasis.', *Cell reports*, 22(12), pp. 3107–3114.

Hong, C. *et al.* (2010) 'The E3 ubiquitin ligase IDOL induces the degradation of the low density lipoprotein receptor family members VLDLR and ApoER2', *Journal of Biological Chemistry*, 285(26), pp. 19720–19726.

Hong, C. and Tontonoz, P. (2014) 'Liver X receptors in lipid metabolism: opportunities for drug discovery', *Nature Reviews Drug Discovery*, 13(6), pp. 433–444.

Horská, A. and Barker, P. B. (2010) 'Imaging of brain tumors: MR spectroscopy and metabolic imaging.', *Neuroimaging clinics of North America*, 20(3), pp. 293–310.

Hou, J. *et al.* (2015) 'Stanniocalicin 2 suppresses breast cancer cell migration and invasion via the PKC/Claudin-1-mediated signaling', *PLoS ONE*, 10(4), pp. 1–16.

Houck, K. A. *et al.* (2004) 'T0901317 is a dual LXR/FXR agonist', *Molecular Genetics and Metabolism*, 83(1–2), pp. 184–187.

Howard, A. and Hirst, B. H. (2011) 'The glycine transporter GLYT1 in human intestine: expression and function.', *Biological & pharmaceutical bulletin*, 34(6), pp. 784–788.

Howe, F. a *et al.* (2003) 'Metabolic profiles of human brain tumors using quantitative in vivo 1H magnetic resonance spectroscopy.', *Magnetic resonance in medicine*, 49(2), pp. 223–32.

Hu, J. *et al.* (2012) 'Dietary cholesterol intake and cancer', *Annals of Oncology*, 23(2), pp. 491–500.

Ichimura, K. *et al.* (2009) 'IDH1 mutations are present in the majority of common adult gliomas but rare in primary glioblastomas.', *Neuro-oncology*, 11(4), pp. 341–7.

Inda, M.-M. *et al.* (2010) 'Tumor heterogeneity is an active process maintained by a mutant EGFR-induced cytokine circuit in glioblastoma.', *Genes & development*, 24(16), pp. 1731–45.

Ivanisevic, J. *et al.* (2014) 'Brain region mapping using global metabolomics.', *Chemistry & biology*, 21(11), pp. 1575–84.

Ivanov, D. P. *et al.* (2014) 'Multiplexing spheroid volume, resazurin and acid phosphatase viability assays for high-throughput screening of tumour spheroids and stem cell neurospheres.', *PloS one*, 9(8), p. e103817.

Jain, M. *et al.* (2012) 'Metabolite profiling identifies a key role for glycine in rapid cancer cell proliferation.', *Science (New York, N.Y.)*, 336(6084), pp. 1040–4.

Jaishy, B. and Abel, E. D. (2016) 'Lipids, lysosomes, and autophagy', *Journal of Lipid Research*, 57(9), pp. 1619–1635.

Jan, Y.-H. *et al.* (2017) 'Adenylate kinase-4 modulates oxidative stress and stabilizes HIF-1α to drive lung cancer metastasis', *bioRxiv*.

Janowski, B. A. *et al.* (1996) 'An oxysterol signalling pathway mediated by the nuclear receptor LXRα', *Nature*, pp. 728–731.

Jeon, S.-M., Chandel, N. S. and Hay, N. (2012) 'AMPK regulates NADPH homeostasis to promote tumour cell survival during energy stress.', *Nature*, 485(7400), pp. 661–5.

Jiang, W. and Napoli, J. L. (2013) 'The retinol dehydrogenase Rdh10 localizes to lipid droplets during acyl ester biosynthesis', *Journal of Biological Chemistry*, 288(1), pp. 589–597.

Johnson, B. E. *et al.* (2014) 'Mutational analysis reveals the origin and therapy-

driven evolution of recurrent glioma.', *Science (New York, N.Y.)*, 343(6167), pp. 189–93.

Jones, C. and Baker, S. J. (2014) 'Unique genetic and epigenetic mechanisms driving paediatric diffuse high-grade glioma.', *Nature reviews. Cancer*, 14(10).

Joseph, S. B., Laffitte, B. A., *et al.* (2002) 'Direct and indirect mechanisms for regulation of fatty acid synthase gene expression by liver X receptors', *Journal of Biological Chemistry*, 277(13), pp. 11019–11025.

Joseph, S. B., McKilligin, E., *et al.* (2002) 'Synthetic LXR ligand inhibits the development of atherosclerosis in mice', *Proceedings of the National Academy of Sciences*, 99(11), pp. 7604–7609.

Kallenberg, K. *et al.* (2009) 'Untreated glioblastoma multiforme: increased myo-inositol and glutamine levels in the contralateral cerebral hemisphere at proton MR spectroscopy.', *Radiology*, 253(3), pp. 805–812.

Kamphorst, J. J. *et al.* (2013) 'Hypoxic and Ras-transformed cells support growth by scavenging unsaturated fatty acids from lysophospholipids', *Proc Natl Acad Sci U S A*, 110(22), pp. 8882–8887.

Kaneko, S. and Kaneko, S. (2016) 'Fluorescence-guided resection of malignant glioma with 5-ALA.', *International journal of biomedical imaging*, 2016, p. 6135293.

Kang, J. H. *et al.* (2016) 'Aldehyde dehydrogenase is used by cancer cells for energy metabolism', *Experimental & molecular medicine*, 48(11), p. e272.

Karremann, M. *et al.* (2013) 'Cerebellar location may predict an unfavourable prognosis in paediatric high-grade glioma.', *British journal of cancer*, 109(4), pp. 844–51.

Karsy, M. *et al.* (2012) 'Established and emerging variants of glioblastoma multiforme: review of morphological and molecular features', *Folia Neuropathologica*, 4(4), pp. 301–321.

Kasumov, T. *et al.* (2005) 'Probing peroxisomal beta-oxidation and the labelling of acetyl-CoA proxies with [1-(13C)]octanoate and [3-(13C)]octanoate in the perfused rat liver.', *The Biochemical journal*, 389(Pt 2), pp. 397–401.

Kathagen-Buhmann, A. *et al.* (2016) 'Glycolysis and the pentose phosphate pathway are differentially associated with the dichotomous regulation of

glioblastoma cell migration versus proliferation.', *Neuro-oncology*, (January), pp. 1–11.

Kathagen, A. *et al.* (2013) 'Hypoxia and oxygenation induce a metabolic switch between pentose phosphate pathway and glycolysis in glioma stem-like cells', *Acta Neuropathologica*, 126(5), pp. 763–780.

Katz, A. *et al.* (2009) 'Safety, pharmacokinetics, and pharmacodynamics of single doses of LXR-623, a novel liver X-receptor agonist, in healthy participants', *The Journal of Clinical Pharmacology*, 49(6), pp. 643–649.

Keats, J. J. *et al.* (2012) 'Clonal competition with alternating dominance in multiple myeloma.', *Blood*, 120(5), pp. 1067–76.

Kennedy, M. A. *et al.* (2005) 'ABCG1 has a critical role in mediating cholesterol efflux to HDL and preventing cellular lipid accumulation', *Cell Metabolism*, 1(2), pp. 121–131.

Kickingereder, P. *et al.* (2015) 'IDH mutation status is associated with a distinct hypoxia/angiogenesis transcriptome signature which is non-invasively predictable with rCBV imaging in human glioma', *Scientific Reports*, 5(July), pp. 1–9.

Kim, D. *et al.* (2015) 'SHMT2 drives glioma cell survival in ischaemia but imposes a dependence on glycine clearance.', *Nature*, 520(7547), pp. 363–7.

Kim, J. *et al.* (2009) 'Overexpression of low-density lipoprotein receptor in the brain markedly inhibits amyloid deposition and increases extracellular A beta clearance.', *Neuron*, 64(5), pp. 632–44.

Kim, J. *et al.* (2015) 'Spatiotemporal evolution of the primary glioblastoma genome.', *Cancer cell*, 28(3), pp. 318–28.

Kim, S. *et al.* (2017) 'Glutaminase 2 expression is associated with regional heterogeneity of 5-aminolevulinic acid fluorescence in glioblastoma.', *Scientific reports*, 7(1), p. 12221.

Klein, M. E. *et al.* (2018) 'CDK4/6 Inhibitors: The mechanism of action may not be as simple as once thought.', *Cancer cell*, 34(1), pp. 9–20.

Koldamova, R. P. *et al.* (2005) 'The liver X receptor ligand T0901317 decreases amyloid beta production in vitro and in a mouse model of Alzheimer's disease.', *The Journal of biological chemistry*, 280(6), pp. 4079–88.

Koppenol, W. H., Bounds, P. L. and Dang, C. V (2011) 'Otto Warburg's contributions to current concepts of cancer metabolism.', *Nature reviews. Cancer*, 11(5), pp. 325–337.

Kramm, C. M. *et al.* (2011) 'Thalamic high-grade gliomas in children: a distinct clinical subset?', *Neuro-oncology*, 13(6), pp. 680–9.

Kreth, F.-W. *et al.* (2013) 'Gross total but not incomplete resection of glioblastoma prolongs survival in the era of radiochemotherapy.', *Annals of oncology : official journal of the European Society for Medical Oncology*, 24(12), pp. 3117–23.

Krupenko, N. I. *et al.* (2010) 'ALDH1L2 is the mitochondrial homolog of 10-formyltetrahydrofolate dehydrogenase', *Journal of Biological Chemistry*, 285(30), pp. 23056–23063.

Kucharzewska, P., Christianson, H. C. and Belting, M. (2015) 'Global profiling of metabolic adaptation to hypoxic stress in human glioblastoma cells.', *PloS one*, 10(1), p. e0116740.

Kurhanewicz, J. *et al.* (2011) 'Analysis of cancer metabolism by imaging hyperpolarized nuclei: prospects for translation to clinical research.', *Neoplasia (New York, N.Y.)*, Inc., 13(2), pp. 81–97.

Labuschagne, C. F. *et al.* (2014) 'Serine, but not glycine, supports one-carbon metabolism and proliferation of cancer cells', *Cell Reports*, 7(4), pp. 1248–1258.

Laffitte, B. A. *et al.* (2003) 'The phospholipid transfer protein gene is a liver X receptor target expressed by macrophages in atherosclerotic lesions.', *Molecular and cellular biology*, 23(6), pp. 2182–91.

Law, A. Y. S. and Wong, C. K. C. (2010) 'Stanniocalcin-2 is a HIF-1 target gene that promotes cell proliferation in hypoxia.', *Experimental cell research*, 316(3), pp. 466–76.

Le, A. *et al.* (2012) 'Glucose-independent glutamine metabolism via TCA cycling for proliferation and survival in B cells.', *Cell metabolism*, 15(1), pp. 110–21.

Lee, J. *et al.* (2016) 'Neurometabolic roles of ApoE and Ldl-R in mouse brain.', *Journal of bioenergetics and biomembranes*, 48(1), pp. 13–21.

Li, X. *et al.* (2002) 'Analysis of the spatial characteristics of metabolic abnormalities in newly diagnosed glioma patients.', *Journal of magnetic*

resonance imaging : JMRI, 16(3), pp. 229–237.

Li, Y.-L. Y.-C. *et al.* (2017) 'GDF15 contributes to radioresistance and cancer stemness of head and neck cancer by regulating cellular reactive oxygen species via a SMAD-associated signaling pathway.', *Oncotarget*, 8(1), pp. 1508–1528.

Liang, Y. *et al.* (2005) 'Gene expression profiling reveals molecularly and clinically distinct subtypes of glioblastoma multiforme.', *Proceedings of the National Academy of Sciences of the United States of America*, 102(16), pp. 5814–5819.

Lietz, C. B., Gemperline, E. and Li, L. (2013) 'Qualitative and quantitative mass spectrometry imaging of drugs and metabolites.', *Advanced drug delivery reviews*. Elsevier B.V., 65(8), pp. 1074–85.

Lin, C.-Y. and Gustafsson, J.-Å. (2015) 'Targeting liver X receptors in cancer therapeutics.', *Nature reviews. Cancer*, 15(4), pp. 216–24.

Lin, H. *et al.* (2017) 'Fatty acid oxidation is required for the respiration and proliferation of malignant glioma cells.', *Neuro-oncology*, 19(1), pp. 43–54.

Liu, M. *et al.* (2014) 'Development of synthetic peptide-modified liposomes with LDL receptor targeting capacity and improved anticancer activity.', *Molecular pharmaceutics*, 11(7), pp. 2305–12.

Liu, W. *et al.* (2012) 'Reprogramming of proline and glutamine metabolism contributes to the proliferative and metabolic responses regulated by oncogenic transcription factor c-MYC', *Proceedings of the National Academy of Sciences*, 109(23), pp. 8983–8988.

Liu, W. *et al.* (2015) 'Proline biosynthesis augments tumor cell growth and aerobic glycolysis: involvement of pyridine nucleotides', *Scientific Reports*., 5(1), p. 17206.

Llaverias, G. *et al.* (2011) 'Role of cholesterol in the development and progression of breast cancer', *American Journal of Pathology*, 178(1), pp. 402–412.

Louis, D. N. *et al.* (2016) 'The 2016 World Health Organization classification of tumors of the central nervous system: a summary', *Acta Neuropathologica*, 131(6), pp. 803–820.

Lu, Z. *et al.* (2014) 'DIRAS3 regulates the autophagosome initiation complex in

dormant ovarian cancer cells', *Autophagy*, 10(6), pp. 1071–1092.

Lulla, R. R., Saratsis, A. M. and Hashizume, R. (2016) 'Mutations in chromatin machinery and pediatric high-grade glioma.', *Science advances*, 2(3), p. e1501354.

Lunt, S. Y. and Vander Heiden, M. G. (2011) 'Aerobic glycolysis: meeting the metabolic requirements of cell proliferation.', *Annual review of cell and developmental biology*, 27, pp. 441–64.

Lyssiotis, C. A. and Kimmelman, A. C. (2017) 'Metabolic interactions in the tumor microenvironment.', *Trends in cell biology*, 27(11), pp. 863–875.

Maher, E. A. *et al.* (2006) 'Marked genomic differences characterize primary and secondary glioblastoma subtypes and identify two distinct molecular and clinical secondary glioblastoma entities', *Cancer Research*, 66(23), pp. 11502–11513.

Maher, E. a *et al.* (2012) 'Metabolism of [U-13 C]glucose in human brain tumors in vivo.', *NMR in biomedicine*, 25(11), pp. 1234–44.

Malhotra, A. *et al.* (2013) 'Breakpoint profiling of 64 cancer genomes reveals numerous complex rearrangements spawned by homology-independent mechanisms', *Genome Research*, 23(5), pp. 762–776.

Markley, J. L. *et al.* (2017) 'The future of NMR-based metabolomics', *Current Opinion in Biotechnology*, 43, pp. 34–40.

Martín, M. G., Pfrieger, F. and Dotti, C. G. (2014) 'Cholesterol in brain disease: sometimes determinant and frequently implicated.', *EMBO reports*, 15(10), pp. 1036–1052.

Marusyk, A. *et al.* (2014) 'Non-cell-autonomous driving of tumour growth supports sub-clonal heterogeneity', *Nature*, 6(7520), pp. 54–58.

Mashimo, T. *et al.* (2014) 'Acetate is a bioenergetic substrate for human glioblastoma and brain metastases.', *Cell*, 159(7), pp. 1603–14.

Di Mauro, C. *et al.* (2017) 'Urokinase-type plasminogen activator receptor (uPAR) expression enhances invasion and metastasis in RAS mutated tumors', *Scientific Reports*, 7(1), pp. 1–12.

McGranahan, N. *et al.* (2015) 'Clonal status of actionable driver events and the timing of mutational processes in cancer evolution.', *Science translational*

medicine, 7(283), p. 283ra54.

McGranahan, N. and Swanton, C. (2017) 'Clonal heterogeneity and tumor evolution: past, present, and the future.', *Cell*, 168(4), pp. 613–628.

Meierhofer, D., Weidner, C. and Sauer, S. (2014) 'Integrative analysis of transcriptomics, proteomics, and metabolomics data of white adipose and liver tissue of high-fat diet and rosiglitazone-treated insulin-resistant mice identified pathway alterations and molecular hubs.', *Journal of proteome research*, 13(12), pp. 5592–602.

Meijer, D. H. *et al.* (2012) 'Separated at birth? The functional and molecular divergence of OLIG1 and OLIG2.', *Nature reviews. Neuroscience*, 13(12), pp. 819–31.

Mellinghoff, I. K. *et al.* (2005) 'Molecular determinants of the response of glioblastomas to EGFR kinase inhibitors.', *The New England journal of medicine*, 353(19), pp. 2012–24.

Menendez, J. a and Lupu, R. (2007) 'Fatty acid synthase and the lipogenic phenotype in cancer pathogenesis.', *Nature reviews. Cancer*, 7(10), pp. 763–77.

Meng, Z., Moroishi, T. and Guan, K. (2016) 'Mechanisms of Hippo pathway regulation', *Genes and Development*, 30(1), pp. 1–17.

Menolfi, D. *et al.* (2015) 'Essential Roles of the Smc5/6 Complex in Replication through Natural Pausing Sites and Endogenous DNA Damage Tolerance', *Molecular Cell*, 60(6), pp. 835–846.

Metallo, C. M. *et al.* (2011) 'Reductive glutamine metabolism by IDH1 mediates lipogenesis under hypoxia.', *Nature*, 481(7381), pp. 380–4.

Meyer, M. *et al.* (2015) 'Single cell-derived clonal analysis of human glioblastoma links functional and genomic heterogeneity.', *Proceedings of the National Academy of Sciences of the United States of America*, 112(3), pp. 851–6.

Miller, G. *et al.* (2009) 'Unraveling delta1-pyrroline-5-carboxylate-proline cycle in plants by uncoupled expression of proline oxidation enzymes.', *The Journal of biological chemistry*, 284(39), pp. 26482–92.

Molino, Y. *et al.* (2017) 'Use of LDL receptor-targeting peptide vectors for in vitro and in vivo cargo transport across the blood-brain barrier.', *FASEB journal :*

official publication of the Federation of American Societies for Experimental Biology, 31(5), pp. 1807–1827.

Möller-Hartmann, W. *et al.* (2002) 'Clinical application of proton magnetic resonance spectroscopy in the diagnosis of intracranial mass lesions', *Neuroradiology*, 44(5), pp. 371–381.

Mukherjee, J. *et al.* (2013) 'Pyruvate kinase M2 expression, but not pyruvate kinase activity, is up-regulated in a grade-specific manner in human glioma.', *PloS one*, 8(2), p. e57610.

Mukhopadhyay, R. *et al.* (2009) 'The GAIT system: a gatekeeper of inflammatory gene expression', *Trends in Biochemical Sciences*, 34(7), pp. 324–331.

Mullen, A. R. *et al.* (2011) 'Reductive carboxylation supports growth in tumour cells with defective mitochondria.', *Nature*, 481(7381), pp. 385–388.

Murakami, S. *et al.* (2002) 'Effect of taurine on cholesterol metabolism in hamsters: up-regulation of low density lipoprotein (LDL) receptor by taurine.', *Life sciences*, 70(20), pp. 2355–66.

Nagel, R., Semenova, E. A. and Berns, A. (2016) 'Drugging the addict: non-oncogene addiction as a target for cancer therapy.', *EMBO reports*, 17(11), pp. 1516–1531.

Nan, J. *et al.* (2018) 'IRF9 and unphosphorylated STAT2 cooperate with NF-κB to drive IL6 expression.', *Proceedings of the National Academy of Sciences of the United States of America*, 115(15), pp. 3906–3911.

Nathanson, D. A. *et al.* (2014) 'Targeted therapy resistance mediated by dynamic regulation of extrachromosomal mutant EGFR DNA.', *Science (New York, N.Y.)*, 343(6166), pp. 72–6.

Nawashiro, H. *et al.* (2005) 'High expression of L-type amino acid transporter 1 in infiltrating glioma cells', *Brain Tumor Pathology*, 22(2), pp. 89–91.

Nguyen-Vu, T. *et al.* (2013) 'Liver X receptor ligands disrupt breast cancer cell proliferation through an E2F-mediated mechanism', *Breast Cancer Research*, 15(3), p. R51.

Nieman, K. M. *et al.* (2011) 'Adipocytes promote ovarian cancer metastasis and provide energy for rapid tumor growth.', *Nature medicine*, 17(11), pp. 1498–

503.

Nikbakht, H. *et al.* (2016) 'Spatial and temporal homogeneity of driver mutations in diffuse intrinsic pontine glioma.', *Nature communications*, 7, p. 11185.

Noushmehr, H. *et al.* (2010) 'Identification of a CpG island methylator phenotype that defines a distinct subgroup of glioma.', *Cancer cell*, 17(5), pp. 510–22.

Nutt, C. L. *et al.* (2003) 'Gene expression-based classification of malignant gliomas correlates better with survival than histological classification gene expression-based classification of malignant gliomas correlates better with survival than histological classification 1', *Cancer research*, 63, pp. 1602–1607.

Ohka, F. *et al.* (2014) 'Quantitative metabolome analysis profiles activation of glutaminolysis in glioma with IDH1 mutation', *Tumor Biology*, 35(6), pp. 5911–5920.

Okegawa, T. *et al.* (2017) 'Intratumor heterogeneity in primary kidney cancer revealed by metabolic profiling of multiple spatially separated samples within tumors', *EBioMedicine*, 19(21), pp. 31–38.

Oliveira, K. A. *et al.* (2018) 'Atorvastatin promotes cytotoxicity and reduces migration and proliferation of human A172 glioma cells', *Molecular Neurobiology*, 55(2), pp. 1509–1523.

Osono, Y. *et al.* (1995) 'Role of the low density lipoprotein receptor in the flux of cholesterol through the plasma and across the tissues of the mouse.', *The Journal of clinical investigation*, 95(3), pp. 1124–32.

Ostrom, Q. T. *et al.* (2017) 'CBTRUS statistical report: Primary brain and other central nervous system tumors diagnosed in the United States in 2010–2014', *Neuro-Oncology*, 19(suppl_5), pp. v1–v88.

Oudshoorn, D. *et al.* (2012) 'HERC6 is the main E3 ligase for global ISG15 conjugation in mouse cells.', *PloS one*, 7(1), p. e29870.

Ozawa, T. *et al.* (2010) 'PDGFRA gene rearrangements are frequent genetic events in PDGFRA-amplified glioblastomas', *Genes and Development*, 24(19), pp. 2205–2218.

Panosyan, E. H. *et al.* (2014) 'Asparagine depletion potentiates the cytotoxic

effect of chemotherapy against brain tumors', *Mol Cancer Res*, 12(5), pp. 694–702.

Parmigiani, A. *et al.* (2014) 'Sestrins inhibit mTORC1 kinase activation through the GATOR complex', *Cell Reports*, 9(4), pp. 1281–1291.

Parsons, D. W. *et al.* (2008) 'An integrated genomic analysis of human glioblastoma multiforme.', *Science (New York, N.Y.)*, 321(5897), pp. 1807–1812.

Patel, A. P. *et al.* (2014) 'Single-cell RNA-seq highlights intratumoral heterogeneity in primary glioblastoma.', *Science (New York, N.Y.)*, 344(6190), pp. 1396–401.

Paugh, B. S. *et al.* (2010) 'Integrated molecular genetic profiling of pediatric high-grade gliomas reveals key differences with the adult disease.', *Journal of clinical oncology : official journal of the American Society of Clinical Oncology*, 28(18), pp. 3061–8.

Paugh, B. S. *et al.* (2011) 'Genome-wide analyses identify recurrent amplifications of receptor tyrosine kinases and cell-cycle regulatory genes in diffuse intrinsic pontine glioma.', *Journal of clinical oncology : official journal of the American Society of Clinical Oncology*, 29(30), pp. 3999–4006.

Paugh, B. S. *et al.* (2013) 'Novel oncogenic PDGFRA mutations in pediatric high-grade gliomas.', *Cancer research*, 73(20), pp. 6219–29.

Pavlova, N. N. and Thompson, C. B. (2016) 'The Emerging Hallmarks of Cancer Metabolism', *Cell Metabolism*, 23(1), pp. 27–47.

Pehkonen, P. *et al.* (2012) 'Genome-wide landscape of liver X receptor chromatin binding and gene regulation in human macrophages.', *BMC genomics*, 13, p. 50.

Pencheva, N. *et al.* (2012) 'Convergent multi-miRNA targeting of ApoE drives LRP1/LRP8-dependent melanoma metastasis and angiogenesis.', *Cell*, 151(5), pp. 1068–82.

Pencheva, N. *et al.* (2014) 'Broad-spectrum therapeutic suppression of metastatic melanoma through nuclear hormone receptor activation', *Cell*, 156(5), pp. 986–1001.

Phillips, H. S. *et al.* (2006) 'Molecular subclasses of high-grade glioma predict prognosis, delineate a pattern of disease progression, and resemble stages in

neurogenesis.', *Cancer cell*, 9(3), pp. 157–73.

Phillips, M. C. (2014) 'Molecular mechanisms of cellular cholesterol efflux', *Journal of Biological Chemistry*, 289(35), pp. 24020–24029.

Pinto, J. A. *et al.* (2017) 'In silico evaluation of DNA Damage Inducible Transcript 4 gene (DDIT4) as prognostic biomarker in several malignancies', *Scientific Reports*, 7(1), pp. 1–11.

Platten, M., Wick, W. and Van Den Eynde, B. J. (2012) 'Tryptophan catabolism in cancer: Beyond IDO and tryptophan depletion', *Cancer Research*, 72(21), pp. 5435–5440.

Pommier, a J. C. *et al.* (2010) 'Liver X Receptor activation downregulates AKT survival signaling in lipid rafts and induces apoptosis of prostate cancer cells.', *Oncogene*, 29(18), pp. 2712–23.

Possemato, R. *et al.* (2011) 'Functional genomics reveal that the serine synthesis pathway is essential in breast cancer.', *Nature*, 476(7360), pp. 346–50.

Della Puppa, A. *et al.* (2013) '5-aminolevulinic acid (5-ALA) fluorescence guided surgery of high-grade gliomas in eloquent areas assisted by functional mapping. Our experience and review of the literature.', *Acta neurochirurgica*, 155(6), p. 965–72.

Qi, J. *et al.* (2012) 'The use of stable isotope-labeled glycerol and oleic acid to differentiate the hepatic functions of DGAT1 and -2.', *Journal of lipid research*, 53(6), pp. 1106–16.

Qiu, B. *et al.* (2015) 'HIF2α-dependent lipid storage promotes endoplasmic reticulum homeostasis in clear-cell renal cell carcinoma.', *Cancer discovery*, 5(6), pp. 652–67.

Qu, H. *et al.* (2010) 'Genome-wide profiling using single-nucleotide polymorphism arrays identifies novel chromosomal imbalances in pediatric glioblastomas.', *Neuro-oncology*, 12(2), pp. 153–63.

Quail, D. F. and Joyce, J. A. (2017) 'The microenvironmental landscape of brain tumors.', *Cancer cell*, 31(3), pp. 326–341.

Quinet, E. M. *et al.* (2009) 'LXR ligand lowers LDL cholesterol in primates, is lipid neutral in hamster, and reduces atherosclerosis in mouse.', *Journal of lipid*

research, 50(12), pp. 2358–70.

Rao, S. *et al.* (1998) 'Lovastatin mediated G1 arrest in normal and tumor breast cells is through inhibition of CDK2 activity and redistribution of p21 and p27, independent of p53.', *Oncogene*, 17(18), pp. 2393–402.

Reitman, Z. J. *et al.* (2011) 'Profiling the effects of isocitrate dehydrogenase 1 and 2 mutations on the cellular metabolome.', *Proceedings of the National Academy of Sciences of the United States of America*, 108(8), pp. 3270–5.

Repa, J. J., Turley, S. D., *et al.* (2000) 'Regulation of absorption and ABC1-mediated efflux of cholesterol by RXR heterodimers.', *Science (New York, N.Y.)*, 289(5484), pp. 1524–9.

Repa, J. J., Liang, G., *et al.* (2000) 'Regulation of mouse sterol regulatory element-binding protein-1c gene (SREBP-1c) by oxysterol receptors, LXRalpha and LXRbeta.', *Genes & development*, 14(22), pp. 2819–30.

Repa, J. J. *et al.* (2002) 'Regulation of ATP-binding cassette sterol transporters ABCG5 and ABCG8 by the liver X receptors α and β', *Journal of Biological Chemistry*, 277(21), pp. 18793–18800.

Ridsdale, A. *et al.* (2006) 'Cholesterol is required for efficient endoplasmic reticulum-to-Golgi transport of secretory membrane proteins.', *Molecular biology of the cell*, 17(4), pp. 1593–605.

Ríos, M. *et al.* (2014) 'Lipoprotein internalisation induced by oncogenic AMPK activation is essential to maintain glioblastoma cell growth.', *European Journal of Cancer*, 50(18), pp. 3187–97.

Ritchie, M. E. *et al.* (2015) 'limma powers differential expression analyses for RNA-sequencing and microarray studies.', *Nucleic acids research*. Oxford University Press, 43(7), p. e47.

Ro, S. H. *et al.* (2016) 'Tumor suppressive role of sestrin2 during colitis and colon carcinogenesis', *eLife*, 5(FEBRUARY2016), pp. 1–20.

Robinet, P. *et al.* (2010) 'A simple and sensitive enzymatic method for cholesterol quantification in macrophages and foam cells', *Journal of Lipid Research*, 51(11), pp. 3364–3369.

Rong, S. *et al.* (2017) 'Expression of SREBP-1c requires SREBP-2-mediated generation of a sterol ligand for LXR in livers of mice', *eLife*, 6, pp. 1–17.

Rosati, A. *et al.* (2013) 'Glutamine synthetase expression as a valuable marker of epilepsy and longer survival in newly diagnosed glioblastoma multiforme.', *Neuro-oncology*, 15(5), pp. 618–25.

Rough, J. J. *et al.* (2010) 'Anti-proliferative effect of LXR agonist T0901317 in ovarian carcinoma cells.', *Journal of ovarian research*, 3, p. 13.

Rubakhin, S. S., Lanni, E. J. and Sweedler, J. V (2013) 'Progress toward single cell metabolomics.', *Current opinion in biotechnology*, 24(1), pp. 95–104.

Rudling, M. J. *et al.* (1990) 'Low density lipoprotein receptor activity in human intracranial tumors and its relation to the cholesterol requirement.', *Cancer research*, 50(3), pp. 483–7.

Ruggiano, A., Foresti, O. and Carvalho, P. (2014) 'ER-associated degradation: Protein quality control and beyond', *Journal of Cell Biology*, 204(6), pp. 869–879.

Saga, I. *et al.* (2014) 'Integrated analysis identifies different metabolic signatures for tumor-initiating cells in a murine glioblastoma model.', *Neuro-oncology*, 16(8), pp. 1048–56.

Sanders, R. P. *et al.* (2007) 'High-grade astrocytoma in very young children', *Pediatric Blood and Cancer*, 49(7), pp. 888–893.

Santandreu, F. M. *et al.* (2008) 'Differences in mitochondrial function and antioxidant systems between regions of human glioma.', *Cellular physiology and biochemistry : international journal of experimental cellular physiology, biochemistry, and pharmacology*, 22(5–6), pp. 757–68.

Santos, C. R. and Schulze, A. (2012) 'Lipid metabolism in cancer', *FEBS Journal*, 279(15), pp. 2610–2623.

Lo Sasso, G. *et al.* (2013) 'Liver X receptors inhibit proliferation of human colorectal cancer cells and growth of intestinal tumors in mice', *Gastroenterology*. Elsevier Inc., 144(7), p. 1497–1507.e13.

Savaryn, J. P., Toby, T. K. and Kelleher, N. L. (2016) 'A researcher's guide to mass spectrometry-based proteomics', *Proteomics*, 16(18), pp. 2435–2443.

Scheltema, R. a. *et al.* (2011) 'PeakML/mzMatch: A file format, Java library, R library, and tool-chain for mass spectrometry data analysis', *Analytical Chemistry*, 83(7), pp. 2786–2793.

Schousboe, A. *et al.* (2014) 'Glutamate metabolism in the brain focusing on astrocytes.', *Advances in neurobiology*, 11, pp. 13–30.

Schultz, J. R. *et al.* (2000) 'Role of LXRs in control of lipogenesis', *Genes and Development*, 14(22), pp. 2831–2838.

Schwartzbaum, J. a *et al.* (2006) 'Epidemiology and molecular pathology of glioma.', *Nature clinical practice. Neurology*, 2(9), pp. 494–503.

Schwartzentruber, J. *et al.* (2012) 'Driver mutations in histone H3.3 and chromatin remodelling genes in paediatric glioblastoma.', *Nature*, 482(7384), pp. 226–31.

Segatto, M. *et al.* (2014) 'Cholesterol homeostasis failure in the brain: implications for synaptic dysfunction and cognitive decline.', *Current medicinal chemistry*, 21(24), pp. 2788–802.

Seliger, C. *et al.* (2016) 'Statin use and risk of glioma: population-based case–control analysis', *European Journal of Epidemiology*, 31(9), pp. 947–952.

Sellers, K. *et al.* (2015) 'Pyruvate carboxylase is critical for non-small-cell lung cancer proliferation.', *The Journal of clinical investigation*, 125(2), pp. 687–98.

Seltzer, M. J. *et al.* (2010) 'Inhibition of glutaminase preferentially slows growth of glioma cells with mutant IDH1', *Cancer Research*, 70(22), pp. 8981–8987.

Senft, C. *et al.* (2011) 'Intraoperative MRI guidance and extent of resection in glioma surgery: A randomised, controlled trial', *The Lancet Oncology*, 12(11), pp. 997–1003.

Sever, N. *et al.* (2004) 'Isolation of mutant cells lacking Insig-1 through selection with SR-12813, an agent that stimulates degradation of 3-hydroxy-3-methylglutaryl-coenzyme A reductase', *Journal of Biological Chemistry*, 279(41), pp. 43136–43147.

Shackelford, D. B. and Shaw, R. J. (2009) 'The LKB1-AMPK pathway: metabolism and growth control in tumour suppression.', *Nature reviews. Cancer*, 9(8), pp. 563–575.

Shai, R. *et al.* (2003) 'Gene expression profiling identifies molecular subtypes of gliomas', *Oncogene*, 22(31), pp. 4918–4923.

Shi, Z. *et al.* (2001) 'S-Phase arrest by nucleoside analogues and abrogation of survival without cell cycle progression by 7-hydroxystaurosporine.', *Cancer*

research, 61(3), pp. 1065–72.

Shibao, S. *et al.* (2017) 'Metabolic heterogeneity and plasticity of glioma stem cells in a mouse glioblastoma model', *Neuro-Oncology*, 20(February), pp. 343–354.

Shirahata, M. *et al.* (2007) 'Gene expression-based molecular diagnostic system for malignant gliomas is superior to histological diagnosis', *Clinical Cancer Research*, 13(24), pp. 7341–7356.

Shushan, B. (2010) 'A review of clinical diagnostic applications of liquid chromatography-tandem mass spectrometry.', *Mass spectrometry reviews*, 29(6), pp. 930–44.

Simons, K. and Ikonen, E. (2000) 'How cells handle cholesterol.', *Science (New York, N.Y.)*, 290(5497), pp. 1721–6.

Simons, K. and Toomre, D. (2000) 'Lipid rafts and signal transduction.', *Nature reviews. Molecular cell biology*, 1(1), pp. 31–9.

Slebe, F. *et al.* (2016) 'FoxA and LIPG endothelial lipase control the uptake of extracellular lipids for breast cancer growth.', *Nature communications*, 7, p. 11199.

Smith, S. J. *et al.* (2012) 'Recapitulation of tumor heterogeneity and molecular signatures in a 3D brain cancer model with decreased sensitivity to histone deacetylase inhibition.', *PloS one*, 7(12), p. e52335.

Snuderl, M. *et al.* (2011) 'Mosaic amplification of multiple receptor tyrosine kinase genes in glioblastoma.', *Cancer cell*, 20(6), pp. 810–7.

Son, J. *et al.* (2013) 'Glutamine supports pancreatic cancer growth through a KRAS-regulated metabolic pathway.', *Nature*, 496(7443), pp. 101–5.

Sorci-Thomas, M. G. *et al.* (2012) 'Nascent high density lipoproteins formed by ABCA1 resemble lipid rafts and are structurally organized by three apoA-I monomers.', *Journal of lipid research*, 53(9), pp. 1890–909.

Sottoriva, A. *et al.* (2013) 'Intratumor heterogeneity in human glioblastoma reflects cancer evolutionary dynamics.', *Proceedings of the National Academy of Sciences of the United States of America*, 110(10), pp. 4009–14.

Sottoriva, A. *et al.* (2015) 'A Big Bang model of human colorectal tumor growth.', *Nature genetics*, 47(3), pp. 209–16.

Sposto, R. *et al.* (1989) 'The effectiveness of chemotherapy for treatment of high grade astrocytoma in children: results of a randomized trial. A report from the Childrens Cancer Study Group.', *Journal of neuro-oncology*, 7(2), pp. 165–77.

Srivastava, N. K. *et al.* (2010) 'In vitro, high-resolution 1H and 31P NMR based analysis of the lipid components in the tissue, serum, and CSF of the patients with primary brain tumors: one possible diagnostic view.', *NMR in biomedicine*, 23(2), pp. 113–22.

Stasinopoulos, I. *et al.* (2013) 'COX-2 in cancer: Gordian knot or Achilles heel?', *Frontiers in pharmacology*, 4(March), p. 34.

Stephan, Z. F., Lindsey, S. and Hayes, K. C. (1987) 'Taurine enhances low density lipoprotein binding. Internalization and degradation by cultured Hep G2 cells.', *The Journal of biological chemistry*, 262(13), pp. 6069–73.

Stummer, W. *et al.* (2006) 'Fluorescence-guided surgery with 5-aminolevulinic acid for resection of malignant glioma: a randomised controlled multicentre phase III trial', *Lancet Oncology*, 7(5), pp. 392–401.

Stupp, R. *et al.* (2005) 'Radiotherapy plus concomitant and adjuvant temozolomide for glioblastoma.', *The New England journal of medicine*, 352(10), pp. 987–96.

Stupp, R. *et al.* (2009) 'Effects of radiotherapy with concomitant and adjuvant temozolomide versus radiotherapy alone on survival in glioblastoma in a randomised phase III study: 5-year analysis of the EORTC-NCIC trial.', *The Lancet. Oncology*. Elsevier Ltd, 10(5), pp. 459–66.

Sturm, D. *et al.* (2012) 'Hotspot mutations in H3F3A and IDH1 define distinct epigenetic and biological subgroups of glioblastoma.', *Cancer cell*, 22(4), pp. 425–37.

Sturm, D. *et al.* (2014) 'Paediatric and adult glioblastoma: multiform (epi)genomic culprits emerge.', *Nature reviews. Cancer*, 14(2), pp. 92–107.

Sugiura, A. *et al.* (2017) 'Newly born peroxisomes are a hybrid of mitochondrial and ER-derived pre-peroxisomes', *Nature*, 542(7640), pp. 251–254.

Sumner, L. W. *et al.* (2007) 'Proposed minimum reporting standards for chemical analysis: Chemical Analysis Working Group (CAWG) Metabolomics

Standards Initiative (MSI)', *Metabolomics*, 3(3), pp. 211–221.

Sumner, L. W. *et al.* (2014) 'Proposed quantitative and alphanumeric metabolite identification metrics', *Metabolomics*, 10(6), pp. 1047–1049.

Sun, X. *et al.* (2016) 'MiR-548c impairs migration and invasion of endometrial and ovarian cancer cells via downregulation of Twist', *Journal of Experimental and Clinical Cancer Research*. Journal of Experimental & Clinical Cancer Research, 35(1), pp. 1–9.

Swanton, C. (2012) 'Intratumor heterogeneity: evolution through space and time.', *Cancer research*, 72(19), pp. 4875–82.

Szerlip, N. J. *et al.* (2012) 'Intratumoral heterogeneity of receptor tyrosine kinases EGFR and PDGFRA amplification in glioblastoma defines subpopulations with distinct growth factor response.', *Proceedings of the National Academy of Sciences of the United States of America*, 109(8), pp. 3041–6.

Szklarczyk, D. *et al.* (2015) 'STRING v10: Protein-protein interaction networks, integrated over the tree of life', *Nucleic Acids Research*, 43(D1), pp. D447–D452.

Tafani, M. *et al.* (2016) 'The interplay of reactive oxygen species, hypoxia, inflammation, and sirtuins in cancer initiation and progression.', *Oxidative medicine and cellular longevity*, 2016, p. 3907147.

Taha, A. Y. *et al.* (2009) 'Brainstem concentrations of cholesterol are not influenced by genetic ablation of the low-density lipoprotein receptor.', *Neurochemical research*, 34(2), pp. 311–5.

Takahashi, Y. *et al.* (2015) 'Three-dimensional (3D) spheroid cultures improve the metabolic gene expression profiles of HepaRG cells', *Bioscience Reports*, pp. 1–7.

Takáts, Z. *et al.* (2004) 'Mass spectrometry sampling under ambient conditions with desorption electrospray ionization.', *Science (New York, N.Y.)*, 306(5695), pp. 471–3.

Tardito, S. *et al.* (2015) 'Glutamine synthetase activity fuels nucleotide biosynthesis and supports growth of glutamine-restricted glioblastoma.', *Nature cell biology*, 17(12), pp. 1556–68.

Tautenhahn, R., Böttcher, C. and Neumann, S. (2008) 'Highly sensitive feature detection for high resolution LC/MS.', *BMC bioinformatics*, 9, p. 504.

Taylor, K. R. *et al.* (2014) 'Recurrent activating ACVR1 mutations in diffuse intrinsic pontine glioma.', *Nature genetics*, 46(5), pp. 457–61.

Terwel, D. *et al.* (2011) 'Critical role of astroglial apolipoprotein E and liver X receptor-α expression for microglial Aβ phagocytosis.', *The Journal of neuroscience : the official journal of the Society for Neuroscience*, 31(19), pp. 7049–59.

The Cancer Genome Atlas Research Network (2008) 'Comprehensive genomic characterization defines human glioblastoma genes and core pathways.', *Nature*, 455(7216), pp. 1061–8.

Tirado-Hurtado, I., Fajardo, W. and Pinto, J. A. (2018) 'DNA damage inducible transcript 4 gene: The switch of the metabolism as potential target in cancer.', *Frontiers in oncology*, 8(April), p. 106.

Tönjes, M. *et al.* (2013) 'BCAT1 promotes cell proliferation through amino acid catabolism in gliomas carrying wild-type IDH1.', *Nature medicine*, 19(7), pp. 901–8.

Tso, C. L. *et al.* (2006) 'Distinct transcription profiles of primary and secondary glioblastoma subgroups', *Cancer Research*, 66(1), pp. 159–167.

Tugnoli, V. *et al.* (2001) 'Characterization of lipids from human brain tissues by multinuclear magnetic resonance spectroscopy.', *Biopolymers*, 62(6), pp. 297–306.

Tulenko, T. N. and Sumner, A. E. (2002) 'The physiology of lipoproteins', *Journal of Nuclear Cardiology*, 9(6), pp. 638–649.

Vance, J. E. and Hayashi, H. (2010) 'Formation and function of apolipoprotein E-containing lipoproteins in the nervous system.', *Biochimica et biophysica acta.*, 1801(8), pp. 806–18.

Del Vecchio, C. *et al.* (2012) 'EGFRvIII gene rearrangement is an early event in glioblastoma tumorigenesis and expression defines a hierarchy modulated by epigenetic mechanisms', *Oncogene*, 32(21), pp. 2670–2681.

Vedhachalam, C. *et al.* (2007) 'Mechanism of ATP-binding cassette transporter A1-mediated cellular lipid efflux to apolipoprotein A-I and formation of high density lipoprotein particles', *Journal of Biological Chemistry*, 282(34), pp. 25123–25130.

Venkateswaran, A. *et al.* (2000) 'Control of cellular cholesterol efflux by the nuclear oxysterol receptor LXR alpha.', *Proceedings of the National Academy of Sciences of the United States of America*, 97(22), pp. 12097–102.

Venneti, S. *et al.* (2015) 'Glutamine-based PET imaging facilitates enhanced metabolic evaluation of gliomas in vivo.', *Science translational medicine*, 7(274), p. 274ra17.

Verhaak, R. G. W. *et al.* (2010) 'Integrated genomic analysis identifies clinically relevant subtypes of glioblastoma characterized by abnormalities in PDGFRA, IDH1, EGFR, and NF1.', *Cancer cell*, 17(1), pp. 98–110.

Viale, A. *et al.* (2014) 'Oncogene ablation-resistant pancreatic cancer cells depend on mitochondrial function.', *Nature*, 514(7524), pp. 628–32.

Viennois, E. *et al.* (2012) 'Selective liver X receptor modulators (SLiMs): What use in human health?', *Molecular and Cellular Endocrinology*, 351(2), pp. 129–141.

Villa, G. R. *et al.* (2016) 'An LXR-cholesterol axis creates a metabolic co-dependency for brain cancers.', *Cancer cell*, 30(5), pp. 683–693.

Villarroya-Beltri, C., Guerra, S. and Sánchez-Madrid, F. (2017) 'ISGylation - a key to lock the cell gates for preventing the spread of threats.', *Journal of cell science*, 130(18), pp. 2961–2969.

Vitols, S. *et al.* (1984) 'Elevated low density lipoprotein receptor activity in leukemic cells with monocytic differentiation.', *Blood*, 63(5), pp. 1186–93.

Vitols, S. *et al.* (1990) 'Uptake of low density lipoproteins by human leukemic cells in vivo: relation to plasma lipoprotein levels and possible relevance for selective chemotherapy.', *Proceedings of the National Academy of Sciences of the United States of America*, 87(7), pp. 2598–602.

Vlashi, E. *et al.* (2011) 'Metabolic state of glioma stem cells and nontumorigenic cells.', *Proceedings of the National Academy of Sciences of the United States of America*, 108(38), pp. 16062–7.

Volmer, R. and Ron, D. (2015) 'Lipid-dependent regulation of the unfolded protein response', *Current Opinion in Cell Biology*, 33, pp. 67–73.

Waitkus, M. S., Diplas, B. H. and Yan, H. (2016) 'Isocitrate dehydrogenase mutations in gliomas', *Neuro-Oncology*, 18(1), pp. 16–26.

Wang, H. and Eckel, R. H. (2014) 'What are lipoproteins doing in the brain?', *Trends in endocrinology and metabolism: TEM*, 25(1), pp. 8–14.

Wang, Y. *et al.* (2015) 'Current state of the art of mass spectrometry-based metabolomics studies – a review focusing on wide coverage, high throughput and easy identification', *RSC Advances*. Royal Society of Chemistry, 5(96), pp. 78728–78737.

Wang, Y. *et al.* (2017) 'MicroRNA-1299 is a negative regulator of STAT3 in colon cancer', *Oncology Reports*, 37(6), pp. 3227–3234.

Wasan, K. M. *et al.* (2008) 'Impact of lipoproteins on the biological activity and disposition of hydrophobic drugs: Implications for drug discovery', *Nature Reviews Drug Discovery*, 7(1), pp. 84–99.

Wei, L. H. *et al.* (2008) 'Changes in tumor metabolism as readout for mammalian target of rapamycin kinase inhibition by rapamycin in glioblastoma', *Clinical Cancer Research*, 14(11), pp. 3416–3426.

Willy, P. J. *et al.* (1995) 'LXR, a nuclear receptor that defines a distinct retinoid response pathway', *Genes and Development*, 9(9), pp. 1033–1045.

Wise, D. R. *et al.* (2008) 'Myc regulates a transcriptional program that stimulates mitochondrial glutaminolysis and leads to glutamine addiction.', *Proceedings of the National Academy of Sciences of the United States of America*, 105(48), pp. 18782–18787.

Wolff, B. *et al.* (2012) 'Pediatric high grade glioma of the spinal cord: results of the HIT-GBM database.', *Journal of neuro-oncology*, 107(1), pp. 139–46.

Wolff, J. E. *et al.* (2008) 'Subpopulations of malignant gliomas in pediatric patients: analysis of the HIT-GBM database.', *Journal of neuro-oncology*, 87(2), pp. 155–64.

Wong, K.-K. *et al.* (2006) 'Genome-wide allelic imbalance analysis of pediatric gliomas by single nucleotide polymorphic allele array.', *Cancer research*, 66(23), pp. 11172–8.

Wong, W. W. *et al.* (2007) 'Determinants of sensitivity to lovastatin-induced apoptosis in multiple myeloma', *Mol Cancer Ther*, 6(6), pp. 1886–1897.

Wrobel, J. *et al.* (2008) 'Indazole-based liver X receptor (LXR) modulators with maintained atherosclerotic lesion reduction activity but diminished stimulation

of hepatic triglyceride synthesis.', *Journal of medicinal chemistry*, 51(22), pp. 7161–8.

Wu, G. *et al.* (2014) 'The genomic landscape of diffuse intrinsic pontine glioma and pediatric non-brainstem high-grade glioma.', *Nature genetics*, 46(5), pp. 444–50.

Wu, J.-Y. and Prentice, H. (2010) 'Role of taurine in the central nervous system.', *Journal of biomedical science*, 17 Suppl 1, p. S1.

Xia, J., Benner, M. J. and Hancock, R. E. W. (2014) 'NetworkAnalyst - Integrative approaches for protein-protein interaction network analysis and visual exploration', *Nucleic Acids Research*, 42(W1), pp. 167–174.

Xia, J. and Wishart, D. S. (2011) 'Web-based inference of biological patterns, functions and pathways from metabolomic data using MetaboAnalyst.', *Nature protocols*. Nature Publishing Group, 6(6), pp. 743–760.

Yachida, S. *et al.* (2010) 'Distant metastasis occurs late during the genetic evolution of pancreatic cancer.', *Nature*, 467, pp. 1114–1117.

Yanae, M. *et al.* (2011) 'Statin-induced apoptosis via the suppression of ERK1/2 and Akt activation by inhibition of the geranylgeranyl-pyrophosphate biosynthesis in glioblastoma.', *Journal of experimental & clinical cancer research : CR*, 30(1), p. 74.

Yanagita, T. *et al.* (2008) 'Taurine reduces the secretion of apolipoprotein B100 and lipids in HepG2 cells.', *Lipids in health and disease*, 7, p. 38.

Yang, C. *et al.* (2009) 'Glioblastoma cells require glutamate dehydrogenase to survive impairments of glucose metabolism or Akt signaling.', *Cancer research*, 69(20), pp. 7986–93.

Yang, K. *et al.* (2017) 'A Comprehensive Analysis of Metabolomics and Transcriptomics in Cervical Cancer.', *Scientific reports*, 7, p. 43353.

Yang, M. and Vousden, K. H. (2016) 'Serine and one-carbon metabolism in cancer', *Nature Reviews Cancer*, 16(10), pp. 650–662.

Ye, J. *et al.* (2014) 'Serine catabolism regulates mitochondrial redox control during hypoxia', *Cancer Discovery*, 4(12), pp. 1406–1417.

Ying, H. *et al.* (2012) 'Oncogenic kras maintains pancreatic tumors through regulation of anabolic glucose metabolism', *Cell*, 149(3), pp. 656–670.

Young, R. M. *et al.* (2013) 'Dysregulated mTORC1 renders cells critically dependent on desaturated lipids for survival under tumor-like stress', *Genes and Development*, 27(10), pp. 1115–1131.

Yue, S. *et al.* (2014) 'Cholesteryl ester accumulation induced by PTEN loss and PI3K/AKT activation underlies human prostate cancer aggressiveness', *Cell Metabolism*, 19(3), pp. 393–406.

Yun, J. *et al.* (2009) 'Glucose deprivation contributes to the development of KRAS pathway mutations in tumor cells.', *Science (New York, N.Y.)*, 325(5947), pp. 1555–9.

Yuneva, M. *et al.* (2007) 'Deficiency in glutamine but not glucose induces MYC-dependent apoptosis in human cells', *The Journal of Cell Biology*, 178(1), pp. 93–105.

Zaugg, K. *et al.* (2011) 'Carnitine palmitoyltransferase 1C promotes cell survival and tumor growth under conditions of metabolic stress.', *Genes & development*, 25(10), pp. 1041–51.

Zelcer, N. *et al.* (2007) 'Attenuation of neuroinflammation and Alzheimer's disease pathology by liver x receptors.', *Proceedings of the National Academy of Sciences of the United States of America*, 104(25), pp. 10601–6.

Zelcer, N. *et al.* (2009) 'Ubiquitination of the LDL Receptor', *Life Sciences*, 325(July), pp. 100–104.

Zenobi, R. (2013) 'Single-cell metabolomics: analytical and biological perspectives.', *Science (New York, N.Y.)*, 342(6163), p. 1243259.

Zhang, B. *et al.* (2013) 'LDLR-mediated peptide-22-conjugated nanoparticles for dual-targeting therapy of brain glioma.', *Biomaterials*, 34(36), pp. 9171–82.

Zhang, J. *et al.* (2014) 'Asparagine plays a critical role in regulating cellular adaptation to glutamine depletion', *Molecular Cell*, 56(2), pp. 205–218.

Zhang, Y. *et al.* (2001) 'Regulation of lipoprotein lipase by the oxysterol receptors, LXRalpha and LXRbeta.', *The Journal of biological chemistry*, 276(46), pp. 43018–24.

Zhao, Y., Wang, L. and Pan, J. (2015) 'The role of L-type amino acid transporter 1 in human tumors.', *Intractable & rare diseases research*, 4(4), pp. 165–9.

Zheng, S. *et al.* (2013) 'A survey of intragenic breakpoints in glioblastoma

identifies a distinct subset associated with poor survival', *Genes and Development*, 27(13), pp. 1462–1472.

Zhu, H. *et al.* (2016) 'miR-1299 suppresses cell proliferation of hepatocellular carcinoma (HCC) by targeting CDK6', *Biomedicine and Pharmacotherapy*, 83, pp. 792–797.